Structural Identification, Health Monitoring and Uncertainty Quantification under Incomplete Information with Minimal Requirements for Identifiability

Suparno Mukhopadhyay

Submitted in partial fulfillment of the

requirements for the degree

of Doctor of Philosophy

in the Graduate School of Arts and Sciences

COLUMBIA UNIVERSITY

2015

ABSTRACT

Structural Identification, Health Monitoring and Uncertainty Quantification under Incomplete Information with Minimal Requirements for Identifiability

Suparno Mukhopadhyay

Structural identification is the inverse problem of estimating the physical parameters, e.g. element masses and stiffnesses, of a model representing a structural system, using response measurements obtained from the actual structure subjected to operational or well-defined experimental excitations. It is one of the principal focal areas of modal testing and structural health monitoring, with the identified model finding a wide variety of applications, from obtaining reliable response predictions to timely detection of structural damage (location and severity) and consequent planning and validating of maintenance/retrofitting operations. However, incomplete instrumentation of the monitored system and ambient vibration testing generally result in spatially incomplete and arbitrarily normalized measured modal information, often making the inverse problem ill-conditioned and resulting in non-unique identification results. The problem of parameter identifiability addresses the question of whether or not a parameter set of interest can be identified from the available information. The identifiability of any parameter set of interest depends on the number and location of sensors on the monitored system.

In this dissertation we study the identifiability of the mass and stiffness parameters of shear-type systems, including 3-dimensional laterally-torsionally coupled rigid floor systems, with incomplete instrumentation, simultaneous to the development of algorithms to identify the complete mass and stiffness matrices of such systems. Both input-output and output-only situations are considered, and mode shape expansion and mass normalization approaches are developed to obtain the complete mass normalized mode shape matrix, starting from the incomplete modal parameters identified using any suitable experimental or operational modal analysis technique. Methods are discussed to decide actuator/sensor locations on the structure which will ensure identifiability of the mass and stiffness parameters. Several possible minimal and near-minimal instrumentation set-ups are also identified.

The minimal *a priori* information necessary in output-only situations is determined, and different scenario of available *a priori* information are considered. Additionally, tests for identifiability are discussed for both pre- and post-experiment applications. The different theoretical discussions are illustrated using numerical simulations and experimental data. It is shown that the proposed identification algorithms are able to obtain reliably accurate physical parameter estimates even under the constraints of minimal instrumentation, minimal *a priori* information, and unmeasured input. The different actuator/sensor placement rules and identifiability tests are useful for both experiment design purposes, to determine the necessary number and location of sensors, as well as in identifying possibilities of multiple solutions post-experiment. The parameter identification methods are applied for structural health monitoring using experimental data, and an approach is discussed for probabilistic characterization of structural damage location and severity. A perturbation based uncertainty propagation approach is also discussed for the identification of the distributions of mass and stiffness parameters, reflecting the variability in the test structure, using very limited measured and *a priori* information.

Table of Contents

List of Figures

List of Tables

Acknowledgments

All along the way in my journey as a Doctoral student, I have been very fortunate to receive help and support, in various ways, from various persons. Attempting to thank all of them will prove an unsurmountable task. Writing this page of "Acknowledgements" provides me with the opportunity to express my sincere gratitude to at least some of them.

Foremost, I would like to thank my advisor Prof. Raimondo Betti for giving me the chance to pursue my Doctoral studies in Columbia, for introducing me to the exciting area of structural identification and health monitoring, and for always providing the perfect balance of independence and guidance in my research. While his unrestrained encouragement has given me the confidence to develop and pursue my ideas, his critical questioning has always refined and enriched them. Moreover, by involving me in different other activities, from mentoring Master's students' research to writing project proposals, he has also helped in my overall development as a researcher, inculcating in me qualities which I will treasure throughout my life.

I have been extremely fortunate to have arrived in Columbia in Fall 2010, when Prof. Hilmi Lus was also visiting Columbia. My collaboration with him has since then strengthened manifold, and has developed into a friendship which I will cherish forever. His comments, and especially his questions, have played a significant role in the development and refinement of this work.

I am also grateful to the other members of my dissertation defense committee, Prof. George Deodatis, Prof. Richard Longman, Prof. Andrew Smyth and Prof. Haim Waisman, for their time in reviewing my work, and for their insightful comments and observations, which, I am sure, will pave the way for my future research. Thanks are also due to Prof. Deodatis for providing me with access to his workstation, and Prof. Smyth for his collaboration during the shake table experiments discussed in this thesis.

Discussions which I have had with some of my friends have found their way to parts of this thesis. I would first like to thank Luciana Balsamo, from whom I have greatly benefited through the regular

discussions on structural damage detection. Her direct help with the idea of using ECDFs in Chapter 5, and with an observation on the work in Appendix D, are duly acknowledged at the respective places. I also thank her, Manolis Chatzis, and Adrian Brugger, for their collaboration during the shake table experiments. Thanks are due to Ah Lum Hong for the many helpful discussions I had with her during the work presented in Appendix D. A helpful suggestion from Luc Berger on the solution discussed in Chapter 4 is also acknowledged in Chapter 4.

I would like to thank the Los Alamos National Laboratory, Engineering Institute, for making their experimental data publicly available for research purposes.

Prof. Vinay K. Gupta, my Master's advisor, was the first to introduce me to research. He also helped me to come to Columbia. I take this opportunity to sincerely thank him for his many help.

I also sincerely acknowledge the financial supports provided by the Department of Civil Engineering and Engineering Mechanics (Columbia University), the Center for Advanced Infrastructure and Transportation (Rutgers), and the National Science Foundation.

Thanks are due to the Departmental administrative and IT staff, King-Tung Chan, Elaine MacDonald and Scott Kelly, for always helping me out of the many difficulties I managed to get myself into. Thanks also to the Laboratory staff, Liming Li and Travis Simmons, for their help during the shake table experiments.

Any attempt to thank my parents, Mallinath and Mahua, and my sister, Samrita, would fall short. They have always trusted and encouraged me in my endeavours. Their unconditional love, be it from across the world, has always been a source of support. The amusing chitchats with my sister have been the best refreshments on any tiring day.

Finally, the last few years would not have been so enjoyable had I not the company of the very good friends one can dream to have. Thanks to Luciana for being the closest friend and ally over the last four years; to Matt, non only for bearing my incessant chatter, but also for being a great friend on many occasions; to Luc, Badri, Malini, Mahesh, Tavishi, Uttam, Mahua, Souvik, Tulika, Ravindra, Arundhati, for the many memorable get-togethers; to Adrian, Andrea, Audrey, Manolis, Patrick, Raphael, Thaleia, for the most delightful happy hours; and to Athina, Brett, Christos, Francesco, Hao, Jenny, Jinwoo, Mady, Simos, Yang, for making the department always a fun place.

Dedicated to my family

Chapter 1

Introduction

The use of representative finite element (FE) models forms an integral part of present day engineering analysis and design. While these models aim to predict the behavior of actual systems, inherent modeling assumptions may often cast doubts on the reliability of such predictions. Furthermore, an initial system may change with time: *gradually* due to aging effects, *periodically* due to diurnal or seasonal loading and environmental variations, and even *suddenly* due to changes incurred during extreme events. It is thus often desirable, and even necessary, to update the initial model or to create a new one to represent the current condition of the system.

Current research trends in vibration based structural identification and health monitoring (SHM) show a sustained effort in developing algorithms to solve the inverse problem of identifying the parameters of an assumed analytical model of a true physical system, so that the identified model mimics the real structure in terms of some response quantities (e.g. the measured response from the actual structure subjected to operational or well-defined experimental excitations, or some derivatives of it, like extracted modal parameters). Such an experimentally identified model may be assumed to represent the structure in its current state, and can be used for response prediction, reliability analysis, etc., as well as in timely detection of structural damage/deterioration and the consequent planning and validation of retrofitting operations.

Model identification techniques usually involve the solution of some nonlinear optimization problem(s), which can efficiently identify (optimize) only a limited number of model parameters, hence requiring a considerable amount of dependence on the *a priori* analytical model. Moreover, such techniques usually work on the premise that "sufficient" information is available for a successful

identification. In situations where the representative model may not be very reliable, leading to an increase in the number of unknown parameters, and/or in situations of incomplete information often encountered in practice, the inverse problem may become ill-conditioned, and the parameter set of interest globally/locally unidentifiable, resulting in multiple physically admissible solutions to the inverse identification problem [1–6]. It is thus important to quantify what constitutes "sufficient" information in a given situation, and what should be measured and what should be (assumed) known *a priori*, so that an identification algorithm may converge to a unique identified system.

In practice it is usually not feasible to instrument the monitored system at all the degrees of freedom (DOFs) defining the model. This situation of incomplete instrumentation results in "spatial incompleteness" [7] in modal information, with the mode shape estimates extracted from any experimental data being initially available only at the measured DOFs. In such cases, either an expansion of these incomplete mode shapes from the observed to the unobserved DOFs [8, 9], or a reduction of the model to the instrumented DOFs [9–11] may emerge as a prerequisite to the physical parameter identification step. Limitations in controllability and/or observability of the monitored system may result in the identification of a reduced number of modes from the experimental data compared to the analytical model, leading to a second type of incompleteness, "modal incompleteness" [7], in modal information. Moreover, in many cases of vibration based health monitoring, it is not feasible to perform an experimental modal analysis consisting of planned forced vibration experiments. Instead, one has to perform the identification using ambient vibration response data, under normal operational conditions of the structure, i.e. operational modal analysis. In these situations, often referred to as output-only situations, the information of the applied input force data is not available, and determining the correct mass scaling (normalization) of the identified mode shapes becomes an issue. While extensive treatment of these issues is by no means trivial, their complete dismissal may lead to ill-conditioning, solution non-uniqueness, and consequent invalidation of the results.

Studies on identifiability generally deal with the situation of spatial incompleteness, investigating whether a given set of input-output data allows a locally/globally unique identification of a parameter set of interest. There have been some attempts to develop generalized tests for identifiability applicable to any model class [2, 6, 12]; such tests do not exploit the specific properties of any particular model class, and hence, while having the advantage of applicability over a wide range of model types, they usually tend to be complex and computationally expensive, especially for larger dimensional sys-

tems. Alternatively, the question of identifiability may be addressed for any particular model class, enabling the explicit use of the properties of that class. Such an approach will have the advantage of straightforward applicability to any system, irrespective of its size, belonging to the model class considered.

The class of shear type systems finds a wide range of applications, modeling structures like "tall buildings, turbine blades and airplane wings" [13], and has thus gained considerable attention in structural identification/health monitoring (see, e.g., [13–16] for efforts solely concerning models belonging to this class, in addition to many other studies considering example applications on such systems). Naturally the identifiability of such systems under various loading scenarios has garnered attention as well [1, 3, 17–20]. It is important to note that these different efforts, although concerning the same model class of shear-type systems, have several situation vis-à-vis necessary *a priori* information specific distinctions, besides formulating the identifiability problem differently: (i) while Franco et al. [3] studies the identifiability problem when the force is applied through a single actuator at some point on the superstructure, Udwadia and his co-workers [1, 17] and Katafygiotis and Beck [18] deal with base excitation inputs; (ii) while Franco et al. [3] does not require any *a priori* knowledge of the system's physical parameters, Udwadia and his co-workers [1, 17], Katafygiotis and Beck [18] and Gladwell [19, 20] require various amounts of knowledge of the system's mass; (iii) while Franco et al. [3] identifies multiple possible instrumentation setups which guarantee global identifiability, in the studies by Udwadia and his co-workers [1, 17] a single such setup is identified.

While the above studies identify certain instrumentation set-ups which guarantee unique solutions, there is still a need to investigate the issue of uniqueness for more general experimental set-ups, catering e.g. to situations with multiple actuators, in order to have alternative experiment designs. Furthermore, while the above studies provide answers to the question of minimal instrumentation, there still exists a need to develop and validate robust methods for unique mode shape expansion and consequent parametric identification using input-output data from prescribed minimal instrumentation set-ups. As Franco et al. [3] clearly states: "...satisfying global identifiability does not mean that the unique solution is found. Indeed, to find this solution it is usually necessary to solve a nonlinear optimization problem that can be quite complex...", and illustrates the complexity one will encounter using a 3-DOF system at the end of their paper. Finally, most of the literature on identifiability address the situation of known inputs. However, as stated before, in many situations of structural/mechanical

testing, it may be only feasible, or at least preferable, to work with output-only data, necessitating an investigation of the identifiability problem for such situations as well.

Resolution of some of the aforementioned issues is the primary objective of this thesis. In particular we investigate the problem of structural identification and identifiability of shear-type systems in various situations: Chapter 2 investigates the global identifiability of shear-type systems for the situation of known forces applied through actuators, considering more general setups than Franco et al. [3], including multiple-input multi-output situations. Chapter 3 addresses the situation where the system is subjected to measured/unmeasured base excitation; the developments in this chapter can be directly applied to any general output-only situation as well. In Chapter 4, the output-only situation is revisited, with an approach alternative to that presented in Chapter 3; moreover, while Chapter 3 considers only the question of global identifiability, Chapter 4 also addresses the question of local identifiability, i.e. when there may be multiple solutions to the inverse problem, but such solutions will be locally isolated. While Chapter 4 is primarily developed for output-only situations, the approach can also be applied in input-output situations, e.g. when the structure is excited by known applied forces from actuators. Finally, while Chapter 3 also explicitly considers 3-dimensional (3-D), possibly laterally-torsionally coupled, rigid floor building systems, Chapters 2 and 4 only consider 1-dimensional systems; however the developments in these chapters may be easily extended/applied to 3-dimensional systems.

In all the chapters, the identifiability question is investigated simultaneous to the development of algorithms to identify the complete $\mathbf{M}$ and $\mathbf{K}$ matrices of the system, given the realistic constraints of spatial incompleteness in modal information due to incomplete instrumentation. The measured responses are however assumed to be sufficiently rich, as in other studies on identifiability, so as to allow the identification of all the structural modes, viz. the natural frequencies, damping ratios and non-mass normalized mode shape components at the sensor locations, using any suitable experimental/operational modal analysis technique. While the assumption of richness of data enabling the identification of a complete set of modal parameters at the sensor locations may not always be practically realizable, leading to modal incompleteness, one can take recourse, in such a situation with not-so-rich data, to the suggestion by Gladwell [19]: "in principle one may augment that experimentally determined spectral data with the calculated higher spectral data corresponding to the FEM model". This principle of mode-mixing, i.e. complementing the experimentally identified modes with

the unidentified modes calculated from an analytical FE model of the system, has also been adopted in several other studies [7]. As will be evident later, the developments in Chapter 4 may be used to address situations when not all the modes are identified at every instrumented DOF. However, as shown with an example by Chatzis et al. [6], even with complete instrumentation of the system, if a mode is not identified at any DOF, then the system may be unidentifiable; hence, even if not all the modes are identified at every instrumented DOF, every mode must be identified (or assumed using mode-mixing) at at least one of the instrumented DOFs.

The proposed identification algorithms obtain the mass and stiffness matrices of the system using the well-known modal orthogonality relations. The pre-requisite for using these orthogonality relations is the availability of the *complete mass normalized* mode shape matrix $\mathbf{V}$, which is unavailable owing to incomplete instrumentation of the system. Moreover, in output-only/base excitation situations, even complete instrumentation will not enable a unique solution to the inverse problem; *a priori* knowledge of the value of some of the system's parameters will be necessary. Insufficient measured and/or available *a priori* information will lead to unidentifiability of the complete $\mathbf{V}$, and hence unidentifiability of the mass and stiffness parameters. Thus the identifiability question: "Is there sufficient information, assumed and/or measured, available for a unique estimation of $\mathbf{M}$ and $\mathbf{K}$?", may be investigated as the equivalent question: "Is there sufficient information, assumed and/or measured, available for a unique estimation of $\mathbf{V}$?". In the proposed identification approaches, mode shape normalization and expansion procedures are developed for various situations. These mode shape normalization and expansion approaches incorporate the structural topology information of the physical system in terms of its modal parameters, except the normalization approach discussed in Chapter 2 for known input forces; the input-output balance normalization in Chapter 2 does not utilize any structural topology information, and is hence not limited to shear-type systems, but is applicable to any linear classically damped system. Since not all instrumentation set-ups and available *a priori* information about the system's physical parameters may give a unique normalization and/or expansion of the mode shapes, the following issues are investigated: (a) what the minimum necessary *a priori* information is, (b) what the minimum number of instrumented DOFs, given certain available *a priori* information, should be, and (c) how to determine which should be the instrumented DOFs, for a unique estimation of the complete mass normalized mode shape matrix? Thus, in the process of developing the identification methodologies catered to various situations, the present study also pro-

vides a technique to determine a wide set of instrumentation set-ups guaranteeing unique solutions to the inverse problem. As will be evident, the proposed identification and instrumentation set-up determination approaches in Chapters 2 and 3 mainly involve solutions of linear systems of equations, and hence have the advantage of straightforward implementation. Although the methodology presented in Chapter 4 involves solving a nonlinear system of equations, even then the implementation is reasonably straightforward, since the involved equations are at most quadratic in the unknowns, and the Jacobian can be analytically written.

The different tests for identifiability and/or rules for instrumentation assuring identifiability are illustrated in the different chapters for experiment designs in various situations. The performance of the identification approaches are discussed at the end of each chapter via numerical simulations as well as using experimental data, considering different situations of possible structural instrumentation and available *a priori* information.

The applicability of the different identification approaches to structural health monitoring and uncertainty quantification problems are examined, using some preliminary results, in Chapters 5 and 6. The identification approaches of Chapters 2 and 3 are applied for structural health monitoring purposes using experimental data in Chapter 5, and a method is discussed to characterize the damage location and severity in a probabilistic sense. In Chapter 6, perturbation based forward uncertainty propagation is used to extend the identification method of Chapter 4 into a probabilistic framework, so as to provide probabilistic descriptions of the estimated mass and stiffness parameters, accounting also for test structure variability.

The thesis ends with four appendices. Appendix A provides a method to determine the centers of mass and lumped mass parameters (floor masses and mass moments of inertia) of all instrumented floors in rigid floor building using an actuator-driven forced vibration test with the input-output balance developed in Chapter 2; it also provides an application of the structural identification method, developed in Chapter 2 for 1-D shear–type systems, to 3-D rigid floor laterally-torsionally coupled shear–buildings, using the minimal permissible instrumentation. Appendix B contains the proofs of some statements made in Chapters 3 and 4. Appendix C provides two pseudo-codes for analytically constructing the Jacobian matrix and another similar matrix necessary in Chapters 4 and 6. Finally, Appendix D investigates, for general linear classically damped dynamic systems, how random errors between identified and "true" mode shapes propagate to the Modal Assurance Criterion (MAC) [21]

and the Coordinate Modal Assurance Criterion (COMAC) [22] values, as well as to the estimated flexibility matrix. Comparison of the statistics of these propagated errors identifies the inconsistency between the magnitude of errors in MAC/COMAC vs. the identified flexibility matrix. Two new indices, the Flexibility Proportional Modal Assurance Criterion (FPMAC) and the Flexibility Proportional Coordinate Modal Assurance Criterion (FPCOMAC), are also proposed, which try to mimic the expected error in the estimated flexibility matrix. The use of these indices for structural damage detection and localization has been considered in Chapter 5 of this thesis, and also within a statistical pattern recognition framework by Balsamo et al. [23] where the FPCOMACs are used as damage sensitive features.

Chapter 2

Structural Identification Using Input-Output Data: Minimal Instrumentation and Global Identifiability Issues[1]

This chapter attempts to develop a simple methodology, based on solutions of linear systems of equations, for the identification of the mass and stiffness parameters of damped shear-type structural systems using input-output measurements, solving the inverse problem under the realistic constraints of incomplete instrumentation. The proposed algorithm obtains the mass, $\mathbf{M}$, and stiffness, $\mathbf{K}$, matrices of the system using the well-known modal orthogonality relations. The pre-requisite for using these orthogonality relations is the availability of the complete mass normalized mode shape matrix $\mathbf{V}$: once one or more rows of $\mathbf{V}$ are identified from the measurements, the remaining, hitherto unknown, rows are obtained by expanding the incomplete mass normalized mode shapes from the observed to the unobserved DOFs. Since not all instrumentation set-ups may give a unique expansion of the mode shapes, it is necessary at this point to also address the following questions: (1) what is

[1]This chapter is almost entirely from an article co-authored with Profs. Raimondo Betti and Hilmi Lus in Mechanical Systems and Signal Processing [4]. The experimental application was presented in the 6th World Conference on Structural Control and Monitoring, Barcelona, 2014 [24].

the minimum number of instrumented DOFs, and (2) which should be the instrumented DOFs, for a unique estimation of the unmeasured rows of $\mathbf{V}$? To this end, a set of statements which address this uniqueness issue are discussed to determine whether the *a priori* knowledge of a certain set of rows of $\mathbf{V}$ will guarantee that the other rows can be uniquely determined. As will be self-evident, the approach employed to address the problem of global identifiability for shear-type systems can itself be interpreted as a procedure to uniquely obtain the unmeasured rows of $\mathbf{V}$ from the measured rows. Since the mass normalized mode shape components at the sensor locations are required in the algorithm, an input-output balance approach to identify these components of $\mathbf{V}$ is also developed. Several possible minimal and near-minimal instrumentation set-ups which guarantee a unique estimation of the unmeasured mode shape components from the measured components are identified for various experimental designs. It is worthwhile to note that, while the proposed input-output balance method yields the mass normalized mode shape components at any instrumented (sensor and/or actuator) location, not all such instrumentation set-ups will guarantee a unique expansion of $\mathbf{V}$. Furthermore, while the proposed input-output balance approach can be applied to other class of systems as well, the mode shape expansion itself is tailored exclusively for the class of shear-type systems, although it may be possible to expand the idea to include other systems. The natural frequencies and modal damping ratios of the system, necessary in the approach proposed herein, may be obtained using various modal analysis techniques; the Eigensystem Realization Algorithm Observer/ Kalman filter Identification (ERA-OKID) approach [25–27] is adopted here for this purpose. The performance of the proposed solution is discussed via numerical simulations of forced vibration testing of a 7-DOF shear-type structure for different actuator-sensor placement scenarios. The robustness of the proposed method to the inevitable presence of measurement noise is also evaluated in the numerical simulations. The method is then applied to experimental data from a 3 storied 1-D frame model, tested in the Los Alamos National Laboratory. Although this frame is 3 storied, the model is 4-DOF, since the frame is not fixed at the base (free-free system instead of shear-type), and thus includes a rigid body translation mode.

2.1 Problem Statement

Suppose we have an N-DOF classically damped shear-type system; with $\mathcal{D}$ denoting the set, with N elements, of all DOFs; $\mathcal{S}$ denoting the set, with N_s elements, of DOFs that are instrumented by accelerometers with which the response of the system is measured; and $\mathcal{A}$ denoting the set, with N_a elements, of DOFs at which there are actuators that excite the system with known inputs. The experimental setup considered here is such that $\mathcal{S} \subseteq \mathcal{D}$ ($N_s \leq N$) and $\mathcal{A} \subseteq \mathcal{D}$ ($N_a \leq N$). Our objectives are (i) to develop a methodology for the identification of the mass, $\mathbf{M}$, and the stiffness, $\mathbf{K}$, matrices of the system, and consequently the element masses and stiffnesses, using measured input-output data, and (ii) to identify different minimal and near-minimal instrumentation set-ups that guarantee a unique identification. For shear-type systems, $\mathbf{M}$ and $\mathbf{K}$ matrices have the following forms:

$$\mathbf{M} = \text{diag}\big(m_1, m_2, \cdots, m_N\big); \;\; \mathbf{K} = \begin{bmatrix} k_1 + k_2 & -k_2 & & & 0 \\ -k_2 & k_2 + k_3 & -k_3 & & \\ & \ddots & \ddots & \ddots & \\ & & -k_{N-1} & k_{N-1} + k_N & -k_N \\ 0 & & & -k_N & k_N \end{bmatrix} \tag{2.1}$$

where m_i and k_i are the ith lumped/floor mass and the ith spring/story stiffness, respectively. These matrices are related with the systems eigenvalues and mode shapes through the generalized eigenvalue problem

$$\mathbf{K}\mathbf{V} = \mathbf{M}\mathbf{V}\mathbf{\Lambda} \tag{2.2}$$

where $\mathbf{\Lambda}$ and $\mathbf{V}$ are the eigenvalue and mode shape matrices, i.e.

$$\begin{aligned} \mathbf{\Lambda} &= \text{diag}\big(\lambda_1, \lambda_2, \cdots, \lambda_N\big) = \text{diag}\big(\omega_1^2, \omega_2^2, \cdots, \omega_N^2\big) \\ \mathbf{V} &= \begin{bmatrix} \mathbf{v}_1 & \mathbf{v}_2 & \cdots & \mathbf{v}_N \end{bmatrix} = \begin{bmatrix} \mathbf{r}_1 \\ \mathbf{r}_2 \\ \vdots \\ \mathbf{r}_N \end{bmatrix} = \begin{bmatrix} v_{1,1} & v_{1,2} & \cdots & v_{1,N} \\ v_{2,1} & v_{2,2} & \cdots & v_{2,N} \\ \vdots & \vdots & \ddots & \vdots \\ v_{N,1} & v_{N,2} & \cdots & v_{N,N} \end{bmatrix} \end{aligned} \tag{2.3}$$

Here, λ_j, ω_j and the column vector $\mathbf{v}_j$ denote the jth modal eigenvalue, frequency and mode shape, respectively, while $v_{i,j}$ denotes the component corresponding to the ith physical coordinate/DOF of

the jth mode shape, and the row vector $\mathbf{r}_i$ denotes the ith row of $\mathbf{V}$. Additionally, if $\mathbf{V}$ is mass normalized, then $\mathbf{M}$ and $\mathbf{K}$ satisfy the modal orthogonality relations and can consequently be evaluated as:

$$\mathbf{V}^T\mathbf{M}\mathbf{V} = \mathbf{I} \Rightarrow \mathbf{M} = \left(\mathbf{V}\mathbf{V}^T\right)^{-1}; \qquad \mathbf{V}^T\mathbf{K}\mathbf{V} = \mathbf{\Lambda} \Rightarrow \mathbf{K} = \left(\mathbf{V}\mathbf{\Lambda}^{-1}\mathbf{V}^T\right)^{-1} \tag{2.4}$$

From here onwards, unless otherwise stated, $\mathbf{V}$ will denote the mass normalized mode shape matrix.

The approach that is proposed in this paper is a two-step procedure, with the complete mass normalized modal information being obtained in the first step, and the modal orthogonality relations of Eq. (2.4) being used to obtain the system's $\mathbf{M}$ and $\mathbf{K}$ matrices in the second.

Although Eq. (2.4) requires the complete mass normalized $\mathbf{V}$, the measured mode shapes are available, in general, only at the instrumented DOFs in $\mathcal{I} = \mathcal{A} \cup \mathcal{S}$ (the clause "in general" is included because, as will be shown later, if the input time histories are proportional, then only under a restricted condition it is possible to estimate the mode shapes for all of $\mathcal{I}$). Thus, the expansion of these incomplete mode shapes from the observed to the unobserved DOFs emerges as a prerequisite to the $\mathbf{M}$-$\mathbf{K}$ identification exercise. (The set of observed DOFs also include the DOFs with actuators. This is because, as will be evident in the section on input-output balance, in general, it is equivalent to have a known input or measured output at a DOF; this concept of input-output equivalence is also discussed in [28].) Since not all instrumentation set-ups may yield a unique expansion, it is also necessary to identify what the minimal instrumentation requirement is and which DOFs should be instrumented for unique estimations. This uniqueness issue is addressed in the next section, and in the process an attempt to develop a unique mode shape expansion procedure catering to different minimal and near-minimal instrumentations of the system is also discussed.

2.2 A Procedure of Mode Shape Expansion and Associated Uniqueness Issue

Assume that the measured responses, obtained from the forced vibration test, are rich enough so that all the structural modes are identified at the instrumented DOFs $\mathcal{I}$; i.e., assume that all the N eigenvalues of the system and all the N elements in each of the rows, corresponding to $\mathcal{I}$, of $\mathbf{V}$ are known. Starting with this *a priori* knowledge of one or more rows of $\mathbf{V}$, the intention is to estimate the coefficients in the rows corresponding to the non-instrumented DOFs $\mathcal{D} \setminus \mathcal{I}$. To this

end, a set of statements are proved in this section, which (i) attempt to identify certain rows of $\mathbf{V}$ whose *a priori* knowledge guarantees a unique estimation of the hitherto unknown rows, and (ii) provide a methodology to obtain the unique estimates of the unknown rows as solutions to sets of linear simultaneous equations. These statements are provided below, with the conclusions that follow at the end of this section.

2.2.1 Some statements on the uniqueness of mode shape expansion

Statement 1: *For any $i \in \{2, 3, \cdots, N-2\}$, knowing the ith and $(i+1)$th rows of $\mathbf{V}$, i.e. $\mathbf{r}_i$ and $\mathbf{r}_{i+1}$, it is possible to uniquely determine:*

1. *the $(i-1)$th row of $\mathbf{V}$, i.e. $\mathbf{r}_{i-1}$, and*
2. *the $(i+2)$th row of $\mathbf{V}$, i.e. $\mathbf{r}_{i+2}$.*

Proof of Statement 1 Case 1: For any mode j, the eigenvalue problem of Eq. (2.2) can be written as:

$$[\mathbf{A} - \lambda_j \mathbf{I}]\mathbf{v}_j = \mathbf{0} \tag{2.5}$$

where

$$\mathbf{A} = \mathbf{M}^{-1}\mathbf{K} = \begin{bmatrix} a_{1,1} & a_{1,2} & & & & 0 \\ a_{2,1} & a_{2,2} & a_{2,3} & & & \\ & \ddots & \ddots & \ddots & & \\ & & a_{N-1,N-2} & a_{N-1,N-1} & a_{N-1,N} & \\ 0 & & & a_{N,N-1} & a_{N,N} & \end{bmatrix} \tag{2.6}$$

The ith row of Eq. (2.5) yields:

$$v_{i-1,j} + \alpha_1 v_{i,j} + \alpha_2 v_{i+1,j} - \alpha_3 \lambda_j v_{i,j} = 0 \quad \forall\, j \in \{1, 2, \cdots, N\} \tag{2.7}$$

where $\alpha_1 = a_{i,i}/a_{i,i1}$, $\alpha_2 = a_{i,i+1}/a_{i,i1}$ and $\alpha_3 = 1/a_{i,i1}$. Since knowing the ith and $(i+1)$th rows of $\mathbf{V}$ means knowing $v_{i,j}$ and $v_{i+1,j}$ $\forall\, j \in \{1, 2, \cdots, N\}$, Eq. (2.7) represents N linear equations in $N+3$ unknowns, the unknowns being the N elements of the $(i-1)$th row of $\mathbf{V}$ (i.e. $v_{i-1,j}$ $\forall$ $j \in \{1, 2, \cdots, N\}$) and the three unknowns α_1, α_2 and α_3. In a shear-type system we must also have:

$$a_{i,i-1} + a_{i,i} + a_{i,i+1} = 0 \quad \Rightarrow \alpha_1 + \alpha_2 = -1 \tag{2.8}$$

which is another linear equation in α_1 and α_2. Finally, since we are trying to obtain the mass normalized mode shapes, and since $\mathbf{M}$, and hence $\mathbf{M}^1$, are diagonal, Eq. (2.4) requires $[\mathbf{V}\mathbf{V}^T]$ to also be a diagonal matrix:

$$\mathbf{r}_k\mathbf{r}_l^T = \sum_{j=1}^{N} v_{k,j}v_{l,j} = 0 \quad \forall\, k \in \{1, 2, \cdots, N-1\},\ l \in \{k+1, k+2, \cdots, N\} \tag{2.9}$$

Substituting $k = i-1$ and $l = i$ and $i+1$ in Eq. (2.9) we get two more linear equations for the components of $\mathbf{r}_{i-1}$, i.e. the $(i-1)$th row of $\mathbf{V}$.

Combining Eqs. (2.7) and (2.8) with the two equations obtained from Eq. (2.9) leads to $N+3$ linear equations in the $N+3$ unknowns. These equations may be expressed in a block matrix form as:

$$\mathbf{P}_{(N+3)\times(N+3)} \begin{Bmatrix} \mathbf{r}_{i-1}^T \\ \alpha_1 \\ \alpha_2 \\ \alpha_3 \end{Bmatrix} = \begin{Bmatrix} \mathbf{0}_{N\times 1} \\ -1 \\ 0 \\ 0 \end{Bmatrix} \tag{2.10}$$

where the coefficient matrix $\mathbf{P}$ is given by:

$$\mathbf{P} = \begin{bmatrix} \mathbf{I}_{N\times N} & \mathbf{r}_i^T & \mathbf{r}_{i+1}^T & -\mathbf{\Lambda}\mathbf{r}_i^T \\ \mathbf{0}_{1\times N} & 1 & 1 & 0 \\ \mathbf{r}_i & 0 & 0 & 0 \\ \mathbf{r}_{i+1} & 0 & 0 & 0 \end{bmatrix} \tag{2.11}$$

The $N+3$ linear equations in Eq. (2.10) can be solved for the $N+3$ unknowns and thereby used to obtain the $(i-1)$th row of $\mathbf{V}$; the solution, however, will be unique if and only if the coefficient matrix is full rank, i.e. the determinant of $\mathbf{P}$, $|\mathbf{P}|$, is non-zero. To show that $|\mathbf{P}| \neq 0$, let us write $|\mathbf{P}|$ by expanding about the $(N+1)$th row of $\mathbf{P}$ as:

$$|\mathbf{P}| = (-1)^{2N+2}(|\mathbf{P}_1| - |\mathbf{P}_2|) = |\mathbf{P}_1| - |\mathbf{P}_2| \tag{2.12}$$

where

$$\mathbf{P}_1 = \begin{bmatrix} \mathbf{I}_{N\times N} & \mathbf{r}_{i+1}^T & -\mathbf{\Lambda}\mathbf{r}_i^T \\ \mathbf{r}_i & 0 & 0 \\ \mathbf{r}_{i+1} & 0 & 0 \end{bmatrix}; \qquad \mathbf{P}_2 = \begin{bmatrix} \mathbf{I}_{N\times N} & \mathbf{r}_i^T & -\mathbf{\Lambda}\mathbf{r}_i^T \\ \mathbf{r}_i & 0 & 0 \\ \mathbf{r}_{i+1} & 0 & 0 \end{bmatrix} \tag{2.13}$$

The determinant of a 2×2 block matrix can be written as:

$$\begin{vmatrix} \mathbf{R}_1 & \mathbf{R}_2 \\ \mathbf{R}_3 & \mathbf{R}_4 \end{vmatrix} = |\mathbf{R}_1| \times |\mathbf{R}_4 - \mathbf{R}_3 \mathbf{R}_1^{-1} \mathbf{R}_2| \tag{2.14}$$

Applying this expansion to $\mathbf{P}_1$ and $\mathbf{P}_2$, and noting that the ith and the $(i+1)$th rows of $\mathbf{V}$ are orthogonal by Eq. (2.9), one gets:

$$|\mathbf{P}_1| = \left(\sum_{j=1}^{N} v_{i+1,j}^2 \right) \left(\sum_{j=1}^{N} \lambda_j v_{i,j}^2 \right); \qquad |\mathbf{P}_2| = - \left(\sum_{j=1}^{N} v_{i,j}^2 \right) \left(\sum_{j=1}^{N} \lambda_j v_{i,j} v_{i+1,j} \right) \tag{2.15}$$

and thus,

$$|\mathbf{P}| = |\mathbf{P}_1| - |\mathbf{P}_2| = \left(\sum_{j=1}^{N} v_{i+1,j}^2 \right) \left(\sum_{j=1}^{N} \lambda_j v_{i,j}^2 \right) + \left(\sum_{j=1}^{N} v_{i,j}^2 \right) \left(\sum_{j=1}^{N} \lambda_j v_{i,j} v_{i+1,j} \right) \tag{2.16}$$

The first product of sums in the summation above is always positive but, the sign of the second product of sums is not readily identified owing to the second parenthesis of this term, although the term in the first parenthesis is again always positive. Considering the mass orthogonality relation of Eq. (2.4) leads to

$$\sum_{j=1}^{N} v_{k,j}^2 = \frac{1}{m_k} \quad \forall\, k \in \{1, 2, \cdots, N\} \tag{2.17}$$

while from the stiffness orthogonality relation one gets $\mathbf{V}\mathbf{\Lambda}\mathbf{V}^T = \mathbf{V}\mathbf{V}^T\mathbf{K}\mathbf{V}\mathbf{V}^T = \mathbf{M}^1\mathbf{K}\mathbf{M}^1$, such that

$$\sum_{j=1}^{N} \lambda_j v_{l,j}^2 = \frac{k_l + k_{l+1}}{m_l^2}; \quad \sum_{j=1}^{N} \lambda_j v_{l,j} v_{l+1,j} = -\frac{k_{l+1}}{m_l m_{l+1}} \quad \forall\, l \in \{1, 2, \cdots, N-1\} \tag{2.18}$$

Using Eqs. (2.17) and (2.18) in the expression for $|\mathbf{P}|$ in Eq. (2.16) finally yields:

$$|\mathbf{P}| = \frac{k_i + k_{i+1}}{m_i^2 m_{i+1}} - \frac{k_{i+1}}{m_i^2 m_{i+1}} = \frac{k_i}{m_i^2 m_{i+1}} \tag{2.19}$$

Note that this expression implies that the determinant $|\mathbf{P}|$ is non-zero since no spring/story stiffness can ever be zero and no lumped/floor mass can ever be infinity. Thus, the coefficient matrix for our system of equations of Eq. (2.10) always has a non-zero determinant and hence a full rank. It is therefore possible to uniquely solve for the $(i-1)$th row of $\mathbf{V}$, given the full ith and the $(i+1)$th rows of $\mathbf{V}$, and all the N eigenvalues. □

Proof of Statement 1 Case 2: Considering now the $(i+1)$th row of Eq. (2.5), and following a similar procedure as for Case (i), it can be shown that we again have a system of $N+3$ linear equations in $N+3$ unknowns as:

$$\mathbf{P}_{(N+3)\times(N+3)} \begin{Bmatrix} \mathbf{r}_{i+2}^T \\ \alpha_1 \\ \alpha_2 \\ \alpha_3 \end{Bmatrix} = \begin{Bmatrix} \mathbf{0}_{N\times 1} \\ -1 \\ 0 \\ 0 \end{Bmatrix} \tag{2.20}$$

where the $N+3$ unknowns are the N elements of the $(i+2)$th row of $\mathbf{V}$, along with the three unknowns $\alpha_1 = a_{i+1,i}/a_{i+1,i+2}$, $\alpha_2 = a_{i+1,i+1}/a_{i+1,i+2}$ and $\alpha_3 = 1/a_{i+1,i+2}$. The coefficient matrix $\mathbf{P}$ is now given by:

$$\mathbf{P} = \begin{bmatrix} \mathbf{I}_{N\times N} & \mathbf{r}_i^T & \mathbf{r}_{i+1}^T & -\mathbf{\Lambda}\mathbf{r}_{i+1}^T \\ \mathbf{0}_{1\times N} & 1 & 1 & 0 \\ \mathbf{r}_i & 0 & 0 & 0 \\ \mathbf{r}_{i+1} & 0 & 0 & 0 \end{bmatrix} \tag{2.21}$$

with its determinant

$$|\mathbf{P}| = \left(\sum_{j=1}^{N} v_{i+1,j}^2\right)\left(\sum_{j=1}^{N} \lambda_j v_{i,j} v_{i+1,j}\right) + \left(\sum_{j=1}^{N} v_{i,j}^2\right)\left(\sum_{j=1}^{N} \lambda_j v_{i+1,j}^2\right) = \frac{k_{i+2}}{m_i m_{i+1}^2} \tag{2.22}$$

obtained as in Case (i). $|\mathbf{P}|$ can again never be zero due to similar reasoning as in Case (i). Thus, the coefficient matrix for the $N+3$ linear system of equations of Eq. (2.20) always has a full rank and the $(i+2)$th row of $\mathbf{V}$ can be uniquely solved given the full ith and the $(i+1)$th rows of $\mathbf{V}$ and all the N eigenvalues. □

Cases (i) and (ii) under Statement 1 lead to the conclusion that all rows of $\mathbf{V}$ may be uniquely determined knowing any two of its consecutive rows, with Eqs. (2.10) and (2.20) serving as the necessary equations for the mode shape expansion procedure in such a situation.

Statement 2: *Knowing the 1st row of* $\mathbf{V}$*, it is possible to uniquely determine the 2nd row, but not vice versa.*

Proof of Statement 2: Let us consider the 1st row of Eq. (2.5). We have

$$(a_{1,1} - \lambda_j)v_{1,j} + a_{1,2}v_{2,j} = 0 \quad \Rightarrow \mathbf{r}_2^T = -\frac{1}{a_{1,2}}[a_{1,1}\mathbf{I} - \mathbf{\Lambda}]\mathbf{r}_1^T \tag{2.23}$$

which, for a known 1st row and an unknown 2nd row of $\mathbf{V}$ leads to N uncoupled linear equations in the N unknowns in $\mathbf{r}_2$, provided that $a_{1,1}$ and $a_{1,2}$ are known. Note that $a_{1,1}$ may be uniquely estimated using Eqs. (2.17) and (2.18) as:

$$a_{1,1} = \frac{k_1 + k_2}{m_1} = \frac{k_1 + k_2}{m_1^2} \times m_1 = \frac{\sum_{j=1}^{N} \lambda_j v_{1,j}^2}{\sum_{j=1}^{N} v_{1,j}^2} \tag{2.24}$$

Furthermore, for a shear-type system, the first element $f_{1,1}$ of the flexibility matrix $\mathbf{F}$ is equal to $1/k_1$, which, on using the stiffness orthogonality relation of Eq. (2.4) can be expressed as:

$$\mathbf{F} = \mathbf{K}^{-1} = \mathbf{V}\mathbf{\Lambda}^{-1}\mathbf{V}^T \quad \Rightarrow f_{1,1} = \frac{1}{k_1} = \sum_{j=1}^{N} \frac{v_{1,j}^2}{\lambda_j} \tag{2.25}$$

Using Eqs. (2.17) and (2.25), the following expression is obtained:

$$a_{1,1} + a_{1,2} = \frac{k_1 + k_2}{m_1} - \frac{k_2}{m_1} = \frac{k_1}{m_1} = \frac{\sum_{j=1}^{N} v_{1,j}^2}{\sum_{j=1}^{N} (v_{1,j}^2/\lambda_j)} \tag{2.26}$$

which, in conjunction with Eq. (2.24), can be used to solve uniquely for the unknown $a_{1,2}$. Once the values of $a_{1,1}$ and $a_{1,2}$ are thus determined, they can be substituted in Eq. (2.23) to solve uniquely for the second row of $\mathbf{V}$. Hence, knowing the 1st row of $\mathbf{V}$, it is possible to uniquely determine its 2nd row; and once the 1st and 2nd rows of $\mathbf{V}$ are both known, it is possible to uniquely solve for all the other rows as claimed in Case (ii) of Statement 1. It should be noted that Eq. (2.23) can also be written as

$$\mathbf{r}_1^T = -a_{1,2}[a_{1,1}\mathbf{I} - \mathbf{\Lambda}]^{-1}\mathbf{r}_2^T \tag{2.27}$$

which, for a known 2nd row and an unknown 1st row, apparently gives again N uncoupled linear equations in the N unknowns in $\mathbf{r}_1$. However, substituting the expressions for $a_{1,1}$ and $a_{1,2}$ from Eqs. (2.24) and (2.26) into Eq. (2.27), these N uncoupled linear equations become N coupled non-linear equations in the unknowns:

$$\left(\frac{\sum_{k=1}^{N} \lambda_k v_{1,k}^2}{\sum_{k=1}^{N} v_{1,k}^2} - \lambda_j \right) v_{1,j} + \left(\frac{\sum_{k=1}^{N} v_{1,k}^2}{\sum_{k=1}^{N} (v_{1,k}^2/\lambda_k)} - \frac{\sum_{k=1}^{N} \lambda_k v_{1,k}^2}{\sum_{k=1}^{N} v_{1,k}^2} \right) v_{2,j} = 0 \quad \forall\, j \in \{1, 2, \cdots, N\} \tag{2.28}$$

This equation may in general have multiple possible solutions owing to the non-linearity: although it is difficult to identify whether or not there indeed are multiple physically admissible solutions, it is later shown with the example of a 3-DOF system that there can exist multiple physically admissible solutions to the 1st row of $\mathbf{V}$ for a given 2nd row. □

Statement 3: *Knowing the Nth row of $\mathbf{V}$, it is possible to uniquely determine the $(N-1)$th row, but not vice versa.*

Proof of Statement 3: Let us now look at the Nth row of Eq. (2.5):

$$a_{N,N-1}v_{N-1,j} + (a_{N,N} - \lambda_j)v_{N,j} = 0 \quad \Rightarrow \mathbf{r}_{N-1}^T = -\frac{1}{a_{N,N-1}}[a_{N,N}\mathbf{I} - \mathbf{\Lambda}]\mathbf{r}_N^T \tag{2.29}$$

which, for a known Nth row and an unknown $(N-1)$th row of $\mathbf{V}$, represents N uncoupled linear equations in the N unknowns in $\mathbf{r}_{N-1}$, provided that $a_{N,N-1}$ and $a_{N,N}$ are known. Pre-multiplying Eq. (2.29) by $\mathbf{r}_N$ and using the fact that the Nth and $(N-1)$th rows of $\mathbf{V}$ are orthogonal by Eq. (2.9), $a_{N,N}$ may be uniquely estimated as:

$$a_{N,N} = \frac{\mathbf{r}_N \mathbf{\Lambda} \mathbf{r}_N^T}{\mathbf{r}_N \mathbf{r}_N^T} = \frac{\sum_{j=1}^N \lambda_j v_{N,j}^2}{\sum_{j=1}^N v_{N,j}^2} \tag{2.30}$$

Moreover, since the system is shear-type, we have:

$$a_{N,N-1} + a_{N,N} = 0 \tag{2.31}$$

with which $a_{N,N-1}$ may be uniquely estimated once $a_{N,N}$ is obtained from Eq. (2.30). Finally, substituting these estimates of $a_{N,N}$ and $a_{N,N-1}$ in Eq. (2.29), we can uniquely estimate the $(N-1)$th row of $\mathbf{V}$. Hence, knowing the Nth row of $\mathbf{V}$, its $(N-1)$th row may be uniquely determined, and once both the Nth and $(N-1)$th rows are known, it is possible to uniquely solve for all the other rows of $\mathbf{V}$ as claimed in Case (i) of Statement 1.

For the case when the $(N-1)$th row is known and the Nth row is unknown, Eq. (2.29), on substitution of Eqs. (2.30) and (2.31), leads to N coupled non-linear equations for the unknowns in $\mathbf{r}_N$:

$$\left(\frac{\sum_{k=1}^N \lambda_k v_{N,k}^2}{\sum_{k=1}^N v_{N,k}^2} - \lambda_j\right) v_{N,j} - \left(\frac{\sum_{k=1}^N \lambda_k v_{N,k}^2}{\sum_{k=1}^N v_{N,k}^2}\right) v_{N-1,j} = 0 \quad \forall\, j \in \{1, 2, \cdots, N\} \tag{2.32}$$

Once again, although difficult to identify, this equation may in general have multiple possible solutions owing to the non-linearity. It is next shown with the example of a 3-DOF system that there can indeed be multiple physically admissible solutions to the Nth row of $\mathbf{V}$ for a given $(N-1)$th row for $N = 3$. □

2.2.1.1 Example of non-uniqueness: 3-DOF system with known 2nd row of V – A geometric interpretation

The problem of the existence of multiple solutions of Eqs. (2.28) or (2.32) becomes more tractable for a 3-DOF system, especially if the lengthy algebraic expressions are avoided via a slightly different geometric interpretation based formulation. This example also serves as a validation of the second parts of both Statements 2 and 3 made regarding all shear-type systems, since a known 2nd row in a 3-DOF system can also be considered as a known $(N-1)$th row in an N-DOF system.

Let us denote the known elements of $\mathbf{V}$ as: $v_{2,1} = \sigma_1$, $v_{2,2} = \sigma_2$, $v_{2,3} = \sigma_3$, and the unknown 3rd and 1st row elements as: $v_{3,1} = x_1$, $v_{3,2} = x_2$, $v_{3,3} = x_3$, and $v_{1,1} = y_1$, $v_{1,2} = y_2$, $v_{1,3} = y_3$, respectively. Knowing the 2nd row, and using the orthogonality of the 2nd and 3rd rows by Eq. (2.9), one has:

$$\sigma_1 x_1 + \sigma_2 x_2 + \sigma_3 x_3 = 0 \tag{2.33}$$

For any general N-DOF shear-type system, the nature of the flexibility matrix $\mathbf{F}$ is such that, any (l,m)th element $f_{l,m}$ in $\mathbf{F}$ can be expressed as:

$$f_{l,m} = f_{m,l} = \sum_{i=1}^{l} \frac{1}{k_i} \quad \forall\, l \in \{1, 2, \cdots, N\},\ m \in \{l, l+1, \cdots, N\} \tag{2.34}$$

Using this property of $\mathbf{F}$ for the 3-DOF system at hand, along with the stiffness orthogonality of Eq. (2.4) expressed in terms of $\mathbf{F}$ as $\mathbf{F} = \mathbf{K}^{-1} = \mathbf{V}\mathbf{\Lambda}^{-1}\mathbf{V}^T$ yields:

$$\begin{aligned} &\sum_{j=1}^{3} \frac{\sigma_j^2}{\lambda_j} = f_{2,2} = \frac{1}{k_2} + \frac{1}{k_3} = f_{2,3} = \sum_{j=1}^{3} \frac{\sigma_j x_j}{\lambda_j} \\ \Rightarrow &\frac{\sigma_1}{\lambda_1} x_1 + \frac{\sigma_2}{\lambda_2} x_2 + \frac{\sigma_3}{\lambda_3} x_3 = \frac{\sigma_1^2}{\lambda_1} + \frac{\sigma_2^2}{\lambda_2} + \frac{\sigma_3^2}{\lambda_3} \end{aligned} \tag{2.35}$$

Finally, using the last row of Eq. (2.5), with $N = 3$ leads first to,

$$a_{3,2}\sigma_j + (a_{3,3} - \lambda_j) x_j = 0 \quad \Rightarrow a_{3,2}\frac{\sigma_j}{x_j} + a_{3,3} - \lambda_j = 0 \quad \forall\, j \in \{1, 2, 3\}$$

and after some algebra to,

$$\sigma_3(\lambda_1 - \lambda_2) x_1 x_2 + \sigma_1(\lambda_2 - \lambda_3) x_2 x_3 + \sigma_2(\lambda_3 - \lambda_1) x_1 x_3 = 0 \tag{2.36}$$

For $\lambda_1 \neq \lambda_2 \neq \lambda_3$, Eqs. (2.33) and (2.35) represent two different planes, in the (x_1, x_2, x_3) space, which are not parallel to each other, and the second of which does not pass through $(0, 0, 0)$. Hence

they must intersect at a line which does not pass through $(0, 0, 0)$. Eq. (2.36) represents an infinite elliptic cone, with its vertex at $(0, 0, 0)$ in the (x_1, x_2, x_3) space. A line can either intersect such a cone (i) at a single point, or (ii) at two distinct points, or (iii) at infinite number of points by lying on the surface of the cone. The third possibility can however be excluded in this case, because the line formed by the intersection of the planes of Eqs. (2.33) and (2.35) does not pass through the cone's vertex at $(0, 0, 0)$. Thus, in this case, the line defined by the intersection of the planes of Eqs. (2.33) and (2.35) can intersect the cone of Eq. (2.36) at either one or two distinct points. Since, it is not possible to know whether the line will intersect the cone at one or two distinct points without *a priori* knowledge of the coefficients in Eqs. (2.33), (2.35) and (2.33), it can be stated that Eqs. (2.33), (2.35) and (2.33) can, in general, have two distinct solutions in the (x_1, x_2, x_3) space leading to two sets of real values to $\{x_1, x_2, x_3\}$ that correspond to two physically admissible solutions for the 3rd row of $\mathbf{V}$ for a given 2nd row.

Consider now the solution for $\{y_1, y_2, y_3\}$, i.e. the 1st row of $\mathbf{V}$, given the 2nd and 3rd rows of $\mathbf{V}$. Since the 1st row of $\mathbf{V}$ is orthogonal to the 2nd and 3rd rows by Eq. (2.9):

$$\begin{aligned} \sigma_1 y_1 + \sigma_2 y_2 + \sigma_3 y_3 &= 0 \\ x_1 y_1 + x_2 y_2 + x_3 y_3 &= 0 \end{aligned} \tag{2.37}$$

Again, using Eq. (2.34) along with the stiffness orthogonality of Eq. (2.4), one gets, after some algebra:

$$\left(\frac{y_1}{\sqrt{\lambda_1}} - \frac{\sigma_1}{2\sqrt{\lambda_1}}\right)^2 + \left(\frac{y_2}{\sqrt{\lambda_2}} - \frac{\sigma_2}{2\sqrt{\lambda_2}}\right)^2 + \left(\frac{y_3}{\sqrt{\lambda_3}} - \frac{\sigma_3}{2\sqrt{\lambda_3}}\right)^2 = \frac{\sigma_1^2}{4\lambda_1} + \frac{\sigma_2^2}{4\lambda_2} + \frac{\sigma_3^2}{4\lambda_3} \tag{2.38}$$

While the two equations in Eq. (2.37) represent two planes, Eq. (2.38) represents an ellipsoid, in the (y_1, y_2, y_3) space. Note that all these three surfaces pass through the point $(0, 0, 0)$. Since $\mathbf{V}$ is always positive definite, the two planes of Eq. (2.37) cannot be parallel ($\{\sigma_1, \sigma_2, \sigma_3\} \neq \{x_1, x_2, x_3\}$) and hence must intersect in a line. This line of intersection of the planes can intersect the ellipsoid of Eq. (2.38) in at most two points, which are the two solutions to Eqs. (2.37) and (2.38). One of these two points must be the trivial solution of $(0, 0, 0)$ since all the three surfaces pass through that point. This point is trivial and not physically admissible since an entire row of $\mathbf{V}$ can never be zero owing to its positive definiteness. Thus, although Eqs. (2.37) and (2.38) give two solutions to $\{y_1, y_2, y_3\}$, only one of them is physically admissible.

Note that in the above solution for $\{y_1, y_2, y_3\}$, the x_i in Eq. (2.37) are assumed to be known. However, as demonstrated earlier, there can, in general, be two physically admissible solutions to $\{x_1, x_2, x_3\}$, leading to two physically admissible solution pairs of $\{\{x_1, x_2, x_3\}, \{y_1, y_2, y_3\}\}$. Hence, for a 3-DOF shear-type system for which the 2nd row of $\mathbf{V}$ is known, there may exist two possible sets of 1st and 3rd rows of $\mathbf{V}$, one of which will correspond to the true system, and the other to an alternative, but also physically admissible, system. An example of such non-uniqueness was also discussed by Franco et al. [3] who showed that the two 3-DOF systems:

System I: $\{m_1, m_2, m_3\} = \{0.85, 1.3, 1.1\}$; $\{k_1, k_2, k_3\} = \{9, 12, 11\}$

System II: $\{m_1, m_2, m_3\} = \{2.369, 1.3, 0.2776\}$; $\{k_1, k_2, k_3\} = \{7.5473, 16.1429, 6.8571\}$

will have the same response at DOF 2 for the same applied force at DOF 2, and thus will have the same eigenvalues and the same 2nd row of $\mathbf{V}$.

Statement 4: *Knowing only the ith row of $\mathbf{V}$, it is not possible to uniquely determine the other rows of $\mathbf{V}$, for any $i \in \{3, \cdots, N-2\}$.*

Proof of Statement 4

The proof of this statement is intuitive. Suppose the ith row of $\mathbf{V}$ is known. If the $(i+1)$th row of $\mathbf{V}$ is estimated, then, using Eqs. (2.10) and (2.20), all the other rows of $\mathbf{V}$ may be solved for. There can, however, be different possible estimates for the $(i+1)$th row as long as the candidate solutions are admissible from the structural topology requirements (such as the $(i+1)$th row being orthogonal to the ith row by Eq. (2.9)). Each of these estimates will lead to different expanded $\mathbf{V}$ matrices, corresponding to different shear-type systems; therefore, it is not possible to uniquely determine all the rows of $\mathbf{V}$ if only the ith row is known to begin with, for any $i \in \{3, \cdots, N-2\}$. □

2.2.2 Summary of expansion statements and nature of estimated $\mathbf{M}$ and $\mathbf{K}$

To summarize, it can be concluded that knowing either (1) two consecutive rows, or (2) the 1st row, or (3) the Nth row of $\mathbf{V}$, its remaining rows may be uniquely determined and a unique mode shape expansion may be accomplished for shear-type systems. Such a mode shape expansion will involve solving systems of linear equations. Since the mode shape matrix $\mathbf{V}$ considered in this discussion is mass normalized, this unique mode shape expansion to a complete $\mathbf{V}$ will enable the use of the modal orthogonality relations of Eq. (2.4) to determine the $\mathbf{M}$ and $\mathbf{K}$ matrices of the system.

Note that the proposed mode shape expansion approach inherently takes into account the diagonal nature of $\mathbf{M}$, through the use of Eq. (2.9), and the tridiagonal nature of $\mathbf{K}$, through the use of the tridiagonal matrix $\mathbf{A}$ in Eqs. (2.7), (2.23) and (2.29). Hence, using the $\mathbf{V}$ so obtained in Eq. (2.4) would also provide identified diagonal $\mathbf{M}$ and tridiagonal $\mathbf{K}$ matrices. The diagonal elements of the thus identified $\mathbf{M}$ (i.e. the estimated lumped masses), $M_{i,i} = m_i = (\mathbf{r}_i\mathbf{r}_i^T)^{-1}$, will always be positive owing to being the reciprocal of an inner product of $\mathbf{r}_i$, the ith row of $\mathbf{V}$. Using $\mathbf{M}^{-1}\mathbf{K}\mathbf{M}^{-1} = \mathbf{V}\mathbf{\Lambda}\mathbf{V}^T$, the diagonal elements of the identified $\mathbf{K}$ can be expressed as $K_{i,i} = (\mathbf{r}_i\mathbf{r}_i^T)^{-2}(\mathbf{r}_i\mathbf{\Lambda}\mathbf{r}_i^T)$, which will again be always positive, being the ratio of an inner product to the product of two inner products. The super and sub-diagonal elements of $\mathbf{K}$ can be similarly expressed as $K_{i,i+1} = K_{i+1,i} = -k_{i+1} = (\mathbf{r}_{i+1}\mathbf{r}_{i+1}^T)^{-1}(\mathbf{r}_i\mathbf{r}_i^T)^{-1}(\mathbf{r}_{i+1}\mathbf{\Lambda}\mathbf{r}_i^T)$, whose sign is governed by the sign of the factor $(\mathbf{r}_{i+1}\mathbf{\Lambda}\mathbf{r}_i^T)$. Pre-multiplying the first N rows of Eq. (2.10) with $\mathbf{r}_{i+1}$, and using the definitions of the variables α_2 and α_3 given for Eq. (2.7), we get $(\mathbf{r}_{i+1}\mathbf{r}_{i+1}^T)^{-1}(\mathbf{r}_{i+1}\mathbf{\Lambda}\mathbf{r}_i^T) = \alpha_2/\alpha_3 = a_{i,i+1}$, which implies that the sign of $(\mathbf{r}_{i+1}\mathbf{\Lambda}\mathbf{r}_i^T)$ is the same as the sign of $a_{i,i+1}$ in the matrix $\mathbf{A}$ of Eq. (2.6). Given that the measured data is coming from a shear-type system for which the underlying matrix $\mathbf{A}$ will have negative super and sub-diagonal elements, it can thus be inferred that the super and sub-diagonal elements of the identified $\mathbf{K}$ matrix will also be negative, and hence the estimated spring (story) stiffnesses, $k_i \; \forall \; i \in \{2, \cdots, N\}$ will be positive. Similarly, the estimated first story stiffness can be expressed as $k_1 = (\mathbf{r}_1\mathbf{r}_1^T)^{-2}(\mathbf{r}_1\mathbf{\Lambda}\mathbf{r}_1^T) + (\mathbf{r}_1\mathbf{r}_1^T)^{-1}(\mathbf{r}_2\mathbf{r}_2^T)^{-1}(\mathbf{r}_2\mathbf{\Lambda}\mathbf{r}_1^T)$; pre-multiplying Eq. (2.23) by $\mathbf{r}_1$ and $\mathbf{r}_2$ gives respectively $(\mathbf{r}_1\mathbf{r}_1^T)^{-1}(\mathbf{r}_1\mathbf{\Lambda}\mathbf{r}_1^T) = a_{1,1}$ and $(\mathbf{r}_2\mathbf{r}_2^T)^{-1}(\mathbf{r}_2\mathbf{\Lambda}\mathbf{r}_1^T) = a_{1,2}$, using which it can be inferred that k_1 will have the same sign as $(a_{1,1} + a_{1,2})$, which, for a shear-type system, will be positive. Hence, the $\mathbf{M}$ and $\mathbf{K}$ matrices, estimated using the complete mass normalized $\mathbf{V}$ matrix, will represent a realistic shear-type system with positive lumped masses and spring stiffnesses, provided the measured input-output data comes from a shear-type system.

The question that still needs to be addressed is how to determine this pre-requisite modal information, i.e. two consecutive rows or the 1st row or the Nth row of the mass normalized $\mathbf{V}$ matrix, so that the mode shape expansion discussed above may be employed. In Section 2.4 this question is addressed for different possible sensor-actuator combinations and input scenarios.

2.3 Comparison with Earlier Studies Based on Symmetric Eigenvalue Problem

At this stage it would be worthwhile to compare the results obtained until now with those discussed by Gladwell in [20], who states similar requirements as the first parts of Statements 2 and 3 for the unitary modeshape matrix ($\mathbf{U}$) of a Jacobi matrix $\mathbf{J} = \mathbf{M}^{-1/2}\mathbf{K}\mathbf{M}^{-1/2}$ ($\mathbf{J}\mathbf{U} = \mathbf{U}\mathbf{\Lambda}$). Since $\mathbf{J}$ is symmetric, the inverse modal problem formulated using $\mathbf{J}$ and the unitary matrix $\mathbf{U}$ can be seen as an "inverse version" of Lanczos's algorithm. Instead, the formulation in this paper is for the mass normalized mode shapes involving the non-symmetric matrix $\mathbf{A} = \mathbf{M}^{-1}\mathbf{K}$, and thus should not be confused as an inverse variant of Lanczos's algorithm. While the two eigenvalue problems are equivalent, being related through a coordinate transformation, the main differences between the two inverse identification approaches are in: (1) the necessary pre-requisite information for mode shape expansion, and (2) the necessary *a priori* knowledge of some physical parameter for the determination of $\mathbf{M}$ and $\mathbf{K}$. The necessary pre-requisite information in the current approach for mode shape expansion are the system's eigenvalues, along with the first or last or any two consecutive rows of $\mathbf{V}$ which can be obtained from a single experiment using the input-output balance approach discussed in the next section. Instead, in [20], the necessary pre-requisite information is the first or last rows of the unitary matrix $\mathbf{U}$, for which it is necessary to know two sets of eigenvalues: one for the system under consideration, and the other for the same system but with the first (or the last) mass constrained/fixed; this second set of eigenvalues may be obtained as the antiresonant frequencies from the frequency response function estimated using the measured input-output data, thus providing both the necessary spectra again from a single experiment. The second difference between the two formulations is that, while the proposed approach does not require any *a priori* information about the system's physical parameters for the estimation of the $\mathbf{M}$ and $\mathbf{K}$ matrices, the formulation using $\mathbf{J}$ instead requires the knowledge of some *a priori* information about the system's mass. This is because, the resulting modeshape matrix $\mathbf{U}$, in the formulation with $\mathbf{J}$, is a function of the system's mass matrix $\mathbf{M}$. In fact, on comparing the two eigenvalue problems: $\mathbf{J}\mathbf{U} = \mathbf{U}\mathbf{\Lambda}$ and $\mathbf{A}\mathbf{V} = \mathbf{V}\mathbf{\Lambda}$, with $\mathbf{J} = \mathbf{M}^{-1/2}\mathbf{K}\mathbf{M}^{-1/2}$ and $\mathbf{A} = \mathbf{M}^{-1}\mathbf{K}$, it can be seen that the two mode shape matrices are related via a coordinate transformation $\mathbf{U} = \mathbf{T}\mathbf{V}$, where $\mathbf{T} = \mathbf{M}^{1/2}$. Thus, in general, unless $\mathbf{M}$ is known, one will not be able to transform the realized mode shape matrix $\mathbf{U}$ in [20] to the mode shape matrix $\mathbf{V}$, and hence the

determination of $\mathbf{K}$ using the eigenvectors of $\mathbf{J}$ will require the *a priori* knowledge of $\mathbf{M}$. In the special case of a shear-type system, at least one information about the system's physical parameters, for example, the knowledge of the total mass of the system used by Gladwell [20], needs to be known *a priori*. While the assumption of known total mass may not be very restrictive in general owing to masses being usually accurately estimated from an engineering drawing of the structure, in certain situations where the mass parameters might not be estimated from the geometry with reasonable confidence, as e.g. in case of a rigid-floor system under torsional vibration, it can be beneficial to perform the identification, if possible, without using this *a priori* information. Thus, in the structural parameter identification problem considered here, neither $\mathbf{M}$ nor the total mass is known, and instead the objective is to find $\mathbf{M}$, along with the usual objective of the identification of $\mathbf{K}$. Formulating the problem using $\mathbf{A}$ enables the direct estimation of the mass normalized mode shape matrix $\mathbf{V}$, thereby bypassing the need of any transformation and the necessity of any *a priori* additional knowledge of the value of any physical parameter. Due to this reason, the formulation of the inverse problem in this chapter uses the non-symmetric $\mathbf{A}$ matrix, instead of the usual treatment of the problem using the symmetric $\mathbf{J}$ matrix adopted in Gladwell [20], Udwadia et al. [1, 17] and Franco et al. [3]. Additionally, the present formulation allows the identification of the simultaneous lower bounds of both the necessary *a priori* information (no *a priori* information necessary) and the necessary instrumentation (only 1 or 2 instrumented DOFs necessary) for a unique identification of $\mathbf{M}$ and $\mathbf{K}$ for shear-type systems.

2.4 Determination of the Necessary Rows of $\mathbf{V}$ Using Input-Output Balance

As in Section 2.2, here also the measured responses are assumed rich enough so as to allow identification of all the modal parameters at the instrumented DOFs. Therefore, prior to estimating the mass normalized rows of $\mathbf{V}$, all the eigenvalues λ_j and modal damping ratios ζ_j, $\forall\ j \in \{1, \cdots, N\}$, of the N-DOF shear-type system under consideration, are assumed to be identified from the measured input-output data using any suitable system identification technique. Starting with these assumptions, the following scenarios need to be discussed:

2.4.1 1 sensor and 1 actuator

Scenario 1: Estimation of the ith row of $\mathbf{V}$ with a co-located sensor-actuator pair at DOF i

The equation of motion of the system is written as:

$$\mathbf{M}\ddot{\mathbf{u}} + \mathbf{C}\dot{\mathbf{u}} + \mathbf{K}\mathbf{u} = \mathbf{f} \tag{2.39}$$

where $\mathbf{u} = [u_1, u_2, \cdots, u_N]^T$ is the displacement response vector in physical coordinates, with u_i being the displacement response at the ith DOF; $\mathbf{f} = [0, 0, \cdots, f_i, \cdots]^T$ is the nodal force vector, with f_i being the applied force at the ith DOF; and $\mathbf{M}$, $\mathbf{C}$, and $\mathbf{K}$ are the system's mass, damping and stiffness matrices, respectively. Transforming Eq. (2.39) to modal coordinates via $\mathbf{u} = \mathbf{V}\boldsymbol{\eta}$ and pre-multiplying Eq. (2.39) by $\mathbf{V}^T$, one gets:

$$\ddot{\boldsymbol{\eta}} + \mathbf{C_m}\dot{\boldsymbol{\eta}} + \boldsymbol{\Lambda}\boldsymbol{\eta} = \mathbf{V}^T\mathbf{f} \tag{2.40}$$

where $\boldsymbol{\eta} = [\eta_1, \eta_2, \cdots, \eta_N]^T$ is the modal displacement response vector, with η_j being the jth modal displacement response, and $\mathbf{C_m} = \mathbf{V}^T\mathbf{C}\mathbf{V}$ is the diagonal modal damping matrix with any jth term on its main diagonal being equal to $2\zeta_j\omega_j$ where $\omega_j = \sqrt{\lambda_j}$ is the jth natural frequency of the system. Since there is a co-located sensor-actuator pair at DOF i, the acceleration response $\ddot{u}_i$ and the applied input force f_i at the ith DOF are measured. Consider the jth modal response from Eq. (2.40):

$$\ddot{\eta}_j + 2\zeta_j\omega_j\dot{\eta}_j + \omega_j^2\eta_j = v_{i,j}f_i \quad \forall\, j \in \{1, 2, \cdots, N\} \tag{2.41}$$

Since the coefficients $\mathbf{r}_i = [v_{i,1}\ v_{i,2}\ \cdots\ v_{i,N}]^T$ on the ith row of $\mathbf{V}$ are yet unknown, the response in the jth mode may not be estimated using Eq. (2.41). Define instead a *pseudo-modal response*, $\tilde{\eta}_j$, proportional to the true modal response as $\eta_j = v_{i,j}\tilde{\eta}_j$ and leading to the *pseudo-modal equation of motion*:

$$\ddot{\tilde{\eta}}_j + 2\zeta_j\omega_j\dot{\tilde{\eta}}_j + \omega_j^2\tilde{\eta}_j = f_i \quad \forall\, j \in \{1, 2, \cdots, N\} \tag{2.42}$$

Since, by assumption, λ_j and $\zeta_j\ \forall\ j \in \{1, \cdots, N\}$ are known, all the pseudo-modal acceleration responses, $\ddot{\tilde{\eta}}_j\ \forall\ j \in \{1, \cdots, N\}$, may be obtained by solving Eq. (2.42) in the time domain. Now writing the measured acceleration response $\ddot{u}_i$ at the ith DOF in terms of the pseudo-modal acceleration responses, one gets a linear system of equations:

$$\begin{aligned} \ddot{u}_i &= \sum_{j=1}^{N} v_{i,j}\ddot{\eta}_j = \sum_{j=1}^{N} v_{i,j}^2\ddot{\tilde{\eta}}_j \\ \Rightarrow \quad & \mathbf{G}\boldsymbol{\Psi} = \mathbf{Y} \end{aligned} \tag{2.43}$$

where, $\mathbf{\Psi} = [v_{i,1}^2\ v_{i,2}^2\ \cdots\ v_{i,N}^2]^T$, $\mathbf{Y} = [\ddot{u}_i(0)\ \ddot{u}_i(\Delta t)\ \ddot{u}_i(2\Delta t)\ \cdots]^T$,

$$\mathbf{G} = \begin{bmatrix} \ddot{\tilde{\eta}}_1(0) & \ddot{\tilde{\eta}}_2(0) & \cdots & \ddot{\tilde{\eta}}_N(0) \\ \ddot{\tilde{\eta}}_1(\Delta t) & \ddot{\tilde{\eta}}_2(\Delta t) & \cdots & \ddot{\tilde{\eta}}_N(\Delta t) \\ \ddot{\tilde{\eta}}_1(2\Delta t) & \ddot{\tilde{\eta}}_2(2\Delta t) & \cdots & \ddot{\tilde{\eta}}_N(2\Delta t) \\ \vdots & \vdots & \vdots & \vdots \end{bmatrix} \tag{2.44}$$

and Δt is the sampling time. The number of equations in Eq. (2.43) is equal to the number of data points in the measured input and output time-histories, and is thus, in general, more than the number N of unknowns. Using the least-squares solution of Eq. (2.43), $\mathbf{\Psi} = \mathbf{G}^{\dagger}\mathbf{Y}$, the ith row of $\mathbf{V}$ can be estimated as $v_{i,j} = \sqrt{\psi_j}\ \forall\ j \in \{1, 2, \cdots, N\}$. Note that, since by definition all the elements of $\mathbf{\Psi}$ are squares, the least squares solution of Eq. (2.43) can be expected to give a vector $\mathbf{\Psi}$ with all non-negative components, hence not affecting the square root operation to estimate $v_{i,j}$.

Note that using the above procedure it is possible to uniquely obtain the ith row of $\mathbf{V}$. If, however, there is no co-located sensor-actuator pair but instead a sensor at DOF i and actuator at DOF k, neither the ith nor the kth row of $\mathbf{V}$ may be determined uniquely. In that case the relation between the true modal and pseudo-modal responses will be $\eta_j = v_{k,j}\tilde{\eta}_j$, and the least squares solution vector $\mathbf{\Psi}$ will thus be of the form $\mathbf{\Psi} = [(v_{i,1}v_{k,1})\ (v_{i,2}v_{k,2})\ \cdots\ (v_{i,N}v_{k,N})]^T$, thereby making it impossible to determine either $v_{i,j}$ or $v_{k,j}$ uniquely. This constitutes an alternative proof for the well-known necessity of at least one co-located sensor-actuator pair for unique identification [28, 29]. (Note: A co-located sensor-actuator pair, while necessary in general, may not always be necessary for an unique identification. For example, a 3-DOF shear-type system with sensors at DOFs 1 and 2 and an actuator at DOF 3, or sensors at DOFs 1 and 3 and actuator at DOF 2, is globally identifiable. This example is discussed in details in Chapter 4 of this thesis using the methodology presented therein, and was also observed by Chatzis et al. [6].)

It should also be mentioned that, although it is possible to uniquely estimate the ith row of $\mathbf{V}$ using Eq. (2.43) when there is a co-located sensor-actuator pair at the ith DOF it will not be possible to uniquely estimate the remaining rows of $\mathbf{V}$ unless $i = 1$ or N as per the discussion in Section 2.2. Thus, if only a single actuator and a single sensor are available, they should be co-located at either the 1st or the Nth DOF, such that either the 1st or the Nth row may first be determined using Eq. (2.43), and then the complete $\mathbf{V}$ may be obtained using the mode shape expansion discussed in Section 2.2.

2.4.2 2 sensors and 1 actuator

Scenario 2: Estimation of the ith row along with the $(i+1)$th or the $(i-1)$th rows of $\mathbf{V}$ with 1 co-located pair at the ith DOF and an extra sensor on the $(i+1)$th or the $(i-1)$th DOF

Suppose the additional sensor is located at the $(i+1)$th DOF. Using Eq. (2.43) of the previous scenario for input-output balance at the ith DOF, the ith row of $\mathbf{V}$ may first be estimated. Then, writing the measured acceleration response at the $(i+1)$th DOF as a linear combination of the pseudo-modal responses, a linear system of equations as in Eq. (2.43) is obtained such that $\mathbf{G}\boldsymbol{\Psi} = \mathbf{Y}$, where $\boldsymbol{\Psi} = [(v_{i+1,1}v_{i,1})\ (v_{i+1,2}v_{i,2})\ \cdots\ (v_{i+1,N}v_{i,N})]^T$, $\mathbf{Y} = [\ddot{u}_{i+1}(0)\ \ddot{u}_{i+1}(\Delta t)\ \ddot{u}_{i+1}(2\Delta t)\ \cdots]^T$, and $\mathbf{G}$ is the same as in Eq. (2.44). Since the ith row of $\mathbf{V}$ has already been determined, the elements of the $(i+1)$th row of $\mathbf{V}$ may be estimated from $v_{i+1,j} = \psi_j / v_{i,j}\ \forall\ j \in \{1, 2, \cdots, N\}$ where the ψ_j's are obtained from the least-squares solution vector $\boldsymbol{\Psi} = \mathbf{G}^{\dagger}\mathbf{Y}$.

If instead the additional sensor is located at DOF $(i-1)$, the process is analogous to the one described above with the index $(i+1)$ in the expressions for $\boldsymbol{\Psi}$ and $\mathbf{Y}$ being replaced with $(i-1)$. Thus, with a co-located sensor-actuator pair at DOF i, and an additional sensor at the $(i+1)$th (or $(i-1)$th) DOF, the ith and $(i+1)$th (or $(i-1)$th) rows of $\mathbf{V}$ may be uniquely estimated. Once two consecutive rows of $\mathbf{V}$ are thus determined, Eqs. (2.10) and (2.20) of Statement 1, Section 2.2, may be used to estimate the remaining rows.

2.4.3 1 sensor and 2 actuators with non-proportional inputs

Scenario 3: Estimation of the ith row along with the $(i+1)$th or the $(i-1)$th rows of $\mathbf{V}$ with 1 co-located pair at the ith DOF and an extra actuator on the $(i+1)$th or the $(i-1)$th DOF considering *non-proportional inputs* from the actuators

Suppose the additional actuator is located at the $(i+1)$th DOF. Also suppose that the inputs from the two actuators, f_i and f_{i+1}, are not proportional to one another. The modal and pseudo-modal responses of Eqs. (2.41) and (2.42) now take the form:

$$\ddot{\eta}_j + 2\zeta_j\omega_j\dot{\eta}_j + \omega_j^2\eta_j = v_{i,j}f_i + v_{i+1,j}f_{i+1} \quad \forall\ j \in \{1, 2, \cdots, N\} \tag{2.45}$$

and

$$\left.\begin{aligned} \ddot{\tilde{\eta}}_{j,i} + 2\zeta_j\omega_j\dot{\tilde{\eta}}_{j,i} + \omega_j^2\tilde{\eta}_{j,i} &= f_i \\ \ddot{\tilde{\eta}}_{j,i+1} + 2\zeta_j\omega_j\dot{\tilde{\eta}}_{j,i+1} + \omega_j^2\tilde{\eta}_{j,i+1} &= f_{i+1} \end{aligned}\right\} \quad \forall\ j \in \{1, 2, \cdots, N\} \tag{2.46}$$

with $\tilde{\eta}_{j,i}$ and $\tilde{\eta}_{j,i+1}$ being the pseudo-modal responses due to the inputs f_i and f_{i+1}, respectively, and $\eta_j = v_{i,j}\tilde{\eta}_{j,i} + v_{i+1,j}\tilde{\eta}_{j,i+1}$. Knowing the two inputs and the λ_j and $\zeta_j \; \forall \, j \in \{1, \cdots, N\}$, the two sets of pseudo-modal responses may be solved for from Eq. (2.46). Writing the measured acceleration $\ddot{u}_i$ in terms of the two sets of pseudo-modal responses, as in Eq. (2.43), again leads to a linear system of equations $\mathbf{G}\boldsymbol{\Psi} = \mathbf{Y}$. In this scenario however, the least squares solution vector, $\boldsymbol{\Psi} = \mathbf{G}^{\dagger}\mathbf{Y}$, is of the form $\boldsymbol{\Psi} = [v_{i,1}^2 \; v_{i,2}^2 \; \cdots \; v_{i,N}^2 \; (v_{i+1,1}v_{i,1}) \; (v_{i+1,2}v_{i,2}) \; \cdots \; (v_{i+1,N}v_{i,N})]^T$ with a dimension of $2N \times 1$. The vector $\mathbf{Y} = [\ddot{u}_i(0) \; \ddot{u}_i(\Delta t) \; \ddot{u}_i(2\Delta t) \; \cdots]^T$ is the same as in Eq. (2.43), containing the measured acceleration response at the ith DOF, while the matrix $\mathbf{G}$ has the form:

$$\mathbf{G} = \begin{bmatrix} \ddot{\tilde{\eta}}_{1,i}(0) & \ddot{\tilde{\eta}}_{2,i}(0) & \cdots & \ddot{\tilde{\eta}}_{N,i}(0) & \ddot{\tilde{\eta}}_{1,i+1}(0) & \ddot{\tilde{\eta}}_{2,i+1}(0) & \cdots & \ddot{\tilde{\eta}}_{N,i+1}(0) \\ \ddot{\tilde{\eta}}_{1,i}(\Delta t) & \ddot{\tilde{\eta}}_{2,i}(\Delta t) & \cdots & \ddot{\tilde{\eta}}_{N,i}(\Delta t) & \ddot{\tilde{\eta}}_{1,i+1}(\Delta t) & \ddot{\tilde{\eta}}_{2,i+1}(\Delta t) & \cdots & \ddot{\tilde{\eta}}_{N,i+1}(\Delta t) \\ \ddot{\tilde{\eta}}_{1,i}(2\Delta t) & \ddot{\tilde{\eta}}_{2,i}(2\Delta t) & \cdots & \ddot{\tilde{\eta}}_{N,i}(2\Delta t) & \ddot{\tilde{\eta}}_{1,i+1}(2\Delta t) & \ddot{\tilde{\eta}}_{2,i+1}(2\Delta t) & \cdots & \ddot{\tilde{\eta}}_{N,i+1}(2\Delta t) \\ \vdots & \vdots & \vdots & \vdots & \vdots & \vdots & \vdots & \vdots \end{bmatrix} \tag{2.47}$$

Using the first N elements of the solution vector $\boldsymbol{\Psi}$, the ith row of $\mathbf{V}$ is first estimated as $v_{i,j} = \sqrt{\psi_j}$ $\forall \, j \in \{1, 2, \cdots, N\}$, and, using the remaining N elements, the $(i+1)$th row of $\mathbf{V}$ is then estimated as $v_{i+1,j} = \psi_{N+j}/v_{i,j} \; \forall \, j \in \{1, 2, \cdots, N\}$.

If instead the additional actuator is located at DOF $(i-1)$, the procedure is analogous to the one discussed above with the index $(i-1)$ replacing $(i+1)$ in the expressions for $\mathbf{G}$, $\boldsymbol{\Psi}$ and $\mathbf{Y}$. Thus, with a co-located sensor-actuator pair at DOF i, and an additional actuator at the $(i+1)$th (or $(i-1)$th) DOF, the ith and $(i+1)$th (or $(i-1)$th) rows of $\mathbf{V}$ may be uniquely estimated, provided that the inputs from the two actuators are not proportional to one another; one can then use Eqs. (2.10) and (2.20) to estimate its remaining rows.

Both Scenarios 2 and 3 involve division by $v_{i,j}$ for the estimation of $v_{i+1,j}$. If however the mode j has a node at DOF i, i.e. $v_{i,j} = 0$, then $v_{i+1,j}$ cannot be thus estimated. In this situation, one would consequently need to perform a second experiment; noting that for the same mode j both DOFs i and $(i+1)$ cannot be nodes (since that would indicate either an infinite stiffness, or the existence of another DOF, between these two DOFs), this second experiment may be performed by shifting the actuator, for Scenario 2, or the sensor, for Scenario 3, from the ith to the $(i+1)$th DOF.

2.4.4 Non-uniqueness from proportional inputs

Scenario 4a: Estimation of the ith row along with the $(i+1)$th or the $(i-1)$th rows of $\mathbf{V}$ with 1 co-located pair at the ith DOF and an extra actuator on the $(i+1)$th or the $(i-1)$th DOF considering *proportional inputs* from the actuators: a *non-unique solution*

This scenario is similar to Scenario 3, with the exception that the inputs from the two actuators, f_i and f_{i+1}, are proportional to one another, such that $f_{i+1} = \beta f_i$, with β being a known time-independent constant. As in Scenario 3, the modal and pseudo-modal responses are defined via Eqs. (2.45) and (2.46), and expressing the measured acceleration $\ddot{u}_i$ as a linear combination of the pseudo-modal responses again leads to the set of linear equations $\mathbf{G\Psi} = \mathbf{Y}$. However, on account of the inputs being proportional, the pseudo-modal responses also become proportional, with $\tilde{\eta}_{j,i+1} = \beta\tilde{\eta}_{j,i}$ $\forall\ j \in \{1, 2, \cdots, N\}$. Thus, the modal and pseudo-modal responses are related in this scenario through $\eta_j = (v_{i,j} + \beta v_{i+1,j})\tilde{\eta}_{j,i}$. This makes the matrix $\mathbf{G}$ of rank N as in Scenario 1, instead of rank $2N$ as in Scenario 3. While $\mathbf{Y}$ remains the same as in Scenario 3, the solution vector $\mathbf{\Psi} = \mathbf{G}^{\dagger}\mathbf{Y}$ now has N elements of the form:

$$v_{i,j}^2 + \beta v_{i,j} v_{i+1,j} = \psi_j \quad \forall\, j \in \{1, 2, \cdots, N\} \tag{2.48}$$

which provide N quadratic equations in terms of the elements of the ith and $(i+1)$th rows of $\mathbf{V}$. As in the last scenario, if the additional actuator is located at DOF $(i-1)$, these equations will be in terms of the elements on the $(i-1)$th row instead of the $(i+1)$th. However, using the elements of the solution vector $\mathbf{\Psi}$, unique solutions may no longer be found for the ith and the $(i+1)$th (or $(i-1)$th) rows.

The quadratic nonlinearity in Eq. (2.48) suggests the possibility of the existence of multiple shear type systems, which can have the same measured response at DOF i, when subjected to the same proportional loadings at DOFs i and $(i+1)$ (or $(i-1)$). For example, it is possible to see that the following two 7 DOF shear-type systems:

$$\text{System I: } \{m_1, m_2, \cdots, m_7\} = \{2.5, 2.5, 2.5, 2.5, 2.5, 2.5, 2.0\} \times 10^3$$
$$\{k_1, k_2, \cdots, k_7\} = \{5, 5, 5, 5, 5, 5, 5\} \times 10^6$$
$$\text{System II: } \{m_1, m_2, \cdots, m_7\} = \{2.3578, 3.0528, 2.2376, 2.1481, 3.3262, 2.5000, 1.4249\} \times 10^3$$
$$\{k_1, k_2, \cdots, k_7\} = \{4.3544, 5.9281, 5.5295, 3.9087, 5.3037, 6.2222, 3.5622\} \times 10^6$$

have the same eigenvalues, and their mass normalized $\mathbf{V}$ matrices are such that, $3v_{6,j}^2 + 2v_{5,j}v_{6,j}$ $\forall\ j\ \in \{1, 2, \cdots, N\}$, are the same for both the systems. Thus, if these two systems are excited with actuators at DOFs 5 and 6, with $2f_6 = 3f_5$, and the response acceleration history at DOF 6 is measured, then it will not be possible to differentiate between the two systems since their measured accelerations will be identical. This shows that *non-uniqueness in identification does not only depend on the number and location of sensors, but also depends on the type of loading. For the same sensor placement scenario, one type of loading may give a unique identification, whereas a different loading situation may lead to non-unique identification.*

2.4.5 2 sensors and 2 actuators for proportional inputs

Scenario 4b: Estimation of the ith and the $(i+1)$th rows of $\mathbf{V}$ with *2 pairs of co-located actuators and sensors* and *proportional inputs* from the actuators

In this case, the input-output balance approach may be applied to the responses of DOFs i and $(i+1)$ separately, as in Scenario 2, to get the following two linear systems of equations:

$$\mathbf{G}\mathbf{\Psi}_i = \mathbf{Y}_i; \qquad \mathbf{G}\mathbf{\Psi}_{i+1} = \mathbf{Y}_{i+1} \tag{2.49}$$

with $\mathbf{Y}_i = [\ddot{u}_i(0)\ \ddot{u}_i(\Delta t)\ \ddot{u}_i(2\Delta t)\ \cdots]^T$, $\mathbf{Y}_{i+1} = [\ddot{u}_{i+1}(0)\ \ddot{u}_{i+1}(\Delta t)\ \ddot{u}_{i+1}(2\Delta t)\ \cdots]^T$, and $\mathbf{G}$ given by Eq. (2.44). The two, $N \times 1$ dimensional, least squares solution vectors, $\mathbf{\Psi}_i = \mathbf{G}^\dagger\mathbf{Y}_i$ and $\mathbf{\Psi}_{i+1} = \mathbf{G}^\dagger\mathbf{Y}_{i+1}$, now have elements of the form:

$$v_{i,j}^2 + \beta v_{i,j}v_{i+1,j} = \psi_{j,i}; \quad \beta v_{i+1,j}^2 + v_{i,j}v_{i+1,j} = \psi_{j,i+1} \quad \forall\, j \in \{1, 2, \cdots, N\} \tag{2.50}$$

where $\psi_{j,i}$ denotes the jth component of the vector $\mathbf{\Psi}_i$. Adding and subtracting β times the second equation from the first equation in Eq. (2.50), and using the formulae $(p+q)^2 = p^2 + 2pq + q^2$ and $(p+q)(p-q) = p^2 - q^2$, one gets:

$$v_{i,j} + \beta v_{i+1,j} = \pm\gamma_j; \quad v_{i,j} - \beta v_{i+1,j} = \pm\delta_j \quad \forall\, j \in \{1, 2, \cdots, N\} \tag{2.51}$$

where $\gamma_j = \sqrt{\psi_{j,i} + \beta\psi_{j,i+1}}$ and $\delta_j = (\psi_{j,i} - \beta\psi_{j,i+1})/\gamma_j$. Since $\psi_{j,i} + \beta\psi_{j,i+1} = (v_{i,j} + \beta v_{i+1,j})^2$ is by definition a square number, the square root operation to estimate γ_j is admissible. Note that the two equations in Eq. (2.51) are linear in $v_{i,j}$ and $v_{i+1,j}$, and can be thus solved to get:

$$v_{i,j} = \pm\frac{\gamma_j + \delta_j}{2}; \quad v_{i+1,j} = \pm\frac{\gamma_j - \delta_j}{2\beta} \quad \forall\, j \in \{1, 2, \cdots, N\} \tag{2.52}$$

which are the unique estimates of the ith and $(i+1)$th rows of $\mathbf{V}$. It should be noted that in Eq. (2.52) the relation between the "$\pm$" signs in the estimates of $v_{i,j}$ and $v_{i+1,j}$ is bijective; specifically, choosing the "$+$" sign for $v_{i,j}$ automatically induces the "$+$" sign in $v_{i+1,j}$, and similarly for the "$-$" sign. The "$\pm$" sign in these estimates are owing to the fact that even scaled (mass normalized) mode shapes have a non-uniqueness in sign; as such, the negative sign may be left off from the "$\pm$" in Eq. (2.52) without introducing any error. Once the ith and $(i+1)$th rows are thus estimated, the remaining rows of $\mathbf{V}$ may be constructed using Eqs. (2.10) and (2.20) of Section 2.2.

2.4.6 Multiple sensors and actuators

Scenario 5: Estimation of the instrumented rows of $\mathbf{V}$ with multiple actuators and sensors

In this situation suppose that the system is instrumented with N_a number of actuators, located at DOFs $a_i \in \mathcal{A} \subseteq \mathcal{D}$, and N_s number of sensors located at DOFs $s_i \in \mathcal{S} \subseteq \mathcal{D}$, with one co-located sensor-actuator pair, say at DOF $c = \mathcal{A} \cap \mathcal{S}$. We assume that none of the inputs from the actuators can be expressed as a linear combination of the other inputs in the time domain. Then, the pseudo-modal responses can be written, as in Eq. (2.46), in the form:

$$\ddot{\tilde{\eta}}_{j,a_i} + 2\zeta_j\omega_j\dot{\tilde{\eta}}_{j,a_i} + \omega_j^2\tilde{\eta}_{j,a_i} = f_{a_i} \quad \forall\, j \in \{1, 2, \cdots, N\},\ a_i \in \mathcal{A} \tag{2.53}$$

Writing the measured responses in terms of the pseudo-modal responses leads to:

$$\ddot{u}_{s_i} = \sum_{j=1}^{N} v_{s_i,j}\ddot{\eta}_j = \sum_{j=1}^{N} v_{s_i,j}\left(\sum_{a_i\in\mathcal{A}} v_{a_i,j}\ddot{\tilde{\eta}}_{j,a_i}\right) \quad \Rightarrow \quad \mathbf{G}\boldsymbol{\Psi}_{s_i} = \mathbf{Y}_{s_i} \quad \forall\, s_i \in \mathcal{S} \tag{2.54}$$

which are a set of N_s least squares problems, with the solution vectors,

$$\boldsymbol{\Psi}_{s_i} = \mathbf{G}^{\dagger}\mathbf{Y}_{s_i} = [(v_{s_i,1}v_{a_1,1})\ \cdots\ (v_{s_i,N}v_{a_1,N})\ \cdots\ \cdots\ (v_{s_i,1}v_{a_{N_a},1})\ \cdots\ (v_{s_i,N}v_{a_{N_a},N})]^T \tag{2.55}$$

$\forall\, s_i \in \mathcal{S}$, being $(N_aN) \times 1$ dimensional vectors, $\mathbf{Y}_{s_i} = [\ddot{u}_{s_i}(0)\ \ddot{u}_{s_i}(\Delta t)\ \ddot{u}_{s_i}(2\Delta t)\ \cdots]^T$, and

$$\mathbf{G} = \begin{bmatrix} \ddot{\tilde{\eta}}_{1,a_1}(0) & \cdots & \ddot{\tilde{\eta}}_{N,a_1}(0) & \cdots & \cdots & \ddot{\tilde{\eta}}_{1,a_{N_a}}(0) & \cdots & \ddot{\tilde{\eta}}_{N,a_{N_a}}(0) \\ \ddot{\tilde{\eta}}_{1,a_1}(\Delta t) & \cdots & \ddot{\tilde{\eta}}_{N,a_1}(\Delta t) & \cdots & \cdots & \ddot{\tilde{\eta}}_{1,a_{N_a}}(\Delta t) & \cdots & \ddot{\tilde{\eta}}_{N,a_{a_{N_a}}}(\Delta t) \\ \ddot{\tilde{\eta}}_{1,a_1}(2\Delta t) & \cdots & \ddot{\tilde{\eta}}_{N,a_1}(2\Delta t) & \cdots & \cdots & \ddot{\tilde{\eta}}_{1,a_{a_{N_a}}}(2\Delta t) & \cdots & \ddot{\tilde{\eta}}_{N,a_{a_{N_a}}}(2\Delta t) \\ \vdots & \vdots & \vdots & \vdots & \vdots & \vdots & \vdots & \vdots \end{bmatrix} \tag{2.56}$$

For ease of representation, suppose the DOF of co-location to be corresponding to sensor location s_1 and actuator location a_1, i.e. $c = a_1 = s_1$. For the measurement from the co-located sensor one gets, using the solution vector $\mathbf{\Psi}_{s_1=c}$:

$$\begin{aligned} v_{c,j} &= \sqrt{\psi_{j,s_1}} \quad \forall\, j \in \{1, 2, \cdots, N\} \\ v_{a_1,j} &= \frac{\psi_{(i-1)\times N+j,s_1}}{v_{c,j}} \quad \forall\, j \in \{1, 2, \cdots, N\},\ \{a_i \in \mathcal{A} : a_i \neq c\} \end{aligned} \tag{2.57}$$

Once the elements of $\mathbf{V}$ corresponding to the actuator locations, i.e. $v_{a_i,j}\ \forall\ j \in \{1, 2, \cdots, N\}$, $a_i \in \mathcal{A}$, are thus determined, the elements of $\mathbf{V}$ corresponding to the non-co-located sensor locations, i.e. $v_{s_i,j}\ \forall\, j \in \{1, 2, \cdots, N\}$, $\{s_i \in \mathcal{S} : s_i \neq c\}$, can be obtained using the solution vectors from the other least squares problems, $\mathbf{\Psi}_{s_i}\ \forall\ \{s_i \in \mathcal{S} : s_i \neq c\}$, as in case of Scenario 2:

$$v_{s_i,j} = \frac{\psi_{j,s_i}}{v_{c,j}} \quad \forall\, j \in \{1, 2, \cdots, N\},\ \{s_i \in \mathcal{S} : s_i \neq c\} \tag{2.58}$$

In this way, it is possible to uniquely estimate the rows of the mass normalized $\mathbf{V}$ matrix corresponding to all the instrumented (i.e. either having an actuator or a sensor) DOFs of the system, provided we have a co-located sensor-actuator pair in at least one DOF, and none of the inputs from the actuators can be expressed as a linear combination of the other inputs.

In the case that some of the inputs can be expressed as a linear combination of some of the other inputs, i.e. if some inputs are "dependent", we will not be able to uniquely determine all the instrumented rows of $\mathbf{V}$ at this stage, and may instead need additional instrumentation for unique identification as in Scenario 4b. Based on which of the inputs are dependent, it may still be possible to uniquely determine some of the instrumented rows of $\mathbf{V}$: for example, if none of the inputs are proportional to the input at the kth DOF, the kth row of $\mathbf{V}$ may be determined uniquely. If, however, the uniquely estimated kth row is the 1st or the Nth row of $\mathbf{V}$, then the complete $\mathbf{V}$ matrix may be estimated via the mode shape expansion approach developed in Section 2.2. Similarly, even in the presence of some dependent inputs, if two consecutive rows of $\mathbf{V}$ can be uniquely estimated through input-output balance, one can still use the mode shape expansion equations developed in Section 2.2 to estimate the remaining rows even though all the instrumented rows of $\mathbf{V}$ may not be evaluated through input-output balance alone.

A special case of the multi-input multi-output scenario is a fully instrumented system, where full instrumentation implies that each DOF has either an actuator or a sensor, with at least one co-located

sensor-actuator pair. If there are a full set of sensors such that $\mathcal{S} = \mathcal{D}$ and there is an actuator at DOF c, then the cth row of $\mathbf{V}$ may first be estimated using the first equation in Eq. (2.57), followed by the other rows via Eq. (2.58), with $\mathbf{\Psi}_{s_i}$ being the $(N \times 1)$ dimensional solution vector obtained using the measured acceleration response at DOF s_i, $\forall\ s_i \in \mathcal{D}$. If instead the system is instrumented with a full set of actuators such that $\mathcal{A} = \mathcal{D}$ and only one sensor at DOF c, and further assuming that all the inputs from the actuators are linearly independent in the time domain, the cth row of $\mathbf{V}$ may first be estimated using the first equation in Eq. (2.57), after which the remaining rows may be found via the second equation in Eq. (2.57), with $\mathbf{\Psi}_{s_i} = \mathbf{\Psi}_c$ being an $(NN \times 1)$ dimensional vector. Finally, for a fully instrumented system with each DOF having either an actuator and/or a sensor, i.e. $\mathcal{I} = \mathcal{A} \cup \mathcal{S} = \mathcal{D}$, with a co-located sensor-actuator pair at DOF c, the cth row of $\mathbf{V}$ may be identified with the first equation in Eq. (2.57), followed by the rows corresponding to the actuator locations $a_i \in \mathcal{A}$, using the second equation in Eq. (2.57), and finally the remaining rows corresponding to the sensor locations $s_i \in \mathcal{S}$ may be obtained via Eq. (2.58). Thus, for a fully instrumented system, it is possible to uniquely determine the complete mass normalized $\mathbf{V}$ matrix by just using the input-output balance approach, provided that the inputs are linearly independent in the time domain. If, however, some of the inputs are not linearly independent in the time domain then additional instrumentation, as in Scenario 4b, may be necessary for a unique identification.

At this point it should be emphasized that Scenario 5, with multi-input multi-output, has been discussed only to show the applicability of the proposed input-output balance in situations where we have multiple actuators and/or sensors. However, from the mode shape expansion procedure of Section 2.2, and from the input-output balance for Scenarios 1 – 4 in this section, it is evident that:

1. only 1 co-located sensor-actuator pair located at the 1st or Nth DOF, or,

2. two consecutive instrumented DOFs, with one co-located sensor-actuator pair and one additional sensor/actuator, and non-proportional inputs from the actuators, or,

3. two consecutive DOFs instrumented with either actuators and/or sensors, plus one co-located sensor-actuator pair at any other DOF, and non-proportional inputs from the actuators, or,

4. two consecutive DOFs instrumented with co-located sensor-actuator pairs in case of proportional inputs from the actuators,

are sufficient for a unique identification and thus define the minimal instrumentation requirement(s). Any additional sensor/actuator does not increase the amount of information, but may, of course, decrease the uncertainty and error in situations with considerable measurement noise. Additionally, while the single actuator – multiple sensors scenario may be the most common practice, the case of multiple actuators can also be important in certain practical situations where to excite the system sufficiently one may need to use more than one actuator. Furthermore, studying the case of multiple actuators also enables the identification of a "non-obvious" source of non-uniqueness in proportional loading from the actuators, which is practically important for experiments where such a situation may arise, and it also leads to the important observation that "incorrect" actuator – sensor placement might not be the only source of non-uniqueness. In Fig. 2.1 we summarize, in a tabulated format, the theoretical developments of Sections 2.2 and 2.4 into possible instrumentation configurations that will ensure a unique estimation of the mass normalized mode-shapes ($\mathbf{V}$) and, consequently, the mass ($\mathbf{M}$) and the stiffness ($\mathbf{K}$) matrices, with minimal instrumentation.

As a conclusion to this section, the following additional observations and comments regarding the applicability of the input-output balance approach presented above may be stated: First, in the derivations presented in this section, the output sensor considered was an accelerometer owing to its wide use in real life systems. This, however, is not a requirement or a necessity, since the approach may be employed also with velocity and displacement measurements, as well as with mixed types of outputs; in such cases the input-output balance equations will have to be modified by writing the $\mathbf{G}$ matrices using the pseudo-modal velocity or displacement responses instead of the pseudo-modal acceleration responses. Second, although the input-output balance approach presented in this section has been formulated in the time domain, it may be similarly applied in the frequency domain, by transforming the $\mathbf{G}$ and $\mathbf{Y}$ matrices to the frequency domain. For a fully instrumented system, the approach can thus be used to directly obtain the complete transfer function matrix. Finally, it is noteworthy that no assumption regarding the shear-type nature of the system has been made while deriving the necessary equations. Thus, while the proposed mode shape expansion procedure in Section 2.2 is applicable to shear-type systems, the input-output balance approach is applicable to any linear classically damped dynamic system. This general applicability of the input-output balance equations, along with the observation for a fully instrumented system discussed under Scenario 5, implies that for any linear classically damped system, fully instrumented with at least one co-located

sensor-actuator pair, the input-output balance equations can be used to estimate the complete mass normalized $\mathbf{V}$ matrix, and consequently the complete $\mathbf{M}$ and $\mathbf{K}$ matrices, of the system, as well as the complete transfer function matrix of the system by writing the equations in the frequency domain. This final observation is in agreement with the conclusion in [28], where it was shown that it is possible to estimate the physical parameters of any linear dynamic system by transforming the identified complex eigenvectors from an identified state-space model of the system to a certain basis, with the requirements for a successful transformation being that all the DOFs should contain either a sensor or an actuator with at least one co-located sensor-actuator pair.

2.5 Numerical Validation of Proposed Algorithms

To verify the performance of the equations developed in Sections 2.2 and 2.4, Monte Carlo simulations are performed on a 7-DOF shear-type structure to address the 10 different cases listed in Table 2.1. These 10 cases are chosen to illustrate the different instrumentation and input scenarios discussed in the preceding sections. The non-uniqueness example given earlier in Scenario 4a is included as Case 6 here; while the response at DOF 6, for this case, is identical to another shear-type system, also measuring the response at DOF 5 makes the identification unique. For each case, 100 simulations for identifying the system parameters are run, and the statistics of the errors in the estimated parameters are calculated using the estimation errors from the 100 simulations. The mean floor (lumped) masses of the structure are taken as $\mathrm{E}[m_i] = 2500$ kg $\forall\ i \in \{1, 2, \cdots, 6\}$, and $\mathrm{E}[m_7] = 2000$ kg, and the mean story (spring) stiffnesses are taken as $\mathrm{E}[k_i] = 5 \times 10^6$ N/m $\forall\ i \in \{1, 2, \cdots, 7\}$, where $\mathrm{E}[\cdot]$ denotes the expected value (mean) of the variable in brackets. For damped systems, modal damping is assumed, with a mean modal damping of $\mathrm{E}[\zeta_j] = 0.05\ \forall\ j \in \{1, 2, \cdots, 7\}$. In each simulation, the lumped masses, spring stiffnesses and modal damping ratios are slightly perturbed, in order to represent a realistic situation with operational variability, as: $m_i = \mathcal{U}(0.995, 1.005)\mathrm{E}[m_i]$, $k_i = \mathcal{U}(0.95, 1.05)\mathrm{E}[k_i]$ and $\zeta_j = \mathcal{U}(0.95, 1.05)\mathrm{E}[\zeta_j]$, $\forall\ i, j \in \{1, 2, \cdots, 7\}$, where $\mathcal{U}(l_l, l_r)$ denotes uniform probability distribution between the two limits l_l and l_r. This slightly perturbed structure in each simulation is excited by zero-mean Gaussian white noise sequences, applied as input force at the actuator locations. Thus, in any of the 10 cases, each of the 100 simulations differs from each other in terms of: (1) the applied input(s), which are different white noise sequences albeit having

Instrumentation Configuration	No. of Actuators	No. of Sensors	Input-Output Balance Scenario	Mode Shape Expansion Statements
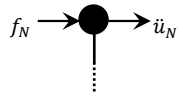	1	1	Scenario 1: Estimate N^{th} row of **V**	Statement 3: Estimate $(N-1)^{\text{th}}$ row of **V** *followed by* Statement 1: Estimate remaining rows of **V**
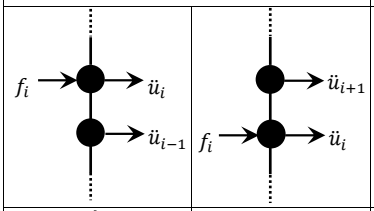	1	2	Scenario 2: Estimate i^{th} and $(i+1)^{\text{th}}$ or $(i-1)^{\text{th}}$ rows of **V**	Statement 1: Estimate remaining rows of **V**
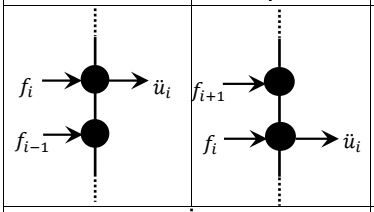	2	1	Scenario 3: Estimate i^{th} and $(i+1)^{\text{th}}$ or $(i-1)^{\text{th}}$ rows of **V**	Statement 1: Estimate remaining rows of **V**
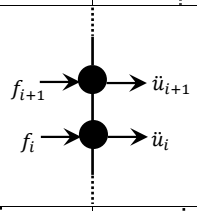	2 ($f_i \propto f_{i+1}$)	2	Scenario 4b: Estimate i^{th} and $(i+1)^{\text{th}}$ rows of **V**	Statement 1: Estimate remaining rows of **V**
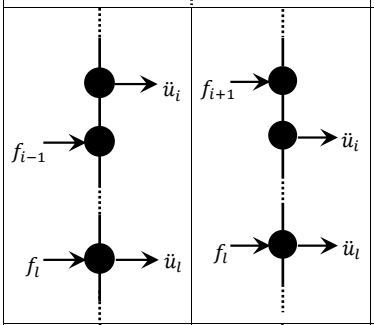	2	2	Scenario 5: Estimate i^{th} and $(i+1)^{\text{th}}$ or $(i-1)^{\text{th}}$ rows of **V**	Statement 1: Estimate remaining rows of **V**
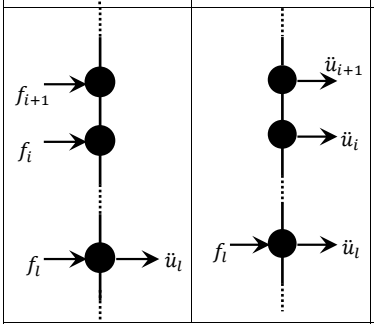	3 (or 1)	1 (or 3)	Scenario 5: Estimate i^{th} and $(i+1)^{\text{th}}$ rows of **V**	Statement 1: Estimate remaining rows of **V**
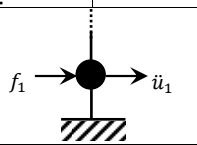	1	1	Scenario 1: Estimate 1^{st} row of **V**	Statement 2: Estimate 2^{nd} row of **V** *followed by* Statement 1: Estimate remaining rows of **V**

Figure 2.1: Minimal instrumentation configurations for unique estimation of $\mathbf{M}$ and $\mathbf{K}$ matrices.

a common underlying Gaussian distribution, and (2) exciting slightly different systems owing to the slight perturbations in the lumped masses, spring stiffnesses, and modal damping ratios. Finally, in order to see the performance of the proposed algorithms in the presence of measurement noise, the true acceleration responses are corrupted by adding zero-mean Gaussian white noise sequences. The noise sequences are scaled to have root-mean-square (RMS) values equal to a certain percentage of the RMS values of the corresponding true response signals. It should be noted that the issue of global identifiability is not related to the presence of measurement noise, but since using "noisy" data is inevitable in a real-life situation we use such artificially "polluted" data to discuss the performance of the proposed identification algorithm.

In order to use the algorithm developed in Sections 2.2 and 2.4, the modal frequencies and modal damping ratios of the system must be initially identified. To this end, we first use the known input and the "measured" (= true + noise) output data in the Eigensystem Realization Algorithm together with the Observer/Kalman filter IDentification algorithm (ERA-OKID) [25–27]. The system's frequencies and modal damping ratios are estimated from the eigenvalues of the identified state matrix. Once the eigenvalues and modal damping ratios are thus identified, we next use the input-output balance equations of Section 2.4 to estimate the instrumented rows of the mass normalized mode shape matrix $\mathbf{V}$, followed by the necessary mode shape expansion equations from Section 2.2 to get the complete $\mathbf{V}$ matrix (except in cases 9 and 10, where, due to complete instrumentation, input-output balance itself gives the complete $\mathbf{V}$). Finally, using the modal orthogonality relations of Eq. (2.4) we estimate the system's mass $\mathbf{M}$ and stiffness $\mathbf{K}$ matrices, from which the floor masses and story stiffnesses are respectively obtained.

While the ERA-OKID method provides good estimates of the system's natural frequencies even in the presence of significant measurement noise, the estimated modal damping ratios suffer from significant amount of errors in case of noisy measurements. Such a significant error in the modal damping will affect the input-output balance equations of Section 2.4, and this in turn will introduce errors in the expanded $\mathbf{V}$ matrix as well as the final estimated $\mathbf{M}$ and $\mathbf{K}$ matrices. To avoid this propagation of error, a nonlinear least squares optimization step is incorporated to obtain improved estimates of the system's natural frequencies and modal damping ratios. Suppose that the initial estimates (from ERA-OKID) of natural frequencies and modal damping ratios for a general N-DOF

shear-type system, are stored in a parameter vector:

$$\hat{\boldsymbol{\Theta}} = \{\hat{\omega}_1, \hat{\omega}_2, \cdots, \hat{\omega}_N, \hat{\zeta}_1, \hat{\zeta}_2, \cdots, \hat{\zeta}_N\} \tag{2.59}$$

Also suppose that the reconstructed outputs obtained from the initial realization (from ERA-OKID) are given by $\ddot{\hat{u}}_{s_i}$, where $s_i \in \mathcal{S} \subseteq \mathcal{D}$ denotes the measured DOFs. It can be shown through numerical simulations that these reconstructed responses usually have higher Signal-to-Noise Ratios than the corresponding original measured responses. Using the known input(s) along with the modal parameters in $\hat{\boldsymbol{\Theta}}$, the pseudo-modal response matrix $\hat{\mathbf{G}}|_{\hat{\boldsymbol{\Theta}}}$ of Section 2.4 may be constructed, and an initial estimate $\hat{\boldsymbol{\Psi}}|_{\hat{\boldsymbol{\Theta}}}$ of the solution may be obtained from the least squares solution of the input-output balance equations of Section 2.4. Note that this estimated $\hat{\boldsymbol{\Psi}}|_{\hat{\boldsymbol{\Theta}}}$ is affected not only by the measurement error in $\ddot{\hat{u}}_{s_i}$, but also by the erroneous modal parameter vector $\hat{\boldsymbol{\Theta}}$ whose effect on $\hat{\mathbf{G}}|_{\hat{\boldsymbol{\Theta}}}$ may be thought of as equivalent to having an erroneous model in the linear least squares problem. While the linear least squares estimate $\hat{\boldsymbol{\Psi}}|_{\hat{\boldsymbol{\Theta}}}$ minimizes, for a fixed $\hat{\mathbf{G}}|_{\hat{\boldsymbol{\Theta}}}$, the residual between the observed (reconstructed in our case) $\ddot{\hat{u}}_{s_i}$ and the model $\hat{\mathbf{G}}|_{\hat{\boldsymbol{\Theta}}}\hat{\boldsymbol{\Psi}}|_{\hat{\boldsymbol{\Theta}}}$, it cannot minimize the error due to erroneous $\hat{\boldsymbol{\Theta}}$ i.e. the modeling error. Using these initial estimates $\hat{\mathbf{G}}|_{\hat{\boldsymbol{\Theta}}}$ and $\hat{\boldsymbol{\Psi}}|_{\hat{\boldsymbol{\Theta}}}$ a second set of reconstructed responses, $\ddot{\hat{u}}^*_{s_i}|_{\hat{\boldsymbol{\Theta}}} = \hat{\mathbf{G}}|_{\hat{\boldsymbol{\Theta}}}\hat{\boldsymbol{\Psi}}|_{\hat{\boldsymbol{\Theta}}}$ are obtained, which will not match the first set of reconstructed responses $\ddot{\hat{u}}_{s_i}$ owing to the modeling error (and also because $\hat{\boldsymbol{\Psi}}|_{\hat{\boldsymbol{\Theta}}}$ is but a least squares solution, and will not be exact except in simulations). A nonlinear optimization problem is then set up to obtain the optimal parameter vector $\hat{\boldsymbol{\Theta}}^*$ which will minimize the mismatch between $\ddot{\hat{u}}^*_{s_i}|_{\hat{\boldsymbol{\Theta}}}$ and $\ddot{\hat{u}}_{s_i}$:

$$\hat{\boldsymbol{\Theta}}^* = \arg\min_{\hat{\boldsymbol{\Theta}}} \left|\left|\mathbf{Y}^* - \mathbf{Y}\right|\right|_2 \tag{2.60}$$

where

$$\begin{aligned}
\mathbf{Y}^* &= [\ddot{\hat{u}}^*_{s_1}|_{\hat{\boldsymbol{\Theta}}}(0)\ \ddot{\hat{u}}^*_{s_1}|_{\hat{\boldsymbol{\Theta}}}(\Delta t)\ \cdots\ \ddot{\hat{u}}^*_{s_2}|_{\hat{\boldsymbol{\Theta}}}(0)\ \ddot{\hat{u}}^*_{s_2}|_{\hat{\boldsymbol{\Theta}}}(\Delta t)\ \cdots\ \cdots\ \ddot{\hat{u}}^*_{s_{N_s}}|_{\hat{\boldsymbol{\Theta}}}(0)\ \ddot{\hat{u}}^*_{s_{N_s}}|_{\hat{\boldsymbol{\Theta}}}(\Delta t)\ \cdots]^T \\
\mathbf{Y} &= [\ddot{\hat{u}}_{s_1}(0)\ \ddot{\hat{u}}_{s_1}(\Delta t)\ \cdots\ \ddot{\hat{u}}_{s_2}(0)\ \ddot{\hat{u}}_{s_2}(\Delta t)\ \cdots\ \cdots\ \ddot{\hat{u}}_{s_{N_s}}(0)\ \ddot{\hat{u}}_{s_{N_s}}(\Delta t)\ \cdots]^T
\end{aligned} \tag{2.61}$$

This optimization problem is solved here using the nonlinear least squares function *lsqnonlin* of MATLAB® [30]. This input-output balance - cum - optimization scheme is essentially a two-step iterative optimization: for a given $\hat{\boldsymbol{\Theta}}$, the optimal $\hat{\boldsymbol{\Psi}}$ is obtained in the first step with input-output balance, while $\hat{\boldsymbol{\Theta}}$ is updated in the second step with nonlinear least squares, and the steps are repeated iteratively till convergence. Once the optimal modal frequencies and damping ratios are obtained,

these values are used in the necessary equations of Sections 2.2 and 2.4 as described in the previous paragraphs. An alternative approach would be based on Total Least Squares [31]; this is not adopted here, but is instead used in the next chapter.

The **M**-**K** identification procedure proposed herein involves several steps: (1) obtaining initial estimates $\{\hat{\omega}_j, \hat{\zeta}_j\}$, (2) obtaining optimized estimates $\{\hat{\omega}_j^*, \hat{\zeta}_j^*\}$ using Eq. (2.60), in presence of measurement noise, (3) estimating $\mathbf{V}$ through input-output balance and mode shape expansion, and (4) estimating $\mathbf{M}$ and $\mathbf{K}$ through modal orthogonality. In the numerical simulations discussed in this section, the errors of the parameter estimates are calculated at each step relative to their true values. Tables 2.2 – 2.5 show the statistics of these errors obtained from the 100 simulations run for each of the 10 cases of Table 2.1: For the ith element of parameter class $\boldsymbol{\theta}$, with $\theta_{i,k}$ and $\hat{\theta}_{i,k}$ respectively denoting its true vale and estimate in the kth simulation, the relative error $\varepsilon(\theta_{i,k})$ (in percent) is first calculated as:

$$\varepsilon(\theta_{i,k}) = \frac{\hat{\theta}_{i,k} - \theta_{i,k}}{\theta_{i,k}} \times 100 \quad \forall\, i \in \{1, 2, \cdots, 7\},\ k \in \{1, 2, \cdots, 100\} \tag{2.62}$$

The sample mean and standard deviation of $\varepsilon(\theta_{i,k})$ are then be calculated as:

$$\mu_{\varepsilon(\theta_i)} = \frac{\sum_{k=1}^{100} \varepsilon(\theta_{i,k})}{100}; \quad \sigma_{\varepsilon(\theta_i)} = \left(\frac{\sum_{k=1}^{100} \varepsilon^2(\theta_{i,k}) - 100\mu^2_{\varepsilon(\theta_i)}}{99} \right)^{1/2} \tag{2.63}$$

The statistics listed in Tables 2.2 – 2.5 are the maximum absolute values, with respect to index i, of these sample means and standard deviations:

$$\mu_{\varepsilon(\theta)} = \max_{i \in \{1, \cdots, 7\}} \left(\left| \mu_{\varepsilon(\theta_i)} \right| \right); \quad \sigma_{\varepsilon(\theta)} = \max_{i \in \{1, \cdots, 7\}} \left(\left| \sigma_{\varepsilon(\theta_i)} \right| \right) \tag{2.64}$$

To quantify the errors in the identified complete $\mathbf{V}$ matrices, we use the deviations from 1 of the Modal Assurance Criterion (MAC) [21], calculated for each mode, and the Coordinate Modal Assurance Criterion (COMAC) [22], calculated for each DOF.

Comparing the errors statistics in Tables 2.2 and 2.3, it is evident that the optimization in Eq. (2.60) does improve the estimates of the modal frequencies and damping ratios. The error statistics in Tables 2.4 and 2.5 illustrate that the proposed input-output balance and mode shape expansion approaches perform reasonably well in estimating the complete $\mathbf{V}$ matrix, and the lumped masses and spring stiffnesses, even under the constraints of very limited instrumentation and no prior information about the physical parameter values. The maximum mean error in the masses and stiffnesses are

Table 2.1: Different cases considered in numerical examples.

Case	Damping, E$[\zeta_j]$ (%)	Noise (%)	Actuator Location (DOFs)	Sensor Location (DOFs)	Notes
1	0	0	1	1	—
2	5	0	1	1	—
3	5	10	7	7	—
4	5	10	6	5,6	—
5	5	10	5,6	6	—
6	5	10	5,6	5,6	$2f_6 = 3f_5$
7	5	10	1,3,7	7	—
8	5	10	3,6	4,6	—
9	5	10	4	1 to 7	Full set of sensors
10	5	10	1 to 7	6	Full set of actuators

mostly less than 1%, and the maximum standard deviation in error are mostly between 0.5% and 3.5%. When the measurements are not corrupted by noise, the estimates are exact, even with only a single sensor, as should be expected from a theoretically exact formulation.

2.6 Implementation with Experimental Data[2]

The structural identification algorithm is applied with experimental data from a set of experiments conducted in the Los Alamos National Laboratory (LANL) on a 3-story model frame structure [32]. These data have been used for experimental verification in several studies on modal identification, model updating and damage detection [32–35]. Here we use this data for modal/physical parameter identification using the minimal instrumentation set-up. The test set-up, shown in Fig. 2.2, consists of a 3-story aluminium frame model; the base plate of the model slides on rails and is excited by means of an electrodynamic shaker. Each floor (including the base) are instrumented using accelerometers located at the centerline, and a load cell measures the input force provided by the shaker. Since the

[2]I would like to thank the Los Alamos National Laboratory, Engineering Institute, for making the experimental data publicly available for research purposes.

Table 2.2: Maximum statistics of estimation errors (%) in $\hat{\omega}$ and $\hat{\zeta}$ estimated using ERA-OKID.

Case	$\mu_{\varepsilon(\omega)}$	$\sigma_{\varepsilon(\omega)}$	$\mu_{\varepsilon(\zeta)}$	$\sigma_{\varepsilon(\zeta)}$
1	2.44×10^{-11}	5.31×10^{-10}	—	—
2	9.18×10^{-13}	1.98×10^{-11}	1.30×10^{-10}	8.87×10^{-10}
3	0.3508	0.6044	7.3643	13.7574
4	0.0051	0.0518	0.6998	1.1394
5	0.0283	0.1425	1.4748	2.7899
6	0.1117	0.5866	4.7269	9.8593
7	0.0127	0.1011	1.8008	1.8108
8	0.0023	0.0461	0.5093	0.9423
9	0.0017	0.0588	0.1516	0.8838
10	0.0442	0.0686	1.2830	1.2084

Table 2.3: Maximum statistics of estimation errors (%) in optimal modal parameters ($\hat{\omega}^*$ and $\hat{\zeta}^*$).

Case	$\mu_{\varepsilon(\omega^*)}$	$\sigma_{\varepsilon(\omega^*)}$	$\mu_{\varepsilon(\zeta^*)}$	$\sigma_{\varepsilon(\zeta^*)}$
1	—	—	—	—
2	—	—	—	—
3	0.0317	0.1916	2.0221	3.9861
4	0.0029	0.0297	0.5569	0.9898
5	0.0088	0.0693	1.2022	2.2315
6	0.0451	0.2692	1.1521	4.3901
7	0.0044	0.0436	1.5102	1.0431
8	0.0028	0.0272	0.4390	0.8288
9	0.0025	0.0273	0.1338	1.0471
10	0.0194	0.0391	1.0605	1.1510

Table 2.4: Maximum statistics of estimation errors (%) in expanded mass normalized mode shape matrix ($\mathbf{V}$).

Case	$\mu_{\varepsilon(\text{MAC})}$	$\sigma_{\varepsilon(\text{MAC})}$	$\mu_{\varepsilon(\text{COMAC})}$	$\sigma_{\varepsilon(\text{COMAC})}$
1	3.00×10^{-17}	2.10×10^{-16}	5.33×10^{-17}	2.51×10^{-16}
2	3.55×10^{-17}	1.96×10^{-16}	3.55×10^{-17}	2.46×10^{-16}
3	0.0010	0.0012	0.0005	0.0005
4	0.0001	0.0001	6.30×10^{-05}	7.36×10^{-05}
5	0.0002	0.0003	0.0001	0.0002
6	0.0114	0.0146	0.0058	0.0075
7	0.0001	0.0001	5.08×10^{-05}	6.48×10^{-05}
8	8.08×10^{-05}	7.18×10^{-05}	5.24×10^{-05}	5.21×10^{-05}
9	0.0002	0.0006	0.0004	0.0007
10	0.0001	0.0001	0.0002	0.0002

Table 2.5: Maximum statistics of estimation errors (%) in estimated lumped masses and spring stiffnesses.

Case	$\mu_{\varepsilon(m)}$	$\sigma_{\varepsilon(m)}$	$\mu_{\varepsilon(k)}$	$\sigma_{\varepsilon(k)}$
1	9.01×10^{-09}	2.81×10^{-07}	9.23×10^{-09}	2.86×10^{-07}
2	1.10×10^{-11}	1.38×10^{-10}	8.09×10^{-12}	1.22×10^{-10}
3	0.3881	0.7810	0.2874	0.8187
4	0.2951	2.1706	0.2727	2.1264
5	0.6110	3.3774	0.4974	3.3917
6	1.0706	4.4682	1.4749	4.6020
7	0.0517	0.2826	0.0381	0.2651
8	0.1907	1.8751	0.2206	1.7779
9	0.1698	2.4299	0.8100	5.7811
10	0.1312	1.2441	0.3843	2.8530

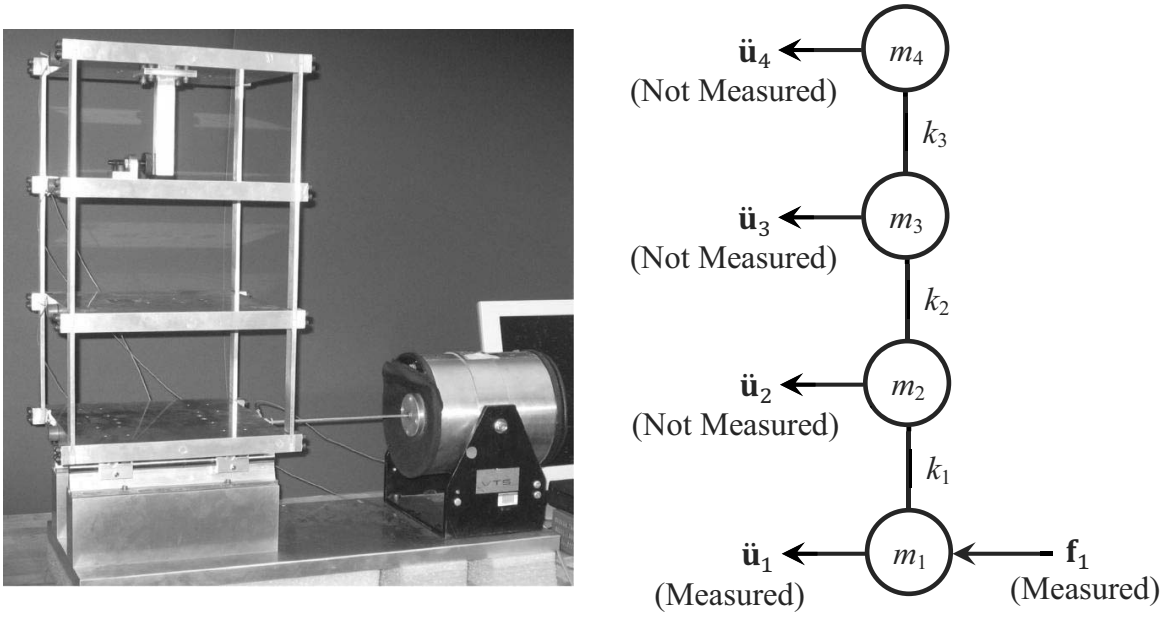

Figure 2.2: LANL test structure (adopted from [32]), and free-free analytical model assumed in this paper (with known input $\mathbf{f}_1$, and measured output $\ddot{\mathbf{u}}_1$).

structure slides on rails (is unconstrained), there exists a rigid body mode in addition to the three structural modes. The input forces are white noise signals, band limited in 20 - 150 Hz so as not to excite the rigid body mode (below 20 Hz). In addition to a baseline frame, several other states of the frame, with added floor masses/changed column cross-sections etc., are also tested; here we only consider the baseline state, while some of the modified states are considered in Chapter 5 for structural health monitoring. Each state of the system is tested 50 times.

We model the frame as a 4-DOF free-free system (neglecting the rail friction), as shown in Fig. 2.2. Although the system was completely instrumented in the actual experiments, as a hypothetical experimental scenario, we consider a single actuator-single sensor set-up, where only the acceleration response of the base plate is measured along with the applied input force. It should be emphasized that, for the 4-DOF model, with this set-up we are measuring *only* 25% of the system.

The measured base acceleration output and the applied input force to the base are first used in the ERA-OKID method to identify the three sets of structural modal frequencies and damping ratios. The means and standard deviations of these experimental modal parameters are then computed using the identifications from the 50 tests. These mean values, and the coefficients of variation (COV (in %) =

standard deviation/mean $\times 100$) are:

$$\mu_f = \{31.3, 55.0, 72.3\} \text{ Hz}; \qquad \text{COV}_f = \{0.1, 0.1, 0.2\} \ \%$$
$$\mu_\zeta = \{4.1, 0.9, 1.1\} \ \%; \qquad \text{COV}_\zeta = \{1.7, 6.1, 18.1\} \ \%$$

The mean estimates compare reasonably well with the corresponding estimates obtained in [32]. From the coefficients of variation, it is evident that the modal frequency estimates from the different tests are very consistent. While the estimated damping ratios from the different tests show some dispersion, with increased dispersion in the higher modes, a high estimation uncertainty associated with identified damping is often encountered in civil structural identification [36,37]. As [37] shows, noise contaminated measurement data usually contains much lesser information about damping compared to frequency. Moreover, structural damping has an inherent variability owing to the "complexity of damping mechanisms", and is, in general, a manifestation of the combined effects of several different types of physical (energy dissipating) phenomenon ([38,39]). In fact, as [38] states: "Quantification of damping is by far the most vexing problem in structural engineering"; although this observation is made by the authors with regard to damping estimation at the structural design stage, it remains similarly true in structural identification exercises.

Once the three sets of structural modal frequencies and damping ratios are identified, they are used in the input-output balance equations, balancing the base acceleration output with the input force to the base, to obtain the coefficients of the three mass normalized mode shapes at the base. The input-output balance is performed with only the three structural modes (modes 2 to 4), i.e. excluding the rigid body translation (mode 1), since, owing to the band limitedness of the applied input, the acceleration response should not contain any rigid body component [32].

The subsequent identification steps require the mode shape expansion from the base to the three higher (unobserved) floors, and then the use of the modal orthogonality relations to estimate $\mathbf{M}$ and $\mathbf{K}$. However, in both these operations, we would need the mass normalized rigid body mode shape. To this end, we use an additional information: the total mass of the system, $M_T = \sum_{i=1}^{4} m_i$. M_T is taken as $6.5 \times 4 = 26$ kg, using the structural dimensions given in [32] and the mass density of aluminium. Then, letting the mass normalized rigid body mode shape be: $\mathbf{v}_1 = \{c, c, c, c\}$, and using mass orthogonality, the constant c can be evaluated as:

$$c = \sqrt{1/M_T} \tag{2.65}$$

Following this, the Statement 2 of the mode shape expansion is applied to estimate the mass normalized mode shapes at the first floor, with the slight modification of $\mathbf{a}_{1,2} = -\mathbf{a}_{1,1}$ for a free-free (instead of a shear-type) system, and with $\lambda_{1,1} = 0$ for the rigid body mode. The mass normalized mode shapes at the second and third floors are then estimated using the Statement 1 of the mode shape expansion. At this stage, we then have a complete (4×4) mass normalized mode shape matrix (including the rigid body mode), and a complete eigenvalue matrix (with $\lambda_{1,1} = 0$) from the identified frequencies, for the 4 DOF model of the system; using the modal orthogonality relations with these we estimate the complete (4×4) $\mathbf{M}$ and $\mathbf{K}$ matrices of the system. The estimated $\mathbf{M}$ and $\mathbf{K}$ matrices are found to be respectively diagonal and tridiagonal symmetric, with $\mathbf{K}$ also being singular and having the form as for a 1-D free-free system (i.e. sum of the elements in any row/column of $\mathbf{K}$ is zero); such properties of the identified $\mathbf{M}$ and $\mathbf{K}$ matrices should be expected as the mode shape expansion equations explicitly utilize these properties. The individual floor masses (including the base mass) and story stiffnesses are finally estimated from the identified $\mathbf{M}$ and $\mathbf{K}$ matrices. The means and coefficients of variation, computed using the estimates from the 50 tests, of these mass and stiffness parameters are:

$$\mu_m = \{7.0, 7.5, 6.3, 5.2\} \text{ kg}; \qquad \text{COV}_m = \{0.6, 0.5, 0.6, 0.7\} \ \%$$

$$\mu_k = \{4.6, 4.3, 3.2\}\ 10^5 \text{ N/m}; \qquad \text{COV}_k = \{1.0, 0.4, 0.9\} \ \%$$

It is evident from these statistics that the parameter estimates are reasonably consistent across the different tests. The distribution of the masses/stiffnesses between the different floors/stories are fairly uniform, as should be expected from the structural geometry, but not exactly uniform, reflecting the inherent individual variabilities (in geometry, connections etc.) in the different floors/stories. Even though measurements from none of the higher floors (1st to 3rd) are used in the identification exercise, the estimated parameter values at these unobserved locations are still realistic. It should be emphasized that the parameter estimates are intricately dependent on the total mass information M_T. This dependency is not that of just a single scalar factor of proportionality (unlike in the next two chapters), since M_T's use here is essentially to determine the rigid body mode; any error in M_T propagates nonlinearly, and not in just a proportional form, to the estimates of the unobserved rows of $\mathbf{V}$. In this current example, the total mass information M_T is not accurate, since we do not include in it the masses of the attachment mechanism of the base to the rails, of the bumper on the 2nd floor and the extra column on the 3rd floor (as we do not know these masses). Even then the final

estimates of the mass and stiffness parameters seem reasonable. Moreover, as is evident from example comparisons in Figs. 2.3 and 2.4, the measured experimental responses are in good agreement with the simulated responses of the identified systems (with both the measured and predicted responses corresponding to the same test/input force), even at the unobserved DOFs (Fig. 2.4) whose response measurements are not used in the identification exercise. Finally, the low coefficients of variation in Table 2.3 (mostly less than 1%), indicating a low uncertainty in the mass/stiffness parameter estimates from the different tests, suggests the possibility of using such parameter estimates in reliable detection of any structural changes, as e.g. in structural health monitoring considered in Chapter 5 with some of the modified states of the frame.

2.7 Conclusions

An algorithm is developed in this chapter for identifying the physical parameters (lumped masses and spring stiffnesses) of shear-type systems using input-output data. The proposed algorithm starts with estimates of the complete sets of modal frequencies and damping ratios. The first major step is to estimate the components of the mass normalized mode shape matrix at the actuator and/or sensor locations, for which an input-output balance procedure has been proposed. The input-output balance attempts to give unique estimates of the mass normalized mode shapes at all the instrumented (with an actuator and/or a sensor) DOFs in the system. In the derivations of this approach, the non-uniqueness owing to absence of co-located sensor-actuator pair, possible non-uniqueness caused by inputs not being independent, as well as the possible unique and complete identification of a fully instrumented structure have been discussed. The situation of dependent inputs may be practically important, e.g. when a 3-dimensional building is tested using only a single actuator; such a situation is illustrated later in the thesis with a numerical example in Appendix A, and as discussed in this chapter, in such situations the direct input-output balance results will need some post-processing. While the input-output balance was formulated in the time domain using acceleration response measurements, it may also be formulated in the frequency domain as well as with velocity or displacement measurements. Moreover, the approach may be applied not only to shear-type systems, but to any linear classically damped dynamic system as well. The approach may also be coupled with a nonlinear least squares optimization step to improve the initial modal frequency and damping ratio estimates in the presence

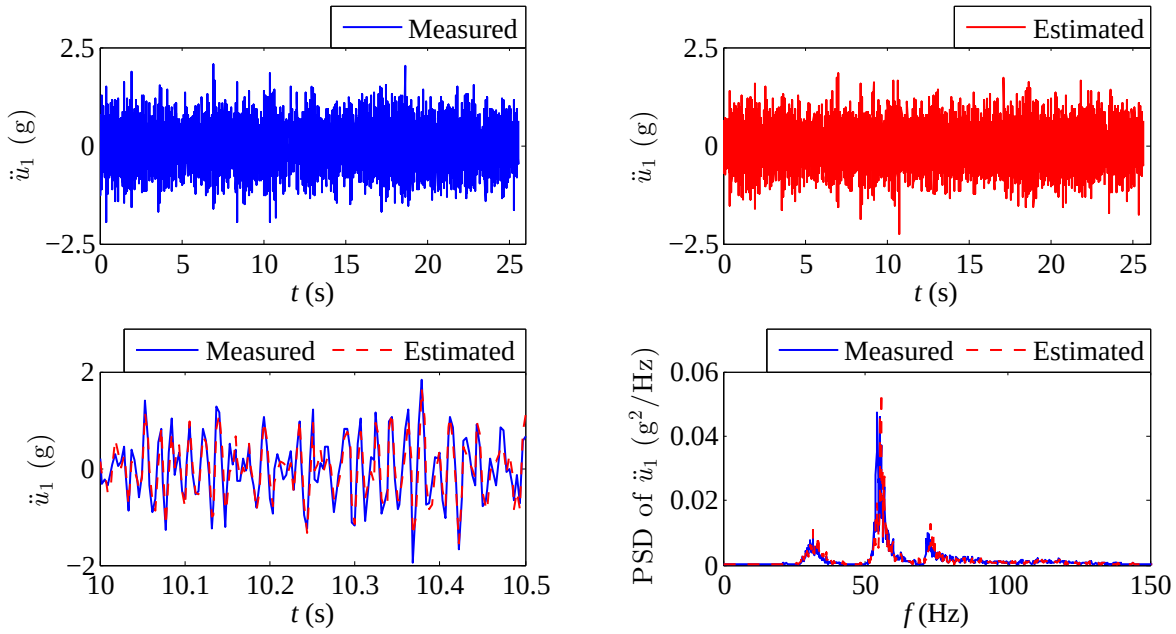

Figure 2.3: Comparison of measured base acceleration response with base acceleration response of estimated system for test 1 of State 1.

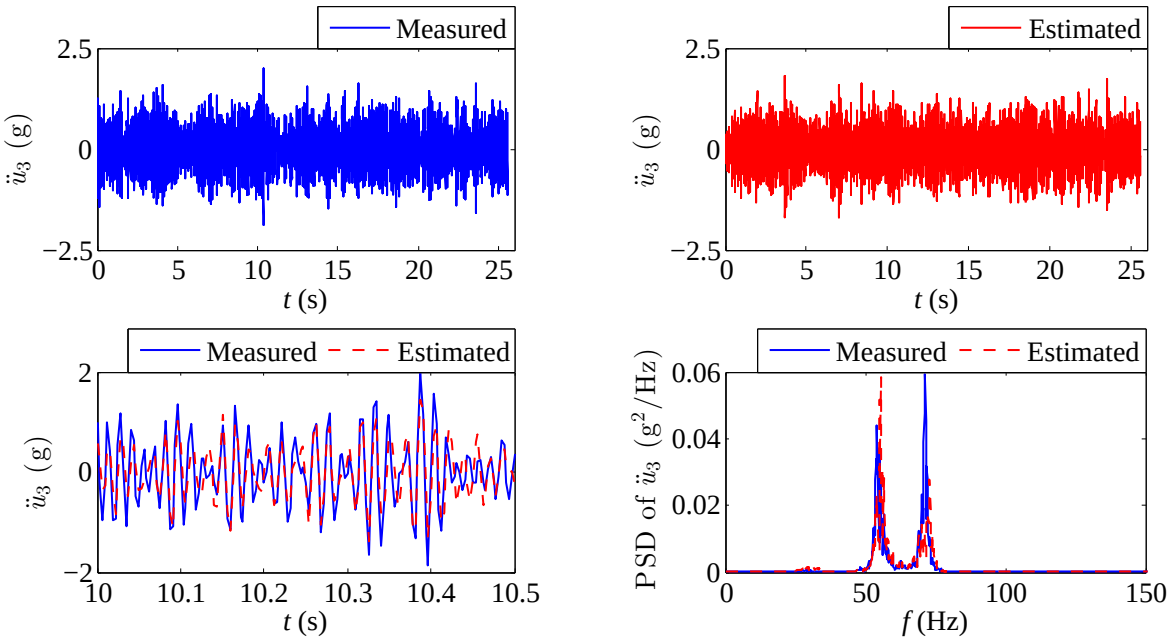

Figure 2.4: Comparison of measured 2nd floor acceleration response with 2nd floor acceleration response of estimated system for test 1 of State 1. (This response is considered *unmeasured*, and not used in the identification of the structural system.)

of measurement noise; when the ERA-OKID approach was used to obtain the initial estimates, this optimization step proved to be especially useful to decrease errors in the identified modal damping ratios.

The second major step comprises a mode shape expansion method which expands the mass normalized mode shapes determined in the first step from the instrumented to the non-instrumented structural DOFs. This expansion method was developed to address the limitations set forth by incomplete instrumentation, and it is formulated in such a way that the non-instrumented rows of the mode shape matrix are successively obtained as solutions to sets of linear simultaneous equations. While deriving the necessary equations for the expansion, the issue of global identifiability vis-a-vis instrumentation set-ups has also been addressed, and it has been shown that a knowledge of either the 1st or the last or any two consecutive rows of the mass normalized mode shape matrix guarantees a unique expansion to a complete mass normalized mode shape matrix for a shear-type system. Once the complete mass normalized mode shape matrix is obtained by the mode shape expansion procedure, the mass and stiffness matrices of the system are to be estimated using modal orthogonality. These estimated physical matrices may be considered to represent the current state/condition of the system, and may be used for model validation and/or damage detection.

Based on the theoretical derivations involved in the input-output balance and mode shape expansion procedures, minimal and near-minimal instrumentation set-ups for shear-type systems which guarantee unique estimation of the mass normalized mode shape matrix, and consequently the mass and stiffness matrices, have also been defined. These optimal instrumentation set-ups require only 1 or 2 actuators and 1 or 2 sensors, and can be summarized as: (i) only 1 co-located sensor-actuator pair located at the 1st or Nth DOF, or (ii) two consecutive instrumented DOFs, with one co-located sensor-actuator pair and one additional sensor/actuator, and non-proportional inputs from the actuators, or (iii) two consecutive DOFs instrumented with either actuators and/or sensors, plus one co-located sensor-actuator pair at any other DOF, and non-proportional inputs from the actuators, or (iv) two consecutive DOFs instrumented with co-located sensor-actuator pairs in case of proportional inputs from the actuators. The discussion on instrumentation is intended to help in experiment design by providing the monitoring personal with an increased flexibility in instrumentation set-ups, using the minimal amount of instruments but meeting the global identifiability requirements by their proper placement. While the discussion specifies only the bare minimum necessary instrumentation, addi-

tional instruments, while not increasing the quantity of information, may be expected to improve the quality of information and hence decrease the estimation uncertainty/error, especially in situations with high measurement noise. Moreover, while all the *permissible* instrumentation set-ups for global identifiability should provide the same information in an ideal situation, in practice, accounting for the facts that all DOFs neither respond to the same extent nor can their responses be expected to have the same signal-to-noise ratio, the quality of information content in the different set-ups will vary, and hence the estimation uncertainty associated with the different set-ups will vary. Thus, once a set of permissible set-ups is obtained satisfying the global identifiability requirements, the individual set-ups in this set may be further ranked according to some information measure ([40,41]), to decide on the optimal (most informative) set-up amongst them.

An extensive suite of numerical examples using simulated data from a 7-DOF system is considered to illustrate the performance of the identification approach. As evidenced by these examples, the advantages of the approach lies: (a) in its ability to obtain reliably accurate estimates of the mass and stiffness parameters using measured data from minimal instrumentation, (b) in its non-requirement of any *a priori* information of the physical parameter values, and (c) in its reasonable robustness to measurement noise. Additionally, the identification exercise mainly involves solutions of linear systems of equations, and hence has the advantage of straightforward implementation.

The identification approach is also applied to experimental data from a 3-story aluminium frame model tested in the Los Alamos National Laboratory [32]. The frame slides on rails, and is hence modeled as a free-free system in this paper. It is shown that using only the applied input and measured acceleration output of the base, the approach provides reasonable identification of the floor masses and stiffnesses, with low estimation uncertainty across different tests. The identified models can also predict the response well, even at unmeasured DOFs. The reliable performance of the method even with incomplete instrumentation of the monitored system and no *a priori* information about the system's physical parameters, highlights its potential in structural identificantion/health monitoring applications.

Chapter 3

Identification with Incomplete Instrumentation and Global Identifiability Requirements under Base Excitation[1]

In this chapter we concentrate on the cases in which a shear-type system is excited not through actuators but through ground motions. The difference between the two excitation types is important and dictates the *a priori* information necessary for the solution. For example, the global identifiability problem has been investigated for a single force actuator case by Franco et al. [3], and for more general sensor/actuator setups in Chapter 2 [4]; neither requires any *a priori* knowledge of the system's physical parameters. On the other hand, Udwadia nd his co-workers [1, 17] deal with the situation where the input is base excitation and require knowledge of the complete mass matrix. Moreover, while in [3, 4] multiple possible instrumentation setups are identified which guarantee unique solutions to the mass and stiffness matrices, in [1, 17] only one such instrumentation setup is identified.

One of the reasons behind this increased complexity may be related to the problem identified in

[1]This chapter is part of an article co-authored with Profs. Raimondo Betti and Hilmi Lus, currently under review in Structural Control and Health Monitoring [5]. A preliminary form of the chapter was presented in the 32nd International Modal Analysis Conference, Orlando, 2014 [42].

Chapter 2 for the case of proportional inputs: if there are two actuators applying proportional forces at two DOFs, then one needs to place sensors at both of these two DOFs in order to uniquely estimate the two corresponding rows of the mass normalized mode shape matrix, whereas only one sensor at either of the DOFs would suffice were the inputs not proportional; base excitation of shear–type systems is equivalent to applying proportional inputs at all DOFs. The second reason stems from the fact that in structures subjected to base accelerations the input is not completely defined unless one knows the complete mass matrix. This incompleteness of information in terms of the applied input, coupled with the incompleteness in modal information from limited instrumentation, makes the base excitation case vis-$\grave{a}$-vis the global identifiability problem of the system a complex affair. Other questions that demand attention in this context are: (i) what is the minimal *a priori* information necessary for a unique identification, i.e. is it possible to identify the system knowing some of the masses instead of the complete mass matrix, or is the knowledge of the complete mass matrix absolutely essential? (ii) what should be the minimal number and the choice of instrumented DOFs for a unique identification?

This chapter attempts to develop a robust algorithm for the identification of the mass and stiffness parameters of rigid-floor shear-building type structures subjected to base excitation, using the measured output along with the base acceleration input (if available), under the constraint of incomplete instrumentation. It should be highlighted that, although the chapter is written for base excitation, the different developments can be directly applied to any general output-only situation as well. The natural frequencies and non-mass normalized mode shape components at the sensor locations that are prerequisites to the approach proposed herein, may be obtained using any suitable experimental/operational modal analysis techniques. As in Chapter 2, the measured responses are assumed to be sufficiently rich so as to allow the identification of all the structural modes at the sensor locations, and the mass and stiffness matrices are estimated using the modal orthogonality relations. To get the complete mass normalized mode shape matrix, a mode shape normalization procedure is developed, and used along with the mode shape expansion method proposed in Chapter 2, and extended to 2/3-dimensional (2/3-D) systems discussed in this chapter. These mode shape normalization and expansion approaches incorporate the structural topology information of the physical system in terms of its modal parameters. Since not all instrumentation set-ups and available *a priori* information about the system's physical parameters may give a unique normalization and/or expansion of the mode shapes, the following issues are investigated: (a) what is the minimum necessary *a priori* in-

formation, (b) what should be the minimum number of instrumented DOFs, given certain available *a priori* information, and (c) how to determine which should be the instrumented DOFs, for a unique estimation of the complete mass normalized mode shape matrix? Thus, in the process of developing the identification methodology, the study also provides a technique to determine a wide set of instrumentation set-ups guaranteeing unique solutions to the inverse problem. The possible implications of low translational-rotational coupling in 2/3-D systems are also highlighted in this context. Although the proposed approach mainly involve solutions of linear systems of equations, and hence have the advantage of straightforward implementation, some practical implementation issues, e.g. induced by noisy data, which may arise in the solution process are also discussed, along with possible strategies to address them. The performance of the method is evaluated using an extensive suite of numerical simulations and shake table experiments.

3.1 Problem Statement and Minimal Necessary *A Priori* Information

Consider a system that can be modelled as an N–DOF classically damped shear–type model: by shear–type is meant a building model in which all floors are rigid plates with 3 DOFs comprising two lateral translations and one in plane rotation. Shear–type models in which only one translation, one translation and the rotation, and all 3 DOFs per floor are active will be called 1 dimensional (1–D), 2 dimensional (2–D) and 3 dimensional (3–D) models, respectively. Let $\mathcal{D}$ denote the set, with N elements, of all DOFs, and $\mathcal{S}$ denote the set, with N_s elements, of DOFs instrumented with sensors which measure the response (acceleration and/or velocity and/or displacement) of the system. For an N_D-dimensional shear-type model subjected to base excitation, the equation of motion in physical coordinates has the form:

$$\mathbf{M\ddot{u}} + \mathbf{C\dot{u}} + \mathbf{Ku} = -\mathbf{M}\boldsymbol{\iota}\mathbf{a_g} \tag{3.1}$$

where $\mathbf{a_g}(t)$ is the vector of ground acceleration input and $\boldsymbol{\iota}$ is the influence matrix of dimension $N \times N_D$, constructed by vertically (row-wise) stacking (N/N_D) many $N_D \times N_D$ identity ($\mathbf{I}$) matrices. Our objectives are (i) to identify the mass and the stiffness matrices of the system's model using the known/unknown applied ground motion input and the response (output) data measured at N_s locations with incomplete instrumentation such that $\mathcal{S} \subseteq \mathcal{D}$, and (ii) to identify different minimal and near-minimal instrumentation set-ups that guarantee a unique identification.

Let $\widetilde{\mathbf{V}}$, with elements $\tilde{v}_{i,j}$, denote any arbitrarily normalized mode shape matrix; while $\mathbf{V}$, as in Chapter 2, specifically denotes the mass normalized mode shape matrix. We make the following assumptions in our analysis:

1. The physical coordinates defining $\mathbf{u}$ in Eq. (3.1) coincide with the centers of masses of the mass elements, and hence $\mathbf{M}$ is diagonal;

2. The data is sufficiently rich so as to allow the identification of all the N modes such that all the eigenvalues λ_j, modal damping ratios ζ_j, and elements of $\widetilde{\mathbf{V}}$ on the rows corresponding to the DOFs in $\mathcal{S}$, $\tilde{v}_{i,j}$, $\forall\, j \in \{1, 2, \cdots, N\}$ and $\forall\, i \in \mathcal{S}$ may be determined.

Note that for a base excited system, the identified system would be non-unique even with a complete set of sensors and known input $\mathbf{a_g}$, since the applied force on the right hand side of Eq. (3.1) is proportional to unknown masses in $\mathbf{M}$. Multiplying both sides of Eq. (3.1) by any matrix $\mathbf{T}$ will not change the response at any of the DOFs for a given $\mathbf{a_g}$. This will also be the case in any general output-only situation, e.g. unmeasured base excitation, ambient vibration etc. Hence, for the cases of known/unknwon ground motion input and output-only situations, some *a priori* information about the system's mass and/or stiffness parameters, additional to the measured responses, is necessary to be able to correctly identify $\mathbf{M}$ and $\mathbf{K}$. On the other hand any general matrix $\mathbf{T}$ will not preserve the topology of $\mathbf{M}$ and $\mathbf{K}$, and hence the model will not be able to represent the physical nature of the structural system; this additional requirement may be used to arrive at the *minimal a priori* information necessary for the unique identification. Assume temporarily that $\mathbf{T}$ is a general $N \times N$ matrix, and an alternative system satisfying the same measured input and output data is given by $\widehat{\mathbf{M}} = \mathbf{TM}$, $\widehat{\mathbf{C}} = \mathbf{TC}$, $\widehat{\mathbf{K}} = \mathbf{TK}$. Then, imposing the condition that $\mathbf{M}$ and $\widehat{\mathbf{M}}$ are both diagonal leads to a diagonal $\mathbf{T}$: $\widehat{M}_{i,j} = t_{i,j} M_{j,j} = 0 \Rightarrow t_{i,j} = 0\, \forall\, i \neq j$. Additionally, imposing the condition that $\mathbf{K}$ and $\widehat{\mathbf{K}}$ are symmetric, one gets that $\mathbf{T} \propto \mathbf{I}$:

$$\left.\begin{aligned} \widehat{K}_{i,j} &= t_{i,i} K_{i,j} \\ \widehat{K}_{j,i} &= t_{j,j} K_{j,i} = t_{j,j} K_{i,j} \end{aligned}\right\} \widehat{K}_{i,j} = \widehat{K}_{j,i} \Rightarrow t_{i,i} = t_{j,j}\, \forall\, i, j \in \{1, 2, \cdots, N\} \tag{3.2}$$

From the above it can be inferred that, for a system with diagonal $\mathbf{M}$ and symmetric $\mathbf{K}$, properly instrumented so as to ensure a *unique* mode shape expansion: (a) it is possible to identify a complete $\mathbf{V}^*$, proportional to the mass normalized $\mathbf{V}$ by a single scalar constant, and (b) this scalar constant can be estimated using a single *a priori* information about the system's physical parameters, e.g. the

total mass of the system. Hence the *minimal necessary a priori information*, given sufficient instrumentation, for the unique identification of $\mathbf{M}$ and $\mathbf{K}$ is one, using which an identified proportional system can be correctly scaled to the true system.

The clause "given sufficient instrumentation" in the last statement is important, since there is a natural trade-off between the instrumentation on the system and the amount of necessary *a priori* information about the system's physical parameter values: for the minimal necessary *a priori* information to suffice, there has to be sufficient instrumentation to identify a unique $\mathbf{V}^*$; and less instrumentation simply necessitates more *a priori* information. The limiting case of the latter scenario is Udwadia and Sharma's [1] proposition that a unique identification of $\mathbf{K}$ of a 1–D shear–type system under known base excitation is possible with only a single sensor at the 1st DOF (1st floor mass) provided that the full $\mathbf{M}$ matrix is known. Here we investigate the possibility of two alternative scenarios to guarantee a unique identification of a shear–type system subjected to base acceleration. In these alternatives, we explore the trade-off between the necessary number of sensors and the necessary *a priori* information, in terms of the element masses. Thus, while Udwadia and Sharma [1] needs only one sensor but all the floor masses, we consider the two scenarios where:

1. We have N_s number of sensors, but know the masses only at these N_s sensor locations;

2. We have N_s number of sensors, and know only the total mass, M_T, of the system.

As will be shown subsequently, these alternatives allow for multiple sensor placement scenarios satisfying global identifiability; these should be expected to help with various issues including working with sensor locations that minimize noise-to-signal ratio, choosing locations where floor masses may be estimated more confidently, or considering the total mass of the system as the *a priori* information, which will be beneficial in many practical situations where the accumulated estimation error in M_T, estimated from an engineering drawing of the structure, can be expected to be lower than the estimation errors in the individual element masses. Finally, while Udwadia and Sharma [1] addresses 1–D systems, we also consider 2–D and 3–D shear–type systems, with possible coupling between the transverse and rotational DOFs which may often be encountered in real-life systems.

The approach proposed in this chapter is the same two-step procedure as in Chapter 2: (i) constructing the complete mass normalized mode shape matrix $\mathbf{V}$, (ii) using the modal orthogonality relations of Eq. (2.4) to obtain the $\mathbf{M}$ and $\mathbf{K}$ matrices. Although Eq. (2.4) requires the complete mass normalized $\mathbf{V}$, the measured mode shapes to be obtained from input–output/output–only data

would initially be available only at the instrumented DOFs in $\mathcal{S}$ ($N_s < N$), and they would be non–mass normalized. The first step therefore involves the estimation of the mass normalization factors of the mode shapes, and consequent normalization of the measured mode shape components. The mass normalized mode shapes at the sensor locations are then expanded from the observed to the unobserved DOFs, using the approach developed for 1-D systems in Chapter 2 but extended here to 2-D and 3-D systems. These theoretical developments are discussed in Sections 3.2 and 3.3, along with the minimal/near–minimal instrumentations of the system allowing the unique estimation of the normalizing factors and unmeasured mode shape components. In order to satisfy the assumption of physical coordinates coinciding with the centers of mass and to estimate the *a priori* knowledge required in the first scenario mentioned above, an approach is discussed in Appendix A to identify the centers of mass and lumped mass parameters, for all instrumented mass elements using a prior actuator–driven forced vibration test. Some implementation issues which may arise in the solution process are discussed in Section 3.4, along with possible strategies to address them. The performance of the proposed solution is then examined in Section 3.5 via numerical simulations of varying complexity. Finally, in Section 3.6, the method is applied to experimental data collected from a 4-story steel frame tested using a shake table facility, considering different situations of possible structural instrumentation and available *a priori* information of the structural mass.

3.2 The Case of One Dimensional Shear-Type System

For N–DOF 1–D shear-type systems (Fig. 3.1(a)), the $\mathbf{M}$ and $\mathbf{K}$ matrices have the forms as given in (2.1). If using sufficient measurements and available *a priori* information one obtains unique estimates of the matrices $\mathbf{M}$ and $\mathbf{K}$, then the unique estimates of the individual lumped masses (m_i's) and spring stiffnesses (k_i's) can be obtained, respectively from the diagonal terms of the identified $\mathbf{M}$ and the diagonal or super/sub-diagonal terms of the identified $\mathbf{K}$. The response of the system under ground excitation is governed by Eq. (3.1) with unidirectional input $\mathbf{a_g} = a_{gx}$, and $\boldsymbol{\iota}$ the column vector $\mathbf{1}$ with 1 in all its elements. The system is instrumented with N_s sensors located at the DOFs in $\mathcal{S} = \{s_1, s_2, \cdots, s_{N_s}\}$. With sufficiently rich measured data, the eigenvalues λ_j and mode shape components $\tilde{v}_{s_i,j}$, $\forall\, j \in \{1, 2, \cdots, N\}$ and $\forall\, s_i \in \mathcal{S}$ are assumed to be estimated from the data prior to the developments explained below.

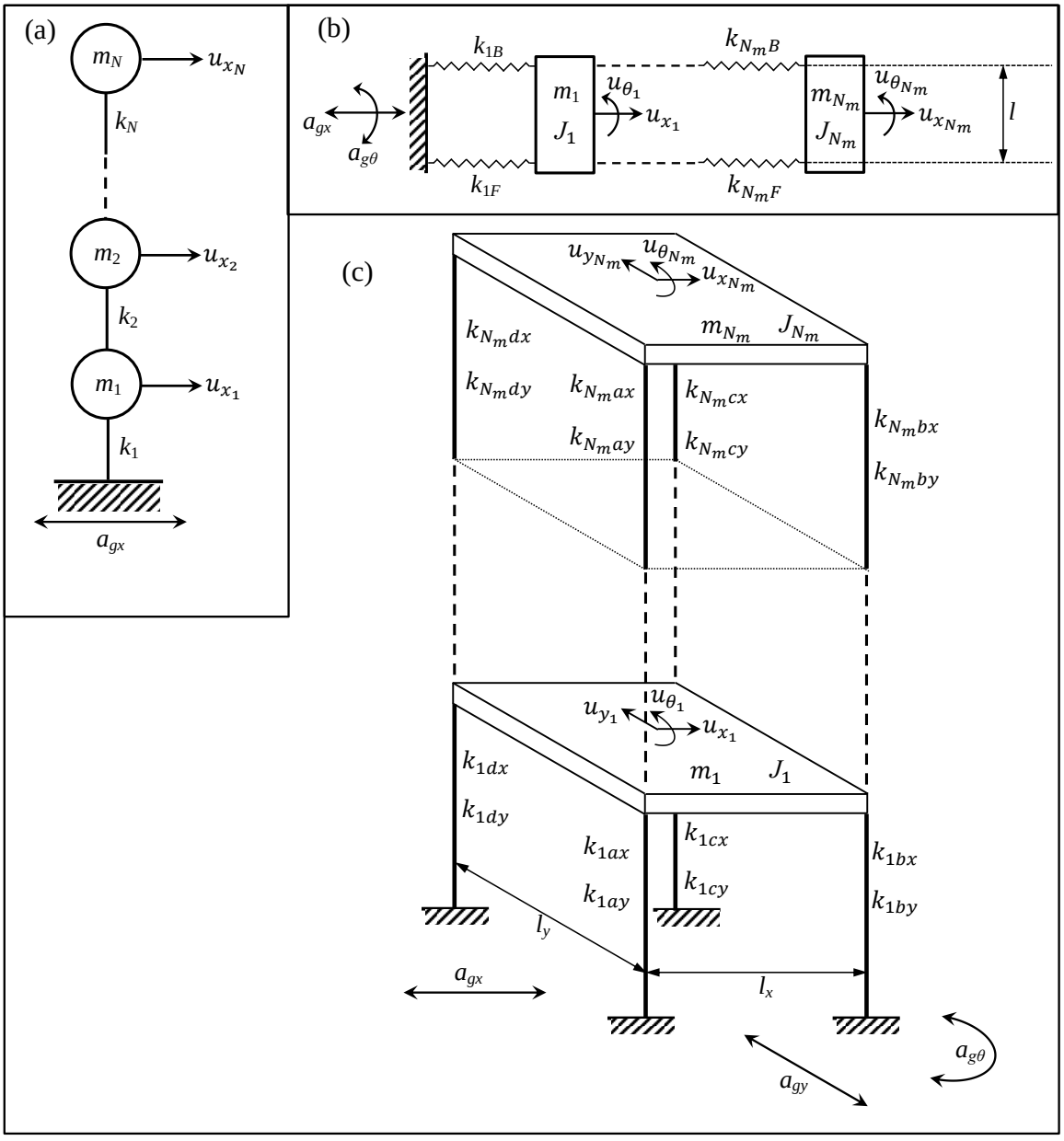

Figure 3.1: (a) 1-D ($N = N_m$ DOFs), (b) 2-D ($N = 2N_m$ DOFs), and (c) 3-D ($N = 3N_m$ DOFs) shear-type systems considered in this chapter.

3.2.1 Identification with masses known at the N_s locations in $\mathcal{S}$

3.2.1.1 Estimation of the mass normalizing factors

Let us denote the mass normalizing factors as $\boldsymbol{\alpha} = \{\alpha_1, \alpha_2, \cdots, \alpha_N\}$, where α_j is the normalizing factor for the jth mode, and the mass normalized mode shape matrix $\mathbf{V}$ is related to the initial mode shape matrix $\widetilde{\mathbf{V}}$ through

$$\mathbf{V} = \widetilde{\mathbf{V}}\text{diag}(\boldsymbol{\alpha}) = \widetilde{\mathbf{V}}\boldsymbol{\alpha}_{\mathbf{D}} \tag{3.3}$$

Noting that $\mathbf{M}$, and hence $\mathbf{M}^{-1}$, are diagonal matrices, the mass orthogonality of Eq. (2.4) leads to:

$$\mathbf{r}_i\mathbf{r}_k^T = 0 \;\forall\, i,k \in \{1,2,\cdots,N\}\,,\; i \neq k; \qquad \mathbf{r}_i\mathbf{r}_i^T = 1/M_{i,i} = 1/m_i \;\forall\, i \in \{1,2,\cdots,N\} \tag{3.4}$$

where $\mathbf{r}_i$ is the ith row of $\mathbf{V}$. In [43] the first equation in Eq. (3.4) is used for estimation of the normalizing factors, assuming that the inverse of the mass matrix associated with the measured DOFs is diagonal. If the mass coefficients m_i are known for the DOFs in $\mathcal{S}$, using Eq. (3.3) in Eq. (3.4) would lead to the following set of $N_s(N_s+1)/2$ equations:

$$\sum_{j=1}^{N} \tilde{v}_{s_i,j}\tilde{v}_{s_k,j}\alpha_j^2 = 0 \quad \forall\, s_i, s_k \in \mathcal{S},\; s_i \neq s_k; \quad \sum_{j=1}^{N} \tilde{v}_{s_i,j}^2\alpha_j^2 = 1/M_{s_i,s_i} = 1/m_{s_i} \quad \forall\, s_i \in \mathcal{S} \tag{3.5}$$

Note that although the first expression in Eq. (3.5) implies $N_s(N_s-1)$ equations, due to symmetry of $\mathbf{M}$ they are in fact a set of only $N_s(N_s-1)/2$ equations. Now, using the mass orthogonality relation in the stiffness orthogonality condition in Eq. (2.4) leads to:

$$\mathbf{M}^{-1}\mathbf{K}\mathbf{M}^{-1} = \mathbf{M}^{-1}\mathbf{V}^{-T}\boldsymbol{\Lambda}\mathbf{V}^{-1}\mathbf{M}^{-1} = \mathbf{V}\boldsymbol{\Lambda}\mathbf{V}^T \tag{3.6}$$

Using the facts that $\mathbf{M}$ is diagonal and $\mathbf{K}$ is tridiagonal in Eq. (3.6), one gets an additional $N_s(N_s-1)/2$ equations, once again accounting for the symmetry of $\mathbf{M}^{-1}\mathbf{K}\mathbf{M}^{-1}$, in terms of the identified modal parameters and the unknown normalizing factors:

$$\sum_{j=1}^{N} \tilde{v}_{s_i,j}\tilde{v}_{s_k,j}\lambda_j\alpha_j^2 = 0 \quad \forall\, s_i, s_k \in \mathcal{S} \text{ such that } s_i \text{ and } s_k \text{ are not of adjacent floors} \tag{3.7}$$

Eqs. (3.5) and (3.7) may be combined, as in Eq. (3.8), to construct a linear non-homogenous system of N_s^2 equations in the N unknowns α_j^2, whose least squares solution, $\mathbf{y} = \mathbf{L}^{\dagger}\mathbf{b}$, will give the mass normalizing factors $\alpha_j = \pm\sqrt{y_j}$. Note that the "$\pm$" sign implies a non-uniqueness in sign; as such, the negative sign may be left off from the "$\pm$" without introducing any error. When the number

of equations are equated to the number of unknowns in Eq. (3.8), the *minimum* number of sensors necessary for unique results is revealed to be equal to $\sqrt{N}$, i.e. one should have $N_s \geq \sqrt{N}$. Since $\sqrt{N}$ will not be a whole number for most values of N, in such cases, we will thus need to choose the next higher whole number after $\sqrt{N}$ as the minimal number of sensors.

$$\begin{bmatrix} \tilde{v}_{s_{1,1}}\tilde{v}_{s_{2,1}} & \cdots & \tilde{v}_{s_{1,N}}\tilde{v}_{s_{2,N}} \\ \vdots & \cdots & \vdots \\ \tilde{v}_{s_{N_s-1,1}}\tilde{v}_{s_{N_s,1}} & \cdots & \tilde{v}_{s_{N_s-1,N}}\tilde{v}_{s_{N_s,N}} \\ \tilde{v}^2_{s_{1,1}} & \cdots & \tilde{v}^2_{s_{1,N}} \\ \vdots & \cdots & \vdots \\ \tilde{v}^2_{s_{N_s,1}} & \cdots & \tilde{v}^2_{s_{N_s,N}} \\ \tilde{v}_{s_{1,1}}\tilde{v}_{s_{2,1}}\lambda_1 & \cdots & \tilde{v}_{s_{1,N}}\tilde{v}_{s_{2,N}}\lambda_N \\ \vdots & \cdots & \vdots \\ \tilde{v}_{s_{N_s-1,1}}\tilde{v}_{s_{N_s,1}}\lambda_1 & \cdots & \tilde{v}_{s_{N_s-1,N}}\tilde{v}_{s_{N_s,N}}\lambda_N \end{bmatrix} \begin{Bmatrix} \alpha_1^2 \\ \vdots \\ \alpha_N^2 \end{Bmatrix} = \mathbf{Ly} = \mathbf{b} = \begin{Bmatrix} 0 \\ \vdots \\ 0 \\ 1/M_{s_{1,s_1}} \\ \vdots \\ 1/M_{s_{N_s,s_{N_s}}} \\ 0 \\ \vdots \\ 0 \end{Bmatrix} \tag{3.8}$$

3.2.1.2 Expanding mode shapes to the unobserved DOFs

Once all the N mass normalizing factors are thus determined, $v_{s_i,j}$ may be calculated using Eq. (3.3) for all modes and $\forall\ s_i \in \mathcal{S}$. The next step is to expand the mass normalized mode shapes from the observed ($\mathcal{S}$) to the unobserved ($\mathcal{D} \setminus \mathcal{S}$) DOFs. To this end, the expansion methodology developed in Chapter 2 (Section 2.2) for 1–D shear-type systems may be used. Recall that the mode shape expansion statements in Section 2.2 imply that, for 1–D shear–type systems an *a priori* knowledge of either (1) two consecutive rows, or (2) the 1st row, or (3) the Nth row of $\mathbf{V}$ will ensure unique estimates of its remaining rows by solving systems of linear equations. Since the mode shape matrix $\mathbf{V}$ considered in this discussion is mass normalized, this unique mode shape expansion will consequently enable the use of the modal orthogonality relations in Eq.(2.4) to determine unique estimates of $\mathbf{M}$ and $\mathbf{K}$.

3.2.2 Identification with only total mass M_T known

3.2.2.1 Estimation of the proportional mass normalizing factors

Consider now the case when only the total mass of the system, $M_T = \sum_{i=1}^{N} m_i$, is known or estimated with some confidence instead of the individual masses at the N_s sensor locations. Since the individual

masses are not known, the available equations for the estimation of the α_j's in this case will include all the equations from Eq. (3.7) (assuming that no two consecutive DOFs are instrumented), and only the first set of equations from Eq. (3.5), constituting a total of $N_s(N_s-1)$ linear simultaneous equations in the N unknown α_j^2's. These equations are, however, homogenous and hence cannot be solved to obtain a non-trivial solution of α_j^2's. One can treat $\alpha_1 = \alpha$ as an undetermined coefficient and obtain a "solution" for $(N-1)$ many $\beta_j^2 = (\alpha_j/\alpha)^2$ for $j \in \{2, \cdots, N\}$ (with $\beta_1 = 1$):

$$\begin{bmatrix} \tilde{v}_{s_1,2}\tilde{v}_{s_2,2} & \cdots & \tilde{v}_{s_1,N}\tilde{v}_{s_2,N} \\ \vdots & \cdots & \vdots \\ \tilde{v}_{s_{N_s-1},2}\tilde{v}_{s_{N_s},2} & \cdots & \tilde{v}_{s_{N_s-1},N}\tilde{v}_{s_{N_s},N} \\ \tilde{v}_{s_1,2}\tilde{v}_{s_2,2}\lambda_2 & \cdots & \tilde{v}_{s_1,N}\tilde{v}_{s_2,N}\lambda_N \\ \vdots & \cdots & \vdots \\ \tilde{v}_{s_{N_s-1},2}\tilde{v}_{s_{N_s},2}\lambda_2 & \cdots & \tilde{v}_{s_{N_s-1},N}\tilde{v}_{s_{N_s},N}\lambda_N \end{bmatrix} \begin{Bmatrix} \beta_2^2 \\ \vdots \\ \beta_N^2 \end{Bmatrix} = \mathbf{L}^*\mathbf{y}^* = \mathbf{b}^* = \begin{Bmatrix} -\tilde{v}_{s_1,1}\tilde{v}_{s_2,1} \\ \vdots \\ -\tilde{v}_{s_{N_s-1},1}\tilde{v}_{s_{N_s},1} \\ -\tilde{v}_{s_1,1}\tilde{v}_{s_2,1}\lambda_1 \\ \vdots \\ -\tilde{v}_{s_{N_s-1},1}\tilde{v}_{s_{N_s},1}\lambda_1 \end{Bmatrix} \tag{3.9}$$

where $\mathbf{L}^*$, $\mathbf{y}^*$ and $\mathbf{b}^*$ are of dimensions $(N_s(N_s-1)) \times (N-1)$, $(N-1) \times 1$ and $(N_s(N_s-1)) \times 1$, respectively. The least squares solution $\mathbf{y}^* = \mathbf{L}^{*\dagger}\mathbf{b}^*$ will give the $(N-1)$ unknown β_j^2's, and thus $\beta_j = \pm\sqrt{y_j}\ \forall\ j\ \in \{2, \cdots, N\}$ (once again the negative sign may be left off from the "$\pm$" without introducing any error). Using these values and defining $\boldsymbol{\beta}_{\mathbf{D}} = \text{diag}(\beta_1 = 1, \beta_2, \cdots, \beta_N)$, the mass normalized mode shapes of Eq. (3.3) may be expressed as $\mathbf{V} = \alpha\widetilde{\mathbf{V}}\boldsymbol{\beta}_{\mathbf{D}} = \alpha\mathbf{V}^*$, and the elements of $\mathbf{V}^*$ can be obtained at the sensor locations. α need not be determined at this stage and will be evaluated at the very final stage. Equating the number of equations to the number of unknowns in Eq. (3.9) leads to the *minimal* sensor requirement of $N_s \geq (1 + \sqrt{4N-3})/2$. Compared with the requirement of $N_s \geq \sqrt{N}$ in the previous case of masses known at the sensor locations, more sensors are needed for this scenario; on the other hand, less *a priori* information about the system's physical parameters (only M_T as compared to N_s known masses) are needed, owing to the natural trade-off between the necessary instrumentation and the necessary *a priori* information.

3.2.2.2 Mode shape expansion and scaling

The next step is to expand $\mathbf{V}^*$ from the observed to the unobserved DOFs. The mode shape expansion equations of Section 2.2 will, by inspection, be seen to remain invariant under a scalar multiplicative transformation of the mode shape matrix; hence, these equations may still be used with the $\mathbf{r}_i$'s being

replaced by $\mathbf{r}_i^*$, where $\mathbf{r}_i^*$ is the ith row of $\mathbf{V}^*$, to obtain the complete proportional mode shape matrix $\mathbf{V}^*$.

If the purpose is to detect structural changes, e.g. due to damage, then the proportionally normalized mode shapes in $\mathbf{V}^*$ may directly be used in appropriate damage detection algorithms [23,44,45]. However, if the objective is the identification of the $\mathbf{M}$ and $\mathbf{K}$ matrices, then the scaling factor α must be evaluated using some known system information. Here it is assumed the total mass of the system, M_T, is known. Note that the estimate of the mass of the system using $\mathbf{V}^*$ would be: $M_T^* = \sum_{i=1}^{N} m_i^* = \sum_{i=1}^{N} \left(\mathbf{r}_i^* \mathbf{r}_i^{*T}\right)^{-1}$. Since $\mathbf{V} = \alpha \mathbf{V}^*$, the scalar constant of proportionality can be estimated as: $\alpha = \sqrt{M_T^*/M_T}$. Once α, and consequently the complete mass normalized mode shape matrix $\mathbf{V}$, are thus estimated, unique estimates of the system's $\mathbf{M}$ and $\mathbf{K}$ matrices can be obtained by using the orthogonality relations of Eq. (2.4). It is important to note that the use of M_T as the *a priori* information rather than some other information such as the mass of a specific floor is not a necessity but rather a choice based on the expectation that the estimation errors for specific various floors would be more pronounced than the error in their sum.

3.2.3 A note on sensor placement

Given that (a) $N_s \geq \sqrt{N}$ for the case with known masses at sensor locations, or (b) $N_s \geq (1 + \sqrt{4N-3})/2$ for the case with known total mass M_T, the following issues should be considered while placing the N_s sensors:

1. If N_s is simply equal to the minimal requirement, then Eq. (3.7) dictates the sensors be placed such that *no two consecutive DOFs are instrumented*.

2. If N_s is more than the minimal requirement, then it may be allowed to place one or more sensors on consecutive DOFs. Consecutively placed sensors will reduce the number of available equations in Eq. (3.7), and one should always ensure to have at least N equations in Eq. (3.8) to solve for the N unknown α_j's for the first scenario, or at least $(N-1)$ equations in Eq. (3.9) to be able to solve for the $(N-1)$ unknown β_j's in the second scenario. Additionally, with $N_s > \sqrt{N}$ in the first scenario, less *a priori* information may also be used; while this may improve the estimation accuracy by excluding those floor masses which cannot be reliably determined, the condition of having at least N equations in Eq. (3.8) must still be satisfied.

3. While placing sensors at consecutive DOFs may be allowed if N_s is greater than the minimal number of necessary sensors, some consecutive sensor placement scenarios, while still seemingly giving sufficient equations to solve for all the unknowns, may actually give less than necessary number of *independent* equations, leading to rank deficient matrices in Eqs. (3.8) (rank($\mathbf{L}$) $< N$) and (3.9) (rank($\mathbf{L}^*$) $< N-1$). For example, placing two consecutive sensors at DOFs $(N-1)$ and N (or at DOFs 1 and 2), and a third sensor at any other DOF q, will make the equation $\mathbf{r}_N \mathbf{\Lambda} \mathbf{r}_q^T = 0$ (or $\mathbf{r}_1 \mathbf{\Lambda} \mathbf{r}_q^T = 0$), obtained for $s_i = N$ (or 1) and $s_k = q$ from Eq. (3.7), a linear combination of the equations $\mathbf{r}_N \mathbf{r}_q^T = 0$ and $\mathbf{r}_{N-1} \mathbf{r}_q^T = 0$ (or $\mathbf{r}_1 \mathbf{r}_q^T = 0$ and $\mathbf{r}_2 \mathbf{r}_q^T = 0$), obtained for $s_i = \{N, N-1\}$ (or $\{1, 2\}$) and $s_k = q$ from Eq. (3.5). It can further be shown that if $q = N-2$ (or 3), i.e the third sensor is also located at a consecutive DOF, there will only be 5 independent equations in Eq. (3.8) and 3 independent equations in Eq. (3.9), as opposed to 7 and 5 total equations, respectively. Thus, when placing sensors at consecutive DOFs, the possibility of some of the estimation equations becoming redundant should be considered and it should be checked whether at least N (or $N-1$) *independent* equations are available to solve for the α_j^2's (or β_j^2's) in Eq. (3.8) (or Eq. (3.9)).

4. Finally note that once the α_j^2's (or β_j's) are uniquely determined, the rows of $\mathbf{V}$ (or $\mathbf{V}^*$) corresponding to the instrumented DOFs may be obtained. The unique expansion of the mode shapes from the observed to the unobserved DOFs using the equations of Section 3.2.1.2, however, also necessitates that the measured rows of $\mathbf{V}$ (or $\mathbf{V}^*$) should either contain the 1st row or the Nth row or two consecutive rows of $\mathbf{V}$ (or $\mathbf{V}^*$). Thus, certain sensor placement scenarios, while giving a unique estimation of the unknown α_j^2's (or β_j^2's) in Section 3.2.1.1 (or 3.2.2.1), and consequently unique estimates of the measured rows of $\mathbf{V}$ (or $\mathbf{V}^*$), will not guarantee a unique estimation of the unmeasured rows of $\mathbf{V}$ (or $\mathbf{V}^*$) due to possible non-uniqueness during the mode shape expansion process, and consequently will not guarantee a unique identification of the $\mathbf{M}$ and $\mathbf{K}$ matrices of the system. One such inadmissible sensor placement scenario, for example, would be to place the sensors at DOFs 2, 4, and 6 in a 1-D, 7-DOF shear-type system subjected to ground acceleration.

The above considerations must be dealt with on a trial–and–error basis and the following methodology may be conveniently applied in experiment design to decide the possible alternative sensor placement configurations on a general N–DOF, 1–D shear–type system subjected to base excitation,

ensuring the unique identification of the $\mathbf{M}$ and $\mathbf{K}$ matrices of the system using the minimal number of necessary sensors. Consider that the system is to be instrumented with $N_{s\text{min}}$ sensors, where $N_{s\text{min}} = \text{ceil}(\sqrt{N})$ for the case of $N_{s\text{min}}$ many known masses, and $N_{s\text{min}} = \text{ceil}((1+\sqrt{4N-3})/2)$ for the case of single *a priori* information, e.g. known total mass M_T, with ceil(.) rounding its argument to the next whole number towards infinity. The proposed experiment design method then involves the following steps:

1. Generate random $\hat{\mathbf{M}}$ and $\hat{\mathbf{K}}$ matrices, satisfying the structural topology given by Eq. (2.1), i.e. $\hat{\mathbf{M}}$ is diagonal with positive diagonal elements, and $\hat{\mathbf{K}}$ is symmetric tridiagonal, with positive diagonal and negative off-diagonal elements, and $\sum_{j=1}^{N} \widehat{K}_{i,j} = 0 \; \forall \; i \in \{2, \cdots, N\}$. Perform an eigenvalue analysis using $\hat{\mathbf{M}}$ and $\hat{\mathbf{K}}$, and scale, if necessary, each eigenvector with a non-zero multiplicative constant to ensure it is not mass normalized.

2. Generate the set $\mathcal{S}_0$ of all possible combinations of the elements in the set $\mathcal{D} = \{1, 2, \cdots, N\}$ choosing $N_{s\text{min}}$ elements at a time (e.g. using the command $nchoosek(\mathcal{D}, N_{s\text{min}})$ in MATLAB® [30]). The total number of such combinations will be ${}^{N}\text{C}_{N_{s\text{min}}}$, each of which will be denoted by $\mathcal{C}_i$, and $\mathcal{S}_0 = \{\mathcal{C}_1, \mathcal{C}_2, \ldots\}$ will be the set of all possible instrumentation configurations of the N–DOF system using $N_{s\text{min}}$ sensors.

3. For each of the instrumentation configurations in $\mathcal{S}_0$, use the eigenvectors and eigenvalues from Step (2) above to construct the $\mathbf{L}$ of Eq. (3.8) (or the $\mathbf{L}^*$ of Eq. (3.9), whichever is relevant). Calculate the rank of $\mathbf{L}$ (or $\mathbf{L}^*$). Discard all the instrumentation configurations $\mathcal{C}_i$ in $\mathcal{S}_0$ for which $\text{rank}(\mathbf{L}) < N$ (or $\text{rank}(\mathbf{L}^*) < N-1$). The resulting reduced set $\mathcal{S}_1 \subseteq \mathcal{S}_0$ of configurations will contain only the instrumentation configurations that will give a unique solution to the true (or proportional) mass normalizing factors, and a unique estimation of the thus instrumented rows of $\mathbf{V}$ (or $\mathbf{V}^*$).

4. From the configurations in $\mathcal{S}_1$, select those which contain the instrumentation of the 1st DOF and/or the Nth DOF and/or any 2 consecutive DOFs, and store them in the set $\mathcal{S}_2 \subseteq \mathcal{S}_1$. The configurations in this final set $\mathcal{S}_2$ will ensure a unique mode shape expansion to the unobserved DOFs; i.e., $\mathcal{S}_2$ comprises the *allowed* sensor placement configurations on the N–DOF system for a unique identification of $\mathbf{M}$ and $\mathbf{K}$ using the minimal $N_{s\text{min}}$ number of sensors.

As an example, Table 3.1 lists permissible configurations for systems up to 7 DOFs. The cardinality of the set $\mathcal{S}_2$, $n(\mathcal{S}_2)$, will generally show a very rapid growth with N leading to combinatorial explosion; e.g., even for $N = 10$, it can be shown that $n(\mathcal{S}_2) = 195$ and 166 for the first and second scenarios, respectively, with $N_{s\text{min}} = 4$ for both the scenarios. An upper limit on the total number of configurations selected in any of the sets ($\mathcal{S}_0$, $\mathcal{S}_1$, $\mathcal{S}_2$) may thus be set by user judgement, if necessary, to avoid this explosion for large N. This wide array of permissible instrumentation configurations should provide a greatly increased flexibility in the experiment design stage, e.g. allowing the location of sensors at DOFs where better signal quality may be expected, or avoiding DOFs where a sensor may not be placed owing to some practical constraints, while always ensuring the global identifiability of the system. Although in the discussions above, only the situation with the minimum necessary number of sensors has been considered, the same exercise should also be performed if $N_s > N_{s\text{min}}$ sensors are available, since having an increased number of sensors may not guarantee a unique estimation of $\mathbf{M}$ and $\mathbf{K}$ if the available sensors are not placed correctly. Once such a set of permissible sensor placement configurations is obtained, they can be further ranked according to some information measure [40,41] to decide on the optimal (most informative) configuration amongst them.

3.3 Two and Three Dimensional Shear–Type Systems

For 2–D (translation + rotation) (Fig. 3.1(b)) and 3–D (2 translations + rotation) (Fig. 3.1(c)) shear–type systems, the $\mathbf{M}$ and $\mathbf{K}$ matrices can be written in the same way as for 1–D systems:

$$\mathbf{M} = \text{diag}\big(\mathbf{m}_1, \mathbf{m}_2, \cdots, \mathbf{m}_{N_m}\big);\ \mathbf{K} = \begin{bmatrix} \mathbf{k}_1 + \mathbf{k}_2 & -\mathbf{k}_2 & & & & 0 \\ -\mathbf{k}_2 & \mathbf{k}_2 + \mathbf{k}_3 & -\mathbf{k}_3 & & & \\ & \ddots & \ddots & \ddots & & \\ & & -\mathbf{k}_{N_m-1} & \mathbf{k}_{N_m-1} + \mathbf{k}_{N_m} & -\mathbf{k}_{N_m} & \\ 0 & & & -\mathbf{k}_{N_m} & \mathbf{k}_{N_m} & \end{bmatrix} \tag{3.10}$$

where N_m is the total number of lumped mass elements/floors in the system, and $\mathbf{m}_i$ and $\mathbf{k}_i$ are now matrices, for the ith floor/story, instead of scalars as in Eq. (2.1) for 1-D systems; i.e., with N_D denoting the number of dimensions ($N = N_D N_m$), and the physical coordinates defining $\mathbf{u}$ in the

Table 3.1: Sensor set-ups for unique estimation of $\mathbf{M}$ and $\mathbf{K}$ of 1-D shear-type systems.

N	Known $m_{s_i}\ \forall\ s_i \in \mathcal{S}$			Known M_T		
	$N_{s\min}$	$\mathcal{S}_2$	$n(\mathcal{S}_2)$	$N_{s\min}$	$\mathcal{S}_2$	$n(\mathcal{S}_2)$
1	1	1	1	1	1	1
2	2	1-2	1	2	1-2	1
3	2	Any 2 DOFs	3	2	1-3	1
4	2	1-3, 1-4, 2-4	3	3	Any 3 DOFs	4
5	3	Any 3 DOFs	10	3	Any 3 DOFs EXCEPT 1-2-3, 3-4-5	8
6	3	Any 3 DOFs EXCEPT 1-2-3, 4-5-6	18	3	1-3-4, 1-3-5, 1-3-6, 1-4-5, 1-4-6, 2-3-5, 2-3-6, 2-4-5, 2-4-6, 3-4-6	10
7	3	Any 3 DOFs EXCEPT 1-2-3, 5-6-7, 2-4-6	32	3	1-3-5, 1-3-6, 1-3-7, 1-4-6, 1-5-7, 2-4-7, 2-5-7, 3-5-7	8

equation of motion, Eq. (3.1), coinciding with the centers of mass of the mass elements:

$$\mathbf{m}_i = \begin{bmatrix} m_i & 0 \\ 0 & J_i \end{bmatrix} \text{ for } N_D = 2; \quad \mathbf{m}_i = \begin{bmatrix} m_i & 0 & 0 \\ 0 & m_i & 0 \\ 0 & 0 & J_i \end{bmatrix} \text{ for } N_D = 3 \tag{3.11}$$

with m_i and J_i respectively being the ith lumped/floor mass and its mass moment of inertia about its center of mass in the x-y plane (i.e. about the z axis), and:

$$\mathbf{k}_i = \begin{bmatrix} k_i^{xx} & k_i^{x\theta} \\ k_i^{\theta x} & k_i^{\theta\theta} \end{bmatrix} \text{ for } N_D = 2; \quad \mathbf{k}_i = \begin{bmatrix} k_i^{xx} & 0 & k_i^{x\theta} \\ 0 & k_i^{yy} & k_i^{y\theta} \\ k_i^{\theta x} & k_i^{\theta y} & k_i^{\theta\theta} \end{bmatrix} \text{ for } N_D = 3 \tag{3.12}$$

For $N_D = 2$: $k_i^{xx} = \sum k_i$, $k_i^{x\theta} = k_i^{\theta x} = (\Delta k_i) l_i/2 + (\sum k_i) e_i$, and $k_i^{\theta\theta} = (\sum k_i) l_i^2/4 + (\sum k_i) e_i^2 + (\Delta k_i) l_i e_i$, where $\sum k_i = k_{iF} + k_{iB}$ and $\Delta k_i = k_{iF} - k_{iB}$, with k_{iF} and k_{iB} respectively being the spring stiffnesses on the two sides ("front" and "back" in the 2-D system of Fig. 3.1(b)) of the center of mass at the ith level, l_i being the distance between the two springs, and e_i being the distance of the center of mass above $l_i/2$ (i.e. from $l_i/2$ towards the spring at the back). Similarly, for $N_D = 3$: $k_i^{xx} = \sum k_{ix}$, $k_i^{yy} = \sum k_{iy}$, $k_i^{x\theta} = k_i^{\theta x} = (\Delta k_{ix}) l_{iy}/2 + (\sum k_{ix}) e_{iy}$, $k_i^{y\theta} = k_i^{\theta y} = (\Delta k_{iy}) l_{ix}/2 - (\sum k_{iy}) e_{ix}$, and $k_i^{\theta\theta} = \{(\sum k_{ix}) l_{iy}^2 + (\sum k_{iy}) l_{ix}^2\}/4 + (\sum k_{ix}) e_{iy}^2 + (\sum k_{iy}) e_{ix}^2 + (\Delta k_{ix}) l_{iy} e_{iy} - (\Delta k_{iy}) l_{ix} e_{ix}$, where $\sum k_{ix} = k_{iFx} + k_{iBx}$ and $\Delta k_{ix} = k_{iFx} - k_{iBx}$, with k_{iFx} and

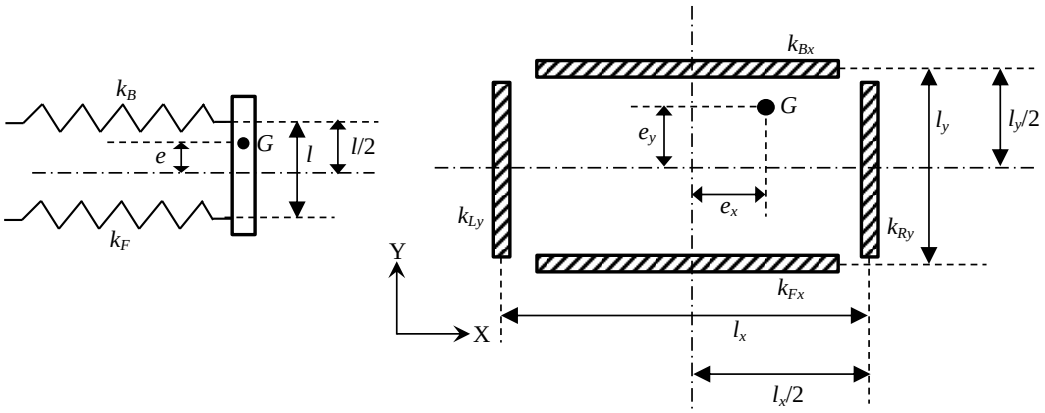

Figure 3.2: Stories of 2-D and 3-D systems showing mass eccentricities from geometric center of springs/frames.

k_{iBx} respectively being the *sum* of all column/spring stiffnesses in the x-direction on the two sides ("front" and "back" in the 3-D system of Fig. 3.1(c)) of the center of mass at the ith floor, l_{iy} being the distance between these two equivalent springs, and e_{iy} being the distance of the center of mass above $l_{iy}/2$; and $\sum k_{iy} = k_{iRy} + k_{iLy}$ and $\Delta k_{iy} = k_{iRy} - k_{iLy}$, with k_{iRy} and k_{iLy} respectively being the sum of all column/spring stiffnesses in the y-direction on the two sides ("right" and "left" in the 3-D system of Fig. 3.1(c)) of the center of mass at the ith floor, l_{ix} being the distance between these two equivalent springs, and e_{ix} being the distance of the center of mass to the right of $l_{ix}/2$. (In Fig. 3.1(c), the additional subscripts to the column stiffnesses, "a", "b", "c" and "d", denotes the four columns, counterclockwise from front-left, at any floor; thus, for any ith floor of this system, $k_{iFx} = k_{iax} + k_{ibx}$, $k_{iBx} = k_{icx} + k_{idx}$, $k_{iRy} = k_{iby} + k_{icy}$, and $k_{iLy} = k_{iay} + k_{idy}$. Also note that, in Figs. 3.1(b) and 3.1(c), the l_i's have been shown to be constants for all i only for the ease of depiction; the theoretical discussions of this section does not require any such constraint on the l_i's and e_i's.)

3.3.1 Unique story stiffness but non-unique spring/frame stiffnesses due to unknown center of mass

Similar to the 1-D system, once unique estimates of the matrices $\mathbf{M}$ and $\mathbf{K}$ are obtained using sufficient measurements and available *a priori* information, the unique estimates of $\mathbf{m}_i$ and $\mathbf{k}_i$, i.e. the mass and stiffness matrices for an story i, can be obtained, respectively using the diagonal blocks

of the identified $\mathbf{M}$ (Eq. (3.11)), and the diagonal or super/sub-diagonal blocks of the identified $\mathbf{K}$ (Eq. (3.12)). Then, for the 2-D system, the individual spring stiffnesses may be estimated as: $k_{iF} = k_i^{xx}/2 + (k_i^{x\theta} - k_i^{xx}e_i)/l_i$ and $k_{iB} = k_i^{xx}/2 - (k_i^{x\theta} - k_i^{xx}e_i)/l_i$; while for the 3-D system, the stiffnesses of the equivalent springs may be estimated as: $k_{iFx} = k_i^{xx}/2 + (k_i^{x\theta} - k_i^{xx}e_{iy})/l_{iy}$, $k_{iBx} = k_i^{xx}/2 - (k_i^{x\theta} - k_i^{xx}e_{iy})/l_{iy}$, $k_{iRy} = k_i^{yy}/2 + (k_i^{y\theta} + k_i^{yy}e_{ix})/l_{ix}$ and $k_{iLy} = k_i^{yy}/2 - (k_i^{y\theta} + k_i^{yy}e_{ix})/l_{ix}$. The distances between the springs (l_i, or, l_{ix} and l_{iy}) may be obtained from the geometric locations of the stiffness elements (columns/frames) in the plan of the floor (Fig. 3.2). However, the mass eccentricities (e_i, or, e_{ix} and e_{iy}) will, in general, not be available. Moreover, using the elements of $\mathbf{k}_i$, the following equations can be obtained for the mass eccentricities in any floor i:

$$\begin{aligned} &e_i^2 - 2(k_i^{x\theta}/k_i^{xx})e_i + (k_i^{\theta\theta}/k_i^{xx} - l_i^2/4) = 0 \qquad \text{for } N_D = 2 \\ &k_i^{yy}e_{ix}^2 + k_i^{xx}e_{iy}^2 + 2k_i^{y\theta}e_{ix} - 2k_i^{x\theta}e_{iy} + (k_i^{\theta\theta} - k_i^{xx}l_{iy}^2/4 - k_i^{yy}l_{ix}^2/4) = 0 \qquad \text{for } N_D = 3 \end{aligned} \tag{3.13}$$

This implies that, in general, two different mass eccentricities, and consequently two different sets of $\{k_{iF}, k_{iB}\}$, will give the same story stiffness matrix $\mathbf{k}_i$ for a 2-D system; this makes $\{k_{iF}, k_{iB}\}$ globally unidentifiable (but locally identifiable) for unknown e_i: e.g. with $l = 1$, the two systems $\{k_F, k_B, e\}_A = \{1500, 1000, 0.1\}$ and $\{k_F, k_B, e\}_B = \{1000, 1500, 0.3\}$ will have the same story stiffness matrix:

$$\mathbf{k}_A = \mathbf{k}_B = \begin{bmatrix} 2500 & 500 \\ 500 & 700 \end{bmatrix}$$

For a 3-D system, an infinite possible combinations of the mass eccentricities $\{e_{ix}, e_{iy}\}$ may, in general, be obtained satisfying Eq. (3.13); thus the set of spring stiffnesses, $\{k_{iFx}, k_{iBx}, k_{iRy}, k_{iLy}\}$, will be both globally and locally unidentifiable for 3-D systems, unless the actual mass eccentricities are known. For example: With $l_x = l_y = 1$, any (e_x, e_y) lying on the ellipse in Fig. 3.3, (k_{Fx}, k_{Bx}) corresponding to that e_y (determined from the blue lines in Fig. 3.3), and (k_{Ly}, k_{Ry}) corresponding to that e_x (determined from the black lines in Fig. 3.3), will have the same story stiffness matrix

$$\mathbf{k} = \begin{bmatrix} 2500 & 0 & 500 \\ 0 & 3500 & -100 \\ 500 & -100 & 1560 \end{bmatrix} \tag{3.14}$$

There are infinite $\{e_x, e_y\}$ pairs lying on the ellipse, and hence, infinite $\{k_F, k_B, k_L, k_R, e_x, e_y\}$ combinations which will give the story stiffness matrix of Eq. (3.14). One such combination,

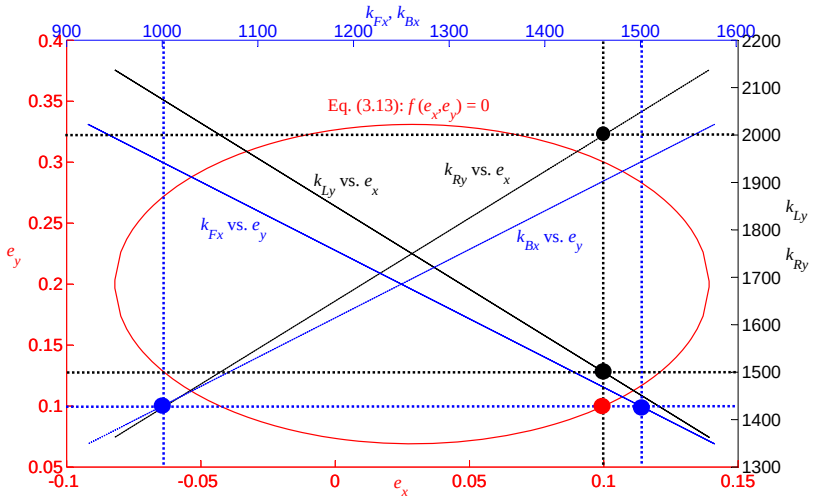

Figure 3.3: An example of non-uniqueness in frame stiffnesses for unique story stiffness matrix due to unknown center of mass in 3-D systems.

$\{k_F, k_B, k_L, k_R, e_x, e_y\} = \{1500, 1000, 1500, 2000, 0.1, 0.1\}$, is shown with the dots in Fig. 3.3. Hence, for 2-D and 3-D systems, even though unique estimates of the global $\mathbf{K}$ matrix as well as the story $\mathbf{k}_i$ matrices may be obtained, satisfying the instrumentation and *a priori* information requirements discussed in the remaining part of this section, this will not guarantee the unique estimation of the individual spring stiffnesses at any story level without knowing the location of the center of mass of the corresponding floor. While the global $\mathbf{K}$ matrix will suffice for simulation/prediction purposes, for structural damage localization it may be necessary to identify also the individual spring stiffnesses. In such a case, one may estimate the necessary centers of mass at the floor under consideration using the approach given in Appendix A. Alternatively, one may ignore the mass eccentricities, i.e. take $e_i = 0$ (or $e_{ix} = e_{iy} = 0$), while estimating the spring stiffnesses; if the springs at a given story have similar stiffnesses ($k_{iF} \approx k_{iB}$, or $\{k_{iFx} \approx k_{iBx}, k_{iLy} \approx k_{iRy}\}$), and the true mass eccentricity is γ percent of the distances between the springs ($e_i = \gamma l_i/100$), then this will result in an error of approximately 2γ percent in the individual spring stiffness estimates, which may be a permissible error for small mass eccentricities.

The response of the 2-D and 3-D systems, under ground excitation, are again governed by Eq.

(3.1), with the response vector $\mathbf{u}(t)$ at time t being of the form:

$$\mathbf{u}(t) = \begin{cases} \{u_{x_1}(t), u_{\theta_1}(t), u_{x_2}(t), u_{\theta_2}(t), \cdots\}^T \text{ for } N_D = 2 \\ \{u_{x_1}(t), u_{y_1}(t), u_{\theta_1}(t), u_{x_2}(t), u_{y_2}(t), u_{\theta_2}(t), \cdots\}^T \text{ for } N_D = 3 \end{cases} \tag{3.15}$$

$\mathbf{a_g}$ being bi- or tri-directional as: $\mathbf{a_g}(t) = \{a_{gx}(t), a_{g\theta}(t)\}^T$ or $\{a_{gx}(t), a_{gy}(t), a_{g\theta}(t)\}^T$ for $N_D = 2$ or 3, respectively; and the $N \times N_D$ influence matrix being $\boldsymbol{\iota} = \{\mathbf{I}_{N_D \times N_D}, \mathbf{I}_{N_D \times N_D}, \cdots\}^T$, where $\mathbf{I}_{N_D \times N_D}$ is the identity matrix. As in the 1-D case, the system is instrumented with N_s sensors located at the DOFs in $\mathcal{S} = \{s_1, s_2, \cdots, s_{N_s}\}$, and using the measured data in an appropriate system identification method, we identify the eigenvalues λ_j, and the elements of $\widetilde{\mathbf{V}}$, $\tilde{v}_{s_i,j}$, $\forall\, j \in \{1, 2, \cdots, N\}$ and $\forall\, s_i \in \mathcal{S}$. Starting with this *a priori* knowledge of the modal parameters, we proceed with the subsequent identification steps following the same approach as for the 1-D system.

3.3.2 Identification with masses known at the N_s locations in $\mathcal{S}$

3.3.2.1 Estimation of the mass normalizing factors

Since the mass matrix $\mathbf{M}$ for the 2 and 3-D systems are still diagonal by Eqs. (3.10) and (3.11), Eq. (3.4) derived for the 1-D case using the mass orthogonality condition is still applicable for 2 and 3-D systems, with $1/M_{i,i}$ in the second equation of Eq. (3.4) now being equal to $1/m_l$ or $1/J_l$, for i being a translational or a rotational DOF corresponding to the lth lumped mass element. Thus, for N_s instrumented DOFs, with the masses/mass moments of inertia known at these DOFs, we will again have the set of $N_s(N_s+1)/2$ equations of Eq. (3.5) for the mass normalizing factors in $\boldsymbol{\alpha} = \{\alpha_1, \alpha_2, \cdots, \alpha_N\}$.

However, since the stiffness matrices for the 2 and 3-D systems are now block tridiagonal by Eqs. (3.10) and (3.12), we cannot make a general statement as to the number of equations which can be derived using Eq. (3.6), as was possible for the 1-D case. Let us define $\mathbf{P}$ as a matrix of 1's and 0's with the same sparsity pattern as $\mathbf{K}$ (i.e. $p_{i,k} = 0$ if $K_{i,k} = 0$, $p_{i,k} = 1$ if $K_{i,k} \neq 0$); since the structure of $\mathbf{K}$ for both the 2-D or 3-D system is known *a priori* from Eqs. (3.10) and (3.12), the matrix $\mathbf{P}$ can be easily obtained. Then using Eq. (3.6), and accounting for the symmetry of $\mathbf{M}^{-1}\mathbf{K}\mathbf{M}^{-1}$, we get a set of N^* equations, analogous to Eq. (3.7) for the 1-D case:

$$\sum_{j=1}^{N} \tilde{v}_{s_i,j}\tilde{v}_{s_k,j}\lambda_j\alpha_j^2 = 0 \;\forall\; s_i, s_k \in \mathcal{S},\; p_{s_i,s_k} = 0 \tag{3.16}$$

Once we have N_s instrumented DOFs such that $N_s(N_s+1)/2 + N^* \geq N$, using Eqs. (3.5) and (3.16) we can get a similar linear system, $\mathbf{Ly} = \mathbf{b}$, as Eq. (3.8), whose least squares solution will give the N unknown α_j^2's, and thus the N mass normalizing factors $\alpha_j \; \forall \; j \in \{1, 2, \cdots, N\}$.

3.3.2.2 Mode shape expansion to unobserved DOFs

Scaling the identified non-normalized mode shapes with the α_j's determined above using Eq. (3.3), we will get the rows of the mass normalized $\mathbf{V}$ matrix corresponding to the observed DOFs in $\mathcal{S}$. We next propose a set of statements, analogous to the statements in Section 2.2, for the expansion of these observed rows of $\mathbf{V}$ to the unobserved rows corresponding to the DOFs in $\mathcal{D} \setminus \mathcal{S}$.

Statement 4: *Knowing the rows of* $\mathbf{V}$ *corresponding to the* i*th and* $(i+1)$*th lumped mass elements, it is possible to uniquely determine*

1. *the rows of* $\mathbf{V}$ *corresponding to the* $(i-1)$*th lumped mass element, and*

2. *the rows of* $\mathbf{V}$ *corresponding to the* $(i+2)$*th lumped mass element,*

for any $i \in \{2, 3, \cdots, N_m - 2\}$.

The rows of $\mathbf{V}$ corresponding to the ith lumped mass element/floor are $\mathbf{r}_{2i-1}$ and $\mathbf{r}_{2i}$ for a 2-D system, or $\mathbf{r}_{3i-2}$, $\mathbf{r}_{3i-1}$ and $\mathbf{r}_{3i}$ for a 3-D system, where $\mathbf{r}_k$ is the kth row of $\mathbf{V}$. Let us denote these set of rows as:

$$\mathbf{r}_{\mathbf{B}i} = \left\{\mathbf{r}_{2i-1}^T, \mathbf{r}_{2i}^T\right\}^T \text{ for } N_D = 2; \quad \mathbf{r}_{\mathbf{B}i} = \left\{\mathbf{r}_{3i-2}^T, \mathbf{r}_{3i-1}^T, \mathbf{r}_{3i}^T\right\}^T \text{ for } N_D = 3 \tag{3.17}$$

Then, knowing $\mathbf{r}_{\mathbf{B}i}$ and $\mathbf{r}_{\mathbf{B}i+1}$, the rows of $\mathbf{V}$ corresponding to the $(i-1)$th and $(i+2)$th lumped mass elements, i.e. $\mathbf{r}_{\mathbf{B}i-1}$ and $\mathbf{r}_{\mathbf{B}i+2}$, can be estimated by solving, respectively, the following two linear systems of equations:

$$\begin{bmatrix} \mathbf{I}_{N\times N} & \mathbf{r}_{\mathbf{B}i}^T & \mathbf{r}_{\mathbf{B}i+1}^T & -\mathbf{\Lambda}\mathbf{r}_{\mathbf{B}i}^T \\ \mathbf{0}_{N_D\times N} & \mathbf{I}_{N_D\times N_D} & \mathbf{I}_{N_D\times N_D} & \mathbf{0}_{N_D\times N_D} \\ \mathbf{r}_{\mathbf{B}i} & \mathbf{0}_{N_D\times N_D} & \mathbf{0}_{N_D\times N_D} & \mathbf{0}_{N_D\times N_D} \\ \mathbf{r}_{\mathbf{B}i+1} & \mathbf{0}_{N_D\times N_D} & \mathbf{0}_{N_D\times N_D} & \mathbf{0}_{N_D\times N_D} \end{bmatrix} \begin{Bmatrix} \mathbf{r}_{\mathbf{B}i-1}^T \\ \tilde{\mathbf{a}}_\mathbf{1}^T \\ \tilde{\mathbf{a}}_\mathbf{2}^T \\ \tilde{\mathbf{a}}_\mathbf{3}^T \end{Bmatrix} = \begin{Bmatrix} \mathbf{0}_{N\times N_D} \\ -\mathbf{I}_{N_D\times N_D} \\ \mathbf{0}_{N_D\times N_D} \\ \mathbf{0}_{N_D\times N_D} \end{Bmatrix} \tag{3.18}$$

and:

$$\begin{bmatrix} \mathbf{I}_{N\times N} & \mathbf{r_B}_i^T & \mathbf{r_B}_{i+1}^T & -\mathbf{\Lambda}\mathbf{r_B}_{i+1}^T \\ \mathbf{0}_{N_D\times N} & \mathbf{I}_{N_D\times N_D} & \mathbf{I}_{N_D\times N_D} & \mathbf{0}_{N_D\times N_D} \\ \mathbf{r}_{\mathbf{B}i} & \mathbf{0}_{N_D\times N_D} & \mathbf{0}_{N_D\times N_D} & \mathbf{0}_{N_D\times N_D} \\ \mathbf{r}_{\mathbf{B}i+1} & \mathbf{0}_{N_D\times N_D} & \mathbf{0}_{N_D\times N_D} & \mathbf{0}_{N_D\times N_D} \end{bmatrix} \begin{Bmatrix} \mathbf{r_B}_{i+2}^T \\ \tilde{\mathbf{b}}_\mathbf{1}^T \\ \tilde{\mathbf{b}}_\mathbf{2}^T \\ \tilde{\mathbf{b}}_\mathbf{3}^T \end{Bmatrix} = \begin{Bmatrix} \mathbf{0}_{N\times N_D} \\ -\mathbf{I}_{N_D\times N_D} \\ \mathbf{0}_{N_D\times N_D} \\ \mathbf{0}_{N_D\times N_D} \end{Bmatrix} \tag{3.19}$$

where $\tilde{\mathbf{a}}_\mathbf{1} = \mathbf{a}_{i,i-1}^{-1}\mathbf{a}_{i,i}$, $\tilde{\mathbf{a}}_\mathbf{2} = \mathbf{a}_{i,i-1}^{-1}\mathbf{a}_{i,i+1}$ and $\tilde{\mathbf{a}}_\mathbf{3} = \mathbf{a}_{i,i-1}^{-1}$ in Eq. (3.18), and $\tilde{\mathbf{b}}_\mathbf{1} = \mathbf{a}_{i+1,i+2}^{-1}\mathbf{a}_{i+1,i}$, $\tilde{\mathbf{b}}_\mathbf{2} = \mathbf{a}_{i+1,i+2}^{-1}\mathbf{a}_{i+1,i+1}$ and $\tilde{\mathbf{b}}_\mathbf{3} = \mathbf{a}_{i+1,i+2}^{-1}$ in Eq. (3.19) are all $N_D \times N_D$ matrices, with $\mathbf{a}_{i,j}$ being the $N_D \times N_D$ sub-matrices in:

$$\mathbf{A} = \mathbf{M}^{-1}\mathbf{K} = \begin{bmatrix} \mathbf{a}_{1,1} & \mathbf{a}_{1,2} & & & & 0 \\ \mathbf{a}_{2,1} & \mathbf{a}_{2,2} & \mathbf{a}_{2,3} & & & \\ & \ddots & \ddots & \ddots & & \\ & & \mathbf{a}_{N_m-1,N_m-2} & \mathbf{a}_{N_m-1,N_m-1} & \mathbf{a}_{N_m-1,N_m} & \\ 0 & & & \mathbf{a}_{N_m,N_m-1} & \mathbf{a}_{N_m,N_m} & \end{bmatrix} \tag{3.20}$$

The first set of N (=$N_D N_m$) equations in Eqs. (3.18) and (3.19) are obtained respectively from the ith and $(i+1)$th row-blocks of the matrix eigenvalue equation: $\mathbf{AV} = \mathbf{V\Lambda}$, considering all the N modes, with the ith row-block constituting of the rows $(N_D i - N_D + 1)$ to $(N_D i)$, and similarly for the $(i+1)$th row-block. The $(N+1)$th to $(N+N_D)$th equations in Eqs. (3.18) and (3.19) are derived from the following condition on the matrix $\mathbf{A}$: $\mathbf{a}_{i,i-1} + \mathbf{a}_{i,i} + \mathbf{a}_{i,i+1} = \mathbf{0}_{N_D\times N_D}\ \forall\, i \in \{2, 3, \cdots, N_m - 1\}$, owing to the nature of the $\mathbf{M}$ and $\mathbf{K}$ matrices given by Eqs. (3.10) to (3.12). Finally, the last two sets, each of N_D equations, in Eqs. (3.18) and (3.19) are from Eq. (3.4), representing the orthogonality of the rows of $\mathbf{V}$ owing to $\mathbf{M}$ being diagonal. The proof of this statement is given in Appendix B; this proof is slightly different from that of Statement 1 in Chapter 2, as we cannot directly apply the cofactor expansion of Eq. (2.12) along any block row of a matrix.

Statement 5: *Knowing the rows of* $\mathbf{V}$ *corresponding to the* 1*st lumped mass element, it is possible to uniquely determine the rows corresponding to the* 2*nd lumped mass element.*

By considering all the N modes in the 1st N_D rows of $\mathbf{AV} = \mathbf{V\Lambda}$, knowing the rows of $\mathbf{V}$ corresponding to the 1st lumped mass element/floor, $\mathbf{r}_{\mathbf{B}1}$, we can estimate the rows corresponding to the 2nd lumped mass element as:

$$\mathbf{r}_{\mathbf{B}2} = -\mathbf{a}_{1,2}^{-1}[\mathbf{a}_{1,1}\mathbf{r}_{\mathbf{B}1} - \mathbf{r}_{\mathbf{B}1}\mathbf{\Lambda}] \tag{3.21}$$

The $N_D \times N_D$ matrices, $\mathbf{a}_{1,1}$ and $\mathbf{a}_{1,2}$, necessary in Eq. (3.21), can be respectively obtained as:

$$\mathbf{a}_{1,1} = [\mathbf{r_{B}}_1 \mathbf{\Lambda} \mathbf{r_{B}}_1^T][\mathbf{r_{B}}_1 \mathbf{r_{B}}_1^T]^{-1}; \quad \mathbf{a}_{1,2} = [\mathbf{r_{B}}_1 \mathbf{r_{B}}_1^T][\mathbf{r_{B}}_1 \mathbf{\Lambda}^{-1} \mathbf{r_{B}}_1^T]^{-1} - \mathbf{a}_{1,1} \tag{3.22}$$

The equation for $\mathbf{a}_{1,1}$ above is derived by pre-multiplying Eq. (3.21) with $\mathbf{a}_{1,2}$ and post-multiplying with $\mathbf{r_{B}}_1^T$, and noting that $\mathbf{r_{B}}_2 \mathbf{r_{B}}_1^T = \mathbf{0}_{N_D \times N_D}$ by Eq. (3.4). The second equation in Eq. (3.22) is derived using Eqs. (3.10) and (3.20) to give $\mathbf{a}_{1,1} + \mathbf{a}_{1,2} = \mathbf{m}_1^{-1}\mathbf{k}_1$, where $\mathbf{m}_1$ and $\mathbf{k}_1$ are the elemental mass and stiffness sub-matrices defined respectively in Eqs. (3.11) and (3.12). Using Eq. (3.4) gives $\mathbf{m}_1^{-1} = \mathbf{r_{B}}_1 \mathbf{r_{B}}_1^T$; moreover for a shear-type system the first $N_D \times N_D$ sub-matrix, $\mathbf{f}_1$, of the flexibility matrix $\mathbf{F} = \mathbf{K}^{-1}$, is equal to $\mathbf{k}_1^{-1}$, and hence $\mathbf{k}_1$ can be obtained, using the stiffness orthogonality relation of Eq. (2.4), as: $\mathbf{k}_1 = \mathbf{f}_1^{-1} = [\mathbf{r_{B}}_1 \mathbf{\Lambda}^{-1} \mathbf{r_{B}}_1^T]^{-1}$ to give the expression for $\mathbf{a}_{1,2}$ in Eq. (3.22).

Statement 6: *Knowing the rows of* $\mathbf{V}$ *corresponding to the* N_m*th lumped mass element, it is possible to uniquely determine the rows corresponding to the* $(N_m - 1)$*th lumped mass element.*

Similarly, considering all the N modes in the last N_D rows of $\mathbf{AV} = \mathbf{V\Lambda}$, knowing the rows of $\mathbf{V}$ corresponding to the N_mth lumped mass element, $\mathbf{r_{B}}_{N_m}$, the rows corresponding to the $(N_m - 1)$th lumped mass element can be obtained as:

$$\mathbf{r_{B}}_{N_m - 1} = -\mathbf{a}_{N_m, N_m - 1}^{-1} [\mathbf{a}_{N_m, N_m} \mathbf{r_{B}}_{N_m} - \mathbf{r_{B}}_{N_m} \mathbf{\Lambda}] \tag{3.23}$$

where, Eqs. (3.10) and (3.20) give $\mathbf{a}_{N_m, N_m - 1} = -\mathbf{a}_{N_m, N_m}$, with $\mathbf{a}_{N_m, N_m}$ given by:

$$\mathbf{a}_{N_m, N_m} = [\mathbf{r_{B}}_{N_m} \mathbf{\Lambda} \mathbf{r_{B}}_{N_m}^T][\mathbf{r_{B}}_{N_m} \mathbf{r_{B}}_{N_m}^T]^{-1} \tag{3.24}$$

Eq. (3.24) is obtained by pre-multiplying and post-multiplying Eq. (3.23) with $\mathbf{a}_{N_m, N_m - 1}$ and $\mathbf{r_{B}}_{N_m}^T$, respectively, and then using $\mathbf{r_{B}}_{N_m - 1} \mathbf{r_{B}}_{N_m}^T = \mathbf{0}_{N_D \times N_D}$ from Eq. (3.4).

Analogous to the 1-D case, it can be further mentioned that knowing only the rows of $\mathbf{V}$ corresponding to the ith lumped mass element will not guarantee the unique estimation of its remaining rows, for any $i \in \{2, \cdots, N_m - 1\}$. Hence, based on the preceding discussion, it can be summarized that, for an N_D-dimensional shear-type system, an *a priori* knowledge of the rows of $\mathbf{V}$ corresponding to either (1) two consecutive lumped mass elements/floors, or (2) the 1st lumped mass element/floor, or (3) the Nth lumped mass element/floor, enables the unique estimation of its remaining rows through the solution of linear systems of equations. Since the complete $\mathbf{V}$ matrix thus obtained is mass normalized, it can then be used in the modal orthogonality relations of Equation (2.4) to determine the $\mathbf{M}$ and $\mathbf{K}$ matrices of the system.

3.3.3 Identification with total mass M_T known

For the second scenario where we know the total mass M_T of the system, we will not have the second set of equations from Eq. (3.5), i.e. we will now only have $N_s(N_s-1)/2$ equations from the mass orthogonality condition. Combining these equations with the N^* equations of Eq. (3.16), we will have a linear system of equations similar to Eq. (3.9); with the N_s instrumented DOFs being such that $N_s(N_s-1)/2 + N^* \geq N-1$, the least squares solution of this linear system will give the $(N-1)$ unknown β_j^2's, and thus the unknown proportional mass normalizing factors, $\beta_j \; \forall \; j \; \in \{2, \cdots, N\}$. With these estimated β_j's, and with $\beta_1 = 1$, we can get the observed rows of the proportional mode shape matrix, from the identified non-mass normalized mode shapes, using $\mathbf{V}^* = \widetilde{\mathbf{V}}\boldsymbol{\beta}_\mathbf{D}$, where $\boldsymbol{\beta}_\mathbf{D} = \text{diag}(\boldsymbol{\beta}) = \text{diag}\,\{\beta_1, \beta_2, \cdots, \beta_N\}$. Subsequently, noting that the mode shape expansion equations of Section 3.3.2.2 are applicable to a proportional mode shape matrix as well (as mentioned in Section 3.2.2.2), using these equations we can estimate the unobserved rows of $\mathbf{V}^*$, and thus get the complete $\mathbf{V}^*$ matrix. While for structural damage detection the proportional mode shapes in $\mathbf{V}^*$ would suffice with appropriate algorithms, in applications requiring the estimates of the $\mathbf{M}$ and $\mathbf{K}$ matrices, the scalar constant of proportionality α relating $\mathbf{V}$ to $\mathbf{V}^*$ should be estimated. To this end, the proportional total mass, following the DOF convention adopted in Eq. (3.15), is estimated as:

$$M_T^* = \sum_{i=1}^{N_m} m_i^* = \begin{cases} \sum_{i=1}^{N_m} \left(\mathbf{r}_{2i-1}^* \mathbf{r}_{2i-1}^{*T}\right)^{-1} \text{ for } N_D = 2 \\ \sum_{i=1}^{N_m} \left(\mathbf{r}_{3i-1}^* \mathbf{r}_{3i-1}^{*T}\right)^{-1} \text{ or } \sum_{i=1}^{N_m} \left(\mathbf{r}_{3i-2}^* \mathbf{r}_{3i-2}^{*T}\right)^{-1} \text{ for } N_D = 3 \end{cases} \tag{3.25}$$

where $\mathbf{r}_i^*$ is the ith row of $\mathbf{V}^*$. The constant α can then be estimated, as for the 1-D system in Section 3.2.2.2, using this estimated M_T^* and the known true total mass M_T: $\alpha = \sqrt{M_T^*/M_T}$. Once α, and consequently the complete mass normalized mode shape matrix $\mathbf{V} = \alpha\mathbf{V}^*$, are thus estimated, the system's $\mathbf{M}$ and $\mathbf{K}$ matrices can be obtained using the orthogonality relations of Eq. (2.4).

3.3.4 A note on sensor placement

3.3.4.1 Complete instrumentation of a set of lumped mass elements

As mentioned in Section 3.3.2.1, owing to the block tridiagonal nature of the $\mathbf{K}$ matrix we are unable to derive a general expression, as was done for the 1-D case, for the number of equations which can be obtained in Eq. (3.16) from the stiffness orthogonality condition, given N_s number of sensors.

One possible observation however is that the number of such equations, N^*, will in general be less than, and at most equal to, $N_s(N_s-1)/2$, which was the number of equations obtained for the 1-D case in Eq. (3.7) with no two consecutive DOFs instrumented. The inability of obtaining a general expression, in terms of N_s, for the number of equations in Eq. (3.16) also prevents us from deriving the minimal number of sensors necessary for a unique identification, unlike the 1-D case.

Instead, in this section, we consider the situation where the instrumentation set-up is such that all the associated N_D DOFs are instrumented for a given lumped mass element, and attempt to derive an expression for the minimum number of such completely instrumented mass elements necessary to have N equations in Eq. (3.8) or $(N-1)$ equations in Eq. (3.9). Let us suppose that we have n_m such instrumented mass elements, and thus a total of $N_s = N_D n_m$ sensors. Then, the total number of equations which can be obtained in Eq. (3.5) from the mass orthogonality condition will be: (a) $N_s(N_s+1)/2 = N_D n_m(N_D n_m+1)/2$ for the case with known M_{s_i,s_i} at all instrumented DOFs $s_i \in \mathcal{S}$, and (b) $N_s(N_s-1)/2 = N_D n_m(N_D n_m-1)/2$ for the case with known total mass M_T. Similarly, in Eq. (3.16), we will get a total number of $N_D^2 n_m(n_m-1)/2$ equations for both $N_D = 2$ and 3, and an additional n_m equations for $N_D = 3$ if we consider uncoupling between the x and y directional spring/elastic forces for the 3-D system (as for the system in Figure 3.1(c)). For instance, suppose we instrument all the translational and rotational DOFs for the i^*th and k^*th lumped mass elements: then for the 2-D system, using these 4 sensors at $(u_{x_{i^*}}, u_{\theta_{i^*}}, u_{x_{k^*}}, u_{\theta_{k^*}})$, we will have a total of 4 equations in Eq. (3.16), since $p_{s_i,s_k} = 0$ will hold for (s_i, s_k) corresponding to the DOF pairs $\big\{(u_{x_{i^*}}, u_{x_{k^*}}), (u_{x_{i^*}}, u_{\theta_{k^*}}), (u_{\theta_{i^*}}, u_{x_{k^*}}), (u_{\theta_{i^*}}, u_{\theta_{k^*}})\big\}$; similarly for the 3-D system we will have 11 equations using the 6 sensors at $(u_{x_{i^*}}, u_{y_{i^*}}, u_{\theta_{i^*}}, u_{x_{k^*}}, u_{y_{k^*}}, u_{\theta_{k^*}})$, with $p_{s_i,s_k} = 0$ for (s_i, s_k) corresponding to the 9 DOF pairs formed as for the 2-D system, and additionally for the pairs $\big\{(u_{x_{i^*}}, u_{y_{i^*}}), (u_{x_{k^*}}, u_{y_{k^*}})\big\}$ due to uncoupling between the x and y directional spring forces.

Equating the number of equations thus obtained with the number of unknowns (mass normalizing factors) in Eq. (3.8), for the scenario of known M_{s_i,s_i} at the instrumented DOFs $s_i \in \mathcal{S}$, we get the following condition for the minimum number of completely instrumented lumped mass elements:

$$n_m \geq \frac{(N_D-1) + \sqrt{(N_D-1)^2 + 16 N_D N_m}}{4 N_D} \tag{3.26}$$

Note that for $N_D = 1$, this requirement reduces to $n_m \geq \sqrt{N_m}$, i.e. $N_s \geq \sqrt{N}$, as was obtained in Section 3.2.1.1 for 1-D systems. The requirement given by Eq. (3.26) is derived without considering any uncoupling between x and y directional spring forces; instead considering this uncoupling,

yielding n_m extra equations for $N_D = 3$, we get the requirement: $n_m \geq \sqrt{N_m/3}$.

Similarly, for the case of known total mass M_T, equating the number of unknowns in Eq. (3.9) with the number of equations, we get the minimal completely instrumented mass elements requirement:

$$n_m \geq \frac{(N_D+1) + \sqrt{(N_D+1)^2 + 16(N_D N_m - 1)}}{4N_D} \tag{3.27}$$

Again, with $N_D = 1$, this requirement reduces to the one obtained in Section 3.2.2.1 for 1-D systems: $n_m \geq (1+\sqrt{4N_m - 3})/2$, i.e. $N_s \geq (1+\sqrt{4N-3})/2$. Moreover, while Eq. (3.27) does not consider any uncoupling between x and y directional spring forces, the requirement on n_m considering this uncoupling for $N_D = 3$ becomes: $n_m \geq (5 + \sqrt{108N_m - 11})/18$.

3.3.4.2 The issue of uncoupling between translational and rotational DOFs

The discussion in the preceding section on the complete instrumentation of a certain n_m number of mass elements, and the minimal n_m necessary for unique identification, assumes the existence of coupling between the translational and the rotational DOFs. However, in case these DOFs are uncoupled, i.e. if in Eq. (3.12), $\Delta k_i = 0$ and $e_i = 0$ for $N_D = 2$, or $\Delta k_{ix} = 0$ and $e_{iy} = 0$, and/or, $\Delta k_{iy} = 0$ and $e_{ix} = 0$ for $N_D = 3$, then some of the equations in Eqs. (3.8) and (3.9) will vanish because of the coefficients (rows in $\mathbf{L}$ or $\mathbf{L}^*$) becoming zero. This is because the mode shapes in such a case will have the elements corresponding to translational–rotational coupling $= 0$; e.g., for a 3-D system with no coupling between the translational and rotational DOFs, if the modes are arranged such that the first N_m columns in $\mathbf{V}$ are the x-directional bending modes, the second N_m columns are the y-directional bending modes, and the last N_m columns are the torsional modes, then, following the DOF numbering convention of Eq. (3.15), $\mathbf{V}$ will have the form:

$$\mathbf{V} = \begin{bmatrix} v_{1,1} & \cdots & v_{1,N_m} & 0 & \cdots & 0 & 0 & \cdots & 0 \\ 0 & \cdots & 0 & v_{2,N_m+1} & \cdots & v_{2,2N_m} & 0 & \cdots & 0 \\ 0 & \cdots & 0 & 0 & \cdots & 0 & v_{3,2N_m+1} & \cdots & v_{3,3N_m} \\ \vdots & \vdots & \vdots & \vdots & \vdots & \vdots & \vdots & \vdots & \vdots \\ v_{N-2,1} & \cdots & v_{N-2,N_m} & 0 & \cdots & 0 & 0 & \cdots & 0 \\ 0 & \cdots & 0 & v_{N-1,N_m+1} & \cdots & v_{N-1,2N_m} & 0 & \cdots & 0 \\ 0 & \cdots & 0 & 0 & \cdots & 0 & v_{N,2N_m+1} & \cdots & v_{N,3N_m} \end{bmatrix} \tag{3.28}$$

This will make the coefficients in the Eqs. (3.5) and (3.16), $\tilde{v}_{s_i,j}\tilde{v}_{s_k,j}$ and $\tilde{v}_{s_i,j}\tilde{v}_{s_k,j}\lambda_j$, equal to zero, unless s_i and s_k correspond to DOFs in the same direction (x/y/θ). Consequently the number of equations available in such a case in Eqs. (3.8) and (3.9) will decrease, and the recommendations in Section 3.3.4.1 as to the minimal number of instrumented mass elements will no longer guarantee a unique solution to the identification problem. In fact, in such a case the N-DOF N_D-D problem will reduce to N_D number of N_m-DOF 1-D problems, and hence, for the scenario with M_{s_i,s_i} known at all the instrumented DOFs $s_i \in \mathcal{S}$ we will need $N_s \geq N_D\sqrt{N_m}$ sensors, and for the scenario with known M_T we will need $N_s \geq N_D(1+\sqrt{4N_m-3})/2$ sensors, with the placement of these sensors determined based on the discussion in Section 3.2.3 for the 1-D case.

Even when the coupling between the translational and rotational DOFs are small, although not completely uncoupled, the coefficients in the concerned equations of Eqs. (3.5) and (3.16) will be very small relative to the coefficients in the other equations (since the corresponding mode shape elements will be small, and, by squaring, become even smaller). This will make the coefficient matrices, $\mathbf{L}$ or $\mathbf{L}^*$, in Eqs. (3.8) and (3.9) ill-conditioned, and will consequently lead to increased errors in the estimates of the different modal and physical parameters. Such an example situation is illustrated later in Section 3.4. Since it is usually not possible to know the degree of coupling between the translational and rotational DOFs prior to the actual experiment and identification exercise, it can be recommended for a real-life application that:

1. In general the sensor placement requirements obtained by treating the N-DOF N_D-D system as N_D number of N_m-DOF 1-D systems should be adopted, as these requirements are more stringent than the ones in Section 3.3.4.1. Combining this with the notion of instrumenting all the N_D DOFs at a given mass element, the number of such instrumented mass elements should then be (a) $n_m \geq \sqrt{N_m}$ for the case of known M_{s_i,s_i} at all the instrumented DOFs $s_i \in \mathcal{S}$, and (b) $n_m \geq (1+\sqrt{4N_m-3})/2$ for the case of known M_T; the location of these instrumented mass elements should be chosen following the sensor location guidelines of Section 3.2.3.

2. However, if for a given situation a high degree of coupling is expected based on engineering/physical judgement, then the necessary minimal number of completely instrumented mass elements can be obtained following the requirements of Section 3.3.4.1.

3. In both the above two cases of instrumentation, we must ensure that the set of completely in-

strumented mass elements include (a) the 1st mass element, and/or (b) the N_Mth mass element, and/or (c) two consecutive mass elements, in order to have a unique mode shape expansion using the approach of Section 3.3.2.2.

4. After the experiment, the non-mass normalized mode shapes at the sensor locations can be estimated using system identification. Then: (a) if these identified mode shape components depict sufficient translational–rotational coupling, the identification strategy discussed in Sections 3.3.2 or 3.3.3 should be used to estimate the remaining modal and physical parameters of the N-DOF N_D-D system; (b) if the identified mode shape components depict negligibly small translational–rotational coupling, the identification of the remaining modal and physical parameters of the system should be performed by treating the system as N_D number of N_m-DOF 1-D systems, and using Sections 3.2.1 and 3.2.2 to identify each of these N_D systems; and (c) if the identified mode shape components show moderate amount of translational–rotational coupling, then both the approaches (a) and (b) above should be used to identify two alternative models of the system, and further engineering judgement used to decide on either of these as the correct model (or an average of the two if the models are close to one another). Here, by moderate translational–rotational coupling is meant situations where, for example, in a dominantly translational mode, the θ directional components are small, but not small enough to be treated as nodes.

3.4 Some Implementation Issues

3.4.1 Weighting of equations from mass orthogonality

While Eqs. (3.8) and (3.9) are theoretically valid for the estimation of the true/proportional mass normalizing factors, their direct implementation has a numerical limitation. This limitation stems from the fact that both Eqs. (3.8) and (3.9) contain two sets of equations, one derived from mass orthogonality (Eq. (3.5)) and the other using stiffness orthogonality (Eqs. (3.7) or (3.16)). The coefficients in the second set of equations are similar to those in the first set weighted by the system's eigenvalues; since the eigenvalues, in the mean sense, have a much higher magnitude than one, the coefficients in the first set of equations have a much smaller magnitude than the coefficients in the second set. This makes the coefficient matrices, $\mathbf{L}$ and $\mathbf{L}^*$, numerically ill-conditioned, which is

undesirable from a numerical aspect. This also inadvertently puts more weight on satisfying the second set of equations compared to the first set, which is unacceptable since we seek that solution which minimizes the error in all the equations equally well while minimizing the overall error as well. One way to circumvent this problem is to multiply all the equations obtained using mass orthogonality with a scalar factor of the same order as the mean of the eigenvalues, thus scaling the coefficients of the first set of equations to a similar order as the mean of the coefficients of the second set of equations. The mean of the identified eigenvalues may be used as this scalar factor.

3.4.2 Using total least squares and optimization for noisy data

In real situations the measured data is inevitably corrupted by noise. This will lead to estimation errors in the modal parameters obtained using system identification, and hence errors in the "known" parameters in Eqs. (3.8) and (3.9). While in the classical least squares problem, $\mathbf{\Phi c} = \mathbf{z} \Rightarrow \mathbf{c} = \mathbf{\Phi}^{\dagger}\mathbf{z}$, it is assumed that the independent variables in $\mathbf{\Phi}$ are error–free, with the measurement noise induced estimation errors, this assumption will not be valid for the matrices $\mathbf{L}$ and $\mathbf{L}^*$ in Eqs. (3.8) and (3.9). Hence, for the solution of these equations in a real situation we must take recourse to alternative approaches which also account for errors in the independent variables: the Total Least Squares method is adopted here for that purpose. Using this method, the solution of Eq. (3.8) is given by [31]:

$$[\mathbf{y}^T \ -1]^T = -\frac{1}{\psi_{N+1,N+1}}\boldsymbol{\psi}_{N+1} \tag{3.29}$$

where $\psi_{N+1,N+1}$ and $\boldsymbol{\psi}_{N+1}$ are respectively the $(N+1, N+1)$th element and $(N+1)$th column of the matrix $\mathbf{\Psi}$ obtained from the singular value decomposition of the augmented matrix $[\mathbf{L}\ \mathbf{b}]$:

$$[\mathbf{L}\ \mathbf{b}] = \mathbf{\Upsilon\Sigma\Psi}^T = [\boldsymbol{\upsilon}_1 \cdots \boldsymbol{\upsilon}_{N_{\text{eq}}}] \begin{bmatrix} \text{diag}\big(\sigma_1, \cdots, \sigma_{N+1}\big) \\ ---------- \\ \mathbf{0}_{(N_{eq}-N-1)\times(N+1)} \end{bmatrix} [\boldsymbol{\psi}_1 \cdots \boldsymbol{\psi}_{N+1}]^T \tag{3.30}$$

where N_{eq} denotes the total number of equations in Eq. (3.8); the $N_{\text{eq}} \times (N+1)$ diagonal matrix $\mathbf{\Sigma}$ contains the $(N+1)$ singular values of $[\mathbf{L}\ \mathbf{b}]$ in its first $(N+1)$ diagonal elements, the $N_{\text{eq}} \times N_{\text{eq}}$ and $(N+1) \times (N+1)$ unitary matrices, $\mathbf{\Upsilon}$ and $\mathbf{\Psi}$, respectively contain the left and right singular vectors of $[\mathbf{L}\ \mathbf{b}]$ as their columns; and σ_i, $\boldsymbol{\upsilon}_i$ and $\boldsymbol{\psi}_i$ are respectively the ith singular value, and ith left and right singular vectors. Moreover, using the $(N+1)$th singular value and singular vectors, the

corrections to $[\mathbf{L}\ \mathbf{b}]$ is given by [31]:

$$[\mathbf{\Delta L}\ \mathbf{\Delta b}] = \sigma_{N+1}\boldsymbol{\upsilon}_{N+1}\boldsymbol{\psi}_{N+1}^{T} \tag{3.31}$$

such that the equation $[\mathbf{L} - \mathbf{\Delta L}]\mathbf{y} = \mathbf{b} - \mathbf{\Delta b}$, where $\mathbf{y}$ is the solution given in Eq. (3.29), is satisfied.

While most efficient system identification techniques usually provide sufficiently accurate estimates of the system's eigenvalues, the estimated non-normalized mode shapes at the sensor locations often suffer from significant amount of errors in case of noisy measurements. The total least squares approach takes this into account, and can thus be assumed to provide a good estimate of the mass normalizing factors; it does not however directly reduce the errors in these observed components of the mode shapes. These errors, if allowed to remain, will adversely affect all the subsequent identification steps, by first propagating to the unobserved mode shape components in the mode shape expansion stage, and finally to the estimated $\mathbf{M}$ and $\mathbf{K}$ matrices. In order to reduce this propagated error, the following optimization step is additionally incorporated to obtain improved estimates of the non-normalized mode shapes at the sensor locations:

$$\mathbf{\Theta}^{*} = \arg\max_{\mathbf{\Theta}} \left|\left|[\mathbf{\Delta L}\ \mathbf{\Delta b}]\right|\right|_{2} \tag{3.32}$$

where $\mathbf{\Theta} = \left\{\tilde{v}_{s_1,1}, \cdots, \tilde{v}_{s_1,N}, \cdots\cdots, \tilde{v}_{s_{N_s},1}, \cdots, \tilde{v}_{s_{N_s},N}\right\}$ contains all the non-normalized mode shapes at the sensor locations, and $||.||_2$ is the 2-norm, i.e. the maximum singular value, of the matrix argument. The optimization problem in Eq. (3.32) takes advantage of the correction matrix of Eq. (3.31) being a function of $\mathbf{\Theta}$, albeit implicit, and may be solved using any suitable optimization algorithm, starting with the $\mathbf{\Theta}$ formed of the mode shape estimates from system identification. Note that $[\mathbf{\Delta L}\ \mathbf{\Delta b}]$ should ideally be zero, for the exact theoretical values of the concerned parameters instead of their erroneous estimates. While Eq. (3.31) is obtained so that $[\mathbf{\Delta L}\ \mathbf{\Delta b}]$ has the minimum Frobenius norm [31] (the square root of the sum of the squares of all the singular values of the matrix), using the 2-norm in Eq. (3.32) ensures that, through the coupled total least squares – optimization approach, we obtain that optimal value $\mathbf{\Theta}^{*}$ which gives a correction matrix $[\mathbf{\Delta L}\ \mathbf{\Delta b}]^{*}$ with the least norm of the singular values as well as the smallest maximum singular value; since the correction matrix is like an error matrix, the proposed approach thus attempts to minimize both the mean error as well as the maximum error. The total least squares - optimization approach can similarly be applied to Eq. (3.9) for obtaining improved and robust estimates of the observed components of the non-normalized mode shapes and the proportional mass normalizing factors.

Finally, note that the total least squares problem is only defined for over-determined systems. Thus, if the number of independent equations just equals the number of unknowns, i.e if Eqs. (3.8) or (3.9) constitutes of just N or $(N-1)$ equations, respectively, then the proposed approach cannot be applied. This is owing to the fact that with the same number of independent linear equations as unknowns an apparently "exact" solution of the unknowns can be obtained, with the solution being "exact" in the sense that the equations will be satisfied with zero error; e.g. with two distinct points we can define a line which passes precisely through the two points. However, if the "known" parameters in these equations have errors, then the "exact" solution thus obtained will not be the "true" solution; e.g. if the two distinct points in the above example are erroneous then the line, although passing through them, will not be the "true" line one is looking for. However, there will be no way to reduce the error in the "known" parameters. Hence, although zero equation error does not imply solution accuracy, in such a situation the thus obtained solution to the unknowns, i.e. $\mathbf{y} = \mathbf{L}^{-1}\mathbf{b}$ or $\mathbf{y}^* = \mathbf{L}^{*-1}\mathbf{b}^*$ for Eqs. (3.8) or (3.9), will be the only and best possible solution. This also suggests that, in order to have a robust estimate of the different parameters in a real situation, the system should not be instrumented with just the bare minimum number of sensors necessary from a theoretical point of view, so as to have over-determined systems in Eqs. (3.8) and (3.9).

3.4.3 Possible modifications in mode shape expansion equations

While the proposed mode shape expansion provide an accurate estimation of the complete $\mathbf{V}$ for *perfectly* shear-type systems, in a real scenario a *perfect* analytical representation of the actual system is usually non-existent. In such situations it might therefore be more prudent to:

1. Convert the linear systems of equations for mode shape expansion, to over-determined systems by considering additional equations, and then obtain total least squares solutions to these over-determined systems of equations. For example, while determining the $(i-1)$th row of $\mathbf{V}$ using the ith and $(i+1)$th rows, if the kth row ($k \neq i$, $k \neq i+1$) is already known because of k being an observed DOF, then one may include the equation $\mathbf{r}_k\mathbf{r}_{i-1}^T = 0$, obtained from mass orthogonality and diagonality of $\mathbf{M}^{-1}$, in the existing system of mode shape expansion equations. Similarly, for the same case, if the DOFs k and $(i-1)$ should be elastically uncoupled ($K_{k,i-1} = 0$), then one may also include the equation $\mathbf{r}_k\mathbf{\Lambda}\mathbf{r}_{i-1}^T = 0$.

2. The different equations in the mode shape expansion reflect different topological aspects of the model (the diagonality of $\mathbf{M}$, the sparsity of $\mathbf{K}$), as well as the satisfaction of the eigenvalue equation. In a practical situation if some of these modeling assumptions seem more reasonable than others, the different equations may be weighted differently, thereby increasing/decreasing the relative importance of some model-related constraints vis-$\grave{a}$-vis others.

3. If $M_{i,i}$ is known *a priori*, but there is no sensor at the ith DOF, then this known mass information cannot be used in the estimation of the mass normalizing factors using Eq. (3.8). However, the information may be used while estimating the ith row of $\mathbf{V}$ in the mode shape expansion stage through the equation $\mathbf{r}_i\mathbf{r}_i^T = 1/M_{i,i}$. Since this equation is quadratic in the elements of the ith row of $\mathbf{V}$, one would need a nonlinear solver (e.g. the Newton-Raphson method) to solve this equation along with the other linear equations of mode shape expansion; the initial guess to the solution may be obtained as the solution to only the linear equations.

3.5 Numerical Validation

The proposed approach is applied to numerically simulated data for the 14 example situations listed in Table 3.2. The systems considered include a 1-D 7-DOF system, two 2-D 6-DOF systems with $l = 1$m for all the 3 levels, and a 3-D 12-DOF system with $l_x = l_y = 1$m for all the 4 stories. Uniform mass distributions are assumed for all the lumped mass elements, and hence their respective centroids and centers of mass coincide. Modal damping is assumed for all the systems. The 14 cases are chosen to illustrate the different possible instrumentation and *a priori* available information scenarios discussed before. The minimal instrumentation set-up necessary for unique identification is adopted in all the cases, and the two types of *a priori* information, viz. known masses at sensor locations and known total mass, are considered for all the instrumentation configurations except Cases 3 and 12 in which the known total mass scenario makes Eq. (3.9) under-determined.

For each of the 14 cases, 100 simulations for identifying the system parameters are run, and the statistics of the errors in the estimated parameters are calculated using the estimation errors from the 100 simulations. In each simulation, the mass and stiffness parameters, and the modal damping ratios are slightly perturbed, in order to represent a realistic situation, by choosing them from corresponding uniform distributions: for any parameter θ, its value in the kth simulation is chosen as

$\theta_{i,k} = E[\theta_i] + \mathcal{U}(-p_\theta, p_\theta)E[\theta_i]$, where $E[.]$ denotes the expected value (mean) of the variable in brackets, and $\mathcal{U}(l_l, l_r)$ denotes uniform probability distribution between the two limits l_l and l_r. The values of these means and limits used in the simulations are given in Table 3.3. The slightly perturbed structure in each of the 100 simulations, for each of the 14 cases, is excited by applying N_D dimensional zero-mean Gaussian white noise sequences, a_{gx}, a_{gy} and $a_{g\theta}$, as input base accelerations to an N_D-D system, and the resulting acceleration responses at the DOFs corresponding to the sensor locations in Table 3.2 are stored. To simulate the effect of measurement noise the true acceleration responses are corrupted by adding 10% RMS zero-mean Gaussian white noise sequences. Thus, each of the 100 simulations is different in terms of: (1) the applied input(s), which are different white noise sequences albeit having a common underlying Gaussian distribution, (2) exciting slightly different systems owing to the slight perturbations in the lumped masses, spring stiffnesses, and modal damping ratios, and (3) the added measurement noise sequences. The necessary *a priori* information are obtained using the mean value(s) of the involved mass parameters from Table 3.3, and are thus inaccurate, being the same for all the simulations in a given case.

Note from Table 3.3 that, while System II(a) represents a 2-D system with considerable translational-rotational coupling, System II(b) represents a similar 2-D system but with much lesser coupling. System II(b) is considered as an example to the discussion in Section 3.3.4.2. In Cases 8 to 11 this slightly coupled 2-D system is identified considering the coupling, using the estimation equations in Section 3.3. On the other hand, for Case 12, the 2-D 6-DOF System II(b) is uncoupled to two 1-D 3-DOF systems, one representing the x-directional motion and the other the θ-directional motion, and the identification is performed for these two 1-D systems individually, using the equations from Section 3.2, with the identified parameters combined at the end to give the matrices for the 2-D 6-DOF system. The results of the uncoupled-system identification in Case 12 is then compared to the coupled-system identification in Cases 8 to 11 to highlight the possible advantages and disadvantages of an uncoupled-system identification.

To estimate the modal frequencies and non-mass normalized mode shapes at the sensor locations we use the input base acceleration(s), along with the (noisy) output accelerations at the sensor locations of Table 3.2, in the ERA-OKID algorithm. Once these initial estimates of the modal parameters at the sensor locations are thus identified, we next use the proposed approach to get the complete mass normalized $\mathbf{V}$ matrix. Finally, using the modal orthogonality relations we estimate the system's

Table 3.2: Different cases considered in the numerical validation.

System	N_D	N_m	N	$\mathcal{S}$	$\mathcal{I}$	Case
I	1-D	7	7	x_3, x_5, x_7	m_3, m_5, m_7	1
					M_T	2
				x_3, x_5, x_6	m_3, m_5, m_6	3
II(a)	2-D	3	6	$x_1, \theta_1, x_3, \theta_3$	m_1, J_1, m_3, J_3	4
					M_T	5
				x_1, x_3, θ_3	m_1, m_3, J_3	6
					M_T	7
II(b)	2-D	3	6	$x_1, \theta_1, x_3, \theta_3$	m_1, J_1, m_3, J_3	8
					M_T	9
				x_1, x_3, θ_3	m_1, m_3, J_3	10
					M_T	11
	2-D (= 2 × 1-D)	3	6 (=2 × 3)	$(x_1, x_3); (\theta_1, \theta_3)$	$(m_1, m_3); (J_1, J_3)$	12
III	3-D	4	12	$x_1, y_1, \theta_1, x_4, y_4, \theta_4$	m_1, J_1, m_4, J_4	13
					M_T	14

N_D: no. of dimensions; N_m: no. of lumped masses; N: no. of DOFs (= $N_D N_m$); $\mathcal{S}$: instrumented DOFs; $\mathcal{I}$: *a priori* information

Table 3.3: Parameters of the structural systems considered in the numerical validation.

System	$E[\theta]$	p_θ
I	$E[m_i] = 2500$ kg $\forall\, i \in \{1, \cdots, 6\}$; $E[m_7] = 2000$ kg	$p_{m_i} = 0.005\ \forall\, i \in \{1, \cdots, 7\}$
	$E[k_i] = 5 \times 10^6$ N/m $\forall\, i \in \{1, \cdots, 7\}$	$p_{k_i} = 0.05\ \forall\, i \in \{1, \cdots, 7\}$
	$E[\zeta_i] = 0.05\ \forall\, i \in \{1, \cdots, 7\}$	$p_{\zeta_i} = 0.05\ \forall\, i \in \{1, \cdots, 7\}$
II(a)	$E[m_1] = E[m_2] = 2500$ kg; $E[m_3] = 2000$ kg	$p_{m_i} = 0.005\ \forall\, i \in \{1, 2, 3\}$
	$E[J_i] = (1/12)E[m_i]$ kg-m^2 $\forall\, i \in \{1, 2, 3\}$	$p_{J_i} = 0.005\ \forall\, i \in \{1, 2, 3\}$
	$E[k_{iF}] = 2.5 \times 10^6$ N/m $\forall\, i \in \{1, 2, 3\}$	$p_{k_{iF}} = p_{k_{iB}} = 0.05\ \forall\, i \in \{1, 2, 3\}$
	$E[k_{iB}] = 0.5E[k_{iF}]\ \forall\, i \in \{1, 2, 3\}$	
	$E[\zeta_i] = 0.05\ \forall\, i \in \{1, \cdots, 6\}$	$p_{\zeta_i} = 0.05\ \forall\, i \in \{1, \cdots, 6\}$
II(b)	$E[k_{iB}] = 2.375 \times 10^6$ N/m $\forall\, i \in \{1, \cdots, 3\}$	Same as System II(a)
	All other parameters same as System II(a)	
III	$E[m_i] = 2500$ kg $\forall\, i \in \{1, 2, 3\}$; $E[m_4] = 2000$ kg	$p_{m_i} = 0.005\ \forall\, i \in \{1, \cdots, 4\}$
	$E[J_i] = (2/12)E[m_i]$ kg-m^2 $\forall\, i \in \{1, \cdots, 4\}$	$p_{J_i} = 0.005\ \forall\, i \in \{1, \cdots, 4\}$
	$E[k_{icx}] = E[k_{idx}] = 1.25 \times 10^6$ N/m $\forall\, i \in \{1, \cdots, 4\}$	$p_{k_{iax}} = p_{k_{ibx}} = p_{k_{icx}} = p_{k_{idx}}$ $= p_{k_{iay}} = p_{k_{iby}} = p_{k_{icy}} = p_{k_{idy}}$ $= 0.05\ \forall\, i \in \{1, \cdots, 4\}$
	$E[k_{iax}] = E[k_{ibx}] = 0.6E[k_{icx}]\ \forall\, i \in \{1, \cdots, 4\}$	
	$E[k_{iby}] = E[k_{icy}] = 1.5 \times 10^6$ N/m $\forall\, i \in \{1, \cdots, 4\}$	
	$E[k_{iay}] = E[k_{idy}] = 0.6E[k_{iby}]\ \forall\, i \in \{1, \cdots, 4\}$	
	$E[\zeta_i] = 0.05\ \forall\, i \in \{1, \cdots, 12\}$	$p_{\zeta_i} = 0.05\ \forall\, i \in \{1, \cdots, 12\}$

mass $\mathbf{M}$ and stiffness $\mathbf{K}$ matrices, and subsequently the element masses and stiffnesses.

The estimation errors in the different parameters identified using the proposed method are calculated in each simulation relative to their true values in that simulation. Table 3.4 show the statistics of these errors obtained from the 100 simulations run for each of the 14 cases. These statistics are calculated in the same way as in the numerical examples in Chapter 2 (Section 2.5), viz. for any parameter class $\boldsymbol{\theta}$, consisting of N_θ elements: (a) the relative percentage error is first computed for each element in each simulation (Eq. (2.62)), (b) the means and standard deviations of these relative percentage errors are then computed over all the 100 simulations (Eq. (2.63)), and (c) the maximum (over all the N_θ elements) absolute values of these means and standard deviations are computed (Eq. (2.64)), and reported in Table 3.4. The number of elements N_θ for parameter class $\boldsymbol{\theta} = \{\text{MAC}, \text{COMAC}\}$ is equal to the number of modes/DOFs of the system under consideration, i.e. 7 for System I, 6 for Systems II(a) and II(b), and 12 for System III. For the parameter class $\hat{\mathbf{m}}$, N_θ equals 7 for System I $(\hat{m}_1, \cdots, \hat{m}_7)$, 6 for Systems II(a) and II(b) $(\hat{m}_1, \widehat{J}_1, \cdots, \hat{m}_3, \widehat{J}_3)$, and 8 for System III $(\hat{m}_1, \widehat{J}_1, \cdots, \hat{m}_4, \widehat{J}_4)$; while for the parameter class $\hat{\mathbf{k}}$, N_θ equals 7 for System I $(\hat{k}_1, \cdots, \hat{k}_7)$, 6 for Systems II(a) and II(b) $(\hat{k}_{1F}, \hat{k}_{1B}, \cdots, \hat{k}_{3F}, \hat{k}_{3B})$, and 16 for System III $(\hat{k}_{1Fx}, \hat{k}_{1Bx}, \hat{k}_{1Ry}, \hat{k}_{1Ly}, \cdots, \hat{k}_{4Fx}, \hat{k}_{4Bx}, \hat{k}_{4Ry}, \hat{k}_{4Ly})$. For the 3-D system of System III, using the elements of the global $\mathbf{K}$ matrix, it is not possible to recover all the individual column stiffnesses in the x and y directions, i.e. k_{iax}, k_{iay} etc. Instead, it is only possible to estimate the equivalent column stiffnesses $k_{iFx} = k_{iax} + k_{ibx}$, $k_{iBx} = k_{icx} + k_{idx}$, $k_{iRy} = k_{iby} + k_{icy}$, and $k_{iLy} = k_{iay} + k_{idy}$. However, this will not be a limitation in most situations, since, (a) if the purpose of the identification exercise is to have an updated model to be used for reliability analysis/structural response prediction, then the identified $\mathbf{K}$ matrix should suffice for most response variables, while (b) if the objective is structural health monitoring, then the identified equivalent column stiffnesses can be used for this purpose, e.g. if both the estimated k_{2Fx} and k_{2Ly} are less than expected, then that will indicate a possible damage in the column a of the 2nd floor (Fig. 3.1(c)).

From the error statistics in Table 3.4, it is evident that the proposed algorithms perform reliably well in estimating the complete $\mathbf{V}$ matrix, as well as the mass and stiffness parameters of the systems. Even with considerable measurement noise and erroneous *a priori* information, for Systems I, II(a) and III, the maximum estimation errors in the mass and stiffness parameters have means and standard deviations mostly in the range of $0.1-2\%$ and $0.5-5\%$, while the estimated $\mathbf{V}$ matrix have minimum

Table 3.4: Maximum statistics of estimation errors (%) in identified parameters.

Case	Complete mass normalized mode shape matrix ($\mathbf{V}$)				Mass parameter ($\hat{m}$)		Stiffness parameter ($\hat{k}$)	
	$\mu_{\varepsilon(\text{MAC})}$	$\sigma_{\varepsilon(\text{MAC})}$	$\mu_{\varepsilon(\text{COMAC})}$	$\sigma_{\varepsilon(\text{COMAC})}$	$\mu_{\varepsilon(\hat{m})}$	$\sigma_{\varepsilon(\hat{m})}$	$\mu_{\varepsilon(\hat{k})}$	$\sigma_{\varepsilon(\hat{k})}$
1	0.002	0.002	0.001	0.001	0.153	2.642	0.200	2.184
2	0.001	0.002	0.001	0.001	0.191	1.113	0.114	0.712
3	0.003	0.004	0.003	0.003	1.432	6.532	1.378	5.475
4	0.000	0.000	0.000	0.000	0.111	0.513	0.094	0.730
5	0.000	0.000	0.000	0.000	0.203	0.974	0.090	0.559
6	0.002	0.003	0.002	0.002	0.285	1.886	0.129	2.654
7	0.002	0.002	0.002	0.002	0.320	2.858	0.355	3.345
8	0.006	0.016	0.152	0.338	2.550	8.780	1.844	4.671
9	0.009	0.018	0.106	0.288	3.899	13.208	0.483	3.816
10	0.010	0.017	0.222	0.398	0.789	9.826	0.458	3.016
11	0.012	0.027	0.238	0.412	0.770	12.591	0.309	2.495
12	0.016	0.011	0.001	0.001	0.164	0.821	2.641	2.065
13	0.002	0.002	0.004	0.005	2.002	2.390	0.915	3.382
14	0.003	0.003	0.005	0.008	2.766	5.012	2.601	9.344

MAC and COMAC values in the order of 0.99.

Comparing the estimation errors in the mode shapes and mass and stiffness parameters for Cases 8-11 with the corresponding estimation errors for Case 12, it is evident that, for System II(b) with low translational-rotational coupling, treating the system as two uncoupled 1-D systems instead of a coupled 2-D system leads to an increased estimation accuracy, when there is measurement noise and uncertainty in the *a priori* information. In fact, the maximum standard deviation of the errors in the estimates of the mass parameters is 8.780% for Case 8, while the corresponding value for Case 12 is only 0.821%, even though both the cases have the same instrumentation configuration and use the same *a priori* information. Similarly, the maximum standard deviation of the errors in the estimates of the stiffness parameters is 4.671% for Case 8, as compared to 2.065% for Case 12. However, in situations with no measurement noise and accurate *a priori* information, the estimates of the parameters obtained in Case 12 are not *exact*, unlike all the other cases (including Cases 8-11), with $\mu_{\varepsilon(\text{MAC})} = 0.014$, $\sigma_{\varepsilon(\text{MAC})} = 0.011$, $\mu_{\varepsilon(\text{COMAC})} = 0.001$, $\sigma_{\varepsilon(\text{COMAC})} = 0.001$, and $\mu_{\varepsilon(\hat{m})} = 0.051$, $\sigma_{\varepsilon(\hat{m})} = 0.149$, $\mu_{\varepsilon(\hat{k})} = 2.337$, $\sigma_{\varepsilon(\hat{k})} = 2.188$ (all values in $\%$). This is because, while the proposed algorithm has the efficiency of identifying the *exact* values of the different parameters if the

necessary inputs to the algorithm are exact and compatible with the true system, for Case 12 the requirement of compatibility gets violated, with the exact eigenvalues and non-normalized mode shapes at the sensor locations of the actual 2-D system being not compatible with the uncoupled systems. Nonetheless, since "no noise" situations are purely hypothetical, it will in general be beneficial to treat such systems with low translational-rotational coupling as uncoupled 1-D systems. A second apparent limitation of uncoupling of the system in Case 12 is that the maximum mean error in the stiffness estimates is higher as compared to Cases 8-11. This is expected since the assumption that the system is uncoupled for a coupled system will invariably introduce some bias in the estimates of the spring stiffnesses, with one of the springs at a given level always having a negative error and the other spring at the same level having a positive error, the errors being approximately of the same magnitude ($\approx |k_{iF} - k_{iB}|/2$; e.g. 2.64% in Case 12 where, $E[k_{iB}] = 0.95E[k_{iF}]$). However, if the translational-rotational coupling in the actual system is indeed small, the error induced by the assumption of uncoupling will also be consequently small, and hence the analysis of such systems as uncoupled 1-D systems will, in general, be advantageous.

It is also seen that Case 14 has higher estimation errors than Case 13. This is owing to the fact that, in spite of having sufficient translational-rotational coupling, the equations in Eqs. (3.8) and (3.9) derived using two rows of the mode shape matrix corresponding to DOFs in different directions (x/y/θ) will have "weaker" coefficients than the equations derived using two rows corresponding to DOFs in the same direction. For the 3-D 12-DOF System III, we have a total of 12 modes, with 4 modes dominating in each of the 3 directions, and thus 12 unknown mass normalizing factors. In Case 13, for the 4 dominating modes in any of the 3 directions, we have 4 corresponding "strong" equations, three from the mass matrix and one from the stiffness matrix, obtained using rows of the mode shape matrix corresponding to DOFs in the same direction. In Case 14, the number of such "strong" equations, corresponding to the 4 dominating modes in any of the 3 directions, reduces to 2, one from the mass matrix and one from the stiffness matrix. In other words, in Case 13 we have 12 independent "strong" equations for the 12 unknown mass normalizing factors, 4 equations for each of the 3 sets of 4 dominating modes, with each set corresponding to one of the 3 directions; whereas, in Case 14, although we have enough independent equations for the 11 unknown proportional mass normalizing factors, only 6 of them are "strong", 2 for each set of 4 dominating modes in each of the 3 directions. This introduces some ill-conditioning in Eq. (3.9) for Case 14, and leads to less accurate

parameter estimates as compared to Case 13. Thus, in general, one should ensure that in a N_D-D system with $N = N_D N_m$ DOFs, there are at least N_m "strong" equations for each of the N_D sets of N_m dominating modes. This requirement will automatically get satisfied if one follows the first recommendation made in the discussion at the end of Section 3.3.4.2. As per this recommendation, the number of sensors on System III for Case 14 should be 9, with 3 in each direction, and for Case 13 should be 6 with 2 per direction; while Case 13 satisfies this requirement, Case 14 does not.

In the above simulations the measurements are assumed to be available at the centers of mass of the mass elements. To see how an error in the center of mass location affects the parameter estimates, the situation of Case 4 is used again, with the true center of mass of the third mass element shifted towards the front of the geometric center (i.e towards the springs denoted as k_{iF} in Fig. 3.1(b)) by $0.05l = 0.05$m. The responses, $\ddot{\mathbf{u}}_{x_3}$ and $\ddot{\mathbf{u}}_{\theta_3}$, are however measured at the geometric center of the third mass element, and the "incorrect" assumption that this geometric center coincides with the center of mass is made in the solution. As before, 100 simulations are run, with 10% measurement noise and inaccurate *a priori* information used in the different simulations. The physical parameter estimation error statistics are: $\mu_{\varepsilon(\hat{m})} = 7.024\%$, $\sigma_{\varepsilon(\hat{m})} = 4.840\%$, $\mu_{\varepsilon(\hat{k})} = 9.135\%$, $\sigma_{\varepsilon(\hat{k})} = 7.722\%$. Comparing these with the values for Case 4 in Table 3.4, the considerable increase in estimation error owing to an error in the center of mass is evident. This increased error is owing to the fact that, with the physical coordinates not coinciding with the center of mass, some of the equations for estimating the mass normalizing factors in Eqs. (3.8) and (3.9) have modeling errors, which propagate through the different identification steps. In fact, excluding the equations $\mathbf{r}_5^T \mathbf{r}_6 = 0$, $\mathbf{r}_5^T \mathbf{r}_5 = 1/m_3$ and $\mathbf{r}_6^T \mathbf{r}_6 = 1/J_3$, which are the ones with modeling error due to the center of mass error in the third mass element, we get: $\mu_{\varepsilon(\hat{m})} = 2.834\%$, $\sigma_{\varepsilon(\hat{m})} = 1.256\%$, $\mu_{\varepsilon(\hat{k})} = 0.151\%$, $\sigma_{\varepsilon(\hat{k})} = 1.719\%$. Also, the error $\mu_{\varepsilon(\hat{m})} = 2.834\%$ corresponds to J_3, and is approximately equal to $(2000 \times 0.05^2)/(2000 \times 1^3/12) \approx 2.99\%$, which is the percentage difference in J_3 defined at the geometric center with respect to J_3 defined at the center of mass, for this scenario. Thus, one approach to increase the accuracy of results, when the center of mass of some mass elements are known with less confidence, is to exclude the equations which may be affected by this uncertainty while estimating the mass normalizing factors; this will however require over-instrumentation of the system so as to have, even after excluding the uncertain equations, at least the necessary number of equations for solving the normalizing factors. An alternative approach, which will not require

over-instrumentation, is to estimate the centers of mass using the method of Appendix A.

3.6 Shake Table Experimental Study[2]

For the experimental application of the structural identification approach, a 4-story single bay laboratory scale A36 steel frame structural model is considered. The frame has an interstory height of 533 mm, floor plate dimensions of $610 \times 457 \times 12.7$ mm, and is diagonally braced in one direction. The columns and the diagonal braces have cross-sectional dimensions of 50.8×9.5 mm and 50.8×6.4 mm, respectively. All the structural connections are bolted using connection plates and angles. The frame is excited in the weak direction of bending, i.e. along the direction without bracing and smaller (9.5 mm) column dimension. The base excitation is provided using the 1.5×1.5 sq. m platform uniaxial hydraulic shaking table facility available at the Carleton Laboratory of Columbia University, New York. The frame is mounted on the table and the structure-table connection is sufficiently bolted to reproduce a fixed-base behaviour. The frame is fully instrumented with accelerometers magnetically attached to the column connection plates at each floor, at the height of the respective floor plates, as well as reference accelerometers located on the shake table platform. In the discussion herein, we use the structural acceleration response measurements from 8 channels; 4 of these (a_9, a_{15}, a_3, a_4) are located as shown in Fig. 3.4, and the other 4 are located at the floor plate levels on the column connection plates of the South-West (S-W) columns. With rigid floor assumption, the accelerations at the center of the floors in the weak direction are estimated using the measurements of these 8 channels; since these accelerations are along the centerlines of the floors they will contain minimal torsional effects, assuming that the centers of mass lie approximately along these centerlines. The base excitation is also oriented so as to induce minimal torsional excitation on the structure. Thus we consider the frame to be modeled as a 1-D 4-DOF system. Six different types of input ground motions, listed in Fig. 3.4, are each applied thrice to the table, thus constituting a total of 18 dynamic tests of the frame. The measured acceleration responses of the table are used as the inputs in the identification exercise.

For analysis using the experimental data, six scenarios of instrumentation and available *a priori*

[2]I would like to thank Ms. Luciana Balsamo, Mr. Adrian Brugger, Prof. Manolis Chatzis and Prof. Andrew Smyth for their collaboration and support during the shake table experiments.

information are considered, as listed in Fig. 3.4. Two of these scenarios consider complete instrumentation, while in three scenarios the second DOF (second floor) is considered to be unobserved, and in one scenario only the first and last DOFs are considered to be instrumented. As available *a priori* knowledge, the first three scenarios assume a complete knowledge of the mass matrix, i.e. all four floor masses known, while the fourth scenario considers a situation where some of the floor masses are known, and in the last two scenarios only the total mass of the system is assumed to be known. The analytical model of the frame is adopted here from [46], and the floor masses of this analytical model is used to get the necessary *a priori* knowledge in any experimental scenario. This 4-DOF analytical model, hereafter denoted as $\mathcal{A}$, has uniform floor masses of 37 kg, and uniform story stiffnesses of 1.7×10^5 N/m.

$$\mathbf{M}_{\mathcal{A}} = \begin{bmatrix} 37.0 & 0.0 & 0.0 & 0.0 \\ 0.0 & 37.0 & 0.0 & 0.0 \\ 0.0 & 0.0 & 37.0 & 0.0 \\ 0.0 & 0.0 & 0.0 & 37.0 \end{bmatrix} \text{kg}; \quad \mathbf{K}_{\mathcal{A}} = \begin{bmatrix} 3.4 & -1.7 & 0.0 & 0.0 \\ -1.7 & 3.4 & -1.7 & 0.0 \\ 0.0 & -1.7 & 3.4 & -1.7 \\ 0.0 & 0.0 & -1.7 & 1.7 \end{bmatrix} \times 10^5 \text{N/m} \quad (3.33)$$

The measured responses (at the center of the floors) at the instrumented DOFs are used, along with the measured table response as the input, to estimate the modal parameters at the measured floors using ERA-OKID. Using these estimated modal parameters in the proposed identification approach, the complete mass normalized mode shape matrix $\mathbf{V}$, the $\mathbf{M}$ and $\mathbf{K}$ matrices, and the floor masses and story stiffnesses, are subsequently obtained (note that the mode shape expansion is not necessary in scenarios $\mathcal{C}_I$ and $\mathcal{C}_V$ owing to complete instrumentation). From the identified $\mathbf{K}$ matrices in this study, as well as from the $\mathbf{K}$ identified in [46], it is evident that the $\mathbf{K}$ matrix of the frame, although dominantly tridiagonal, is not strictly shear-type in nature. Thus, for all the scenarios excepting $\mathcal{C}_{III}$, in the estimation of the mass normalizing factors, the set of equations derived using the tridiagonality of $\mathbf{K}$ is not used. For scenario $\mathcal{C}_{III}$, however, this will lead to an undetermined system (3 equations and 4 unknowns), and hence the equation $\mathbf{r}_1 \mathbf{\Lambda} \mathbf{r}_4^T = 0$ given by this condition is also included. In the mode shape expansion in scenarios $\mathcal{C}_{II}$, $\mathcal{C}_{IV}$ and $\mathcal{C}_{VI}$, the 2nd (unobserved) row of the mode shape matrix is estimated from the 1st row (Statement 2 in Chapter 2); for scenario $\mathcal{C}_{III}$ the 2nd and 3rd rows are estimated respectively from the 1st and 4th rows (Statements 2 and 3 in Chapter 2). Note that these equations inherently take into account the shear-type nature of $\mathbf{K}$. However, owing to the fact that $\mathbf{K}$ is not strictly shear-type, in the mode shape expansion we give more importance

to the equations derived using the condition of diagonality of $\mathbf{M}$ than the other equations which involve the condition of shear-type nature of $\mathbf{K}$. This reflects that we have more confidence in the diagonality of $\mathbf{M}$, which seems to be a more reasonable modeling assumption, than in the shear-type nature of $\mathbf{K}$. This increased dependence of the mode shape expansion procedure on the diagonality of $\mathbf{M}$ vis-$\grave{a}$-vis the shear-type nature of $\mathbf{K}$ is achieved, following Section 3.4.3, by: (1) including the orthogonality of the unobserved rows to *all* the observed rows of the mode shape matrix, and (2) weighting the equations depicting the diagonality of $\mathbf{M}$ by 10, as compared to the weight of 1 for the other equations involved in the mode shape expansion. Additionally, for scenarios $\mathcal{C}_{II}$ and $\mathcal{C}_{III}$, the estimates of the unobserved rows of $\mathbf{V}$ obtained as above are treated as initial estimates, and a Newton-Raphson procedure starting from these estimates is employed to get the final estimates; in this Newton-Raphson solution step the quadratic equations (weighted by 10) representing the condition of known *a priori* masses at the unobserved DOFs also get included.

After estimating the different parameters in each of the 18 runs (6 inputs, each run thrice), the statistics (mean μ, standard deviation σ and coefficient of variation (COV = σ/μ in %)) of these estimates are computed, for each instrumentation - available *a priori* information scenario. The COV is a measure of the dispersion between the parameter estimates from the different test runs, and reflects the uncertainty induced by ambient effects/measurement noise and variability of the input excitations in the different tests.

Table 3.5 lists the statistics of the modal frequencies and damping ratios identified using ERA-OKID, along with the analytical model's modal frequencies ($\mathcal{A}$), and those identified in [46] for the completely instrumented healthy system and known $\mathbf{M} = \mathbf{M}_{\mathcal{A}}$ situation ($\mathcal{E}$). (The identification results from [46], referred here and also later in this section, correspond to a *different* set of experiments, conducted earlier on the same frame.) It is evident that while the identified frequencies are reasonably consistent across all the three instrumentation set-ups considered, the damping ratios show some dispersion between the different instrumentation set-ups. Also, the uncertainty in the frequency estimates is reasonably small, with the COV being mostly less than 1%, signifying a robust estimation of the structural frequencies. The uncertainty in the damping ratio estimates is however considerable. This high uncertainty can be primarily attributed to the variability in input excitation; as reported in [46] the identified modal damping ratios "depend strongly on the type of input excitation". Ambient effects/measurement noise, and possible variability in the structural connections

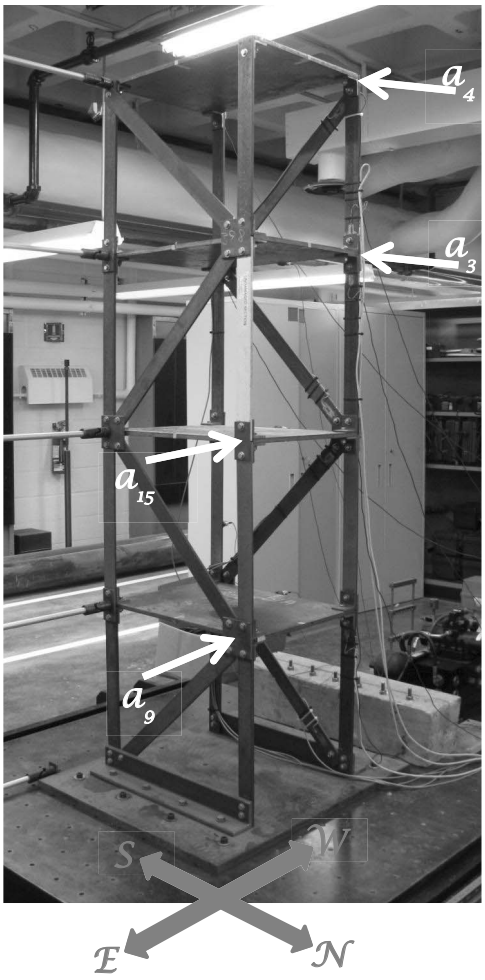

Inputs:

Band limited white noise, EC8, El Centro, Hachinohe, Kobe, Northridge

Experimental scenarios:

Scenario	Instrumented DOFs (floors)	*A priori* Information
C_I	1, 2, 3, 4	m_1, m_2, m_3, m_4
C_{II}	1, 3, 4	m_1, m_2, m_3, m_4
C_{III}	1, 4	m_1, m_2, m_3, m_4
C_{IV}	1, 3, 4	m_1, m_3, m_4
C_V	1, 2, 3, 4	M_T
C_{VI}	1, 3, 4	M_T

Figure 3.4: Experimental 4-story frame model on the shake table, and lists of inputs and instrumentation - available *a priori* information scenarios.

Table 3.5: Statistics of modal frequency (Hz) and damping ratio (%) estimates using ERA-OKID.

Scenario	μ_f (Hz)	σ_f (Hz)	COV$_f$ (%)
$\mathcal{A}$	$3.75, 10.79, 16.53, 20.27$	————	————
$\mathcal{E}$	$3.68, 10.60, 18.21, 25.81$	$0.03, 0.09, 0.07, 0.12$	$0.82, 0.85, 0.38, 0.46$
$\mathcal{C}_I, \mathcal{C}_V$	$3.59, 10.76, 17.96, 25.45$	$0.02, 0.15, 0.07, 0.07$	$0.68, 1.38, 0.40, 0.29$
$\mathcal{C}_{II}, \mathcal{C}_{IV}, \mathcal{C}_{VI}$	$3.59, 10.77, 17.96, 25.44$	$0.03, 0.15, 0.07, 0.07$	$0.70, 1.39, 0.40, 0.26$
$\mathcal{C}_{III}$	$3.59, 10.76, 17.96, 25.45$	$0.03, 0.15, 0.07, 0.08$	$0.79, 1.36, 0.40, 0.31$
	μ_ζ (%)	σ_ζ (%)	COV$_\zeta$ (%)
$\mathcal{E}$	$0.95, 0.51, 0.47, 0.61$	$0.19, 0.11, 0.10, 0.17$	$20, 21.57, 21.28, 27.87$
$\mathcal{C}_I, \mathcal{C}_V$	$0.57, 0.54, 0.36, 0.36$	$0.10, 0.16, 0.08, 0.05$	$16.95, 29.63, 21.24, 13.26$
$\mathcal{C}_{II}, \mathcal{C}_{IV}, \mathcal{C}_{VI}$	$0.63, 0.54, 0.36, 0.35$	$0.08, 0.16, 0.08, 0.04$	$12.89, 30.36, 21.36, 12.66$
$\mathcal{C}_{III}$	$0.56, 0.61, 0.40, 0.39$	$0.11, 0.10, 0.09, 0.04$	$20.24, 16.89, 21.30, 10.97$

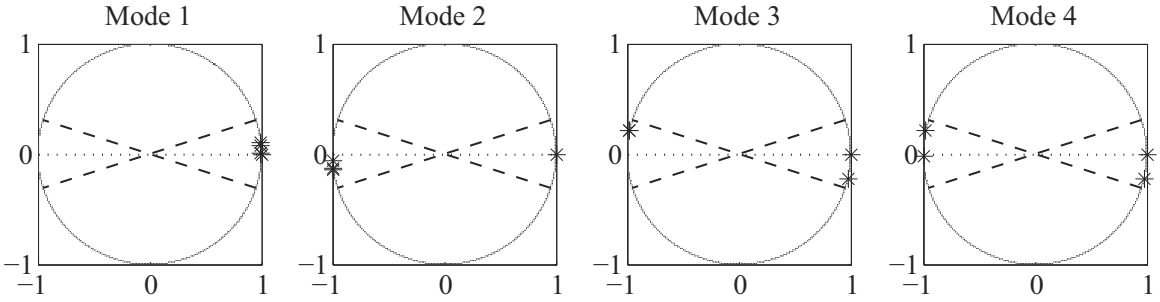

Figure 3.5: Phase angles of the complex mode shape components identified using ERA-OKID for a Kobe earthquake excitation and complete instrumentation.

during and between experiments due to slight loosening of bolts, also add to this dispersion. However, since the damping ratios are not involved in the identification approach used in this chapter, this high uncertainty will not affect the identified $\mathbf{V}$, $\mathbf{M}$ and $\mathbf{K}$ matrices.

The mode shape components identified using ERA-OKID are initially complex. Since this may suggest non-proportional damping, to check how complex the modes are, we follow the approach used in [47]: after normalizing each mode shape so as to have the maximum component equal to one, the phases of the different components are calculated and plotted on the unit circle. Fig. 3.5 shows such an example plot for one of the Kobe earthquake runs and complete instrumentation. The phases of each component are denoted by asterisks on the unit circle, and the $\pm 0.1\pi$ bounds are shown by dashed lines. While for "real modes" the phase should be 0 or π, accounting for the effects of

Table 3.6: Statistics of MAC between OKID/ERA estimates of complete non-normalized modes and estimates of complete mass-normalized modes from proposed approach.

Scenario	μ_{MAC}	σ_{MAC} (10^{-2})	COV_{MAC} (%)
$\mathcal{C}_I$	$0.99, 0.99, 1.00, 1.00$	$0.31, 0.33, 0.11, 0.04$	$0.31, 0.33, 0.11, 0.04$
$\mathcal{C}_{II}$	$1.00, 0.99, 0.99, 1.00$	$0.16, 0.54, 0.31, 0.09$	$0.16, 0.55, 0.32, 0.09$
$\mathcal{C}_{III}$	$0.97, 0.96, 0.99, 0.99$	$1.21, 1.52, 0.20, 0.49$	$1.24, 1.58, 0.20, 0.50$
$\mathcal{C}_{IV}$	$0.99, 0.99, 0.99, 1.00$	$0.21, 0.32, 0.31, 0.10$	$0.21, 0.32, 0.31, 0.10$
$\mathcal{C}_V$	$1.00, 1.00, 1.00, 1.00$	$0.02, 0.01, 0.01, 0.02$	$0.02, 0.01, 0.01, 0.02$
$\mathcal{C}_{VI}$	$0.99, 1.00, 0.99, 0.99$	$0.02, 0.02, 0.22, 0.11$	$0.02, 0.02, 0.22, 0.11$

measurement noise etc., variations within these $\pm 0.1\pi$ bounds may be considered acceptable. As can be seen, all the components of all the modes, lie within these bounds, and this is found to be true also for other inputs and sensor set-ups (except at nodes where both the real and imaginary parts of the identified modes are close to zero). This suggests that the system is proportionally damped, and the identified modal frequencies and the real mode shapes obtained by minimizing the imaginary parts of the initial complex modes, may be used in the subsequent steps of identification.

Once the identified real mode shapes are normalized and, if necessary, expanded using the proposed approach, the MAC values comparing these with the non-normalized real mode shapes identified through ERA-OKID for complete instrumentation, are calculated, and their statistics presented in Table 3.6. Although scenarios $\mathcal{C}_I$ and $\mathcal{C}_V$ represent complete instrumentation, the MAC values corresponding to these scenarios are slightly different from 1, owing to the optimization exercise in Eq. (3.32). As per the MAC values, the normalized complete mode shapes estimated across the different scenarios are consistent with each other, with MAC values close to 1. Also, in any given scenario, the estimated mode shapes from the 18 different test runs are consistent, with the COV being less than 1% in general. Fig. 3.6 compares the mean of the complete mass normalized mode shapes (scaled by a factor of 4 to aid in representation) obtained in Scenarios $\mathcal{C}_I$ and $\mathcal{C}_{VI}$. Based on the first modes in Fig. 3.6, it is seen that in scenario $\mathcal{C}_I$ the 4th story seems to be almost infinitely stiff as compared to the rest of the structure, unlike in scenario $\mathcal{C}_{VI}$; while scenarios $\mathcal{C}_{II}$ to $\mathcal{C}_{IV}$ show a similar behaviour as $\mathcal{C}_I$, scenario $\mathcal{C}_V$ is similar to $\mathcal{C}_{VI}$ on this issue. This behaviour may be owing to the assumption of the known 4th floor mass value of 37 kg (same as the other floors) in scenarios $\mathcal{C}_I$ to $\mathcal{C}_{IV}$. As can be seen later from Table 3.8, when we do not make this assumption (in scenarios $\mathcal{C}_V$ and $\mathcal{C}_{VI}$), the

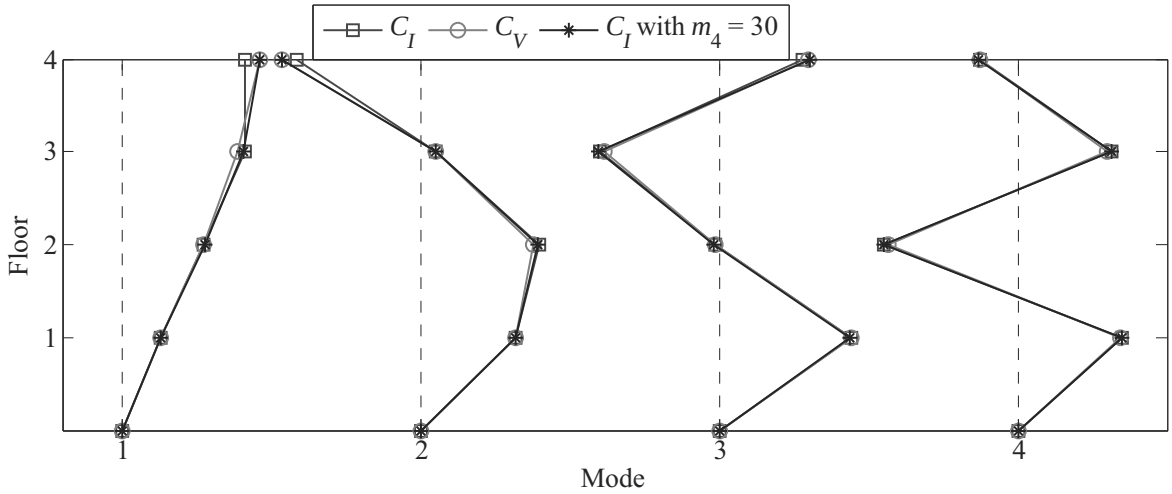

Figure 3.6: Comparison of mean mass normalized mode shapes in scenarios $\mathcal{C}_I$, $\mathcal{C}_{VI}$, and $\mathcal{C}_I$ with $m_4 = 30$ kg.

4th floor mass is estimated as around 29 - 30 kg. Assuming the presence of a larger mass at the 4th floor, than what actually is, will force any algorithm to assign a "larger than the actual stiffness" to the 4th story, in order to produce the same response. This is again seen in Table 3.8, where the 4th story stiffness estimates are larger in scenarios $\mathcal{C}_I$ to $\mathcal{C}_{IV}$ than in scenarios $\mathcal{C}_V$ and $\mathcal{C}_{VI}$. This over estimation of the stiffness may be reflected in the apparent non-deformability of the 4th story in the 1st mode for scenarios $\mathcal{C}_I$ to $\mathcal{C}_{IV}$. In fact, as seen from Fig. 3.6, when we assume $m_4 = 30$ kg in scenario $\mathcal{C}_I$, the deformation of the 4th story in the 1st mode is closer to scenario $\mathcal{C}_{VI}$, than to the original scenario $\mathcal{C}_I$ with $m_4 = 37$ kg.

Table 3.7 presents the statistics of the identified $\mathbf{M}$ and $\mathbf{K}$ matrices obtained, using the complete mass-normalized $\mathbf{V}$ matrices and the identified eigenvalues (frequencies), in the two scenarios $\mathcal{C}_I$ and $\mathcal{C}_{VI}$ (the matrices identified in the other scenarios are similar). The $\mathbf{K}$ matrix of the healthy system identified in [46], using the M-L-K algorithm [28] with complete instrumentation and known $\mathbf{M} = \mathbf{M}_{\mathcal{A}}$, is also shown for comparison purposes. From these identified matrices it is evident that $\mathbf{K}$, although dominantly tridiagonal, is not strictly shear-type in nature. Also, although the MAC values in Table 3.6 are all close to 1, there is noticeable dispersion between the identified $\mathbf{M}$ and $\mathbf{K}$ matrices across the different experimental scenarios. This indicates that a near 1 value of MAC does not necessarily imply a good match between the two systems, as shown in Appendix D [48]. The dis-

Table 3.7: Statistics of mass and stiffness matrix estimates for experimental scenarios $\mathcal{C}_I$ and $\mathcal{C}_{VI}$.

Scenario	$\mu_{\mathbf{M}}$ (kg)	$\sigma_{\mathbf{M}}$ (kg)	$\mu_{\mathbf{K}}$ (10^5 N/m)	$\sigma_{\mathbf{K}}$ (10^5 N/m)
$\mathcal{E}$	37.00 0.00 0.00 0.00	———	5.94 -3.43 0.83 -0.14	0.05 0.09 0.02 0.02
	0.00 37.00 0.00 0.00		-3.43 5.02 -2.75 0.40	0.09 0.12 0.06 0.03
	0.00 0.00 37.00 0.00		0.83 -2.75 4.21 -2.03	0.02 0.06 0.06 0.03
	0.00 0.00 0.00 37.00		-0.14 0.40 -2.03 1.67	0.02 0.03 0.03 0.03
$\mathcal{C}_I$	37.03 0.22 -0.09 -0.02	0.11 0.92 0.36 0.09	5.14 -2.92 0.50 -0.11	0.09 0.12 0.08 0.06
	0.22 37.14 0.10 -0.09	0.92 0.58 0.43 0.39	-2.92 5.00 -2.84 0.58	0.12 0.09 0.05 0.15
	-0.09 0.10 37.20 0.11	0.36 0.43 0.87 0.46	0.50 -2.84 3.96 -2.06	0.08 0.05 0.07 0.09
	-0.02 -0.09 0.11 36.77	0.09 0.39 0.46 0.97	-0.11 0.58 -2.06 1.91	0.06 0.15 0.09 0.10
$\mathcal{C}_{VI}$	38.08 -0.00 -0.00 0.00	0.63 0.00 0.00 0.00	5.22 -3.09 0.00 0.00	0.06 0.06 0.00 0.00
	-0.00 38.98 6.14 -0.42	0.00 1.05 0.26 0.73	-3.09 5.45 -2.28 0.41	0.06 0.09 0.02 0.02
	-0.00 6.14 42.70 -0.07	0.00 0.26 0.76 0.11	0.00 -2.28 3.58 -1.80	0.00 0.02 0.04 0.06
	0.00 -0.42 -0.07 30.13	0.00 0.73 0.11 2.28	0.00 0.41 -1.80 1.51	0.00 0.02 0.06 0.13

persion between the different identified systems in the different scenarios may be expected owing to the different modeling assumptions and amounts of measured experimental data used in the different scenarios. The different amounts of measured data, owing to different levels of instrumentation, also introduce a source of discrepancy in terms of the relative importance given to the model vis-$\grave{a}$-vis the data. In spite of these sources of discrepancies, the differences in the diagonal terms of $\mathbf{M}$ and the diagonal and super/subdiagonal terms of $\mathbf{K}$ identified in the different scenarios, are not significant enough to classify any of the identified models as an outlier. Figs. 3.7 and 3.8 compare the measured acceleration responses, their autocorrelations, and the frequency response function magnitudes of the frame, with the corresponding quantities of the estimated system under a Hachinohe earthquake run. While Fig. 3.7 considers the 4th floor acceleration and Scenario $\mathcal{C}_{VI}$, with the 4th floor being an observed DOF in this scenario, Fig. 3.8 considers the 2nd floor acceleration and Scenario $\mathcal{C}_{II}$ in which the 2nd floor is unobserved. From these figures it is evident that for an observed DOF the estimated system can reconstruct the responses with a high accuracy; while for the unobserved DOF considered in Fig. 3.8, the responses are slightly underestimated, the estimated responses still capture the dominant frequencies and the pattern of the measured responses with reasonable accuracy. These results illustrate the potential of the proposed approach in identifying reliable structural models which may be used for response prediction purposes.

Once the $\mathbf{M}$ and $\mathbf{K}$ matrices are identified, the floor masses of the frame are estimated as the diagonal terms of the identified $\mathbf{M}$ matrices, i.e. $m_i = M_{i,i}$, and the story stiffnesses are estimated as the super/subdiagonal terms of the identified $\mathbf{K}$ matrices, i.e. $k_i = -K_{i,i+1}$ (with the first story stiffness calculated as $k_1 = K_{1,1} + K_{1,2}$). The statistics of the estimated floor masses and story stiffnesses are respectively listed in Table 3.8. Although there exists a variability between the different (mean) models identified in the six different experimental scenarios, the mean mass and stiffness distributions (amongst the floors and stories) in the different identified models bear reasonable resemblance, given the aforementioned discrepancies in the amount of data and modeling assumptions in the different experimental scenarios. The COVs are mostly around $0-2\%$ for the estimated floor masses, and around $0-3\%$ for the estimated story stiffnesses, indicating that the uncertainty in these estimates are not unreasonably high in general, given the obvious presence of unknown/uncontrolled variables in any experimental application. This in turn highlights the reasonable robustness of the proposed structural identification algorithm in handling real data and in realistic situations comprising of incomplete instrumentation of the monitored system, uncertain and/or incomplete *a priori* information about the system etc. Moreover, from these coefficients it can be inferred that, even for low levels of damage, it is less likely that the uncertainties in the story stiffness estimates would mask the damage induced stiffness reduction. This observation propounds the possibility of using the proposed identification algorithm in structural health monitoring/damage detection exercises, as done in Chapter 5.

Note that, in spite of using known floor mass values of 37 kg in some of the scenarios, the estimated masses are not exactly 37 kg. This is because, in the estimation of the mass normalizing factors or in the mode shape expansion, these *a priori* information are used along with other conditions obtained from imposing structural topology requirements and satisfaction of the eigenvalue problem. The unknown normalization factors or mode shape components are then solved for in a least squares sense. In this way, the *a priori* known mass values are not strictly imposed, and that solution is sought which optimally satisfies all the conditions considered together. This should be seen as an advantage of the proposed method, as it inherently allows for uncertainties in the available *a priori* information as well as uncertainties in the other conditions like structural topology requirements. The non-shear type nature of the identified $\mathbf{K}$ matrices illustrate the ability of the method, primarily developed for the identification of shear-type systems, to identify near-shear type systems, thus allowing for uncertainty in the structural topology requirements. Also, as mentioned earlier, and

Table 3.8: Statistics of floor mass (in kg) and story stiffness (in 10^5 N/m) estimates.

Scenario	μ_m (kg)	σ_m (kg)	COV$_m$ (%)
$\mathcal{A}$	$37.00, 37.00, 37.00, 37.00$	————————	————————
$\mathcal{E}$	$37.00, 37.00, 37.00, 37.00$	————————	————————
$\mathcal{C}_I$	$37.03, 37.14, 37.20, 36.77$	$0.11, 0.58, 0.87, 0.97$	$0.29, 1.55, 2.33, 2.64$
$\mathcal{C}_{II}$	$37.00, 37.49, 37.12, 37.03$	$0.00, 0.17, 0.02, 0.01$	$0.00, 0.46, 0.07, 0.03$
$\mathcal{C}_{III}$	$37.98, 39.68, 39.13, 38.31$	$0.30, 0.60, 0.73, 0.38$	$0.78, 1.51, 1.87, 0.99$
$\mathcal{C}_{IV}$	$37.00, 41.45, 37.13, 37.03$	$0.00, 1.82, 0.03, 0.01$	$0.00, 4.38, 0.08, 0.04$
$\mathcal{C}_V$	$36.90, 39.65, 41.26, 30.19$	$0.70, 0.65, 1.16, 2.42$	$1.90, 1.63, 2.80, 8.02$
$\mathcal{C}_{VI}$	$38.08, 38.98, 42.70, 30.13$	$0.63, 1.05, 0.76, 2.28$	$1.64, 2.71, 1.77, 7.57$
	μ_k (10^5 N/m)	σ_k (10^5 N/m)	COV$_k$ (%)
$\mathcal{A}$	$1.70, 1.70, 1.70, 1.70$	————————	————————
$\mathcal{E}$	$2.51, 3.43, 2.75, 2.03$	————————	————————
$\mathcal{C}_I$	$2.22, 2.92, 2.84, 2.06$	$0.05, 0.12, 0.05, 0.09$	$2.20, 4.16, 1.62, 4.61$
$\mathcal{C}_{II}$	$2.44, 2.95, 2.50, 2.05$	$0.13, 0.04, 0.09, 0.07$	$5.15, 1.25, 3.67, 3.22$
$\mathcal{C}_{III}$	$2.46, 3.66, 3.60, 2.87$	$0.16, 0.06, 0.12, 0.24$	$6.45, 1.74, 3.42, 8.45$
$\mathcal{C}_{IV}$	$2.29, 3.10, 2.62, 2.05$	$0.07, 0.04, 0.05, 0.06$	$2.88, 1.27, 1.87, 3.14$
$\mathcal{C}_V$	$2.07, 3.05, 3.16, 1.91$	$0.02, 0.03, 0.06, 0.01$	$0.92, 0.95, 1.94, 0.75$
$\mathcal{C}_{VI}$	$2.13, 3.09, 2.28, 1.80$	$0.01, 0.06, 0.02, 0.06$	$0.53, 1.89, 0.86, 3.56$

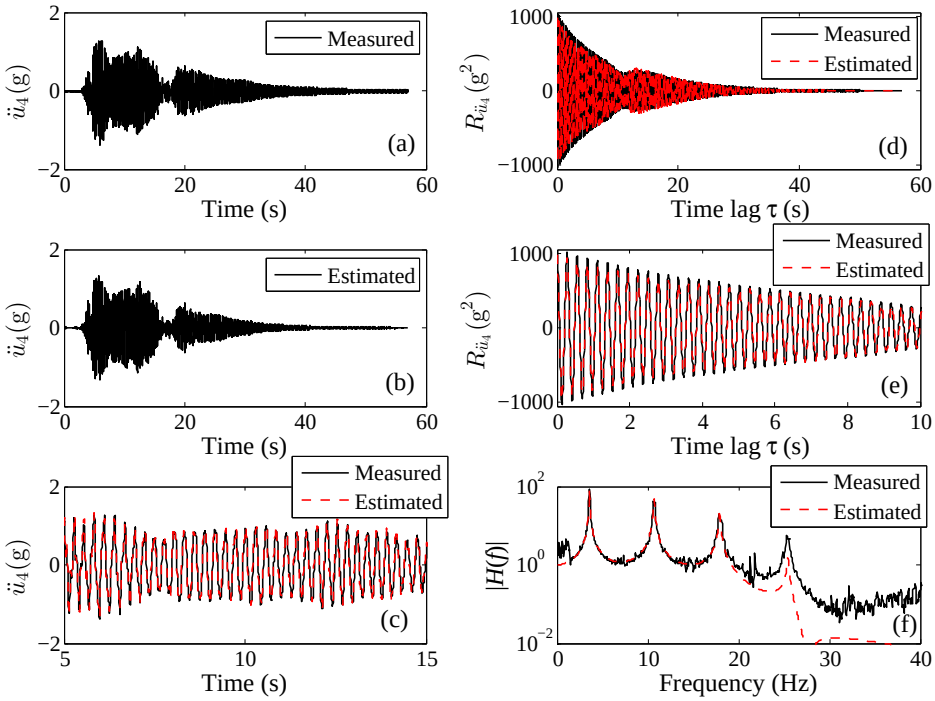

Figure 3.7: 4th floor (observed DOF) acceleration under a Hachinohe earthquake: (a) measured response, (b) estimated response in Scenario $\mathcal{C}_{VI}$, (c) measured and estimated responses during strong shaking, (d) autocorrelations of measured and estimated responses, (e) autocorrelation up to time lag $= 10$ s, and (f) measured and estimated frequency response function magnitudes.

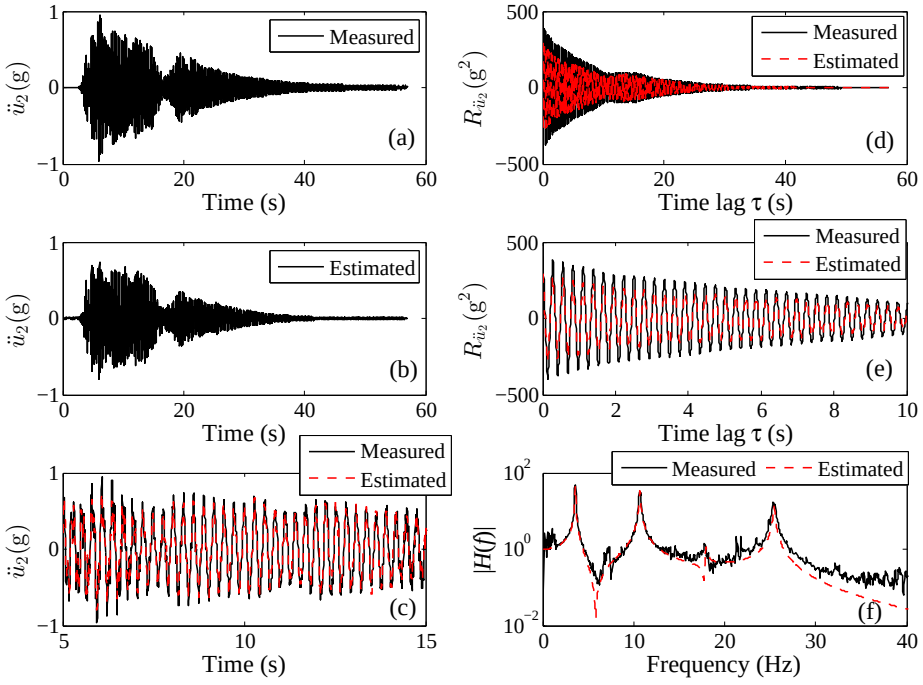

Figure 3.8: 2nd floor (unobserved DOF) acceleration under a Hachinohe earthquake: (a) measured response, (b) estimated response in Scenario $\mathcal{C}_{II}$, (c) measured and estimated responses during strong shaking, (d) autocorrelations of measured and estimated responses, (e) autocorrelation up to time lag $= 10$ s, and (f) measured and estimated frequency response function magnitudes.

implemented in this experimental application, the different levels of confidence that one may have in the different conditions can be imposed using different weighting factors. A second observation from Table 3.8 is that, in scenarios $\mathcal{C}_V$ and $\mathcal{C}_{VI}$, where the total mass M_T is used as the only available *a priori* information, the estimated 4th floor mass is lower than the estimated masses of the other floors. This can be expected to be a more realistic picture of the mass distribution between the different floors, since the 4th floor mass can be expected to have contribution from approximately only half the 4th story columns, braces and connections, while the other floors will have a contribution from approximately a full story's columns, braces and connections (one-half from the story below and one-half from the story above). Using a mass density of 7800 kg/m^3 for A36 steel, the mass of any of the floor plates is approximately 27 kg, i.e. approximately 10 kg mass is contributed in each floor by the columns, braces and connections. Finally, it should be mentioned that, amongst the six experimental scenarios considered in this study, scenario $\mathcal{C}_V$ possibly provides the most ideal conditions for identification, since it involves the least *a priori* information and complete instrumentation, and hence relies almost exclusively on experimental data. This increased reliance on experimental observation is also evidenced by the MAC values reported in Table 3.6, where the mean MAC values corresponding to scenario $\mathcal{C}_V$ are all equal to 1, with COVs in the range $0.00 - 0.02\%$, the minimum COV_{MAC} amongst all the six scenarios. Hence, the identified models in scenario $\mathcal{C}_V$ are possibly the closest representations of the true system, in the premise that we trust the experimental data more than any modeling assumption(s).

To test the performance of the identification approach with error in the center of mass/*a priori* mass information, an additional set of 18 tests were performed with an added eccentric 5 kg mass on the 2nd floor. This mass was attached at the center of the north side ($\mathcal{N}$) of the floor, and thus shifts the center of mass of the 2nd floor towards the north side, in addition to increasing its mass by 5 kg. In the identification using the measured data, two different cases are considered to obtain the *a priori* information necessary in any scenario: (a) $\mathbf{M}_{\mathcal{A}} = \text{diag}(37.00, 37.00, 42.00, 37.00)$, and (b) $\mathbf{M}_{\mathcal{A}} = \text{diag}(37.00, 37.00, 37.00, 37.00)$ (same as before); these two cases are respectively denoted by $\mathcal{I}_I$ and $\mathcal{I}_{II}$. While case $\mathcal{I}_I$ is affected only by the error in the 2nd floor's center of mass, case $\mathcal{I}_{II}$ is additionally affected by the errors in the 2nd floor mass value m_2 (in scenarios $\mathcal{C}_I$ to $\mathcal{C}_{III}$) and the value of the total mass M_T (in scenarios $\mathcal{C}_V$ and $\mathcal{C}_{VI}$). An error in the center of mass in a 1-D model does not explicitly affect the proposed approach by introducing modelling errors in some

of the normalizing factor estimation and mode shape expansion equations, unlike in 2-D and 3-D models (see the discussion at the end of Section 3.5). However, in this case, such an error affects the responses used in the identification, which are calculated by averaging the measured responses from accelerometers located at the corners of the floors, and hence correspond to the accelerations at the geometric centers of the floor; with a sufficiently shifted center of mass, the accelerations at the center of floor and center of mass will no longer be even *approximately* the same. Table 3.9 lists the means and standard deviations of the different floor masses and story stiffnesses for both cases $\mathcal{I}_I$ and $\mathcal{I}_{II}$. Comparing Tables 3.9 and 3.8 it is evident that the stiffness estimates for all the stories, as well as the mass estimates for floors 1, 3 and 4, are not affected to any significant extent by the shift in the 2nd floor's center of mass or the errors in the *a priori* information. Also, in all the scenarios except $\mathcal{C}_{IV}$, only the shift in the center of mass does not introduce any considerable error in the estimate of m_2. Additionally, in scenarios $\mathcal{C}_V$ and $\mathcal{C}_{VI}$, even the error in the *a priori* information M_T does not affect the estimate of m_2 significantly, while for scenarios $\mathcal{C}_I$ to $\mathcal{C}_{III}$, the error in the *a priori* value of m_2 is reflected in the estimates of m_2, as may be expected. In scenario $\mathcal{C}_{IV}$, the mean estimate of m_2 is considerably larger (38% overestimation with respect to the analytical value of 42 kg), as is the associated standard deviation. The estimates in scenario $\mathcal{C}_{IV}$ are identical for both cases $\mathcal{I}_I$ and $\mathcal{I}_{II}$, since in this scenario, the same measurements and the same *a priori* information are used in both cases. The high error in the estimate of m_2 in scenario $\mathcal{C}_{IV}$ may be attributed to the effects of (a) neither measuring the 2nd floor's acceleration, which has a considerable disturbance in its mass owing to the added 5 kg ($\approx 13.5\%$ of 37 kg), (b) nor using the mass of the 2nd floor as an *a priori* information, (c) but, at the same time, putting too much constraints on the solution process through the *a priori* information of all the other floor masses, instead of allowing sufficient latitude to explore different mass distributions while still controlling the mass through the single *a priori* information M_T (as in scenarios $\mathcal{C}_V$ and $\mathcal{C}_{VI}$). Nonetheless, even in scenario $\mathcal{C}_{IV}$, the reasonable estimates of the other floor masses and all the story stiffnesses ensure that the identified model may be reliably used for both response predictions at floors 1, 3 and 4 and in structural damage detection.

Table 3.9: Floor mass and story stiffness estimates with an added eccentric mass on the 2nd floor.

Scenario	μ_m (kg)	σ_m (kg)	μ_k (10^5 N/m)	σ_k (10^5 N/m)
$\mathcal{C}_I$ ($\mathcal{I}_I$)	$36.97, 42.27, 37.19, 36.79$	$0.15, 1.13, 0.82, 0.90$	$2.46, 2.83, 2.69, 2.08$	$0.02, 0.10, 0.03, 0.07$
$\mathcal{C}_{II}$ ($\mathcal{I}_I$)	$36.99, 43.46, 37.88, 36.68$	$0.11, 0.53, 1.01, 0.44$	$2.91, 2.76, 2.29, 2.05$	$0.26, 0.13, 0.12, 0.02$
$\mathcal{C}_{III}$ ($\mathcal{I}_I$)	$37.84, 44.70, 39.13, 38.06$	$0.02, 0.05, 0.06, 0.03$	$2.82, 3.32, 3.22, 2.71$	$0.03, 0.03, 0.02, 0.02$
$\mathcal{C}_{IV}$ ($\mathcal{I}_I$)	$36.99, 58.77, 37.92, 36.70$	$0.11, 7.46, 1.04, 0.43$	$2.47, 3.20, 2.62, 2.04$	$0.11, 0.04, 0.01, 0.02$
$\mathcal{C}_V$ ($\mathcal{I}_I$)	$36.01, 47.75, 40.85, 28.39$	$0.22, 0.28, 0.43, 0.07$	$2.15, 3.02, 3.07, 1.84$	$0.02, 0.03, 0.02, 0.01$
$\mathcal{C}_{VI}$ ($\mathcal{I}_I$)	$36.79, 48.19, 42.30, 28.40$	$0.27, 0.24, 0.45, 0.15$	$2.16, 3.09, 2.21, 1.75$	$0.03, 0.04, 0.02, 0.01$
$\mathcal{C}_I$ ($\mathcal{I}_{II}$)	$36.80, 38.52, 37.51, 36.02$	$0.39, 2.94, 0.98, 1.89$	$2.61, 2.60, 2.48, 2.03$	$0.02, 0.17, 0.08, 0.13$
$\mathcal{C}_{II}$ ($\mathcal{I}_{II}$)	$36.99, 38.50, 37.87, 36.68$	$0.11, 0.40, 1.01, 0.44$	$3.07, 2.60, 2.16, 2.06$	$0.26, 0.12, 0.11, 0.02$
$\mathcal{C}_{III}$ ($\mathcal{I}_{II}$)	$37.85, 39.64, 39.14, 38.03$	$0.02, 0.04, 0.06, 0.03$	$3.02, 3.14, 3.04, 2.70$	$0.03, 0.03, 0.02, 0.02$
$\mathcal{C}_{IV}$ ($\mathcal{I}_{II}$)	$36.99, 58.77, 37.92, 36.70$	$0.11, 7.46, 1.04, 0.43$	$2.47, 3.20, 2.62, 2.04$	$0.11, 0.04, 0.01, 0.02$
$\mathcal{C}_V$ ($\mathcal{I}_{II}$)	$34.84, 46.19, 39.51, 27.46$	$0.22, 0.27, 0.41, 0.07$	$2.08, 2.92, 2.97, 1.78$	$0.02, 0.03, 0.02, 0.01$
$\mathcal{C}_{VI}$ ($\mathcal{I}_{II}$)	$35.59, 46.61, 40.92, 27.47$	$0.26, 0.23, 0.44, 0.15$	$2.09, 2.99, 2.14, 1.69$	$0.03, 0.04, 0.02, 0.01$

3.7 Conclusions

An algorithm is developed for the identification of the mass and stiffness parameters of 1, 2 and 3-D rigid–floor shear–type structural systems subjected to base excitation. The proposed algorithm starts with estimates of the complete sets of eigenvalues and non-normalized mode shape components at the sensor locations, obtained using any suitable system identification technique. The structural identification involves a two-step procedure, with the complete mass normalized mode shape matrix being obtained in the first step, and the modal orthogonality relations employed in the second step to estimate the system's mass and stiffness matrices. The first step in turn involves two stages: the estimation of the mass normalizing factors followed by the expansion of the mode shapes from the observed to the unobserved DOFs. It is assumed that the physical coordinates coincide with the centers of mass of the floors; the input–output balance method of Appendix A may be used to estimate the thus necessary centers of mass, along with the lumped masses and mass moments of inertia, of all instrumented floors, using data from a prior actuator–driven forced vibration test.

Since in base excitation the input is not completely defined, some *a priori* information is necessary to uniquely identify the system's mass and stiffness parameters. It is shown that, for any system with diagonal mass matrix, only a single such information is sufficient for a unique identification, and

this defines the *minimal a priori* information requirement for such systems. Two different scenarios, based on available *a priori* information, are studied: (a) with the masses known at all the sensor locations, and (b) with the total mass of the system known. For each of these two scenarios, the *minimal number of sensors* necessary for a unique identification is derived. Additionally, different considerations regarding instrumentation of the system are discussed, and guidelines are provided for determining different possible instrumentation set-ups necessary for global identifiability. The possible implication of low translational-rotational coupling in 2 and 3-D systems vis-$\grave{a}$-vis instrumentation requirements is also highlighted, and possible measures to address this issue are discussed in view of a realistic situation with no prior knowledge of the amount of translational-rotational coupling. The discourse on instrumentation presented throughout this chapter is aimed to help in experiment design by providing multiple choices of possible instrumentation set-ups, using the minimum number of sensors while assuring global identifiability.

Some practical implementation issues and strategies are discussed. An extensive set of numerical simulations is considered for validating the proposed identification approach. As evidenced by these simulations, the approach has the ability to obtain reliably accurate estimates of the system's physical parameters under the constraints of minimal instrumentation and minimal *a priori* information of the system's mass. In fact, since the mode shape normalization and expansion approaches are based on the structural topology, a near perfect estimation of the mass and stiffness parameters can generally be obtained for truly shear-type systems, even with noisy measurements.

In the experimental phase, a 4 storied laboratory scale steel frame, and three damaged versions of the frame, are tested on a shake table facility. The identification method is applied to the measured data, considering different scenarios of instrumentation and available *a priori* information. It is shown from the identified stiffness matrices that the frames under study are not perfectly shear-type. Nonetheless, reasonably consistent identification of the mass and stiffness parameters are obtained, highlighting the ability of the method to also work with near-shear type systems, inherently allowing for some amounts of modeling uncertainty. The responses and frequency response functions of the identified models agree very accurately with the measurements at observed DOFs and reasonably well at unobserved DOFs. The reliable performance of the method even with non-stationary earthquake inputs, incomplete instrumentation of the monitored system, and incomplete and uncertain available *a priori* information, highlights its potential in structural identification applications in

realistic scenarios.

In the applications considered in this chapter, the input base acceleration(s) are known, and thus an input-output system identification technique is used to get the necessary non-normalized modal parameter estimates at the sensor locations. These parameters can also be estimated with output-only identification techniques using only the "measured" acceleration response data. Hence, the structural identification method developed here can also be used in output-only (unmeasured ground motion, ambient vibration) situations. Also, while structural accelerations are considered as outputs in this chapter, system identification methods like ERA-OKID can also work with velocity or displacement measurements, and hence the proposed technique is also suitable for use with such outputs.

Chapter 4

Output-Only Structural Identification with Incomplete Information and Local/Global Identifiability Requirements[1]

While most studies on identifiability analyze the situation of known inputs, in structural/mechanical testing it may often be feasible/preferable to work only with output (response) data. The identification method and identifiability requirtements/tests in Chapter 3, albeit developed for base excitation, can also be directly applied to general output-only situations. In this chapter, the problem of identifiability of the mass and stiffness parameters of shear-type systems in output-only situations is revisited, with an approach alternative to that in Chapter 3. Moreover, while Chapter 3 considers only the question of global identifiability, here we also consider the question of local identifiability, i.e. there may be multiple solutions to the inverse problem, but such solutions will be locally isolated. The relaxation of the identifiability requirement to local from global can be expected to relax to some extent the instrumentation requirements prescribed in Chapter 3, while still being functional, especially when used

[1]This chapter is to be submitted as a journal article co-authored with Profs. Raimondo Betti and Hilmi Lus. A very preliminary form of the chapter was presented in the 31st International Modal Analysis Conference, Garden Grove, 2013 [49].

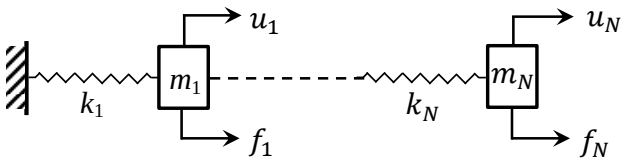

Figure 4.1: Shear-type system under dynamic loads.

in conjunction with engineering judgement to exclude improbable local solutions. The first objective of this chapter is to develop a method for the identification of the mass and stiffness parameters of a shear-type system under the constraints of output-only data, incomplete instrumentation, and minimal available *a priori* information about the system's physical parameters; this is pursued by extending the preliminary ideas in [49]. The second objective is to develop a method of analysis to determine the amount of independent information that is contained in the measurements from a given sensor set-up, and to use this analysis to define some rules for selecting the necessary number and location of sensors from the point of view minimum necessary information. The third and final objective of this chapter is to develop some tests for local and global identifiability for given sensor set-ups, which may be used both in the experiment design stage to find the allowed sensor set-ups, as well as post-experiment to identify the possible existence of multiple solutions. In the following section we outline the scope of the chapter by formally stating the problems that we address here, and the general solution strategy that we adopt.

4.1 Problem Statement and Solution Strategy Outline

Suppose we have a system that can be modelled as an N–DOF 1–D classically damped shear–type model (Fig. 4.1), subjected to some dynamic loading. Its equation of motion in physical coordinates is:

$$\mathbf{M}\ddot{\mathbf{u}} + \mathbf{C}\dot{\mathbf{u}} + \mathbf{K}\mathbf{u} = \mathbf{f} \tag{4.1}$$

The $\mathbf{M}$ and $\mathbf{K}$ matrices have the forms as given in Chapter 2 (Eq. (2.1)), and may be obtained using the modal orthogonality relation of Eq. (2.4). As in Chapter 3, let $\mathbf{V}$ specifically denote the mass normalized mode shape matrix, and let $\widetilde{\mathbf{V}}$ denote any arbitrarily normalized mode shape matrix.

Let the system in Eq. (4.1) be instrumented with N_s sensors which measure the response (acceleration and/or velocity and/or displacement) of the system at N_s DOFs. Let $\mathcal{S} = \{s_1, \cdots, s_{N_s}\}$ be

the set of these observed DOFs, and $\mathcal{D}$ be the set of all the N DOFs. We consider the situation when $\mathbf{f}$ is unknown (output-only) and $\mathcal{S} \subseteq \mathcal{D}$ (incomplete instrumentation). Our first objective is to identify the matrices $\mathbf{M}$ and $\mathbf{K}$ in this situation, and consequently estimate all the m_i's and k_i's. We make the assumption that the measured responses are sufficiently rich so as to allow the identification of all the structural modes at the sensor locations, i.e. using the measured responses at the N_s DOFs in any operational modal analysis technique, we can identify the eigenvalues, λ_j, and arbitrarily normalized mode shape components, $\tilde{v}_{i,j}$, $\forall\ j\ \in \{1, 2, \cdots, N\}$, $i\ \in\ \mathcal{S}$. While such an assumption may not always be practically realizable, in practice one may use analytical (FE) modes, corresponding to the unidentified ones, to complement the identified experimental modes at the sensor locations (mode-mixing) [7, 19]. Moreover, as will be evident at the end of Section 4.4, it is not strictly necessary to be able to identify the $\tilde{v}_{i,j}, \forall\ j \in \{1, 2, \cdots, N\}, i \in \mathcal{S}$; the developments in Section 4.4 may be used to address situations when not all the modes are identified at every DOF in $\mathcal{S}$. However, as shown with an example in Chatzis et al. [6], even with complete instrumentation of the system, if a mode is not identified at any DOF then the system may be unidentifiable; hence, even if not all the modes are identified at every DOF in $\mathcal{S}$, every mode must be identified (or assumed using mode-mixing) at at least one of the DOFs in $\mathcal{S}$.

Since the input is unknown, along with the measured modal information, we will also need to have some *a priori* information about the values of some physical parameters of the system to be able to identify unique $\mathbf{M}$ and $\mathbf{K}$ matrices. As shown in Chapter 3, for systems with diagonal $\mathbf{M}$ and symmetric $\mathbf{K}$, given sufficient instrumentation, the *minimal* amount of such necessary *a priori* information is one. In other words, assuming that the system is sufficiently instrumented, we can identify a complete normalized mode shape matrix, $\mathbf{V}^*$, proportional to the mass normalized $\mathbf{V}$ by a single scalar factor. Hence, our solution to the inverse problem first involves a method to estimate this complete $\mathbf{V}^*$, starting from the measured modal information and expressing the structural topological requirements in terms of modal parameters. The scalar factor of proportionality is then estimated using one additional information; we consider two types of additional information: (a) the sum-total of all the lumped masses in the system, or (b) a second set of measured data obtained from the system with some added masses, with the sum-total of all the added masses known. Using this scalar factor, the complete $\mathbf{V}^*$ is then scaled to the true mass normalized $\mathbf{V}$. The $\mathbf{M}$ and $\mathbf{K}$ matrices are finally obtained using $\mathbf{V}$ in the orthogonality relations of Eq. (2.4). The identification algorithm is discussed

in details in Section 4.2.

The identification framework of Section 4.2 also sets the stage for investigating the question of mass and stiffness parameter identifiability. In the first step of this framework we have made the assumption that there is sufficient instrumentation to identify a complete $\mathbf{V}^*$. Insufficient measured information will lead to unidentifiability of the complete $\mathbf{V}^*$, and hence unidentifiability of the mass and stiffness parameters. Hence, the question: "Is this instrumentation set-up sufficient for unique estimation of all the m_i's and k_i's?", is equivalent to the question: "Is this instrumentation set-up sufficient for unique estimation of $\mathbf{V}^*$?"; in Sections 4.3 to 4.5 we attempt to address this latter question. Section 4.3 illustrates, using a simple 3-DOF system instrumented with 2 sensors, that the sufficiency of measured information depends not only on the number of sensors but also on their location on the structure, and highlights the importance of identifiability in the context of structural health monitoring. In Section 4.4 we attempt to develop a method of analysis to determine the minimum independent information carried by any given sensor set-up; using such analysis one may check whether the total available independent information, from measurements and structural topology, meets the minimum information necessary to uniquely solve for $\mathbf{V}^*$. While insufficient measured information would result in global unidentifiability, the parameter set of interest may still be locally identifiable, i.e. when the multiple solutions to the inverse problem are locally isolated. A globally unidentifiable, but locally identifiable, parameter set may be practically useful; e.g. in situations where one may exclude most of the local solutions based on engineering judgement. Hence, it would be useful to test whether a given instrumentation set-up makes the mass and stiffness parameters at least locally identifiable, and if the parameters are globally identifiable as well. This is attempted in Section 4.5, where the implicit function theorem and the strong real Jacobian conjecture are respectively used to develop tests for local and global identifiability. The developments in Sections 4.4 and 4.5 can be used for experiment design to find different possible sensor set-ups, using the minimal/near-minimal number of sensors, but satisfying local/global identifiability. The tests in Section 4.5 can also be used post-experiment to test whether there may be more solutions around an identified solution; signalling the possible presence of multiple solutions will encourage the engineer to look for these alternative solutions, instead of blindly trusting only the identified solution. It is emphasized that, although our treatment of the identifiability issue is based on the identification framework of Section 4.2, the final answers are general. This is firstly because, identifiability is only dependent on the measured data

and assumptions on the model class, and independent of the identification algorithm; using different algorithms will not make an unidentifiable parameter set identifiable or vice versa. Moreover, our treatment of the problem is in terms of modal parameters, which are the basic components making up the structural response; hence investigating identifiability using directly the measured response data should be equivalent to investigating identifiability using the modal information extracted from the measured data. The different theoretical discussions are illustrated in Section 4.6 using an extensive suite of numerical simulations, and in Section 4.7 using the 4-story steel frame shaking table experimental data considered in Chapter 3.

4.2 M-K Identification Methodology

4.2.1 Estimation of proportional mode shape matrix

For the system in Eq. (4.1), instrumented with N_s sensors, suppose using the measured output data in any output-only system identification method we have identified the eigenvalues, λ_j, and arbitrarily normalized mode shape components, $\tilde{v}_{i,j}, \forall\, j \in \{1, 2, \cdots, N\}$, $i \in \mathcal{S}$, where $\mathcal{S} = \{s_1, \cdots, s_{N_s}\}$ is the set of DOFs with sensors. In this section we discuss a method to estimate the complete mode shape matrix $\mathbf{V}^*$, which is proportional to the mass normalized mode shape matrix $\mathbf{V}$ by a single scalar factor. Let any (i,j)th element of $\mathbf{V}^*$ be denoted by $v^*_{i,j}$. Since $\mathbf{V}^*$ can be any matrix proportional to $\mathbf{V}$, we choose $\mathbf{V}^*$ such that $\mathbf{V}^*_{s_1,1} = 1$, i.e. $\mathbf{V} = v_{s_1,1}\mathbf{V}^*$. We next proceed to determine the remaining $N^2 - 1$ elements of $\mathbf{V}^*$. To this end, we first derive two sets of equations involving the unknown elements in $\mathbf{V}^*$.

4.2.1.1 Equations from structural topology

The first set of equations is derived from the structural topology of a shear type system, namely the nature of the mass $\mathbf{M}$ and flexibility $\mathbf{F}$ matrices. Let us first consider the $\mathbf{M}$ matrix. Since we are trying to obtain the mass normalized mode shapes, and since $\mathbf{M}$, and thus $\mathbf{M}^{-1}$, are diagonal, from the mass orthogonality of Eq. (2.4), we get:

$$\sum_{j=1}^{N} v^*_{i,j} v^*_{k,j} = 0 \quad \forall\, i \in \{1, 2, \cdots, N-1\}, k \in \{i+1, i+2, \cdots, N\} \tag{4.2}$$

i.e. the rows of $\mathbf{V}^*$ are orthogonal to each other. Eq. (4.2) gives us $N(N-1)/2$ quadratic equations in terms of the elements of $\mathbf{V}^*$. Now let us consider the flexibility matrix of a shear type system, which has the form such that any (j,l)th element of $\mathbf{F}$ is given by: $F_{j,l} = F_{j,j} = \sum_{i=1}^{j} 1/k_i, \forall\, l \geq j$, and $j \in \{1, 2, \cdots, N\}$. Using this nature of $\mathbf{F} = \mathbf{K}^{-1}$ in the stiffness orthogonality of Eq. (2.4), we get an additional $N(N-1)/2$ quadratic equations in terms of the elements of $\mathbf{V}^*$:

$$\sum_{j=1}^{N} \frac{v^*_{i,j} v^*_{k,j} - v^{*2}_{i,j}}{\lambda_j} = 0 \quad \forall\, i \in \{1, 2, \cdots, N-1\}, k \in \{i+1, i+2, \cdots, N\} \tag{4.3}$$

The terms in Eq. (4.3) involve division by the eigenvalues, which, in the mean sense, having a much higher magnitude than one. This will make the terms in Eq. (4.3) much smaller than the terms in Eq. (4.2), which may lead to numerical ill-conditioning of the system of equations, as well as inadvertently put more weight on satisfying Eq. (4.3) compared to Eq. (4.2). To circumvent this problem, all the equations in Eq. (4.3) may be multiplied with the harmonic mean of the identified eigenvalues, thus scaling the mean of the terms in Eq. (4.3) to a similar order as the terms in Eq. (4.2).

4.2.1.2 Equations from measured mode shape components

With N_s sensors we have N_s components of all the N identified mode shapes. Since these modes are arbitrarily normalized, we can get $N(N_s - 1)$ linear equations, in terms of the elements of $\mathbf{V}^*$, from these measured modes, such as:

$$v^*_{s_i,j} - \frac{\tilde{v}_{s_i,j}}{\tilde{v}_{s_1,j}} v^*_{s_1,j} = 0 \quad \forall\, j \in \{1, 2, \cdots, N\},\ s_i \in \mathcal{S},\ s_i \neq s_1 \tag{4.4}$$

The measured DOF s_1 is not necessarily the lowest (or highest) of the measured DOFs, and the choice of s_1 should be governed by s_1 not being a node in any mode. Thus, one way to choose which of the measured DOFs should be s_1, is to treat each measured DOF in turn as s_1, construct an $(N_s - 1) \times N$ matrix of the ratios $\tilde{v}_{s_i,j}/\tilde{v}_{s_1,j}$ for this s_1, and choose that measured DOF as s_1 for which the above matrix has the minimum norm. Also, writing the equations as in Eq. (4.4) is just one way; the information contained by the measured mode shape components can of course be expressed in several other ways similar to Eq. (4.4); e.g. if $\tilde{v}_{s_1,j} = 0$ and $\tilde{v}_{s_i,j} \neq 0$, then the equation $v^*_{s_i,j} - v^*_{s_1,j}\tilde{v}_{s_i,j}/\tilde{v}_{s_1,j} = 0$ may be written as $v^*_{s_1,j} - v^*_{s_i,j}\tilde{v}_{s_1,j}/\tilde{v}_{s_i,j} = v^*_{s_1,j} = 0$. Finally, given sufficient sensors, some of the equations from Eq. (4.4) may be excluded from the analysis; this may

be useful in cases where all the measured DOFs have a node in some mode or the other, and one would like to discard the equations involving these nodes so as to avoid any numerical ill-conditioning.

4.2.1.3 Solution using modified Newton-Raphson method[2]

Let us now store all the unknowns, i.e. the elements of $\mathbf{V}^*$ with $v^*_{s_1,1}$ arbitrarily assumed to be 1, in a $(N^2-1)\times 1$ vector $\boldsymbol{\theta}$, and all the known parameters, i.e. the identified modal parameters, in a $NN_s \times 1$ vector $\boldsymbol{\alpha}$:

$$\begin{aligned}\boldsymbol{\theta} &= \{v^*_{1,1},\cdots,v^*_{1,N},v^*_{2,1},\cdots\cdots,v^*_{N,N}\}^T \setminus \{v^*_{s_1,1}\}\\ \boldsymbol{\alpha} &= \{\lambda_1,\cdots,\lambda_N,\frac{\tilde{v}_{s_2,1}}{\tilde{v}_{s_1,1}},\cdots,\frac{\tilde{v}_{s_2,N}}{\tilde{v}_{s_1,N}},\cdots\cdots,\frac{\tilde{v}_{s_{N_s},N}}{\tilde{v}_{s_1,N}}\}^T\end{aligned} \tag{4.5}$$

Eqs. (4.2), (4.3) and (4.4) can be augmented to get a nonlinear system of $N(N+N_s-2)$ total equations in the (N^2-1) unknown elements of $\mathbf{V}^*$. Let us denote this nonlinear system of equations as:

$$\mathbf{g}(\boldsymbol{\alpha},\boldsymbol{\theta}) = \mathbf{0}_{N(N+N_s-2)\times 1} \tag{4.6}$$

Although Eq. (4.6) appears to be a homogenous system, the assumption of $v^*_{s_1,1} = 1$ makes it non-homogenous. Eq. (4.6) can be solved using any nonlinear equation solver, e.g. the damped Newton-Raphson method as used here. In this case, the estimate of the unknown vector $\boldsymbol{\theta}$ in the kth iteration is given as:

$$\boldsymbol{\theta}^k = \boldsymbol{\theta}^{k-1} - \gamma^k[\mathbf{J}^{k-1}]^\dagger \mathbf{g}^{k-1} \tag{4.7}$$

where,

$$\mathbf{g}^{k-1} = \mathbf{g}(\boldsymbol{\alpha},\boldsymbol{\theta})|_{\boldsymbol{\theta}=\boldsymbol{\theta}^{k-1}}; \quad \mathbf{J}^{k-1} = \frac{\partial \mathbf{g}(\boldsymbol{\alpha},\boldsymbol{\theta})}{\partial \boldsymbol{\theta}}\Big|_{\boldsymbol{\theta}=\boldsymbol{\theta}^{k-1}} \tag{4.8}$$

and γ^k is a scalar damping parameter obtained by solving the constrained optimization problem:

$$\gamma^k = \underset{\varepsilon\le\gamma\le 1}{\arg\min} \left|\left|\mathbf{g}(\boldsymbol{\theta}^{k-1} - \gamma[\mathbf{J}^{k-1}]^\dagger \mathbf{g}^{k-1})\right|\right| \tag{4.9}$$

where $\|\cdot\|$ represents the Euclidean norm of the concerned vector argument, and ε is an arbitrarily chosen very small positive number. For the vector of nonlinear functions $\mathbf{g}$ involved in this problem,

[2] I would like to thank Mr. Luc Berger-Vergiat for helpful discussions on choosing the initial guess for the Newton-Raphson solution.

the elements of the Jacobian matrix $\mathbf{J}$ can be easily defined analytically, and incorporated in a computer program without much difficulty; this will avoid any numerical approximation, as e.g would be introduced by finite difference schemes, in the computation of $\mathbf{J}$. A pseudo-code for analytically constructing the Jacobian is given in Appendix C. The initial guess for the Newton-Raphson method can be obtained by solving the eigenvalue problem for any arbitrary N-DOF shear-type system and taking the elements of the resultant eigenvector matrix as the elements of $\boldsymbol{\theta}$ for the 1st iteration. Although a random non-zero assumption for the initial guess would also suffice, the guess using the modes of any arbitrary shear-type system is found to lead to a more controlled convergence of the iterations in this chapter, as in this way we incorporate the expected nature of the mode shapes of a shear-type system in our initial guess. The convergence criterion can be set in any conventional way, e.g. through a maximum number of iterations and/or through a tolerance on the Euclidean norm of the error $\|\mathbf{g}_{k-1}\|$, etc. The different equations in Eq. (4.6) may also be weighted with different factors, reflecting different amounts of confidences in the different types of information (see the experimental application in Section 4.7).

4.2.2 Scaling $\mathbf{V}^*$ to $\mathbf{V}$

In Section 4.2.1 we first estimate the complete $\boldsymbol{\Lambda}$ using any output-only system identification method, and then the complete $\mathbf{V}^*$, which is proportional to the true mass normalized $\mathbf{V}$ as $\mathbf{V} = v_{s_1,1}\mathbf{V}^*$. If our sole purpose is to detect structural changes, e.g. induced by damage, then at this stage itself we can use the proportional mode shapes in $\mathbf{V}^*$, in appropriate damage detection algorithms [23,44,45], or to identify a proportional system whose comparison with an *initial* proportional system would enable the detection of damage locations and severities. However, if our objective is to estimate the true $\mathbf{M}$ and $\mathbf{K}$ matrices, as in model updating/validation tasks, then we need to estimate the scaling factor $v_{s_1,1}$ using some additional information. Different types of such information are discussed below. Once $v_{s_1,1}$, and consequently the complete mass normalized $\mathbf{V}$ matrix, are estimated, the system's $\mathbf{M}$ and $\mathbf{K}$ matrices can be obtained using the orthogonality relations of Eq. (2.4).

4.2.2.1 Some/all individual lumped masses known

Suppose we know some, say n_m, lumped masses: $m_p \; \forall \; p \in \mathcal{P} = \{p_1, \cdots, p_{n_m}\}$, where $\mathcal{P}$ is the set of known lumped mass locations (DOFs). Then, we can write Eq. (4.6) directly in terms of

the elements of $\mathbf{V}$, instead of $\mathbf{V}^*$, and augment these equations with the following additional n_m equations:

$$\sum_{j=1}^{N} v_{p,j}^2 = 1/m_p \quad \forall\, p \in \mathcal{P} \tag{4.10}$$

The resulting system of nonlinear equations can then be solved directly for the N^2 elements of $\mathbf{V}$. Alternatively, after having solved for $\mathbf{V}^*$ in Section 4.2.1, we can also estimate the scalar factor of proportionality $v_{s_1,1}$ as:

$$v_{s_1,1} = \sqrt{\frac{\sum_{p\in\mathcal{P}} m_p m_p^*}{\sum_{p\in\mathcal{P}} m_p^2}}; \quad \text{where } m_p^* = \frac{1}{\sum_{j=1}^{N} v_{p,j}^{*2}} \tag{4.11}$$

by minimizing, in the least squares sense, the mismatch between the estimated and known lumped masses at the n_m locations.

4.2.2.2 Total mass of structure known

Suppose instead that we know the total mass of the structure, $M_T = \sum_{i=1}^{N} m_i$. This information was also used in Chapter 3 to find the final scalar proportionality factor, and has the advantage that, while each floor/lumped mass can be approximately estimated from an engineering drawing, the estimation errors in the various floors can be assumed to have a cancelling effect with each other, thus reducing the final estimation error in the total mass M_T. In this case, the factor is given as:

$$v_{s_1,1} = \sqrt{M_T^*/M_T}; \quad \text{where } M_T^* = \sum_{i=1}^{N} m_i^* \tag{4.12}$$

Here M_T^* is the total mass of the proportional system, and the proportional lumped masses, m_i^*'s, can be evaluated as in Eq. (4.11).

4.2.2.3 Second set of measured data with added masses and total added mass known

In this case we suppose that we do not have any information on the value of the physical parameters of the system. However, we have an additional set of measured data, recorded from a slightly modified structure; the modified structure is obtained by adding some lumped masses on the lumped masses of the original structure. Let us define a vector of the added masses at the N locations: $\triangle\mathbf{m} = \{\triangle m_1, \cdots, \triangle m_N\}$; if there is no mass added at DOF i then $\triangle m_i = 0$, otherwise $\triangle m_i$ is the value of the mass added at DOF i. Also, let us denote the total added mass by $\triangle\mathbf{m}_T = \sum_{i=1}^{N} \triangle m_i$. Using

the two sets of measured data, we can obtain the proportional mode shape matrices, $\mathbf{V}^*$ and $\mathbf{V}_b^*$, respectively of the original and the modified structures, following Section 4.2.1. Then, we can first obtain the mass and stiffness matrices of the two proportional systems as:

$$\begin{aligned} \mathbf{M}^* &= (\mathbf{V}^*\mathbf{V}^{*T})^{-1}; \quad \mathbf{K}^* = (\mathbf{V}^*\mathbf{\Lambda}^{-1}\mathbf{V}^{*T})^{-1} \\ \mathbf{M}_b^* &= (\mathbf{V}_b^*\mathbf{V}_b^{*T})^{-1}; \quad \mathbf{K}_b^* = (\mathbf{V}_b^*\mathbf{\Lambda}_b^{-1}\mathbf{V}_b^{*T})^{-1} \end{aligned} \tag{4.13}$$

where the subscript b denotes quantities belonging to the modified system. From the diagonal terms of $\mathbf{M}^*$ and $\mathbf{M}_b^*$, and the diagonal or super/sub-diagonal terms of $\mathbf{K}^*$ and $\mathbf{K}_b^*$, we can now get the proportional lumped masses and spring stiffnesses of the two systems: $\{m_i^*, k_i^*, m_{bi}^*, k_{bi}^*\}\ \forall\ i\ \in \{1, \cdots, N\}$. Although the true (not proportional) masses and stiffnesses of the two systems are not known at this point, they can still be expressed in terms of their proportional masses and stiffnesses and their scalar factors of proportionality. The scalar factor of proportionality of the original system can then be estimated, by equating the modified system's total mass to the sum of the original system's total mass and the total added mass, as:

$$\sum_{i=1}^{N} m_{bi} = \sum_{i=1}^{N} m_i + \triangle\mathbf{m}_T \Rightarrow v_{s_1,1} = \sqrt{\frac{\alpha \sum_{i=1}^{N} m_{bi}^* - \sum_{i=1}^{N} m_i^*}{\triangle\mathbf{m}_T}} \tag{4.14}$$

where α is obtained by minimizing, in the least squares sense, the mismatch between all the corresponding spring stiffnesses of the original and modified systems:

$$k_{bi} = k_i\ \forall\ i \in \{1, \cdots, N\} \Rightarrow \alpha = \frac{\sum_{i=1}^{N} k_{bi}^* k_i^*}{\sum_{i=1}^{N} k_{bi}^{*2}} \tag{4.15}$$

The factor α is the square of the ratio of the scalar factor of proportionality of the original system to that of the modified system; hence the scalar proportionality factor for the modified system can be obtained as:

$$(v_{s_1,1})_b = v_{s_1,1}/\sqrt{\alpha} \tag{4.16}$$

At this point some remarks need to be made: (1) The sensor location s_1 does not need to be the same in the two systems, i.e. if s_1 is DOF i in the original system, it can be DOF i or DOF $j \neq i$ in the modified system. (2) The modified system's proportionality factor, $(v_{s_1,1})_b$, does not need to be computed, since we are interested in identifying only the original system. However, computing this factor, estimating the $\mathbf{M}_b$ and $\mathbf{K}_b$ matrices of the modified system, and comparing these with the estimated $\mathbf{M}$ and $\mathbf{K}$ matrices of the original system, can give an idea about the uncertainty/errors in the

estimates; if the differences between the estimated matrices of the two systems are explainable, e.g. by the added masses, then the estimates can be regarded to be reliably accurate, otherwise signalling the possible presence of high estimation errors and the need for cautious use of such estimates. (3) When estimating $v_{s_1,1}$ in Eq. (4.14) we use the total added mass $\triangle\mathbf{m}_T$; it is also possible to instead consider each individual added mass separately and solve for the factor in a least squares sense (as in Eqs. (4.11) and (4.15)). Using the total added mass has a similar advantage as using the total structural mass in the last section, with the error in the known value of $\triangle\mathbf{m}_T$ being expected to be less pronounced than the errors in the known values of the individual added masses. (4) The accuracy of the estimate of the scalar factor of proportionality using the above equations will depend on the modes of the two systems being noticeably different, beyond the measurement noise and ambient fluctuations effects. Thus, while adding mass only at a single location is theoretically sufficient, such an added mass will need to be significant so as to introduce noticeable difference in the modes. Adding such a very large mass at a single location will make the dynamics of the modified structure badly behaved. Hence, to get both a noticeable difference in the modes, as well as maintain good dynamics of the modified system, it may be recommended that a more uniform distribution of the masses be added at many locations. However, there is no requirement that the distribution of the added masses be *strictly* uniform or that it needs to be proportional to the lumped mass distribution in the original structure, i.e. $\triangle\mathbf{M}$ does not need to be proportional to $\mathbf{I}$ or $\mathbf{M}$. (5) Starting with the first paper by Parloo et al. [50], using an added mass experiment for mass normalizing the modes in output-only situations has been considered in a number of studies [51–54]. Here however the modes are already normalized in Section 4.2.1 up to an unknown scalar factor; the data from the modified structure is only used to find this single factor of proportionality. Hence the formulation above is different from the formulations in [50–54], not involving any sensitivity based expression or any direct projection of the modes of the modified system on the modes of the original system. Avoiding any sensitivity based formulation also allows us to add larger masses so as to induce noticeable changes in the modes, above any noise/ambient effects.

4.2.2.4 Case of known input: Base excitation/Actuator generated

While this chapter is on output-only situations, the formulation in Section 4.2.1 can also be used in input-output situations. When the input is a measured base excitation, the arbitrarily normalized

modes at the sensor locations can be obtained using any input-output system identification method, Section 4.2.1 can be used to estimate $\mathbf{V}^*$, and the scalar factor of proportionality may be estimated as in any of the aforementioned cases. If the known input force(s) are generated by actuator(s), with at least one co-located actuator-sensor pair on the system, then the mass normalized modes at all the DOFs instrumented with either an actuator and/or a sensor can be obtained using input-output balance (Chapter 2); the mass normalized mode shapes at the non-instrumented DOFs may then be obtained by writing Eqs. (4.2) and (4.3) in terms of the elements of $\mathbf{V}$ and solving for the unknown elements. In this way it will be possible to directly solve for the elements of $\mathbf{V}$ in the case of actuator generated force inputs. Of course the uniqueness of the solution to Eqs. (4.2) and (4.3) will depend on the actuator - sensor placement on the structure, i.e on which rows of $\mathbf{V}$ have been identified using input-output balance; the instrumentation set-ups identified in Chapter 2 for global identifiability can be used to assure solutions uniqueness.

4.3 3-DOF System with 2 Sensors: An Example of Non-Unique Solution

In this section we use the identification framework of Section 4.2 to illustrate the problem of solution non-uniqueness using the example of a 3-DOF system with 2 sensors. The equations from structural topology (Eqs. (4.2) and (4.3) in Section 4.2.1) for this system are:

$$\begin{aligned}
&v^*_{1,1}v^*_{2,1} + v^*_{1,2}v^*_{2,2} + v^*_{1,3}v^*_{2,3} = 0\\
&v^*_{1,1}v^*_{3,1} + v^*_{1,2}v^*_{3,2} + v^*_{1,3}v^*_{3,3} = 0\\
&v^*_{2,1}v^*_{3,1} + v^*_{2,2}v^*_{3,2} + v^*_{2,3}v^*_{3,3} = 0\\
&v^*_{1,1}v^*_{2,1}/\lambda_1 + v^*_{1,2}v^*_{2,2}/\lambda_2 + v^*_{1,3}v^*_{2,3}/\lambda_3 - v^{*2}_{1,1}/\lambda_1 - v^{*2}_{1,2}/\lambda_2 - v^{*2}_{1,3}/\lambda_3 = 0\\
&v^*_{1,1}v^*_{3,1}/\lambda_1 + v^*_{1,2}v^*_{3,2}/\lambda_2 + v^*_{1,3}v^*_{3,3}/\lambda_3 - v^{*2}_{1,1}/\lambda_1 - v^{*2}_{1,2}/\lambda_2 - v^{*2}_{1,3}/\lambda_3 = 0\\
&v^*_{2,1}v^*_{3,1}/\lambda_1 + v^*_{2,2}v^*_{3,2}/\lambda_2 + v^*_{2,3}v^*_{3,3}/\lambda_3 - v^{*2}_{2,1}/\lambda_1 - v^{*2}_{2,2}/\lambda_2 - v^{*2}_{2,3}/\lambda_3 = 0
\end{aligned} \tag{4.17}$$

Case 1: $\mathcal{S} = \{1, 3\}$ — Assume that the 2 sensors are located on the lumped masses m_1 and m_3 (see Fig. 4.1 for the numbering); from the measurements of these 2 sensors we identify $\{\lambda_j, \tilde{v}_{1,j}, \tilde{v}_{3,j}\}\ \forall\ j \in \{1, 2, 3\}$. Then, with $s_1 = 1$, i.e. $v^*_{1,1} = 1$, and $\alpha_j = \tilde{v}_{3,j}/\tilde{v}_{1,j}$, the equations: $v^*_{3,j} - \alpha_j v^*_{1,j} = 0$

$\forall\, j \in \{1,2,3\}$, along with Eq. (4.17), can be solved after some algebra to give:

$$\begin{aligned}
&v^*_{1,2} = \sqrt{\frac{\lambda_2[\alpha_1\alpha_3(\lambda_3-\lambda_1)+\alpha_1\lambda_1-\alpha_3\lambda_3]}{\lambda_1[\alpha_2\alpha_3(\lambda_2-\lambda_3)+\alpha_3\lambda_3-\alpha_2\lambda_2]}}; \quad v^*_{1,3} = \sqrt{\frac{-\alpha_1-\alpha_2 v^{*2}_{1,2}}{\alpha_3}};\\
&v^*_{2,1} = \frac{1/\lambda_1 + v^{*2}_{1,2}/\lambda_2 + v^{*2}_{1,3}/\lambda_3}{1/\lambda_1 + (\alpha_1-\alpha_3)/[\lambda_2(\alpha_3-\alpha_2)] + (\alpha_2-\alpha_1)/[\lambda_3(\alpha_3-\alpha_2)]};\\
&v^*_{2,2} = \frac{\alpha_1-\alpha_3}{v^*_{1,2}(\alpha_3-\alpha_2)}v^*_{2,1}; \quad v^*_{2,3} = \frac{\alpha_2-\alpha_1}{v^*_{1,3}(\alpha_3-\alpha_2)}v^*_{2,1};\\
&v^*_{3,1} = \alpha_1; \quad v^*_{3,2} = \alpha_2 v^*_{1,2}; \quad v^*_{3,3} = \alpha_3 v^*_{1,3}
\end{aligned} \tag{4.18}$$

Case 2: $\mathcal{S} = \{1,2\}$ — Assume now that the 2 sensors are located on the lumped masses m_1 and m_2. Again taking $s_1 = 1$, i.e. $v^*_{1,1} = 1$, and $\alpha_j = \tilde{v}_{2,j}/\tilde{v}_{1,j}$, the equations: $v^*_{2,j} - \alpha_j v^*_{1,j} = 0\ \forall\ j \in \{1,2,3\}$, along with Eq. (4.17), can be solved to give:

$$\begin{aligned}
&v^*_{1,2} = \sqrt{\frac{\lambda_2[\alpha_1\alpha_3(\lambda_3-\lambda_1)+\alpha_1\lambda_1-\alpha_3\lambda_3]}{\lambda_1[\alpha_2\alpha_3(\lambda_2-\lambda_3)+\alpha_3\lambda_3-\alpha_2\lambda_2]}}; \quad v^*_{1,3} = \sqrt{\frac{-\alpha_1-\alpha_2 v^{*2}_{1,2}}{\alpha_3}};\\
&v^*_{3,1} = \frac{1/\lambda_1 + v^{*2}_{1,2}/\lambda_2 + v^{*2}_{1,3}/\lambda_3}{1/\lambda_1 + (\alpha_1-\alpha_3)/[\lambda_2(\alpha_3-\alpha_2)] + (\alpha_2-\alpha_1)/[\lambda_3(\alpha_3-\alpha_2)]};\\
&v^*_{3,2} = \frac{\alpha_1-\alpha_3}{v^*_{1,2}(\alpha_3-\alpha_2)}v^*_{3,1}; \quad v^*_{3,3} = \frac{\alpha_2-\alpha_1}{v^*_{1,3}(\alpha_3-\alpha_2)}v^*_{3,1};\\
&v^*_{2,1} = \alpha_1; \quad v^*_{2,2} = \alpha_2 v^*_{1,2}; \quad v^*_{2,3} = \alpha_3 v^*_{1,3}
\end{aligned} \tag{4.19}$$

Case 3: $\mathcal{S} = \{2,3\}$ — Finally, assume the 2 sensors to be located on the lumped masses m_2 and m_3. With $s_2 = 2$, i.e. $v^*_{2,1} = 1$, and $\alpha_j = \tilde{v}_{3,j}/\tilde{v}_{2,j}$, the equations: $v^*_{3,j} - \alpha_j v^*_{2,j} = 0\ \forall\ j \in \{1,2,3\}$, along with Eq. (4.17), is now solved to give:

$$\begin{aligned}
&v^*_{2,2} = \sqrt{\frac{\lambda_2[\alpha_1\alpha_3(\lambda_3-\lambda_1)+\alpha_1\lambda_1-\alpha_3\lambda_3]}{\lambda_1[\alpha_2\alpha_3(\lambda_2-\lambda_3)+\alpha_3\lambda_3-\alpha_2\lambda_2]}}; \quad v^*_{2,3} = \sqrt{\frac{-\alpha_1-\alpha_2 v^{*2}_{2,2}}{\alpha_3}};\\
&v^*_{1,1} = \frac{1/\lambda_1 + (\alpha_1-\alpha_3)/[\lambda_2(\alpha_3-\alpha_2)] + (\alpha_2-\alpha_1)/[\lambda_3(\alpha_3-\alpha_2)]}{1/\lambda_1 + (\alpha_1-\alpha_3)^2/[\lambda_2 v^{*2}_{2,2}(\alpha_3-\alpha_2)^2] + (\alpha_2-\alpha_1)^2/[\lambda_3 v^{*2}_{2,3}(\alpha_3-\alpha_2)^2]};\\
&v^*_{1,2} = \frac{\alpha_1-\alpha_3}{v^*_{2,2}(\alpha_3-\alpha_2)}v^*_{1,1}; \quad v^*_{1,3} = \frac{\alpha_2-\alpha_1}{v^*_{2,3}(\alpha_3-\alpha_2)}v^*_{1,1};\\
&v^*_{3,1} = \alpha_1; \quad v^*_{3,2} = \alpha_2 v^*_{2,2}; \quad v^*_{3,3} = \alpha_3 v^*_{2,3}
\end{aligned} \tag{4.20}$$

Although as per Eqs. (4.18) to (4.20), all the elements of $\mathbf{V}^*$ have a unique parametric expression in all the three cases, the sensor configuration in Case 3, $\mathcal{S} = \{2,3\}$, actually results in a, globally as well as locally, unidentifiable parameter set. This is because the denominator in the expression for $v^*_{2,2}$ in this case, i.e. $\lambda_1[\alpha_2\alpha_3(\lambda_2-\lambda_3)+\alpha_3\lambda_3-\alpha_2\lambda_2]$, is identically zero for any 3-DOF system. This

can be shown by considering the last equation (row) in the eigenvalue problem: $[\mathbf{A} - \lambda_j \mathbf{I}]\tilde{\mathbf{v}}_j = \mathbf{0}$, where $\mathbf{A} = \mathbf{M}^{-1}\mathbf{K}$. Denoting the (i,l)th element of $\mathbf{A}$ by $a_{i,l}$, we have:

$$a_{3,2}\tilde{v}_{2,j} + (a_{3,3} - \lambda_j)\tilde{v}_{3,j} = 0 \quad \Rightarrow a_{3,2} + (a_{3,3} - \lambda_j)\alpha_j = 0 \quad \forall\, j \in \{1,2,3\} \tag{4.21}$$

where $\alpha_j = \tilde{v}_{3,j}/\tilde{v}_{2,j}$. Using that fact that $a_{3,2} = -a_{3,3}$ for a shear-type system, and after some algebra, we get from Eq. (4.21):

$$\begin{aligned} a_{3,3} = \frac{\lambda_j \alpha_j}{\alpha_j - 1} \quad \forall\, j \in \{1,2,3\} \qquad & \Rightarrow \frac{\lambda_2 \alpha_2}{\alpha_2 - 1} = \frac{\lambda_3 \alpha_3}{\alpha_3 - 1} \\ & \Rightarrow \alpha_2\alpha_3(\lambda_2 - \lambda_3) + \alpha_3\lambda_3 - \alpha_2\lambda_2 = 0 \end{aligned} \tag{4.22}$$

This implies that, in Case 3, we can choose $v^*_{2,2}$ to be any real number and solve for the remaining elements of $\mathbf{V}^*$, resulting in an infinite number of physically admissible shear-type systems, which will have the same eigenvalues, $\{\lambda_1, \lambda_2, \lambda_3\}$, and the same ratios between the modes at DOFs 3 and 2, $\{\tilde{v}_{3,1}/\tilde{v}_{2,1}, \tilde{v}_{3,2}/\tilde{v}_{2,2}, \tilde{v}_{3,3}/\tilde{v}_{2,3}\}$. As an example, two such systems are:

$$\begin{aligned} \text{System I} : & \{m_1, m_2, m_3\} = \{2.4468, 2.2678, 2\} \times 10^3 \text{ kg}; \\ & \{k_1, k_2, k_3\} = \{5.0592, 4.3870, 5\} \times 10^6 \text{ N/m} \\ \text{System II} : & \{m_1, m_2, m_3\} = \{2.5684, 2.7798, 2\} \times 10^3 \text{ kg}; \\ & \{k_1, k_2, k_3\} = \{5.0524, 5.6525, 5\} \times 10^6 \text{ N/m} \end{aligned} \tag{4.23}$$

The fact that the set-up $\mathcal{S} = \{2,3\}$ results in an unidentifiable parameter set is in agreement with Chatzis et al. [6], where it was shown that, with a known input at DOF 1, and known displacements at DOFs 2 and 3, a 3-DOF shear-type system is unobservable, and hence unidentifiable; the case of a single applied input at DOF 1 falls within the general output-only situation, and if, even with this input known the system is unidentifiable, then with it unknown it is definitely unidentifiable.

Evidently, the consequences of such unidentifiability can be significant, especially in the context of structural health monitoring. For example, let System II of Eq. (4.23) represent an initial *healthy* state of a structure, and let System I denote its current *damaged* state, with damage in the 2nd story/spring. If we monitor the system via its modal parameters extracted from output-only data recorded at DOFs 2 and 3, then the measured non-mass normalized modal parameters from the current *damaged* state will be the same as those from the initial *healthy* state, thereby wrongly signalling the current state as healthy, illustrating a case of *false safety* due to unidentifiability. This will also

be the case if we monitor the system using any modal parameter derivatives, e.g. flexibility/stiffness proportional damage sensitive features [23, 44].

It should be highlighted that, unidentifiability in output-only situations does not necessarily imply that the responses at the measured DOFs will be identically equal for all the alternative systems, but only that the non-normalized modal parameters identified from the measured responses will be the same for all such systems. However, under certain loading conditions, even the responses at the measured DOFs will be identically equal. For example, let the two systems of Eq. (4.23) be excited with the input forces $\mathbf{f}^I(t) = [f_1^I(t), f_2^I(t), f_3^I(t)]$ and $\mathbf{f}^{II}(t) = [f_1^{II}(t), f_2^{II}(t), f_3^{II}(t)]$, respectively, where $f_1^I(t)$ is the input at DOF 1 (floor 1) of System I, etc. Further, let $\mathbf{f}^{II}(t) = \mathbf{f}^I(t)\mathbf{G}$, where:

$$\mathbf{G} = \mathbf{V}^I \mathbf{R}_3^I [\mathbf{R}_3^{II}]^{-1} [\mathbf{V}^{II}]^{-1} = \begin{bmatrix} 0.9987 & 0 & 0 \\ -0.1711 & 1.2258 & 0 \\ 0.2565 & 0 & 1 \end{bmatrix} \text{ in this example} \tag{4.24}$$

where $\mathbf{V}^I$ is the mass normalized mode shape matrix of System I, $\mathbf{R}_3^I = \text{diag}(\mathbf{r}_3^I)$, and $\mathbf{r}_3^I$ is the third row (i.e. corresponding to DOF 3) of $\mathbf{V}^I$, and similarly for System II. In this loading situation the responses of the two systems will be identically equal at both DOFs 2 and 3, and hence, not only the identified non-normalized modal parameters, but no derivatives of such measurements (e.g. AR coefficients [55], cepstral features [35], etc.) should be able to distinguish between the two systems. Since the scenario is output-only, and we have no control on the applied inputs, such a loading scenario cannot be ruled out in practice. This is especially true since, by Eq. (4.24), both $\mathbf{f}^I(t)$ and $\mathbf{f}^{II}(t)$ will have similar power content, time-frequency characteristics etc., making such a loading situation physically realizable in practice. Moreover, the requirement $\mathbf{f}^{II}(t) = \mathbf{f}^I(t)\mathbf{G}$ may be relaxed to $\mathbf{F}^{II}(\omega) = \mathbf{F}^I(\omega)\mathbf{G}$, i.e. the two sets of inputs are only related in the frequency domain; in such a case, the responses of the two systems at DOFs 2 and 3 will no longer be identical in time, but they will still be identical in the frequency domain (e.g. their PSDFs will be same). Such a scenario can be visualized as: the initial system II has suffered damage, changing into System I, and at the same time, the initial loading conditions of $\mathbf{F}^{II}(\omega)$ has changed into $\mathbf{F}^I(\omega)$. If now, we assume that we have several sets of measured data from DOFs 2 and 3, then these data will be statistically similar for both the systems, and hence, statistical models of any response derivatives, constructed using these measured data sets, should not be able to distinguish between the two systems. This last operation defines the main underlying principle of several statistical pattern recognition based SHM

schemes [35, 44, 55, 56]; hence, in such situations, not only model identification based methods, but also such solely data based statistical schemes may fail to provide reliable results.

4.3.1 Nonnecessity of collocated actuator–sensor in input–output identification

Most structural identification methods using input-output data require at least one collocated sensor-actuator pair to uniquely scale the identified mode shapes. This requirement was also shown as necessary in the input-output balance approach of Chapter 2 (Section 2.4) to obtain the mass normalized mode shapes at all the instrumented DOFs. However, in specific cases this requirement may be violated, yet resulting in the identification of an unique system. For example, consider the **Case 1** above, i.e. $\mathcal{S} = \{1, 3\}$, with an actuator located at DOF 2 applying a known input force. Then, using input–output balance of Chapter 2, we can identify the following products:

$$\begin{aligned} v_{1,1}v_{2,1} = \beta_1; \quad v_{1,2}v_{2,2} = \beta_2; \quad v_{1,3}v_{2,3} = \beta_3 \\ v_{3,1}v_{2,1} = \gamma_1; \quad v_{3,2}v_{2,2} = \gamma_2; \quad v_{3,3}v_{2,3} = \gamma_3 \end{aligned} \tag{4.25}$$

where any $v_{i,j}$ is an element of the mass normalized $\mathbf{V}$. Then, $\alpha_j = v^*_{3,j}/v^*_{1,j} = v_{3,j}/v_{1,j} = \gamma_j/\beta_j$, are also known for all $j \in \{1, 2, 3\}$, and the elements of the proportional mass normalized mode shape matrix $\mathbf{V}^*$, with $v^*_{1,1} = 1$, can be uniquely estimated as Eq. (4.18). In the output-only case we use some assumed *a priori* information to solve for $v_{1,1}$, and scale $\mathbf{V}^*$ to $\mathbf{V}$. But in this input-output case, since we already know that $v_{1,1}v_{2,1} = \beta_1$, the scaling factor $v_{1,1}$ may be estimated as:

$$v_{1,1}v_{2,1} = \beta_1 \quad \Rightarrow \; v^2_{1,1}v^*_{2,1} = \beta_1 \quad \Rightarrow \; v_{1,1} = \sqrt{\frac{\beta_1}{v^*_{2,1}}} \tag{4.26}$$

thus leading to an unique estimation of $\mathbf{V}$, and consequently of $\mathbf{M}$ and $\mathbf{K}$, without requiring a collocated actuator-sensor pair or any assumed *a priori* information of the system's physical parameters. Such an unique identification is similarly possible for the **Case 2** above, with $\mathcal{S} = \{1, 2\}$ and an actuator at DOF 3; but not possible for **Case 3**, with $\mathcal{S} = \{2, 3\}$ and an actuator at DOF 1, due to the unidentifiability of the $\mathbf{V}^*$ matrix in this case, as discussed before. These observations on the global identifiability/unidentifiability of a 3-DOF shear–type system, in input–output scenarios without any collocated sensor-actuator pair, agree with the results of an identifiability test performed on the same system in Chatzis et al. [6].

The nonnecessity of any collocated sensor-actuator pair is not only limited to 3-DOF systems. By a similar analysis as above, in any N-DOF system if a certain sensor set-up satisfies local/global

identifiability in the output–only scenario, then this sensor set-up plus an actuator located at *any*, not necessarily collocated, DOF will satisfy local/global identifiability in the input–output scenario: (a) first, using input–output balance with the known input and the measured outputs we will be able to find similar unique products as in Eq. (4.25); (b) next, using these products we will be able to find the mode shape ratios, similar to the α_j's above; (c) since the sensor set-up satisfies local/global identifiability in the output–only situation, using these mode shape ratios and the equations from structural topology in the approach of Section 4.2.1, we will be able to solve for an unique $\mathbf{V}^*$; and finally (d) using any one of the known products obtained in step (a) above, we will be able to solve for the unknown scaling factor, thereby scaling $\mathbf{V}^*$ to an unique $\mathbf{V}$.

4.4 Independent Measured Information from a Sensor Set-Up

The example in Section 4.3 shows that the issue of correctly locating sensors on the monitored system is related to its identifiability and is crucial for the success of any structural identification/health monitoring activity. In this and the next section, we study the identifiability of the proportional mode shape matrix $\mathbf{V}^*$. If an unique solution for $\mathbf{V}^*$ is obtained, scaling it to $\mathbf{V}$ will just require one more information; the absence of any such information will of course make the system unidentifiable, since there can be an infinite number of systems with the same $\mathbf{V}^*$. However, this latter case of unidentifiability is not solvable via proper instrumentation, and is unavoidable in output-only/base excitation situations, unless one has some such information as discussed in Section 4.2.2. The identifiability of the $\mathbf{V}^*$ is however directly dependent on sensor locations through the information contained in the measurements. Thus, in this section we investigate the issue of sensor location by developing a method of analysis which attempts to answer the following question: What is the amount of independent information that is contained in the measurements recorded by any given sensor set-up? Recall that, with $v^*_{s_1,1} = 1$, solving for $\mathbf{V}^*$ means solving for a total of $N^2 - 1$ unknowns. Hence, we would like to have equations which represent at least $N^2 - 1$ independent information. Now, from the structural topology we have a total of $N(N-1)$ equations in Section 4.2.1.1, each of which represents a particular information about the $\mathbf{M}$ or $\mathbf{F} = \mathbf{K}^{-1}$ matrix; hence these equations may be treated as $N(N-1)$ independent information. Then, we will still need to have $N-1$ independent information, which will be in the form of the measured mode shape components used to form the equations in

Section 4.2.1.2. Thus, we want to locate the sensors in such a way that the mode shape components extracted from the measurements contain $N-1$ independent information. In the following, we study the amount of independent information contained by the extracted mode shape components extracted for any given sensor set-up, and decide on the permissibility of the sensor set-up based on the minimum $N-1$ independent information requirement. For this purpose, we use some statements on the mode shapes of shear-type systems. These statements hold for any arbitrary normalization (including mass normalization) of the modes. The proofs of the statements are given in Appendix B. Although the method is developed here for output-only situations, it can also be similarly applied for situations with known input.

4.4.1 Two sensors on an N-DOF system

Statement 1: *For an N-DOF shear-type system, for any mode $j \in \{1,\cdots,N\}$, the mode shape components at any two DOFs i_1, $i_2 \in \{1,\cdots,N\}$, are related as:*

$$\left(\sum_{l=0}^{i_1-1} \bar{c}_{l,i_1}\lambda_j^l\right)\tilde{v}_{i_2,j} - \left(1+\sum_{l=1}^{i_2-1} \bar{c}_{l,i_2}\lambda_j^l\right)\tilde{v}_{i_1,j} = 0 \tag{4.27}$$

where $\bar{c}_{l,i_1}\ \forall\ l \in \{0,\cdots,i_1-1\}$, and $\bar{c}_{l,i_2}\ \forall\ l \in \{1,\cdots,i_2-1\}$, are respectively i_1 and (i_2-1) number of mode independent constants. (See Appendix B for proof.)

Statement 2: *For an N-DOF shear-type system, for any mode $j \in \{1,\cdots,N\}$, the mode shape components at any two DOFs i_1, $i_2 \in \{1,\cdots,N\}$, are related as:*

$$\left(1+\sum_{l=1}^{N-i_1} d_{l,N-i_1}\lambda_j^l\right)\tilde{v}_{i_2,j} - \left(1+\sum_{l=1}^{N-i_2} d_{l,N-i_2}\lambda_j^l\right)\tilde{v}_{i_1,j} = 0 \tag{4.28}$$

where $d_{l,i_1}\ \forall\ l \in \{1,\cdots,N-i_1\}$, and $d_{l,i_2}\ \forall\ l \in \{1,\cdots,N-i_2\}$, are respectively $(N-i_1)$ and $(N-i_2)$ number of mode independent constants. (See Appendix B for proof.)

Now suppose that the system is instrumented with 2 sensors at $\mathcal{S} = \{s_1, s_2\}$. Then, the measured mode shape components at DOFs s_1 and s_2 are related as per both Statements 1 and 2 above. From Statement 1, we have a total of s_1+s_2-1 unknowns (the $\bar{c}_{l,s_1}$'s and $\bar{c}_{l,s_2}$'s) relating the mode shape components at s_1 and s_2. Similarly, from Statement 2, we have a total of $2N-s_1-s_2$ unknowns (the d_{l,s_1}'s and d_{l,s_2}'s) relating these mode shape components. Let the minimum number of unknowns relating these mode shape components be denoted as:

$$\mathcal{I}_2^{s_1,s_2} = \min(s_1+s_2-1, 2N-s_1-s_2) \tag{4.29}$$

So, knowing any $\mathcal{I}_2^{s_1,s_2}$ pairs of $(\tilde{v}_{s_1,j}, \tilde{v}_{s_2,j})$, one can solve for these $\mathcal{I}_2^{s_1,s_2}$ unknowns, and then solve for the remaining $(N - \mathcal{I}_2^{s_1,s_2})$ pairs of $(\tilde{v}_{s_1,j}, \tilde{v}_{s_2,j})$. (Note: each pair corresponds to a distinct mode, i.e. a distinct value of $j \in \{1, \cdots, N\}$.) Thus, it can be argued that, only $\mathcal{I}_2^{s_1,s_2}$ pairs of $(\tilde{v}_{s_1,j}, \tilde{v}_{s_2,j})$ contain independent information. Since each pair of $(\tilde{v}_{s_1,j}, \tilde{v}_{s_2,j})$ contains one information in the output-only situation (the ratio $\tilde{v}_{s_2,j}/\tilde{v}_{s_1,j}$ or $\tilde{v}_{s_1,j}/\tilde{v}_{s_2,j}$), the sensors located at $\{s_1, s_2\}$ will contain a total of $\mathcal{I}_2^{s_1,s_2}$ independent information. Since we need to have at least $N-1$ independent information, the two sensor should be so located such that:

$$\mathcal{I}_2^{s_1,s_2} \geq N - 1 \quad \text{i.e. } \min(s_1 + s_2 - 1, 2N - s_1 - s_2) \geq N - 1 \tag{4.30}$$

Recall that in the last section we showed that $\mathcal{S} = \{2, 3\}$ for a 3-DOF system leads to unidentifiability; this agrees with Eq. (4.30), as $\mathcal{I}_2^{s_1,s_2}$ in this case becomes 1, which is $< N - 1 = 2$. Considering the two possibilities in Eq. (4.30) individually, the requirement can also be written as:

$$N \leq s_1 + s_2 \leq N + 1 \quad \text{i.e. } s_1 + s_2 = N \text{ or } N + 1 \tag{4.31}$$

based on which the $\geq$ sign in Eq. (4.30) actually becomes an $=$ sign. It can further be shown that the above requirement results in a total of $(N - 1)$ possible sensor placement choices, using 2 senors, for any N-DOF shear-type system; e.g. $\mathcal{S} = \{1, 2\}$ and $\{1, 3\}$, for $N = 3$, as in Section 4.3.

4.4.2 A rule for N_s sensors

First suppose we have three sensors at $\mathcal{S} = \{s_1, s_2, s_3\}$. We want to find how much independent information, in terms of the identified mode shape components, the measurements from these 3 sensors will contain. We can argue as follows: Selecting any two of these three sensors, e.g. $\{s_1, s_2\}$, they will contain $\mathcal{I}_2^{s_1,s_2}$ independent information; then the addition of the third sensor, s_3, will lead to an increase of information equal to $\min(\mathcal{I}_2^{s_1,s_3}, \mathcal{I}_2^{s_2,s_3})$. Repeating this with all the three pairs of sensors we can write:

$$\begin{aligned} \mathcal{J}_3^{s_1,s_2,s_3} = \min \{ & \mathcal{I}_2^{s_1,s_2} + \min(\mathcal{I}_2^{s_1,s_3}, \mathcal{I}_2^{s_2,s_3}), \mathcal{I}_2^{s_1,s_3} + \min(\mathcal{I}_2^{s_1,s_2}, \mathcal{I}_2^{s_2,s_3}), \\ & \mathcal{I}_2^{s_2,s_3} + \min(\mathcal{I}_2^{s_1,s_2}, \mathcal{I}_2^{s_1,s_3}) \} \end{aligned} \tag{4.32}$$

which may be considered to be a measure of the amount of independent information carried by the three sensors. However, since the addition of a sensor cannot lead to a decrease in information, the

information carried by the three sensors should at least be equal to $\max(\mathcal{I}_2^{s_1,s_2}, \mathcal{I}_2^{s_1,s_3}, \mathcal{I}_2^{s_2,s_3})$. Taking this into account, the amount of information provided by the three sensors may be written as:

$$\mathcal{I}_3^{s_1,s_2,s_3} = \max\left\{\mathcal{J}_3^{s_1,s_2,s_3}, \mathcal{I}_2^{s_1,s_2}, \mathcal{I}_2^{s_1,s_3}, \mathcal{I}_2^{s_2,s_3}\right\} \tag{4.33}$$

Extending the argument to the case of N_s sensors, located at the DOFs in $\mathcal{S} = \{s_1, \cdots, s_{N_s}\}$, we may write the amount of independent information provided by these sensors as:

$$\mathcal{I}_{N_s}^{\mathcal{S}} = \max\left\{\mathcal{J}_{N_s}^{\mathcal{S}}, \mathcal{I}_{N_s-1}^{\mathcal{S}\setminus s_1}, \mathcal{I}_{N_s-1}^{\mathcal{S}\setminus s_2}, \cdots, \mathcal{I}_{N_s-1}^{\mathcal{S}\setminus s_{N_s}}\right\} \tag{4.34}$$

where

$$\begin{aligned}\mathcal{J}_{N_s}^{\mathcal{S}} = \min\Big\{&\mathcal{I}_{N_s-1}^{\mathcal{S}\setminus s_1} + \min(\mathcal{I}_2^{s_1,s_2}, \mathcal{I}_2^{s_1,s_3}, \cdots, \mathcal{I}_2^{s_1,s_{N_s}}),\\ &\mathcal{I}_{N_s-1}^{\mathcal{S}\setminus s_2} + \min(\mathcal{I}_2^{s_2,s_1}, \mathcal{I}_2^{s_2,s_3}, \cdots, \mathcal{I}_2^{s_2,s_{N_s}}), \cdots,\\ &\mathcal{I}_{N_s-1}^{\mathcal{S}\setminus s_i} + \min(\mathcal{I}_2^{s_i,s_1}, \mathcal{I}_2^{s_i,s_2}, \cdots, \mathcal{I}_2^{s_i,s_{N_s}}), \cdots,\\ &\mathcal{I}_{N_s-1}^{\mathcal{S}\setminus s_{N_s}} + \min(\mathcal{I}_2^{s_{N_s},s_1}, \mathcal{I}_2^{s_{N_s},s_2}, \cdots, \mathcal{I}_2^{s_{N_s},s_{N_s-1}})\Big\}\end{aligned} \tag{4.35}$$

and the symbol "\" denotes the set-minus operation. The N_s sensors should be so located as to provide at least $N-1$ independent information, i.e.:

$$\mathcal{I}_{N_s}^{\mathcal{S}} \geq N-1 \tag{4.36}$$

Given N_s sensors located at the DOFs in $\mathcal{S}$, the recursive formulae of Eqs. (4.34) and (4.35) may be used to compute $\mathcal{I}_{N_s}^{\mathcal{S}}$, which can be checked against the requirement in Eq. (4.36). Also, given N_s sensors to be located on an N-DOF system, all the ${}^{N}\mathcal{C}_{N_s}$ possible sensor set-ups using these sensors may be first determined; $\mathcal{I}_{N_s}^{\mathcal{S}}$ can then be computed for each of these set-ups and checked using Eq. (4.36), to come up with a final set of *permissible* sensor set-ups using these N_s sensors, with *permissible* being in the sense of providing at least $N-1$ independent information as per the above analysis.

4.4.3 The case of 3 sensors with 2 at consecutive DOFs

The above rule for testing the information content in the measurements from N_s sensors may over-estimate the information in some cases when there are sensors located on consecutive DOFs. That consecutively located sensors may decrease the amount of independent information was also observed

in Chapter 3 in the context of estimating the mass normalization factors vis-$\grave{a}$-vis identifiability requirements. The reason behind this decrease in information is the nature of the $\mathbf{M}$ and $\mathbf{K}$ matrices in shear-type systems, which makes the sum of the elements in any ith row ($i \neq 1$) of the matrix $\mathbf{A} = \mathbf{M}^{-1}\mathbf{K}$ equal to zero, as well as $\mathbf{A}$ tridiagonal. Since we want to find the amount of *independent* information contained in the measurements from the sensors, such information should not include, even implicitly, any information from the structural topological requirements, as we have already included all possible information from structural topology in our first set of equations in Section 4.2.1.1. In other words, while determining the amount of independent information provided by a given sensor set-up, any information provided already by the structural topology should be carefully filtered out. The nature of the $\mathbf{A}$ matrix stated above, being an information on structural topology, thus reduces the amount of independent information when we have consecutively located sensors. In this section we discuss such a case of decreased information, where we have 3 sensors on the system, with 2 of them located on consecutive DOFs; the decrease in information is reflected in the statement below.

Statement 3: *For an N-DOF shear-type system, for any mode $j \in \{1, \cdots, N\}$, the mode shape components at the three DOFs $\{i-1, i, i+k\}$ (respectively $\{i-k, i, i+1\}$), for any $i \in \{2, \cdots, N-1\}$ and $k \in \{1, \cdots, N-i\}$ (respectively $k \in \{1, \cdots, i-1\}$), are related as:*

$$\begin{aligned} &\tilde{v}_{i+k,j} = \left(1 + p_{0,k} + \sum_{l=1}^{k-1} q_{l,k}\lambda_j^l\right)\tilde{v}_{i-1,j} - \left(p_{0,k} + \sum_{l=1}^{k} r_{l,k}\lambda_j^l\right)\tilde{v}_{i,j} \\ &\left(\text{respectively } \tilde{v}_{i-k,j} = \left(1 + p_{0,k} + \sum_{l=1}^{k-1} q_{l,k}\lambda_j^l\right)\tilde{v}_{i+1,j} - \left(p_{0,k} + \sum_{l=1}^{k} r_{l,k}\lambda_j^l\right)\tilde{v}_{i,j}\right) \end{aligned} \tag{4.37}$$

where $p_{0,k}$, $q_{l,k}\ \forall\ l \in \{1, \cdots, k-1\}$, and $r_{l,k}\ \forall\ l \in \{1, \cdots, k\}$, are $2k$ number of mode independent constants. (See Appendix B for proof. Also note: the $p_{0,k}$, $q_{l,k}$'s and $r_{l,k}$'s are particular to i as well, and should indeed be written as $p_{0,i,k}$, $q_{l,i,k}$'s and $r_{l,i,k}$'s; however, for ease of presentation, we do not explicitly show this dependence on i, here as well as in Appendix B.)

Suppose we have the 3 senors at the DOFs in $\mathcal{S} = \{s_1, s_2, s_3\} = \{i-1, i, i+k\}$. Then, for any mode j, the measured mode shape components are related via $2k$ number of mode independent constants, as per Statement 3. Knowing any $2k$ number of $\{\tilde{v}_{i-1,j}, \tilde{v}_{i,j}, \tilde{v}_{i+k,j}\}$ triplets, one can solve for these $2k$ unknowns, and then solve for the remaining $(N-2k)$ triplets of $\{\tilde{v}_{i-1,j}, \tilde{v}_{i,j}, \tilde{v}_{i+k,j}\}$ from Eq. (4.37). Hence, only $2k$ number of $\{\tilde{v}_{i-1,j}, \tilde{v}_{i,j}, \tilde{v}_{i+k,j}\}$ triplets contain independent information.

Since each triplet of $\{\tilde{v}_{i-1,j}, \tilde{v}_{i,j}, \tilde{v}_{i+k,j}\}$ contains two information in the output-only scenario (e.g. $\tilde{v}_{i,j}/\tilde{v}_{i-1,j}$ and $\tilde{v}_{i+k,j}/\tilde{v}_{i-1,j}$), the sensors located at DOFs $\{i-1, i, i+k\}$, when considered all together, will provide a total of $4k$ independent information, as per Statement 3.

Alternatively, one can also consider the three sensors as follows: consider any 2 of the 3 senors, e.g. the ones at s_1 and s_2. Then, as per Section 4.4.1, using any $\mathcal{I}_2^{s_1,s_2}$ pairs of $(\tilde{v}_{s_1,j}, \tilde{v}_{s_2,j})$, one can first determine the involved $\mathcal{I}_2^{s_1,s_2}$ number of mode independent constants, and then the remaining pairs of $(\tilde{v}_{s_1,j}, \tilde{v}_{s_2,j})$. Once all the pairs of $(\tilde{v}_{s_1,j}, \tilde{v}_{s_2,j})$ are thus determined, one can then use any $2k$ number of the mode shape components, $\tilde{v}_{s_3,j}$, from the third sensor at DOF s_3, to first solve for the $2k$ unknowns in Eq. (4.37), and then determine the remaining $\tilde{v}_{s_3,j}$ components. Thus, in this case the three sensors will provide a total of $\mathcal{I}_2^{s_1,s_2} + 2k$ independent information. Since any 2 of the 3 sensors can be chosen to begin with, the amount of information from the 3 sensors at DOFs $\{i-1, i, i+k\}$, based on the present line of thought, will be $\min(\mathcal{I}_2^{i-1,i}, \mathcal{I}_2^{i-1,i+k}, \mathcal{I}_2^{i,i+k}) + 2k$.

Combining the above two ways of counting the information provided by the sensors at DOFs $\{i-1, i, i+k\}$, along with the information count given by Eq. (4.32), we can write:

$$\mathcal{J}_3^{i-1,i,i+k} = \min\left\{4k, \min(\mathcal{I}_2^{i-1,i}, \mathcal{I}_2^{i-1,i+k}, \mathcal{I}_2^{i,i+k}) + 2k, \widetilde{\mathcal{J}}_3^{i-1,i,i+k}\right\} \tag{4.38}$$

where $\widetilde{\mathcal{J}}_3^{i-1,i,i+k}$ is evaluated using Eq. (4.32). The $\mathcal{J}_3^{i-1,i,i+k}$, computed as above, can then be used in Eq. (4.33) to get the amount of independent information, $\mathcal{I}_3^{i-1,i,i+k}$, provided by the 3 sensors at DOFs $\{i-1, i, i+k\}$. One can similarly find the amount of independent information when the 3 sensors are located at DOFs $\{i-k, i, i+1\}$. This computed $\mathcal{I}_3^{i-1,i,i+k}$ (or $\mathcal{I}_3^{i-k,i,i+1}$) can finally be checked for the minimum $N-1$ independent information requirement, as in Eq. (4.36).

In Table 4.1 we give some examples of the above analysis, with 3 sensors on different N-DOF shear-type systems; these examples include both cases when none of the sensors are placed on consecutive DOFs, as well as cases when 2 or all the sensors are consecutively located. The last column in this table shows whether the sensor placement meets the $N-1$ minimum information requirement of Eq. (4.36): a ✓ indicates that it meets the requirement, while a X mark indicates that it doesn't. The examples are carefully chosen so as to illustrate the different cases when different counts of the information become the final governing condition: e.g. in the first case ($N = 7$, $\mathcal{S} = \{1, 6, 7\}$) the final information count is governed by the $\widetilde{\mathcal{J}}$ from Eq. (4.32); in the last case ($N = 10$, $\mathcal{S} = \{2, 5, 6\}$) the $\mathcal{J}$ from Eq. (4.38), specifically, the count of $4k$, governs the final information count; while in the

Table 4.1: Examples of 3 sensors on different N-DOF shear-type systems.

N	$\mathcal{S}$	k	$\widetilde{\mathcal{J}}$ (Eq. (4.32))	$\mathcal{J}$ (Eq. (4.38))	$\mathcal{I}_3$ (Eq. (4.33))	Check Requirement (Eq. (4.36))
7	$\{1,6,7\}$	5	7	7	7	✓
9	$\{3,8,9\}$	5	7	7	7	X
6	$\{1,2,3\}$	1	5	4	4	X
6	$\{2,3,4\}$	1	9	4	5	✓
8	$\{2,4,8\}$	—	9	9	9	✓
8	$\{4,6,8\}$	—	6	6	6	X
7	$\{4,5,6\}$	1	7	4	5	X
10	$\{2,5,6\}$	3	13	12	12	✓

fourth and seventh cases ($N = 6$, $\mathcal{S} = \{2,3,4\}$; and $N = 7$, $\mathcal{S} = \{4,5,6\}$) the $\mathcal{I}_3$ from Eq. (4.33), specifically, the maximum of the $\mathcal{I}_2$'s, govern the final information count.

4.4.4 Some general comments

We end this section with some general comments on the analysis discussed herein. Firstly, it should be emphasized that, although throughout this section we talk about different mode shape components being related through a number of mode independent constant (the $\bar{c}_{l,i}$'s, $d_{l,i}$'s, $p_{0,k}$'s, $q_{l,k}$'s and $r_{l,k}$'s), these constants do not need to be actually evaluated. We just need to know that there exists some constants which relate the mode shape components as in the above statements; then, in any scenario, we just use the number of such constants to count the number of independent information provided by the corresponding mode shape components.

The analysis presented in this section provides a framework to choose the location of sensors, such that the total amount of independent information, represented through the linear/nonlinear equations of Section 4.2.1, is at least equal to the number of unknowns that we want to determine. However, since the involved equations are nonlinear, having the same number of information as the number of unknowns *does not guarantee* solution uniqueness; e.g. a circle and a parabola, representing 2 independent sources of information in the x-y plane, may intersect at 0 to 4 points. Similarly, we may, in some cases, have a unique solution to a nonlinear system of equations even with an *apparently* less number of information than unknowns; e.g. 2 spheres, representing 2 independent sources of information in the x-y-z space, may intersect at 0, 1 or infinitely many points. (In the

last sentence we use the term "*apparently*" since such cases of less information than unknowns with an unique solution should usually be reducible to a lesser dimensional space with same number of information as unknowns; e.g. the case of 2 spheres - 1 point of intersection in x-y-z (3-D) space may be reduced to a 2 circles - 1 point of intersection problem in a 2-D space.)

In the next section we attempt to directly address the issue of solution uniqueness. But as would be evident later, this direct treatment is only possible by numerically defining a region within which the system's physical (mass and stiffness) parameters must lie. On the other hand, although in this section we do not directly address the question of solution uniqueness, we do address the question of necessary and available independent information, which is related to identifiability; moreover, our treatment in this section is more global, being not limited to any given structure or any given region within which the physical parameters must lie. In addition, this section, based on the algebra of the eigenvalue problem of the underlying $\mathbf{A} = \mathbf{M}^{-1}\mathbf{K}$ matrix, also provides us with an understanding of how much information we gain/loose on placing/removing sensors from certain DOFs. Irrespective of identifiability, such an understanding may be used to locate sensors at DOFs where we may expect to have the most independent information.

In practice it may be suggested that, given an N_s number of available sensors, one first employs the developments in this section to find the different sensor set-ups using the N_s sensors which satisfy the minimum $(N-1)$ independent information requirement. Then, for each of these sensor set-ups one can apply the identifiability tests of the next section, after defining from engineering judgements a particular region within which the system's physical parameters must lie. Those sensor set-ups which pass these region-specific identifiability tests may then be adopted for the structure in question. Note that the region specific tests of the next section are particularly important to address the presence of nodes, which may lead to ill-conditioning of the system of equations. Since the presence of nodes is particular to a structure, it will be governed by the particular region in which the physical parameters belong, and will not be a general property of all models in the model class of N-DOF shear-type systems; hence the presence of nodes will go undetected using the developments in this section, which are based only on the general properties of N-DOF shear-type systems.

Besides the application for which the method discussed here is developed, it may also find some other applications. Two such applications may be in evaluating (a) the accuracy of identified mode shapes, or (b) the validity of the model class assumption. In experimental modal analysis, frequencies

can usually be estimated with a higher accuracy than mode shapes, especially in output only scenarios [57]. The usual tests for the reliability/accuracy of experimentally obtained mode shape are via their direct comparison with corresponding analytical mode shapes, using some inner product norms, e.g. the Modal Assurance Criterion or Coordinate Modal Assurance Criterion, testing their linear dependence (Cauchy-Schwarz inequality); however, as shown in Appendix D [48], the differences reflected by such measures can be expected to be of a lower order than the actual differences in the structural flexibility matrix. Given the model class, the analysis discussed here may be applied to test the reliability/accuracy of the experimentally identified mode shapes by: (a) first using the necessary number of identified frequencies and corresponding identified mode shapes to compute the different involved mode independent constants, and (b) then using these known constants with the remaining identified frequencies to estimate the corresponding semi-analytical mode shapes. These mode shapes are "semi-analytical" since they are dependent both on the experimentally identified frequencies, and on the theoretically derived equations/statements. The mismatch between these "semi-analytical" mode shapes and the corresponding experimentally identified ones may be interpreted as a measure of inaccuracy in the identified modes, and/or a measure of error in the model class assumption. Finally, such a set of "semi-analytical" mode shapes may also be used to complement the experimentally identified mode shapes, in a situation when not all the modes are identified at every sensor location. This can often occur in practice, e.g. when different DOFs are instrumented with different types of sensors; such heterogenous sensing and data fusion is often desirable since different sensors work well at different bandwidths [6]. Assume that in such a case, the complete spectrum of eigenvalues have been identified considering all the measurements, but only the low frequency mode shapes are identified at some of the instrumented DOFs (with say displacement sensors), while the high frequency mode shapes are identified at the other instrumented DOFs (with say accelerometers). Then, the "semi-analytical" modes shapes obtained as above may be used to complement these identified mode shapes so as to complete the spectra of the non-normalized mode shapes at all the DOFs with sensors.

4.5 Tests for Identifiability

Given that the measured data comes from a system which can be reliably modeled as a shear-type system, the unknown parameters of the model ($\boldsymbol{\theta}$ in Eq. (4.5), Section 4.2.1) will exist somewhere in the solution space, thus ensuring the existence of solution to the system of equations $\mathbf{g}(\boldsymbol{\alpha}, \boldsymbol{\theta}) = \mathbf{0}$ (Eq. (4.6), Section 4.2.1). While it is reasonable to assume that there exists at least one solution, owing to the nonlinearity of $\mathbf{g}(\boldsymbol{\alpha}, \boldsymbol{\theta})$, the uniqueness of such a solution cannot be guaranteed merely by the fact of having sufficient number of independent equations. For a nonlinear system of equations defined only parametrically, guaranteeing uniqueness of solution is generally an untractable problem, especially when the number of equations are not very small. The question of solution uniqueness for any nonlinear system of equations is thus usually answered with the parameters numerically defined and the unknowns lying within some defined region. In this section we use such an approach to investigate identifiability in our problem; specifically, we define a region in which the mass and stiffness parameters may lie, and test whether any system within this region is identifiable given a certain sensor set-up, i.e. whether, for a given parameter vector $\boldsymbol{\alpha}$ (see Eq. (4.5) in Section 4.2.1), the solution to the elements of $\mathbf{V}^*$ is unique within this region. Although the tests are discussed here for output-only situations, they may be similarly applied in input-output situations by suitably modifying Eq. (4.5) following Section 4.2.2.4, as well as in situations when some *a priori* information is included in Eq. (4.5) (e.g. including Eq. (4.10) from Section 4.2.2.1).

4.5.1 Implicit function theorem and local identifiability

The implicit function theorem [58, 59] may be used to test whether, for a given instrumentation set-up, the solution to $\mathbf{g}(\boldsymbol{\alpha}, \boldsymbol{\theta}) = \mathbf{0}$ will be locally unique, i.e. unique in a neighborhood around a solution $\boldsymbol{\theta} = \boldsymbol{\theta}_0$. With N_s instrumented DOFs, we have $(N^2 - 1)$ unknowns in the vector $\boldsymbol{\theta} \in \mathbf{R}^{N^2-1}$, and NN_s known parameters in the vector $\boldsymbol{\alpha} \in \mathbf{R}^{NN_s}$; thus $\boldsymbol{\theta}$ and $\boldsymbol{\alpha}$ respectively contain our dependent and independent variables. The equations $\mathbf{g}(\boldsymbol{\alpha}, \boldsymbol{\theta}) = \mathbf{0}$ implicitly relates these dependent and independent variables. Suppose that there are a total of $(N^2 - 1)$ equations (= the number of unknowns) in $\mathbf{g}(\boldsymbol{\alpha}, \boldsymbol{\theta}) = \mathbf{0}$, i.e. $\mathbf{g}(\boldsymbol{\alpha}, \boldsymbol{\theta}) : \mathcal{U} \to \mathbf{R}^{N^2-1}$ for the open set $\mathcal{U} \subset \mathbf{R}^{NN_s+N^2-1}$. Also let $(\boldsymbol{\alpha}^*, \boldsymbol{\theta}^*)$ be a fixed point of $\mathbf{g}(\boldsymbol{\alpha}, \boldsymbol{\theta})$, i.e. $\mathbf{g}(\boldsymbol{\alpha}^*, \boldsymbol{\theta}^*) = \mathbf{0}$. Then, for our purpose, the implicit function theorem can be stated (adopting the phraseology of [59, Theorem 1.3.4, pp. 11]) as:

Implicit Function Theorem: *If* $\mathbf{g}(\boldsymbol{\alpha}, \boldsymbol{\theta})$ *is continuously differentiable in* $\mathcal{U}$ *and*

$$\det[\mathbf{J}|_{(\boldsymbol{\alpha},\boldsymbol{\theta})=(\boldsymbol{\alpha}^*,\boldsymbol{\theta}^*)}] = \det\left[\frac{\partial \mathbf{g}(\boldsymbol{\alpha}, \boldsymbol{\theta})}{\partial \boldsymbol{\theta}}\Big|_{(\boldsymbol{\alpha},\boldsymbol{\theta})=(\boldsymbol{\alpha}^*,\boldsymbol{\theta}^*)}\right] \neq 0 \tag{4.39}$$

then there exists a product neighbourhood $\mathcal{V} \times \mathcal{W} \subseteq \mathcal{U}$*, with* $\boldsymbol{\alpha}^* \in \mathcal{V} \subseteq \mathbf{R}^{NN_s}$ *and* $\boldsymbol{\theta}^* \in \mathcal{W} \subseteq \mathbf{R}^{N^2-1}$*, and a unique, continuously differentiable function,* $\mathbf{h}(\boldsymbol{\alpha}) : \mathcal{V} \to \mathcal{W}$*, such that* $\boldsymbol{\theta}^* = \mathbf{h}(\boldsymbol{\alpha}^*)$*, and* $\mathbf{g}(\boldsymbol{\alpha}, \mathbf{h}(\boldsymbol{\alpha})) = \mathbf{0}$ *for all* $\boldsymbol{\alpha} \in \mathcal{V}$*.*

The implication of the local existence and uniqueness of such a function $\mathbf{h}(\boldsymbol{\alpha}) = \boldsymbol{\theta}$ is the local uniqueness of the solution $\boldsymbol{\theta}$ to the system of equations $\mathbf{g}(\boldsymbol{\alpha}, \boldsymbol{\theta}) = \mathbf{0}$; given any parameter set $\boldsymbol{\alpha} \in \mathcal{V}$, the unique function $\mathbf{h}(\boldsymbol{\alpha})$ will map it to a unique solution $\boldsymbol{\theta} \in \mathcal{W}$. It is not necessary, and in fact may not be generally possible, to determine this function $\mathbf{h}(\boldsymbol{\alpha})$; just ensuring, as per the theorem, that such a function exists and is unique in a local region is sufficient for our purpose, which is to ensure the uniqueness of the solution vector $\boldsymbol{\theta}^*$, given a parameter vector $\boldsymbol{\alpha}^*$, in the local region.

4.5.1.1 Continuous differentiability of $\mathbf{g}(\boldsymbol{\alpha}, \boldsymbol{\theta})$

The implicit function theorem requires the differential of $\mathbf{g}(\boldsymbol{\alpha}, \boldsymbol{\theta})$, with respect to $\boldsymbol{\alpha}$ and $\boldsymbol{\theta}$, to exist and be continuous everywhere in the local region containing the fixed point $(\boldsymbol{\alpha}^*, \boldsymbol{\theta}^*)$. This property of continuous differentiability may be ascertained by observing the different functions, Eqs. (4.2) to (4.4), in $\mathbf{g}(\boldsymbol{\alpha}, \boldsymbol{\theta})$. These functions are (a) multivariate quadratic or linear polynomials in the unknown $v_{i,j}^*$'s in $\boldsymbol{\theta}$, (b) reciprocal functions of the known λ_j's in $\boldsymbol{\alpha}$, and (c) linear functions of the known $\tilde{v}_{s_i,j}/\tilde{v}_{s_1,j}$'s in $\boldsymbol{\alpha}$. Hence, their derivatives, with respect to any element of $\boldsymbol{\theta}$ or $\boldsymbol{\alpha}$, will always exist and be continuous, unless any $v_{i,j}^* = \infty$ or any $\lambda_j = 0$ or any $\tilde{v}_{s_1,j} = 0$. All eigenvalues, λ_j's, of a properly constrained system are positive; any mode shape component, $v_{i,j}^*$, being infinity is physically meaningless; $\tilde{v}_{s_1,j}$ is zero if DOF s_1 is a node for mode j. However, if s_1 is a node in any mode j, the concerned equations in Eq. (4.4) may either be expressed in a different way or excluded (see Section 4.2.1.2). (Also, see Section 4.2.1.2 for a way to select s_1 which minimizes the possibility of s_1 being a node.) Thus, with Eq. (4.4) being properly written so as to exclude any division by zero, $\mathbf{g}(\boldsymbol{\alpha}, \boldsymbol{\theta})$ will be continuously differentiable in any physically meaningful parameter space.

4.5.1.2 Same number of equations as unknowns

The application of the implicit function theorem also requires having the same number of equations as unknowns. However, with N_s sensors we have a total of $N(N + N_s - 2)$ equations, which is more than the $(N^2 - 1)$ unknowns. So we need to rewrite these equations in a reduced form of only $(N^2 - 1)$ equations to be able to apply the theorem. This reduction should be such that we do not loose any independent information. Since all the equations from structural topology represent independent information, each particular to a distinct element of the $\mathbf{M}$ or $\mathbf{F} = \mathbf{K}^{-1}$ matrix, let us keep the $N(N-1)$ equations in Eqs. (4.2) and (4.3) unchanged. Then, we need to reduce the $N(N_s-1)$ equations in Eq. (4.4) to $(N-1)$ equations. This can be done by first re-writing Eq. (4.4) as the N equations:

$$\boldsymbol{\theta}_a - \boldsymbol{\Gamma}^{\dagger}\boldsymbol{\theta}_b = \mathbf{0}_{N\times 1} \tag{4.40}$$

where: $\boldsymbol{\theta}_a = \{v^*_{s_1,1}, v^*_{s_1,2}, \cdots, v^*_{s_1,N}\}^T$ is an $N \times 1$ vector with its first element $v^*_{s_1,1} = 1$, $\boldsymbol{\theta}_b = \{v^*_{s_2,1}, \cdots, v^*_{s_2,N}, \cdots, v^*_{s_{N_s},N}\}^T$ is an $N(N_s-1)\times 1$ vector, and $\boldsymbol{\Gamma}$ is the $N(N_s-1)\times N$ matrix:

$$\boldsymbol{\Gamma} = \begin{bmatrix} \tilde{v}_{s_2,1}/\tilde{v}_{s_1,1} & & & \cdots & \tilde{v}_{s_{N_s},1}/\tilde{v}_{s_1,1} & & \\ & \ddots & & \cdots & & \ddots & \\ & & \tilde{v}_{s_2,N}/\tilde{v}_{s_1,N} & \cdots & & & \tilde{v}_{s_{N_s},N}/\tilde{v}_{s_1,N} \end{bmatrix}^T \tag{4.41}$$

Each equation in Eq. (4.40) correspond to a different mode. As shown in Section 4.4, mode shape components belonging to the same mode may be related via some mode independent constants, i.e. any mode is equivalent to another in terms of independent information content in the mode shape components. Thus, any arbitrary $(N-1)$ of the N equations in Eq. (4.40) may be selected, and augmented with the $N(N-1)$ equations from structural topology, to get a reduced set of $(N^2 - 1)$ nonlinear equations, $\mathbf{g}(\boldsymbol{\alpha}, \boldsymbol{\theta}) = \mathbf{0}$, on which the implicit function theorem can be used. The continuous differentiability of $\mathbf{g}(\boldsymbol{\alpha}, \boldsymbol{\theta})$ does not change with this re-definition; this can be verified by first using using $\boldsymbol{\Gamma}^{\dagger} = (\boldsymbol{\Gamma}^T\boldsymbol{\Gamma})^{-1}\boldsymbol{\Gamma}^T$ for explicitly writing out any jth equation of Eq. (4.40) as:

$$v^*_{s_1,j} - \frac{\sum_{i=2}^{N_s} \tilde{v}_{s_i,j} v^*_{s_i,j}/\tilde{v}_{s_1,j}}{\sum_{i=2}^{N_s} \tilde{v}^2_{s_i,j}/\tilde{v}^2_{s_1,j}} = 0 \quad \forall\, j \in \{1, \cdots, N\} \tag{4.42}$$

and then following similar arguments as in Section 4.5.1.1. Finally, note that the re-definition of $\mathbf{g}(\boldsymbol{\alpha}, \boldsymbol{\theta})$ is only necessary for the application of the implicit function theorem (and the real Jacobian

conjecture in Section 4.5.2); the identification of $\mathbf{V}^*$ may be performed using the original $\mathbf{g}(\boldsymbol{\alpha}, \boldsymbol{\theta})$ as in Section 4.2.1.2.

4.5.1.3 Pre-experiment use for experiment design

The local uniqueness of solution test using the implicit function theorem may be applied in the experiment design stage to find sensor set-ups assuring local identifiability of the system. Since this has to be performed prior to the actual experiment, we will need to use a nominal model which exists prior to identification. Let this nominal model be characterized by the structural matrices $(\bar{\mathbf{M}}, \bar{\mathbf{K}})$. We choose a model space $\mathcal{M}$ around our nominal model (i.e. $(\bar{\mathbf{M}}, \bar{\mathbf{K}}) \in \mathcal{M}$), with all models in $\mathcal{M}$ belonging to the same class of shear-type systems. Then, using any sampling technique, we generate $N_{\mathcal{M}}$ models from $\mathcal{M}$: $(\mathbf{M}_i, \mathbf{K}_i) \in \mathcal{M},\ \forall i \in \{1, 2, \cdots, N_{\mathcal{M}}\}$. For each model, we solve the eigenvalue problem to get the corresponding mode shape and eigenvalue matrices: $(\mathbf{V}, \boldsymbol{\Lambda})|_{\mathcal{M}}\ \forall\, i \in \{1, 2, \cdots, N_{\mathcal{M}}\}$. Now, let us choose a set of instrumented DOFs $\mathcal{S}$. Given this sensor set-up, we can get $N_{\mathcal{M}}$ sets of independent and dependent parameter vectors: $(\boldsymbol{\alpha}_i, \boldsymbol{\theta}_i)|_{\mathcal{M},\mathcal{S}}\ \forall\, i \in \{1, 2, \cdots, N_{\mathcal{M}}\}$, where $|_{\mathcal{M},\mathcal{S}}$ denote that the concerned parameters are particular to the model space $\mathcal{M}$ and sensor set-up $\mathcal{S}$. Unlike in the actual identification exercise, the dependent parameters in $\boldsymbol{\theta}_i|_{\mathcal{M},\mathcal{S}}$, being obtained from solving the forward eigenvalue problem, are known in the experiment design. Once the $N_{\mathcal{M}}$ sets of $(\boldsymbol{\alpha}_i, \boldsymbol{\theta}_i)|_{\mathcal{M},\mathcal{S}}$ are obtained, we can compute the determinants of the corresponding Jacobian matrices, $\det[\mathbf{J}_i|_{\mathcal{M},\mathcal{S}}]$, with $\mathbf{J}_i|_{\mathcal{M},\mathcal{S}}$ evaluated at $(\boldsymbol{\alpha}, \boldsymbol{\theta}) = (\boldsymbol{\alpha}_i, \boldsymbol{\theta}_i)$ for the ith model. If each of these $N_{\mathcal{M}}$ determinants is non-zero, then we can say that, given the sensor set-up $\mathcal{S}$, the system is locally identifiable if it belongs to the model space $\mathcal{M}$; otherwise it **may** not be locally identifiable in $\mathcal{M}$ with the sensor set-up $\mathcal{S}$. Different sensor set-ups can be similarly tested to find those which assure local identifiability in $\mathcal{M}$. The model space $\mathcal{M}$ is similar to the search space of parameters in an optimization problem, and should be exhaustive enough to include all possible and feasible sets of physical parameters' values that, from an engineering judgement, may describe the current state of the system; a larger model space should correspond to a larger number of generated models $N_{\mathcal{M}}$.

It may be argued that all the $N_{\mathcal{M}}$ $\det[\mathbf{J}_i|_{\mathcal{M},\mathcal{S}}]$'s being $\neq 0$ does not necessarily imply that no other Jacobian matrix, for the same space $\mathcal{M}$ and set-up $\mathcal{S}$, can have a zero determinant. A stricter condition will of course be to ensure that all the $N_{\mathcal{M}}$ $\det[\mathbf{J}_i|_{\mathcal{M},\mathcal{S}}]$'s be of the same sign. However, the latter condition should not be treated as necessary. This is because, for a given model class, the eigen-

values and mode shape components do not vary continuously with the mass and stiffness parameters; i.e. even though $\mathcal{M}$ defines a continuous space of the mass and stiffness matrices, the associated space of the eigenvalues and mode shape components is not continuous. Hence, the determinant of the Jacobian matrix will not be a continuous function in $\mathcal{M}$, and so the requirement that the $N_{\mathcal{M}}$ $\det[\mathbf{J}_i|_{\mathcal{M},\mathcal{S}}]$'s be of the same sign is not necessary. Note that, the space $\mathcal{U}$ in the statement of the theorem is not the same as the space of the eigenvalues and mode shape components associated with $\mathcal{M}$, and hence the discontinuity of the eigenvalues, mode shape components and Jacobian determinant in $\mathcal{M}$, does not violate any hypothesis of the theorem. In the experiment design discussed above, we consider $N_{\mathcal{M}}$ number of $\mathcal{U}_i|_{\mathcal{M},\mathcal{S}}$, each containing a distinct $(\boldsymbol{\alpha}_i, \boldsymbol{\theta}_i)|_{\mathcal{M},\mathcal{S}}$'s; i.e. we apply the implicit function theorem individually to each of the $N_{\mathcal{M}}$ models in $\mathcal{M}$. If the theorem gives a positive result, $\det[\mathbf{J}_i|_{\mathcal{M},\mathcal{S}}] \neq 0$, for all these $N_{\mathcal{M}}$ models, we infer that, since all the $N_{\mathcal{M}}$ models in $\mathcal{M}$ are locally identifiable, any model in $\mathcal{M}$ should be locally identifiable. While this is certainly not necessary, since there can still be some un-sampled models for which the test fails, ascertaining that the test is positive for a sufficiently large number $N_{\mathcal{M}}$ of sampled models, decreases the likelihood of such a negative situation.

4.5.1.4 Post-experiment use

Suppose that after an experiment with a given sensor set-up, we have identified $\boldsymbol{\alpha}^*$ from the measured data, and $\boldsymbol{\theta}^*$ using Section 4.2.1. We would like to know whether this solution $\boldsymbol{\theta}^*$ is the only possible solution satisfying our equations, for the identified $\boldsymbol{\alpha}^*$. This can be checked by computing the determinant of the Jacobian matrix $\mathbf{J}$ evaluated at $(\boldsymbol{\alpha}, \boldsymbol{\theta}) = (\boldsymbol{\alpha}^*, \boldsymbol{\theta}^*)$; if this determinant is non-zero then we can say that our solution $\boldsymbol{\theta}^*$, given the identified $\boldsymbol{\alpha}^*$, is the only solution in a neighbourhood around $\boldsymbol{\theta}^*$. If, on the other hand, the determinant is equal to zero, then we have to conclude that there *may* exist other solutions in the neighbourhood of our identified solution $\boldsymbol{\theta}^*$. The latter case will imply that there may exist an infinite number of systems, with exactly the same frequencies and measured mode shape components but different, albeit close to one another, mode shape components at the unmeasured DOFs.

4.5.1.5 Two remarks on the inferences from local identifiability test

(1) The implicit function theorem gives a *sufficient*, but *not necessary*, condition for the local uniqueness of solution. Hence, for any $(\boldsymbol{\alpha}^*, \boldsymbol{\theta}^*)$, the Jacobian determinant being non-zero definitely implies the local uniqueness of the solution $\boldsymbol{\theta}^*$, but the Jacobian determinant being zero does not imply the non-uniqueness of $\boldsymbol{\theta}^*$. (2) Even if the implicit function theorem is satisfied, i.e the determinant of the Jacobian is non-zero, everywhere in $\mathcal{U}$, that does not guarantee that $\boldsymbol{\theta}$ is globally identifiable in $\mathcal{U}$; it just implies that, if there are multiple solutions to $\mathbf{g}(\boldsymbol{\alpha}, \boldsymbol{\theta}) = \mathbf{0}$, these solutions are locally isolated in $\mathcal{U}$ [60].

4.5.2 Real Jacobian conjecture and global identifiability

While we can not use the implicit function theorem to test for global identifiability, since the equations in $\mathbf{g}(\boldsymbol{\alpha}, \boldsymbol{\theta}) = \mathbf{0}$ are at most of degree 2, we may use the real Jacobian conjecture to develop such a test. For our problem, this conjecture can be stated as:

Real Jacobian Conjecture: *Given* $\boldsymbol{\alpha}^*$*, if the polynomial map* $\mathbf{g}(\boldsymbol{\alpha}^*, \boldsymbol{\theta}) : \mathbf{R}^{N^2-1} \to \mathbf{R}^{N^2-1}$ *has*

$$\det[\mathbf{J}] = \det\left[\frac{\partial \mathbf{g}(\boldsymbol{\alpha}^*, \boldsymbol{\theta})}{\partial \boldsymbol{\theta}}\right] \neq 0 \quad \forall\, \boldsymbol{\theta} \in \mathcal{W} \subseteq \mathbf{R}^{N^2-1} \tag{4.43}$$

and $\mathbf{g}(\boldsymbol{\alpha}^*, \boldsymbol{\theta})$ *is at most degree 2 in* $\boldsymbol{\theta}$*, then* $\mathbf{g}(\boldsymbol{\alpha}^*, \boldsymbol{\theta})$ *is injective in* $\mathcal{W}$*.*

The original (real or complex) Jacobian conjecture requires $\det[\mathbf{J}]$ to be not only $\neq 0$, but a non-zero constant everywhere in $\mathcal{W}$; it is still a conjecture and its proof/disproof remains an open problem [61], except in special cases [62,63]. The real Jacobian conjecture requiring only $\det[\mathbf{J}] \neq 0$ has been proved to be generally false in [64], by a counterexample of two polynomials of degrees 10 and 35; however, the conjecture is true, for any number of polynomials, if the degree of any polynomial is at most 2 (see Appendix B for a proof from [65], or [62, 63] for alternative proofs). Hence, for our problem, we can treat the **Real Jacobian Conjecture** stated above as a theorem, since this statement includes the requirement that any polynomial in $\mathbf{g}(\boldsymbol{\alpha}^*, \boldsymbol{\theta})$ is at most degree 2 in the elements of $\boldsymbol{\theta}$, and this requirement is indeed satisfied by our $\mathbf{g}(\boldsymbol{\alpha}^*, \boldsymbol{\theta})$ (Section 4.2.1).

If $\mathbf{g}(\boldsymbol{\alpha}^*, \boldsymbol{\theta})$ is injective in $\mathcal{W}$, then every unique $\boldsymbol{\theta} \in \mathcal{W}$ will be mapped to an unique $\mathbf{g}(\boldsymbol{\alpha}^*, \boldsymbol{\theta})$. Hence, in such a situation, corresponding to $\mathbf{g}(\boldsymbol{\alpha}^*, \boldsymbol{\theta}) = \mathbf{0}$, there will be an unique solution $\boldsymbol{\theta} = \boldsymbol{\theta}^*$ in $\mathcal{W}$, i.e. $\boldsymbol{\theta}$ will be globally identifiable in $\mathcal{W}$. Note that we cannot claim $\boldsymbol{\theta}$ to be *simply* globally

identifiable, as there may be some $\boldsymbol{\theta}$ outside $\mathcal{W}$ satisfying $\mathbf{g}(\boldsymbol{\alpha}^*, \boldsymbol{\theta}) = \mathbf{0}$; we can only claim that, in the above situation, there will be only one $\boldsymbol{\theta}$ in $\mathcal{W}$ which will satisfy $\mathbf{g}(\boldsymbol{\alpha}^*, \boldsymbol{\theta}) = \mathbf{0}$.

4.5.2.1 Post-experiment use

Suppose using the measured data from a given sensor set-up, we have identified $\boldsymbol{\alpha}^*$ using system identification, and $\boldsymbol{\theta}^*$ using Section 4.2.1. Let us first define a space $\mathcal{W}$ around $\boldsymbol{\theta}^*$. The space $\mathcal{W}$ should cover the expected range of variation of the solution vector $\boldsymbol{\theta}$; such a range may, for example, be estimated as the range of values $\boldsymbol{\theta}$ takes for a range of possible values, from engineering judgement, of the physical parameters. Next, using any sampling technique, we generate $N_{\mathcal{W}}$ number of $\boldsymbol{\theta}$ vectors, say $\boldsymbol{\theta}_i \; \forall \; i \in \{1, \cdots, N_{\mathcal{W}}\}$, from $\mathcal{W}$; a larger $\mathcal{W}$ should correspond to a larger $N_{\mathcal{W}}$. For each $\boldsymbol{\theta}_i$, we compute the determinant of the corresponding Jacobian evaluated at $(\boldsymbol{\alpha}^*, \boldsymbol{\theta}_i)$. If all these $N_{\mathcal{W}}$ determinants are of the same sign (either strictly positive or strictly negative), then we can say that, the parameter vector $\boldsymbol{\theta}$ is globally identifiable in $\mathcal{W}$, with $\boldsymbol{\theta}^*$ being the unique solution in $\mathcal{W}$; otherwise it **may** not be globally identifiable in $\mathcal{W}$ for the given measured data. The latter situation will be a signal that we should solve $\mathbf{g}(\boldsymbol{\alpha}^*, \boldsymbol{\theta}) = \mathbf{0}$ multiple times starting from different initial guesses of $\boldsymbol{\theta}$ (Section 4.2.1.3). If we converge to the same $\boldsymbol{\theta}^*$ from all the initial guesses, then again we may assume that this $\boldsymbol{\theta}^*$ is the unique solution to $\mathbf{g}(\boldsymbol{\alpha}^*, \boldsymbol{\theta}) = \mathbf{0}$ in $\mathcal{W}$; if, however, we converge to more than one solution, then all these solutions may be taken to be equivalent given the measured data and structural topology requirements. In the latter case, engineering judgement and/or additional measurements from a different sensor set-up will be necessary to distinguish the "true" model from the pool of equivalent models.

Although seemingly similar, the above application is different from the implicit function theorem application of Section 4.5.1.3. Firstly, in Section 4.5.1.3 we consider different models sampled from a model space $\mathcal{M}$ (pre-experiment), whereas above we consider different $\boldsymbol{\theta}$ vectors sampled from a space around a solution $\boldsymbol{\theta}^*$ (post-experiment). While all the models sampled from $\mathcal{M}$ belong to the same class of models (here shear-type), the different $\boldsymbol{\theta}$ vectors sampled from $\mathcal{W}$ are arbitrary; in fact, the sampled $\boldsymbol{\theta}$'s may not even correspond to *any* physically meaningful structural model. This definitely makes the satisfaction of the real jacobian conjecture rarer than the satisfaction of the implicit function theorem, as should be expected given that they respectively test global and local identifiability. Secondly, for the implicit function theorem we only ensure that the Jacobian

determinant is non-zero for each of the $N_{\mathcal{M}}$ models in $\mathcal{M}$; whereas here we want to ensure that the Jacobian determinant is non-zero for all $\boldsymbol{\theta}$ in $\mathcal{W}$, and hence ensure that the determinant is of the same sign for all the $N_{\mathcal{W}}$ sampled $\boldsymbol{\theta}$ vectors. This difference is a consequence of the continuous variation of $\boldsymbol{\theta}$ in $\mathcal{W}$, as against a discontinuous variation of $\boldsymbol{\theta}$ in $\mathcal{M}$ (see Section 4.5.1.3).

In some cases when $\boldsymbol{\theta}$ is not globally identifiable, the solution strategy of Section 4.2.1.3 involving Newton-Raphson iterations may fail owing to the Jacobian matrix becoming singular at an intermediate iteration. This of course follows directly from the real Jacobian conjecture. Again, such an occurrence does not necessarily imply multiple solutions; e.g. a single variable monotonic function $f(x)$ will have a single zero but may have a saddle point at which its derivative vanishes. But it does signal the possibility of multiple solutions, which should be checked by solving $\mathbf{g}(\boldsymbol{\alpha}^*, \boldsymbol{\theta}) = \mathbf{0}$ multiple times starting from different initial guesses of $\boldsymbol{\theta}$.

4.5.2.2 Possible pre-experiment use

The test for the local identifiability of the system in $\mathcal{M}$ discussed in Section 4.5.1.3, may theoretically be extended to test also for global identifiability in $\mathcal{M}$. This extension will simply involve: (a) generating a space $\mathcal{W}_i$ around each of the $\boldsymbol{\theta}_i$'s, $i \in \{1, \cdots, N_{\mathcal{M}}\}$, corresponding to the $N_{\mathcal{M}}$ sampled models in Section 4.5.1.3; (b) sampling $N_{\mathcal{W}}$ number of $\boldsymbol{\theta}_{i,j}$ vectors, $j \in \{1, \cdots, N_{\mathcal{W}}\}$, from $\mathcal{W}_i$; and (c) assuring that, for each $i \in \{1, \cdots, N_{\mathcal{M}}\}$, all the corresponding $N_{\mathcal{W}}$ Jacobian determinants, $\det[\mathbf{J}]_{i,j}$ evaluated at $(\boldsymbol{\alpha}_i, \boldsymbol{\theta}_{i,j})$, $j \in \{1, \cdots, N_{\mathcal{W}}\}$, are of the same sign. (Note: the $\det[\mathbf{J}]_{i,j}$'s $\forall$ $i \in \{1, \cdots, N_{\mathcal{M}}\}$, $j \in \{1, \cdots, N_{\mathcal{W}}\}$, need not be of the same sign, but, for any given i, the $\det[\mathbf{J}]_{i,j}$'s $\forall$ j should be of the same sign; this is following the argument of $\boldsymbol{\theta}$ being continuous in $\mathcal{W}$, but discontinuous in $\mathcal{M}$.) If the above test is satisfied, then we can say that, with the sensor set-up under consideration, the system is globally identifiable in $\mathcal{M}$. However, based on our experience, we do not recommend the above test in assessing global identifiability pre-experiment. This is because, since the sampled $\boldsymbol{\theta}_{i,j}$'s are arbitrary, it is very likely that there is (at least) one $\mathcal{W}_i$ in which the condition of everywhere non-singular Jacobian is not satisfied; this leads to the test usually failing, especially for larger systems. However, since the real Jacobian conjecture gives a sufficient, but not a necessary, condition for the involved polynomial map to be injective, for any sensor set-up, the failing of the above test does not rule out global identifiability of the system in $\mathcal{M}$. In fact, Chapter 3 shows that there are sensor set-ups which will guarantee the global identifiability of the system in the model

space $\mathcal{M}$, and also provides a method to determine such sensor set-ups; thus for experiment design requiring guaranteed global identifiability in $\mathcal{M}$, we recommend the use of Chapter 3, at the cost of using an increased number of sensors.

4.5.2.3 Other Jacobian based tests for global identifiability

We close this section by noting some other possibilities for assessing global identifiability: (1) An alternative to the real Jacobian conjecture is Hadamard's theorem which asserts that $\mathbf{g}(\boldsymbol{\alpha}^*, \boldsymbol{\theta})$ is injective in $\overline{\mathcal{W}}$, the interior of $\mathcal{W}$, if (a) $\mathbf{g}(\boldsymbol{\alpha}^*, \boldsymbol{\theta})$ is continuously differentiable with respect to $\boldsymbol{\theta}$ in $\overline{\mathcal{W}}$, (b) its Jacobian matrix is non-singular $\forall\ \boldsymbol{\theta} \in \overline{\mathcal{W}}$, and (c) $|\mathbf{g}(\boldsymbol{\alpha}^*, \boldsymbol{\theta})| \to +\infty$ when $\boldsymbol{\theta}$ approaches the boundary of $\mathcal{W}$ [63]. The first condition is satisfied since no element of $\boldsymbol{\theta}$, i.e. no $v^*_{i,j}$, can be infinity (see Section 4.5.1.1); the second condition is the same as the real Jacobian conjecture, and hence is satisfied whenever the conjecture is satisfied; however, the third condition is obviously not satisfied in our case. Hence we cannot apply this theorem in our problem. (2) Yet another test can be satisfying Samuelson's conjecture that, for some arrangement of the equations and variables, if all the leading principal minors of the Jacobian are non-zero $\forall\ \boldsymbol{\theta} \in \mathcal{W}$, then the system of equations have a unique solution [60]; while this conjecture is not generally true [66], it is true for rational (and so polynomial) maps [67]. However, all tests that we have performed, on systems of different DOFs with different sensors set-ups, have failed to guarantee uniqueness as per this conjecture, possibly owing to the more stringent conditions as compared to the real Jacobian conjecture. Again, since this conjecture provides a sufficient, but not necessary, condition for solution uniqueness, such failures do not rule out the possibility of solution uniqueness. (3) Finally, there is the Gale-Nikaido theorem [66], by which if all the principal minors of the Jacobian matrix is positive then the function is univalent, i.e. the system of equations will have a unique solution. Since Samuelson's conjecture has failed to give any conclusive result in our case, this theorem will lead to inconclusive results as well. Moreover, for our system of N^2-1 equations, the application of this theorem will require the evaluation of $2^{N^2-1}-1$ determinants (principal minors), which, with increasing N, will be very soon computationally infeasible. Based on this discussion, we may conclude that the real Jacobian conjecture seems to be the one ideally suited for assessing global identifiability using the Jacobian matrix; it is computationally feasible, has the least conditions on the Jacobian or the function, while providing the same assertion on global identifiability (sufficient, but not necessary) as the other approaches.

4.6 Numerical Examples

4.6.1 Experiment design using Sections 4.4 and 4.5.1

In this section we illustrate the method discussed in Section 4.4 and the local identifiability test of Section 4.5.1.3 using four example situations: a 3 DOF system with 2 sensors ($N = 3$, $N_s = 2$), a 7 DOF system with 2 sensors ($N = 7$, $N_s = 2$), an 8 DOF system with 2 sensors ($N = 8$, $N_s = 2$), and a 7 DOF system with 3 sensors ($N = 7$, $N_s = 3$). Recall that the method of independent information from measurements (Section 4.4) does not require the definition of any model space $\mathcal{M}$. On the contrary, we need to define a model space $\mathcal{M}$ within which the local identifiability of the system can be tested using the implicit function theorem. In these examples, we define $\mathcal{M}$ as follows: (a) Define a nominal model with $m_i = 2500$ kg $\forall\ i \in \{1, \cdots, N-1\}$, $m_N = 2000$ kg, $k_i = 5 \times 10^6$ N/m $\forall\ i \in \{1, \cdots, N\}$ (this model can be an existing FE model); (b) Define a range for each of these parameters as $[p_l, p_u] = [0.70, 1.30]p$, where $p \in \{m_1, \cdots, m_N, k_1, \cdots, k_N\}$ as defined in (a), and p_l and p_u are respectively the lower and upper bounds of the range of p. The model space $\mathcal{M}$ is defined as the space of all models whose parameters belong in the above ranges, i.e. a space covering $\pm$ 30% around the nominal model's parameter values. We then generate $N_{\mathcal{M}} = 10,000$ models in $\mathcal{M}$, using latin hypercube sampling (LHS) to sample the parameter values from the above defined ranges; this is done using the function *lhsdesign* in MATLAB® [30]. The test of Section 4.5.1.3 is applied with these $10,000$ models. In each example, all the ${}^{N}C_{N_s}$ possible sensor set-ups are tested.

Fig. 4.2 presents the results of the tests: a ✓ sign indicates that the corresponding sensor set-up is allowed as per the requirement tested, while a ✗ sign indicates otherwise. It is noteworthy that the results from the two different tests agree in all the cases, although Section 4.4 tests only the independent information content, and does not depend on $\mathcal{M}$, while Section 4.5.1.3 tests local identifiability in $\mathcal{M}$. This highlights the very definite connection between parameter identifiability and the amount of available information. Both the tests also corroborate the observations of Section 4.3 on the 3-DOF 2-sensor problem. Comparing the $N_s = 2$ and $N_s = 3$ cases for $N = 7$, it is seen that the number of allowed set-ups increase with the number of sensors, as may be expected.

In any example, for each sensor set-up, the maximum and minimum values of the ranks of all the $10,000$ Jacobian matrices are computed, and plotted in Fig. 4.3. In these plots, the sensor set-ups are in lexicographic ordering, as in Fig. 4.2. It is seen that, in any given case, the minimum

and the maximum ranks of the Jacobians are the same, i.e. all the $10,000$ Jacobians have the same rank. Hence, for any given sensor set-up, either all models are locally identifiable in $\mathcal{M}$, or all are unidentifiable. In other words, if any 1 model in $\mathcal{M}$ is locally identifiable, then all models in $\mathcal{M}$ are locally identifiable, and vice versa; this means that testing any 1 of the $10,000$ models would have been sufficient to assess local identifiability. While this is indeed a very strong statement, and should be merely treated as an observation pertaining to the example discussed here, it is also possibly the reason why, in Fig. 4.2, the results of the two different tests match, even when one of the tests is model independent.

Fig. 4.3 also shows the $N(N-1)+\mathcal{I}_2$ (or $N(N-1)+\mathcal{I}_3$) values in the different sensor set-ups, where $\mathcal{I}_2$ (or $\mathcal{I}_3$), computed as per Section 4.4, is the amount of independent information provided by the sensors in any set-up. Since $N(N-1)$ is the number of equations from structural topology (Section 4.2.1.1), $N(N-1)+\mathcal{I}_2$ (or $N(N-1)+\mathcal{I}_3$) denotes the total information available in any set-up. It is interesting that these values match the corresponding Jacobian ranks, in all cases of 2 sensors and in all cases when the total information count is less than the minimum necessary N^2-1 (= the number of unknowns). This implies that the analysis of Section 4.4 may be used to detect situations of unidentifiability whenever the total available information becomes less than the minimum necessary, the available information being the rank of the Jacobian and thus indicating the Jacobian becoming rank deficient, hence singular. The total information counts in all the cases with 2 sensors also show that we can have at most the minimum necessary information with 2 sensors. For the case of 3 sensors however, in many cases we do have more than N^2-1 available information; some such additional information may be redundant, especially given the way we reduce the number of equations in Section 4.5.1.2 for the identifiability tests of Section 4.5. Having such redundant information may be beneficial in decreasing the uncertainty in the estimated parameters. Also, with some redundant information, some equations pertaining to nodes may be excluded, *only* in case they tend to make the problem numerically ill-conditioned; any such exclusion should involve caution so as not to remove any essential information. One way to exclude such potential sources of ill-conditioning without loss of essential information is to use the $\mathbf{\Gamma}$ matrix of Eq. (4.41) (Section 4.5.1.2), removing any row(s) of $\mathbf{\Gamma}$ with numerically too small/too large an entry as compared to the other rows, ensuring that such a removal reduces the condition number of $\mathbf{\Gamma}$ but does not make it rank deficient (rank $< N$). The equations corresponding to such removed row(s) may then be excluded from Eq. (4.4).

$N = 3$; $N_s = 2$; Possible set-ups = 3; Allowed set-ups = 2

$\mathcal{S}$	1,2	1,3	2,3
Sec. 4	✓	✓	×
Sec. 5.1.3	✓	✓	×

$N = 7$; $N_s = 2$; Possible set-ups = 21; Allowed set-ups = 6

$\mathcal{S}$	1 2	1 3	1 4	1 5	1 6	1 7	2 3	2 4	2 5	2 6	2 7	3 4	3 5	3 6	3 7	4 5	4 6	4 7	5 6	5 7	6 7
Sec. 4	×	×	×	×	✓	✓	×	×	✓	✓	×	✓	✓	×	×	×	×	×	×	×	×
Sec. 5.1.3	×	×	×	×	✓	✓	×	×	✓	✓	×	✓	✓	×	×	×	×	×	×	×	×

$N = 8$; $N_s = 2$; Possible set-ups = 28; Allowed set-ups = 7

$\mathcal{S}$	1 2	1 3	1 4	1 5	1 6	1 7	1 8	2 3	2 4	2 5	2 6	2 7	2 8	3 4	3 5	3 6	3 7	3 8	4 5	4 6	4 7	4 8	5 6	5 7	5 8	6 7	6 8	7 8
Sec. 4	×	×	×	×	×	✓	✓	×	×	×	✓	✓	×	✓	×	×	✓	×	✓	×	×	×	×	×	×	×	×	×
Sec. 5.1.3	×	×	×	×	×	✓	✓	×	×	×	✓	✓	×	✓	×	×	✓	×	✓	×	×	×	×	×	×	×	×	×

$N = 7$; $N_s = 3$; Possible set-ups = 35; Allowed set-ups = 29

$\mathcal{S}$	1 2 3	1 2 4	1 2 5	1 2 6	1 2 7	1 3 4	1 3 5	1 3 6	1 3 7	1 4 5	1 4 6	1 4 7	1 5 6	1 5 7	1 6 7	2 3 4	2 3 5	2 3 6	2 3 7	2 4 5	2 4 6	2 4 7	2 5 6	2 5 7	2 6 7	3 4 5	3 4 6	3 4 7	3 5 6	3 5 7	3 6 7	4 5 6	4 5 7	4 6 7	5 6 7
Sec. 4	×	✓	✓	✓	✓	✓	✓	✓	✓	✓	✓	✓	✓	✓	✓	✓	✓	✓	✓	✓	✓	✓	✓	✓	✓	✓	✓	✓	✓	✓	✓	✓	✓	✓	✓
Sec. 5.1.3	×	✓	✓	✓	✓	✓	✓	✓	✓	✓	✓	✓	✓	✓	✓	✓	✓	✓	✓	✓	✓	✓	✓	✓	✓	✓	✓	✓	✓	✓	✓	✓	✓	✓	✓

Figure 4.2: Possible and allowed sensor set-ups, for different N (number of DOFs) and N_s (number of sensors) combinations, determined using the concept of independent measured information (Section 4.4, and the implicit function theorem based test for local identifiability (Section 4.5.1.3).

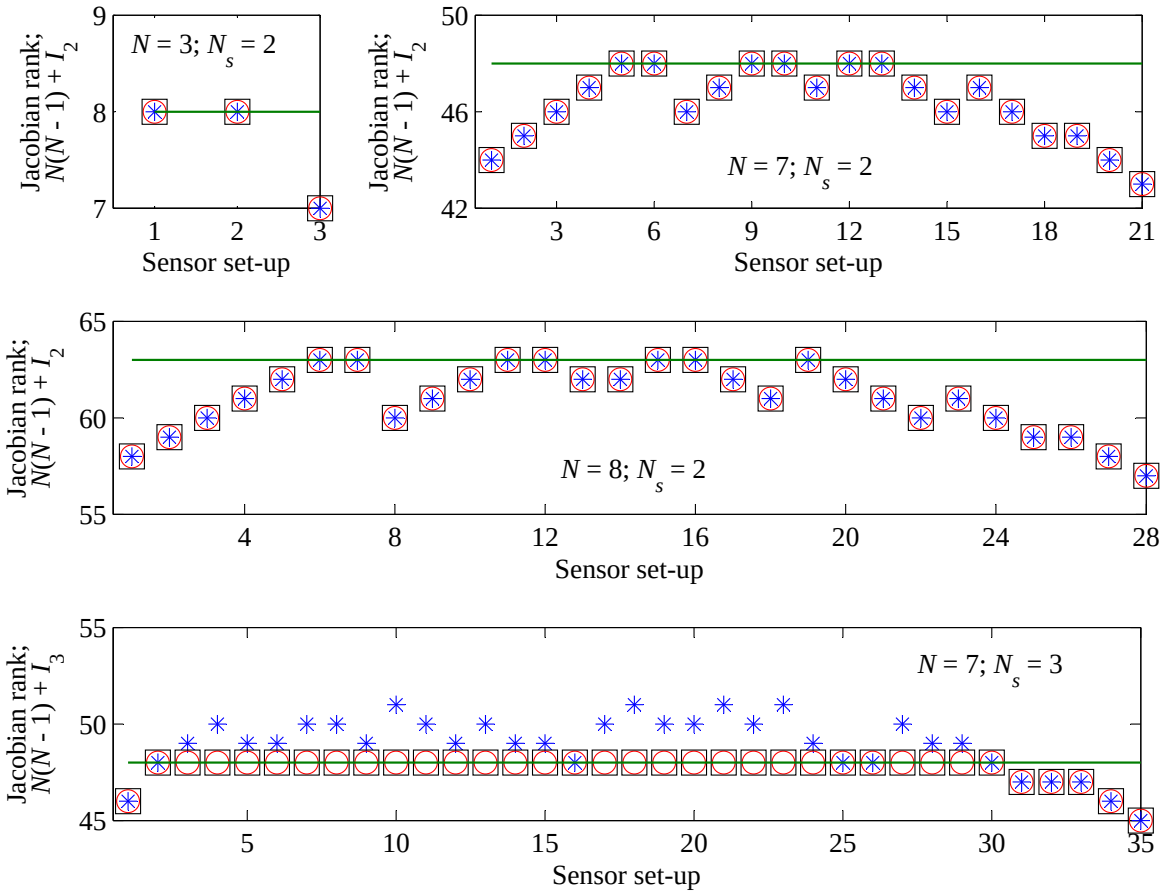

Figure 4.3: Maximum (black square) and minimum (red circle) ranks of Jacobians; total available information $= N(N-1) + \mathcal{I}_2$ (or $N(N-1) + \mathcal{I}_3$) (blue stars); number of unknowns $= N^2 - 1$ (green line), in different sensor set-ups, for different N and N_s combinations.

4.6.2 Structural identification using Section 4.2

In this section we validate the structural identification algorithm of Section 4.2 using numerical simulations of ambient vibration testing. 10 example cases are considered, with a 7 and an 8-DOF system, instrumented with 2 or 3 accelerometers in different set-ups (see Table 4.2). Note: for the $N = 8$ DOF system, both $N_s = 2$ and 3 sensors are less than the prescribed minimum number of sensors, $(1 + \sqrt{4N-3})/2$, necessary for global identifiability as per Chapter 3; for the $N = 7$ DOF system, $N_s = 2$ is below this minimal sensor requirement; the set-ups $\mathcal{S} = \{1, 3, 4\}$ and $\{2, 3, 4\}$ for $N = 7$ violate the sensor placement guideline: "no consecutive sensors when $N_s =$ the minimum necessary number of sensors", given in Chapter 3; only the sensor set-up $\mathcal{S} = \{1, 3, 4\}$ for $N = 7$ satisfies

all the requirements of Chapter 3. The cases here are chosen to illustrate that even when sensors are placed violating the guidelines of Chapter 3, it may still be possible to identify the system if it is locally identifiable, even though the system may not be globally identifiable in such a case.

Both the systems are assumed to have modal damping characteristics. In each case, 100 simulations are run; in each simulation, the mass, stiffness and damping parameters are slightly perturbed, to represent a realistic situation, by choosing them from uniform distributions: for any parameter ϕ, its value in the kth simulation is chosen as $\phi_{i,k} = \mathcal{U}(1-p_\phi, 1+p_\phi)E[\phi_i]$, where $E[.]$ denotes the mean value of the variable in brackets, and $\mathcal{U}(l_l, l_r)$ denotes uniform probability distribution between l_l and l_r. The mean values and limits used here are: $E[m_i] = 2500$ kg $\forall\ i \in \{1, \cdots, N-1\}$, $E[m_N] = 2000$ kg, $E[k_i] = 5 \times 10^6$ N/m $\forall\ i \in \{1, \cdots, N\}$, and $E[\zeta_j] = 5 \times 10^6$ N/m $\forall\ j \in \{1, \cdots, N\}$, where ζ_j is the modal damping ratio in the jth mode; and $p_{m_i} = 0.005$, $p_{k_i} = 0.05$, $p_{\zeta_j} = 0.05$, $\forall\ i, j \in \{1, \cdots, N\}$. The slightly perturbed structure in each simulation is excited by applying zero-mean Gaussian white noise input forces at all the DOFs, and the resulting acceleration responses at the DOFs with accelerometers are stored. To simulate the effect of measurement noise the true acceleration responses are corrupted by adding 10% RMS zero-mean Gaussian white noise sequences. Thus, each simulation differs in terms of: (1) the applied input(s), which are different white noise sequences, (2) exciting slightly different systems owing to the slight perturbations in the system parameters, and (3) the added measurement noise sequences. Two different scenarios are considered based on the available *a priori* information: (1) the total mass of the system is known as $M_T = 2500(N-1) + 2000$ kg (Section 4.2.2.2), and (2) two sets of measured data are available, one from the original structure, and the other from the structure with masses of ≈ 500 kg added on all the floors, i.e. $\triangle \mathbf{m}_T = 500N$ kg (Section 4.2.2.3). The second set of (noisy) output data is simulated in the same way as the first set, with added masses in each simulation being also perturbed between $\pm 0.5\%$ of 500 kg, as is done for the floor masses. The *a priori* information used in identification are based on the mean parameter values, as would be in a realistic situation, and are thus not strictly accurate, being uninformed of the parameter perturbations.

The modal frequencies and non-mass normalized mode shapes at the sensor locations are estimated using the (noisy) output accelerations at the sensor locations in the Enhanced Canonical Correlation Analysis (ECCA) [68], a recently developed system identification technique in the stochastic subspace identification framework. The proposed approach of Section 4.2 is next used to get the

Table 4.2: Maximum statistics of estimation errors (%) in identified parameters.

N	$\mathcal{S}$	Known M_T				Second experiment with known added mass			
		$\mu_{\varepsilon(m)}$	$\sigma_{\varepsilon(m)}$	$\mu_{\varepsilon(k)}$	$\sigma_{\varepsilon(m)}$	$\mu_{\varepsilon(m)}$	$\sigma_{\varepsilon(m)}$	$\mu_{\varepsilon(k)}$	$\sigma_{\varepsilon(m)}$
7	$\{1,7\}$	0.39	1.32	0.21	1.46	0.28	2.35	0.44	2.37
	$\{1,6\}$	0.52	2.96	0.46	3.07	0.40	2.99	0.40	2.92
	$\{1,3,4\}$	0.19	1.61	0.16	1.85	0.12	2.18	0.22	2.26
	$\{1,4,7\}$	0.62	3.35	0.43	2.17	0.55	4.27	0.39	2.93
	$\{2,3,4\}$	0.24	2.57	0.31	2.34	0.14	4.07	0.28	3.54
8	$\{1,8\}$	0.43	2.22	0.22	2.21	0.45	3.39	0.31	3.36
	$\{3,5\}$	0.63	2.53	0.29	2.44	0.87	3.03	0.67	2.88
	$\{4,5\}$	0.29	2.62	0.48	3.29	0.87	3.55	1.52	4.37
	$\{1,4,6\}$	0.62	2.73	0.32	3.03	0.55	3.32	0.58	3.90
	$\{2,7,8\}$	0.26	3.03	0.48	2.38	0.69	3.17	0.59	2.76

complete mass normalized $\mathbf{V}$ matrix; the initial guess for the Newton-Raphson method is obtained as the elements of the mode shape matrix of a 7 (or 8) DOF shear-type system with all $m_i = 1$ and all $k_i = 10$. Finally, the modal orthogonality relations are used to estimate the $\mathbf{M}$ and $\mathbf{K}$ matrices, from which the floor masses and story stiffnesses are estimated.

Table 4.2 show the statistics of the estimation errors in the identified mass and stiffness parameters, obtained from the 100 simulations run for each case. These statistics are calculated in the same way as in the numerical examples in Chapters 2 and 3 (see Section 2.5), viz. for any m_i or k_i, $i \in \{1, \cdots, N\}$: (a) the relative percentage error is first computed in each simulation (Eq. (2.62)), (b) the means and standard deviations of these relative percentage errors are then computed over all the 100 simulations (Eq. (2.63)), and (c) the maximum (over all $i \in \{1, \cdots, N\}$, i.e. across all floors/stories) absolute values of these means and standard deviations are computed (Eq. (2.64)), and reported in Table 4.2. It is evident from Table 4.2 that the proposed algorithm performs reasonably well in estimating the floor masses and story stiffnesses, with the maximum absolute mean errors being mostly less than 1%, and the maximum absolute standard deviations in the errors being mostly between 1.5 and 4%, even with noisy measurements, very limited number of sensors, and very limited *a priori* information of physical parameter values.

4.6.3 Heterogenous sensing and estimation of unobserved modes

In this section we present two examples of the possible use of Section 4.4 in estimating the complete mode shape spectra at some DOFs with sensors, when not all the modes are identified directly from the measurements at every DOF with sensor. Such a possibility is briefly discussed at the end of Section 4.4.4. Treating the different modes identified at the different DOFs as complementary information, one may be able to estimate the unobserved mode shape components at some/all of the DOFs with sensors.

Consider a 4-DOF shear-type system with $m_i = 2500$ kg and $k_i = 5\times10^6$ N/m, $\forall\, i \in \{1, \cdots, 4\}$, and with accelerometers at DOFs 1 and 2, and a displacement sensor at DOF 4. The system is excited with white noise forces applied at all the DOFs. The true acceleration and displacement responses at the DOFs with sensors are now corrupted by adding colored noise sequences, scaled to have 10% RMS of the corresponding true signals: (a) in the accelerations we add red noise (power spectral density $\propto 1/f^2$, where f is frequency), adversely affecting the low frequency modes, and (b) in the displacement we add violet noise (power spectral density $\propto f^2$), adversely affecting the high frequency modes. Moreover, the displacement measurements are sampled at 20Hz, so that the Nyquist frequency is less than the third modal frequency of the system. The acceleration and displacement signals are used separately in ECCA for modal identification. As expected, using the two "noisy" acceleration signals we identify only modes 2, 3 and 4, while using the single displacement record we are only able to consistently (based on 100 simulations) identify mode 1. Statement **1** of Section 4.4.1 is then applied, with DOFs $i_1 = 1$ and $i_2 = 2$, as follows: (a) using the identified $\{\lambda_j, \tilde{v}_{1,j}, \tilde{v}_{2,j}\}$, $\forall\, j \in \{2, 3, 4\}$, we first find the 3 involved mode independent constants; and (b) using these constants, along with the λ_1 identified from the displacement record, we estimate $\tilde{v}_{2,1}/\tilde{v}_{1,1}$, or $\tilde{v}_{2,1}$ for any assumed $\tilde{v}_{1,1}$. This gives the complete non-normalized modal spectra at DOFs 1 and 2. Using the estimates from 100 such simulations, the identified $\tilde{v}_{2,j}/\tilde{v}_{1,j}$ has a mean: $\{1.90, 0.98, -0.26, -1.58\}$, and standard deviation: $\{0.02, 0.01, 0.01, 0.02\}$, where the components respectively correspond to modes $j = 1$ to 4. Thus, while the last three components are from the ECCA estimates, the first component is from the estimates using Section 4.4.1. Comparing with the true $\tilde{v}_{2,j}/\tilde{v}_{1,j} = \{1.88, 1.00, -0.35, -1.53\}$, it is evident that the estimate of the first mode shape is reasonably accurate, and as accurate as the ECCA estimates of the other mode shapes. Also, the standard deviations show that the estimates, for all the modes, are consistent across different runs.

The same example is repeated with displacement sensors at DOFs 3 and 4, and a single accelerometer at DOF 1. With DOFs $i_1 = 4$ and $i_2 = 3$, Statement 2 of Section 4.4.1 is now applied as follows: (a) using the ECCA identified $\{\lambda_1, \tilde{v}_{3,1}, \tilde{v}_{4,1}\}$ we first estimate the single involved mode independent constant; and (b) we next use this constant, along with the λ_j's identified from the acceleration signal, to estimate the corresponding $\tilde{v}_{3,j}/\tilde{v}_{4,j}$'s, $\forall\ j \in \{2, 3, 4\}$. The mean and standard deviation of the estimated $\tilde{v}_{3,j}/\tilde{v}_{4,j}$'s, from 100 such simulations, are respectively: $\{0.88, 0.05, -1.28, -2.37\}$, and $\{0.00, 0.01, 0.02, 0.03\}$; the first component is from ECCA estimates, while the remaining three components are from the estimates using Section 4.4.1. The true $\tilde{v}_{3,j}/\tilde{v}_{4,j} = \{0.88, 0.00, -1.35, -2.53\}$. In this example, we were also able to identify the second mode from the displacement signals at DOFs 3 and 4 using ECCA, with a mean of -0.03 and standard deviation of 0.01, based on the 100 simulations. Note that the 2nd mode has a node at DOF 3. From these results, it is evident that Section 4.4.1 is able to identify the mode shape ratios $\tilde{v}_{3,j}/\tilde{v}_{4,j}$, for all modes $j = 2$ to 4, with reasonable accuracy and consistency, using only the measured information pertaining to mode 1 at DOFs 3 and 4, but complemented with the measured information on modes 2 to 4 from DOF 1. Such fusion of modal information may be a possible approach to combine information contained in heterogenous measurements, and may serve as a necessary precursor to subsequent structural identification and/or damage detection operations.

4.7 Experimental Application

For the experimental application, we again use the shaking table experimental data from the 4-story laboratory scale steel frame (Fig. 3.4) considered in Chapter 3 (Section 3.6). Recall that the experimental campaign included six different input ground motions (Fig. 3.4), each applied thrice, thus constituting a total of 18 dynamic tests of the frame.

In the identification, we use various sub-sets of the weak direction measured acceleration responses transformed to the centerline of the floors. While the input to the structure (table acceleration) was measured in the experiments, we do not use them in the identification. We consider the frame, along the weak direction, to be modeled as a 4-DOF shear-type system. As in Chapter 3, the analytical model of the frame adopted here is from [46]: this model has uniform floor masses of 37 kg, and uniform story stiffnesses of 1.7×10^5 N/m. This analytical model is used (1) to test local

Table 4.3: Pre-identification determination of allowed sensor set-ups, using Sections 4.4 and 4.5.1.3.

N_s	$\mathcal{S}$	Section 4.4	$N(N-1)+\mathcal{I}_{N_s}$	Section 4.5.1.3	rank(**J**)
2	$\{1,2\}$	X	14	X	14
	$\{1,3\}$	✓	15	✓	15
	$\{1,4\}$	✓	15	✓	15
	$\{2,3\}$	✓	15	✓	15
	$\{2,4\}$	X	14	X	14
	$\{3,4\}$	X	13	X	13
3	$\{1,2,3\}$	✓	16	✓	15
	$\{1,2,4\}$	✓	16	✓	15
	$\{1,3,4\}$	✓	16	✓	15
	$\{2,3,4\}$	✓	15	✓	15
4	$\{1,2,3,4\}$	✓	17	✓	15

identifiability for various sensor set-ups pre-identification, (2) to get the initial guess of the elements of $\mathbf{V}^*$ for the Newton-Raphson method, and (3) to get the *a priori* information of known total mass, $M_T = 148$ kg, for scaling $\mathbf{V}^*$ to $\mathbf{V}$.

First, the concept of independent information of Section 4.4, and the local identifiability test of Section 4.5.1.3, are used to decide permissible sensor set-ups. For the application of Section 4.5.1.3, the same procedure as Section 4.6.1 is followed: the model space $\mathcal{M}$ is defined covering $\pm$ 30% around the analytical model's parameter values [46], and a latin hypercube sample of $10,000$ models is generated from $\mathcal{M}$; the test of Section 4.5.1.3 is applied on these $10,000$ models. Table 4.3 presents the results of these tests, for all possible set-ups with $N_s \geq 2$ observed floors; e.g. $\mathcal{S} = \{1,2\}$ means the acceleration responses at the centerlines of the 1st and 2nd floors are observed, etc. A ✓ sign indicates that the corresponding set-up is allowed, while a X sign indicates otherwise. Table 4.3 also shows the total information, $N(N-1)+\mathcal{I}_{N_s}$, from Section 4.4, and the rank of the Jacobians computed in the local identifiability test; note that, for any set-up, all the $10,000$ Jacobians had the same rank. The results here agree with those in Section 4.6.1. As per Table 4.3, we have a total of 8 sets of observed floors which satisfies local identifiability requirements. These set-ups are considered for identification in the remaining part of this section. In a real situation, such a test will be performed prior to the actual data collection, and will govern the sensor placements on the structure.

For each of the allowed set-ups, the corresponding floor accelerations in each test are used in

Table 4.4: Statistics of modal frequency (in Hz) and damping ratio (in %) estimates using ECCA.

$\mathcal{S}$	μ_f (Hz)	COV$_f$ (%)	μ_ζ (%)	COV$_\zeta$ (%)
$\{1,3\}$	$3.6, 10.7, 17.9, 25.4$	$0.7, 1.4, 0.5, 0.3$	$0.3, 0.6, 0.6, 0.6$	$37.2, 27.4, 58.4, 27.7$
$\{1,4\}$	$3.6, 10.7, 17.9, 25.4$	$0.7, 1.3, 0.7, 0.3$	$0.3, 0.7, 0.6, 0.7$	$31.2, 28.6, 59.4, 32.0$
$\{2,3\}$	$3.6, 10.7, 17.9, 25.4$	$0.6, 1.3, 0.4, 0.3$	$0.3, 0.4, 0.4, 0.5$	$29.2, 20.1, 49.0, 18.3$
$\{1,2,3\}$	$3.6, 10.7, 17.9, 25.4$	$0.7, 1.3, 0.5, 0.3$	$0.3, 0.4, 0.6, 0.5$	$39.2, 22.7, 59.1, 28.0$
$\{1,2,4\}$	$3.6, 10.7, 17.9, 25.4$	$0.7, 1.2, 0.5, 0.3$	$0.3, 0.6, 0.5, 0.6$	$32.8, 23.3, 54.2, 28.4$
$\{1,3,4\}$	$3.6, 10.7, 17.9, 25.4$	$0.6, 1.3, 0.4, 0.3$	$0.2, 0.7, 0.5, 0.6$	$35.1, 27.5, 52.7, 24.0$
$\{2,3,4\}$	$3.6, 10.8, 17.9, 25.4$	$0.6, 1.2, 0.5, 0.3$	$0.3, 0.5, 0.4, 0.5$	$26.7, 19.4, 48.3, 18.8$
$\{1,2,3,4\}$	$3.6, 10.7, 17.9, 25.4$	$0.6, 1.2, 0.4, 0.3$	$0.2, 0.5, 0.5, 0.5$	$38.4, 22.8, 52.7, 25.2$

Table 4.5: Statistics of MAC between ECCA estimates of complete non-normalized modes and estimates of complete mass-normalized modes using proposed approach.

$\mathcal{S}$	μ_{MAC}	COV$_{\text{MAC}}$ (%)
$\{1,3\}$	$1.00, 0.90, 0.96, 0.95$	$0.01, 0.69, 0.65, 1.00$
$\{1,4\}$	$1.00, 0.92, 0.99, 0.81$	$0.02, 1.09, 0.16, 3.18$
$\{2,3\}$	———-	———-
$\{1,2,3\}$	$1.00, 0.96, 0.99, 1.00$	$0.01, 0.45, 0.40, 0.05$
$\{1,2,4\}$	$1.00, 1.00, 0.99, 1.00$	$0.00, 0.04, 0.25, 0.13$
$\{1,3,4\}$	$1.00, 1.00, 1.00, 1.00$	$0.01, 0.09, 0.01, 0.22$
$\{2,3,4\}$	$1.00, 1.00, 0.98, 1.00$	$0.07, 0.02, 0.58, 0.07$
$\{1,2,3,4\}$	$1.00, 1.00, 1.00, 1.00$	$0.00, 0.00, 0.00, 0.00$

ECCA to identify the modal frequencies, damping ratios and non-mass normalized mode shapes at the observed floors. These mode shapes are initially complex. Using the same data in an input-output identification algorithm, it was shown in Chapter 3 that the structure may be assumed to be proportionally damped. Hence, the real mode shapes, obtained by minimizing the imaginary parts of the corresponding identified complex modes, are used in further analysis. The initial guess for the Newton-Raphson solution, and the *a priori* information of total mass for scaling, are obtained from the analytical model [46]. In the Newton-Raphson solution, the equations from the measured mode shape components (Eq. (4.4)) are weighted by a factor of 100, as compared to a weight of 1 for the other equations; this reflects that we have more confidence in the experimental data as compared to the assumed model topology. For each set-up, after estimating 18 sets of the different parameters, corresponding to the 18 tests (6 inputs $\times$ 3 runs), the mean μ, standard deviation σ, and coefficient of variation (COV = σ/μ in %), of these estimates are computed. Tables 4.4 to 4.7 lists the estimation statistics, respectively for: (a) the modal frequencies and damping ratios identified using ECCA; (b) the MAC values comparing the non-mass normalized modes identified using ECCA for $\mathcal{S} = \{1, 2, 3, 4\}$, with the complete mass-normalized modes obtained using the proposed approach for different $\mathcal{S}$; (c) the identified $\mathbf{M}$ and $\mathbf{K}$ matrices; and (d) the identified floor masses, obtained as the diagonal elements of $\mathbf{M}$, and story stiffness, obtained from the super/sub-diagonal elements of $\mathbf{K}$ (with k_1 estimated as $K_{1,1} + K_{1,2}$). Note: for the case $\mathcal{S} = \{2, 3\}$, the Newton-Raphson solution failed owing to the Jacobian becoming singular at an intermediate step; as mentioned at the end of Section 4.5.2.1, this indicates that there may be multiple solutions to $\mathbf{V}^*$ for this set-up.

The following observations can be made from these results: (1) The different mean parameter estimates are, in most cases, reasonably consistent across the different observation set-ups. (2) The uncertainty in the different parameter estimates, represented by the COV or σ values, are also not unreasonably high, excepting in case of the damping ratios. The high COVs in the damping ratios may be due to input variability [46], and possible variability in the structural connections during and between experiments (see also Chapter 3); however, since these ratios are not used in the further steps of identification, this high uncertainty does not propagate to the other parameters. (3) The estimates obtained here agree well with the estimates obtained from the same same data, but using a different approach with the input known, in Chapter 3. This agreement with results from a different approach, and the reasonable consistency across different tests and different set-ups, indicate a robust

Table 4.6: Statistics of mass (in kg) and stiffness (in 10^5 N/m) matrix estimates.

$\mathcal{S}$	$\mu_{\mathbf{M}}$ (kg)	$\sigma_{\mathbf{M}}$ (kg)	$\mu_{\mathbf{K}}$ (10^5 N/m)	$\sigma_{\mathbf{K}}$ (10^5 N/m)
$\{1,3\}$	25.62 0.02 -0.03 0.01 0.02 38.78 0.04 -0.11 -0.03 0.04 32.36 -0.02 0.01 -0.11 -0.02 51.24	0.42 0.00 0.00 0.00 0.00 1.32 0.00 0.01 0.00 0.00 0.61 0.00 0.00 0.01 0.00 0.70	3.99 -2.32 0.86 -0.52 -2.32 3.88 -2.33 0.55 0.86 -2.33 4.26 -2.48 -0.52 0.55 -2.48 2.27	0.06 0.04 0.03 0.02 0.04 0.06 0.03 0.02 0.03 0.03 0.05 0.03 0.02 0.02 0.03 0.04
$\{1,4\}$	21.53 0.02 -0.04 0.03 0.02 50.90 0.08 -0.05 -0.04 0.08 42.35 0.00 0.03 -0.05 0.00 33.23	0.69 0.00 0.00 0.00 0.00 0.67 0.01 0.00 0.00 0.01 2.12 0.00 0.00 0.00 0.00 1.76	3.87 -2.09 1.10 -0.71 -2.09 3.58 -2.42 0.64 1.10 -2.42 4.53 -2.71 -0.71 0.64 -2.71 2.47	0.05 0.02 0.04 0.03 0.02 0.09 0.08 0.02 0.04 0.08 0.06 0.04 0.03 0.02 0.04 0.04
$\{2,3\}$	————-	————-	————-	————-
$\{1,2,3\}$	30.93 -0.40 0.26 -0.08 -0.40 35.39 1.25 -0.08 0.26 1.25 39.27 -0.02 -0.08 -0.08 -0.02 42.51	0.41 0.10 0.06 0.04 0.10 0.67 0.22 0.03 0.06 0.22 0.46 0.01 0.04 0.03 0.01 1.09	4.34 -2.72 0.62 -0.07 -2.72 4.62 -2.68 0.37 0.62 -2.68 4.41 -2.23 -0.07 0.37 -2.23 1.99	0.10 0.05 0.02 0.02 0.05 0.08 0.06 0.03 0.02 0.06 0.05 0.03 0.02 0.03 0.03 0.03
$\{1,2,4\}$	31.11 0.87 0.35 0.05 0.87 39.08 0.64 1.55 0.35 0.64 48.92 0.52 0.05 1.55 0.52 29.11	0.77 0.11 0.05 0.06 0.11 0.79 0.02 0.14 0.05 0.02 0.90 0.02 0.06 0.14 0.02 0.57	4.25 -2.58 0.56 -0.08 -2.58 5.21 -3.46 0.73 0.56 -3.46 4.95 -2.16 -0.08 0.73 -2.16 1.63	0.15 0.06 0.02 0.02 0.06 0.09 0.08 0.02 0.02 0.08 0.06 0.02 0.02 0.02 0.02 0.02
$\{1,3,4\}$	36.21 0.29 0.98 0.86 0.29 37.45 0.40 0.37 0.98 0.40 43.46 1.81 0.86 0.37 1.81 31.17	1.25 0.02 0.12 0.09 0.02 1.30 0.02 0.02 0.12 0.02 0.75 0.07 0.09 0.02 0.07 0.71	5.03 -2.92 0.65 0.00 -2.92 4.97 -3.15 0.37 0.65 -3.15 4.61 -1.84 0.00 0.37 -1.84 1.49	0.12 0.05 0.08 0.06 0.05 0.07 0.03 0.06 0.08 0.03 0.04 0.05 0.06 0.06 0.05 0.03
$\{2,3,4\}$	28.34 -0.01 -0.02 -0.05 -0.01 41.31 1.47 1.47 -0.02 1.47 47.00 0.84 -0.05 1.47 0.84 31.61	0.51 0.02 0.08 0.07 0.02 0.54 0.08 0.11 0.08 0.08 0.51 0.02 0.07 0.11 0.02 0.49	3.90 -2.57 0.49 -0.11 -2.57 5.42 -3.46 0.64 0.49 -3.46 5.00 -2.10 -0.11 0.64 -2.10 1.60	0.03 0.05 0.04 0.02 0.05 0.06 0.03 0.02 0.04 0.03 0.04 0.03 0.02 0.02 0.03 0.04
$\{1,2,3,4\}$	35.12 0.36 0.71 1.01 0.36 40.78 0.73 1.21 0.71 0.73 42.19 1.97 1.01 1.21 1.97 30.34	0.66 0.22 0.35 0.18 0.22 0.50 0.23 0.15 0.35 0.23 0.23 0.28 0.18 0.15 0.28 0.39	4.88 -2.99 0.60 -0.02 -2.99 5.37 -3.20 0.44 0.60 -3.20 4.46 -1.82 -0.02 0.44 -1.82 1.45	0.15 0.06 0.03 0.02 0.06 0.05 0.05 0.03 0.03 0.05 0.05 0.03 0.02 0.03 0.03 0.02

Table 4.7: Statistics of floor mass (in kg) and story stiffness (in 10^5 N/m) estimates.

$\mathcal{S}$	μ_m (kg)	COV$_m$ (%)	μ_k (10^5 N/m)	COV$_k$ (%)
$\{1,3\}$	$25.6, 38.8, 32.4, 51.2$	$1.6, 3.4, 1.9, 1.4$	$1.7, 2.3, 2.3, 2.5$	$1.8, 1.7, 1.5, 1.4$
$\{1,4\}$	$21.5, 50.9, 42.3, 33.2$	$3.2, 1.3, 5.0, 5.3$	$1.8, 2.1, 2.4, 2.7$	$2.3, 1.1, 3.3, 1.4$
$\{2,3\}$	———-	———-	———-	———-
$\{1,2,3\}$	$30.9, 35.4, 39.3, 42.5$	$1.3, 1.9, 1.2, 2.6$	$1.6, 2.7, 2.7, 2.2$	$4.6, 2.0, 2.2, 1.3$
$\{1,2,4\}$	$31.1, 39.1, 48.9, 29.1$	$2.5, 2.0, 1.8, 2.0$	$1.7, 2.6, 3.5, 2.2$	$6.2, 2.3, 2.2, 0.9$
$\{1,3,4\}$	$36.2, 37.5, 43.5, 31.2$	$3.4, 3.5, 1.7, 2.3$	$2.1, 2.9, 3.1, 1.8$	$4.0, 1.7, 1.1, 2.8$
$\{2,3,4\}$	$28.3, 41.3, 47.0, 31.6$	$1.8, 1.3, 1.1, 1.6$	$1.3, 2.6, 3.5, 2.1$	$3.4, 2.0, 0.9, 1.3$
$\{1,2,3,4\}$	$35.1, 40.8, 42.2, 30.3$	$1.9, 1.2, 0.5, 1.3$	$1.9, 3.0, 3.2, 1.8$	$5.9, 2.1, 1.4, 1.5$

estimation of the different parameters. This is further validated in Fig. 4.4, which compares the measured frequency response function magnitudes with those of the estimated systems in two of the set-ups, under a Northridge earthquake run. The reasonable matching between the frequency response functions, at both observed and unobserved DOFs, validates the identified models, and highlights the ability of the proposed method to identify reliable complete structural models even with incomplete measured information. Note: Fig. 4.4 is included only as a validation of the proposed approach; since it requires the input, such a validation will not be possible in real-life output-only situations; it is possible here as we have actually measured the inputs (table accelerations), although we did not use them in the identification. (4) From the estimated $\mathbf{M}$ and $\mathbf{K}$ matrices, it is evident that the structure is not perfectly shear-type, as also noted in Chapter 3 and [46]; this shows that the proposed method may also work when the model class assumption is not strictly valid, i.e with near-shear type structures. In such cases, as done here, the experimental data should be weighted more than structural topology requirements. (5) From the identified $\mathbf{M}$ matrices, the structure looks more non-shear type when more floors are observed; this is owing to the fact that more experimental data is used with more observed floors, and highlights the trade-off between assumed and measured information. (6) This trade-off between measured and assumed information also creates some variations between the identified $\mathbf{M}$-$\mathbf{K}$ matrices, and floor masses/story stiffnesses, across the different observation set-ups, owing to different amounts of measured data being used in the different set-ups. (7) From Tables 4.5 to 4.7, it is evident that some of the estimated parameters in set-ups $\mathcal{S} = \{1,2\}$ and $\{1,4\}$ are significantly different when compared with the other set-ups. This is owing to the fact that these

set-ups do not result in global identifiability of the system, and the identified solutions in Tables 4.5 to 4.7 for these set-ups are not the true solutions. This issue is further discussed next.

The post-identification local and global identifiability tests, discussed respectively in Section 4.5.1.4 and 4.5.2.1, are performed with the converged solutions to $\mathbf{V}^*$, for each of the 18 experiments (6 inputs $\times$ 3 runs). Table 4.8 presents the results of these tests for the different set-ups. These results are presented in a fractional form, where the fraction $x/18$ means that the test declares the set-up to be identifiable in x of the 18 experiments. The parameter space $\mathcal{W}$ necessary in the global identifiability test is defined as the space around the converged solution $\boldsymbol{\theta}^*$, such that any element θ_i of any $\boldsymbol{\theta} \in \mathcal{W}$ is within the range $[0.80, 1.20]\theta_i$, i.e. $\mathcal{W}$ covers a space of $\pm 20\%$ around the solution $\boldsymbol{\theta}^*$. Note that such a variation in $\boldsymbol{\theta}$, which contains the elements of $\mathbf{V}^*$, corresponds to an approximate variation of $\pm 40\%$ in the proportional mass and stiffness parameters, and hence such a variation in $\mathcal{W}$ may be considered to be exhaustive enough. $N_{\mathcal{W}} = 20,000$ $\boldsymbol{\theta}$ vectors are sampled from $\mathcal{W}$ using LHS, and the global identifiability test in performed with these $20,000$ $\boldsymbol{\theta}$'s. From Table 4.8 it is seen that the converged solutions, in all the set-ups and experiments, are at least locally identifiable, agreeing with the pre-identification results of Table 4.3. The global identifiability test however fails for all the 18 experiments for set-ups $\mathcal{S} = \{1, 3\}$, $\{1, 4\}$, $\{1, 2, 3\}$, and $\{2, 3, 4\}$. This corroborates the last observation, concerning set-ups $\mathcal{S} = \{1, 2\}$ and $\{1, 4\}$, made in the preceding paragraph. While the failure of the global identifiability tests do not necessarily mean that these set-ups result in globally unidentifiability, they indicate that the system may be unidentifiable with these set-ups. Hence, as per Section 4.5.2.1, for these cases, as well as for $\mathcal{S} = \{2, 3\}$ where the Jacobian becomes singular at an intermediate step, we will need to repeat the identification starting with multiple initial guesses for the Newton-Raphson solution, in order to confirm solution uniquness/non-uniqueness.

We next repeat the identification multiple times corresponding to multiple initial guesses for the Newton-Raphson solution. These multiple initial guesses are generated as follows: (a) A space $\mathcal{M}$ is defined around the analytical model of [46], such that any parameter (floor mass or story stiffness) p_i of any model in $\mathcal{M}$ lies in the range $[0.5, 2.0]p_0$, where p_0 is the corresponding parameter of the analytical model of [46]; (b) 50 models are generated from $\mathcal{M}$ using LHS, and the corresponding 50 sets of mode shapes are used as the initial guesses. Fig. 4.5 shows the corresponding 50 sets of floor masses and story stiffnesses, obtained from the identified $\mathbf{M}$ and $\mathbf{K}$ matrices as before, in four of the observation set-ups. The following comments can be made from Fig. 4.5: (1) For set-up $\mathcal{S} = \{1, 3\}$,

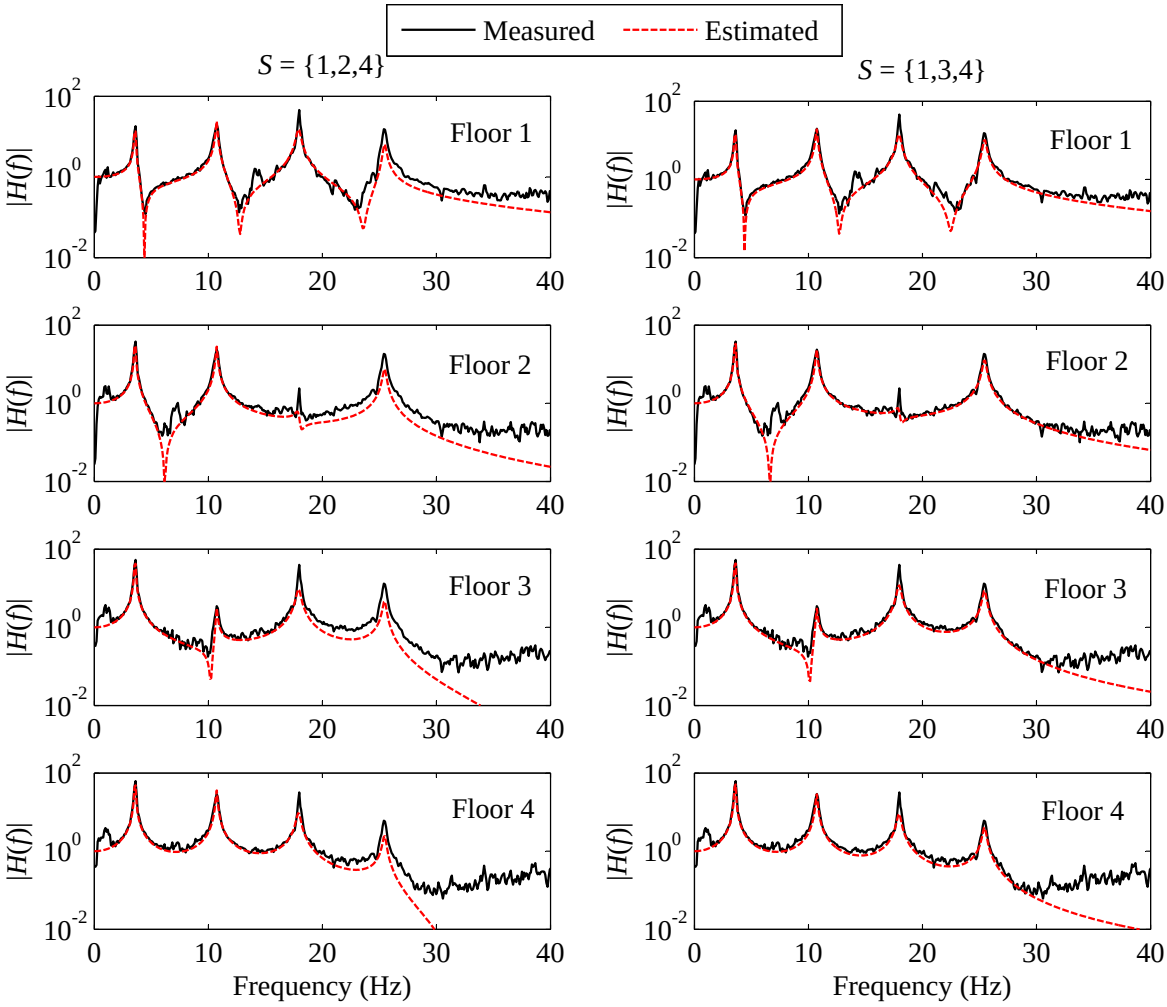

Figure 4.4: Comparison of measured frequency response function magnitudes at different floors, with those corresponding to the estimated systems in set-ups $\mathcal{S} = \{1, 2, 4\}$ and $\{1, 3, 4\}$, under a Northridge earthquake.

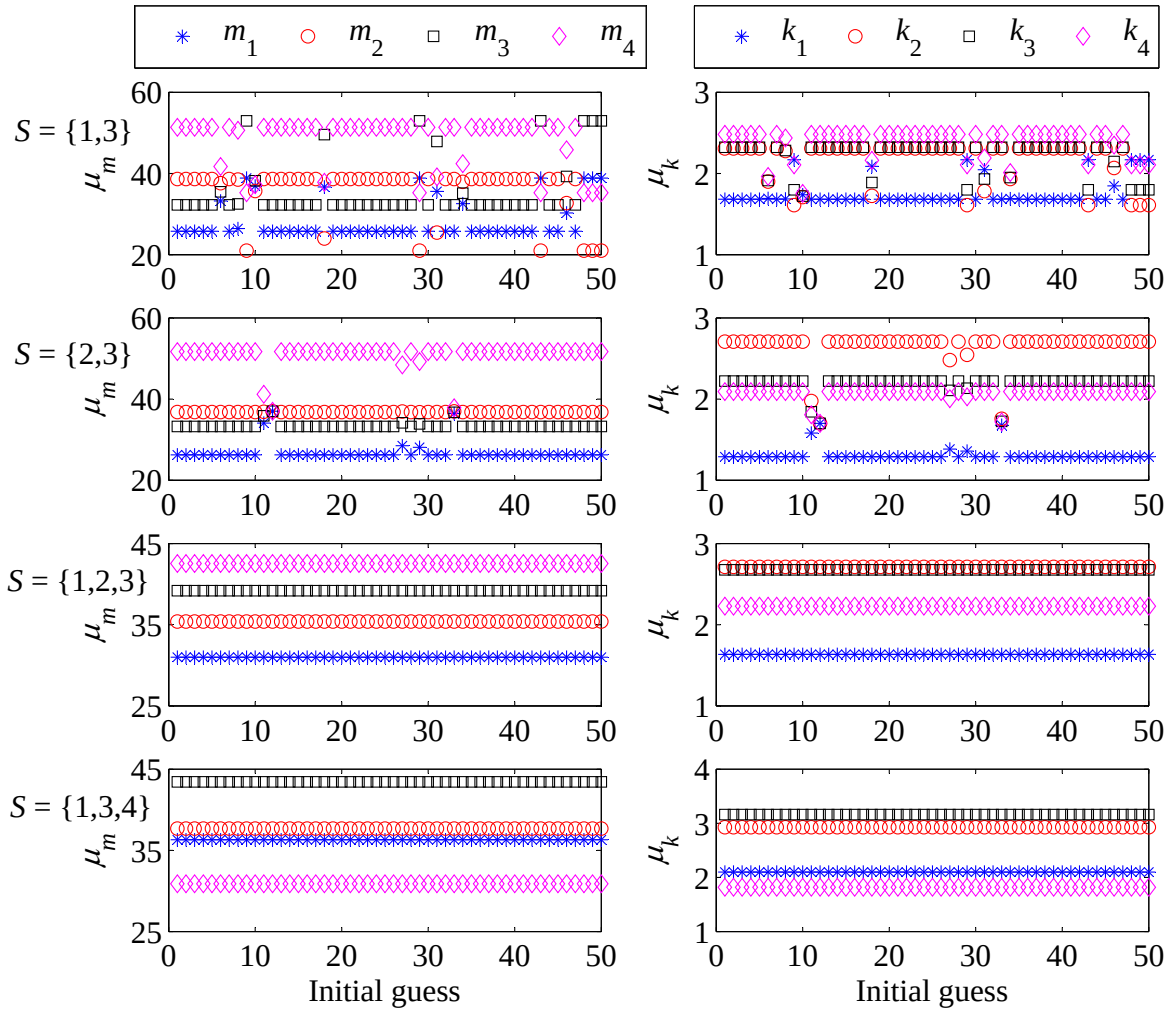

Figure 4.5: Mean (over 18 tests) floor mass and story stiffness estimates corresponding to 50 different initial guesses for the Newton-Raphson solutions.

Table 4.8: Local and global identifiability check at solution.

$\mathcal{S}$	Local identifiability (Section 4.5.1.4)	Global identifiability (Section 4.5.2.1)
$\{1,3\}$	✓ $(18/18)$	X $(0/18)$
$\{1,4\}$	✓ $(18/18)$	X $(0/18)$
$\{2,3\}$	————	————
$\{1,2,3\}$	✓ $(18/18)$	X $(0/18)$
$\{1,2,4\}$	✓ $(18/18)$	✓ $(18/18)$
$\{1,3,4\}$	✓ $(18/18)$	✓ $(18/18)$
$\{2,3,4\}$	✓ $(18/18)$	X $(0/18)$
$\{1,2,3,4\}$	✓ $(18/18)$	✓ $(18/18)$

there are indeed multiple locally distinct solutions to the inverse problem, the possibility of which was indicated in Table 4.8. The same was also observed for $\mathcal{S} = \{1,4\}$. (2) The Newton-Raphson solutions now do converge for $\mathcal{S} = \{2,3\}$; again, there are multiple solutions for $\mathcal{S} = \{2,3\}$, which possibility was indicated by the Jacobian becoming singular at an intermediate step before. (3) All the 50 solutions are identical in set-ups $\mathcal{S} = \{1,2,3\}$ and $\{1,3,4\}$, and the same was also observed for $\mathcal{S} = \{1,2,4\}$, $\{2,3,4\}$ and $\{1,2,3,4\}$, although for $\mathcal{S} = \{1,2,3\}$ and $\{2,3,4\}$ the global identifiability test indicated the possibility of multiple solutions. This exemplifies that the real Jacobian conjecture provides a *sufficient, but not necessary, condition* for global identifiability (see Section 4.5.2). (5) For set-ups which result in a globally unidentifiable parameter set, when finding multiple solutions, corresponding to multiple initial guesses, the most occurring solution is not necessarily the "true" solution. For example, in Fig. 4.5, the most occurring solutions for $\mathcal{S} = \{1,3\}$ and $\{2,3\}$ have some parameters significantly different from those identified in the cases with 3 or more observed floors; thus, although these models apparently have the largest basins of attraction, they are not the "true" models. In such cases, the identification approach should involve methods with superior global search capabilities, e.g. heuristic optimization schemes [69], so as to effectively and efficiently scan the entire parameter space, finding as many distinct solutions as possible. Distinguishing the "true" model will then require engineering insight, some weighted combination in case of closely spaced models, or even additional data using more/rearranged sensors.

We end this section by presenting an application of Section 4.2.2.3. An additional set of 18 tests (6 inputs $\times$ 3 runs) were performed with an added ≈ 7.5 kg mass on the 2nd floor of the structure.

The proportional mode shape matrices of this modified structure were obtained in the same way as for the original structure discussed before. The method of Section 4.2.2.3 was then applied to scale the $\mathbf{V}^*$ matrices of the original structure to the mass normalized $\mathbf{V}$ matrices. The identification was only carried out for the globally identifiable observation set-ups; Table 4.9 presents the statistics, computed over the 18 tests, of the thus identified $\mathbf{M}$ and $\mathbf{K}$ matrices of the original structure. The mean matrices in Table 4.9 agree reasonably well with the corresponding matrices in Table 4.6 in all the set-ups except $\mathcal{S} = \{1, 2, 3\}$. As expected, the dominant entries (diagonal of $\mathbf{M}$, diagonal and super/sub-diagonal of $\mathbf{K}$), as well as most other entries, in the mean matrices, differ between Tables 4.6 and 4.9 in terms of a multiplicative factor, which is relatively constant across the different entries, in any given set-up. This is also true for set-up $\mathcal{S} = \{1, 2, 3\}$; while the factor is ≈ 1 for the other set-ups, it is ≈ 1.3 for $\mathcal{S} = \{1, 2, 3\}$. The factors are not strictly constant across all the entries of a matrix, since the matrices are the mean of the identified matrices, and not the actual identified ones. Note however that the standard deviations in Table 4.9 are much higher than those in Table 4.6 for all the set-ups, and especially for $\mathcal{S} = \{1, 2, 3\}$. As mentioned in Section 4.2.2.3, an added mass at a single location may not induce a sufficiently discernible difference in the identified proportional modes, especially given the presence of other effects, e.g. ambient effects/measurement noise etc., in the measured data. This is possibly the reason behind the high standard deviations in all set-ups, and the over-estimation of the $\mathbf{M}$ and $\mathbf{K}$ matrices for $\mathcal{S} = \{1, 2, 3\}$.

4.8 Conclusions

An algorithm is developed for the identification of all the lumped masses and spring stiffnesses of shear-type structures using ambient vibration response data. The proposed algorithm starts with the complete spectra of eigenvalues and non-normalized mode shape components, identified only at the DOFs with sensors using any suitable system identification technique. A mode shape expansion-cum-normalization approach, based on satisfying the structural topology requirements and the measured modal information, is next used to estimate a complete mode shape matrix, proportional to the mass normalized mode shape matrix by a single scalar. The proportionality constant is then estimated using any one additional information, e.g. a set of known floor masses, or known total mass of the system, or a second set of measured data with some known added masses, etc. The situations of

Table 4.9: Statistics of mass (in kg) and stiffness (in 10^5 N/m) matrix estimates of original system, obtained using second experiment with known added mass (Section 4.2.2.3).

$\mathcal{S}$	$\mu_{\mathbf{M}}$ (kg)	$\sigma_{\mathbf{M}}$ (kg)	$\mu_{\mathbf{K}}$ (10^5 N/m)	$\sigma_{\mathbf{K}}$ (10^5 N/m)
$\{1,2,3\}$	39.78 -0.52 0.34 -0.11	10.27 0.19 0.08 0.06	5.56 -3.48 0.80 -0.09	1.39 0.91 0.22 0.04
	-0.52 45.56 1.61 -0.10	0.19 12.33 0.48 0.05	-3.48 5.93 -3.45 0.49	0.91 1.60 0.95 0.15
	0.34 1.61 50.37 -0.03	0.08 0.48 13.39 0.01	0.80 -3.45 5.66 -2.86	0.22 0.95 1.49 0.74
	-0.11 -0.10 -0.03 54.34	0.06 0.05 0.01 13.11	-0.09 0.49 -2.86 2.55	0.04 0.15 0.74 0.64
$\{1,2,4\}$	32.32 0.96 0.37 0.07	5.64 0.15 0.05 0.07	4.40 -2.67 0.58 -0.09	0.72 0.47 0.11 0.02
	0.96 40.46 0.68 1.70	0.15 7.99 0.13 0.29	-2.67 5.36 -3.56 0.74	0.47 1.05 0.71 0.14
	0.37 0.68 49.77 0.54	0.05 0.13 8.93 0.12	0.58 -3.56 5.06 -2.20	0.11 0.71 0.96 0.40
	0.07 1.70 0.54 29.82	0.07 0.29 0.12 5.65	-0.09 0.74 -2.20 1.66	0.02 0.14 0.40 0.29
$\{1,3,4\}$	35.19 0.29 0.94 0.81	4.52 0.04 0.19 0.15	4.86 -2.83 0.62 0.02	0.58 0.32 0.07 0.04
	0.29 36.35 0.38 0.36	0.04 3.59 0.06 0.04	-2.83 4.83 -3.06 0.34	0.32 0.54 0.33 0.04
	0.94 0.38 42.04 1.73	0.19 0.06 5.08 0.22	0.62 -3.06 4.46 -1.76	0.07 0.33 0.48 0.18
	0.81 0.36 1.73 29.83	0.15 0.04 0.22 3.02	0.02 0.34 -1.76 1.43	0.04 0.04 0.18 0.15
$\{2,3,4\}$	25.92 -0.02 -0.08 -0.09	2.96 0.02 0.09 0.08	3.58 -2.33 0.47 -0.08	0.37 0.27 0.07 0.02
	-0.02 37.42 1.35 1.35	0.02 4.26 0.20 0.22	-2.33 4.87 -3.12 0.57	0.27 0.56 0.34 0.06
	-0.08 1.35 42.36 0.76	0.09 0.20 4.29 0.09	0.47 -3.12 4.50 -1.88	0.07 0.34 0.46 0.19
	-0.09 1.35 0.76 28.23	0.08 0.22 0.09 2.88	-0.08 0.57 -1.88 1.43	0.02 0.06 0.19 0.14
$\{1,2,3,4\}$	33.94 0.44 0.69 0.95	4.91 0.24 0.38 0.25	4.69 -2.87 0.58 -0.02	0.63 0.43 0.11 0.02
	0.44 39.43 0.69 1.26	0.24 6.44 0.29 0.23	-2.87 5.17 -3.10 0.43	0.43 0.81 0.51 0.08
	0.69 0.69 40.67 1.84	0.38 0.29 6.24 0.21	0.58 -3.10 4.31 -1.75	0.11 0.51 0.69 0.29
	0.95 1.26 1.84 29.11	0.25 0.23 0.21 4.57	-0.02 0.43 -1.75 1.40	0.02 0.08 0.29 0.22

known applied input forces or base excitation is also discussed. Once the complete mass normalized mode shape matrix is estimated, the modal orthogonality relations are used to estimate the complete mass and stiffness matrices of the system. Application of the method in several numerical examples, as well as with experimental data from shake table testing of a 4 story steel frame, show the potential of the method in identifying structural parameters with reasonable accuracy, under the constraints of very limited number of sensors, unmeasured input, minimal *a priori* information, and noisy data.

Using an example of a 3-DOF system with 2 sensors, the effect of sensor locations in the identifiability of the system is highlighted. It is shown that there may be multiple structures, which are close enough for one to be a damaged version of the other, with the same frequencies and non-normalized mode shapes at certain DOFs. Observing these DOFs and monitoring the system using extracted modal parameters or their functions may lead to false indications of the structural health. Moreover, if the loading pattern also changes, then there can be instances when the structural response of these systems become identical at the observed DOFs; in such situations no model-based or data-based health monitoring techniques would be able to distinguish the damaged system. With the same example, it is also shown that the requirement of at least one collocated actuator-sensor pair in input–output identification may be violated in specific cases, while still giving an unique identification without using any assumed *a priori* information.

Two approaches to investigate the issue of sensor locations vis-$\grave{a}$-vis identifiability of the system are explored. First, a method is developed which aims to determine the amount of independent information contained by the measurements from a given sensor set-up. This method considers the algebra of the eigenvalue problem, and is based on a set of statements relating the modal information between different DOFs. Alternatively, tests for (a) local identifiability, using the implicit function theorem, and (b) global identifiability, using the real Jacobian conjecture, are developed. The real Jacobian conjecture can be treated as a theorem in our problem, since the involved polynomials are of at most degree 2. The method based on measured independent information is general, in the sense that its application does not require the knowledge of any nominal model and definition of any parameter space; the tests for identifiability however require the definition of a parameter space, within which the identifiability of the parameters are tested. On the other hand, while the former only assesses the amount of available independent information, which is related to identifiability, the latter tests directly address the issue of identifiability. The local identifiability test may be applied

both prior to the actual data collection, for deciding the sensor location on the structure, as well as post-experiment, testing local identifiability around an identified solution. The global identifiability test is however recommended only for post-experiment applications, identifying situations where there is a possibility of multiple solutions in a region around the identified solution. It is emphasized that both the tests provide sufficient, but not necessary, conditions for identifiability; hence, failing the tests do not imply that the system is locally/globally unidentifiable. The method of measured independent information may be seen more as a necessary condition, since it attempts to balance the number of unknowns with the available independent information. These approaches were applied to both numerical examples and the shake table experimental data. The results of the method of independent information were found to always agree with the implicit function theorem based local identifiability test. The global identifiability test was able to identify situations with multiple locally isolated solutions using the experimental data.

The statements relating the modal information between different DOFs may also be applied to estimate the complete non-normalized mode shape spectra, at some/all observed DOFs, in situations where not all modes are directly identified from the measurements at every observed DOF. Such a situation may be envisaged as when different types of sensors are located at different DOFs; since different sensors work well at different bandwidths, some, e.g accelerometers, may measure the high frequency modes better, while others, e.g. displacement sensors, may measure the low frequency modes better. The application of the proposed statements in the fusion of modal information, extracted from such heterogenous measurements, was shown with some numerical examples. However, this issue will need to be investigated more formally, especially in relation to the identifiability question. Broadening the applicability of the ideas discussed in this chapter by possible extensions to other model classes will be another potential direction of future research.

Chapter 5

Structural Health Monitoring Applications

This chapter focuses on the application of the structural identification methods of Chapters 2 and 3 for structural health monitoring. In Section 5.1, the method of Chapter 3 is applied to shake table experimental data collected from different "damaged" versions of the 4-story steel frame used in Chapters 3 and 4, considering different situations of possible structural instrumentation and available *a priori* information of the structural mass. The effects of damage on the identified modal and physical parameters are discussed. A fundamental axiom for structural health monitoring states: "Damage assessment requires a comparison between two system states" [56]. We successively consider the viability of the mean identified modal parameters and the mean identified physical parameters, as comparative measures for damage assessment purposes. Attempts are made to detect the existence and location of damage using the modal parameter comparative measures of Appendix D. The mean of the identified story stiffnesses are used to detect the existence, location and severity of damage. A method is also discussed to characterize the damage location and severity in a probabilistic sense, based on the identified story stiffnesses from each individual test, rather than their mean estimates from several tests. Finally, in Section 5.2, damage assessment is performed, with the mean identified physical parameters and the probabilistic approach, using experimental data from different damaged versions of the 3 storied Los Alamos National Laboratory frame, whose healthy version was used in Chapter 2; the method of Chapter 2 is used for the necessary structural identification.

5.1 4-Story Steel Frame Shake Table Experimental Study

Shaking table experimental data from a 4-story laboratory scale steel frame were used in Chapters 3 and 4 as applications of the identification approaches discussed in those chapters. Recall that the experimental campaign included six different input ground motions, each applied thrice, thus constituting a total of 18 dynamic tests of the frame. To assess the applicability of the identification approach of Chapter 3 for structural damage detection purposes, in addition to the above frame, here onwards referred to as the "healthy" system (DS0), three different "damaged" frames (DS1 to DS4) are also tested using the same set of 6 inputs, each applied thrice. In these damaged frames, structural damage is simulated as stiffness reduction, by replacing one or more columns of the "healthy" frame with columns of reduced cross-sectional area (50.8×7 sq. mm). The same six scenarios of instrumentation and available *a priori* information, as considered in Chapter 3, are also used here for analyses using the damaged frames. Fig. 5.1 lists these experimental scenarios, along with the inputs and damage states' descriptions. The same identification methodology used in Chapter 3 on the "healthy" frame, is used here with each of the damaged states of the frame. Details of the identification method, and further details of the experiment is given in Chapter 3 (Section 3.6). In the remaining parts of this section, we present the identification results of the damaged frames; for convenience in comparison, we also include the identification results of the healthy frame. The effect of damage on the different identified modal/physical parameters are studied, and the possible use of different parameters for different levels of structural damage assessment, viz. damage existence, location, and severity assessment, are explored.

5.1.1 Identified frequencies and damping ratios of damaged frames

Table 5.1 compares the statistics of the modal frequencies of the different frames identified using ERA-OKID from the 18 tests. These statistics agree with the observations in Section 3.6, viz. consistent identification across all instrumentation set-ups, and reasonably small estimation uncertainty. As expected, the identified frequencies, in general, show a decreasing trend with damage. For DS3 however, the identified frequencies for the second mode, f_2, are comparable to/slightly more than those identified for the healthy system DS0. A possible reason for this may be that for this frame, the damage induced in DS3 does not affect the second mode to any noticeable extent. This is seen in Fig.

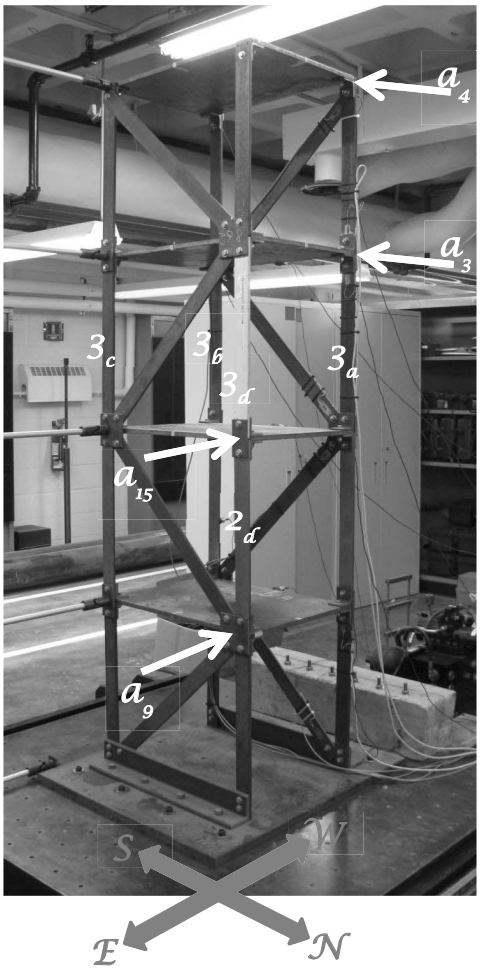

Inputs:

Band limited white noise, EC8, El Centro, Hachinohe, Kobe, Northridge

Damage states:

State	Description
DS0	Healthy system
DS1	Columns 3_c and 3_d damaged
DS2	Columns 3_a, 3_b, 3_c and 3_d damaged
DS3	Columns 2_d and 3_d damaged

Experimental scenarios:

Scenario	Instrumented DOFs (floors)	*A priori* Information
C_I	1, 2, 3, 4	m_1, m_2, m_3, m_4
C_{II}	1, 3, 4	m_1, m_2, m_3, m_4
C_{III}	1, 4	m_1, m_2, m_3, m_4
C_{IV}	1, 3, 4	m_1, m_3, m_4
C_V	1, 2, 3, 4	M_T
C_{VI}	1, 3, 4	M_T

Figure 5.1: Experimental 4-story frame model on the shake table, and lists of inputs, damage states and instrumentation - available *a priori* information scenarios.

Table 5.1: Statistics of modal frequency estimates (in Hz) using OKID/ERA.

State	Scenario	μ_f (Hz)	COV$_f$ (%)
DS0	$\mathcal{C}_I, \mathcal{C}_V$	$3.59, 10.76, 17.96, 25.45$	$0.68, 1.38, 0.40, 0.29$
	$\mathcal{C}_{II}, \mathcal{C}_{IV}, \mathcal{C}_{VI}$	$3.59, 10.77, 17.96, 25.44$	$0.70, 1.39, 0.40, 0.26$
	$\mathcal{C}_{III}$	$3.59, 10.76, 17.96, 25.45$	$0.79, 1.36, 0.40, 0.31$
DS1	$\mathcal{C}_I, \mathcal{C}_V$	$3.55, 10.47, 17.58, 23.90$	$0.24, 0.23, 0.06, 0.09$
	$\mathcal{C}_{II}, \mathcal{C}_{IV}, \mathcal{C}_{VI}$	$3.55, 10.48, 17.58, 23.90$	$0.19, 0.23, 0.06, 0.09$
	$\mathcal{C}_{III}$	$3.55, 10.47, 17.58, 23.90$	$0.22, 0.24, 0.06, 0.10$
DS2	$\mathcal{C}_I, \mathcal{C}_V$	$3.41, 10.02, 16.97, 22.70$	$0.23, 0.44, 0.21, 0.12$
	$\mathcal{C}_{II}, \mathcal{C}_{IV}, \mathcal{C}_{VI}$	$3.41, 10.02, 16.97, 22.70$	$0.40, 0.43, 0.21, 0.12$
	$\mathcal{C}_{III}$	$3.41, 10.02, 16.98, 22.70$	$0.34, 0.43, 0.18, 0.12$
DS3	$\mathcal{C}_I, \mathcal{C}_V$	$3.50, 10.98, 17.66, 23.98$	$1.10, 0.51, 0.09, 0.22$
	$\mathcal{C}_{II}, \mathcal{C}_{IV}, \mathcal{C}_{VI}$	$3.51, 10.98, 17.66, 23.98$	$1.17, 0.52, 0.09, 0.22$
	$\mathcal{C}_{III}$	$3.54, 10.98, 17.66, 23.96$	$0.51, 0.42, 0.09, 0.23$

5.2, which compares the theoretical frequencies obtained for DS1 to DS3, by introducing the theoretical level of damage (15% reduction in story stiffness for damage in each column) in the healthy frame's identified story stiffnesses, and using the healthy frame's identified floor masses (see Scenario $\mathcal{C}_I$ in Table 3.8 for the values of these identified masses and stiffnesses of the healthy frame). It can be seen from Fig. 5.2 that, the second modal frequency for DS3 is almost 98% of that for DS0, and so there is a strong possibility that the estimated second modal frequencies in these two cases appear comparable to each other, especially given the effects of other factors like measurement noise, actual level of damage etc. From Fig. 5.2 it is also evident that for modes 1, 3 and 4, the modal frequencies for DS1 and DS3 are almost indistinguishable from each other, which is also apparent in Table 5.1.

Table 5.2 lists the statistics of the modal damping ratios of the different frames identified using ERA-OKID from the 18 tests. Again, as observed in Section 3.6, the identified modal damping ratios show some dispersion across the different instrumentation set-ups show some dispersion, and also the estimate uncertainty is considerable. Possible reasons for this high uncertainty were noted in Chapter 3; since these ratios do not appear in the subsequent steps of identification, the high uncertainty does not affect the identified $\mathbf{V}$, $\mathbf{M}$ and $\mathbf{K}$ matrices. Although there is a slight decreasing trend of the identified damping ratios with damage for modes 2 to 4, and a slight increasing trend for mode 1, these trends are neither very dominant nor consistent. Note however that, for DS3, the fourth mode's

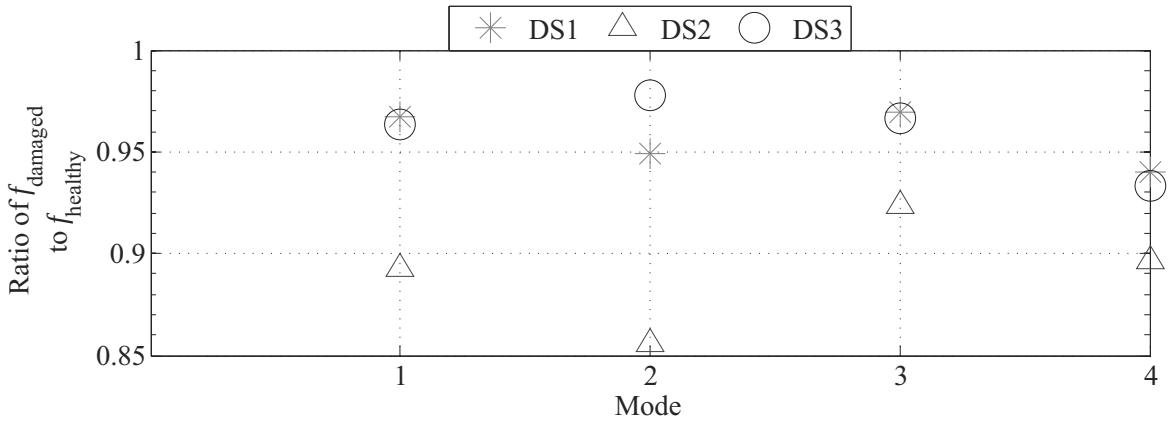

Figure 5.2: Ratio of theoretical modal frequencies of the different damaged states to corresponding identified frequencies of the healthy state.

damping ratio is distinctly higher than for the other states. This may be owing to the fact that, the first torsional mode of the frame (around 25% Hz as reported in [46]) interacts with the fourth bending mode in this case, and this leads to an increased energy dissipation at the connections. This is because, with torsion, tangential forces will develop at the interface connected by the bolts, and this will lead to an increase in energy dissipation at the connections [70, 71].

5.1.2 A note on damage induced frequency changes

To see if the damage induced reductions in the structural frequency estimates of Table 5.1 are consistent with the damage level, we consider the damage states DS1 and DS2. Since the damage in each column is introduced in the same way, the total damage in DS2 should be approximately twice that in DS1. Then, noting that the sum of the eigenvalues should equal the trace of the matrix $\mathbf{M}^{-1}\mathbf{K}$, and depicting the fractional reduction in stiffness due to damage in any one column by x, we can write:

$$\frac{\sum_{j=1}^{4}(f_j^{\text{DS0}})^2 - \sum_{j=1}^{4}(f_j^{\text{DS2}})^2}{\sum_{j=1}^{4}(f_j^{\text{DS0}})^2 - \sum_{j=1}^{4}(f_j^{\text{DS1}})^2} = \frac{\sum_{j=1}^{4}\lambda_j^{\text{DS0}} - \sum_{j=1}^{4}\lambda_j^{\text{DS2}}}{\sum_{j=1}^{4}\lambda_j^{\text{DS0}} - \sum_{j=1}^{4}\lambda_j^{\text{DS1}}} = \frac{4xk_3(\frac{1}{m_2}+\frac{1}{m_3})}{2xk_3(\frac{1}{m_2}+\frac{1}{m_3})} = 2 \tag{5.1}$$

Indeed, using the mean identified frequencies of Table 5.1, this ratio comes out to be 1.90 (for scenarios $\mathcal{C}_I$ and $\mathcal{C}_V$), 1.91 (for scenarios $\mathcal{C}_{II}$, $\mathcal{C}_{IV}$ and $\mathcal{C}_{VI}$) and 1.90 (for scenario $\mathcal{C}_{III}$).

Now, if we assume that all the frequencies get affected by damage in the same way, then for any mode j, the modal frequency (f_j) should be related with the total damage (x) as:

$$f_j^2 = -a_j x + b_j \tag{5.2}$$

Table 5.2: Statistics of modal damping ratio estimates (in %) using OKID/ERA.

State	Scenario	μ_ζ (%)	COV$_\zeta$ (%)
DS0	$\mathcal{C}_I, \mathcal{C}_V$	$0.57, 0.54, 0.36, 0.36$	$16.95, 29.63, 21.24, 13.26$
	$\mathcal{C}_{II}, \mathcal{C}_{IV}, \mathcal{C}_{VI}$	$0.63, 0.54, 0.36, 0.35$	$12.89, 30.36, 21.36, 12.66$
	$\mathcal{C}_{III}$	$0.56, 0.61, 0.40, 0.39$	$20.24, 16.89, 21.30, 10.97$
DS1	$\mathcal{C}_I, \mathcal{C}_V$	$0.67, 0.50, 0.29, 0.32$	$12.65, 16.61, 24.26, 5.63$
	$\mathcal{C}_{II}, \mathcal{C}_{IV}, \mathcal{C}_{VI}$	$0.65, 0.49, 0.29, 0.32$	$8.27, 11.96, 23.13, 6.21$
	$\mathcal{C}_{III}$	$0.63, 0.52, 0.29, 0.33$	$9.96, 18.07, 24.89, 5.73$
DS2	$\mathcal{C}_I, \mathcal{C}_V$	$0.70, 0.50, 0.23, 0.31$	$9.00, 23.44, 42.29, 11.38$
	$\mathcal{C}_{II}, \mathcal{C}_{IV}, \mathcal{C}_{VI}$	$0.69, 0.49, 0.23, 0.31$	$13.49, 21.89, 40.92, 11.60$
	$\mathcal{C}_{III}$	$0.73, 0.55, 0.26, 0.30$	$9.49, 24.16, 42.24, 10.68$
DS3	$\mathcal{C}_I, \mathcal{C}_V$	$0.92, 0.38, 0.28, 0.70$	$22.16, 25.28, 27.16, 8.96$
	$\mathcal{C}_{II}, \mathcal{C}_{IV}, \mathcal{C}_{VI}$	$0.66, 0.38, 0.27, 0.69$	$35.77, 24.33, 29.42, 8.86$
	$\mathcal{C}_{III}$	$0.77, 0.49, 0.28, 0.79$	$30.98, 52.89, 27.95, 10.64$

where a_j and b_j are positive constants, with $b_j = f_j^2|_{x=0}$. To see if indeed the squares of each modal frequency decrease linearly with damage severity, we consider the mean identified frequencies for scenarios $\mathcal{C}_I$ and $\mathcal{C}_V$ from Table 5.1, and the damage severities of $x = 0$, 0.30, and 0.60, respectively for the states DS0, DS1 and DS2. In Fig. 5.3 we plot the squares of these frequencies against the damage severity x, along with the best fit line (in a least squares sense) describing the f^2–x relationship. As evident from the R^2 values (coefficients of determination), these best-fit lines approximate the relationships reasonable well. Moreover, the squares of the frequencies of the healthy (DS0) system are 12.89, 115.78, 322.56 and 647.70, respectively for modes 1 to 4, and they compare reasonably well with the b_j values of 13.00, 116.29, 323.82 and 644.27, obtained as coefficients in corresponding best-fit line equations. Eq. (5.2) also gives for any mode j:

$$2f_j \frac{\mathrm{d}f_j}{\mathrm{d}x} = -a_j; \qquad \frac{\mathrm{d}f_j}{f_j} = \frac{a_j \mathrm{d}x}{2(a_j x - b_j)}; \qquad \frac{\mathrm{d}f_j^2}{\mathrm{d}x} = -a_j \Rightarrow \frac{\mathrm{d}\lambda_j}{\mathrm{d}x} = -4\pi^2 a_j \tag{5.3}$$

If a_j is indeed a constant independent of the damage severities, then the first relation would suggest that: as the damage (x) increases, f_j will decrease, and hence $|\mathrm{d}f_j/\mathrm{d}x|$ will increase, i.e. the (absolute value of) the rate of change of the modal frequencies with damage will increase with damage. This means that higher levels of damage can be more easily detected from the *absolute* frequency changes than lower levels of damage. Similarly, from the second equation above, we can say that as damage

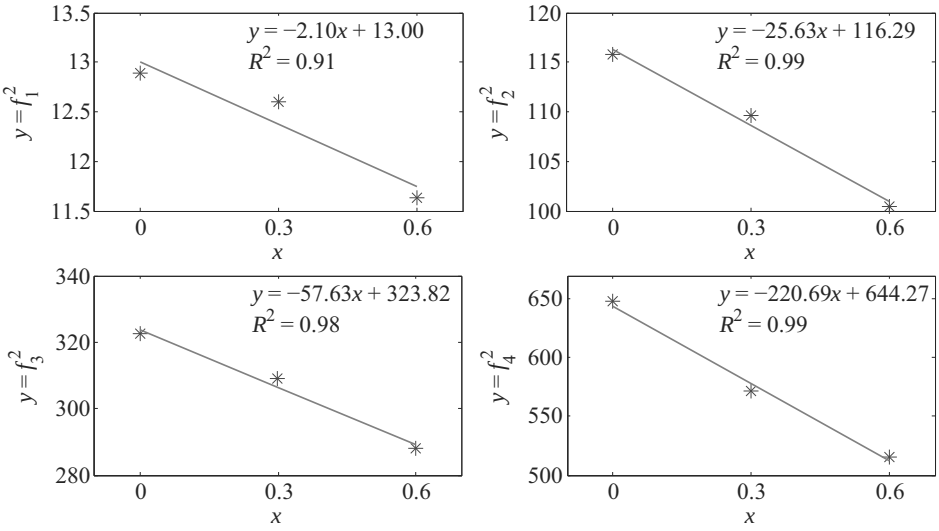

Figure 5.3: Relationship between square of structural frequencies and damage severity.

x increases, the absolute value of the denominator inn the right hand side expression will decrease, and hence the absolute value of $\mathrm{d}f_j/f_j$ will increase; this again implies that, any incremental damage can be more easily detected from the *relative* changes in frequency at higher levels of damage than at lower levels of damage. Finally, from the equations of the best-fit lines in Fig. 5.3, we can see that a_j is higher for higher modes. Based on the third relationship above, this indicates that the (absolute value of the) rate of change of the eigenvalues/square of frequencies with damage is higher for higher modes, i.e. damage may be more easily detected by the changes in the higher mode eigenvalues/square of frequencies than changes in the lower mode ones.

5.1.3 Identified mode shapes and damage detection

The complete mass normalized $\mathbf{V}$ matrix is obtained for each of the damage states and experimental scenarios following the approach detailed in Section 3.6. Fig. 5.4 compares the mean of the complete mass normalized mode shapes (scaled by a factor of 4 to aid in representation) for the different damage states, in two of the experimental scenarios. While there is no discernible difference between the first mode shapes of the different damage states of the system, for modes 2 to 4 there is an obvious damage-induced difference, evidencing that damage affects the higher modes more, as may be expected from localized damage [56]. However, for modes 3 and 4, there is a considerable mismatch between the damaged and the undamaged mode shapes at the first floor level, which is an undamaged location

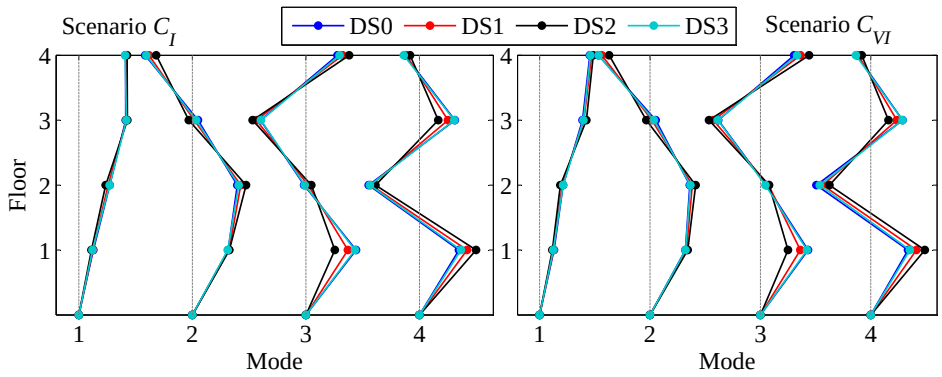

Figure 5.4: Comparison of mean mass normalized mode shapes (scaled by 4), estimated in scenarios $\mathcal{C}_I$ and $\mathcal{C}_{VI}$, for different damage states.

removed from the damage location (story 3 in case of DS1 to DS3, and story 2 as well for DS3). This indicates that just by observing the mismatch between the mode shapes, while it may be possible to identify the existence of damage, it may not be possible to accurately locate the damaged zone(s) and quantify the severity of damage.

Table 5.3 compares the corresponding mean mass normalized mode shapes of the different damaged states with those of the healthy state using MAC and FPMAC (Appendix D, Eq. D.48). Note that, the values of FPMAC over 1 indicate an increase in modal flexibility. Again it is evident that comparing the mode shapes, especially through FPMAC, it is possible to say whether or not the structure is damaged, even for low damage levels; e.g. while for DS2 and DS3 the MAC values comparing damaged to healthy states are near 1, the FPMAC values indicate a change in the state of the system.

Table 5.4 compares the corresponding mean mass normalized mode shapes of the different damaged states with those of the healthy state at the different DOFs using COMAC and FPCOMAC (Appendix D, Eq. D.52). Note that the deviation of FPCOMAC from 1, as defined in Appendix D, is expected to give an approximate value of the relative change in the corresponding diagonal element of the structure's flexibility matrix; i.e. $\text{eFPCOMAC}_k = 1 - \text{FPCOMAC}_k \approx \left(F_{k,k} - \widehat{F}_{k,k}\right)/F_{k,k}$, where $\mathbf{F}_{k,k}$ and $\widehat{\mathbf{F}}_{k,k}$ are respectively the flexibility matrices of the healthy and the possibly damaged states; a greater than 1 value of FPCOMAC_k would signal an increase in the kth diagonal element of the flexibility matrix. It can be seen from Table 5.4 that the COMAC values may also indicate the existence damage in the structure, especially for severe and localized damage (DS2). Nonetheless, the maximum deviation of the COMAC values occur at DOF 1 (the first floor), possibly reflecting the

Table 5.3: Comparison of damaged and healthy states using mean mass normalized mode shapes: MAC and FPMAC for different modes.

Index	Scenario	DS1 vs. DS0	DS2 vs. DS0	DS3 vs. DS0
MAC	$\mathcal{C}_I$	$1.00, 0.99, 0.98, 0.98$	$1.00, 0.95, 0.88, 0.89$	$1.00, 1.00, 1.00, 1.00$
	$\mathcal{C}_{II}$	$1.00, 0.99, 0.97, 0.97$	$1.00, 0.95, 0.88, 0.88$	$1.00, 1.00, 1.00, 1.00$
	$\mathcal{C}_{III}$	$1.00, 0.99, 0.98, 0.97$	$0.99, 0.96, 0.88, 0.88$	$1.00, 1.00, 1.00, 1.00$
	$\mathcal{C}_{IV}$	$1.00, 1.00, 0.97, 0.96$	$0.99, 0.97, 0.88, 0.86$	$1.00, 1.00, 1.00, 0.99$
	$\mathcal{C}_V$	$1.00, 0.99, 0.97, 0.98$	$0.99, 0.95, 0.87, 0.89$	$1.00, 1.00, 1.00, 1.00$
	$\mathcal{C}_{VI}$	$1.00, 0.99, 0.98, 0.97$	$1.00, 0.96, 0.88, 0.88$	$1.00, 1.00, 1.00, 1.00$
FPMAC	$\mathcal{C}_I$	$0.97, 1.01, 1.08, 0.96$	$0.91, 1.02, 1.19, 0.88$	$0.97, 1.00, 1.03, 1.04$
	$\mathcal{C}_{II}$	$0.97, 0.99, 1.09, 0.97$	$0.91, 1.00, 1.21, 0.86$	$0.97, 0.99, 1.03, 1.05$
	$\mathcal{C}_{III}$	$0.95, 0.99, 1.09, 0.89$	$0.88, 0.98, 1.21, 0.76$	$0.95, 0.99, 1.03, 1.02$
	$\mathcal{C}_{IV}$	$0.95, 1.01, 1.10, 0.98$	$0.88, 1.04, 1.21, 0.86$	$0.96, 1.00, 1.03, 1.06$
	$\mathcal{C}_V$	$0.96, 1.03, 1.08, 0.95$	$0.90, 1.07, 1.19, 0.86$	$0.97, 1.00, 1.03, 1.03$
	$\mathcal{C}_{VI}$	$0.95, 1.04, 1.07, 1.00$	$0.88, 1.09, 1.16, 0.94$	$0.97, 1.01, 1.03, 1.07$

mode shape mismatch at DOF 1 noted earlier in Fig. 5.4, although this is an undamaged location. Thus, while COMAC may be used to identify the existence of damage in a system, for severe and localized damage, it may not be used to identify the damage location. On the other hand, noting the instances where FPCOMAC > 1 helps us to identify damage existence, as well as possible damage locations, even for milder and distributed damage (DS3); note that the FPCOMAC values at DOF 4 are also expected to be more than 1, although the 4th story is undamaged, since the flexibility at DOF 4 is also affected by the third story stiffness, which is damaged. There are however some instances where the FPCOMAC values become less than 1, indicating an apparent decrease in flexibility, especially at DOF 1. This is also noted later in the Section 5.5, where the mean story stiffness estimates are used for damage detection, along with possible reasons for this apparent stiffness increase.

While FPCOMAC is only defined for the diagonal terms of $\mathbf{F}$ in Appendix D, using a similar formulae as Eq. D.52, we may also compute FPCOMAC corresponding to the non-diagonal terms of $\mathbf{F}$, i.e.:

$$\text{FPCOMAC}_{i,k} = \frac{\sum_{j=1}^{N_m} \frac{\|\mathbf{v}_j\|^2}{\|\widehat{\mathbf{v}}_j\|^2} \frac{\widehat{v}_{i,j}\widehat{v}_{k,j}}{\widehat{\lambda}_j}}{\sum_{j=1}^{N_m} \frac{v_{i,j}v_{k,j}}{\lambda_j}} \tag{5.4}$$

Table 5.4: Comparison of damaged and healthy states using mean mass normalized mode shapes: COMAC and FPCOMAC at different DOFs.

Index	Scenario	DS1 vs. DS0	DS2 vs. DS0	DS3 vs. DS0
COMAC	$\mathcal{C}_I$	$0.98, 0.99, 0.99, 0.99$	$0.87, 0.97, 0.92, 0.95$	$1.00, 1.00, 1.00, 1.00$
	$\mathcal{C}_{II}$	$0.97, 0.99, 0.99, 0.99$	$0.87, 0.97, 0.92, 0.95$	$1.00, 1.00, 1.00, 1.00$
	$\mathcal{C}_{III}$	$0.97, 1.00, 0.99, 0.99$	$0.86, 0.98, 0.94, 0.93$	$1.00, 1.00, 1.00, 1.00$
	$\mathcal{C}_{IV}$	$0.97, 0.99, 0.99, 0.99$	$0.87, 0.96, 0.92, 0.95$	$1.00, 1.00, 1.00, 1.00$
	$\mathcal{C}_V$	$0.98, 0.99, 0.98, 0.99$	$0.87, 0.97, 0.92, 0.95$	$1.00, 1.00, 1.00, 1.00$
	$\mathcal{C}_{VI}$	$0.97, 0.99, 0.99, 0.99$	$0.87, 0.96, 0.93, 0.95$	$1.00, 1.00, 1.00, 1.00$
FPCOMAC ($=$ FPCOMAC$_{k,k}$)	$\mathcal{C}_I$	$1.00, 0.98, 1.06, 1.04$	$0.97, 0.99, 1.19, 1.15$	$0.96, 1.04, 1.08, 1.03$
	$\mathcal{C}_{II}$	$0.96, 1.03, 1.01, 1.05$	$0.95, 1.03, 1.18, 1.13$	$0.95, 1.06, 1.05, 1.04$
	$\mathcal{C}_{III}$	$0.96, 0.98, 1.10, 0.98$	$0.93, 0.95, 1.31, 1.04$	$0.93, 1.02, 1.09, 0.95$
	$\mathcal{C}_{IV}$	$1.00, 0.87, 1.04, 1.09$	$1.02, 0.86, 1.20, 1.17$	$0.97, 0.97, 1.06, 1.06$
	$\mathcal{C}_V$	$0.98, 0.97, 1.05, 1.04$	$0.95, 0.98, 1.24, 1.12$	$0.95, 1.05, 1.07, 1.04$
	$\mathcal{C}_{VI}$	$0.99, 0.98, 1.04, 1.04$	$1.01, 0.98, 1.20, 1.13$	$0.96, 1.02, 1.06, 1.04$
FPCOMAC$_k^{II}$ $= \max_i$ (FPCOMAC$_{i,k}$) $i, k = \{1, 2, 3, 4\}$	$\mathcal{C}_I$	$1.00, 0.99, 1.06, 1.05$	$1.01, 0.99, 1.20, 1.20$	$1.00, 1.06, 1.08, 1.06$
	$\mathcal{C}_{II}$	$1.02, 1.03, 1.04, 1.05$	$0.98, 1.03, 1.18, 1.18$	$1.02, 1.07, 1.05, 1.07$
	$\mathcal{C}_{III}$	$0.96, 0.99, 1.10, 1.04$	$0.96, 0.98, 1.31, 1.18$	$0.93, 1.05, 1.09, 1.02$
	$\mathcal{C}_{IV}$	$1.01, 0.94, 1.06, 1.09$	$1.02, 0.93, 1.21, 1.21$	$1.02, 1.02, 1.07, 1.07$
	$\mathcal{C}_V$	$0.98, 0.98, 1.06, 1.06$	$0.98, 0.98, 1.24, 1.21$	$1.00, 1.06, 1.07, 1.07$
	$\mathcal{C}_{VI}$	$0.99, 0.98, 1.05, 1.05$	$1.01, 0.98, 1.20, 1.19$	$0.99, 1.05, 1.06, 1.06$

where N_m is the number of available modes, $\{\lambda_j, \mathbf{v}_j\}$ are the jth modal eigenvalue and mode shape of the healthy system, with $v_{i,j}$ being the ith element of $\mathbf{v}_j$, and $\{\widehat{\lambda}_j, \widehat{\mathbf{v}}_j, \widehat{v}_{i,j}\}$ being the corresponding parameters of the damaged system. Then, as per Appendix D, eFPCOMAC$_{i,k} = 1 -$ FPCOMAC$_{i,k} \approx \left(F_{i,k} - \widehat{F}_{i,k}\right)/F_{i,k}$, i.e. eFPCOMAC$_{i,k}$ is the (i,k)th element of the matrix $\left(\mathbf{F} - \widehat{\mathbf{F}}\right)/\mathbf{F}$. One common approach [56, 72] for damage detection using a matrix of flexibility change: $\Delta\mathbf{F} = \mathbf{F} - \widehat{\mathbf{F}}$, is to compute the $\bar{\delta}_k = \max_i \|\Delta F_{i,k}\|$'s, i.e. the maximum number in each column of $\Delta\mathbf{F}$, for all the columns; then the column k corresponding to the maximum $\bar{\delta}_k$ should give the damage location. Following a similar argument, we can say that the k corresponding to the maximum of the computed FPCOMAC$_k^{II}$'s, where:

$$\text{FPCOMAC}_k^{II} = \max_i \left(\text{FPCOMAC}_{i,k}\right) \tag{5.5}$$

should also give the damage location. Table 5.4 also lists the values of the FPCOMAC$_k^{II}$'s computed using the mean mass normalized mode shapes obtained in the different experimental scenarios. Evidently, the damage location results obtained with this second definition of FPCOMAC (Eq. (5.5)) is very similar to those obtained with the first definition (Appendix D, Eq. D.52). Figs. 5.5 and 5.5 show the FPCOMAC$_{i,k} - 1 = -$eFPCOMAC$_{i,k}$ values, for all $i, k = \{1, 2, 3, 4\}$, computed in Scenarios $\mathcal{C}_V$ and $\mathcal{C}_{VI}$, for all the damage states. (The negative of the eFPCOMAC$_{i,k}$'s were plotted in these figures for ease of representation.) From these figures it is clear that using the FPCOMAC values one may be able to detect a region containing the damaged elements with reasonable accuracy. Recall that: in state DS1, two 3rd story columns are damaged; in state DS2, all four 3rd story columns are damaged; while in state DS3, one 3rd and one 2nd story columns are damaged. Comparing the three damage states in these figures, we can also infer that the severity of damage is greatest in DS2; while the damage severity at story 3 seems comparable in DS1 and DS3, DS3 also has a similarly severe damage at story 2. Note also the better damage localization in Scenario $\mathcal{C}_V$ than in Scenario $\mathcal{C}_{VI}$; while both the scenarios use the same a priori information (total mass M_T), in Scenario $\mathcal{C}_V$ we measure all the 4 floors, while in $\mathcal{C}_{VI}$ we do not measure the 2nd floor.

5.1.4 Damage detection using mean identified story stiffnesses

Once the $\mathbf{M}$ and $\mathbf{K}$ matrices are identified using the complete mass-normalized $\mathbf{V}$ matrices and the identified eigenvalues (frequencies), the floor masses and story stiffnesses of the frame are estimated as in Section 3.6: $m_i = M_{i,i}$, $k_1 = K_{1,1} + K_{1,2}$, and any other $k_i = -K_{i,i+1}$. The identified

physical parameters in the different damage states are similar in nature to the identified parameters of the healthy state in Section 3.6, i.e.: diagonal $\mathbf{M}$ and tridiagonal $\mathbf{K}$, but not strictly shear–type nature; dispersion between the identifications in the different instrumentation/*a priori* information scenarios, owing to the differences in modeling assumptions and amounts of measured data, etc. The individual identification results are not essential in the following discussion on damage detection, and hence are not presented here.

The ratios of the mean (over the 18 tests) identified story stiffnesses in the different damage states (DS1 to DS3) to the corresponding mean stiffnesses in the healthy state (DS0) of the frame, listed in Table 5.5, are used here for this comparison. From these ratios it is evident that, if the identification exercise of the undamaged and damaged structure is consistent in terms of instrumentation, modeling assumptions and solution strategy, then the damage location and severity can both be identified with reasonable accuracy. For example, in the case of DS1, replacing two 50.8×9.5 mm columns in the 3rd story with two 50.8×7 mm columns introduces a stiffness reduction of approximately 30%, and hence a stiffness retention of approximately 70% in the damaged 3rd story with respect to the undamaged 3rd story. Similarly, in DS2 the stiffness retention in the 3rd story is approximately 40%, while in DS3 the stiffness retentions in the 2nd and 3rd stories are each 85%, with respect to the story stiffnesses in DS0. These theoretical approximates of story stiffness retention in the damaged frames are also listed in Table 5.5 (first row) for comparison purposes, and may be expected to serve as approximate lower bounds of the ratio of the damaged to the undamaged frames' damaged story stiffnesses, since they ignore the stiffness contribution from the braces, and the fact that the column cross-sections were not uniformly reduced throughout the interstory height as additional plates were inserted between the damaged columns and angles at the connections to maintain proper fixity. From Table 5.5 it can be seen that this ratio for the 3rd story varies between 0.71 and 0.79 in case of DS1 for the different scenarios considered, thus identifying both the damage location and severity with reasonable accuracy. Similarly, this ratio for the 3rd story in case of DS2 varies between 0.44 and 0.55, while in case of DS3 these ratios for the 2nd and 3rd stories respectively vary between 0.82 to 0.91 and 0.81 to 0.90. Note that scenario $\mathcal{C}_{III}$ represents a situation where measurements from the damaged floor are not available; the accurate damage location and severity assessment even in this case exemplifies the potential of the proposed method for structural health monitoring in realistic situations where incomplete instrumentation may lead to unavailable measurements from potentially

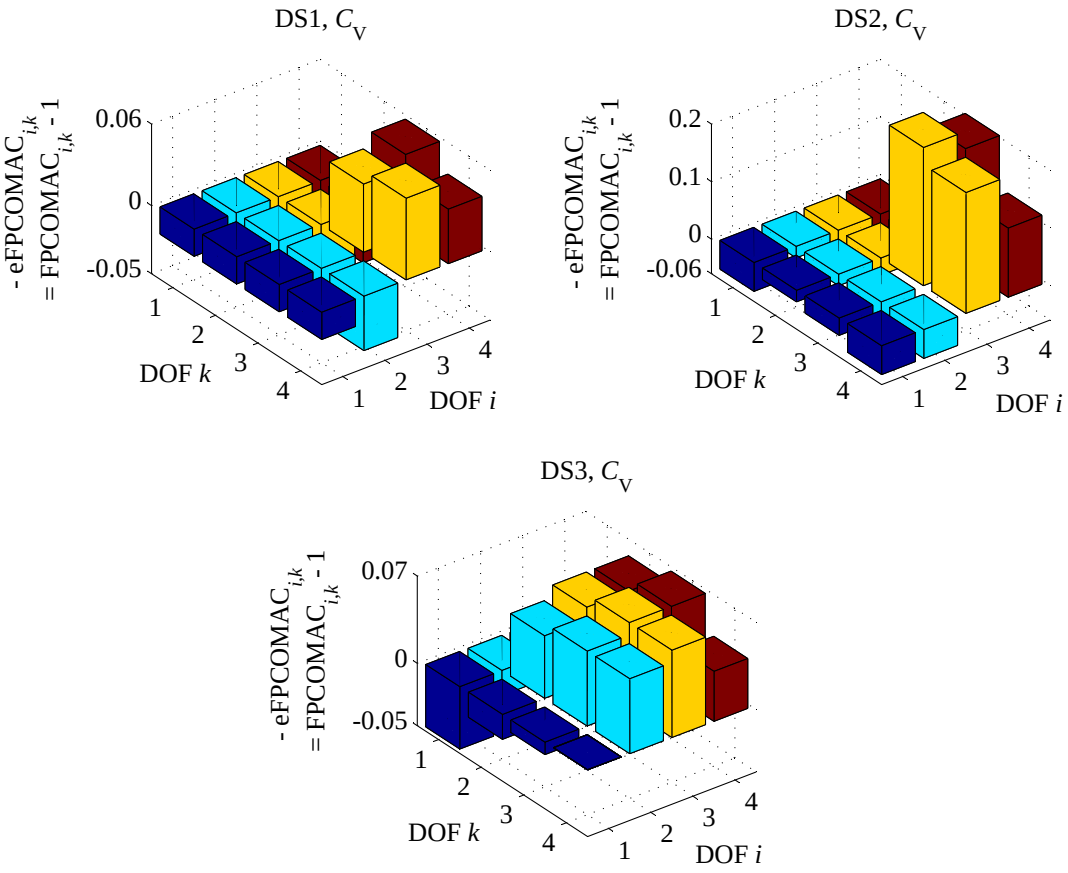

Figure 5.5: Computed $-\text{eFPCOMAC}_{i,k} = \text{FPCOMAC}_{i,k} - 1$ values between the three damage states (DS1 to DS3) and the healthy state (DS0)in scenario $\mathcal{C}_V$.

damaged region(s). Also, in scenarios $\mathcal{C}_V$ and $\mathcal{C}_{VI}$, for the purpose of structural damage detection, the *a priori* information of the total mass of the system (M_T) may not be unnecessary; as long as the total mass of the system remains unchanged between the healthy and the damaged states, the story stiffness ratios in Table 5.5 are independent of the exact value of M_T, and any assumed value of M_T may be used to scale the proportional systems (with this value being the same for both the healthy and damaged states).

From the ratios of the story stiffnesses of the other stories it is observed that, while in most cases the ratios are close to 1, in some cases the stories above and below a damaged story show some reduction is stiffness, while in some cases the ratios for the the 1st story indicate an increase in stiffness. The stiffness reduction in the stories above and below a damaged story may be owing to the

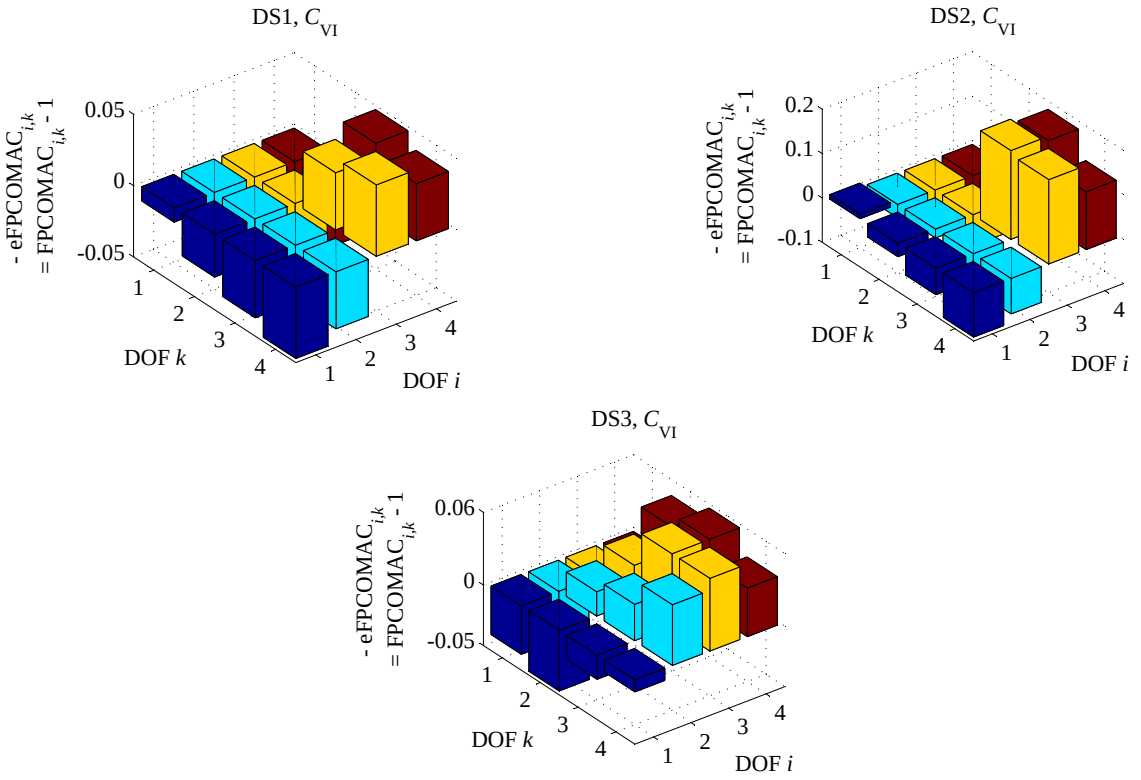

Figure 5.6: Computed $-\text{eFPCOMAC}_{i,k} = \text{FPCOMAC}_{i,k} - 1$ values between the three damage states (DS1 to DS3) and the healthy state (DS0) in scenario $\mathcal{C}_{VI}$.

Table 5.5: Ratio of damaged to healthy mean story stiffness estimates.

Scenario	$\mu_{k_{\text{DS1}}}/\mu_{k_{\text{DS0}}}$	$\mu_{k_{\text{DS2}}}/\mu_{k_{\text{DS0}}}$	$\mu_{k_{\text{DS3}}}/\mu_{k_{\text{DS0}}}$
Theoretical	$1.00, 1.00, 0.70, 1.00$	$1.00, 1.00, 0.40, 1.00$	$1.00, 0.85, 0.85, 1.00$
$\mathcal{C}_I$	$1.07, 0.97, 0.73, 0.95$	$1.18, 0.93, 0.47, 0.90$	$1.08, 0.87, 0.85, 0.97$
$\mathcal{C}_{II}$	$1.18, 0.93, 0.71, 0.94$	$1.19, 0.90, 0.49, 0.90$	$1.11, 0.86, 0.84, 0.97$
$\mathcal{C}_{III}$	$1.14, 0.86, 0.71, 0.86$	$1.25, 0.75, 0.44, 0.73$	$1.08, 0.82, 0.81, 0.91$
$\mathcal{C}_{IV}$	$1.06, 1.03, 0.79, 0.94$	$1.05, 1.02, 0.55, 0.90$	$1.06, 0.91, 0.88, 0.97$
$\mathcal{C}_V$	$1.12, 0.98, 0.73, 0.95$	$1.24, 0.94, 0.47, 0.90$	$1.11, 0.88, 0.86, 0.97$
$\mathcal{C}_{VI}$	$0.99, 1.00, 0.78, 0.94$	$0.99, 0.99, 0.53, 0.89$	$1.02, 0.90, 0.90, 0.96$

reduction of the joint stiffnesses at the columns–floor plate connections of the damaged story to the stories above and below. It may also imply some *leaking* of damage sensitive information from the damaged to the neighbouring stories, since we are primarily working with modal information which represents global information about the system. This will signal to us that the structure is damaged, and will indicate a possible damaged zone consisting of a particular story, where damage is most likely present based on the estimated severity, and also of the neighbouring stories, where damage may be present, but with less likelihood based on their estimated severities. The apparent increase in the 1st story stiffness is greater if the damage is localized and severe (e.g. $\{1.08, 1.11, 1.08, 1.11\}$ in case of $\mu_{k_{\text{DS3}}}/\mu_{k_{\text{DS0}}}$ vs. $\{1.18, 1.19, 1.25, 1.24\}$ in case of $\mu_{k_{\text{DS2}}}/\mu_{k_{\text{DS0}}}$), and may also be due to the global picture given by the estimated modal parameters, whereby a significant (true) decrease in some story stiffness also shows up as a relative (fictitious) increase in the 1st story stiffness. Another possible explanation of this increase stiffness in the 1st story may be the activation of some strengthening mechanism (e.g. increased participation of the braces in load resistance) in the 1st story when there is damage at some other story. A similar unexpected increase in stiffness has been observed for the same structure also in [44, 73], where the stiffness identification/damage detection have been performed using different, though modal parameter based, approaches.

Similar to the ratios of the mean identified story stiffnesses in Table 5.5, we also compute the ratios of the mean of the identified floor masses in the different damage states to the corresponding mean floor masses of the healthy frame, as listed in Table 5.6. Since structural damage, in the form of story stiffness reduction (reduction in some columns' cross-sectional area), should not affect the mass matrix to any significant extent, the ratios of the mean identified floor masses are expected to be approximately 1.00. This is verified from Table 5.6, where all these ratios (excepting for the 2nd floor mass in Scenario $\mathcal{C}_{IV}$) are near 1.00. In case of Scenario $\mathcal{C}_{IV}$, the 2nd floor masses are overestimated in the damaged states. Recall that such overestimation was also observed in Section 3.6 for the test with an added eccentric 2nd floor mass. As per Section 3.6, such overestimation is possibly owing to neither measuring the 2nd floor acceleration, nor assuming *a priori* the 2nd floor mass, while putting too much constraints on the solution process through the *a priori* assumption of all the other floor masses. Moreover, noting that the 2nd floor is a location just next to the damaged story in any damaged state of the frame, measured data from such a location may be expected to be more informative than expanded mode shape components obtained using theoretical considerations.

Table 5.6: Ratio of damaged to healthy mean floor mass estimates.

Scenario	$\mu_{m_{\text{DS1}}}/\mu_{m_{\text{DS0}}}$	$\mu_{m_{\text{DS2}}}/\mu_{m_{\text{DS0}}}$	$\mu_{m_{\text{DS3}}}/\mu_{m_{\text{DS0}}}$
Theoretical	$1.00, 1.00, 1.00, 1.00$	$1.00, 1.00, 1.00, 1.00$	$1.00, 1.00, 1.00, 1.00$
$\mathcal{C}_I$	$1.00, 1.00, 1.00, 1.00$	$1.00, 1.00, 1.00, 1.00$	$1.00, 1.00, 1.00, 0.99$
$\mathcal{C}_{II}$	$1.00, 1.02, 1.01, 0.99$	$1.00, 1.02, 1.00, 0.99$	$1.00, 1.01, 1.01, 1.00$
$\mathcal{C}_{III}$	$0.99, 0.98, 1.00, 0.99$	$0.98, 0.97, 1.00, 0.98$	$0.99, 0.98, 1.00, 0.99$
$\mathcal{C}_{IV}$	$1.00, 1.25, 1.01, 0.99$	$1.00, 1.30, 1.00, 0.99$	$1.00, 1.14, 1.01, 1.00$
$\mathcal{C}_V$	$1.02, 1.00, 1.00, 0.98$	$1.03, 1.01, 0.97, 0.99$	$1.02, 0.99, 1.01, 0.98$
$\mathcal{C}_{VI}$	$0.98, 1.09, 0.95, 0.95$	$0.97, 1.17, 0.89, 0.93$	$0.99, 1.06, 0.98, 0.95$

Nonetheless, as evident from Tables 5.6 and 5.5, even in Scenario $\mathcal{C}_{IV}$, we are able to estimate the damage locations and severities with reasonable accuracy, along with the assurance that the other floor masses do not suffer any significant change. While the computation of the mean identified floor mass ratios do not directly help us in damage detection, these ratios being close to 1.00 in most cases do help us in gaining some confidence in the identified models, and hence confidence in the damage detection results obtained using such models.

5.1.5 A method of probabilistic damage characterization[1]

It has been widely reported in the literature that modal parameters are significantly affected by "non-damage" related structural variations, induced, for example, by temperature changes, or other environmental/operational fluctuations [13, 33, 74–80]. Moreover, the data from the healthy and damaged states may correspond to different inputs, e.g. ambient inputs for the healthy system vs. earthquake input for the damaged system. Hence: (1) identification results from different tests performed on a single state of the system will show some variability, not only induced by estimation errors, but also introduced by exogenous factors like input/environmental/operational condition variability, and thus (2) the difference in the identification results between two states of the system may not only be owing to damage induced changes, but also due to the above mentioned exogenous disturbances. It may thus be more appropriate if the damage assessment is performed in a probabilistic framework, accounting for the effects of these exogenous, often unmeasured, variables.

[1] I would like to thank Ms. Luciana Balsamo for many helpful discussions on structural damage detection using statistical methods, and particularly for the idea of using ECDFs for the distributions of the k_R ratios.

Let us first compare each test on the damaged state with each and every test on the healthy state, as well as, for the purpose of building a benchmark, compare each test on the healthy state with each of the remaining tests on the healthy state. For this comparison, we define the following ratio:

$$k_R^{i,j} = \frac{k^i}{k_H^j} \tag{5.6}$$

where k^i represents the story stiffness estimate, for any story, in the ith test on any state DS$\#$ ($\# = \{0, 1, 2, 3\}$), while k_H^j represents the story stiffness estimate, for the same story, in the jth test on state DS0 (the healthy or baseline state), with $i \neq j$ when $\# = 0$. Thus, in any experimental scenario, for the damage states DS1 to DS3, we have a total of $18 \times 18 = 324$ sets of the above ratio, while for the healthy state DS0, we have a total of $18 \times 17 = 306$ sets of the ratio. Table 5.7 lists the means, standard deviations and coefficients of variations of these k_R values. These coefficients of variation are, in most cases, less than 5%, indicating that the approach may be used to reliably detect even low levels of damage (e.g. $5 - 10\%$ reduction in story stiffness), with the damage assessment being more reliable if measurements from the damaged region are available. Also, the mean values in Table 5.7 for the damaged stories match reasonably well with the theoretical estimates of story stiffness retention, and the values of $\mu_{k_{\text{DS}\#}}/\mu_{k_{\text{DS0}}}$, listed in Table 5.5 previously, thus indicating that the severity of damage may also be well estimated, in the mean sense, even if only single sets of test data are available for the comparison of the healthy and the damaged states. We next evaluate the empirical cumulative distribution functions (ECDFs) of the computed k_R values (see e.g. [44, 81, 82] for ECDF computation); the ECDFs of the k_R values comparing the baseline state to itself are denoted as F_H, while, for any of the damaged states DS$\#$ ($\# = \{1, 2, 3\}$), the ECDFs of the k_R values comparing it to the baseline state are denoted by $F_\#$. Fig. 5.7 illustrates the comparison of the ECDFs obtained for the different states in scenario $\mathcal{C}_{VI}$. These ECDFs show that, while for undamaged stories the distributions for the damaged states have significant overlap with those of the healthy state, for the damaged stories the overlaps are minimal, signifying that the probability of classifying a damaged story as undamaged is negligibly small.

Based on the above discussion, it is evident that the present approach has the potential for successful application, through Eq. (5.6), in structural damage detection problems. We now attempt to develop a method to probabilistically characterize the presence of damage at a given location, as well as the severity of damage, if present. To detect the presence of damage at a location in a possibly

Table 5.7: Statistics of k_R comparing different states with healthy state.

State	Scenario	μ_{k_R}	COV$_{k_R}$ (%)
DS0	$\mathcal{C}_I$	$1.00, 1.00, 1.00, 1.00$	$3.05, 6.37, 2.34, 6.85$
	$\mathcal{C}_{II}$	$1.00, 1.00, 1.00, 1.00$	$7.52, 1.76, 5.07, 4.68$
	$\mathcal{C}_{III}$	$1.00, 1.00, 1.00, 1.01$	$9.70, 2.49, 5.00, 13.05$
	$\mathcal{C}_{IV}$	$1.00, 1.00, 1.00, 1.00$	$4.14, 1.81, 2.62, 4.57$
	$\mathcal{C}_V$	$1.00, 1.00, 1.00, 1.00$	$1.31, 1.34, 2.78, 1.06$
	$\mathcal{C}_{VI}$	$1.00, 1.00, 1.00, 1.00$	$0.76, 2.71, 1.22, 4.93$
DS1	$\mathcal{C}_I$	$1.07, 0.97, 0.73, 0.95$	$2.14, 4.83, 1.70, 5.48$
	$\mathcal{C}_{II}$	$1.18, 0.93, 0.72, 0.94$	$10.52, 3.50, 5.77, 3.32$
	$\mathcal{C}_{III}$	$1.14, 0.86, 0.71, 0.87$	$7.05, 1.77, 3.57, 9.63$
	$\mathcal{C}_{IV}$	$1.06, 1.03, 0.79, 0.94$	$5.26, 2.40, 1.79, 3.28$
	$\mathcal{C}_V$	$1.12, 0.98, 0.73, 0.95$	$1.10, 0.99, 2.00, 0.76$
	$\mathcal{C}_{VI}$	$0.99, 1.00, 0.78, 0.94$	$0.65, 1.95, 1.03, 3.32$
DS2	$\mathcal{C}_I$	$1.18, 0.93, 0.47, 0.91$	$2.27, 4.69, 1.77, 4.99$
	$\mathcal{C}_{II}$	$1.19, 0.90, 0.49, 0.90$	$6.50, 1.72, 4.03, 3.35$
	$\mathcal{C}_{III}$	$1.25, 0.75, 0.44, 0.73$	$7.13, 1.77, 3.58, 9.63$
	$\mathcal{C}_{IV}$	$1.05, 1.02, 0.55, 0.90$	$3.48, 1.59, 2.00, 3.27$
	$\mathcal{C}_V$	$1.24, 0.94, 0.47, 0.90$	$1.37, 0.97, 2.26, 0.92$
	$\mathcal{C}_{VI}$	$0.99, 0.99, 0.53, 0.89$	$0.87, 1.91, 1.08, 3.41$
DS3	$\mathcal{C}_I$	$1.08, 0.87, 0.85, 0.97$	$3.20, 6.20, 2.35, 6.31$
	$\mathcal{C}_{II}$	$1.12, 0.86, 0.84, 0.97$	$10.45, 3.27, 5.52, 3.50$
	$\mathcal{C}_{III}$	$1.08, 0.82, 0.81, 0.92$	$7.11, 1.90, 3.74, 9.78$
	$\mathcal{C}_{IV}$	$1.06, 0.91, 0.88, 0.97$	$5.68, 2.78, 2.38, 3.48$
	$\mathcal{C}_V$	$1.11, 0.88, 0.86, 0.97$	$1.63, 1.14, 2.01, 0.96$
	$\mathcal{C}_{VI}$	$1.02, 0.90, 0.90, 0.96$	$2.82, 2.06, 2.67, 3.37$

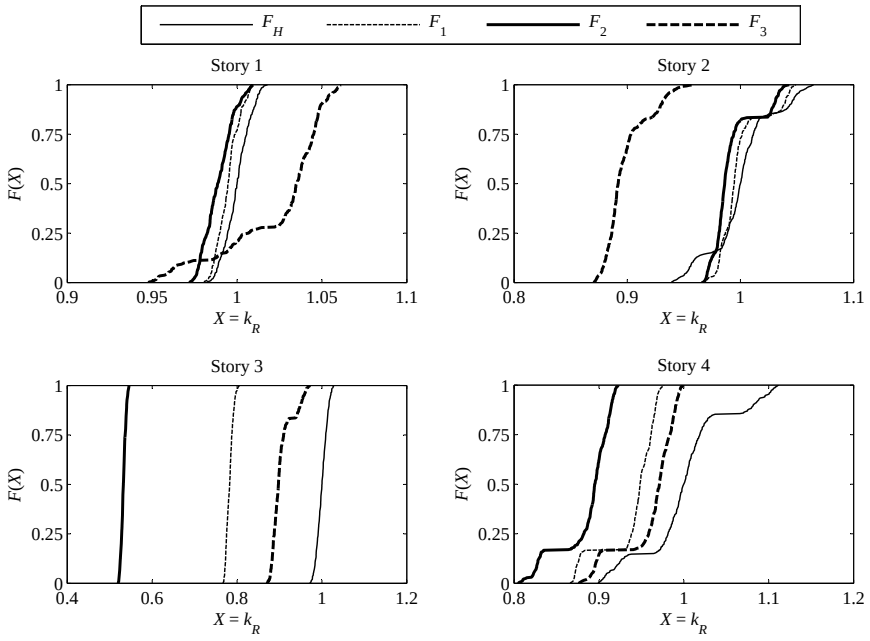

Figure 5.7: ECDFs of k_R comparing different states with healthy state in scenario $\mathcal{C}_{VI}$.

damaged state $\#$, we define a measure to compare the the ECDFs $F_{\#}$ and F_H. Let X_L and X_U respectively be the k_R values corresponding to the 2.5th and 97.5th percentiles of F_H. The comparative measure, $\mathcal{P}$, is then defined as a a degree of mismatch between $F_{\#}$ and F_H, determined as:

$$\mathcal{P} = 1 - P(X_L < Y < X_U) = 1 - (F_{\#}(k_R = X_U) - F_{\#}(k_R = X_L)) \tag{5.7}$$

where $Y = k_R$ in state DS$\#$, and $P(X_L < Y < X_U)$ is the probability that k_R values in the state DS$\#$ will lie between X_L and X_U, i.e. within the central 95% probability region of the k_R values in the baseline state. A $\mathcal{P}$ value of p will indicate that the k_R values in state DS$\#$ will fall outside the $X_L - X_U$ range with a probability of p, and within this range with a probability of $(1 - p)$; thus higher the value of $\mathcal{P}$ more is the chance that the k_R in state DS$\#$ will lie outside the central 95% probability region of k_R in the baseline state. The measure $\mathcal{P}$ thus denotes how much the k_R ratios in the two states differ in a statistical sense, with a higher $\mathcal{P}$ indicating a possible change in the state of the structure from the healthy state, and thus the possibility of the presence of damage in the structure at the location under consideration. Fig. 5.8 illustrates the calculation of the $\mathcal{P}$ values, for stories 2 (undamaged) and 3 (damaged) in the damage state DS1, for scenario $\mathcal{C}_{VI}$. Table 5.8 lists the $\mathcal{P}$ values obtained for the different damage states in the different experimental scenarios.

To classify a given location as damaged or healthy using the $\mathcal{P}$ values, we would need to select a threshold for $\mathcal{P}$; in this discussion, we select this threshold as 0.90, i.e. $\mathcal{P} > 0.90$ would indicate that the story under consideration is damaged, otherwise healthy. Considering the classification for each of the 4 stories in each of the 3 damaged states and 6 scenarios as a separate event, we have a total of $4 \times 3 \times 6 = 72$ such events, 24 of which should be damaged (story 3 in states DS1 to DS3, and story 2 as well in state DS3, for all 6 scenarios), and the remaining 48 should be undamaged. Using the threshold of 0.90 with the $\mathcal{P}$ values in Table 5.8, we classify correctly all the damage cases except one (DS3, story 2, scenario $\mathcal{C}_I$), while 10 healthy cases are misclassified as damaged; thus the misclassification rates are 4% false-negative (damaged classified as healthy) and 20% false-positive (healthy classified as damaged) [56], indicating a conservative damage detection. Note that, out of the 10 misclassifications of healthy locations, 4 are at the first story, where the stiffness estimate shows an apparent increase relative to the healthy state, thus classifying the current state as *healthier*; this issue was also highlighted at the end of Section 5.1.4. The remaining 6 false-positive misclassifications incorrectly indicate the presence of damage in the neighbouring stories of a true damaged story; this issue was also discussed at the end of Section 5.1.4, and as will be shown later, the severity of damage in these misclassified cases are in fact much lower compared to the severity in the correctly classified damaged stories. Both the false-positive and false-negative error rates will of course depend on: (a) the percentiles of F_H defining X_L and X_U, and thus defining $\mathcal{P}$ in Eq. (5.7), and (b) the threshold value for $\mathcal{P}$. However, it should be mentioned that, although the false-positive error rate of 20% may seem high, in the context of structural health monitoring, the consequences of a higher false-negative error are "potentially even more severe" [56]; in fact, as stated in [56]: "If a damaged system is allowed to continue to operate in a misdiagnosed damaged state, there will be a threat to safety and there may even be complete loss of the structure and consequent loss of life."

Once a given location/story is classified as potentially damaged using the above procedure, the damage severity, in terms of percentage reduction in k_R, may also be assessed in a probabilistic sense by comparing different percentiles of the two ECDFs, F_H and $F_{\#}$. An example of such an assessment is shown in Fig. 5.9, for the damage in the 3rd story in state DS1, using the ECDFs obtained in scenario $\mathcal{C}_{VI}$. From this figure we can say: (a) there is a 95% probability of at least 20.4% damage with respect to the median k_R ($= 1.00$) in the healthy state, (b) there is a 50% probability of at least 21.8% damage with respect to the median k_R in the healthy state, (c) there is a 95% probability of at

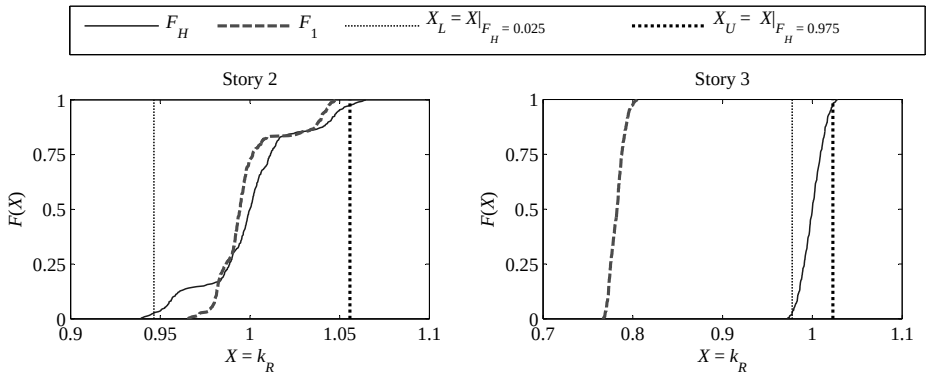

Figure 5.8: Calculation of $\mathcal{P}$ values for stories 2 (undamaged) and 3 (damaged) in State DS1, using ECDFs obtained in scenario $\mathcal{C}_{VI}$: $\mathcal{P} = 1 - (F_1|_{k_R=X_U} - F_1|_{k_R=X_L})$.

least 18.8% damage with respect to the 5th percentile k_R ($= 0.98$) in the healthy state, (d) there is a 50% probability of at least 20.2% damage with respect to the 5th percentile k_R in the healthy state, etc. In general: let X_{γ_H} be the value of k_R corresponding to the γ_Hth percentile of F_H, and X_{γ_D} be the value of k_R corresponding to the γ_Dth percentile of $F_\#$. The damage severity may then be expressed in a probabilistic sense as: there is a γ_D percentage probability of at least d percentage damage with respect to the γ_Hth percentile baseline (healthy) k_R, where $d = (X_{\gamma_H} - X_{\gamma_D})/X_{\gamma_H} \times 100$, denotes the percentage reduction in k_R due to damage. In other words, if Y represents the k_R values in state DS$\#$, then [44, 82, 83]:

$$\gamma_D = P(Y \leq X_{\gamma_D}) = P\left(\frac{X_{\gamma_H} - Y}{X_{\gamma_H}} \times 100 \geq d\right) \tag{5.8}$$

i.e. γ_D is the probability that the percentage decrease in k_R in state DS$\#$, with respect to the healthy state, is at least d. Note that, for any given damage severity d, we do not have a single associated probability of exceedance γ_D, but a set of associated (γ_D, γ_H) values, with γ_H representing the inherent variability, induced by noise/estimation error/environmental and operational fluctuations etc., in the healthy state. Using all possible values of γ_H and $\gamma_D \in (0, 1)$, we can express the damage severity using a color surface plot as in Fig. 5.10. In this figure, F_D denotes the probability of exceedance for any given damage severity, while F_H, as before, denotes the different percentiles of k_R in the healthy state. As expected, the damage severity increases with: (a) decreasing probability of exceedance for any given percentile in F_H, and (b) increasing percentiles in F_H for any given probability of exceedance. While such a color surface plot would contain the complete information

Table 5.8: Mismatch between damaged states and healthy state ECDFs of k_R given by $\mathcal{P}$ values.

Scenario	$\mathcal{P}$(DS1/DS0)	$\mathcal{P}$(DS2/DS0)	$\mathcal{P}$(DS3/DS0)
$\mathcal{C}_I$	$0.31, 0.00, 1.00, 0.00$	$1.00, 0.00, 1.00, 0.00$	$0.40, 0.12, 1.00, 0.06$
$\mathcal{C}_{II}$	$0.44, 0.81, 1.00, 0.02$	$0.61, 1.00, 1.00, 0.84$	$0.28, 1.00, 0.99, 0.00$
$\mathcal{C}_{III}$	$0.17, 1.00, 1.00, 0.00$	$0.68, 1.00, 1.00, 0.84$	$0.17, 1.00, 1.00, 0.00$
$\mathcal{C}_{IV}$	$0.37, 0.48, 1.00, 0.06$	$0.21, 0.19, 1.00, 0.84$	$0.32, 0.97, 1.00, 0.01$
$\mathcal{C}_V$	$1.00, 0.42, 1.00, 1.00$	$1.00, 1.00, 1.00, 1.00$	$1.00, 1.00, 1.00, 0.82$
$\mathcal{C}_{VI}$	$0.10, 0.00, 1.00, 0.17$	$0.42, 0.00, 1.00, 0.71$	$0.85, 0.99, 1.00, 0.17$

of a probabilistic assessment of damage severity, it may also be helpful to derive from such a plot, probability of exceedance vs. damage severity curves corresponding to some particular percentiles in F_H. Such curves, for the 5th, 50th (median) and 95th percentiles of F_H are also shown in Fig. 5.10, with the 95th percentile curve being the most conservative (safe), corresponding to a "very stiff" condition of the healthy state, and the 5th percentile being the least safe, corresponding to a "very flexible" condition of the healthy state, amongst the three. Finally, in Fig. 5.11, a similar damage severity assessment is performed as in Fig. 5.10, but for a story which was misclassified as damaged using the $\mathcal{P}$ value. As is evident, although erroneously declared damaged, the estimated damage severities in this case is much lower, as compared to the damage severities in Fig. 5.10.

The probabilistic approach to assess the existence and location of damage using $\mathcal{P}$ values, and to estimate the probability of exceedance vs. damage severity curves, may be expected to help in decision making for maintenance and retrofitting operations, prioritizing emergency response after earthquakes etc. The approach takes into account the inherent variability in k_R values in both the healthy and possibly damaged conditions, and would thus, in a continuous health monitoring scheme, help in a robust assessment of damage, accounting for the uncertainties induced by measurement noise, environmental/ambient fluctuations etc. Note however that the performance of the approach will depend on: (a) how reliable the ECDFs of k_R are, and (b) the choice of the threshold for $\mathcal{P}$ and the different percentiles necessary in the approach. In continuous health monitoring, it may be expected that several sets of data will be available from the baseline/healthy system. An initialization phase would first need to be performed using sufficient number of such data sets, to construct an initial set of stable and reliable ECDFs of k_R of the healthy system [83]. Once this initial set of ECDFs for the healthy system is obtained, the ECDFs obtained using any current sets of data can be

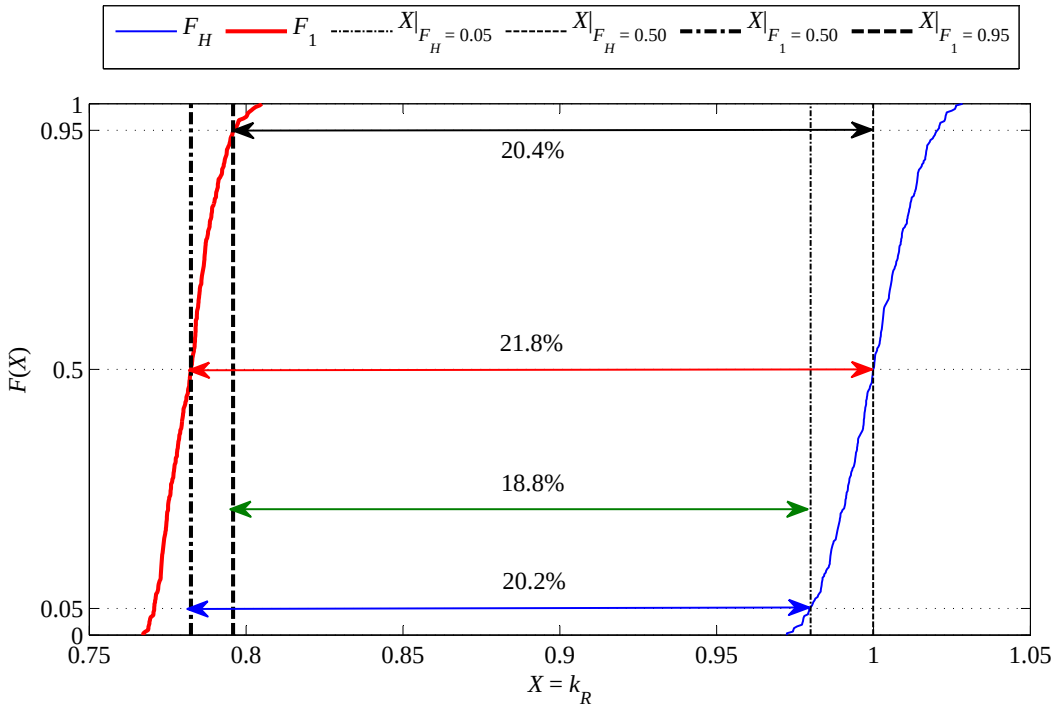

Figure 5.9: Probabilistic characterization of damage severity at 3rd story using ECDFs of k_R in scenario $\mathcal{C}_{VI}$.

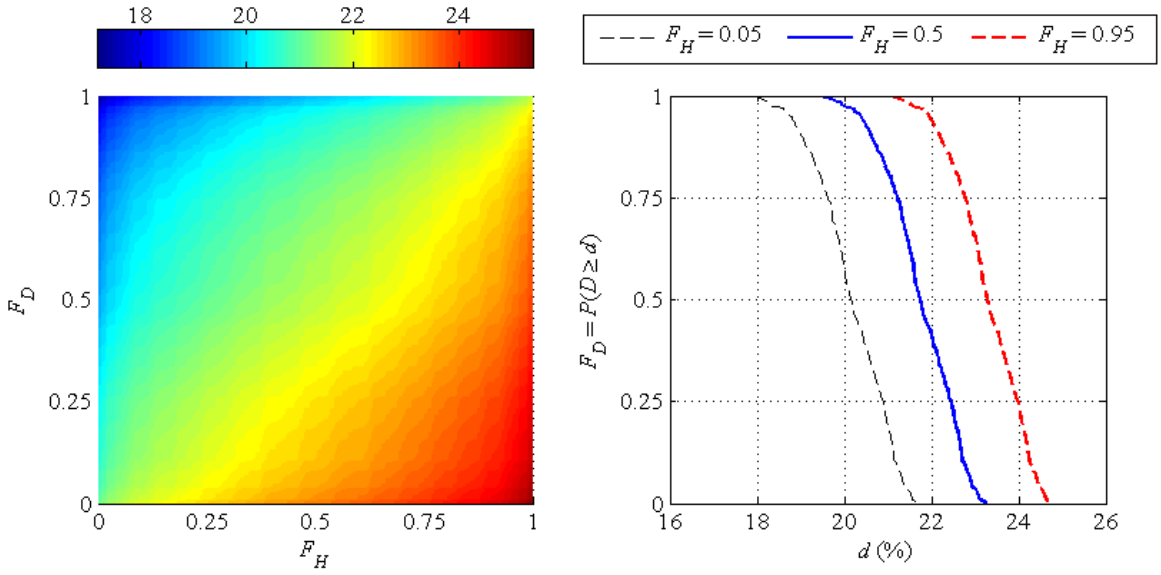

Figure 5.10: Probabilistic characterization of damage severity at 3rd story in state DS1, using ECDFs of k_R in scenario $\mathcal{C}_{VI}$.

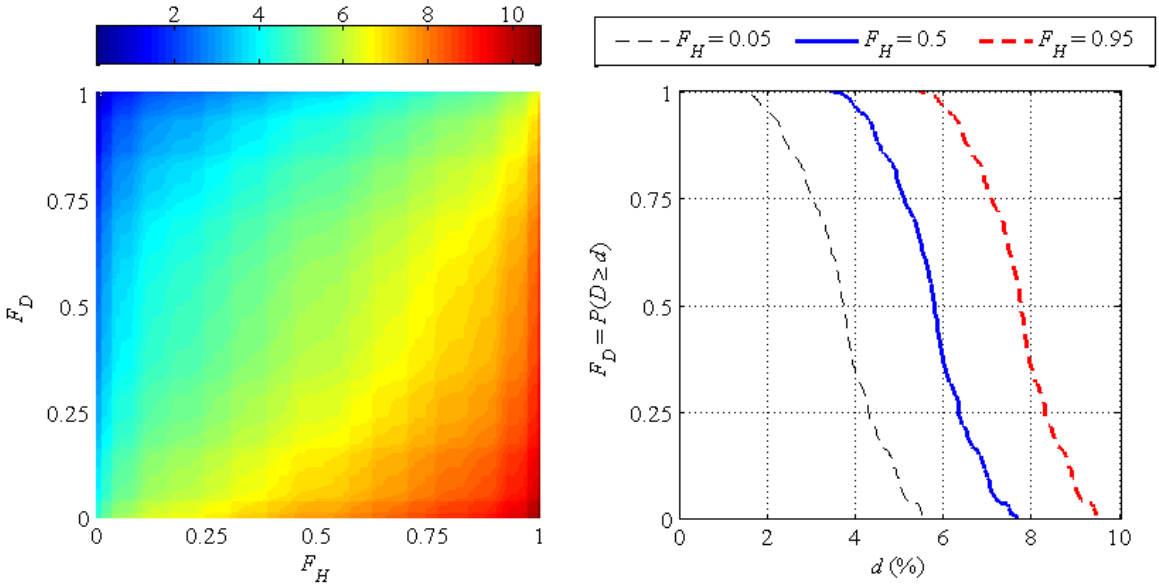

Figure 5.11: Probabilistic characterization of damage severity at 2nd story in state DS2, using ECDFs of k_R in scenario $\mathcal{C}_V$ (a case of *false alarm*).

compared against this initial set. If the current state is found healthy, then the current sets of data may be augmented with the initial set. Note that the number of data sets constituting the current data may be much smaller than the number of data sets used in the initialization process; as long as a sufficient number of story stiffness estimates are available using the initial sets of data, we can get a sufficient population of k_R ratios comparing the current state of the structure to the initial state. For example, if the initialization phase uses 20 data sets, then these will give 20 sets of story stiffness estimates, and the initial ECDF will be constructed using 20×19 sets of reference k_R ratios; from the current state, if we now have 5 data sets, then these will give 5 sets of story stiffness estimates, and 5×20 sets of k_R ratios comparing the current to the initial (reference) state. While the choice of the threshold for $\mathcal{P}$ and the different necessary percentiles can be from the engineer's judgement, these parameters may also be chosen using other objective techniques when a large enough initial data set is available [35, 84]. Since the structural identification approach of Chapter 3 employed here only requires the non-normalized modal parameter estimates at the sensor locations, it may be applied with both known/unknown ground excitations, as well as in other output only (ambient vibration) situations. Thus, the multiple data sets necessary in the present probabilistic approach, would not require multiple experiments, but may be simply obtained from a sufficiently long length of ambient

vibration data, by breaking up the data into several windows and performing the modal and structural identification for each of these windows individually. In continuous monitoring, sufficient lengths of ambient vibration data would, in general, be available.

5.2 3-Story LANL Frame Experimental Study[2]

In this section we consider the applicability of the structural identification approach of Chapter 2 in damage assessment problems. Experimental data from a 3-story frame model, tested in the Los Alamos National Laboratory (LANL) [32], was used in Chapter 2 (Section 2.6) as an application of the identification approach. Here, we consider different modified versions of this frame, also tested in the LANL; these modified states are listed in Table 5.9, and were obtained by adding a floor mass or replacing column(s) with column(s) of reduced cross-section. Like the healthy state, each of the modified states were tested 50 times, using band limited white noise signals as input forces applied to the base. The test set-up, the structural model assumed to represent the frame, and the assumed instrumentation set-up, is again shown in Fig. 5.12. As in Section 2.6: (a) all the states of the frame are modeled as 4-DOF free-free systems, owing to the base being allowed to slide on rails (neglecting rail friction), and (b) the applied input force at the base and only the base acceleration output are used for identification. Using these input and output data in the structural identification approach of Chapter 2, we identify the complete physical model of the frame, in the different experiments and for the different states. Further details of the experiment and the identification procedure can be found in Section 2.6.

5.2.1 Comparing identified modal parameters

While the damping ratios in Table 5.10 do not show any consistent trend with damage, the mean frequency estimates, as expected, show a mostly consistent decrease with damage (story stiffness reduction), and may thus be used to signal the existence of damage in the system. However, they may not be used to locate/assess the severity of damage. Moreover, the decrease in modal frequencies may also be induced by an increase in mass (State 2), and this will be indistinguishable from a stiffness

[2]This section was presented as a conference paper, co-authored with Profs. Raimondo Betti and Hilmi Lus, in the 6th World Conference on Structural Control and Monitoring, Barcelona, 2014 [24].

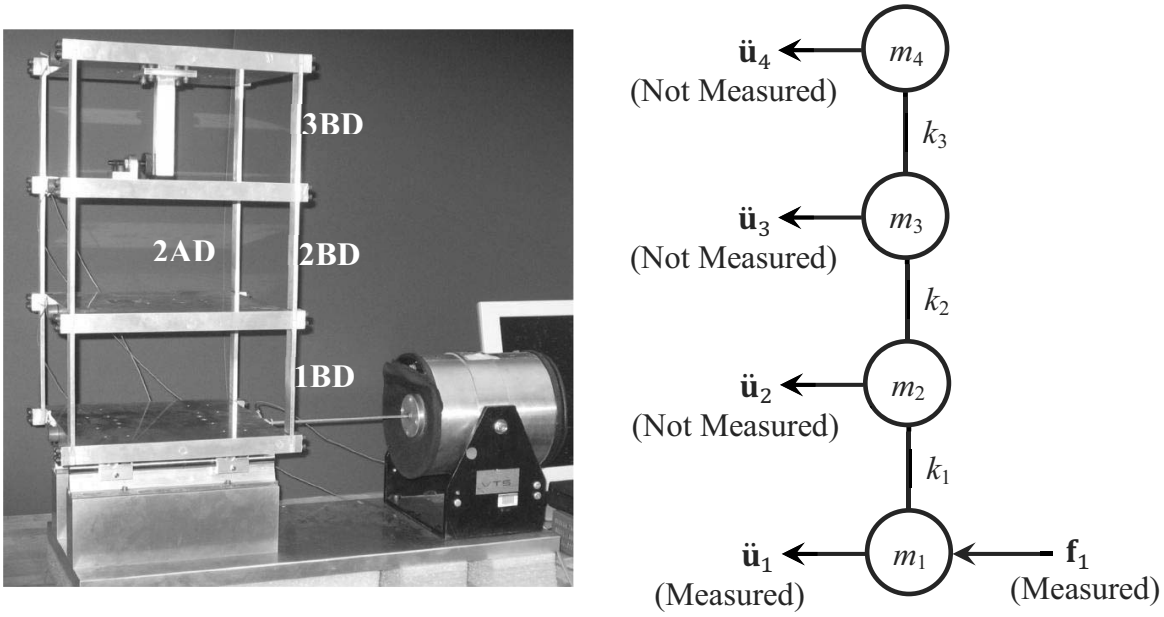

Figure 5.12: LANL test structure (adopted from [32]), and free-free analytical model assumed in this paper (with known input $\mathbf{f}_1$, and measured output $\ddot{\mathbf{u}}_1$).

Table 5.9: Different states of the LANL test structure (from [32]) considered in this paper.

State	Description	*Approximate* (*theoretical*) effect on baseline condition model
DS0	Baseline condition	
DS1	1.2 kg mass added at base	$m_1 = 1.19 m_{1_{\text{State 1}}}$
DS2	Stiffness of column 1BD reduced	$k_1 = 0.78 k_{1_{\text{State 1}}}$
DS3	Stiffness of column 2BD reduced	$k_2 = 0.78 k_{2_{\text{State 1}}}$
DS4	Stiffness of columns 2AD and 2BD reduced	$k_2 = 0.56 k_{2_{\text{State 1}}}$
DS5	Stiffness of column 3BD reduced	$k_3 = 0.78 k_{3_{\text{State 1}}}$

Table 5.10: Statistics of modal frequency and damping ratio estimates using OKID/ERA, for modes 2 to 4 of the LANL test structure.

State	μ_f (Hz)	COV$_f$ (%)	μ_ς (%)	COV$_\varsigma$ (%)
DS0	$31.3, 55.0, 72.3$	$0.1, 0.1, 0.2$	$4.1, 0.9, 1.1$	$1.7, 6.1, 18.1$
DS1	$30.5, 53.9, 71.8$	$0.2, 0.0, 0.1$	$4.3, 0.8, 0.8$	$2.4, 7.7, 17.8$
DS2	$31.0, 51.8, 70.3$	$0.3, 0.1, 0.1$	$4.3, 1.1, 0.5$	$2.9, 7.2, 19.3$
DS3	$30.4, 55.2, 68.1$	$0.3, 0.1, 0.2$	$3.8, 0.9, 1.7$	$2.1, 6.2, 17.4$
DS4	$27.7, 54.8, 63.1$	$0.3, 0.0, 0.1$	$4.5, 0.7, 2.0$	$2.1, 6.3, 12.4$
DS5	$30.1, 51.7, 70.5$	$0.2, 0.1, 0.1$	$3.8, 1.2, 0.6$	$2.3, 5.8, 12.6$

reduction. In Fig. 5.13 we plot the squares of the frequencies against the damage severity x, for states DS0, DS3 and DS4, along with the best fit line (in a least squares sense) describing the f^2–x relationship. Note that both DS3 and DS4 have second story damage of different severities. This figure agrees with the discussion in Section 5.1.2, i.e.: (a) the squares of each modal frequency decrease linearly with damage severity, for damage at any single floor, (b) the squares of the frequencies of the baseline (DS0) system, $\{979.69, 3025, 5227.29\}$, are comparable to the corresponding constant terms (b_j in Eq. (5.2)) in these linear relationships, and (c) the slopes (a_j in Eq. (5.2)) are higher for higher modes, i.e. damage may be more easily detected from changes in the higher mode eigenvalues (see the third relationship in Eq. (5.3), Section 5.1.2). Although the third modal frequency seems to contradict this discussion on the linear f^2–x relationship, from the frequencies in Table 5.10 and the slope to constant term ratios for the best-fit lines in Fig. 5.13, it is evident that this mode is not significantly affected by damage in the second floor.

Fig. 5.14 compares the mean (from the 50 tests) identified complete mass normalized mode shapes of the healthy state, with those identified in states DS3 and DS4 (both having a 2nd story stiffness reduction, with different severities). Evidently, by just looking at the mode shape plots, although it may be possible to infer that the three depicted states are different, it is not possible to decipher what/where are the changes. The mode shapes obtained in the other states are similar, and are not included here as they do not provide any additional information. To condense the information in mode shape comparison, we again use the MAC, COMAC, FPMAC and FPCOMAC values. Table 5.11 lists these measures comparing the different states with the baseline (healthy) state. Note that:

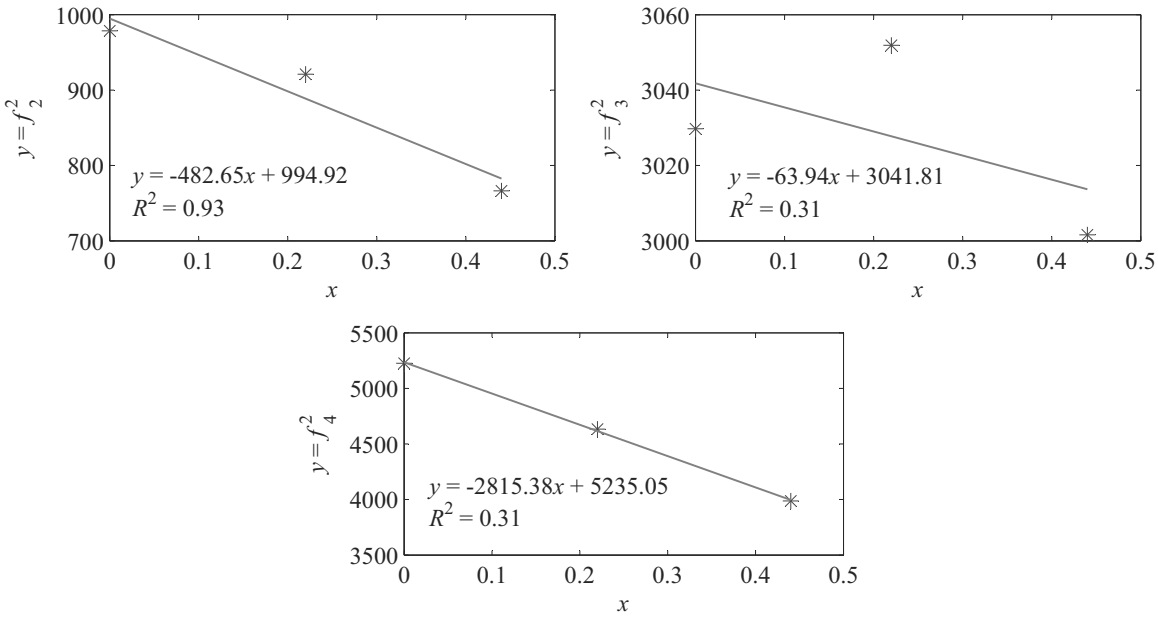

Figure 5.13: Square of structural frequencies vs. damage severity for LANL frame.

(a) the MAC and FPMAC values are only presented for modes 2 to 4, since for the rigid body mode, MAC and FPMAC are always identically 1.00, (b) in the COMAC and FPCOMAC computations we have not used the rigid body mode, and (c) FPMAC/FPCOMAC values over 1 indicate an increase in modal/coordinate flexibility. Evidently, these measures (especially FPCOMAC) may be used to signal a departure from the baseline state, although it is still not possible to distinguish between structural mass changes and structural stiffnesses changes. The maximum of the FPCOMAC values ($\{1.12, 1.13, 1.39, 1.19\}$ in States $\{\text{DS2}, \text{DS3}, \text{DS4}, \text{DS5}\}$) also seems to indicate an approximate location of structural damage. In State DS5, the FPMAC values do not show an increase in modal flexibility induced by damage; this is possibly due to FPMAC not including the effect of frequency changes, unlike FPCOMAC. Although FPMAC/FPCOMAC signals the presence of damage in this example, for free-free systems the use of these measures may not be very suitable, since they were defined to mimic the changes in the structural flexibility matrix, which is undefined for a free-free system due to $\mathbf{K}$ being singular. This is found to be especially true when evaluating (using Eq. (5.4)) and plotting the complete eFPCOMAC matrix, i.e. the $\text{FPCOMAC}_{i,k} - 1 = -\text{eFPCOMAC}_{i,k}$ values, for all $i, k = \{1, 2, 3, 4\}$, as in Section 5.1.3. Fig. 5.15 shows this plot for the different damaged states of the LANL frame; it is apparent that we cannot correctly detect the possible location of damage from

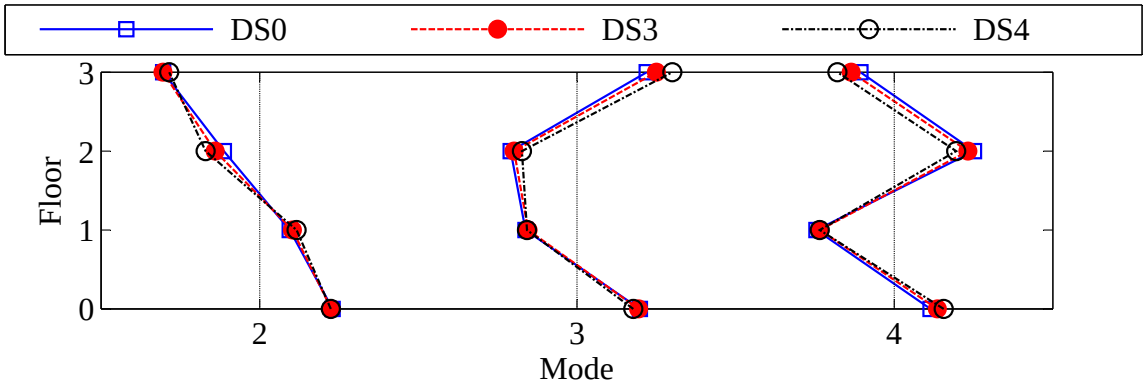

Figure 5.14: Comparison of mean mass normalized mode shapes estimated for States DS0 (baseline), DS3 ($\approx 20\%$ damage in k_2) and DS4 ($\approx 40\%$ damage in k_2).

Table 5.11: Comparison of baseline state (State DS0) with other states using mean mass normalized mode shapes.

State	MAC	FPMAC	COMAC	FPCOMAC
DS1	1.00, 0.99, 1.00	0.98, 1.02, 0.96	1.00, 0.99, 1.00, 1.00	0.99, 1.02, 1.09, 1.08
DS2	1.00, 0.98, 0.97	0.94, 1.04, 1.01	0.99, 0.98, 0.97, 1.00	1.12, 0.96, 1.01, 1.03
DS3	1.00, 0.99, 0.99	1.13, 0.98, 1.21	1.00, 1.00, 0.99, 0.99	0.99, 1.05, 1.13, 1.07
DS4	0.98, 0.95, 0.93	1.35, 0.96, 1.53	0.98, 0.99, 0.94, 0.95	1.13, 1.29, 1.39, 1.21
DS5	0.99, 0.99, 0.99	0.90, 0.97, 0.95	1.00, 0.99, 0.99, 0.99	0.98, 1.02, 1.05, 1.19

this plot, unlike the earlier case of the 4-story fixed-base frame (Figs. 5.5 and 5.6 in Section 5.1.3).

5.2.2 Comparing mean identified physical parameters

Table 5.12 lists the ratios of the mean identified floor masses and story stiffnesses in the different states to the corresponding mean estimates in the healthy state. Comparing the stiffness ratios with the theoretical approximates listed in Table 5.9, it is evident that the mean of the identified story stiffnesses may be used to detect both the damage location and severity with reasonable accuracy. On the other hand, from the ratio of the floor masses, although the location and amount of an increase in the base mass is accurately reflected in State DS1, even in the other states (especially for State DS4 with severe damage) the floor mass ratios show some departure from 1.00. This may be attributed to the

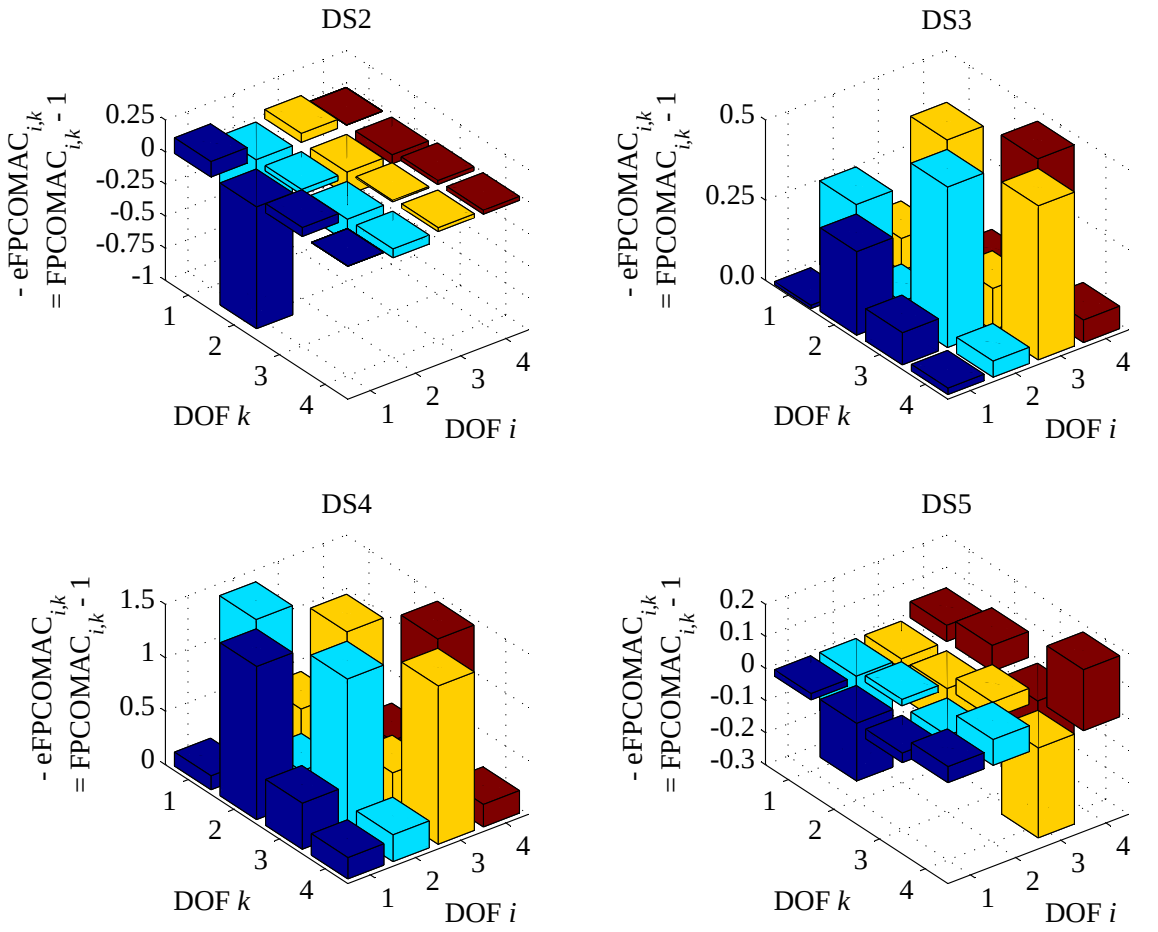

Figure 5.15: Computed $-\text{eFPCOMAC}_{i,k} = \text{FPCOMAC}_{i,k} - 1$ values between the four damaged states (DS2 to DS5) and the healthy state (DS0) of the LANL frame.

Table 5.12: Comparison of baseline state (State DS0) with other states using mean floor mass and story stiffness estimates.

State	$\mu_{m_{\text{State}\#}}/\mu_{m_{\text{State1}}}$	$\mu_{k_{\text{State}\#}}/\mu_{k_{\text{State1}}}$
DS1	$1.15, 1.00, 1.01, 1.01$	$0.99, 1.01, 1.02$
DS2	$0.97, 1.07, 0.99, 0.95$	$0.81, 1.03, 0.97$
DS3	$0.99, 1.05, 1.04, 0.90$	$1.01, 0.82, 0.99$
DS4	$0.99, 1.01, 1.16, 0.79$	$0.95, 0.60, 0.97$
DS5	$1.03, 1.01, 0.99, 0.96$	$0.98, 1.00, 0.79$

error induced by the inaccuracy in the total mass information M_T, whose use in the identification is not simply for scaling purposes (see Section 2.6). Moreover, the "fictitious" change in the estimated floor mass being more pronounced in case of severe damage, in the neighbourhood of the damage location, indicates that a "true" severe decrease in story stiffness possibly also shows up as a "fictitious" increase in the floor mass at the same location; this may be due to the fact that an increase in mass and decrease in stiffness affect the system's dynamics (especially eigenvalues) in a similar way. Nonetheless, unlike the modal parameter based damage assessment discussed previously, comparing the mean identified physical parameters provide us with a more complete and accurate damage assessment, detecting the existence, location and severity of story stiffness reduction, as well as letting the "true" stiffness change estimation be uncorrupted by any "true"/"fictitious" mass change.

5.2.3 Probabilistic damage assessment

The probabilistic damage assessment approach discussed in Section 5.1.5 is applied on the data from the LANL frame in this section. This approach attempts to account for the inherent variability within any given state of the system by characterizing the damage location and severity in a probabilistic sense. In this section, we additionally consider the situation where we may have a lot of test data from the healthy state, but a much reduced set of data from a possibly damaged (or healthy) state. This may be a very realistic scenario, where any incipient damage in the structure needs to be detected as soon as possible, to avoid further deterioration or even structural failures leading to casualties. Thus it is necessary that a damage detection method be able to perform reliably well even with limited data

from the possibly damaged state of the system.

Based on the above discussion, out of the 50 tests performed on the healthy state (DS0), we randomly choose 40 tests for which we *know* that the system is healthy (*baseline* state). The remaining 10 tests on DS0 are treated as tests where we do not know whether or not the system is healthy. (These 10 tests are treated as unknown state since it is as important to be able to identify an undamaged structure as undamaged, as it is to be able to classify a damaged structure as damaged, so as not to unnecessarily interrupt the normal operations on the structure, leading to economic losses and reduced confidence in the health monitoring system [56].) Similarly, 10 tests are randomly picked (from the 50 tests) for each of the other states (DS1 to DS5). The identified story stiffnesses in each test are then used to compute the k_R values using Eq. (5.6); in this way, we have a total of $40 \times 39 = 1560$ k_R values comparing the baseline state to itself, through different tests; and $10 \times 40 = 400$ k_R values comparing the unknown states to the baseline state. The means and coefficients of variation of the 1560 k_R values comparing the baseline state to itself are respectively $\{1, 1, 1\}$ and $\{1.38, 0.56, 1.31\}$. Table 5.13 lists the means and coefficients of variation of the 400 k_R values comparing the unknown states to the baseline state, for each of the 6 states considered in this example. The mean values in Table 5.13 being close to the ratios in Table 5.12 indicates that the k_R values can be used for accurate detection of damage location and severity, even when much lesser data is available from the unknown state. The low coefficients of variation of the k_R values suggest that even significantly low levels of damage may be detected using the k_R values. Fig. 5.16 shows as an example the comparison of the ECDFs obtained for the unknown States DS0, DS3 and DS4, with the baseline ECDF F_H; note that the ECDFs in State DS0 (baseline state treated as unknown) almost overlap with the corresponding F_H's.

To detect the presence of damage at a story in an unknown state $\#$, the $\mathcal{P}$ values are computed using Eq. (5.7), as in Section 5.1.5. Such a calculation is also illustrated in Fig. 5.17 for State DS5, and the $\mathcal{P}$ values for all the 3 stories in the 6 states are listed in Table 5.13. Recall that these $\mathcal{P}$ values denote the mismatch between an ECDF of k_R values comparing an unknown state to the baseline state, $F_{\#}$, and the corresponding ECDF of k_R values comparing the baseline state to itself, F_H; the higher the $\mathcal{P}$ value the greater is the mismatch between the involved ECDFs and higher is the probability of damage existence at that location. We again arbitrarily select 0.90 (same as in Section 5.1.6) as a threshold for the $\mathcal{P}$ values to classify a given location as damaged or healthy, i.e. $\mathcal{P} > 0.90$

Table 5.13: Statistics of k_R, and $\mathcal{P}$ values of mismatch between ECDFs of k_R in different states (10 tests) with baseline ECDF (40 tests).

State	μ_{k_R}	COV_{k_R} (%)	$\mathcal{P}$
DS0	$1.00, 1.00, 1.00$	$1.48, 0.52, 1.39$	$0.06, 0.05, 0.07$
DS1	$0.99, 1.01, 1.02$	$1.19, 0.57, 1.12$	$0.10, 0.33, 0.19$
DS2	$0.81, 1.03, 0.97$	$1.31, 0.75, 1.33$	$1.00, 1.00, 0.73$
DS3	$1.01, 0.82, 0.99$	$1.64, 0.65, 1.48$	$0.12, 1.00, 0.27$
DS4	$0.95, 0.60, 0.97$	$1.15, 0.67, 1.04$	$1.00, 1.00, 0.80$
DS5	$0.98, 1.00, 0.79$	$1.05, 0.55, 1.04$	$0.23, 0.11, 1.00$

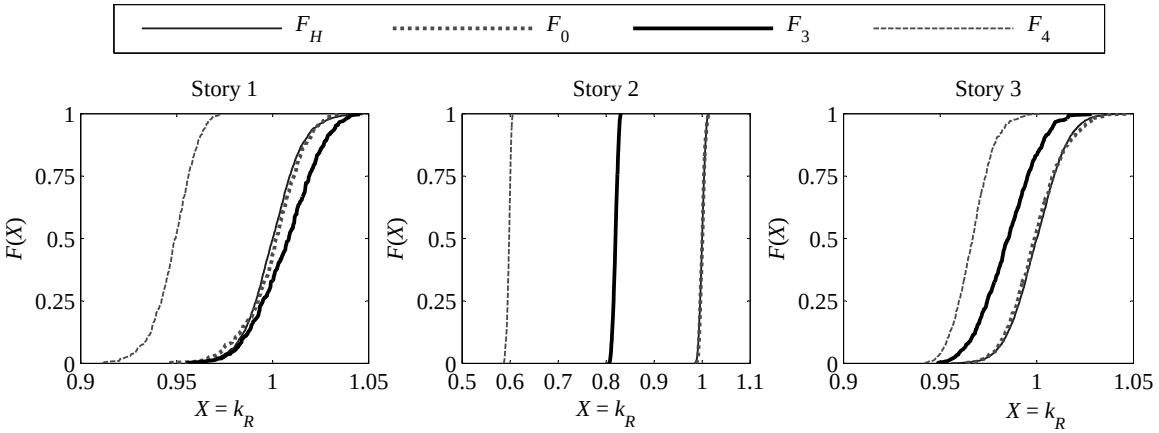

Figure 5.16: ECDFs of k_R comparing States DS0 (baseline), DS3 ($\approx 20\%$ damage in k_2) and DS4 ($\approx 40\%$ damage in k_2), with baseline ECDFs.

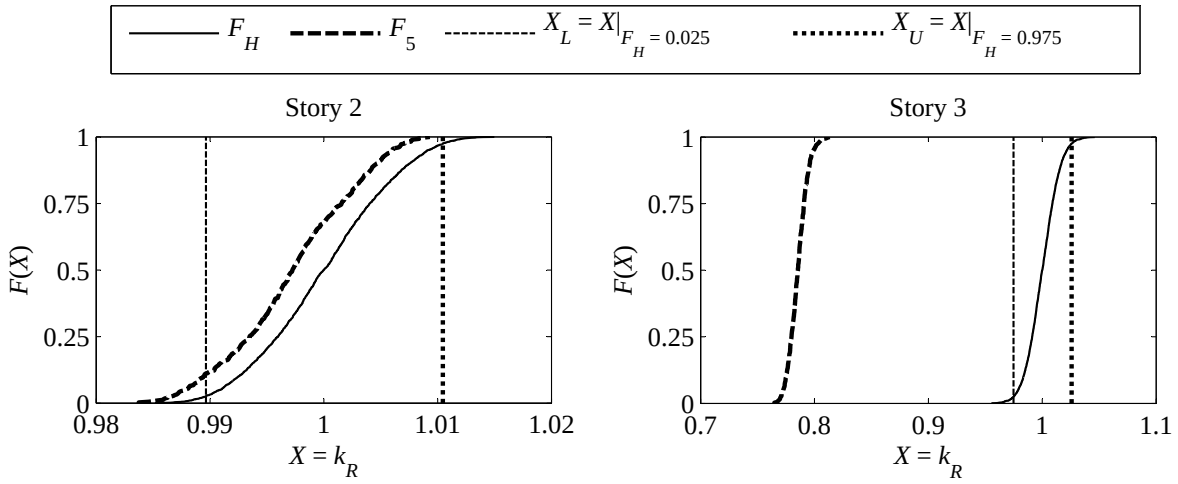

Figure 5.17: Calculation of $\mathcal{P}$ values for 2nd and 3rd stories in State DS5: $\mathcal{P} = 1 - (F_5|_{k_R=X_U} - F_5|_{k_R=X_L})$.

would indicate that the story under consideration is damaged, otherwise healthy. Considering the classifications for each of the 3 stories in each of the 6 damaged states as separate events, we have a total of $3 \times 6 = 18$ such events, 4 of which should be damaged (story 1 in states DS2, and story 2 in states DS3 and DS4, and story 3 in state DS5), and the remaining 14 should be undamaged. With the threshold of 0.90, the $\mathcal{P}$ values in Table 5.13 correctly classify all the 4 damaged stories, while 2 healthy stories are misclassified as damaged; thus the misclassification rates are 0% false-negative (damaged classified as healthy) and 14% false-positive (healthy classified as damaged).

Finally, the damage severity assessment is also performed as in Section 5.1.5, by comparing different percentiles of the ECDFs of the healthy-to-healthy and damaged-to-healthy k_R values, F_H and $F_\#$. Figs. 5.18 show some example percentile comparison for the 3rd story in State DS5; the color surface plot obtained by comparing all the percentiles of F_H and F_5 is shown in Fig. 5.19, along with the exceedance probability ($F_D(d)$) vs. damage severity (d) curves corresponding to the 5th (least safe), 50th and 95th (most conservative) percentiles of F_H. As in Section 5.1.6, here too we see the increase of damage severity with decreasing probability of exceedance for a given percentile of F_H, and increasing percentiles of F_H for a given probability of exceedance. Fig. 5.20 shows the color surface plots for the damage severities at the 1st and 2nd stories in State DS4; note that the range of damage severity is much lower in the 1st story, which is actually an undamaged location,

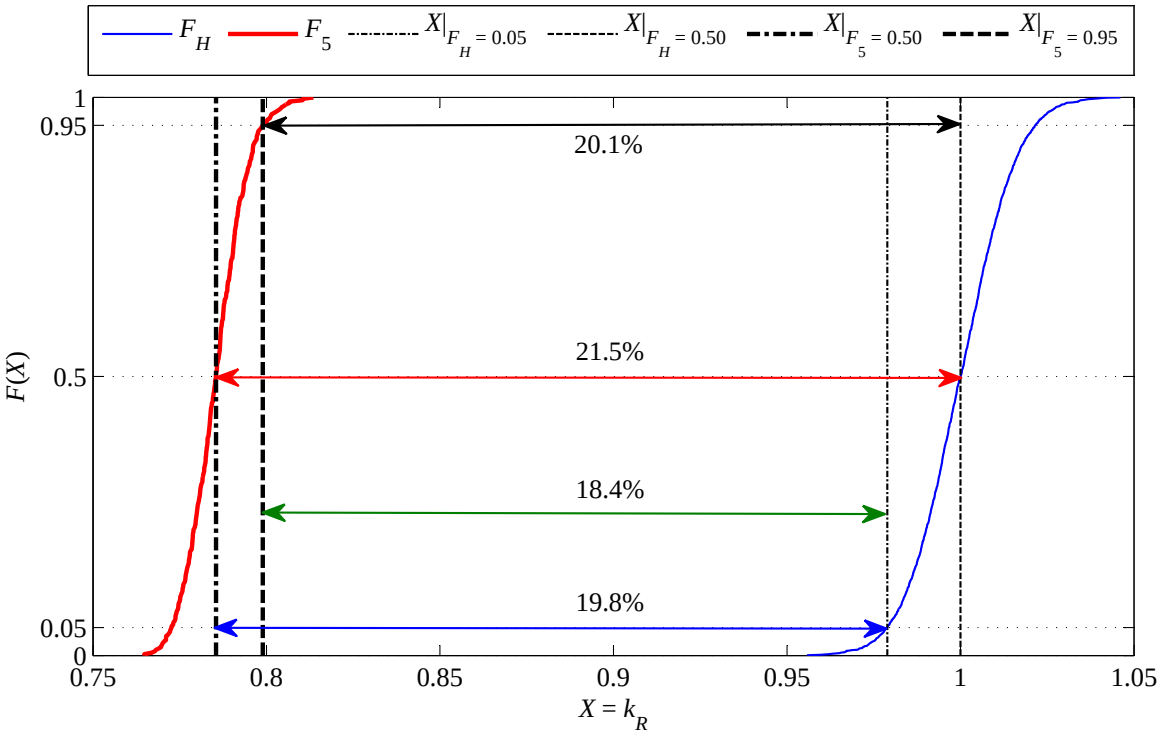

Figure 5.18: Probabilistic characterization of damage severity at 3rd story in State DS5. There is: (a) a 95% probability of at least 20.1% damage with respect to the median baseline k_R (= 1.00), (b) a 50% probability of at least 21.5% damage with respect to the median baseline k_R, (c) a 95% probability of at least 18.4% damage with respect to the 5th percentile baseline k_R (= 0.98), (d) a 50% probability of at least 19.8% damage with respect to the 5th percentile baseline k_R, etc.

classified as damaged using the $\mathcal{P}$ value threshold of 0.90 in Table 5.13.

5.3 Conclusions

In this chapter the applicability of the structural identification methods, discussed in Chapters 2 and 3, in structural health monitoring is studied. Experimental data from different damaged versions of a 4 story steel frame subjected to base excitation on a shake table facility are used with the method in Chapter 3; while experimental data from different damaged versions of a 3 story frame tested in the LANL are used with the method of Chapter 2. The healthy versions of these two frames were respectively used in Chapters 3 and 2 earlier as experimental applications. Structural damages in these

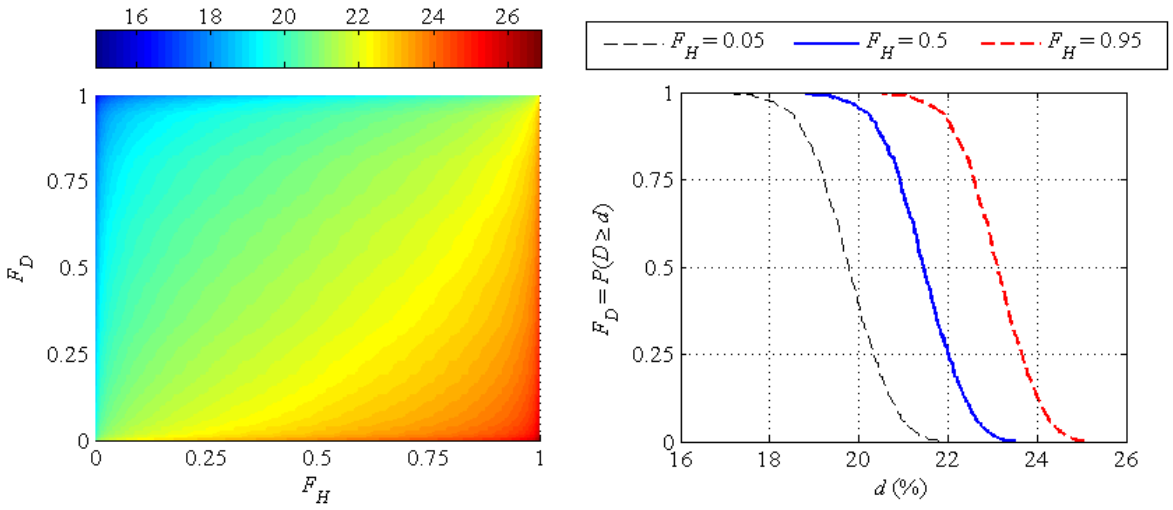

Figure 5.19: Complete probabilistic description of damage severity at 3rd story in State DS5, including baseline variability; and probability of exceedance vs. damage severity curves for some particular percentiles of F_H.

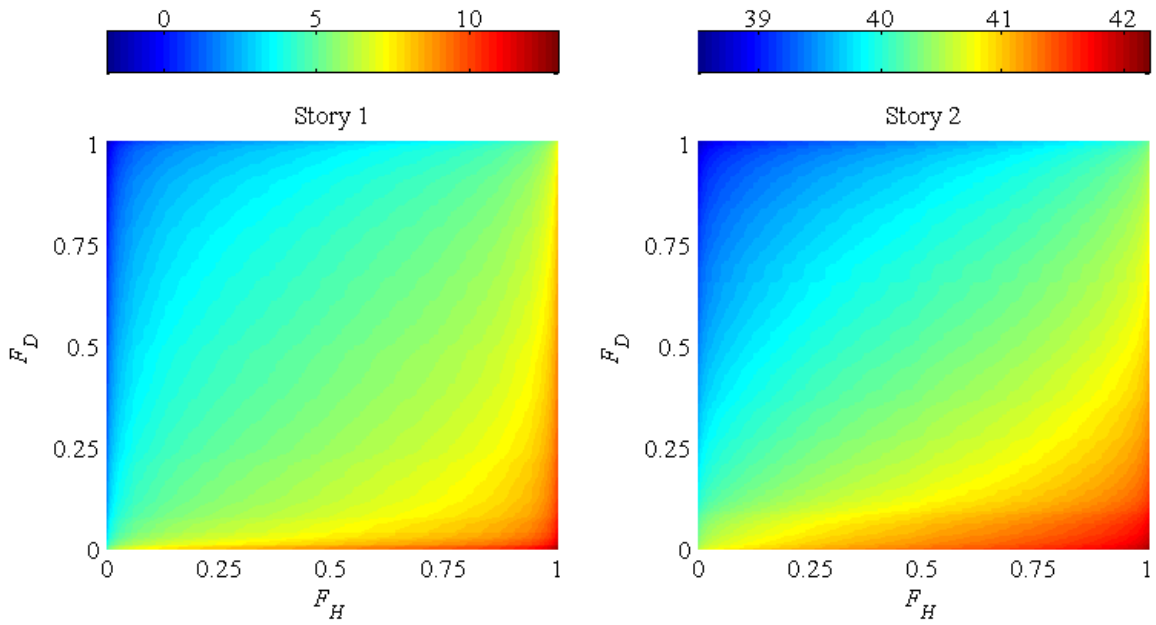

Figure 5.20: Comparison of complete probabilistic descriptions of damage severity at 1st and 2nd stories in State DS4.

frames are simulated by replacing some columns of the healthy frames with columns of reduced cross-sectional area; for the LANL frame, a case of mass modification, with an added mass on the base plate of the frame, is also included. The structural identification methods are applied to these experimental data, considering different scenarios of instrumentation and available *a priori* information. The different identified modal and physical parameters are then used for different levels of structural damage assessment. It is seen that, using the modal parameter comparative measures defined in Appendix D, one may be able to identify the existence and location of damage in a system. Moreover, while the discrepancies in the available amount of data and modeling assumptions in the different experimental scenarios, as well as the different types of inputs used in different tests and the presence of measurement noise/ambient effects, introduce discrepancies in the identified physical models, if the instrumentation, modeling assumptions, and operations in the identification exercise are consistent between the healthy and the damaged states of the system, reasonably accurate estimation of both the damage location and severity is achieved using the mean identified physical parameters. A probabilistic damage detection framework based on the structural identification results is also proposed, which intends to account for the uncertainties induced by exogenous factors like environmental/operational fluctuations, measurement noise etc. This framework considers the ratio between estimated story stiffnesses from two tests for damage assessment. The possible existence/location of damage is detected using a measure of mismatch, $\mathcal{P}$, between the distributions of these ratios obtained comparing the possibly damaged state to the healthy state, and the healthy state to itself. The reasonably low misclassification rates, and the generally wide separation of the $\mathcal{P}$ values between the damaged and most of the undamaged locations, highlights the potential of the present analysis in meeting both the requirements of a useful classification tool, i.e. classifying undamaged as undamaged and damaged as damaged; the simultaneous satisfaction of both these requirements is necessary for the successful application of any algorithm solving classification problems, and damage detection problems are a subset of such problems. The severity of damage is also expressed in a probabilistic sense. The advantages of such a probabilistic description of damage severity are: (a) accounting for the uncertainty in the baseline (healthy) state and the current state, and (b) providing exceedance probability vs. damage severity curves, for different levels of confidence in the baseline state, which may be expected to help the concerned authorities in the decision making process. The reasonable accuracy in damage detection even with incomplete instrumentation, lack of measurements from a damaged story, and

incomplete and uncertain available *a priori* information about the system, highlights the potential of the structural identification approaches in structural health monitoring applications.

5.3.1 Directions for future research

While this chapter presents some preliminary attempts on structural damage assessment in a probabilistic framework, using the ratios of identified story stiffnesses (k_R) from different tests, there exists an extensive scope of possible future research and improvements in this direction. Firstly, the use of the $\mathcal{P}$ values for classifying a story as damaged or undamaged requires the selection of a threshold to define the boundary between damaged and undamaged; this threshold is selected arbitrarily in this chapter, and hence suffers from a degree of subjectivity. An objective selection criteria needs to be investigated, possibly using the k_R values comparing the baseline state to itself, and employing statistical distance calculations as in [35, 84]. Secondly, while the statistical damage detection here considers each story individually, it may be better to consider all the stories together, using a vector of k_R ratios and multivariate statistical analysis. This is because, non-damage induced variability in the story stiffnesses may often be expected to have a similar nature or moderately well-defined pattern, e.g. ambient mean temperature changes should affect all the columns approximately alike, heating due to facing the sun should affect all the columns at the sun-facing side in much the same way, etc. Thirdly, while the color plots of damage severity and/or the exceedance probability vs. damage severity curves may be expected to help in making decisions on whether or not to indulge in repairing/retrofitting the current state of the system, the appropriate way to interpret these plots/curves to arrive at a finite set of numbers or indices for decision making still needs to be explored. It needs to be studied whether the information contained by such plots/curves may be incorporated in remaining service life assessments, and in cost-benefit analyses of possible intervention (maintenance and repairing) strategies. Fourthly, the approach discussed here should also theoretically be applicable with other damage sensitive features (here the k_R values), e.g. simply the identified story stiffnesses, as long as sufficient data is available to construct stable ECDF representations of the variability in the features considered. However, performance of the approach with other features needs to be verified using experimental data. Applying the approach with other features may also help in identifying the sensitivity of different features to (a) exogenous factors, e.g. environemntal/operational variability, vis-a-vis damage, as well as (b) different types of damage; this in turn would help in choosing

appropriate features for damage detection. Finally, an alternative probabilistic damage assessment procedure, which also attempts to account for non-damage induced variabilities, involves the use of lower and upper bound ECDFs of damage sensitive features to define a normal (non-damage induced) range of variability of such features [44]. This approach is similar to the one discussed here, in that the damage detection is performed by comparing the ECDFs obtained from tests on the current state of the system with the baseline ECDFs built from tests on the baseline (healthy) system. However, the two approaches differ in the way they attempt to account for the inherent (non-damage induced) variability in the different states of the system, and consequently they also differ in their final probabilistic representation of damage severity. The comparative advantages/disadvatages of the two approaches, and their possible integration needs to be studied.

Chapter 6

Uncertainty Propagation in Output-Only Structural Identification with Incomplete Information[1]

The inevitable presence of measurement noise, uncertainties introduced by environmental/ambient fluctuations, incompleteness in the measured information, and incomplete and uncertain available *a priori* information about the system, often necessitates that the identification of the structural parameters be performed in a probabilistic framework [86]. In this chapter, we consider a possible probabilistic description of the problems of mode shape expansion, normalization, and subsequent physical parameter identification, under the constraints of incomplete measured/assumed information and ambient vibration testing condition, by extending the structural topology based identification approach of Chapter 4 to a probabilistic framework. The proposed extension starts from a probabilistic description of the incomplete non-normalized modal parameters at the sensor locations; this description contains the uncertainty in these parameters induced by measurement noise and ambient fluctuation effects. This uncertainty is next propagated through the nonlinear system of equations involved in the mode shape expansion (Section 4.2.1), and through the subsequent nonlinear parameter estimation equations (Section 4.2.2), using a mean centered first order perturbation approach (see,

[1] A preliminary form of this chapter was presented as a conference paper, co-authored with Profs. Raimondo Betti and Hilmi Lus, in the 11th International Conference on Structural Safety and Reliability, New York, 2013 [85].

e.g., [87]). This forward propagation of uncertainty also takes into account the uncertainty in any assumed *a priori* information, e.g. the total mass of the system, necessary for scaling the identified proportional system. The performance of the perturbation approach, in quantifying the uncertainty induced by measurement noise and ambient structural variability, is evaluated using simulated data and comparing the estimated probability distributions with those obtained from Monte Carlo simulations.

6.1 Uncertainty Propagation Using Mean Centered First Order Perturbation

We make two assumptions in our analysis: (1) the distributions of the different involved modal and physical parameters can be well approximated by Gaussian distributions, i.e. these distributions may be described using only the means and variances, and (2) the uncertainties in the different parameters are not very high, i.e. a first order perturbation may be applied. The second assumption may be expected to be valid for estimates obtained from tests on the same state of the structure, so that the variability in the parameters result mainly from estimation errors and environmental/ambient fluctuations, and there is no severe damage induced change.

Let us first consider the proportional mode shape matrix estimation approach of Section 4.2.1. For an N-DOF shear–type system, instrumented with N_s sensors located at the DOFs in $\mathcal{S} = \{s_1, \cdots, s_{N_s}\}$, we have the following nonlinear system of $N(N + N_s - 2)$ equations:

$$\mathbf{g}(\boldsymbol{\alpha}, \boldsymbol{\theta}) = \mathbf{0} \tag{6.1}$$

where:

$$\begin{aligned} \boldsymbol{\theta} &= \{v^*_{1,1}, \cdots, v^*_{1,N}, v^*_{2,1}, \cdots\cdots, v^*_{N,N}\}^T \setminus \{v^*_{s_1,1}\} \\ \boldsymbol{\alpha} &= \{\lambda_1, \cdots, \lambda_N, \frac{\tilde{v}_{s_2,1}}{\tilde{v}_{s_1,1}}, \cdots, \frac{\tilde{v}_{s_2,N}}{\tilde{v}_{s_1,N}}, \cdots\cdots, \frac{\tilde{v}_{s_{N_s},N}}{\tilde{v}_{s_1,N}}\}^T \end{aligned} \tag{6.2}$$

are respectively the $(N^2 - 1) \times 1$ and $NN_s \times 1$ vectors of unknown and known parameters; the $v^*_{i,j}$'s are the unknown elements of the proportional normalized mode shape matrix $\mathbf{V}^*$, with $v^*_{s_1,1}$ arbitrarily assumed to be 1; the λ_j's are the known (identified) eigenvalues; and the $\tilde{v}_{s_i,j}$'s are known (identified) non-normalized mode shape components at the sensor locations in $\mathcal{S}$. The symbol "\" in Eq. (6.2) denotes the set difference operation. In Section 4.2.1, we solve Eq. (6.1) for the unknowns in $\boldsymbol{\theta}$, given the known parameters in $\boldsymbol{\alpha}$.

We now attempt to cast the above deterministic equations in a probabilistic framework. To that end, assume that we have an estimate of the mean vector, $\boldsymbol{\mu}_{\boldsymbol{\alpha}}$, and of the covariance matrix, $\mathbf{C}_{\boldsymbol{\alpha}\boldsymbol{\alpha}}$, of the modal parameter vector $\boldsymbol{\alpha}$. Such estimates may be obtained by statistical processing of multiple sets of output records [88], or even from a single set of output time histories [89, 90]. Let $\boldsymbol{\theta} = \boldsymbol{\theta}^*$ satisfy Eq. (6.1) for $\boldsymbol{\alpha} = \boldsymbol{\mu}_{\boldsymbol{\alpha}}$, i.e. let $\mathbf{g}(\boldsymbol{\mu}_{\boldsymbol{\alpha}}, \boldsymbol{\theta}^*) = \mathbf{0}$. Knowing $\boldsymbol{\mu}_{\boldsymbol{\alpha}}$, $\boldsymbol{\theta}^*$ can be estimated following the Newton-Raphson procedure discussed in Section 4.2.1. Then, approximating $\mathbf{g}(\boldsymbol{\alpha}, \boldsymbol{\theta})$ through a first–order Taylor series expansion about $(\boldsymbol{\mu}_{\boldsymbol{\alpha}}, \boldsymbol{\theta}^*)$, for any $(\boldsymbol{\alpha}, \boldsymbol{\theta})$ in the neighborhood of $(\boldsymbol{\mu}_{\boldsymbol{\alpha}}, \boldsymbol{\theta}^*)$ and satisfying Eq. (6.1) (i.e. $\mathbf{g}(\boldsymbol{\alpha}, \boldsymbol{\theta}) = \mathbf{0}$), we get:

$$\mathbf{g}(\boldsymbol{\alpha}, \boldsymbol{\theta}) \approx \mathbf{g}(\boldsymbol{\mu}_{\boldsymbol{\alpha}}, \boldsymbol{\theta}^*) + \left.\frac{\partial \mathbf{g}(\boldsymbol{\alpha}, \boldsymbol{\theta})}{\partial \boldsymbol{\alpha}}\right|_{\substack{\boldsymbol{\alpha}=\boldsymbol{\mu}_{\boldsymbol{\alpha}} \\ \boldsymbol{\theta}=\boldsymbol{\theta}^*}} \{\boldsymbol{\alpha} - \boldsymbol{\mu}_{\boldsymbol{\alpha}}\} + \left.\frac{\partial \mathbf{g}(\boldsymbol{\alpha}, \boldsymbol{\theta})}{\partial \boldsymbol{\theta}}\right|_{\substack{\boldsymbol{\alpha}=\boldsymbol{\mu}_{\boldsymbol{\alpha}} \\ \boldsymbol{\theta}=\boldsymbol{\theta}^*}} \{\boldsymbol{\theta} - \boldsymbol{\theta}^*\}$$

$$\Rightarrow \{\boldsymbol{\theta} - \boldsymbol{\theta}^*\} \approx -\mathbf{S}\{\boldsymbol{\alpha} - \boldsymbol{\mu}_{\boldsymbol{\alpha}}\} \tag{6.3}$$

where

$$\mathbf{S} = \left(\left[\frac{\partial \mathbf{g}(\boldsymbol{\alpha}, \boldsymbol{\theta})}{\partial \boldsymbol{\theta}}\right]^{\dagger} \left[\frac{\partial \mathbf{g}(\boldsymbol{\alpha}, \boldsymbol{\theta})}{\partial \boldsymbol{\alpha}}\right] \right) \Bigg|_{\substack{\boldsymbol{\alpha}=\boldsymbol{\mu}_{\boldsymbol{\alpha}} \\ \boldsymbol{\theta}=\boldsymbol{\theta}^*}} \tag{6.4}$$

From Eq. (6.3), the statistics of vector $\boldsymbol{\theta}$, and hence those of the elements of the proportional mode shape matrix $\mathbf{V}^*$, can be estimated as:

$$\boldsymbol{\mu}_{\boldsymbol{\theta}} \approx \boldsymbol{\theta}^*; \qquad \mathbf{C}_{\boldsymbol{\theta}\boldsymbol{\theta}} = \mathbf{S}\mathbf{C}_{\boldsymbol{\alpha}\boldsymbol{\alpha}}\mathbf{S}^T \tag{6.5}$$

The proportional and mass normalized mode shape matrices are related as $\mathbf{V}^* = v_{s_1,1}\mathbf{V}$. The scaling factor $v_{s_1,1}$ can be estimated using some assumed *a priori* information, as discussed in Section 4.2.2. Here we consider the total mass of the system, M_T, as this *a priori* information, so that $v_{s_1,1} = \sqrt{M_T^*/M_T}$, where $M_T^* = \sum_{i=1}^{N} m_i^*$ and $m_i^* = \left(\sum_{j=1}^{N} v_{i,j}^{*2}\right)^{-1}$, as per Section 4.2.2. Let μ_{M_T} and σ_{M_T} respectively denote the expected value and standard deviation of the total mass; μ_{M_T} may estimated from an engineering drawing of the structure, while σ_{M_T}, reflecting the uncertainty in this estimate, may be assumed depending on the confidence in the *a priori* system model/drawing. Then, applying a similar analysis as for $\boldsymbol{\theta}$, i.e. through a first–order expansion of $v_{s_1,1}$ about its estimate using $\boldsymbol{\mu}_{\boldsymbol{\theta}}$ and μ_{M_T}, followed by taking the statistical moments, with the statistical independence of

the uncertainties in the *a priori* information (M_T) and the experimental data, we get:

$$\begin{aligned}\mu_{v_{s_1,1}} &\approx v_{s_1,1}\big|_{\substack{M_T=\mu_{M_T}\\ \boldsymbol{\theta}=\boldsymbol{\mu}_{\boldsymbol{\theta}}}}\\ \sigma^2_{v_{s_1,1}} &\approx \left(\sigma^2_{M_T}\left(\frac{\partial v_{s_1,1}}{\partial M_T}\right)^2 + \left\{\frac{\partial v_{s_1,1}}{\partial \boldsymbol{\theta}}\right\}\mathbf{C}_{\boldsymbol{\theta}\boldsymbol{\theta}}\left\{\frac{\partial v_{s_1,1}}{\partial \boldsymbol{\theta}}\right\}^T\right)\Bigg|_{\substack{M_T=\mu_{M_T}\\ \boldsymbol{\theta}=\boldsymbol{\mu}_{\boldsymbol{\theta}}}}\end{aligned} \tag{6.6}$$

After the mean and variance of the scaling factor $v_{s_1,1}$ are estimated, the estimates of the mean vector and the covariance matrix of a vector $\boldsymbol{\phi}$ of the elements of $\mathbf{V}$:

$$\boldsymbol{\phi} = \{v_{1,1}, \cdots, v_{1,N}, v_{2,1}, \cdots\cdots, v_{N,N}\}^T \tag{6.7}$$

need to be determined. Let us first define a rearranged vector:

$$\mathbf{z} = \{v_{s_1,1}, \boldsymbol{\phi}^T_{1:N(s_1-1)}, \boldsymbol{\phi}^T_{N(s_1-1)+2:N^2}\}^T \tag{6.8}$$

where the indices in the subscripts denote the position of elements in the concerned vector/matrix, i.e. for any matrix $\mathbf{\Pi}$, $\mathbf{\Pi}_{i:j,k:l}$ denotes the sub-matrix constituted by the ith to jth rows and kth to lth columns of $\mathbf{\Pi}$. The rearrangement in (6.8) is only necessary for the ease of discussion and computer implementation of the equations, and accounts for the fact that the measured DOF s_1 is not necessarily DOF 1. The statistics of the rearranged vector $\mathbf{z}$ can be obtained from the first–order Taylor series expansion of $\mathbf{z} = v_{s_1,1}\left\{1 \quad \boldsymbol{\theta}^T\right\}^T$ as:

$$\begin{aligned}\boldsymbol{\mu}_{\mathbf{z}} \approx& \mu_{v_{s_1,1}}\left\{1 \quad \boldsymbol{\mu}^T_{\boldsymbol{\theta}}\right\}^T\\ \mathbf{C}_{\mathbf{zz}} \approx& \sigma^2_{v_{s_1,1}}\begin{bmatrix}1 & \boldsymbol{\mu}^T_{\boldsymbol{\theta}}\\ \boldsymbol{\mu}_{\boldsymbol{\theta}} & \boldsymbol{\mu}_{\boldsymbol{\theta}}\boldsymbol{\mu}^T_{\boldsymbol{\theta}}\end{bmatrix} + \mu^2_{v_{s_1,1}}\begin{bmatrix}0 & \mathbf{0}_{1\times(N^2-1)}\\ \mathbf{0}_{(N^2-1)\times 1} & \mathbf{C}_{\boldsymbol{\theta}\boldsymbol{\theta}}\end{bmatrix}\\ &+ \boldsymbol{\mu}_{\mathbf{z}}\left\{0 \quad \mathbf{C}_{v_{s_1,1}\boldsymbol{\theta}}\right\} + \left[\boldsymbol{\mu}_{\mathbf{z}}\left\{0 \quad \mathbf{C}_{v_{s_1,1}\boldsymbol{\theta}}\right\}\right]^T\end{aligned} \tag{6.9}$$

where, again using the statistical independence of M_T and the experimental data:

$$\mathbf{C}_{v_{s_1,1}\boldsymbol{\theta}} = \left\{\left\{\frac{\partial v_{s_1,1}}{\partial \boldsymbol{\theta}}\right\}\mathbf{C}_{\boldsymbol{\theta}\boldsymbol{\theta}}\right\}\Bigg|_{\substack{M_T=\mu_{M_T}\\ \boldsymbol{\theta}=\boldsymbol{\mu}_{\boldsymbol{\theta}}}} \tag{6.10}$$

The mean vector and covariance matrix of the vector $\boldsymbol{\phi}$ of Eq. (6.7) can then be obtained by rear-

rangement as:

$$\begin{aligned}\boldsymbol{\mu}_{\boldsymbol{\phi}} &= \left\{\{\boldsymbol{\mu}_{\mathbf{z}}^T\}_{2:N(s_1-1)+1}, \{\boldsymbol{\mu}_{\mathbf{z}}^T\}_1, \{\boldsymbol{\mu}_{\mathbf{z}}^T\}_{N(s_1-1)+2:N^2}\right\}^T \\ \mathbf{C}_{\boldsymbol{\phi}\boldsymbol{\phi}} &= \begin{bmatrix} \mathbf{C}_{\boldsymbol{\phi}\boldsymbol{\phi}}^{aa} & \mathbf{C}_{\boldsymbol{\phi}\boldsymbol{\phi}}^{ab} & \mathbf{C}_{\boldsymbol{\phi}\boldsymbol{\phi}}^{ac} \\ \mathbf{C}_{\boldsymbol{\phi}\boldsymbol{\phi}}^{ab\ T} & \mathbf{C}_{\boldsymbol{\phi}\boldsymbol{\phi}}^{bb} & \mathbf{C}_{\boldsymbol{\phi}\boldsymbol{\phi}}^{bc} \\ \mathbf{C}_{\boldsymbol{\phi}\boldsymbol{\phi}}^{ac\ T} & \mathbf{C}_{\boldsymbol{\phi}\boldsymbol{\phi}}^{bc\ T} & \mathbf{C}_{\boldsymbol{\phi}\boldsymbol{\phi}}^{cc} \end{bmatrix}\end{aligned} \tag{6.11}$$

where

$$\begin{aligned}\mathbf{C}_{\boldsymbol{\phi}\boldsymbol{\phi}}^{aa} &= [\mathbf{C}_{\mathbf{zz}}]_{2:N(s_1-1)+1,2:N(s_1-1)+1} \\ \mathbf{C}_{\boldsymbol{\phi}\boldsymbol{\phi}}^{bb} &= [\mathbf{C}_{\mathbf{zz}}]_{1,1} \\ \mathbf{C}_{\boldsymbol{\phi}\boldsymbol{\phi}}^{cc} &= [\mathbf{C}_{\mathbf{zz}}]_{N(s_1-1)+2:N^2,N(s_1-1)+2:N^2} \\ \mathbf{C}_{\boldsymbol{\phi}\boldsymbol{\phi}}^{ab} &= [\mathbf{C}_{\mathbf{zz}}]_{2:N(s_1-1)+1,1} \\ \mathbf{C}_{\boldsymbol{\phi}\boldsymbol{\phi}}^{ac} &= [\mathbf{C}_{\mathbf{zz}}]_{2:N(s_1-1)+1,N(s_1-1)+2:N^2} \\ \mathbf{C}_{\boldsymbol{\phi}\boldsymbol{\phi}}^{bc} &= [\mathbf{C}_{\mathbf{zz}}]_{1,N(s_1-1)+2:N^2}\end{aligned} \tag{6.12}$$

Eq. (6.11) provides the means and variances/covariances of the elements of the mass normalized mode shape matrix $\mathbf{V}$. Recall that, from the nature of the $\mathbf{M}$ and $\mathbf{F} = \mathbf{K}^{-1}$ matrices, any $M_{i,i} = m_i$ and any $F_{l,l} = \sum_{i=1}^{l} 1/k_i$, where m_i and k_i are the ith lumped (floor) mass and ith spring (story) stiffness, respectively. Using modal orthogonality, we can then write:

$$\begin{aligned} m_i &= \left(\sum_{j=1}^{N} v_{i,j}^2\right)^{-1} \qquad \forall\, i \in \{1, \cdots, N\} \\ k_i &= \begin{cases} \left(\sum_{j=1}^{N} \dfrac{v_{i,j}^2}{\lambda_j}\right)^{-1} & \text{for } i = 1 \\ \left(\sum_{j=1}^{N} \dfrac{v_{i,j}^2 - v_{i-1,j}^2}{\lambda_j}\right)^{-1} & \forall\, i \in \{2, \cdots, N\} \end{cases}\end{aligned} \tag{6.13}$$

From the first-order expansion of the above expressions, the means and variances/covariances of these masses and stiffnesses may finally be obtained, respectively as:

$$\begin{aligned} \mu_{m_i} &\approx m_i\big|_{\boldsymbol{\phi}=\boldsymbol{\mu}_{\boldsymbol{\phi}}} \\ \sigma_{m_i}^2 &\approx \left(\left\{\frac{\partial m_i}{\partial \boldsymbol{\phi}}\right\} \mathbf{C}_{\boldsymbol{\phi}\boldsymbol{\phi}} \left\{\frac{\partial m_i}{\partial \boldsymbol{\phi}}\right\}^T\right)\Bigg|_{\boldsymbol{\phi}=\boldsymbol{\mu}_{\boldsymbol{\phi}}} \\ \sigma_{m_i m_j} &\approx \left(\left\{\frac{\partial m_i}{\partial \boldsymbol{\phi}}\right\} \mathbf{C}_{\boldsymbol{\phi}\boldsymbol{\phi}} \left\{\frac{\partial m_j}{\partial \boldsymbol{\phi}}\right\}^T\right)\Bigg|_{\boldsymbol{\phi}=\boldsymbol{\mu}_{\boldsymbol{\phi}}}\end{aligned} \tag{6.14}$$

and

$$\begin{aligned}
\mu_{k_i} \approx & k_i\big|_{\boldsymbol{\phi}=\boldsymbol{\mu}_{\boldsymbol{\phi}},\boldsymbol{\lambda}=\boldsymbol{\mu}_{\boldsymbol{\lambda}}} \\
\sigma^2_{k_i} \approx & \left(\left\{\frac{\partial k_i}{\partial \boldsymbol{\phi}}\right\}\mathbf{C}_{\boldsymbol{\phi}\boldsymbol{\phi}}\left\{\frac{\partial k_i}{\partial \boldsymbol{\phi}}\right\}^T\right)\Bigg|_{\substack{\boldsymbol{\phi}=\boldsymbol{\mu}_{\boldsymbol{\phi}}\\ \boldsymbol{\lambda}=\boldsymbol{\mu}_{\boldsymbol{\lambda}}}} + \left(\left\{\frac{\partial k_i}{\partial \boldsymbol{\lambda}}\right\}\mathbf{C}_{\boldsymbol{\lambda}\boldsymbol{\lambda}}\left\{\frac{\partial k_i}{\partial \boldsymbol{\lambda}}\right\}^T\right)\Bigg|_{\substack{\boldsymbol{\phi}=\boldsymbol{\mu}_{\boldsymbol{\phi}}\\ \boldsymbol{\lambda}=\boldsymbol{\mu}_{\boldsymbol{\lambda}}}} \\
& + 2\left(\left\{\frac{\partial k_i}{\partial \boldsymbol{\lambda}}\right\}\mathbf{C}_{\boldsymbol{\lambda}\boldsymbol{\phi}}\left\{\frac{\partial k_i}{\partial \boldsymbol{\phi}}\right\}^T\right)\Bigg|_{\substack{\boldsymbol{\phi}=\boldsymbol{\mu}_{\boldsymbol{\phi}}\\ \boldsymbol{\lambda}=\boldsymbol{\mu}_{\boldsymbol{\lambda}}}} \\
\sigma_{k_ik_j} \approx & \left(\left\{\frac{\partial k_i}{\partial \boldsymbol{\phi}}\right\}\mathbf{C}_{\boldsymbol{\phi}\boldsymbol{\phi}}\left\{\frac{\partial k_j}{\partial \boldsymbol{\phi}}\right\}^T\right)\Bigg|_{\substack{\boldsymbol{\phi}=\boldsymbol{\mu}_{\boldsymbol{\phi}}\\ \boldsymbol{\lambda}=\boldsymbol{\mu}_{\boldsymbol{\lambda}}}} + \left(\left\{\frac{\partial k_i}{\partial \boldsymbol{\lambda}}\right\}\mathbf{C}_{\boldsymbol{\lambda}\boldsymbol{\lambda}}\left\{\frac{\partial k_j}{\partial \boldsymbol{\lambda}}\right\}^T\right)\Bigg|_{\substack{\boldsymbol{\phi}=\boldsymbol{\mu}_{\boldsymbol{\phi}}\\ \boldsymbol{\lambda}=\boldsymbol{\mu}_{\boldsymbol{\lambda}}}} \\
& + \left(\left\{\frac{\partial k_i}{\partial \boldsymbol{\lambda}}\right\}\mathbf{C}_{\boldsymbol{\lambda}\boldsymbol{\phi}}\left\{\frac{\partial k_j}{\partial \boldsymbol{\phi}}\right\}^T\right)\Bigg|_{\substack{\boldsymbol{\phi}=\boldsymbol{\mu}_{\boldsymbol{\phi}}\\ \boldsymbol{\lambda}=\boldsymbol{\mu}_{\boldsymbol{\lambda}}}} + \left(\left\{\frac{\partial k_j}{\partial \boldsymbol{\lambda}}\right\}\mathbf{C}_{\boldsymbol{\lambda}\boldsymbol{\phi}}\left\{\frac{\partial k_i}{\partial \boldsymbol{\phi}}\right\}^T\right)\Bigg|_{\substack{\boldsymbol{\phi}=\boldsymbol{\mu}_{\boldsymbol{\phi}}\\ \boldsymbol{\lambda}=\boldsymbol{\mu}_{\boldsymbol{\lambda}}}}
\end{aligned} \tag{6.15}$$

where, $\boldsymbol{\lambda} = \{\lambda_1, \cdots, \lambda_N\}^T$, $\boldsymbol{\mu}_{\boldsymbol{\lambda}} = \boldsymbol{\mu}_{\boldsymbol{\alpha}}(1:N)$, $\mathbf{C}_{\boldsymbol{\lambda}\boldsymbol{\lambda}} = \mathbf{C}_{\boldsymbol{\alpha}\boldsymbol{\alpha}}(1:N, 1:N)$, $\mathbf{C}_{\boldsymbol{\lambda}\boldsymbol{\phi}} = -\mathbf{C}_{\boldsymbol{\alpha}\boldsymbol{\alpha}}(1:N, 1:NN_s)\mathbf{S}^T\mathbf{G}$, and

$$\mathbf{G} = \begin{bmatrix}\mathbf{G}^*_{1:N^2-1,2:N(s_1-1)+1} & \mathbf{G}^*_{1:N^2-1,1} & \mathbf{G}^*_{1:N^2-1,N(s_1-1)+2:N^2}\end{bmatrix} \tag{6.16}$$

with $\mathbf{G}^*$ being the $(N^2-1)\times N^2$ matrix

$$\mathbf{G}^* = \left[\left\{\frac{\partial v_{s_1,1}}{\partial \boldsymbol{\theta}}\right\}^T \begin{Bmatrix}1 & \boldsymbol{\mu}^T_{\boldsymbol{\theta}}\end{Bmatrix}\right]\Bigg|_{\substack{M_T=\mu_{M_T}\\ \boldsymbol{\theta}=\boldsymbol{\mu}_{\boldsymbol{\theta}}}} + \mu_{v_{s_1,1}}\begin{bmatrix}\mathbf{0}_{(N^2-1)\times 1} & \mathbf{I}_{(N^2-1)\times(N^2-1)}\end{bmatrix} \tag{6.17}$$

The covariances between the different masses and stiffnesses may similarly be estimated as:

$$\sigma_{m_ik_j} \approx \left(\left\{\frac{\partial m_i}{\partial \boldsymbol{\phi}}\right\}\mathbf{C}_{\boldsymbol{\phi}\boldsymbol{\phi}}\left\{\frac{\partial k_j}{\partial \boldsymbol{\phi}}\right\}^T\right)\Bigg|_{\substack{\boldsymbol{\phi}=\boldsymbol{\mu}_{\boldsymbol{\phi}}\\ \boldsymbol{\lambda}=\boldsymbol{\mu}_{\boldsymbol{\lambda}}}} + \left(\left\{\frac{\partial k_j}{\partial \boldsymbol{\lambda}}\right\}\mathbf{C}_{\boldsymbol{\lambda}\boldsymbol{\phi}}\left\{\frac{\partial m_i}{\partial \boldsymbol{\phi}}\right\}^T\right)\Bigg|_{\substack{\boldsymbol{\phi}=\boldsymbol{\mu}_{\boldsymbol{\phi}}\\ \boldsymbol{\lambda}=\boldsymbol{\mu}_{\boldsymbol{\lambda}}}} \tag{6.18}$$

6.1.1 Analytical expressions for the derivatives

The different derivatives involved in the perturbation approach may be expressed analytically. In Appendix C, pseudo-codes are provided for analytically constructing the matrices $[\partial \mathbf{g}(\boldsymbol{\alpha}, \boldsymbol{\theta})/\partial \boldsymbol{\theta}]$ and $[\partial \mathbf{g}(\boldsymbol{\alpha}, \boldsymbol{\theta})/\partial \boldsymbol{\alpha}]$. The expressions for the remaining derivatives are listed here to enable a straightforward implementation of the approach.

Given a vector $\boldsymbol{\theta}$ of the N^2-1 proportional mode shape components, with $v^*_{s_1,1} = 1$, the floor masses, m^*_i's, and total mass, M^*_T, of the proportional system may be computed using modal orthogonality (Section 4.2.2). Then, for the vector $\boldsymbol{\theta}$ arranged as in Eq. (6.2), the derivatives of the scaling

factor, $v_{s_1,1}$, with respect to M_T and $\boldsymbol{\theta}$, may respectively be written as:

$$\frac{\partial v_{s_1,1}}{\partial M_T} = -\frac{1}{2}\sqrt{\frac{M_T^*}{M_T^3}} \tag{6.19}$$

and

$$\frac{\partial v_{s_1,1}}{\partial \boldsymbol{\theta}} = -\sqrt{\frac{1}{M_T M_T^*}}\{\boldsymbol{\theta} \circ \mathbf{m}^* \circ \mathbf{m}^*\} \tag{6.20}$$

where $\circ$ denotes the element-by-element (Hadamard) product, and $\mathbf{m}^*$ is the $(N^2-1)\times 1$ vector:

$$\mathbf{m}^* = \{m_1^*\mathbf{1}_N, m_2^*\mathbf{1}_N, \cdots, m_{s_1}^*\mathbf{1}_{N-1}, \cdots, m_N^*\mathbf{1}\}^T \tag{6.21}$$

with $\mathbf{1}_N$ being the $N \times 1$ dimensional vector with all elements equal to 1, and similarly $\mathbf{1}_{N-1}$.

Again, given a vector $\boldsymbol{\phi}$ of the N^2 mass normalized mode shape components, and a vector $\boldsymbol{\lambda}$ of the N eigenvalues, the floor masses and story stiffnesses may be computed from modal orthogonality. Then, for the vector $\boldsymbol{\phi}$ arranged as in Eq. (6.7), the derivatives of the floor masses with respect to the elements of $\boldsymbol{\phi}$ may be expressed as:

$$\frac{\partial m_i}{\partial \phi_l} = \begin{cases} -2m_i^2\phi_l & \text{for } N(i-1)+1 \le l \le Ni \\ 0 & \text{otherwise} \end{cases} \tag{6.22}$$

Similarly, the derivatives of the first story stiffness with respect to the elements of $\boldsymbol{\phi}$ and $\boldsymbol{\lambda}$ can be written as:

$$\begin{aligned} \frac{\partial k_1}{\partial \phi_l} &= \begin{cases} -2k_1^2\dfrac{\phi_l}{\lambda_l} & \text{for } 1 \le l \le N \\ 0 & \text{otherwise} \end{cases} \\ \frac{\partial k_1}{\partial \lambda_l} &= k_1^2\frac{\phi_l^2}{\lambda_l^2} \qquad \forall\, l \in \{1, \cdots, N\} \end{aligned} \tag{6.23}$$

while those of the remaining story stiffnesses ($i \in \{2, \cdots, N\}$) may be written as:

$$\begin{aligned} \frac{\partial k_i}{\partial \phi_l} &= \begin{cases} -2k_i^2\dfrac{\phi_l}{\lambda_{l-N(i-1)}} & \text{for } N(i-1)+1 \le l \le Ni \\ 2k_i^2\dfrac{\phi_l}{\lambda_{l-N(i-2)}} & \text{for } N(i-2)+1 \le l \le N(i-1) \\ 0 & \text{otherwise} \end{cases} \\ \frac{\partial k_i}{\partial \lambda_l} &= k_i^2\frac{\phi_{N(i-1)+l}^2 - \phi_{N(i-2)+l}^2}{\lambda_l^2} \qquad \forall\, l \in \{1, \cdots, N\} \end{aligned} \tag{6.24}$$

6.2 Numerical Examples

To evaluate the performance of the perturbation approach in quantifying the uncertainties induced by test structure variability, e.g. due to ambient/environmental effects, we consider a 7-DOF shear-type system. We assume the structure to be instrumented with 2 sensors, located at DOFs $\mathcal{S} = \{1, 7\}$, i.e. $s_1 = 1$ and the vector of known non-normalized modal parameters in Eq. (6.2) is:

$$\boldsymbol{\alpha} = \{\lambda_1, \cdots, \lambda_N, \frac{\tilde{v}_{7,1}}{\tilde{v}_{1,1}}, \cdots, \frac{\tilde{v}_{7,N}}{\tilde{v}_{1,N}}\}^T \tag{6.25}$$

The floor masses and story stiffnesses of the structure are assumed to be independent random variables, defined by the Gaussian distributions: $m_i \sim \mathcal{N}(2500, 125^2)$ kg $\forall\ i \in \{1, \cdots, 6\}$, $m_7 \sim \mathcal{N}(2000, 100^2)$ kg, and $k_i \sim \mathcal{N}(5 \times 10^6, (25 \times 10^4)^2)$ N/m $\forall\ i \in \{1, \cdots, 7\}$, where $\mathcal{N}(\mu, \sigma^2)$ denotes a Gaussian distribution with mean μ and standard deviation σ. Note that the assumed standard deviations are 5% of the corresponding mean values. First, we generate 5000 realizations of the masses and stiffnesses from these distributions, i.e. create 5000 sample structures; next, we perform an eigenvalue analysis of each of these structures, resulting in 5000 sets of the eigenvalues and mode shape matrices; from these, we compute the mean vector, $\boldsymbol{\mu}_{\boldsymbol{\alpha}}$, and covariance matrix, $\mathbf{C}_{\boldsymbol{\alpha}\boldsymbol{\alpha}}$, corresponding to the $\boldsymbol{\alpha}$ defined in Eq. (6.25). Using these $\boldsymbol{\mu}_{\boldsymbol{\alpha}}$ and $\mathbf{C}_{\boldsymbol{\alpha}\boldsymbol{\alpha}}$ in the perturbation approach, we then successively compute the statistics of all the subsequent parameters; in these computations we assumed $\mu_{M_T} = 17 \times 10^3$ kg (i.e. the sum of all the mean masses), and $\sigma_{M_T} = 0$. For comparison purposes, we also perform a Monte Carlo simulation by first generating 500 sample $\boldsymbol{\alpha}$ vectors from the distribution $\mathcal{N}(\boldsymbol{\mu}_{\boldsymbol{\alpha}}, \mathbf{C}_{\boldsymbol{\alpha}\boldsymbol{\alpha}})$, and then identifying the corresponding 500 structures using the identification approach of Chapter 4. Figs. 6.1 and 6.2, respectively for the floor masses and story stiffnesses, compare the true distributions, in terms of the probability density functions, with those obtained from the perturbation approach, and from fitting normal distributions to the identified parameters in the Monte Carlo simulation; the histograms of the parameters identified in the Monte Carlo simulation are also shown, after scaling them so as to match the corresponding density functions. From this comparison it is evident that the density functions obtained using the perturbation approach approximate the corresponding true distributions reasonably well, and as well as the distributions obtained from the Monte Carlo simulation. It should be emphasized however that, to obtain the simulation results shown in Figs. 6.1 and 6.2, the time spent in the Monte Carlo simulations was approximately 500 times the time spent in the perturbation approach. This is because the Monte Carlo results are based

on 500 sets of identified parameters, and thus require the execution of the identification algorithm 500 times, while in the perturbation approach we only need to run the identification approach once, corresponding to the mean vector $\boldsymbol{\mu}_{\boldsymbol{\alpha}}$; although the perturbation approach involves some additional computational effort, this extra effort is negligible when compared to the computations involved in the identification approach, owing to the latter involving the solution of a moderately large system of nonlinear equations.

6.2.1 Possible updating of σ_{M_T}

In the above example we considered the uncertainty in the *a priori* information of the total mass, σ_{M_T}, to be zero. To first see the effect of σ_{M_T} on the estimated distributions, we repeat the perturbation approach with $\sigma_{M_T} = 0.01\%\mu_{M_T}$ and $\sigma_{M_T} = 0.02\%\mu_{M_T}$; Fig. 6.3 shows, for some example masses and stiffnesses, the comparison of the actual distributions, with those obtained using the perturbation approach for the different σ_{M_T}'s. The closeness of the estimated distributions for the different σ_{M_T}'s in these plots suggest their relative insensitivity to reasonable levels of uncertainty in the *a priori* information of total mass vis-a-vis the uncertainty induced by structural variability.

The true σ_{M_T} will be non-zero owing to the variability of the test structure. It should emphasized that, remaining mathematically correct, it is not possible to identify the true σ_{M_T}; this is because σ_{M_T}, being in some sense analogous to the *minimal a priori* information necessary for scaling the system, is unidentifiable, just as M_T is unidentifiable and has to be assumed in the deterministic case (see Chapters 3 and 4). It may also be numerically verified that the assumed σ_{M_T} and the estimated variances/covariances of the floor masses satisfy the following relationship:

$$\sigma^2_{M_T} = \sum_{i=1}^{N} \sigma^2_{m_i} + 2 \sum_{i=1}^{N} \sum_{\substack{j=1 \\ j \neq i}}^{N} \sigma_{m_i m_j} \tag{6.26}$$

which is expected since M_T is the sum of the N normally distributed m_i's. Now, if we make the assumption that the different m_i's are independent, then one can write:

$$\sigma^2_{M_T} = \sum_{i=1}^{N} \sigma^2_{m_i} \tag{6.27}$$

where the right hand side is not equal to the assumed $\sigma^2_{M_T}$. Then, we can update the initially assumed σ_{M_T} with the σ_{M_T} computed from Eq. (6.27), and repeat the perturbation approach; this process

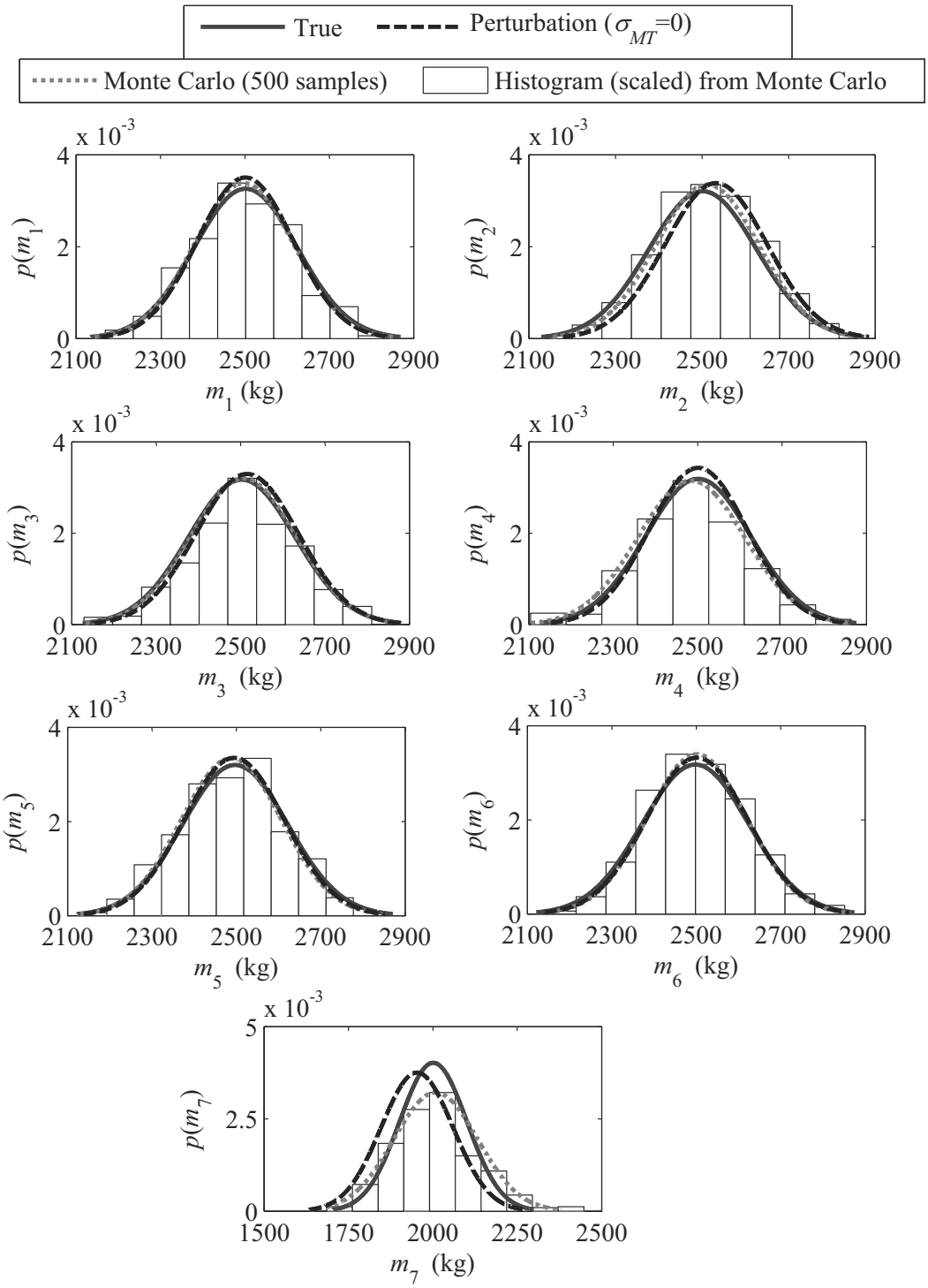

Figure 6.1: Comparison of probability density functions of the true floor mass distributions, with those obtained from the perturbation approach and the Monte Carlo simulation. Also shown are the histograms (scaled to match the density functions) from the Monte Carlo simulation.

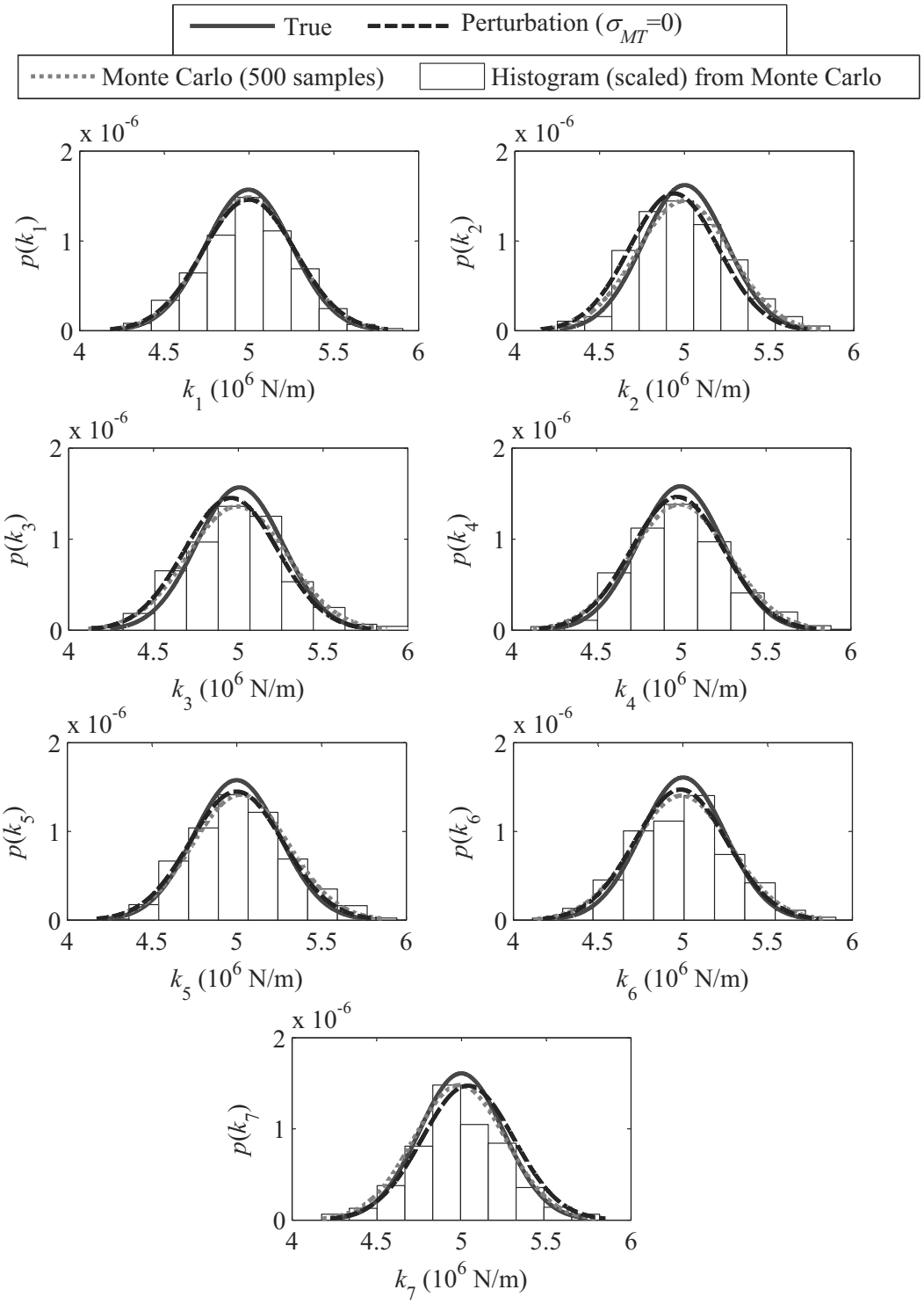

Figure 6.2: Comparison of probability density functions of the true story stiffness distributions, with those obtained from the perturbation approach and the Monte Carlo simulation. Also shown are the histograms (scaled to match the density functions) from the Monte Carlo simulation.

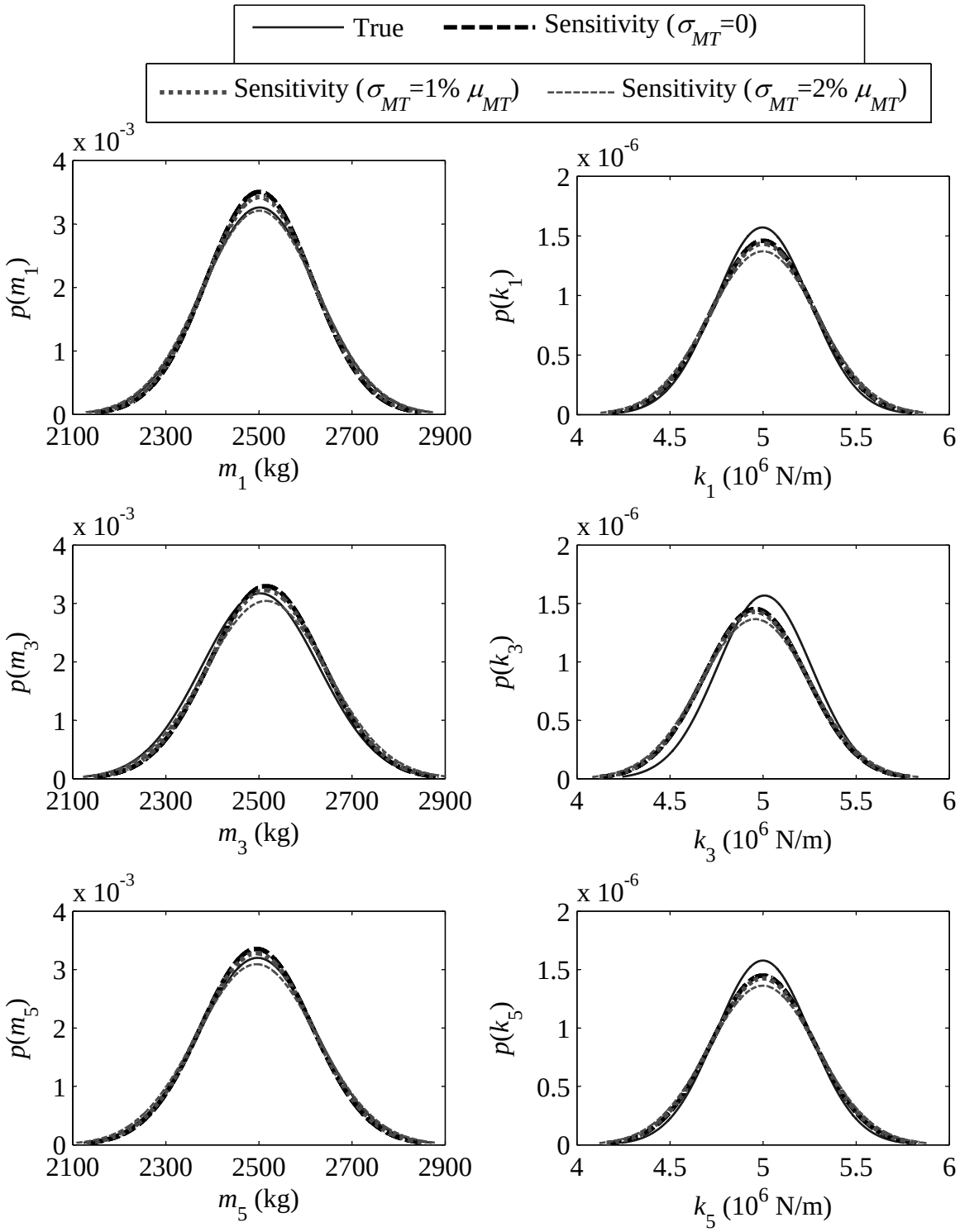

Figure 6.3: Comparison of the true probability density functions, with those obtained using the perturbation approach assuming $\sigma_{M_T} = 0$, $\sigma_{M_T} = 0.01\%\mu_{M_T}$ and $\sigma_{M_T} = 0.02\%\mu_{M_T}$, for the 1st, 3rd and 5th floor masses and story stiffnesses.

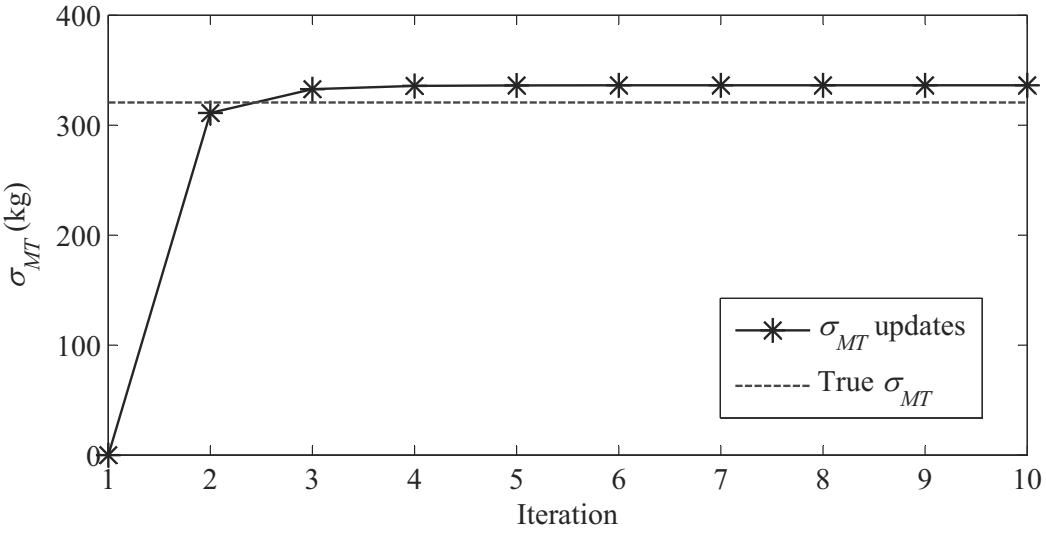

Figure 6.4: Convergence of σ_{M_T} updates starting from assumed $\sigma_{M_T} = 0$.

can then be executed iteratively. Note that, in this way the process will be adjusting the estimates of the variances/covariances of the different parameters trying to satisfy Eq. (6.27), while at the same time always identically satisfying (6.26). For the example considered before, implementing such an iterative computation leads to the convergence of the σ_{M_T} updates as shown in Figs. 6.4 and 6.5, with the initial assumed σ_{M_T}'s being respectively 0 and $5\%\mu_{M_T}$. It is evident that using this strategy one is able to improve on the initial guess of the assumed σ_{M_T}. Since the assumption of independent floor masses is true in this example, the converged σ_{M_T} indeed approximates the true σ_{M_T} with reasonable accuracy, having an error of 4.8% and 2% respectively in the cases of Figs. 6.4 and 6.5. As will be shown later, the approximation is not as good in case the masses are correlated; but even in these cases, the converged σ_{M_T} may be expected to be a better approximation of the true σ_{M_T} than the initial assumption, since the initial assumption will be affected by lack of knowledge, and hence subjectivity. Fig. 6.6 compares the true distributions of some example masses and stiffnesses, with the corresponding distributions estimated using the perturbation approach, for $\sigma_{M_T} = 0$ (iteration 1) and the converged value of σ_{M_T} (iteration 10) in Fig. 6.4. Fig. 6.6 agrees with the earlier observation from Fig. 6.3, i.e. the updating of σ_{M_T} does not have any significant effect on the estimated distributions, even though it definitely improves the value of σ_{M_T}. This seems to indicate that the updating mainly affects the covariances between different floor masses as compared to the variances; this will be illustrated in a later example concerning correlated floor masses.

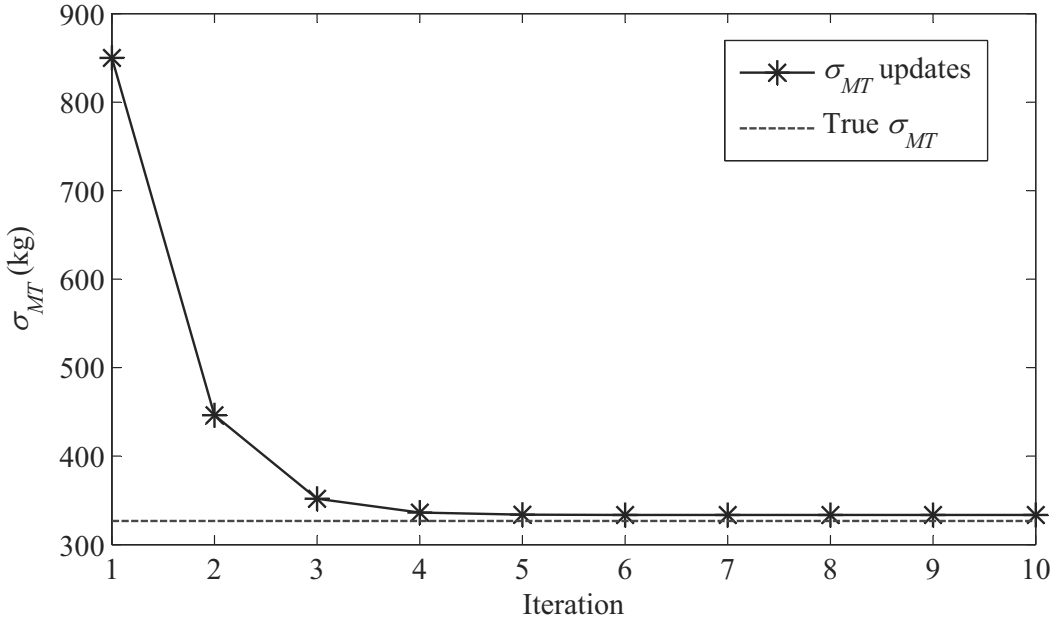

Figure 6.5: Convergence of σ_{M_T} updates starting from assumed $\sigma_{M_T} = 5\%\mu_{M_T}$.

6.2.2 Effect of errors in $\boldsymbol{\mu}_{\boldsymbol{\alpha}}$ and $\mathbf{C}_{\boldsymbol{\alpha\alpha}}$

In the last example, the statistics of the initial non-normalized modal parameters, $\boldsymbol{\mu}_{\boldsymbol{\alpha}}$ and $\mathbf{C}_{\boldsymbol{\alpha\alpha}}$, are computed from the eigenvalue analyses of the 5000 structures whose parameters are sampled from the true distributions. So these initial statistics are free from any errors, as, for instance, would be introduced if they were identified from measured data. To evaluate the performance of the perturbation approach vis-a-vis the Monte Carlo simulations, with errors in $\boldsymbol{\mu}_{\boldsymbol{\alpha}}$ and $\mathbf{C}_{\boldsymbol{\alpha\alpha}}$, we now: (a) randomly pick 100 structures from the set of 5000 sample structures; (b) excite each of these 100 structures at all the DOFs using Gaussian white noise inputs; (c) pollute the true acceleration responses at the sensor locations, DOFs 1 and 7, using 10% RMS Gaussian white noise sequences; (d) use these noise corrupted acceleration responses in ECCA [68] to identify 100 corresponding sets of eigenvalues and non-normalized mode shapes at DOFs 1 and 7; and (e) compute $\boldsymbol{\mu}_{\boldsymbol{\alpha}}$ and $\mathbf{C}_{\boldsymbol{\alpha\alpha}}$ from these 100 sets of identified modal parameters. Figs. 6.7 and 6.8 compare the marginal distributions of these modal parameters obtained based on the identified 100 sets, with the true marginal distributions obtained from the eigenvalue analyses of all the 5000 sample structures. It is apparent that the distributions based on the identified parameters show some deviation from the corresponding true distributions, especially in case of the ratios between the mode shape components at DOFs 7 and 1. The perturbation

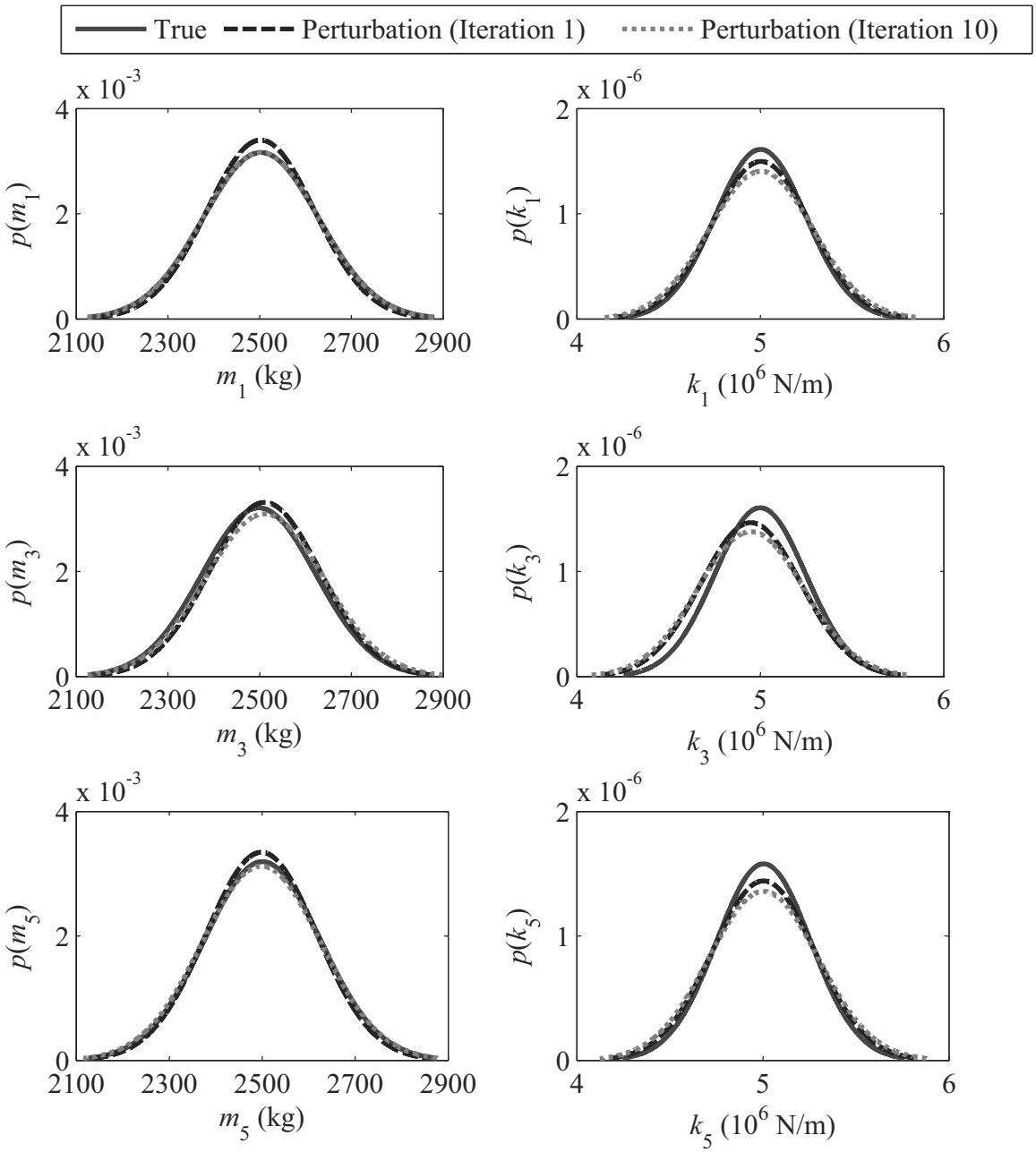

Figure 6.6: Comparison of the true probability density functions, with those obtained from the perturbation approach with assumed $\sigma_{M_T} = 0$ (iteration 1) and converged σ_{M_T} (iteration 10) from Fig. 6.4, for the 1st, 3rd and 5th floor masses and story stiffnesses.

approach is next applied with the $\boldsymbol{\mu}_{\boldsymbol{\alpha}}$ and $\mathbf{C}_{\boldsymbol{\alpha}\boldsymbol{\alpha}}$ obtained from the identified parameters; μ_{M_T} is again taken as 17×10^3 kg, and σ_{M_T} is iteratively updated, as in Section 6.2.1, starting from $\sigma_{M_T} = 0$. Also, for the Monte Carlo simulation, 500 realization of $\boldsymbol{\alpha}$ are sampled from the distribution described by these $\boldsymbol{\mu}_{\boldsymbol{\alpha}}$ and $\mathbf{C}_{\boldsymbol{\alpha}\boldsymbol{\alpha}}$, and 500 corresponding structural systems are identified. Figs. 6.9 and 6.10 respectively compare the true probability density functions of the floor masses and story stiffnesses, with the corresponding distributions obtained from the perturbation approach (with $\sigma_{M_T} = 0$ and converged σ_{M_T}), and from fitting normal distributions to the parameters identified in the Monte Carlo simulation. Although the discrepancy between the estimated and true distributions are more pronounced in this case, owing to the errors in the initial modal parameter statistics $\boldsymbol{\mu}_{\boldsymbol{\alpha}}$ and $\mathbf{C}_{\boldsymbol{\alpha}\boldsymbol{\alpha}}$, the estimated distributions from both the Monte Carlo simulations and the perturbation approach still approximate the true distributions reasonably well.

6.2.3 An example of correlated m_i's and k_i's

As a final example we consider a case where the floor masses and story stiffnesses have the same means and variances as in the preceding examples, but now they are correlated with the following

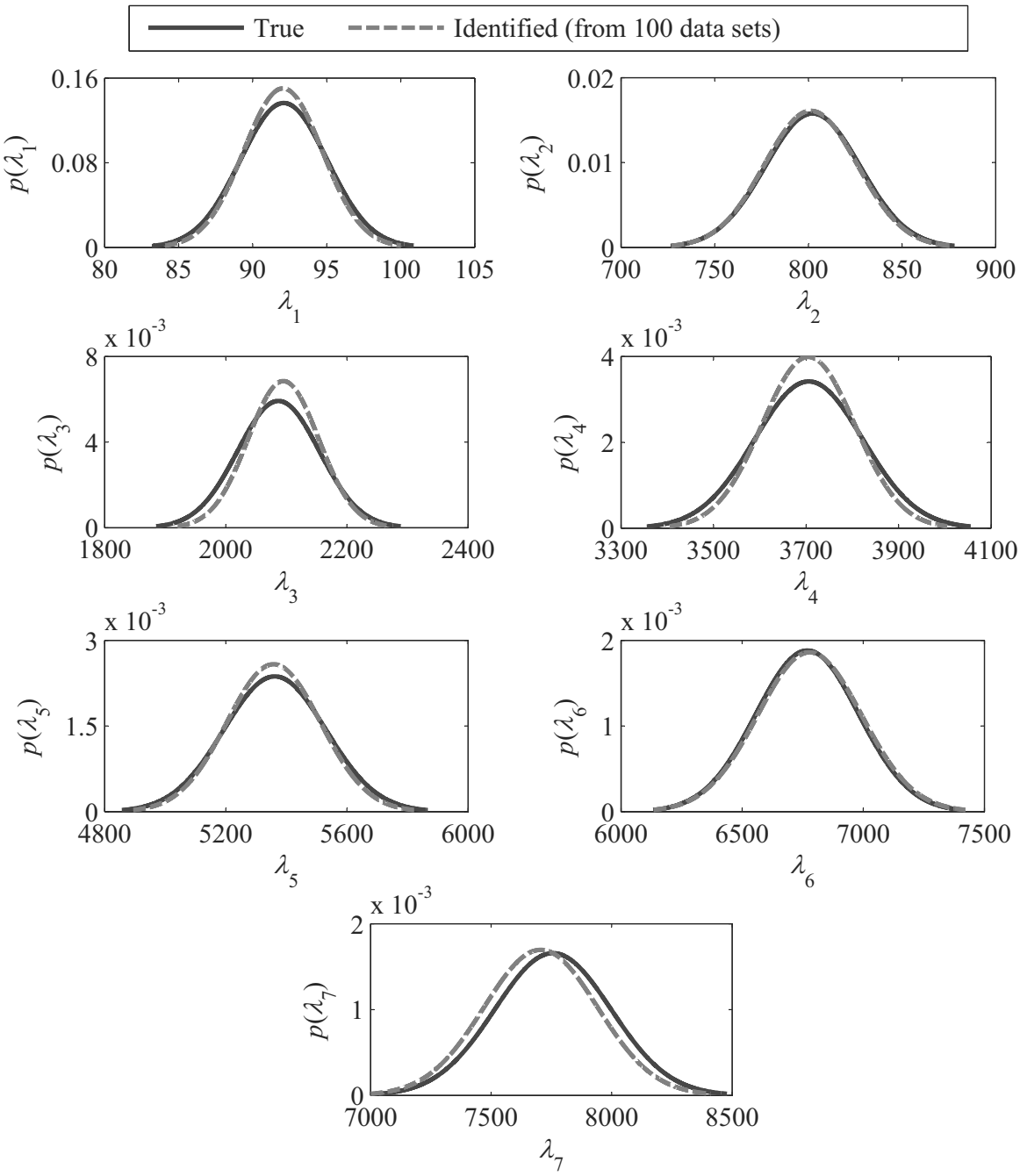

Figure 6.7: Comparison of the marginal probability density functions of the true eigenvalues, obtained from eigenvalue analyses of 5000 sample structures, with the corresponding density functions obtained from the 100 sets of identified eigenvalues.

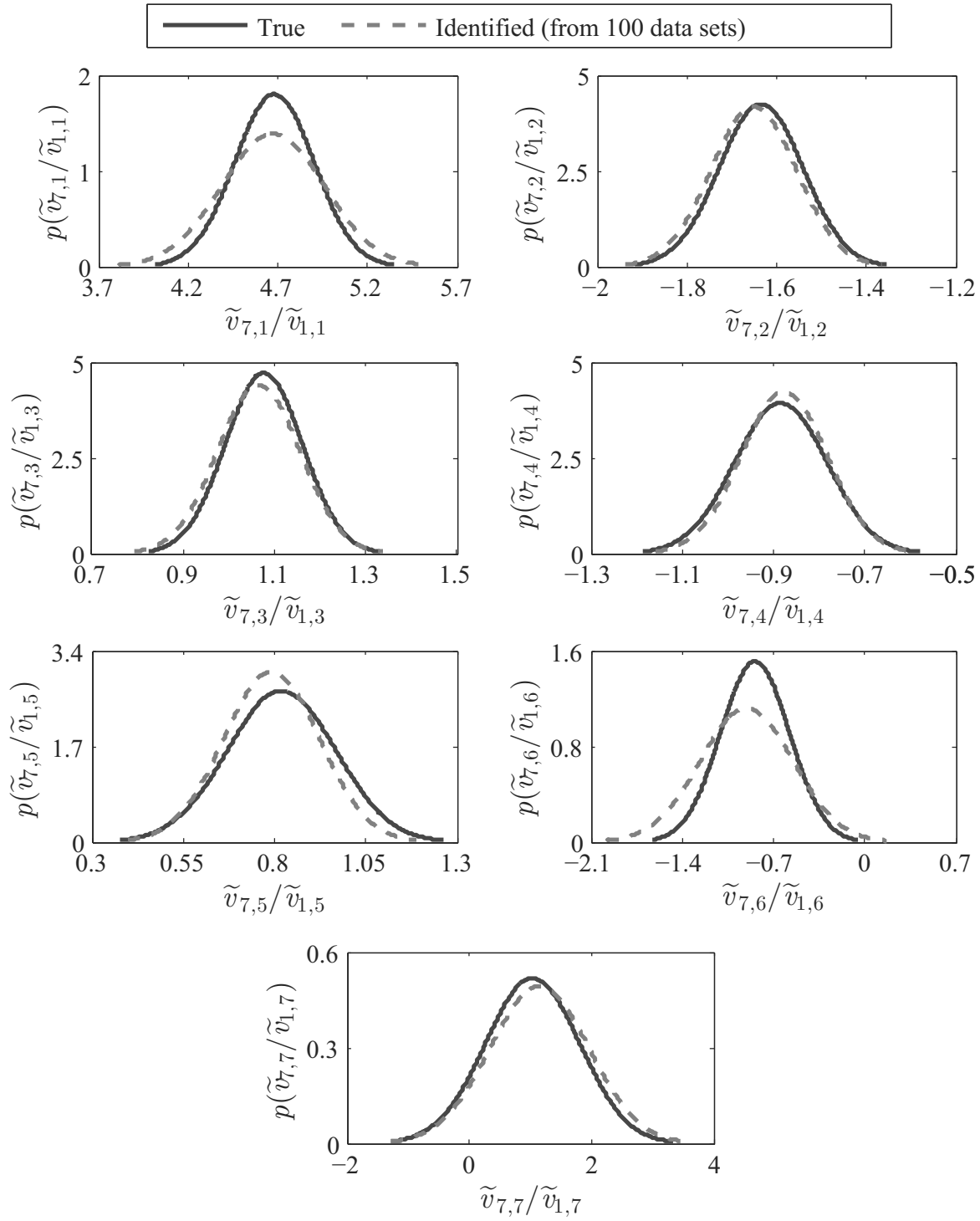

Figure 6.8: Comparison of the marginal probability density functions of the true $\frac{\tilde{v}_{7,j}}{\tilde{v}_{1,j}}$ ratios, obtained from eigenvalue analyses of 5000 sample structures, with the corresponding density functions obtained from the 100 sets of identified $\frac{\tilde{v}_{7,j}}{\tilde{v}_{1,j}}$ ratios.

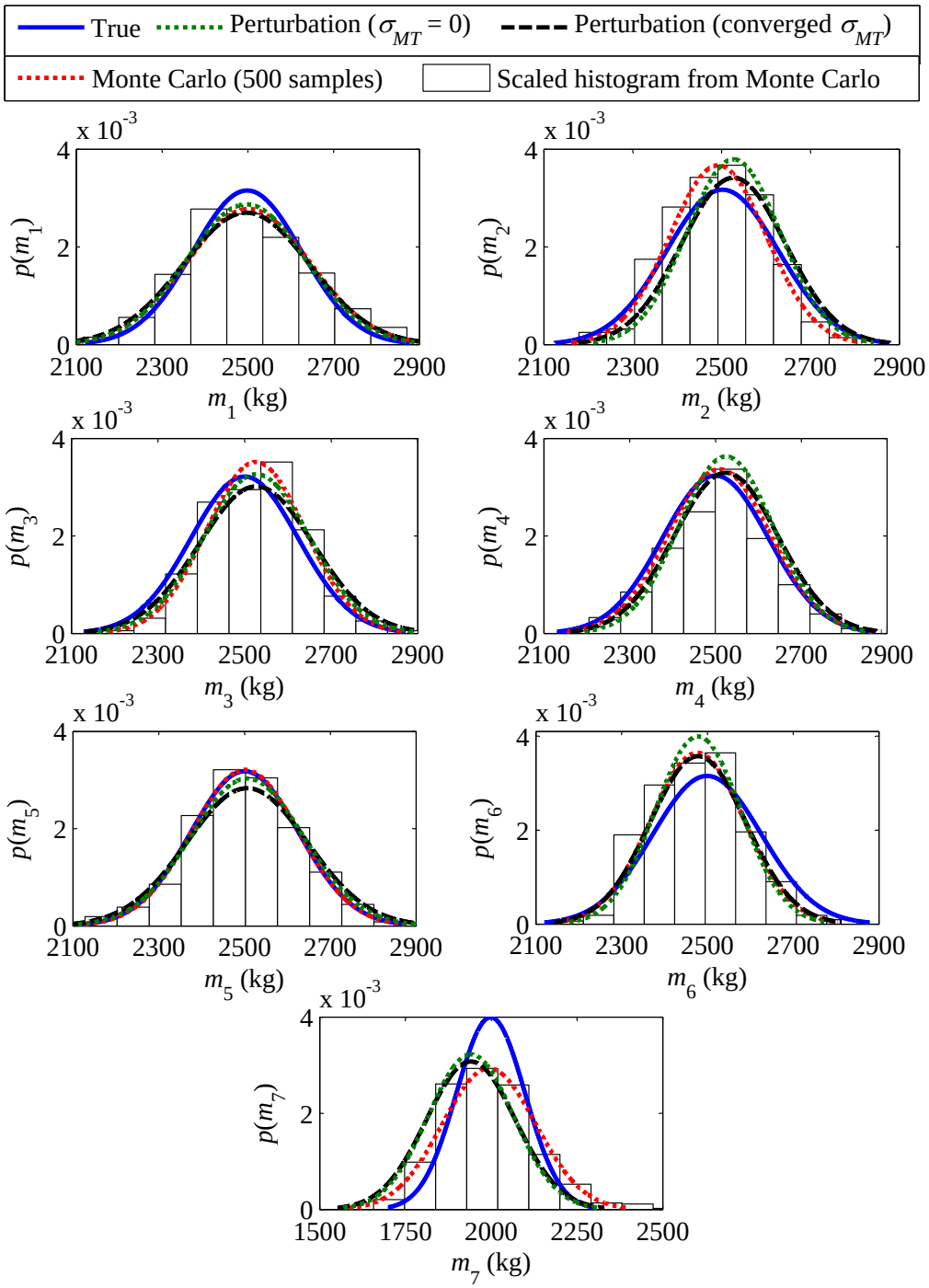

Figure 6.9: Comparison of true probability density functions with those obtained from the perturbation approach (with $\sigma_{M_T} = 0$ and converged σ_{M_T}) and the Monte Carlo simulation, for the different floor masses, in the case of estimation errors in $\boldsymbol{\mu}_{\boldsymbol{\alpha}}$ and $\mathbf{C}_{\boldsymbol{\alpha}\boldsymbol{\alpha}}$. Also shown are the histograms (scaled to match the density functions) from the Monte Carlo simulation.

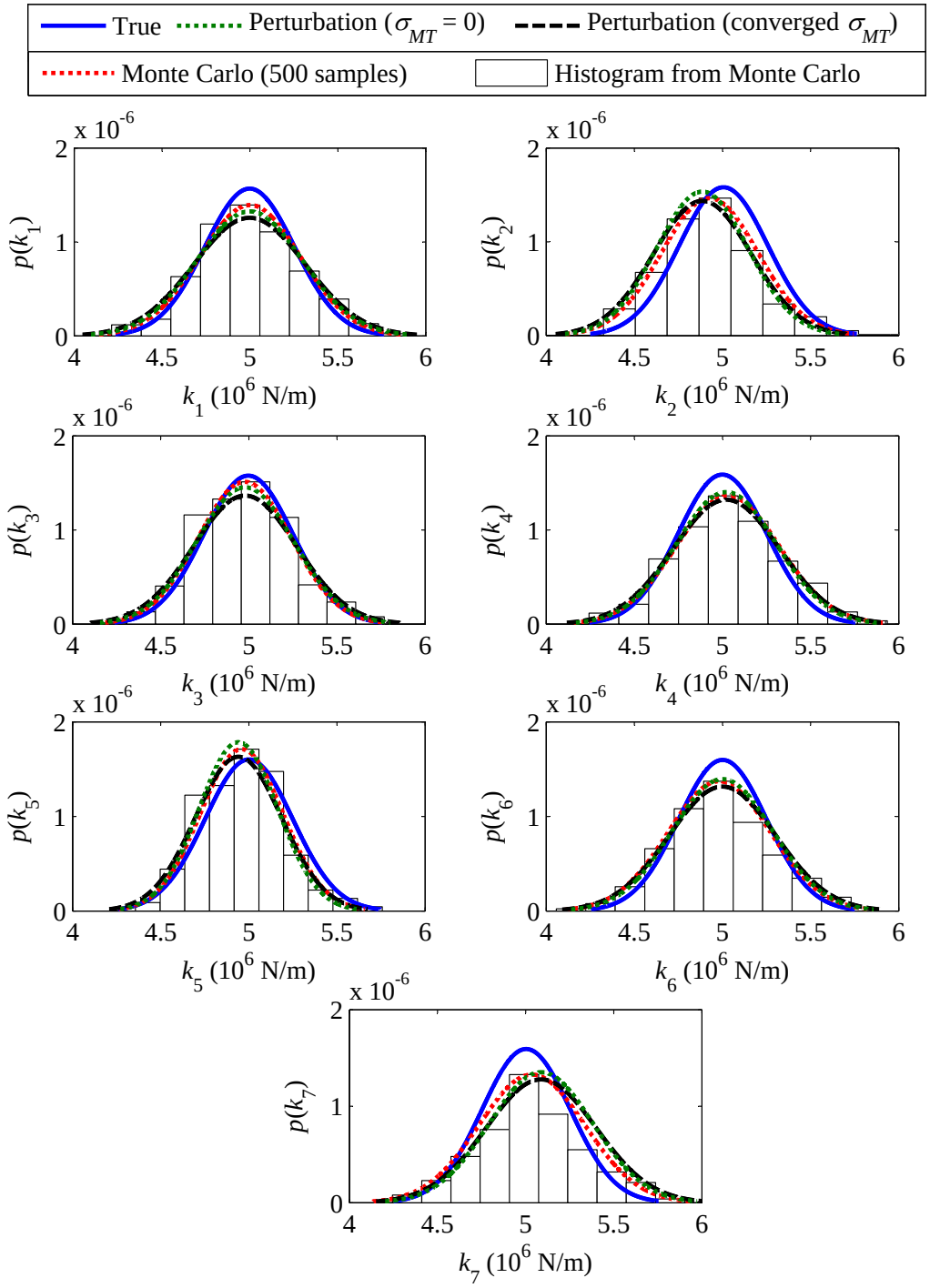

Figure 6.10: Comparison of true probability density functions with those obtained from the perturbation approach (with $\sigma_{M_T} = 0$ and converged σ_{M_T}) and the Monte Carlo simulation, for the different story stiffnesses, in the case of estimation errors in $\boldsymbol{\mu}_{\boldsymbol{\alpha}}$ and $\mathbf{C}_{\boldsymbol{\alpha\alpha}}$. Also shown are the histograms (scaled to match the density functions) from the Monte Carlo simulation.

correlation matrices:

$$\boldsymbol{\rho}_{mm} = \begin{bmatrix} 1.00 & 0.50 & 0.10 & 0.05 & 0.05 & 0.10 & 0.05 \\ 0.50 & 1.00 & 0.50 & 0.10 & 0.05 & 0.05 & 0.10 \\ 0.10 & 0.50 & 1.00 & 0.50 & 0.10 & 0.05 & 0.05 \\ 0.05 & 0.10 & 0.50 & 1.00 & 0.50 & 0.10 & 0.05 \\ 0.05 & 0.05 & 0.10 & 0.50 & 1.00 & 0.50 & 0.10 \\ 0.10 & 0.05 & 0.05 & 0.10 & 0.50 & 1.00 & 0.50 \\ 0.05 & 0.10 & 0.05 & 0.05 & 0.10 & 0.50 & 1.00 \end{bmatrix}$$

$$\boldsymbol{\rho}_{kk} = \begin{bmatrix} 1.00 & 0.50 & 0.10 & 0.05 & 0.05 & 0.10 & 0.05 \\ 0.50 & 1.00 & 0.50 & 0.10 & 0.05 & 0.05 & 0.10 \\ 0.10 & 0.50 & 1.00 & 0.50 & 0.10 & 0.05 & 0.05 \\ 0.05 & 0.10 & 0.50 & 1.00 & 0.50 & 0.10 & 0.05 \\ 0.05 & 0.05 & 0.10 & 0.50 & 1.00 & 0.50 & 0.10 \\ 0.10 & 0.05 & 0.05 & 0.10 & 0.50 & 1.00 & 0.50 \\ 0.05 & 0.10 & 0.05 & 0.05 & 0.10 & 0.50 & 1.00 \end{bmatrix} \tag{6.28}$$

$$\boldsymbol{\rho}_{mk} = \begin{bmatrix} 0.50 & 0.30 & 0.10 & 0.05 & 0.05 & 0.10 & 0.05 \\ 0.30 & 0.50 & 0.30 & 0.10 & 0.05 & 0.05 & 0.10 \\ 0.10 & 0.30 & 0.50 & 0.30 & 0.10 & 0.05 & 0.05 \\ 0.05 & 0.10 & 0.30 & 0.50 & 0.30 & 0.10 & 0.05 \\ 0.05 & 0.05 & 0.10 & 0.30 & 0.50 & 0.30 & 0.10 \\ 0.10 & 0.05 & 0.05 & 0.10 & 0.30 & 0.50 & 0.30 \\ 0.05 & 0.10 & 0.05 & 0.05 & 0.10 & 0.30 & 0.50 \end{bmatrix}$$

By Eq. (6.28), any ith floor mass/story stiffness is moderately correlated with the (i+1)th and (i-1)th floor masses/story stiffnesses, and any ith floor mass is also moderately correlated with the ith story stiffness. We follow the same procedure as before, i.e. generate 5000 sample structures from the multivariate Gaussian distribution describing the mass-stiffness variability, and compute $\boldsymbol{\mu}_{\boldsymbol{\alpha}}$ and $\mathbf{C}_{\boldsymbol{\alpha\alpha}}$ from an eigenvalue analyses of these structures. These $\boldsymbol{\mu}_{\boldsymbol{\alpha}}$ and $\mathbf{C}_{\boldsymbol{\alpha\alpha}}$ are then used in the perturbation approach, as well as to generate 500 sample $\boldsymbol{\alpha}$ vectors used in the Monte Carlo approach; as before, we assume $\mu_{M_T} = 17 \times 10^3$ kg. Fig. 6.11 shows the convergence of the σ_{M_T} updates on using the approach discussed in Section 6.2.1. Figs. 6.12 and 6.13 respectively compare the true marginal

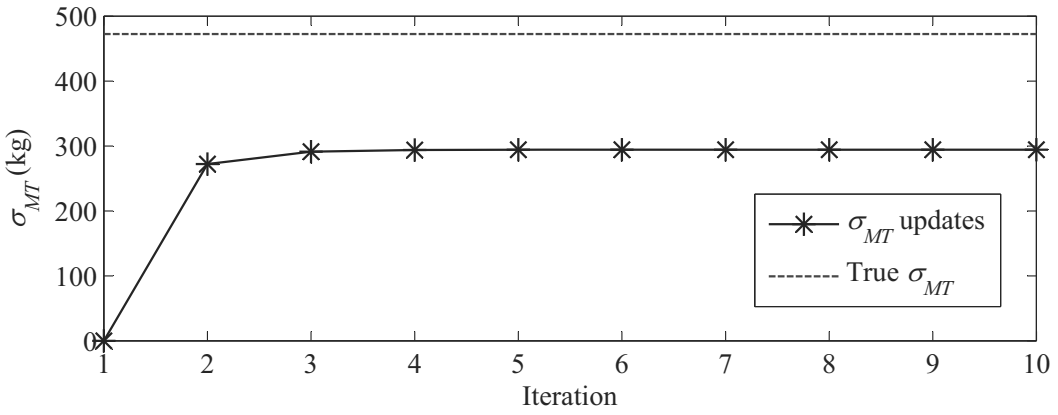

Figure 6.11: Convergence of σ_{M_T} updates starting from assumed $\sigma_{M_T} = 0$, in the case of correlated m_i's and k_i's.

distributions of the floor masses and story stiffnesses with the estimated marginal distributions from the perturbation approach and the Monte Carlo simulations; Figs. 6.14 to 6.16 compare the true and the estimated correlation matrices, respectively for $\boldsymbol{\rho}_{mm}$, $\boldsymbol{\rho}_{kk}$ and $\boldsymbol{\rho}_{mk}$. Note in Fig. 6.11 that the converged value of σ_{M_T} is no longer a good approximation of the true standard deviation in the total structural mass, having an error of 37.8%; nonetheless it is still a better approximation that the initial guess of $\sigma_{M_T} = 0$. Interestingly, the error between the converged σ_{M_T} and the square root of the sum of the variances in the floor masses is much less, 8.6%, indicating that the updated $\sigma^2_{M_T}$ possibly attempts to converge to the sum of the variances. Another observation that needs to be highlighted, based on Fig. 6.14, is that updating the σ_{M_T} tends to decrease the correlations between different masses, i.e. the off-diagonal terms of $\boldsymbol{\rho}_{mm}$. It is also worth noting that the estimated $\boldsymbol{\rho}_{mm}$ from perturbation with $\sigma_{M_T} = 0$ matches more closely with the Monte Carlo estimate; this may be expected owing to the fact that in the Monte Carlo simulations, each of the 500 structures is identified with the same given value of $M_T = \mu_{M_T} = 17 \times 10^3$ kg, and thus the standard deviation of the total structural mass in the Monte Carlo simulations is zero. While the effect of updating σ_{M_T} is not apparent in the marginal distributions in Figs. 6.12 and 6.13, the correlation matrices in Figs. 6.14 to 6.16 instead show a noticeable improvement with updating, with the matrices obtained using perturbation with the converged σ_{M_T} being closer to the true matrices than those obtained from the Monte Carlo simulations and perturbation with $\sigma_{M_T} = 0$.

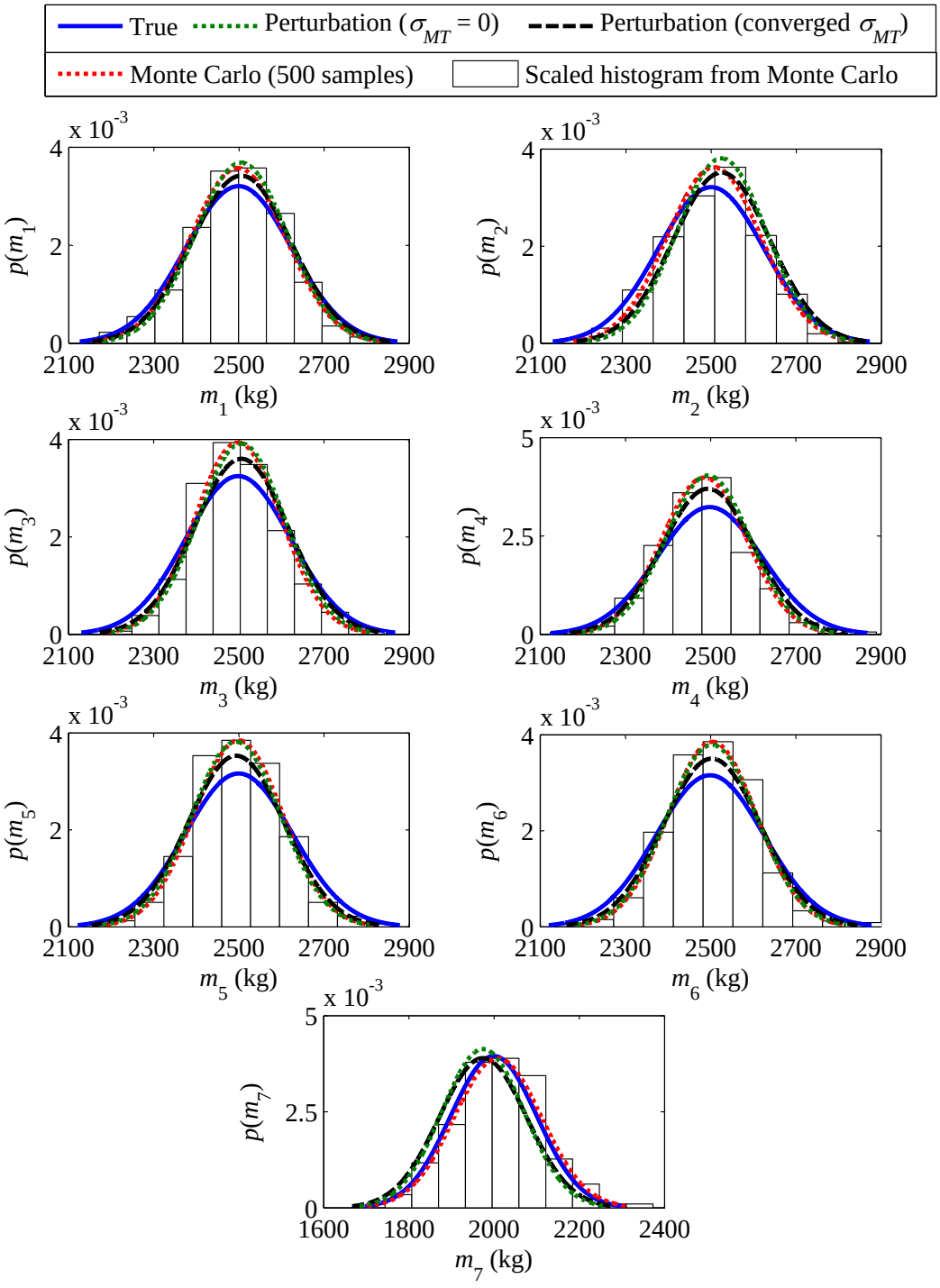

Figure 6.12: Comparison of true marginal probability density functions with those obtained from the perturbation approach (with $\sigma_{M_T} = 0$ and converged σ_{M_T}) and the Monte Carlo simulation, for the different floor masses, in the case of correlated m_i's and k_i's. Also shown are the histograms (scaled to match the density functions) from the Monte Carlo simulation.

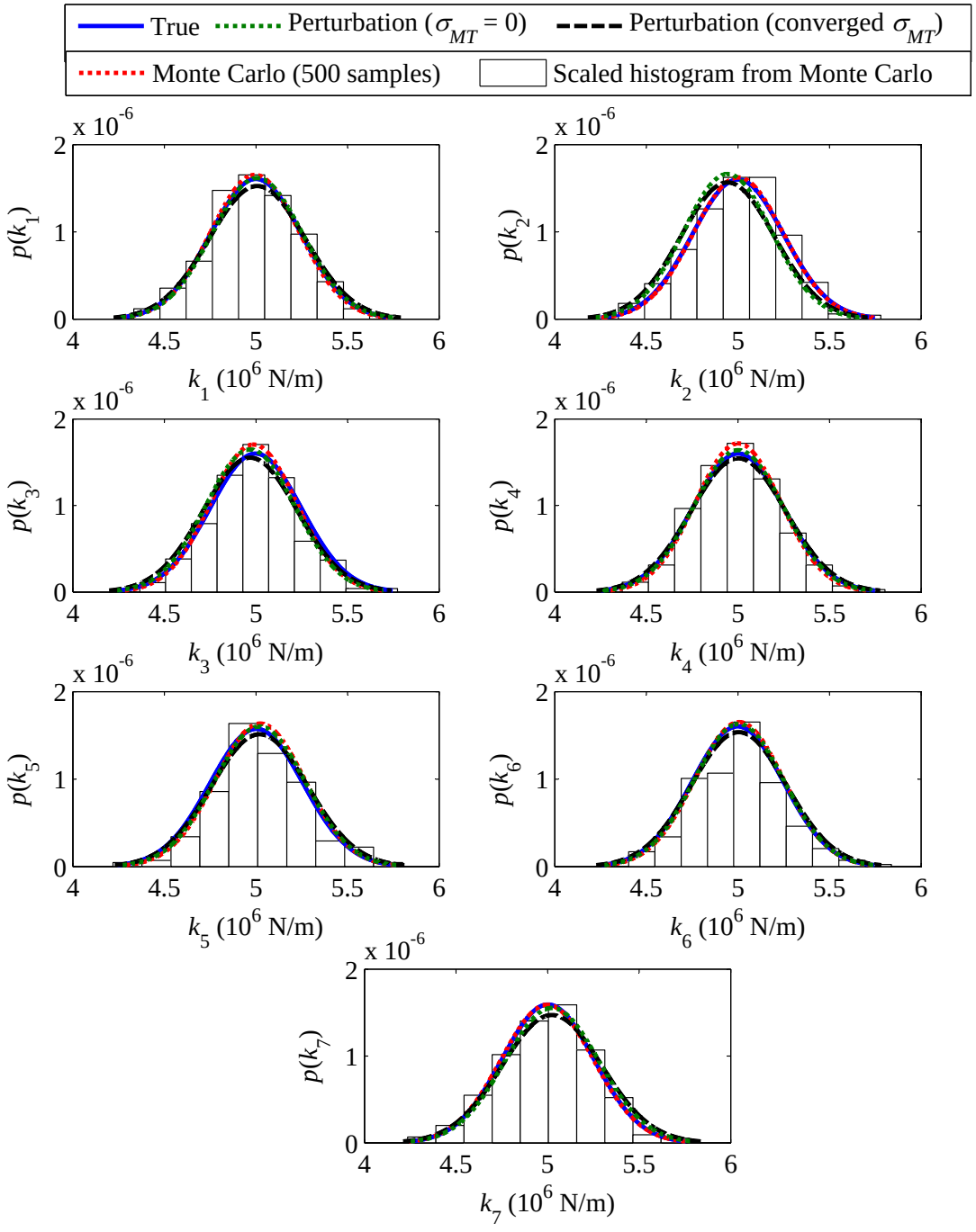

Figure 6.13: Comparison of true marginal probability density functions with those obtained from the perturbation approach (with $\sigma_{M_T} = 0$ and converged σ_{M_T}) and the Monte Carlo simulation, for the different story stiffnesses, in the case of correlated m_i's and k_i's. Also shown are the histograms (scaled to match the density functions) from the Monte Carlo simulation.

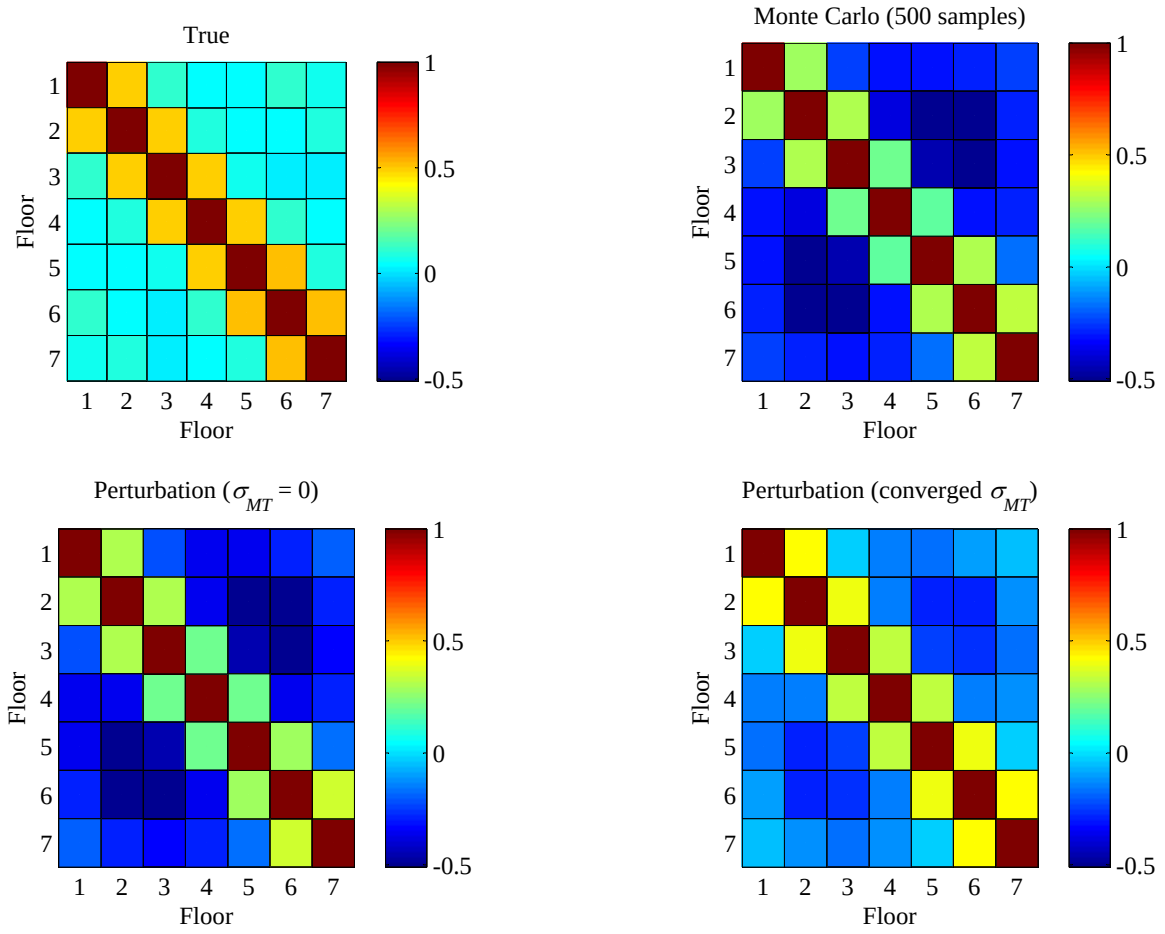

Figure 6.14: Comparison of the true correlation matrices for the floor masses, with those obtained from the perturbation approach (with $\sigma_{M_T} = 0$ and converged σ_{M_T}) and the Monte Carlo simulation.

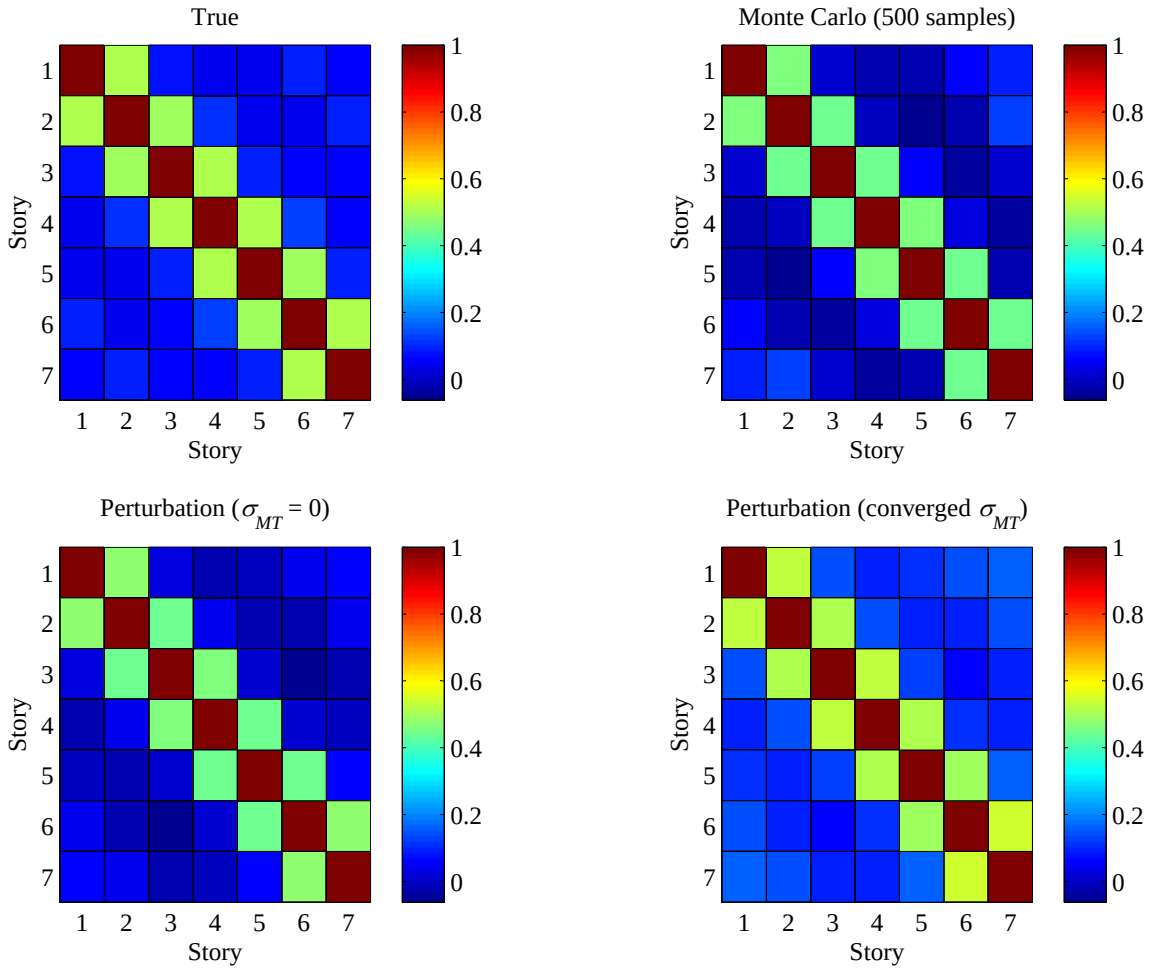

Figure 6.15: Comparison of the true correlation matrices for the story stiffnesses, with those obtained from the perturbation approach (with $\sigma_{M_T} = 0$ and converged σ_{M_T}) and the Monte Carlo simulation.

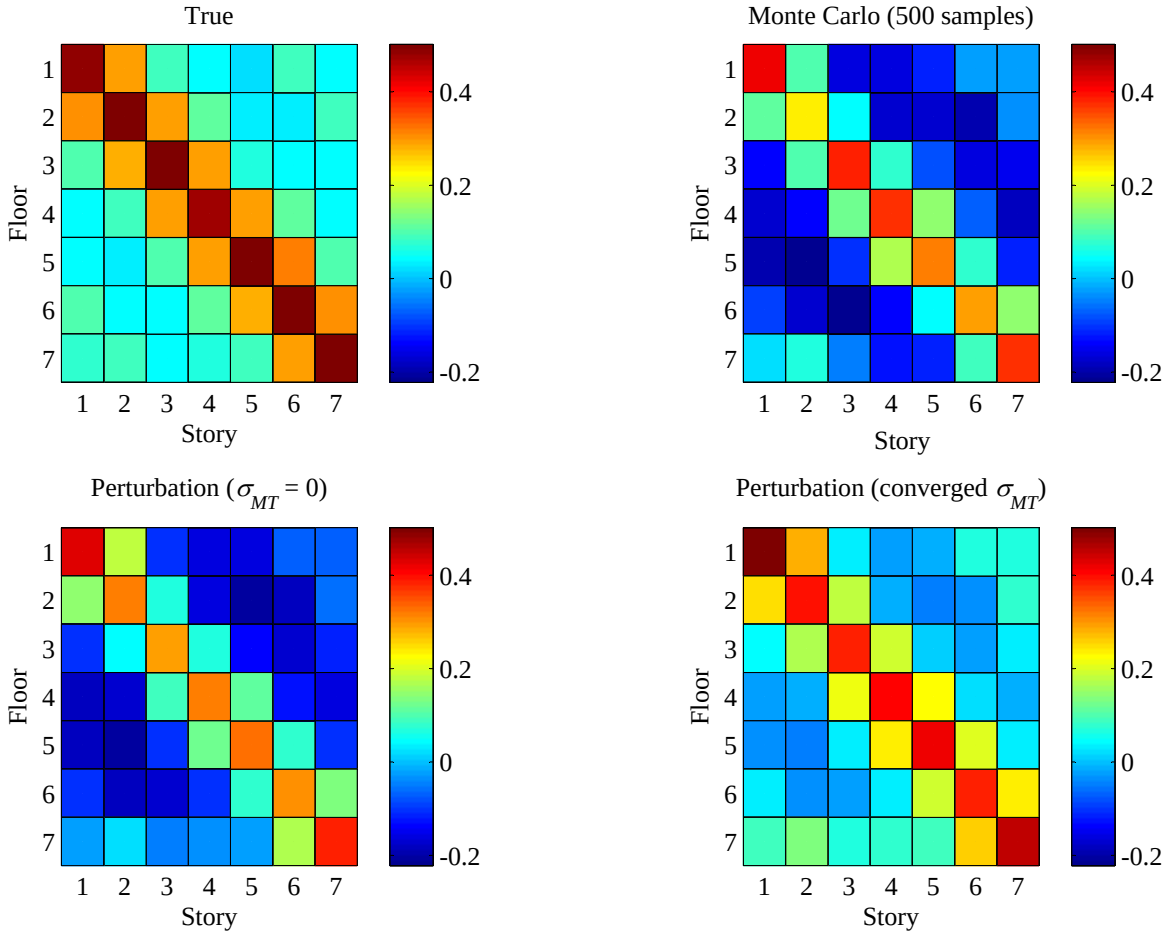

Figure 6.16: Comparison of the true correlation matrices between the floor masses and story stiffnesses, with those obtained from the perturbation approach (with $\sigma_{M_T} = 0$ and converged σ_{M_T}) and the Monte Carlo simulation.

6.3 Conclusions

In this chapter a perturbation based forward uncertainty propagation method is discussed to quantify the uncertainty in parameter identification of shear–type systems using output-only data. The uncertainty propagation is achieved by casting the deterministic mode shape expansion – parameter estimation equations of Chapter 4 in a probabilistic framework, through first-order mean centered expansion of these nonlinear equations followed by estimation of the statistical moments (mean vectors and covariance matrices) of the different parameters. These statistical moments are then used to quantify the estimation uncertainty through approximate Gaussian distributions of the parameter estimates. This perturbation based method requires the mean vector and covariance matrix of the initial non-normalized modal parameters, i.e. the eigenvalues and ratios of mode shape components at the measured DOFs, and the mean and variance of the *a priori* information. Using numerical simulations and comparing with Monte Carlo simulations, it is shown that the perturbation approach can obtain reliably accurate probabilistic descriptions of the physical parameters using the minimal necessary instrumentation (only two sensors), and the minimal necessary *a priori* information about the physical parameters (only the total mass of the system). Importantly, the approach can account for test structure variability, induced e.g. by ambient/environmental fluctuations, as well as correlations between the floor masses and story stiffnesses. A method is also suggested to iteratively update the variance of the *a priori* information, based on the assumption of uncorrelated floor masses; even when the masses are correlated, the converged variance of the *a priori* information may be expected to be a better approximation of the true variance, given the lack of knowledge induced subjectivity that would be involved in an initial guess of the variance. The final probabilistic descriptions, in terms of marginal probability density functions and correlation matrices, of the element masses and stiffnesses of the system, may be expected to help in health monitoring/damage detection [44], reliability analysis [91], etc.

6.3.1 Directions for future research

There exists an immense scope of future research starting from the discussions in this chapter. Firstly, with an example in this chapter, the perturbation approach is shown to perform reasonably well in the presence of errors in the initial non-normalized modal parameter statistics. However, the said

example involved 100 sets of measured data; in a real situation the available sets of measured data may be very limited. Hence, the proposed perturbation approach needs to be combined with a preceding probabilistic modal identification technique (e.g. [89, 90]), which would enable the identification of the initial modal parameter statistics using very limited sets of measured data. The estimation errors in such statistics may be expected to be different from the errors in the example considered in this chapter, owing to the reduction in the measured data. The performance of the perturbation approach with such errors remains to be assessed. Secondly, the perturbation approach is based on the assumption that the parameter distributions are Gaussian; the case of non-Gaussian distributions needs to be addressed, e.g. using Laplace's method of asymptotic approximation for the integrals defining the different parameter statistics [87, 92, 93]. Thirdly, the method discussed to iteratively update the variance of the *a priori* information needs to be studied in more details with respect to its convergence properties, e.g. the rate of convergence, the converged value, whether there can be some other assumption than Eq. (6.27) which leads to an improved converged value etc. Fourthly, the proposed approach should be compared with some other existing uncertainty quantification methods with similar objectives, e.g. the Bayesian approach discussed in [94]. While Bayesian approaches would have certain advantages, e.g. they may not require the re-formulation of the involved estimation equations of the inverse problem for different model classes, they would also be computationally more intensive and would, in general, require more *a priori* information. Finally, the proposed perturbation approach needs to be tested with experimental data, and its performance in structural health monitoring applications remains to be examined.

Chapter 7

Concluding Remarks

While chapter specific conclusions, contributions, and future research scope have been identified at the end of each chapter, here we reiterate the important findings, and list the general contributions of this dissertation, its general limitations and the ensuing scope of future research.

7.1 Contributions

The primary objective of this dissertation has been to investigate the structural identification problem under the constraint of incomplete information, and to specifically attempt to answer the following question: "Is the available information, assumed and/or measured, sufficient for an unique estimation of the structural mass, $\mathbf{M}$, and stiffness, $\mathbf{K}$, matrices?". This question and the associated identification problem have been addressed for shear-type structural systems, including 2-D and 3-D laterally-torsionally coupled rigid-floor systems (2 translations and 1 rotation per floor), under different testing scenarios. The general identification framework adopted in this study has involved the following successive steps: (a) identifying the complete spectrum of modal parameters, i.e. natural frequencies, modal damping ratios, and non-mass normalized mode shape components at the DOFs with sensors/actuators using any appropriate experimental/operational modal analysis technique, (b) mass-normalizing the measured mode shape components, (c) expanding the mode shape components to the unobserved DOFs to get the complete mass normalized mode shape matrix $\mathbf{V}$, and (d) using the modal orthogonality relations to estimate the complete $\mathbf{M}$ and $\mathbf{K}$ matrices. Thus, the identifiability question framed above has been reframed and investigated as: "Is the available information,

assumed and/or measured, sufficient for an unique normalization and expansion of the vibration mode shapes of the structure?". The normalization and expansion strategies have been formulated expressing the information available from the structural topology in terms of the modal parameters, and conditions/tests attempting to ensure unique normalization and expansion have been discussed for various testing scenarios.

In Chapter 2, the scenario when a shear-type structure is excited using actuator generated known input forces has been considered. An input-output balance approach has been introduced to obtain mass-normalized mode shape components at all the instrumented, with an actuator and/or a sensor, DOFs of the system. This approach is not limited to only shear-type structures, but is applicable to any linear classically damped structural system. In Chapter 3 the scenario when a 3-D rigid floor shear–building type structure is excited by known/unknown base excitation has been considered. The discussions in this chapter are however applicable to any output-only situation. Mass normalizing the observed mode shape components has involved satisfying the structural topology requirements and any available *a priori* information. An approach to expand the mass normalized mode shapes from the instrumented to the non-instrumented DOFs has been developed for 1-D systems in Chapter 2, and extended to 2-D and 3-D systems in Chapter 3, to get the complete mass normalized mode shape matrix. An alternative approach has been studied in Chapter 4, where a simultaneous mode shape expansion-cum-mass normalization approach to obtain the complete mass normalized mode shape matrix has been developed. This approach involves the solution of a system of nonlinear equations, derived from structural topology requirements and the measured non-normalized mode shape components. The performance of the different identification schemes have been assessed using numerical examples of various complexities as well as using experimental data. These example applications have illustrated the ability of the proposed approaches to obtain reliably accurate estimates of the system's mass and stiffness parameters, even under the constraints of very limited and noisy measured data, unmeasured input, and minimal assumed *a priori* information of the system's physical parameters.

For a test with known inputs applied through actuators one does not need to assume *a priori* the value of any physical parameter. On the other hand, for systems with diagonal $\mathbf{M}$, it has been shown that a single *a priori* information of the value of any physical parameter is sufficient for a unique identification, given sufficient measured information, in output-only/base excitation situations. This

implies that, given sufficient measured information, one can always estimate a system proportional system to the true system by a single scalar factor. The single *a priori* information can then be used to scale the proportional to the true system. Different alternatives of available *a priori* information have been considered: (a) a set of known lumped/floor masses, or (b) the known total mass of the system, or (c) an additional set of measured data from a modified system with known added lumped masses. As shown in Appendix A, the input-output balance method of Chapter 2 may be used with a prior forced vibration test to identify the centers of mass and lumped mass parameters of all instrumented floors, providing necessary *a priori* information for a base excitation/output-only test.

The importance of actuator/sensor locations in identifiability has been established through various discussions/examples appearing throughout this thesis. Moreover, the importance of identifiability in health monitoring has been highlighted through an example of a 3-DOF system in Chapter 4. The mode shape expansion method developed in Chapters 2 and 3 has simultaneously addressed the problem of global identifiability through a set of statements, from which it is concluded that a knowledge of either the 1st or the last or any two consecutive rows (or block rows for 2-D/3-D systems) of the mass normalized mode shape matrix $\mathbf{V}$ guarantees a unique expansion to the complete $\mathbf{V}$ matrix for a shear-type system. Considering the input-output balance along with the mode shape expansion statements, several minimal and near-minimal instrumentation set-ups have been identified for a unique estimation of the mass and stiffness matrices of rigid floor shear-type buildings, from tests with known input forces applied through actuators. These set-ups have been listed in Chapter 2 for 1-D systems and Appendix A for 3-D systems; for a general N_D system with N_m floors/lumped masses, these set-ups require instrumenting: (i) only the 1st or the N_mth floor with one actuator and N_D sensors, or (ii) two consecutive floors, with one actuator and N_D sensors at one floor, and an additional N_D actuators/sensors at the other floor, with independent inputs from the actuators, or (iii) two consecutive floors with either N_D actuators and/or N_D sensors per floor, and *any other* additional floor with one actuator and N_D sensors, with independent inputs from the actuators, or (iv) two consecutive floors, with one actuator and N_D sensors per floor, for dependent inputs from the actuators. For 1-D systems these set-ups require only 1 or 2 actuators and sensors. The case of dependent inputs from the actuators leading to possible solution non-uniqueness has been identified while studying the input-output balance approach, and highlights the fact that non-uniqueness in identification does not only depend on the instrumentation, but also on the type of loading.

For the output-only/base excitation situations, theoretical constraints regarding minimal instrumentation, given some available *a priori* information, have been addressed in Chapter 3, vis-$\grave{a}$-vis the requirements for global identifiability. Some guidelines and an experiment design method have been discussed to decide sensor placement configurations ensuring global identifiability, and possible implications of low translational-rotational coupling in 2-D and 3-D systems have been highlighted. It has also been shown that an unique estimation of the story stiffness matrix does not imply an unique estimation of the individual frame stiffnesses, if one does not know the floor center of mass. In Chapter 4, a different approach has been explored to determine the minimum necessary number and location of sensors from the point of view of minimum necessary information. This approach is based on a set of statements and a method of analysis to determine the minimum independent information contained in the measurements from any given sensor set-up. Additionally, tests for local and global identifiability, using the implicit function theorem and the real Jacobian conjecture, have also been discussed for pre- and post-experiment applications; these tests provide sufficient, but not necessary, conditions for identifiability.

The different sensor placement rules and identifiability tests appearing in Chapters 2 to 4 are expected to be useful for experiment design purposes, in determining the necessary number of sensors/actuators, and identifying a wide array of alternative choices for sensor/actuator locations. Having such alternative choices will provide the engineer with an increased flexibility in avoiding locations where placing instruments may be difficult due to physical constraints, or where one may expect to have a low signal-to-noise ratio in the measurements, etc., while still satisfying the requirements of global/local identifiability. While all the sensor/actuator placement configurations satisfying global identifiability requirements would contain at least the minimal necessary information to identify a unique system, the quality of information for the different configurations would be different, and would depend on the particular structure under consideration. Hence, the individual configurations may further be ranked according to some information measure [40,41] to find the optimal, in the sense of most informative, instrumentation configuration, given a nominal model of the structure. The identifiability tests developed in Chapter 4 may also be used in identifying possibilities of multiple solutions post-experiment. The different identifiability requirements/tests have been verified using both numerical and experimental examples, by performing structural identification with the permissible instrumentation set-ups obtained from satisfying these requirements/tests.

The structural identification approaches developed in Chapters 2 and 3 have been applied to structural health monitoring problems in Chapter 5, using experimental data from two different sets of experiments. In these experiments, structural damage has been represented by a reduction in the cross-sectional area of some columns of the corresponding "healthy" system. Different modal and physical parameter comparative measures have been considered for damage detection. It has been shown that just using modal parameters (frequencies and mode shapes), while one may be able to detect whether the structure is damaged or not, in general one may not be able to identify the possible location and extent of any damage. The only exception to this is possibly the FPCOMAC, a modal parameter comparative measure introduced in Appendix D, using which one may also be able to locate a likely region containing the damaged element(s). On the other hand, it has been shown using the mean identified physical parameters that, if the instrumentation, modeling assumptions, and operations in the identification exercise are consistent between the healthy and the damaged states of the system, reasonably accurate estimation of both the damage location and severity can be achieved. An approach has also been discussed to characterize the damage location and severity in a probabilistic sense. This approach aims to account for the inherent variability, induced by exogenous factors like environmental/operational fluctuations etc., in both the healthy and possibly damaged states of the structure, providing different damage severity vs. exceedance probability curves corresponding to different conditions of the healthy state.

The deterministic structural identification approach developed in Chapter 4 has been extended to a probabilistic framework in Chapter 6, using a mean-centered perturbation based forward uncertainty propagation approach. With numerical examples it has been shown that this approach can quantify the uncertainty in the mass and stiffness parameter estimates with reasonable accuracy, using the minimal necessary instrumentation and *a priori* information. The source of uncertainty considered in this chapter has been the inherent structural variability, induced e.g by ambient fluctuations, represented through Gaussian distributions of the structural parameters. Cases with correlations between the different masses and stiffnesses have also been considered. The estimated marginal distributions and correlation matrices, statistically defining the parameters of the monitored system, may be expected to help in structural health assessment and reliability analysis problems.

7.2 Directions for Future Research

Some possible directions for future research particular to the works presented in Chapters 5 and 6 have been respectively included at the end of these chapters. Here instead we list some general potential future research directions, stemming mainly from the limitations of the research conducted in this thesis.

Firstly, the entire study in this dissertation has been concerned with shear-type systems, including 2-D/3-D laterally-torsionally coupled rigid floor building systems. A natural next step would be to investigate if similar analysis, as presented in this dissertation, may be extended to other classes of linear structural systems. The general framework discussed here involved explicitly using the information available from structural topology in developing the identification schemes and studying identifiability. Since for a given model class, the structural topology, in terms of connectivity, sparsity pattern in the $\mathbf{M}$ and $\mathbf{K}$ matrices, etc., would be known from a FE model, there certainly exists the possibility of generalizing the framework of this dissertation.

Secondly, in this study we have always considered classically damped systems, with the damping represented via modal damping ratios. The case of non-classically damped systems may be considered in the future. For such systems, a complete instrumentation, with every DOF having either an actuator and/or a sensor and at least one co-located actuator-sensor pair, will ensure the unique estimation of the complete mass, damping and stiffness matrices [28]. If however only N_s number of DOFs are instrumented, assuming the identification of the complete spectrum at the measured DOFs, one would have a total of $2N(N - N_s)$ unknowns in the mode shape matrix, considering the real and imaginary parts, which would need to be estimated. Finding the minimal N_s, and their allowed locations, which will ensure a unique estimation of these $2N(N - N_s)$ unknowns, can be a direction of future research.

Thirdly, we have consistently made the assumption that the complete spectrum of modal parameters have been identified at the instrumented DOFs. While this assumption is very common in studies on identifiability, it will seldom be satisfied in practice. Thus, the situation of unidentified modes certainly needs to be considered in the future. While this is possibly going to be the most challenging direction of future research amongst the ones listed here, there are some potential courses one may follow, e.g.: (a) Investigating whether knowing a certain set of modes would allow an unique identification, and any associated conditions which would need to be satisfied in such a case; (b) Whether

identifying certain modes at certain DOFs, e.g using heterogenous sensing, would ensure identifiability (see e.g. Section 4.6.3 and [6]); (c) Whether one can use mode mixing, i.e. complementing the identified modes with analytical modes from a FE model, to account for unidentified modes, and how much error does such a strategy introduce in the solution, etc.

Finally, it will also be interesting to investigate strategies which would enable the identification of all the solutions, within a feasible space defined from engineering judgements, in cases where the parameter sets of interest are globally unidentifiable but locally identifiable. It should be emphasized that identifiability of the parameter set of interest is exclusively dependent on the instrumented DOFs (measured data) and available *a priori* information. Even if these information do not ensure identifiability, one can still obtain a single solution by discarding the other solutions using regularization techniques, limiting the search space, or using informative priors in Bayesian updating; however, this does not mean that the identified solution is the correct one, as the correct solution may in fact be amongst the ones discarded. One possible way to identify all the solutions within a feasible model space would be to use a non-informative (uniform) prior in Bayesian updating, thereby letting only the measured data influence the identification; in this case the posterior probability density function may be expected to be multi-modal, with the different peaks corresponding to the different solutions. An alternative method may be to engage in multi-model FE model updating/identification techniques [95, 96]. The crucial requirement will be to employ efficient identification schemes, possibly using optimization methods with good global search capabilities [97, 98], which will attempt to find all the possible solutions at a reasonable computational expense.

Bibliography

[1] Udwadia FE, Sharma DK. Some uniqueness results related to building structural identification. *SIAM Journal on Applied Mathematics* 1978; **34**:104–118.

[2] Katafygiotis LS, Beck JL. Updating models and their uncertainties. II: Model identifiability. *ASCE Journal of Engineering Mechanics* 1998; **124**:463–467.

[3] Franco G, Betti R, Longman RW. On the uniqueness of solutions for the identification of linear structural systems. *ASME Journal of Applied Mechanics* 2006; **73**:153–162.

[4] Mukhopadhyay S, Luş H, Betti R. Modal parameter based structural identification using input-output data: Minimal instrumentation and global identifiability issues. *Mechanical Systems and Signal Processing* 2014; **45**(2):283–301.

[5] Mukhopadhyay S, Luş H, Betti R. Structural identification with incomplete instrumentation and global identifiability requirements under base excitation. *Structural Control and Health Monitoring* 2014; **under review**.

[6] Chatzis MN, Chatzi EN, Smyth AW. On the observability and identifiability of nonlinear structural and mechanical systems. *Structural Control and Health Monitoring* 2014; **DOI: 10.1002/stc.1690**.

[7] Friswell MI, Mottershead JE. *Finite element model updating in structural dynamics*. Kluwer Academic Publishers, 1995.

[8] Chen HP. Mode shape expansion using perturbed force approach. *Journal of Sound and Vibration* 2010; **329**:1177–1190.

[9] O'Callahan JC, Avitabile P, Riemer R. System equivalent reduction expansion process. *Proceedings of the 7th International Modal Analysis Conference*, Las Vegas, NV, USA, 1989; 29–37.

[10] Guyan RJ. Reduction of stiffness and mass matrices. *AIAA Journal* 1965; **3**:380.

[11] Paz M. Dynamic condensation. *AIAA Journal* 1984; **22**:724–727.

[12] Ljung L, Glad T. On global identifiability for arbitrary model parameterizations. *Automatica* 1994; **30**:265–276.

[13] Nayeri RD, Masri SF, Ghanem RG, Nigbor RL. A novel approach for the structural identification and monitoring of a full-scale 17-story building based on ambient vibration measurements. *Smart Materials and Structures* 2008; **17**:025 006.

[14] Yuan P, Wu Z, Ma X. Estimated mass and stiffness matrices of shear building from modal test data. *Earthquake Engineering and Structural Dynamics* 1998; **27**:415–421.

[15] Camillacci R, Gabriele S. Mechanical identification and model validation for shear-type frames. *Mechanical Systems and Signal Processing* 2005; **19**:597–614.

[16] Omrani R, Hudson RE, Taciroglu E. Story-by-story estimation of the stiffness parameters of laterally-torsionally coupled buildings using forced or ambient vibration data: I. Formulation and verification. *Earthquake Engineering and Structural Dynamics* 2012; **41**:1609–1634.

[17] Udwadia FE, Sharma DK, Shah PC. Uniqueness of damping and stiffness distributions in the identification of soil and structural systems. *ASME Journal of Applied Mechanics* 1978; **45**:181–187.

[18] Katafygiotis LS, Beck JL. Uniqueness in structural system identification. *Proceedings of the U.S. National Workshop on Structural Control Research*, Los Angeles, CA, USA, 1990; 136–140.

[19] Gladwell GML. Inverse finite element vibration problems. *Journal of Sound and Vibration* 1999; **211**:309–324.

[20] Gladwell GML. *Inverse problems in vibration, 2nd Edition*. Kluwer Academic Publishers, 2004.

[21] Allemang RJ, Brown DL. A correlation coefficient for modal vector analysis. *Proceedings of the 1st International Modal Analysis Conference (IMAC)*, Kissimmee, FL, USA, 1982; 110–116.

[22] Lieven NAJ, Ewins DJ. Spatial correlation of mode shapes, the Coordinate Modal Assurance Criterion (COMAC). *Proceedings of the 6th International Modal Analysis Conference (IMAC)*, Bethel, CT, USA, 1988; 690–695.

[23] Balsamo L, Mukhopadhyay S, Betti R, Luş H. Damage detection using Flexibility Proportional Modal Assurance Criterion. *Proceedings of the 31st International Modal Analysis Conference*, Garden Grove, CA, USA, 2013.

[24] Mukhopadhyay S, Betti R, Luş H. Minimal instrumentation for global identifiability in structural identification using input-output data. *Proceedings of the 6th World Conference on Structural Control and Monitoring*, Barcelona, Spain, 2014.

[25] Juang JN, Pappa RS. An eigensystem realization algorithm for model parameter identification and model reduction. *Journal of Guidance, Control, and Dynamics* 1985; **8**:620–627.

[26] Juang JN, Phan M, Horta LG, Longman RW. Identification of observer/kalman filter markov parameters: Theory and experiments. *Journal of Guidance, Control, and Dynamics* 1993; **16**:320–329.

[27] Luş H, Betti R, Longman RW. Identification of linear structural systems using earthquake-induced vibration data. *Earthquake Engineering and Structural Dynamics* 1999; **28**:1449–1467.

[28] Angelis MD, Luş H, Betti R, Longman RW. Extracting physical parameters of mechanical models from identified state space representations. *ASME Journal of Applied Mechanics* 2002; **69**(9):617–625.

[29] Alvin K, Park K. Second-order structural identification procedure via state-space-based system identification. *AIAA Journal* 1994; **32**:397–406.

[30] MATLAB®. *R2012b*. The MathWorks Inc., Natick, MA, 2012.

[31] Huffel SV, Vandewalle J. *The Total Least Squares Problem: Computational Aspects and Analysis*. Society for Industrial and Applied Mathematics, Philadelphia, 1991.

[32] Figueiredo E, Park G, Figueiras J, Farrar C, Worden K. Structural health monitoring algorithm comparisons using standard data sets. *Technical Report LA-14393*, Los Alamos National Laboratory, Los Alamos, New Mexico 87545 2009.

[33] Figueiredo E, Park G, Farrar CR, Worden K, Figueiras J. Machine learning algorithms for damage detection under operational and environmental variability. *Structural Health Monitoring* 2011; **10**:559–572.

[34] Bao C, Hao H, Li ZX. Multi-stage identification scheme for detecting damage in structures under ambient excitations. *Smart Materials and Structures* 2013; **22**:045 006.

[35] Balsamo L, Betti R, Beigi H. A structural health monitoring strategy using cepstral features. *Journal of Sound and Vibration* 2014; **333**:4526–4542.

[36] Moaveni B, Barbosa AR, Panagiotou M, Conte JP, Restrepo JI. Uncertainty analysis of identified damping ratios in nonlinear dynamic systems. *Proceedings of the 27th International Modal Analysis Conference*, Orlando, FL, USA, 2009.

[37] Hernandez EM, Polanco NR. Uncertainty quantification of identified modal parameters using the Fisher information criterion. *Proceedings of the 32nd International Modal Analysis Conference*, Orlando, FL, USA, 2014.

[38] Kareem A, Sun WJ. Dynamic response of structures with uncertain damping. *Engineering Structures* 1990; **12**:2–8.

[39] Kareem A, Gurley K. Damping in structures: its evaluation and treatment of uncertainty. *Journal of Wind Engineering and Industrial Aerodynamics* 1996; **59**:131–157.

[40] Udwadia FE. Methodology for optimal sensor locations for parameter identification in dynamic systems. *ASCE Journal of Engineering Mechanics* 1994; **120**:368–390.

[41] Papadimitriou C. Optimal sensor placement methodology for parametric identification of structural systems. *Journal of Sound and Vibration* 2004; **278**:923–947.

[42] Mukhopadhyay S, Betti R, Luş H. Structural identification using response measurements under base excitation. *Proceedings of the 32nd International Modal Analysis Conference*, Orlando, FL, USA, 2014.

[43] Bernal D, Gunes B. Flexibility based approach for damage characterization: Benchmark application. *ASCE Journal of Engineering Mechanics* 2004; **130**(1):61–70.

[44] Balsamo L, Mukhopadhyay S, Betti R. A statistical framework for structural health monitoring with stiffness proportional damage sensitive features. *Smart Structures and Systems* 2014; **under review**.

[45] Catbas FN, Gul M, Burkett JL. Damage assessment using flexibility and flexibility-based curvature for structural health monitoring. *Smart Materials and Structures* 2008; **17**:015 024.

[46] Fraraccio G, Brugger A, Betti R. Experimental studies on damage detection in frame structures using vibration measurements. *Shock and Vibration* 2010; **17**:697–721.

[47] Luş H, Betti R, Longman RW. Obtaining refined first-order predictive models of linear structural systems. *Earthquake Engineering and Structural Dynamics* 2002; **31**:1413–1440.

[48] Mukhopadhyay S, Luş H, Hong AL, Betti R. Propagation of mode shape errors in structural identification. *Journal of Sound and Vibration* 2012; **331**(17):3961–3975.

[49] Mukhopadhyay S, Betti R, Luş H. Output only structural identification with minimal instrumentation. *Proceedings of the 31st International Modal Analysis Conference*, Garden Grove, CA, USA, 2013.

[50] Parloo E, Verboven P, Guillaume P, Overmeire MV. Sensitivity-based operational mode shape normalization. *Mechanical Systems and Signal Processing* 2002; **16**:757–767.

[51] Brincker R, Andersen P. A way of getting scaled mode shapes in output only modal analysis. *Proceedings of the 21st International Modal Analysis Conference (IMAC)*, Orlando, USA, 2003; 141.

[52] Bernal D. Modal scaling from known mass perturbations. *ASCE Journal of Engineering Mechanics* 2004; **130**(9):1083–1088.

[53] Bernal D. A receptance based formulation for modal scaling using mass perturbations. *Mechanical Systems and Signal Processing* 2011; **25**:621–629.

[54] Lopez-Aenlle M, Brincker R, Pelayo F, Canteli A. On exact and approximated formulations for scaling mode shapes in operational modal analysis by mass and stiffness change. *Journal of Sound and Vibration* 2012; **331**:622–637.

[55] Gul M, Catbas FN. Statistical pattern recognition for structural health monitoring using time series modeling: Theory and experimental verifications. *Mechanical Systems and Signal Processingl* 2009; **23**:2192–2204.

[56] Farrar CR, Worden K. *Structural health monitoring: A machine learning perspective*. John Wiley & Sons, Ltd, Chichester, UK, 2013.

[57] Friswell MI. Damage identification using inverse methods. *Philosophical transactions of the Royal Society A* 2007; **365**:393–410.

[58] Spivak M. *Calculus on manifolds*. Addison-Wesley/WA Benjamin, New York, 1965.

[59] Krantz S, Parks H. *The implicit function theorem: History, theory, and applications*. Springer, 2002.

[60] Samuelson P. Prices of factors and goods in general equilibrium. *The Review of Economic Studies* 1953-54; **21**:1–20.

[61] Smale S. Mathematical problems for the next century. *The Mathematical Intelligencer* 1998; **20**:7–15.

[62] van den Essen A. Polynomial automorphisms and the Jacobian conjecture. *Algbre non commutative groupes quantiques et invariants: Septiemes Rencontres du contact Franco-Belge en Algebre*, Societe Mathematique de France: Reims, France, 1995.

[63] Parthasarathy T, Ravindran G. Global univalence and the Jacobian conjecture. *Applied Mathematics in the Golden Age*, Misra J (ed.). Narosa Publishing House: New Delhi, India, 2003; 378–409.

[64] Pinchuk S. A counterexample to the string real jacobian conjecture. *Mathematische Zeitschrift* 1994; **217**:1–4.

[65] Kurdyka K, Rusek K. Polynomial rational bijections of R^n. *Proceedings of the American Mathematical Society* 1988; **102**:804–808.

[66] Gale D, Nikaido H. The Jacobian matrix and global univalence of mappings. *Mathematische Annalen* 1965; **159**:81–93.

[67] Campbell LA. Rational Samuelson maps are univalent. *Journal of Pure and Applied Algebra* 1994; **92**:227–240.

[68] Hong AL, Ubertini F, Betti R. New stochastic subspace approach for system identification and its application to long-span bridges. *ASCE Journal of Engineering Mechanics* 2013; **139**:724–736.

[69] Sun H, Betti R. Simultaneous identification of structural parameters and dynamic input with incomplete output-only measurements. *Structural Control and Health Monitoring* 2014; **21**:868–889.

[70] Padmanabhan KK, Murty ASR. Damping in structural joints subjected to tangential loads. *Proceedings of the Institution of Mechanical Engineers, Part C: Journal of Mechanical Engineering Science* 1991; **205**:121.

[71] Ouyang H, Oldfield JE, Mottershead JE. Experimental and theoretical studies of a bolted joint excited by a torsional dynamic load. *International Journal of Mechanical Sciences* 2006; **48**:1447–1455.

[72] Pandey AK, Biswas M. Damage detection in structures using changes in flexibility. *Journal of Sound and Vibration* 1994; **169**:3–17.

[73] Fraraccio G, Brugger A, Betti R. Identification and damage detection in structures subjected to base excitation. *Experimental Mechanics* 2008; **48**:521–528.

[74] Sohn H, Dzwonczyk M, Straser E, Kiremidjian A, Law K, Meng T. An experimental study of temperature effect on modal parameters of the Alamosa Canyon bridge. *Earthquake Engineering and Structural Dynamics* 1999; **28**:879–897.

[75] Peeters B, Roeck GD. One-year monitoring of the Z24-bridge: Environmental effects versus damage events. *Earthquake Engineering and Structural Dynamics* 2001; **30**:149–171.

[76] Clinton J, Bradford S, Heaton T, Favela J. The observed wander of the natural frequencies in a structure. *Bulletin of Seismological Society of America* 2006; **96**:237–257.

[77] Sohn H. Effects of environmental and operational variability on structural health monitoring. *Philosophical Transactional of the Royal Society A* 2007; **365**:539–560.

[78] Soyoz S, Feng M. Long-term monitoring and identification of bridge structural parameters. *Computer Aided Civil and Infrastructure Engineering* 2009; **24**:82–92.

[79] Yuen KV, Kuok SC. Ambient interference in long-term monitoring of buildings. *Engineering Structures* 2010; **32**:2379–2386.

[80] Moser P, Moaveni B. Environmental effects on the identified natural frequencies of the Dowling Hall footbridge. *Mechanical Systems and Signal Processing* 2011; **25**:2336–2357.

[81] Hanselmann A, Schrempf O, Hanebeck U. Optimal parametric density estimation by minimizing an analytic distance measure. *Proceedings of the 10th International Conference on Information Fusion*, 2007.

[82] Balsamo L. *Statistical pattern recognition based structural health monitoring strategies*. PhD Thesis, Columbia Univeristy, NY, 2014.

[83] Vanik MW, Beck JL, Au SK. Bayesian probabilistic approach to structural health monitoring. *ASCE Journal of Engineering Mechanics* 2000; **126**:738–745.

[84] Balsamo L, Mukhopadhyay S, Betti R, Luş H. Modal parameter based damage detection in operational modal analysis: A statistical pattern recognition approach. *Proceedings of the 11th International Conference on Structural Safety and Reliability (ICOSSAR)*, New York, NY, USA, 2013.

[85] Mukhopadhyay S, Betti R, Luş H. Structural identification and uncertainty quantification in operational modal analysis with minimal instrumentation. *Proceedings of the 11th International Conference on Structural Safety and Reliability*, New York, NY, USA, 2013.

[86] Beck JL, Katafygiotis LS. Updating models and their uncertainties. I: Bayesian statistical framework. *ASCE Journal of Engineering Mechanics* 1998; **124**:455–461.

[87] Khodaparast H, Mottershead J, Friswell M. Perturbation methods for the estimation of parameter variability in stochastic model updating. *Mechanical Systems and Signal Processing* 2008; **22**:1751–1773.

[88] Doebling SW, Farrar CR. Estimation of statistical distributions for modal parameters identified from averaged frequency response function data. *Journal of Vibration and Control* 2001; **7**:603–624.

[89] Yuen KV, Katafygiotis LS. Bayesian time-domain approach for modal updating using ambient data. *Probabilistic Engineering Mechanics* 2001; **16**:219–231.

[90] Reynders E, Pintelon R, Roeck GD. Uncertainty bounds on modal parameters obtained from stochastic subspace identification. *Mechanical Systems and Signal Processing* 2008; **22**:948–969.

[91] Soyoz S, Feng MQ, Shinozuka M. Structural reliability estimation with vibration-based identified parameters. *ASCE Journal of Engineering Mechanics* 2010; **136**:100–106.

[92] Papadimitriou C, Beck J, Katafygiotis L. Asymptotic expansion for reliability and moments of uncertain systems. *ASCE Journal of Engineering Mechanics* 1997; **123**:1219–1229.

[93] Adhikari S, Friswell M. Random matrix eigenvalue problems in structural dynamics. *International Journal for Numerical Methods in Engineering* 2007; **69**:562–591.

[94] Yuen KV, Beck JL, Katafygiotis LS. Efficient model updating and health monitoring methodology using incomplete modal data without mode matching. *Structural Control and Health Monitoring* 2006; **13**:91–107.

[95] Zarate BA, Caicedo JM. Finite element model updating: Multiple alternatives. *Engineering Structures* 2008; **30**:3724–3730.

[96] Goulet JA, Kripakaran P, Smith IFC. Multimodel structural performance monitoring. *ASCE Journal of Structural Engineering* 2010; **136**:1309–1318.

[97] Chatzi EN, Hiriyur B, Waisman H, Smyth AW. Experimental application and enhancement of the XFEM-GA algorithm for the detection of flaws in structures. *Computers & Structures* 2011; **89**:556–570.

[98] Sun H, Luş H, Betti R. Identification of structural models using a modified Artificial Bee Colony algorithm. *Computers & Structures* 2013; **116**:59–74.

[99] Toksoy T, Aktan AE. Bridge-condition assessment by modal flexibility. *Experimental Mechanics* 1994; **34**:271–278.

[100] Mayes RL. An experimental algorithm for detecting damage applied to the I-40 bridge over the Rio Grande. *Proceedings of the 13th International Modal Analysis Conference, Nashville, TN, USA* 1995; :219–225.

[101] Li GQ, Hao KC, Lu Y, Chen SW. A flexibility approach for damage identification of cantilever-type structures with bending and shear deformation. *Computers and Structures* 1999; **73**:565–572.

[102] Bernal D. Load vectors for damage localization. *ASCE Journal of Engineering Mechanics* 2002; **128**(1):7–14.

[103] Salawu OS, Williams C. Bridge assessment using forced-vibration testing. *Journal of Structural Engineering* 1995; **121**(2):161–173.

[104] Fryba L, Pirner M. Load tests and modal analysis of bridges. *Engineering Structures* 2001; **23**:102–109.

[105] Banerjee S, Ricci F, Monaco E, Mal A. A wave propagation and vibration-based approach for damage identification in structural components. *Journal of Sound and Vibration* 2009; **322**:167–183.

[106] Zhao J, DeWolf JT. Sensitivity study for vibrational parameters used in damage detection. *ASCE Journal of Structural Engineering* 1999; **125**:410–416.

[107] Nelson RB. Simplified calculation of eigenvector derivatives. *AIAA Journal* 1976; **14**(9):1201–1205.

[108] dos Santos JVA, Soares CMM, Soares CAM, Pina HLG. A damage identification numerical model based on the sensitivity of orthogonality conditions and least squares techniques. *Computers and Structures* 2000; **78**:283–291.

[109] Ren WX, Roeck GD. Structural damage identification using modal data. I: Simulation verification. *Journal of Structural Engineering* 2002; **128**(1):87–95.

[110] Yang QW, Liu JK. Structural damage identification based on residual force vector. *Journal of Sound and Vibration* 2007; **305**:298–307.

[111] Chen HP, Bicanic N. Identification of structural damage in buildings using iterative procedure and regularisation method. *International Journal for Computer Aided Engineering and Software* 2010; **27**:930–950.

[112] Ang AHS, Wilson HT. *Probability Concepts in Engineering Planning and Design: Vol. 2. Decision, Risk and Reliability*. John Wiley and Sons, New York, 1984.

[113] Allemang RJ. The modal assurance criterion (MAC) – Twenty years of use and abuse. *Proceedings of the 20th International Modal Analysis Conference*, Los Angeles, CA, USA, 2002; 397–405.

[114] Cornwell P, SW Doebling CF. Application of the strain energy damage detection method to plate-like structures. *Journal of Sound and Vibration* 1999; **224**:359–374.

[115] Duan Z, Yan G, Ou J, Spencer B. Damage detection in ambient vibration using proportional flexibility matrix with incomplete measured DOFs. *Structural Control and Health Monitoring* 2007; **14**:186–196.

Appendix A

Actuator-Driven Test of 3-D Buildings and Floor Centers of Mass Identification

A.1 Identification of Centers of Mass and Lumped Mass Parameters of Instrumented Floors from a Prior Actuator-Driven Forced Vibration Test[1]

In the approach discussed in Chapter 3, we assume that structural response measurements are available at the centers of mass of the instrumented mass elements. As illustrated with a numerical example in Chapter 3, this assumption plays a vital role in the identification of the 2-D and 3-D systems, since the mode shape normalization and expansion approaches explicitly use this condition, expressed through the diagonality of $\mathbf{M}$. As per this assumption, the *a priori* knowledge of the lumped masses/mass moments of inertia of the instrumented mass elements, necessary in the first scenario, also need to be defined with respect to the centers of mass of these elements. However, in general, the centers of mass may be unknown. To address this issue we present here a method to estimate the centers of mass, as well as the lumped masses/mass moments of inertia defined with respect to the centers of mass, of all the instrumented mass elements. For this we need to perform a separate forced vibration test, prior to the base excitation test, using actuator generated force inputs, and use

[1]This section is part of an article co-authored with Profs. Raimondo Betti and Hilmi Lus, currently under review in Structural Control and Health Monitoring [5].

these known input force(s) with the measured responses at the instrumented DOFs, to first identify the individual mass matrices, and then identify the centers of mass and lumped mass parameters, of all the instrumented mass elements. Although in Chapter 3 the physical coordinates of the structural system are defined with respect to the centers of mass at *all* the mass elements, both instrumented and non-instrumented, for the application of the method we need to know the centers of mass of only the instrumented elements; once these are known, using the proposed method we can estimate the *complete* $\mathbf{M}$ and $\mathbf{K}$ matrices, defined at the centers of mass of *all* the mass elements, even though the centers of mass of the non-instrumented elements are not explicitly known.

We present the center of mass/lumped mass parameter estimation methodology for a 3-D system consisting of N_m lumped mass elements, i.e. $N = 3N_m$ DOFs (it can be similarly applied for a 2-D system). Suppose: (a) we completely instrument n_m of these mass elements (total $3n_m$ measured DOFs), and (b) we apply known input forces at *any one* of these n_m instrumented mass elements. Fig. A.1(a) shows such a lumped mass element (floor of a building), containing applied inputs ($\mathbf{f}_{x_3}$, $\mathbf{f}_{x_4}$, $\mathbf{f}_{y_4}$) and measured outputs ($\ddot{\mathbf{u}}_{x_1}$, $\ddot{\mathbf{u}}_{y_1}$, $\ddot{\mathbf{u}}_{y_2}$). In this prior test, we use the applied input force(s) and the measured output responses defined at the centroids of the instrumented mass elements, since centroids can be easily determined from geometry (engineering drawing/architectural floor plan). However, it may not always be possible to *physically* locate sensors at the centroids, e.g. in a square floor with a central cut-out; here too, the actuators and sensors do not need to be *physically* located at the centroids (Fig. A.1). If the centroid (O) is the origin of the X–Y coordinate system, using rigid floor assumption, the forces and responses at O may be written as:

$$\begin{aligned} &\mathbf{f}_{x_O} = \mathbf{f}_{x_3} + \mathbf{f}_{x_4}; \quad \mathbf{f}_{y_O} = \mathbf{f}_{y_4}; \quad \mathbf{f}_{\theta_O} = -\mathbf{f}_{x_3} y_3 - \mathbf{f}_{x_4} y_4 + \mathbf{f}_{y_4} x_4 \\ &\ddot{\mathbf{u}}_{x_O} = \ddot{\mathbf{u}}_{x_1} + y_1 \ddot{\mathbf{u}}_{\theta_O}; \quad \ddot{\mathbf{u}}_{y_O} = \ddot{\mathbf{u}}_{y_1} - x_1 \ddot{\mathbf{u}}_{\theta_O}; \quad \ddot{\mathbf{u}}_{\theta_O} = \frac{\ddot{\mathbf{u}}_{y_2} - \ddot{\mathbf{u}}_{y_1}}{x_2 - x_1} \end{aligned} \tag{A.1}$$

where (x_1, y_1) to (x_4, y_4) are known from the actuator/sensor locations. The mass matrix with physical coordinates defined at centroids is: $\mathbf{M}_O = \text{diag}\big(\mathbf{m}_{O_1}, \mathbf{m}_{O_2}, \cdots, \mathbf{m}_{O_{N_m}}\big)$, where:

$$\mathbf{m}_{O_i} = \begin{bmatrix} m_i & 0 & -m_i y_{G_i} \\ 0 & m_i & m_i x_{G_i} \\ -m_i y_{G_i} & m_i x_{G_i} & J_i + m_i (x_{G_i}^2 + y_{G_i}^2) \end{bmatrix} \tag{A.2}$$

is the mass matrix of the ith mass element/floor defined at its centroid, with m_i being the ith lumped/floor mass, and J_i its mass moment of inertia defined at its center of mass located at (x_{G_i}, y_{G_i}). Hence, if

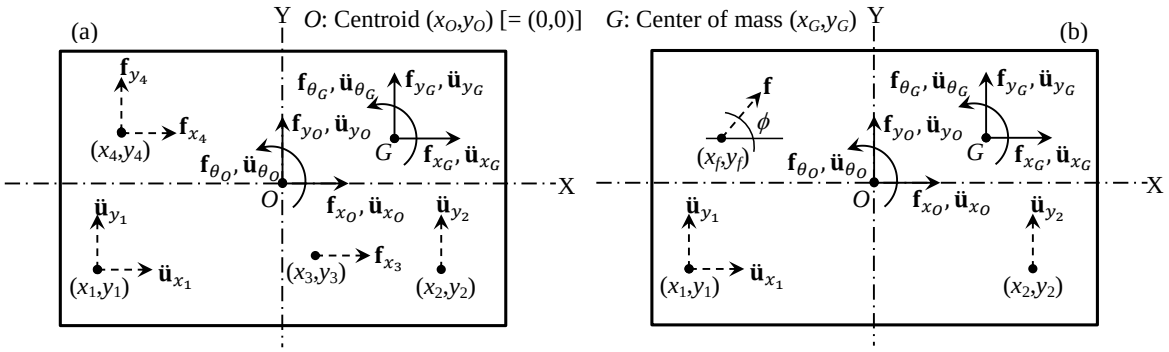

Figure A.1: Completely instrumented lumped mass with (a) three applied inputs, and (b) a single applied input.

we can estimate the mass matrices, defined at the centroids, of all the n_m instrumented mass elements, then, using Eq. (A.2), we can determine their corresponding centers of mass (x_{G_i}, y_{G_i}), lumped masses (m_i) and mass moments of inertia at the centers of mass (J_i). Let us denote by $\mathbf{V}_O$ the mass normalized mode shape matrix of the system for the physical coordinates defined at the centroids, by $\mathbf{r}_{O_i}$ the ith row of $\mathbf{V}_O$, and by $\mathbf{r}_{\mathbf{B}O_i} = \left\{\mathbf{r}_{O_{3i-2}}^T, \mathbf{r}_{O_{3i-1}}^T, \mathbf{r}_{O_{3i}}^T\right\}^T$ the set of rows of $\mathbf{V}_O$ corresponding to the DOFs of the ith mass element/floor. Then, using mass orthogonality ($\mathbf{M}_O^{-1} = \mathbf{V}_O\mathbf{V}_O^T$), and noting that $\mathbf{M}_O$ is block diagonal, and hence $\mathbf{M}_O^{-1} = \text{diag}\big(\mathbf{m}_{O_1}^{-1}, \mathbf{m}_{O_2}^{-1}, \cdots, \mathbf{m}_{O_{Nm}}^{-1}\big)$, the matrix $\mathbf{m}_{O_i}$ can be expressed as:

$$\mathbf{m}_{O_i} = (\mathbf{r}_{\mathbf{B}O_i}\mathbf{r}_{\mathbf{B}O_i}^T)^{-1} \tag{A.3}$$

The problem then reduces to the estimation of the $\mathbf{r}_{\mathbf{B}O_i}$'s for all the completely instrumented mass elements, for which we use the input–output balance method of Chapter 2.

Let ${}^m\mathcal{S} = \{{}^m s_1, {}^m s_2, \cdots, {}^m s_{n_m}\}$ denote the set of n_m completely measured mass elements; here ${}^m s_i$ is the ith *instrumented* floor, but not necessarily the ith floor. Then, the set of all measured DOFs, $\mathcal{S} = \{s_1, s_2, \cdots, s_{N_s}\}$ with $N_s = 3n_m$, is related to ${}^m\mathcal{S}$ as: $\{s_{3i-2}, s_{3i-1}, s_{3i}\}$ being the measured DOFs, respectively in the $\{x, y, \theta\}$ directions, at the centroid of the ith instrumented mass element ${}^m s_i$. Let the 3 inputs be located on the lth instrumented element ${}^m s_l$, and let us denote the 3 DOFs with these collocated inputs as $c_x(= s_{3l-2})$, $c_y(= s_{3l-1})$ and $c_\theta(= s_{3l})$. Let us also denote the 3 responses of any ith instrumented mass element by $\{(\ddot{\mathbf{u}}_{x_O})_{{}^m s_i}, (\ddot{\mathbf{u}}_{y_O})_{{}^m s_i}, (\ddot{\mathbf{u}}_{\theta_O})_{{}^m s_i}\}$, and the 3 input forces by $\{(\mathbf{f}_{x_O})_{{}^m s_l}, (\mathbf{f}_{y_O})_{{}^m s_l}, (\mathbf{f}_{\theta_O})_{{}^m s_l}\}$. We first use these known inputs and outputs in any system identification algorithm to identify $\{\omega_j, \zeta_j\}\ \forall\ j \in \{1, 2, \cdots, N\}$. Three sets of N *pseudo*-modal

responses are then computed by solving the following differential equations:

$$\left.\begin{aligned}(\ddot{\tilde{\boldsymbol{\eta}}}_j)_x + 2\zeta_j\omega_j(\dot{\tilde{\boldsymbol{\eta}}}_j)_x + \omega_j^2(\tilde{\boldsymbol{\eta}}_j)_x &= (\mathbf{f}_{x_O})_{^m s_l}\\ (\ddot{\tilde{\boldsymbol{\eta}}}_j)_y + 2\zeta_j\omega_j(\dot{\tilde{\boldsymbol{\eta}}}_j)_y + \omega_j^2(\tilde{\boldsymbol{\eta}}_j)_y &= (\mathbf{f}_{y_O})_{^m s_l}\\ (\ddot{\tilde{\boldsymbol{\eta}}}_j)_\theta + 2\zeta_j\omega_j(\dot{\tilde{\boldsymbol{\eta}}}_j)_\theta + \omega_j^2(\tilde{\boldsymbol{\eta}}_j)_\theta &= (\mathbf{f}_{\theta_O})_{^m s_l}\end{aligned}\right\} \quad \forall\, j \in \{1, 2, \cdots, N\} \tag{A.4}$$

where $(\ddot{\tilde{\boldsymbol{\eta}}}_j)_x$, $(\ddot{\tilde{\boldsymbol{\eta}}}_j)_y$, $(\ddot{\tilde{\boldsymbol{\eta}}}_j)_\theta$ are all $n_t \times 1$ dimensional vectors, n_t being the length of the input/output records. We next solve the least squares problem, $\mathbf{G}\boldsymbol{\Psi} = \mathbf{Y}$, where $\mathbf{G}$ is the $n_t \times 3N$ matrix:

$$\mathbf{G} = [(\ddot{\tilde{\boldsymbol{\eta}}}_1)_x\ (\ddot{\tilde{\boldsymbol{\eta}}}_2)_x\ \cdots\ (\ddot{\tilde{\boldsymbol{\eta}}}_N)_x\ (\ddot{\tilde{\boldsymbol{\eta}}}_1)_y\ (\ddot{\tilde{\boldsymbol{\eta}}}_2)_y\ \cdots\ (\ddot{\tilde{\boldsymbol{\eta}}}_N)_y\ (\ddot{\tilde{\boldsymbol{\eta}}}_1)_\theta\ (\ddot{\tilde{\boldsymbol{\eta}}}_2)_\theta\ \cdots\ (\ddot{\tilde{\boldsymbol{\eta}}}_N)_\theta] \tag{A.5}$$

and $\mathbf{Y}$ is the $n_t \times 3n_m$ matrix of the measured responses at the centroids of the instrumented floors:

$$\mathbf{Y} = [(\ddot{\mathbf{u}}_{x_O})_{^m s_1}\ (\ddot{\mathbf{u}}_{y_O})_{^m s_1}\ (\ddot{\mathbf{u}}_{\theta_O})_{^m s_1}\ \cdots\ (\ddot{\mathbf{u}}_{x_O})_{^m s_{n_m}}\ (\ddot{\mathbf{u}}_{x_O})_{^m s_{n_m}}\ (\ddot{\mathbf{u}}_{x_O})_{^m s_{n_m}}] \tag{A.6}$$

The $3N \times 3n_m$ dimensional least squares solution matrix, $\boldsymbol{\Psi} = \mathbf{G}^\dagger\mathbf{Y}$, is then of the form:

$$\boldsymbol{\Psi} = \left[\begin{array}{cccccccc}
\breve{v}_{s_1,1}\breve{v}_{c_x,1} & \breve{v}_{s_2,1}\breve{v}_{c_x,1} & \cdots & \breve{v}^2_{c_x,1} & \breve{v}_{c_y,1}\breve{v}_{c_x,1} & \breve{v}_{c_\theta,1}\breve{v}_{c_x,1} & \cdots & \breve{v}_{s_{N_s},1}\breve{v}_{c_x,1}\\
\breve{v}_{s_1,2}\breve{v}_{c_x,2} & \breve{v}_{s_2,2}\breve{v}_{c_x,2} & \cdots & \breve{v}^2_{c_x,2} & \breve{v}_{c_y,2}\breve{v}_{c_x,2} & \breve{v}_{c_\theta,2}\breve{v}_{c_x,2} & \cdots & \breve{v}_{s_{N_s},2}\breve{v}_{c_x,2}\\
\vdots & \vdots & \cdots & \vdots & \vdots & \vdots & \cdots & \vdots\\
\breve{v}_{s_1,N}\breve{v}_{c_x,N} & \breve{v}_{s_2,N}\breve{v}_{c_x,N} & \cdots & \breve{v}^2_{c_x,N} & \breve{v}_{c_y,N}\breve{v}_{c_x,N} & \breve{v}_{c_\theta,N}\breve{v}_{c_x,N} & \cdots & \breve{v}_{s_{N_s},N}\breve{v}_{c_x,N}\\
\hline
\breve{v}_{s_1,1}\breve{v}_{c_y,1} & \breve{v}_{s_2,1}\breve{v}_{c_y,1} & \cdots & \breve{v}_{c_x,1}\breve{v}_{c_y,1} & \breve{v}^2_{c_y,1} & \breve{v}_{c_\theta,1}\breve{v}_{c_y,1} & \cdots & \breve{v}_{s_{N_s},1}\breve{v}_{c_y,1}\\
\breve{v}_{s_1,2}\breve{v}_{c_y,2} & \breve{v}_{s_2,2}\breve{v}_{c_y,2} & \cdots & \breve{v}_{c_x,2}\breve{v}_{c_y,2} & \breve{v}^2_{c_y,2} & \breve{v}_{c_\theta,2}\breve{v}_{c_y,2} & \cdots & \breve{v}_{s_{N_s},2}\breve{v}_{c_y,2}\\
\vdots & \vdots & \cdots & \vdots & \vdots & \vdots & \cdots & \vdots\\
\breve{v}_{s_1,N}\breve{v}_{c_y,N} & \breve{v}_{s_2,N}\breve{v}_{c_y,N} & \cdots & \breve{v}_{c_x,N}\breve{v}_{c_y,N} & \breve{v}^2_{c_y,N} & \breve{v}_{c_\theta,N}\breve{v}_{c_y,N} & \cdots & \breve{v}_{s_{N_s},N}\breve{v}_{c_y,N}\\
\hline
\breve{v}_{s_1,1}\breve{v}_{c_\theta,1} & \breve{v}_{s_2,1}\breve{v}_{c_\theta,1} & \cdots & \breve{v}_{c_x,1}\breve{v}_{c_\theta,1} & \breve{v}_{c_y,1}\breve{v}_{c_\theta,1} & \breve{v}^2_{c_\theta,1} & \cdots & \breve{v}_{s_{N_s},1}\breve{v}_{c_\theta,1}\\
\breve{v}_{s_1,2}\breve{v}_{c_\theta,2} & \breve{v}_{s_2,2}\breve{v}_{c_\theta,2} & \cdots & \breve{v}_{c_x,2}\breve{v}_{c_\theta,2} & \breve{v}_{c_y,2}\breve{v}_{c_\theta,2} & \breve{v}^2_{c_\theta,2} & \cdots & \breve{v}_{s_{N_s},2}\breve{v}_{c_\theta,2}\\
\vdots & \vdots & \cdots & \vdots & \vdots & \vdots & \cdots & \vdots\\
\breve{v}_{s_1,N}\breve{v}_{c_\theta,N} & \breve{v}_{s_2,N}\breve{v}_{c_\theta,N} & \cdots & \breve{v}_{c_x,N}\breve{v}_{c_\theta,N} & \breve{v}_{c_y,N}\breve{v}_{c_\theta,N} & \breve{v}^2_{c_\theta,N} & \cdots & \breve{v}_{s_{N_s},N}\breve{v}_{c_\theta,N}
\end{array}\right] \tag{A.7}$$

where $\breve{v}_{i,j}$ is the (i,j)th element of $\mathbf{V}_O$. Remembering that the DOFs c_x, c_y and c_θ are the ones with collocated inputs and outputs, we can first solve for the elements of any of the corresponding three rows of $\mathbf{V}_O$, i.e. $\breve{v}_{c_x,j}$ (or $\breve{v}_{c_y,j}$ or $\breve{v}_{c_\theta,j}$) $\forall\ j \in \{1, 2, \cdots, N\}$, from the $(3l-2)$th (or $(3l-1)$th or $(3l)$th) column of $\boldsymbol{\Psi}$, considering the first (or the second or the third) set of N rows of $\boldsymbol{\Psi}$. Once

one of these three rows of $\mathbf{V}_O$ is estimated, the remaining $3n_m - 1$ measured rows of $\mathbf{V}_O$ may be estimated from the remaining $3n_m - 1$ columns of $\mathbf{\Psi}$, considering the same set of N rows of $\mathbf{\Psi}$ (e.g. the first N rows if the c_xth row was estimated in the previous step). Once all the instrumented rows of $\mathbf{V}_O$ are thus determined, one can use Eqs. (A.3) and (A.2) to estimate the centers of mass, lumped masses and mass moments of inertia at the centers of mass of all the instrumented mass elements.

In practical situations, the modal frequencies and damping ratios identified using system identification will contain estimation errors due to noisy measurements. To limit the propagation of these errors through the different steps of identification one can implement a coupled optimization/input-output balance technique as discussed in Chapter 2. Additionally, to reduce the errors from measurement noise, as well as to address the issue of unknown coupling between the translational and rotational DOFs in the different modes, it will be more prudent to estimate the instrumented rows of $\mathbf{V}_O$ using all the $3N$ rows of $\mathbf{\Psi}$, instead of using only one set of N rows. The issue of unknown coupling is important, since in case there is low level of coupling between the x, y and θ directional DOFs, the estimated $\breve{v}_{c_x,j}$'s will be close to zero for the j's corresponding to the y directional and torsional modes, and hence one will not be able to estimate, in this situation, the other $v_{s_i,j}$'s for these j's. To instead use all the $3N$ rows of $\mathbf{\Psi}$, we define a reduced matrix, $\mathbf{\Psi}^R$, obtained by element-wise summing of the matrices defined by the three sets of N rows in $\mathbf{\Psi}$:

$$\mathbf{\Psi}^R = \mathbf{\Psi}(1:N,:) + \mathbf{\Psi}(N+1:2N,:) + \mathbf{\Psi}(2N+1:3N,:) \tag{A.8}$$

Then, any (j,i)th element of $\mathbf{\Psi}^R$, can be written as:

$$\psi^R_{j,i} = \breve{v}_{s_i,j}(\breve{v}_{c_x,j} + \breve{v}_{c_y,j} + \breve{v}_{c_\theta,j}) \quad \forall\, s_i \in \mathcal{S},\ j \in \{1,2,\cdots,N\} \tag{A.9}$$

Once $\left\{\breve{v}_{c_x,j}, \breve{v}_{c_y,j}, \breve{v}_{c_\theta,j}\right\}\ \forall\, j \in \{1,2,\cdots,N\}$ are obtained, the remaining $3n_m - 3$ measured rows of $\mathbf{V}_O$ ($\breve{v}_{s_i,j}\ \forall\, s_i \in \mathcal{S} \setminus \{c_x, c_y, c_\theta\}\ ,\ j \in \{1,2,\cdots,N\}$) can be estimated using Eq. (A.9). Using the formulae $(p+q+r)^2 = p^2+q^2+r^2+2(pq+qr+rp)$ and $(p+q)(p-q) = p^2-q^2$, we obtain:

$$\left.\begin{aligned}
\breve{v}_{c_x,j} + \breve{v}_{c_y,j} + \breve{v}_{c_\theta,j} &= \sqrt{\psi^R_{j,3l-2} + \psi^R_{j,3l-1} + \psi^R_{j,3l}} \\
\breve{v}_{c_x,j} + \breve{v}_{c_y,j} - \breve{v}_{c_\theta,j} &= \frac{\psi^R_{j,3l-2} + \psi^R_{j,3l-1} - \psi^R_{j,3l}}{\sqrt{\psi^R_{j,3l-2} + \psi^R_{j,3l-1} + \psi^R_{j,3l}}} \\
\breve{v}_{c_x,j} - \breve{v}_{c_y,j} + \breve{v}_{c_\theta,j} &= \frac{\psi^R_{j,3l-2} - \psi^R_{j,3l-1} + \psi^R_{j,3l}}{\sqrt{\psi^R_{j,3l-2} + \psi^R_{j,3l-1} + \psi^R_{j,3l}}}
\end{aligned}\right\} \quad \forall\, j \in \{1,2,\cdots,N\} \tag{A.10}$$

whose solutions will give the estimates of $\left\{\breve{v}_{c_x,j}, \breve{v}_{c_y,j}, \breve{v}_{c_\theta,j}\right\}\ \forall\ j\ \in\ \{1, 2, \cdots, N\}$. The term $\psi^R_{j,3l-2} + \psi^R_{j,3l-1} + \psi^R_{j,3l}$ can be expected to be always non-negative since it equals the square number $(\breve{v}_{c_x,j} + \breve{v}_{c_y,j} + \breve{v}_{c_\theta,j})^2$; it may however be zero if the jth mode has a node in all the three directions (x,y and θ) at the lth instrumented mass element ${}^m s_l$, in which case the actuators will need to be shifted to a different instrumented mass element.

The method discussed above needs actuators at only one of the instrumented floors to estimate the centers of mass/lumped mass parameters of all the instrumented floors. Moreover, the location of the sensors for this prior actuator-driven test can be the same as their locations in case of the base excitation test; once the centers of mass have been obtained, the measured responses during the base excitation test may be transformed to the centers of mass using Eq. (A.1) with (x_i, y_i) replaced with $(x_i - x_G, y_i - y_G)\ \forall\ i\ \in\ \{1, 2, 3, 4\}$. These observations highlight the advantages of the method in its simplicity in experimental implementation. However, one still needs to have three actuators providing three independent inputs on one of the instrumented floors. It would be more useful if the same can be accomplished using a single actuator. Such a situation is illustrated in Fig. A.1(b), where a single input $\mathbf{f}$ is applied on a completely measured mass element. As before, (x_f, y_f, ϕ) are known from the actuator's location and orientation. The transformed forces at the centroid are now written as: $\mathbf{f}_{x_O} = \mathbf{f}\cos\phi$; $\mathbf{f}_{y_O} = \mathbf{f}\sin\phi$; $\mathbf{f}_{\theta_O} = (x_f \sin\phi - y_f \cos\phi)\mathbf{f}$, and hence the inputs at the centroid are no longer independent, but instead proportional in the time domain. The input-output balance procedure needs some adjustments for proportional inputs (Chapter 2), as the matrix $\mathbf{G}$ becomes rank N (instead of $3N$). Hence, let us now compute only one set of pseudo-modal responses:

$$\ddot{\tilde{\boldsymbol{\eta}}}_j + 2\zeta_j\omega_j\dot{\tilde{\boldsymbol{\eta}}}_j + \omega_j^2\tilde{\boldsymbol{\eta}}_j = (\mathbf{f})_{{}^m s_l}\ \forall\ j \in \{1, 2, \cdots, N\} \tag{A.11}$$

Then we construct $\mathbf{G} = [\ddot{\tilde{\boldsymbol{\eta}}}_1\ \ddot{\tilde{\boldsymbol{\eta}}}_2\ \cdots\ \ddot{\tilde{\boldsymbol{\eta}}}_N]$, of dimension $n_t \times N$; $\mathbf{Y}$ is the same as in Eq. (A.6); and the $N \times 3n_m$ least squares solution, $\boldsymbol{\Psi} = \mathbf{G}^\dagger\mathbf{Y}$, has any (j, i)th element of the form:

$$\psi_{j,i} = \breve{v}_{s_i,j}(\breve{v}_{c_x,j}\cos\phi + \breve{v}_{c_y,j}\sin\phi + \breve{v}_{c_\theta,j}(x_f\sin\phi - y_f\cos\phi))\ \forall\ s_i \in \mathcal{S},\ j \in \{1, 2, \cdots, N\} \tag{A.12}$$

Using the same algebraic expansion formulae as used for Eq. (A.10), we get the linear systems:

$$\begin{bmatrix} \cos\phi & \sin\phi & (x_f\sin\phi - y_f\cos\phi) \\ \cos\phi & \sin\phi & -(x_f\sin\phi - y_f\cos\phi) \\ \cos\phi & -\sin\phi & (x_f\sin\phi - y_f\cos\phi) \end{bmatrix} \begin{Bmatrix} \breve{v}_{c_x,j} \\ \breve{v}_{c_y,j} \\ \breve{v}_{c_\theta,j} \end{Bmatrix} = \begin{Bmatrix} d_{1_j} \\ d_{2_j} \\ d_{3_j} \end{Bmatrix} \quad \forall\ j \in \{1, 2, \cdots, N\} \tag{A.13}$$

where:

$$\left.\begin{aligned} d_{1_j} &= \sqrt{\psi_{j,3l-2}\cos\phi + \psi_{j,3l-1}\sin\phi + \psi_{j,3l}(x_f\sin\phi - y_f\cos\phi)} \\ d_{2_j} &= \frac{\psi_{j,3l-2}\cos\phi + \psi_{j,3l-1}\sin\phi - \psi_{j,3l}(x_f\sin\phi - y_f\cos\phi)}{d_{1_j}} \\ d_{3_j} &= \frac{\psi_{j,3l-2}\cos\phi - \psi_{j,3l-1}\sin\phi + \psi_{j,3l}(x_f\sin\phi - y_f\cos\phi)}{d_{1_j}} \end{aligned}\right\} \quad \forall\, j \in \{1, 2, \cdots, N\} \tag{A.14}$$

One can first estimate $\left\{\breve{v}_{c_x,j}, \breve{v}_{c_y,j}, \breve{v}_{c_\theta,j}\right\}\ \forall\, j \in \{1, 2, \cdots, N\}$ from Eq. (A.13), and then the remaining $3n_m - 3$ measured rows of $\mathbf{V}_O$ from Eq. (A.12). Again, the term $\psi_{j,3l-2}\cos\phi + \psi_{j,3l-1}\sin\phi + \psi_{j,3l}(x_f\sin\phi - y_f\cos\phi)$ equals the square number $(\breve{v}_{c_x,j}\cos\phi + \breve{v}_{c_y,j}\sin\phi + \breve{v}_{c_\theta,j}(x_f\sin\phi - y_f\cos\phi))^2$, and would always be non-negative; if any jth mode has a node in all the three directions at the floor ${}^m s_l$, this term will be zero, and the actuator will need to be placed on a different instrumented floor. In this single actuator test, the angle ϕ cannot be 0^0 or 90^0 or $\tan^{-1}(y_f/x_f)$, as otherwise the coefficient matrix in Eq. (A.13) will have a column of zeros.

To validate the method, we consider the 3-story building shown in Fig. A.2, with the DOFs defined at the centroid. For all the floors, $l_x = l_y = 1$ m. The stiffnesses of the columns are: $k_{icx} = k_{idx} = 1.25 \times 10^6$ N/m, $k_{iax} = k_{ibx} = 0.6k_{icx}$, $k_{iby} = k_{icy} = 1.5 \times 10^6$ N/m, and $k_{iay} = k_{idy} = 0.6k_{iby}$, $\forall\ i \in \{1, 2, 3\}$. The first and second floors have a uniform mass distribution, with $m_1 = m_2 = 2500$ kg; hence the centroids and centers of mass of these floors coincide ($(x_G, y_G) = (0, 0)$), and $J_1 = J_2 = 416.67$ kg-m^2 at their centers of mass. The third floor has a non-uniform mass distribution as shown in Fig. A.2, with $(x_G, y_G) = (0.2, -0.15)$ m with respect to its centroid at $(0, 0)$; $m_3 = 2000$ kg, and $J_3 = 208.33$ kg-m^2 with respect to its center of mass, and 333.33 kg-m^2 with respect to its centroid. 5% modal damping is assumed in all the 9 modes. The first and third floors are completely instrumented, i.e. we measure $\{(\ddot{\mathbf{u}}_{x_O})_1, (\ddot{\mathbf{u}}_{y_O})_1, (\ddot{\mathbf{u}}_{\theta_O})_1, (\ddot{\mathbf{u}}_{x_O})_3, (\ddot{\mathbf{u}}_{y_O})_3, (\ddot{\mathbf{u}}_{\theta_O})_3\}$. We consider both the multiple and single actuator cases discussed above, with input force(s) applied on the third floor: in the first case, three independent Gaussian white noise inputs are applied at the centroid of the third floor, while in the second case, a single Gaussian white noise input is applied at an angle of $\phi = 30^0$ at the point $(x_f, y_f) = (-0.5, -0.5)$ with respect to the centroid at $(0, 0)$. To simulate the effect of measurement noise, the true acceleration responses are corrupted by adding zero-mean Gaussian white noise sequences with root-mean-square (RMS) values equal to 10% of the RMS values of the corresponding true signals. In both cases, 100 simulations are run, with each

simulation differing in (1) the applied input(s), which are different white noise sequences from a common underlying Gaussian distribution, and (2) the additive measurement noise sequences. For each simulation, the ERA-OKID approach is first used to identify the modal frequencies and damping ratios using the input - (noisy) output sequences, following which the centers of mass, lumped masses and mass moments of inertia (at the centers of mass), of the first and third floors, are estimated using the proposed approach. The means and standard deviations of the estimates from the 100 simulations are then computed. For the multi–actuator case, the mean of the parameter estimates for the first floor are: $\mu_{x_G} = -0.0003$ m, $\mu_{y_G} = 0.0002$ m, $\mu_{m_1} = 2489.92$ kg, and $\mu_{J_1} = 416.22$ kg-m^2, and the standard deviations are: $\sigma_{x_G} = 0.0011$ m, $\sigma_{y_G} = 0.0011$ m, $\sigma_{m_1} = 33.84$ kg, and $\sigma_{J_1} = 1.23$ kg-m^2; while for the third floor, the mean estimates are: $\mu_{x_G} = 0.2005$ m, $\mu_{y_G} = -0.1504$ m, $\mu_{m_3} = 1995.01$ kg, and $\mu_{J_3} = 207.99$ kg-m^2 (at the center of mass), with standard deviations of: $\sigma_{x_G} = 0.0014$ m, $\sigma_{y_G} = 0.0010$ m, $\sigma_{m_3} = 13.39$ kg, and $\sigma_{J_3} = 0.83$ kg-m^2. For the single actuator case, the estimation statistics for the first floor are: $\mu_{x_G} = 0.0002$ m, $\mu_{y_G} = -0.0001$ m, $\mu_{m_1} = 2498.62$ kg, and $\mu_{J_1} = 416.39$ kg-m^2; $\sigma_{x_G} = 0.0004$ m, $\sigma_{y_G} = 0.0004$ m, $\sigma_{m_1} = 3.15$ kg, and $\sigma_{J_1} = 0.95$ kg-m^2; and for the third floor are: $\mu_{x_G} = 0.2000$ m, $\mu_{y_G} = -0.1502$ m, $\mu_{m_3} = 1998.27$ kg, and $\mu_{J_3} = 207.99$ kg-m^2; $\sigma_{x_G} = 0.0005$ m, $\sigma_{y_G} = 0.0003$ m, $\sigma_{m_3} = 2.40$ kg, and $\sigma_{J_3} = 0.81$ kg-m^2. Thus, even with 10% measurement noise, the method performs reasonably well (with no noise, the mean estimates are numerically exact, with standard deviations of the order of $10^{-10} - 10^{-15}$).

A.2 Minimal/Near-Minimal Instrumentation for 3-D Rigid Floor Building Identification Using Actuator-Driven Forced Vibration Test

Different minimal/near-minimal instrumentation set-ups for global identifiability in actuator driven forced vibration tests of 1-D shear-type systems were identified in Chapter 2. These set-ups can be extended to 2 and 3-D systems following the recommendation in Chapter 3: the complete instrumentation (i.e. measurement of all the active DOFs) of a set of floors for N_D-dimensional rigid-floor systems, with the set of floors to be completely instrumented being the same as the set of DOFs (lumped masses) to be necessarily instrumented in 1-D systems. Thus, in an actuator driven test of an N_D-dimensional N-DOF rigid-floor system with N_m floors/lumped masses, instrumenting:

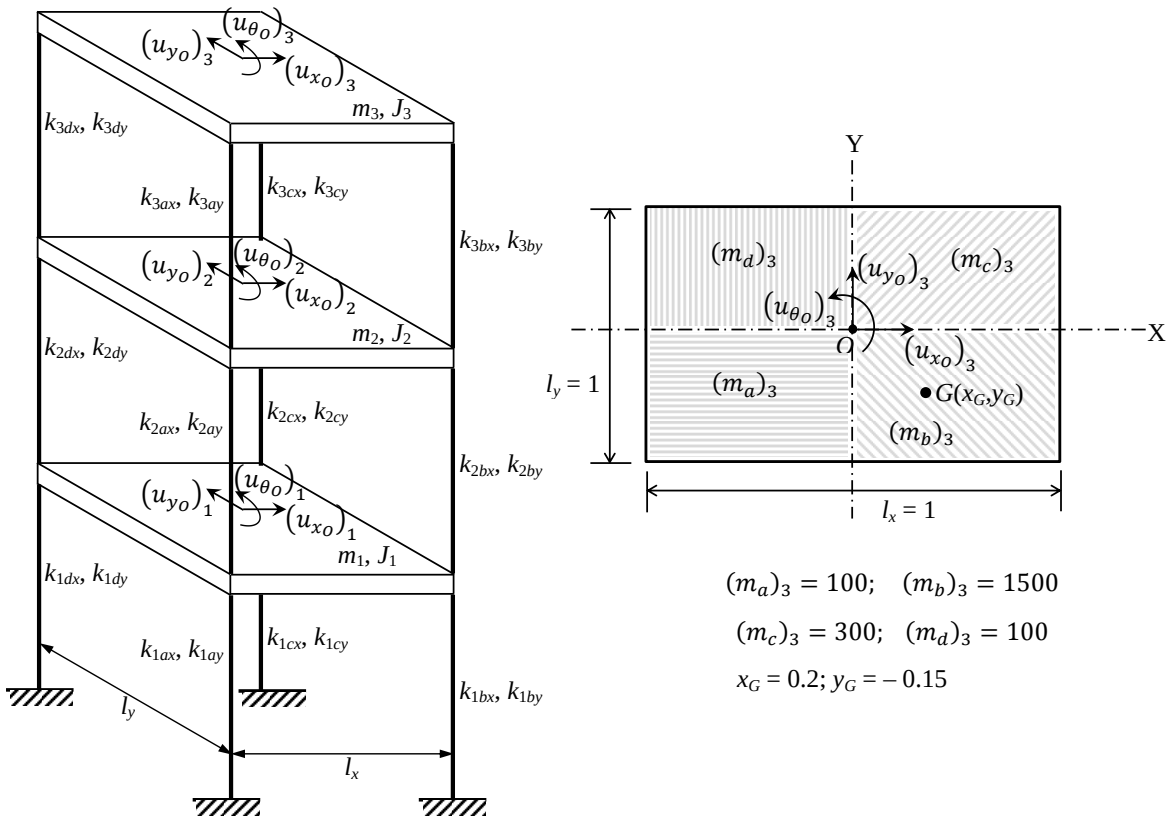

Figure A.2: Three storied building with non-uniform mass distribution on third floor: an example of 3-D shear-type system ($N = 3N_m = 9$ DOFs) considered in the present study.

1. only the 1st or N_mth floor with one actuator and N_D sensors, or,

2. two consecutive floors, with one actuator and N_D sensors at one floor, and an additional N_D actuators/sensors at the other floor, with independent inputs from the actuators, or,

3. two consecutive floors with either N_D actuators and/or N_D sensors per floor, and *any other* additional floor with one actuator and N_D sensors, with independent inputs from the actuators, or,

4. two consecutive floors, with one actuator and N_D sensors per floor, for dependent inputs from the actuators,

is sufficient for a unique identification of the complete mass normalized $\mathbf{V}$, and consequently the $\mathbf{M}$ and $\mathbf{K}$ matrices, of the system, and hence the above list defines the minimal/near-minimal instrumentation requirement(s) for global identifiability. In case of 2/3-D systems the single actuator in any floor needs to be so located and oriented as to excite all the 2/3 active DOFs (i.e. eccentrically located and oriented in a direction not parallel to the two translational DOFs).

As an example, consider again the 3-storied building of Fig. A.2, with the masses in all the floors uniformly distributed. The structure is excited by applying a zero-mean Gaussian white noise force, through a single actuator located on the 3rd floor (roof), at an angle of $\phi = 30^0$ at the point $(x_f, y_f) = (-0.5, -0.5)$ with respect to the centroid at $(0, 0)$. Only the three 3rd floor responses of the system are measured; the "measured" responses are the true responses corrupted with 10% RMS Gaussian white noise. Using the same approach as before (i.e. ERA-OKID + input-output balance) with the applied input and "measured" output data, the modal frequencies, damping ratios and mass normalized mode shape components at the 3rd floor are first identified. The mode shape expansion equations of Chapter 3 (Statements 6 and 4) are then used to estimate the complete mass normalized $\mathbf{V}$ matrix. The individual floor masses, mass moments of inertia and story stiffnesses ($k_L = k_{ay} + k_{dy}$, $k_R = k_{by} + k_{cy}$, $k_F = k_{ax} + k_{bx}$, $k_B = k_{cx} + k_{dx}$) are then estimated from the $\mathbf{M}$ and $\mathbf{K}$ matrices identified using modal orthogonality. 100 such simulations are run; Tables A.1 and A.2 show the means and coefficients of variation of the physical parameter estimates from the 100 simulations. Evidently, even with 10% RMS measurement noise and only a single instrumented floor (only 1 actuator and 3 sensors), reliably accurate estimates of the mass and stiffness parameters are obtained using the proposed approach, with the maximum (amongst all 6 parameters) error in

Table A.1: Statistics of identified floor mass parameters.

Floor	μ_m	COV$_m$	μ_J	COV$_J$
1	2.48 (2.5)	0.01	4.15 (4.17)	0.10
2	2.48 (2.5)	0.02	4.15 (4.17)	0.09
3	2.00 (2.0)	0.01	3.33 (3.33)	0.05

μ_m in 10^3 kg; μ_J in 10^2 kg-m^2; COV in %; true values in parenthesis.

Table A.2: Statistics of identified story stiffness parameters.

Story	μ_{k_L}	COV$_{k_L}$	μ_{k_R}	COV$_{k_R}$	μ_{k_F}	COV$_{k_F}$	μ_{k_B}	COV$_{k_B}$
1	1.78 (1.8)	0.47	2.98 (3.0)	0.51	1.50 (1.5)	0.79	2.49 (2.5)	0.94
2	1.77 (1.8)	0.62	2.97 (3.0)	0.50	1.49 (1.5)	0.79	2.49 (2.5)	0.89
3	1.78 (1.8)	0.46	2.98 (3.0)	0.27	1.50 (1.5)	0.31	2.49 (2.5)	0.33

μ_k in 10^6 N/m; COV in %; true values in parenthesis.

the mean estimates being 1.7% (in k_L), and the maximum COV being 0.94%. It is also interesting that the COVs tend to increase from the 3rd to the 1st floor, indicating that the estimation uncertainty increases as one moves away from the instrumented location, as may be expected.

Appendix B

Proofs of Some Statements from Chapters 3 and 4

B.1 Proof of Statement 4 from Chapter 3

For the first case, to show that the estimate of $\mathbf{r}_{\mathbf{B}i-1}$ is unique, we need to show that the determinant of the coefficient matrix in Eq. (3.18) is non-zero. To this end, we repeatedly apply the block matrix determinant expansion of Eq. (2.14) as follows:

$$
\begin{aligned}
&\begin{vmatrix}
\mathbf{I}_{N\times N} & \mathbf{r}_{\mathbf{B}i}^T & \mathbf{r}_{\mathbf{B}i+1}^T & -\mathbf{\Lambda}\mathbf{r}_{\mathbf{B}i}^T \\
\mathbf{0}_{N_D\times N} & \mathbf{I}_{N_D\times N_D} & \mathbf{I}_{N_D\times N_D} & \mathbf{0}_{N_D\times N_D} \\
\mathbf{r}_{\mathbf{B}i} & \mathbf{0}_{N_D\times N_D} & \mathbf{0}_{N_D\times N_D} & \mathbf{0}_{N_D\times N_D} \\
\mathbf{r}_{\mathbf{B}i+1} & \mathbf{0}_{N_D\times N_D} & \mathbf{0}_{N_D\times N_D} & \mathbf{0}_{N_D\times N_D}
\end{vmatrix} \\
&= |\mathbf{I}_{N\times N}| \times \begin{vmatrix}
\mathbf{I}_{N_D\times N_D} & \mathbf{I}_{N_D\times N_D} & \mathbf{0}_{N_D\times N_D} \\
-\mathbf{r}_{\mathbf{B}i}\mathbf{r}_{\mathbf{B}i}^T & \mathbf{0}_{N_D\times N_D} & \mathbf{r}_{\mathbf{B}i}\mathbf{\Lambda}\mathbf{r}_{\mathbf{B}i}^T \\
\mathbf{0}_{N_D\times N_D} & -\mathbf{r}_{\mathbf{B}i+1}\mathbf{r}_{\mathbf{B}i+1}^T & \mathbf{r}_{\mathbf{B}i+1}\mathbf{\Lambda}\mathbf{r}_{\mathbf{B}i}^T
\end{vmatrix} \\
&= |\mathbf{I}_{N_D\times N_D}| \times \begin{vmatrix}
\mathbf{r}_{\mathbf{B}i}\mathbf{r}_{\mathbf{B}i}^T & \mathbf{r}_{\mathbf{B}i}\mathbf{\Lambda}\mathbf{r}_{\mathbf{B}i}^T \\
-\mathbf{r}_{\mathbf{B}i+1}\mathbf{r}_{\mathbf{B}i+1}^T & \mathbf{r}_{\mathbf{B}i+1}\mathbf{\Lambda}\mathbf{r}_{\mathbf{B}i}^T
\end{vmatrix}
\end{aligned}
$$

$$
\begin{aligned}
&= \left|\mathbf{r}_{\mathbf{B}i}\mathbf{r}_{\mathbf{B}i}^T\right| \times \left|\mathbf{r}_{\mathbf{B}i+1}\mathbf{\Lambda}\mathbf{r}_{\mathbf{B}i}^T + \left[\mathbf{r}_{\mathbf{B}i+1}\mathbf{r}_{\mathbf{B}i+1}^T\right]\left[\mathbf{r}_{\mathbf{B}i}\mathbf{r}_{\mathbf{B}i}^T\right]^{-1}\left[\mathbf{r}_{\mathbf{B}i}\mathbf{\Lambda}\mathbf{r}_{\mathbf{B}i}^T\right]\right| \\
&= \left|\mathbf{m}_i^{-1}\right| \times \left|-\mathbf{m}_{i+1}^{-1}\mathbf{k}_i\mathbf{m}_i^{-1} + \mathbf{m}_{i+1}^{-1}\mathbf{m}_i\mathbf{m}_i^{-1}\left[\mathbf{k}_i + \mathbf{k}_{i+1}\right]\mathbf{m}_i^{-1}\right| \\
&\qquad\qquad \text{(using mass and stiffness orthogonality, with the notation of Section 3.3)} \\
&= \left|\mathbf{m}_i^{-1}\right|\left|\mathbf{m}_{i+1}^{-1}\mathbf{k}_{i+1}\mathbf{m}_i^{-1}\right|
\end{aligned}
\tag{B.1}
$$

which cannot be zero as neither any floor mass matrix can have an infinite determinant, nor any story stiffness matrix can have a zero determinant.

Similarly, for the second case in can be shown that the coefficient matrix in Eq. (3.19) has a determinant:

$$
\begin{aligned}
&\begin{vmatrix}
\mathbf{I}_{N\times N} & \mathbf{r}_{\mathbf{B}i}^T & \mathbf{r}_{\mathbf{B}i+1}^T & -\mathbf{\Lambda}\mathbf{r}_{\mathbf{B}i+1}^T \\
\mathbf{0}_{N_D\times N} & \mathbf{I}_{N_D\times N_D} & \mathbf{I}_{N_D\times N_D} & \mathbf{0}_{N_D\times N_D} \\
\mathbf{r}_{\mathbf{B}i} & \mathbf{0}_{N_D\times N_D} & \mathbf{0}_{N_D\times N_D} & \mathbf{0}_{N_D\times N_D} \\
\mathbf{r}_{\mathbf{B}i+1} & \mathbf{0}_{N_D\times N_D} & \mathbf{0}_{N_D\times N_D} & \mathbf{0}_{N_D\times N_D}
\end{vmatrix} \\
&= \left|\mathbf{m}_i^{-1}\right|\left|\mathbf{m}_{i+1}^{-1}\mathbf{k}_{i+2}\mathbf{m}_{i+1}^{-1}\right|
\end{aligned}
\tag{B.2}
$$

which is again non-zero, and so the estimate of $\mathbf{r}_{\mathbf{B}i+2}$ is unique. □

B.2 Proof of Statement 7 from Chapter 4

Statement 7 used in Chapter 4 is a corollary of another statement; so, we first give below this statement, and its proof by induction.

Statement 10: *For a shear-type system, for any mode $j \in \{1, \cdots, N\}$, the mode shape component at any DOF $i \in \{2, \cdots, N\}$, is related to the component at DOF 1 as:*

$$
\tilde{v}_{i,j} = \left(\sum_{l=0}^{i-1} c_{l,i}\lambda_j^l\right)\tilde{v}_{1,j} \tag{B.3}
$$

where $c_{l,i}\ \forall\ l \in \{0, \cdots, i-1\}$, are i number of mode independent constants.

Proof of Statement 10: Consider the eigenvalue problem, for any mode $j \in \{1, \cdots, N\}$:

$$
[\mathbf{A} - \lambda_j\mathbf{I}]\tilde{\mathbf{v}}_j = \mathbf{0} \tag{B.4}
$$

where $\mathbf{A} = \mathbf{M}^{-1}\mathbf{K}$, and let any (i,k)th element of $\mathbf{A}$ be denoted by $a_{i,k}$. (Note: even though $\mathbf{M}$ and $\mathbf{K}$ are symmetric, $\mathbf{A}$ is not necessarily symmetric.) Then, considering the first row of Eq. (B.4), it

can be shown that Statement 10 is true for $i = 2$:

$$(a_{1,1} - \lambda_j)\tilde{v}_{1,j} + a_{2,2}\tilde{v}_{2,j} = 0 \quad \Rightarrow \tilde{v}_{2,j} = (c_{0,2} + c_{1,2}\lambda_j)\tilde{v}_{2,j} \tag{B.5}$$

where $c_{0,2} = -a_{1,1}/a_{1,2}$ and $c_{1,2} = 1/a_{1,2}$. Assume that Statement 10 is true for $i = i^* - 1$ and $i = i^*$, i.e.:

$$\tilde{v}_{i^*-1,j} = \left(\sum_{l=0}^{i^*-2} c_{l,i^*-1}\lambda_j^l\right)\tilde{v}_{1,j}; \quad \tilde{v}_{i^*,j} = \left(\sum_{l=0}^{i^*-1} c_{l,i^*}\lambda_j^l\right)\tilde{v}_{1,j} \tag{B.6}$$

Then, considering the i^*th row of Eq. (B.4), we get:

$$\begin{aligned}
&a_{i^*,i^*-1}\tilde{v}_{i^*-1,j} + (a_{i^*,i^*} - \lambda_j)\tilde{v}_{i^*,j} + a_{i^*,i^*+1}\tilde{v}_{i^*+1,j} = 0 \\
\Rightarrow &\tilde{v}_{i^*+1,j} = -\frac{1}{a_{i^*,i^*+1}}\left[a_{i^*,i^*-1}\left(\sum_{l=0}^{i^*-2} c_{l,i^*-1}\lambda_j^l\right) + (a_{i^*,i^*} - \lambda_j)\left(\sum_{l=0}^{i^*-1} c_{l,i^*}\lambda_j^l\right)\right]\tilde{v}_{1,j} \\
&\qquad\qquad \text{(rearranging and using Eq. (B.6))} \\
\Rightarrow &\tilde{v}_{i^*+1,j} = \left(\sum_{l=0}^{i^*} c_{l,i^*+1}\lambda_j^l\right)\tilde{v}_{1,j} \qquad \text{(collecting like powers of } \lambda_j\text{)}
\end{aligned} \tag{B.7}$$

where:

$$c_{l,i^*+1} = \begin{cases}
-(a_{i^*,i^*-1}c_{l,i^*-1} + a_{i^*,i^*}c_{l,i^*})/a_{i^*,i^*+1} & \text{for } l = 0 \\
-(a_{i^*,i^*-1}c_{l,i^*-1} + a_{i^*,i^*}c_{l,i^*} - c_{l-1,i^*})/a_{i^*,i^*+1} & \text{for } l \in \{1, \cdots, i^* - 2\} \\
-(a_{i^*,i^*}c_{l,i^*} - c_{l-1,i^*})/a_{i^*,i^*+1} & \text{for } l = i^* - 1 \\
c_{l-1,i^*}/a_{i^*,i^*+1} & \text{for } l = i^*
\end{cases} \tag{B.8}$$

Eq. (B.7) shows that Statement 10, if true for $i = i^* - 1$ and $i = i^*$, is also true for $i = i^* + 1$. This completes the proof of Statement 10 by induction. □

The proof of Statement 7 follows directly from Statement 10.

Proof of Statement 7: Consider $i = i_1$ and $i = i_2$ in Statement 10. Then:

$$\begin{aligned}
&\tilde{v}_{i_1,j} = \left(\sum_{l=0}^{i_1-1} c_{l,i_1}\lambda_j^l\right)\tilde{v}_{1,j}; \quad \tilde{v}_{i_2,j} = \left(\sum_{l=0}^{i_2-1} c_{l,i_2}\lambda_j^l\right)\tilde{v}_{1,j} \\
\Rightarrow &\frac{\tilde{v}_{i_2,j}}{\tilde{v}_{i_1,j}} = \frac{\sum_{l=0}^{i_2-1} c_{l,i_2}\lambda_j^l}{\sum_{l=0}^{i_1-1} c_{l,i_1}\lambda_j^l} = \frac{1 + \sum_{l=1}^{i_2-1} \bar{c}_{l,i_2}\lambda_j^l}{\sum_{l=0}^{i_1-1} \bar{c}_{l,i_1}\lambda_j^l} \\
\Rightarrow &\left(\sum_{l=0}^{i_1-1} \bar{c}_{l,i_1}\lambda_j^l\right)\tilde{v}_{i_2,j} - \left(1 + \sum_{l=1}^{i_2-1} \bar{c}_{l,i_2}\lambda_j^l\right)\tilde{v}_{i_1,j} = 0
\end{aligned} \tag{B.9}$$

where $\bar{c}_{l,i_1} = c_{l,i_1}/c_{0,i_2}$ and $\bar{c}_{l,i_2} = c_{l,i_2}/c_{0,i_2}$. □

B.3 Proof of Statement 8 from Chapter 4

Statement 8 used in Chapter 4 is again a corollary of another statement. We first give below this statement, and its proof by induction.

Statement 11: *For a shear-type system, for any mode $j \in \{1, \cdots, N\}$, the mode shape component at any DOF $N-k$, $k \in \{1, \cdots, N-1\}$, is related to the component at DOF N as:*

$$\tilde{v}_{N-k,j} = \left(1 + \sum_{l=1}^{k} d_{l,k} \lambda_j^l\right) \tilde{v}_{N,j} \tag{B.10}$$

where $d_{l,k}\ \forall\ l \in \{1, \cdots, k\}$, are k number of mode independent constants.

Proof of Statement 11: Considering the Nth row of the eigenvalue Eq. (B.4), and using $a_{N,N-1} = -a_{N,N}$ for a shear-type system, it is evident that Statement 11 is true for $k = 1$:

$$a_{N,N-1}\tilde{v}_{N-1,j} + (a_{N,N} - \lambda_j)\tilde{v}_{N,j} = 0 \quad \Rightarrow \tilde{v}_{N-1,j} = (1 + d_{1,1}\lambda_j)\tilde{v}_{N,j} \tag{B.11}$$

where $d_{1,1} = -1/a_{N,N}$. Assume that Statement 11 is true for $k = k^* - 1$ and $k = k^*$, i.e.:

$$\tilde{v}_{N-k^*+1,j} = \left(1 + \sum_{l=1}^{k^*-1} d_{l,k^*-1}\lambda_j^l\right) \tilde{v}_{N,j}; \quad \tilde{v}_{N-k^*,j} = \left(1 + \sum_{l=1}^{k^*} d_{l,k^*}\lambda_j^l\right) \tilde{v}_{N,j} \tag{B.12}$$

Then, considering the $(N-k^*)$th row of Eq. (B.4), we get:

$$a_{N-k^*,N-k^*-1}\tilde{v}_{N-k^*-1,j} + (a_{N-k^*,N-k^*} - \lambda_j)\tilde{v}_{N-k^*,j} + a_{N-k^*,N-k^*+1}\tilde{v}_{N-k^*+1,j} = 0$$

$$\Rightarrow \tilde{v}_{N-k^*-1,j} = -\frac{1}{a_{N-k^*,N-k^*-1}} \left[a_{N-k^*,N-k^*+1} \left(1 + \sum_{l=1}^{k^*-1} d_{l,k^*-1}\lambda_j^l\right) + (a_{N-k^*,N-k^*} - \lambda_j) \left(1 + \sum_{l=1}^{k^*} d_{l,k^*}\lambda_j^l\right) \right] \tilde{v}_{N,j}$$

(rearranging and using Eq. (B.12))

$$\Rightarrow \tilde{v}_{N-k^*-1,j} = \frac{1}{a_{N-k^*,N-k^*-1}} \left[a_{N-k^*,N-k^*-1} + \lambda_j - a_{N-k^*,N-k^*+1} \left(\sum_{l=1}^{k^*-1} d_{l,k^*-1}\lambda_j^l\right) - (a_{N-k^*,N-k^*} - \lambda_j) \left(\sum_{l=1}^{k^*} d_{l,k^*}\lambda_j^l\right) \right] \tilde{v}_{N,j}$$

(using $a_{N-k^*,N-k^*} + a_{N-k^*,N-k^*+1} = -a_{N-k^*,N-k^*-1}$ for a shear-type system)

$$\Rightarrow \tilde{v}_{N-k^*-1,j} = \left(1 + \sum_{l=1}^{k^*+1} d_{l,k^*+1}\lambda_j^l\right) \tilde{v}_{N,j}$$

(collecting like powers of λ_j)

(B.13)

where:

$$d_{l,k^*+1} = \begin{cases} (1 - a_{N-k^*,N-k^*+1}d_{l,k^*-1} & \\ \quad -a_{N-k^*,N-k^*}d_{l,k^*})\,/a_{N-k^*,N-k^*-1} & \text{for } l = 1 \\ (d_{l-1,k^*} - a_{N-k^*,N-k^*+1}d_{l,k^*-1} & \\ \quad -a_{N-k^*,N-k^*}d_{l,k^*})\,/a_{N-k^*,N-k^*-1} & \text{for } l \in \{2,\cdots,k^*-1\} \\ (d_{l-1,k^*} - a_{N-k^*,N-k^*}d_{l,k^*})/a_{N-k^*,N-k^*-1} & \text{for } l = k^* \\ d_{l-1,k^*}/a_{N-k^*,N-k^*-1} & \text{for } l = k^*+1 \end{cases} \tag{B.14}$$

Eq. (B.13) shows that Statement 11, if true for $k = k^* - 1$ and $k = k^*$, is also true for $k = k^* + 1$. This completes the proof of Statement 11 by induction. □

The proof of Statement 8 follows directly from Statement 11.

Proof of Statement 8: Consider $k = k_1 = N - i_1$ and $k = k_2 = N - i_2$ in Statement 11. Then:

$$\begin{aligned} &\tilde{v}_{i_1,j} = \tilde{v}_{N-k_1,j} = \left(1 + \sum_{l=1}^{k_1} d_{l,k_1}\lambda_j^l\right)\tilde{v}_{N,j}; \quad \tilde{v}_{i_2,j} = \tilde{v}_{N-k_2,j} = \left(1 + \sum_{l=1}^{k_2} d_{l,k_2}\lambda_j^l\right)\tilde{v}_{N,j} \\ &\Rightarrow \frac{\tilde{v}_{i_2,j}}{\tilde{v}_{i_1,j}} = \frac{1 + \sum_{l=1}^{k_2} d_{l,k_2}\lambda_j^l}{1 + \sum_{l=1}^{k_1} d_{l,k_1}\lambda_j^l} = \frac{1 + \sum_{l=1}^{N-i_2} d_{l,N-i_2}\lambda_j^l}{1 + \sum_{l=1}^{N-i_1} d_{l,N-i_1}\lambda_j^l} \\ &\Rightarrow \left(1 + \sum_{l=1}^{N-i_1} d_{l,N-i_1}\lambda_j^l\right)\tilde{v}_{i_2,j} - \left(1 + \sum_{l=1}^{N-i_2} d_{l,N-i_2}\lambda_j^l\right)\tilde{v}_{i_1,j} = 0 \end{aligned} \tag{B.15}$$

□

B.4 Proof of Statement 9 from Chapter 4

This proof will also be by induction. We will consider here the case of the DOFs $\{i-1, i, i+k\}$; the proof for the case of the DOFs $\{i-k, i, i+1\}$ is similar. To show that Statement 9 is true for $k = 1$, consider the ith row of the eigenvalue Eq. (B.4):

$$\begin{aligned} &a_{i,i-1}\tilde{v}_{i-1,j} + (a_{i,i} - \lambda_j)\tilde{v}_{i+1,j} + a_{i,i+1}\tilde{v}_{i+1,j} = 0 \\ \Rightarrow &\tilde{v}_{i+1,j} = (1 + p_{0,1})\tilde{v}_{i-1,j} - (p_{0,1} + r_{1,1}\lambda_j)\tilde{v}_{i,j} \\ &\qquad \text{(after rearrangement and using } a_{i,i-1} + a_{i,i} + a_{i,i+1} = 0) \end{aligned} \tag{B.16}$$

where $p_{0,1} = a_{i,i}/a_{i,i+1}$ and $r_{1,1} = -1/a_{i,i+1}$. Since the $q_{l,k}$ terms don't appear for $k = 1$, we also need to show that Statement 9 holds for $k = 2$. Hence, from the $i + 1$th row of Eq. (B.4):

$$\begin{aligned}
&a_{i+1,i}\tilde{v}_{i,j} + (a_{i+1,i+1} - \lambda_j)\tilde{v}_{i+1,j} + a_{i+1,i+2}\tilde{v}_{i+2,j} = 0 \\
\Rightarrow &\tilde{v}_{i+2,j} = -\frac{\{a_{i+1,i} - (a_{i+1,i+1} - \lambda_j)(p_{0,1} + r_{1,1}\lambda_j)\}\tilde{v}_{i,j} + (a_{i+1,i+1} - \lambda_j)(1 + p_{0,1})\tilde{v}_{i-1,j}}{a_{i+1,i+2}} \\
&\qquad\qquad \text{(rearranging and using Eq. (B.16))} \\
\Rightarrow &\tilde{v}_{i+2,j} = (1 + p_{0,2} + q_{1,2}\lambda_j)\tilde{v}_{i-1,j} - (p_{0,2} + r_{1,2}\lambda_j + r_{2,2}\lambda_j^2)\tilde{v}_{i,j} \\
&\qquad\qquad \text{(after some algebra and using } a_{i+1,i} + a_{i+1,i+1} + a_{i+1,i+2} = 0)
\end{aligned} \tag{B.17}$$

where:

$$\begin{aligned}
&p_{0,2} = -1 - (1 + p_{0,1})a_{i+1,i+1}/a_{i+1,i+2}; \quad q_{1,2} = (1 + p_{0,1})/a_{i+1,i+2}; \\
&r_{1,2} = (p_{0,1} - r_{1,1}a_{i+1,i+1})/a_{i+1,i+2}; \quad r_{2,2} = r_{1,1}/a_{i+1,i+2}
\end{aligned} \tag{B.18}$$

Assume that Statement 9 holds for $k = k^* - 1$ and $k = k^*$, i.e.:

$$\begin{aligned}
\tilde{v}_{i+k^*-1,j} &= \left(1 + p_{0,k^*-1} + \sum_{l=1}^{k^*-2} q_{l,k^*-1}\lambda_j^l\right)\tilde{v}_{i-1,j} - \left(p_{0,k^*-1} + \sum_{l=1}^{k^*-1} r_{l,k^*-1}\lambda_j^l\right)\tilde{v}_{i,j} \\
\tilde{v}_{i-k^*,j} &= \left(1 + p_{0,k^*} + \sum_{l=1}^{k^*-1} q_{l,k^*}\lambda_j^l\right)\tilde{v}_{i-1,j} - \left(p_{0,k^*} + \sum_{l=1}^{k^*} r_{l,k^*}\lambda_j^l\right)\tilde{v}_{i,j}
\end{aligned} \tag{B.19}$$

Then, from the $(i + k^*)$th row of Eq. (B.4), we get:

$$\begin{aligned}
&a_{i+k^*,i+k^*-1}\tilde{v}_{i+k^*-1,j} + (a_{i+k^*,i+k^*} - \lambda_j)\tilde{v}_{i+k^*,j} + a_{i+k^*,i+k^*+1}\tilde{v}_{i+k^*+1,j} = 0 \\
\Rightarrow &\tilde{v}_{i+k^*+1,j} = (1 + e_1)\left(1 + p_{0,k^*-1} + \sum_{l=1}^{k^*-2} q_{l,k^*-1}\lambda_j^l\right)\tilde{v}_{i-1,j} \\
&\qquad - (1 + e_1)\left(p_{0,k^*-1} + \sum_{l=1}^{k^*-1} r_{l,k^*-1}\lambda_j^l\right)\tilde{v}_{i,j} \\
&\qquad - (e_1 + e_2\lambda_j)\left(1 + p_{0,k^*} + \sum_{l=1}^{k^*-1} q_{l,k^*}\lambda_j^l\right)\tilde{v}_{i-1,j} \\
&\qquad + (e_1 + e_2\lambda_j)\left(p_{0,k^*} + \sum_{l=1}^{k^*} r_{l,k^*}\lambda_j^l\right)\tilde{v}_{i,j} \\
&\qquad\qquad \text{(rearranging, and using Eq. (B.19) and } a_{i+k^*,i+k^*-1} + a_{i+k^*,i+k^*} + a_{i+k^*,i+k^*+1} = 0)
\end{aligned} \tag{B.20}$$

where:

$$e_1 = \frac{a_{i+k^*,i+k^*}}{a_{i+k^*,i+k^*+1}} = -1 - \frac{a_{i+k^*,i+k^*-1}}{a_{i+k^*,i+k^*+1}}; \quad e_2 = -\frac{1}{a_{i+k^*,i+k^*+1}} \tag{B.21}$$

After some algebra, and collecting like powers of λ_j and like terms in $\tilde{v}_{i-1,j}$ and $\tilde{v}_{i,j}$, we get from Eq. (B.20):

$$\tilde{v}_{i+k^*+1,j} = \left(1 + p_{0,k^*+1} + \sum_{l=1}^{k^*} q_{l,k^*+1}\lambda_j^l\right)\tilde{v}_{i-1,j} - \left(p_{0,k^*+1} + \sum_{l=1}^{k^*+1} r_{l,k^*+1}\lambda_j^l\right)\tilde{v}_{i,j} \tag{B.22}$$

where:

$$p_{0,k^*+1} = (1+e_1)p_{0,k^*-1} - e_1 p_{0,k^*}$$

$$q_{l,k^*+1} = \begin{cases} -e_2(1+p_{0,k^*}) + (1+e_1)q_{l,k^*-1} - e_1 q_{l,k^*} & \text{for } l = 1 \\ (1+e_1)q_{l,k^*-1} - e_1 q_{l,k^*} - e_2 q_{l-1,k^*} & \text{for } l \in \{2,\cdots,k^*-2\} \\ -e_1 q_{l,k^*} - e_2 q_{l-1,k^*} & \text{for } l = k^*-1 \\ -e_2 q_{l-1,k^*} & \text{for } l = k^* \end{cases}$$

$$r_{l,k^*+1} = \begin{cases} -e_2 p_{0,k^*} + (1+e_1)r_{l,k^*-1} - e_1 r_{l,k^*} & \text{for } l = 1 \\ (1+e_1)r_{l,k^*-1} - e_1 r_{l,k^*} - e_2 r_{l-1,k^*} & \text{for } l \in \{2,\cdots,k^*-1\} \\ -e_1 r_{l,k^*} - e_2 r_{l-1,k^*} & \text{for } l = k^* \\ -e_2 r_{l-1,k^*} & \text{for } l = k^*+1 \end{cases} \tag{B.23}$$

Eqs. (B.20) and (B.22) show that Statement 9, if true for $k = k^* - 1$ and $k = k^*$, is also true for $k = k^* + 1$. This completes the proof of Statement 9 by induction. □

B.5 Proof of Real Jacobian Conjecture for Degree 2

$\mathbf{g}(\boldsymbol{\alpha}^*, \boldsymbol{\theta}) : \mathbf{R}^{N^2-1} \to \mathbf{R}^{N^2-1}$ is a polynomial map in the elements of $\boldsymbol{\theta}$, with any polynomial being at most of degree 2. Let us choose two $\boldsymbol{\theta}$'s, viz. $\boldsymbol{\theta}_a \neq \boldsymbol{\theta}_b$, and let $\boldsymbol{\theta}_c = (\boldsymbol{\theta}_a + \boldsymbol{\theta}_b)/2$. Then:

$$\begin{aligned} \mathbf{g}(\boldsymbol{\alpha}^*, \boldsymbol{\theta} = \boldsymbol{\theta}_a) &= \mathbf{g}(\boldsymbol{\alpha}^*, \boldsymbol{\theta} = \boldsymbol{\theta}_c) + \mathbf{J}|_{\boldsymbol{\theta}_c}\{\boldsymbol{\theta}_a - \boldsymbol{\theta}_c\} + \mathbf{p}(\boldsymbol{\theta}_a, \boldsymbol{\theta}_c) \\ \mathbf{g}(\boldsymbol{\alpha}^*, \boldsymbol{\theta} = \boldsymbol{\theta}_b) &= \mathbf{g}(\boldsymbol{\alpha}^*, \boldsymbol{\theta} = \boldsymbol{\theta}_c) + \mathbf{J}|_{\boldsymbol{\theta}_c}\{\boldsymbol{\theta}_b - \boldsymbol{\theta}_c\} + \mathbf{p}(\boldsymbol{\theta}_b, \boldsymbol{\theta}_c) \end{aligned} \tag{B.24}$$

where, since any polynomial in $\mathbf{g}(\boldsymbol{\alpha}^*, \boldsymbol{\theta})$ is of degree at most 2 and $\boldsymbol{\theta}_c = (\boldsymbol{\theta}_a + \boldsymbol{\theta}_b)/2$, the vectors $\mathbf{p}(\boldsymbol{\theta}_a, \boldsymbol{\theta}_c)$ and $\mathbf{p}(\boldsymbol{\theta}_b, \boldsymbol{\theta}_c)$ are equal. Subtracting the two equations above:

$$\mathbf{g}(\boldsymbol{\alpha}^*, \boldsymbol{\theta}_a) - \mathbf{g}(\boldsymbol{\alpha}^*, \boldsymbol{\theta}_b) = \mathbf{J}|_{\boldsymbol{\theta}_c}\{\boldsymbol{\theta}_a - \boldsymbol{\theta}_b\} \tag{B.25}$$

by which, since $\boldsymbol{\theta}_a \neq \boldsymbol{\theta}_b$, $\mathbf{g}(\boldsymbol{\alpha}^*, \boldsymbol{\theta}_a) = \mathbf{g}(\boldsymbol{\alpha}^*, \boldsymbol{\theta}_b)$, if and only if $\mathbf{J}|_{\boldsymbol{\theta}_c}$ is singular, i.e. $\det[\mathbf{J}|_{\boldsymbol{\theta}_c}] = 0$. Hence, if $\det[\mathbf{J}] \neq 0 \; \forall \; \boldsymbol{\theta} \in \mathcal{W}$, then $\mathbf{g}(\boldsymbol{\alpha}^*, \boldsymbol{\theta})$ is injective in $\mathcal{W}$. □

The above proof is a direct result of the mean-value theorem represented by Eq. (B.25) [65]. There is also an alternative proof, a proof by contradiction, given in [62, 63].

Appendix C

Constructing the Matrices $\mathbf{J}_{\boldsymbol{\theta}}$ and $\mathbf{J}_{\boldsymbol{\alpha}}$

In this appendix, pseudo-codes are provided for analytically constructing the matrices $[\partial \mathbf{g}(\boldsymbol{\alpha}, \boldsymbol{\theta})/\partial \boldsymbol{\theta}]$ and $[\partial \mathbf{g}(\boldsymbol{\alpha}, \boldsymbol{\theta})/\partial \boldsymbol{\alpha}]$ necessary in Chapters 4 and 6. The pseudo-codes are written for an N-DOF shear–type system, instrumented with N_s sensors located at the DOFs in $\mathcal{S} = \{s_1, \cdots, s_{N_s}\}$. The $N(N + N_s - 2)$ nonlinear equations in $\mathbf{g}(\boldsymbol{\alpha}, \boldsymbol{\theta}) = \mathbf{0}$ are arranged such that: (a) the first $N(N-1)/2$ equations are from the diagonality of $\mathbf{M}$, (b) the next $N(N-1)/2$ equations are from the nature of $\mathbf{F} = \mathbf{K}^{-1}$, and (c) the last $N(N_s - 1)$ equations are from the measured mode shape components, $\tilde{v}_{s_i,j}$'s (see Section 4.2.1 for the equations). The unknown and known parameters are respectively arranged in the vectors $\boldsymbol{\theta}$, of dimension $(N^2 - 1) \times 1$, and $\boldsymbol{\alpha}$, of dimension $NN_s \times 1$, as in Eqs. (4.5) or (6.2). Given an estimate of $\boldsymbol{\theta}$, and with $v^*_{s_1,1} = 1$, one can construct the matrix $\mathbf{V}^*$. The Jacobian matrix $\mathbf{J} = \mathbf{J}_{\boldsymbol{\theta}} = [\partial \mathbf{g}(\boldsymbol{\alpha}, \boldsymbol{\theta})/\partial \boldsymbol{\theta}]$, necessary in Chapters 4 and 6, may then be obtained as:

$\mathbf{J}_{\boldsymbol{\theta}} = \mathbf{0}_{N(N+N_s-2)\times N^2}$
$l = 1$
for $i = 1$ to $N - 1$ **do**
  for $k = i + 1$ to N **do**
    for $j = 1$ to N **do**
      $[\mathbf{J}_{\boldsymbol{\theta}}]_{l,N(i-1)+j} = v^*_{k,j}$
      $[\mathbf{J}_{\boldsymbol{\theta}}]_{l,N(k-1)+j} = v^*_{i,j}$
      $[\mathbf{J}_{\boldsymbol{\theta}}]_{N(N-1)/2+l,N(i-1)+j} = (v^*_{k,j} - 2v^*_{i,j})/\lambda_j$
      $[\mathbf{J}_{\boldsymbol{\theta}}]_{N(N-1)/2+l,N(k-1)+j} = v^*_{i,j}/\lambda_j$
    end for

$l = l + 1$

end for

end for

for $i = 2$ to N_s **do**

for $j = 1$ to N **do**

$[\mathbf{J}_{\boldsymbol{\theta}}]_{N(N-1)+N(i-2)+j,N(s_1-1)+j} = -\tilde{v}_{s_i,j}/\tilde{v}_{s_1,j}$

$[\mathbf{J}_{\boldsymbol{\theta}}]_{N(N-1)+N(i-2)+j,N(s_i-1)+j} = 1$

end for

end for

$\mathbf{J}_{\boldsymbol{\theta}} = \left[[\mathbf{J}_{\boldsymbol{\theta}}]_{1:N(N+N_s-2),1:N(s_1-1)} \quad [\mathbf{J}_{\boldsymbol{\theta}}]_{1:N(N+N_s-2),N(s_1-1)+2:N^2}\right]$

The matrix $\mathbf{J}_{\boldsymbol{\alpha}} = [\partial \mathbf{g}(\boldsymbol{\alpha}, \boldsymbol{\theta})/\partial \boldsymbol{\alpha}]$, necessary in Chapter 6, may be obtained as:

$\mathbf{J}_{\boldsymbol{\alpha}} = \mathbf{0}_{N(N+N_s-2)\times NN_s}$

$l = N(N-1)/2 + 1$

for $i = 1$ to $N - 1$ **do**

for $k = i + 1$ to N **do**

for $j = 1$ to N **do**

$[\mathbf{J}_{\boldsymbol{\alpha}}]_{l,j} = -(v^*_{i,j}v^*_{k,j} - v^{*2}_{i,j})/\lambda^2_j$

end for

$l = l + 1$

end for

end for

for $i = 2$ to N_s **do**

for $j = 1$ to N **do**

$[\mathbf{J}_{\boldsymbol{\theta}}]_{N(N-1)+N(i-2)+j,N(i-1)+j} = -v^*_{s_1,j}$

end for

end for

Appendix D

Propagation of Mode Shape Errors in Structural Identification[1]

D.1 Introduction

Experimentally identified modal parameters are often used in structural damage detection, for example by directly comparing them with the corresponding ones obtained from an initial analytical model of the structure, or by using them to estimate the stiffness/flexibility matrices of the structural model. In assessing structural damage, an increase in structural flexibility has often been considered as indicative of damage (see, e.g. [72, 99–102], amongst others).

Another approach, especially for ascertaining the presence of damage and for damage localization, has been the direct comparison of experimental and analytical modal parameters. In [103] the authors have shown that the comparison of mode shapes gives a better indication of damage in the structure than the comparison of natural frequencies. The comparison of two mode shapes obtained from different sources but corresponding to the same mode of vibration is conventionally conducted via the Modal Assurance Criterion (MAC) [21]. MAC is a scalar constant which expresses the consistency between two selected mode shapes. It can take values between 0 and 1; if the two mode shapes are consistent, i.e. they differ only by a scalar factor of proportionality, MAC takes a value of 1; if the

[1] This appendix is almost entirely from an article, co-authored with Profs. Raimondo Betti and Hilmi Lus, and Dr. Ah Lum Hong, in the Journal of Sound and Vibration [48].

two mode shapes are orthogonal to each other, MAC takes a value of 0. On the other hand, a commonly used criterion to test how two sets of mode shapes (obtained from different sources) compare at a given degree of freedom (DOF) is the Coordinate Modal Assurance Criterion, or COMAC [22]. The COMAC also takes a value between 0 and 1 and, for a given DOF, gives us a global index indicating how all the corresponding mode shapes from the two different sets compare at that specific DOF. A low value of COMAC implies that the two sets of mode shapes, at the selected DOF, are not consistent or similar to each other, while a high value of COMAC implies a concordance between the two sets of mode shapes for that DOF. [103] used MAC values to ascertain the presence of damage, and COMAC values to indicate the location of damage in a multispan reinforced concrete highway bridge, whereas [104] used COMAC values to assess the quality of repair and damage localizations in a prestressed concrete bridge. [105] used MAC values to identify changes in the modal parameters obtained from vibration measurements from both damaged and undamaged metallic and composite panels. Comparing the natural frequencies, mode shapes and modal flexibility, [106] found the modal flexibilities to be most sensitive to damage.

For algorithms using mode shapes for damage detection, it is ideal that the experimental mode shapes be error free; it is, however, not possible to obtain error free estimates. It is thus important that one should be able to quantify how errors that occur in the mode shape estimates propagate to the estimates of the structural flexibility matrix, as well as to the calculation of MAC and COMAC values for these estimated mode shapes and the corresponding exact ones. From a different perspective, if "error" in any estimated mode shape is the change due to damage, this error propagation analysis will show how the changes in mode shapes due to damage show up in the estimated structural flexibility matrix and MAC/COMAC values. Since both changes in the flexibility matrix as well as the MAC/COMAC values are used for damage detection purposes, it will also be interesting to compare these propagated errors, i.e. how changes induced in the modal parameters by damage propagate to the estimated structural flexibility matrix and the MAC/COMAC values.

One stream of research has tried to address how changes in the structural parameters affect the structural frequencies and mode shapes using sensitivity analysis (see, e.g. [107] for eigenvector derivatives). In this appendix, we instead try to address a somewhat inverse issue, namely how changes in the mode shapes of linear classically damped systems affect the structural flexibility matrix and the MAC/COMAC values obtained from comparing the corresponding changed and unchanged

mode shapes. To this end, a random multiplicative error in each component of each estimated mode shape is assumed, and the nonlinear functions thus obtained are simplified by expanding them in Taylor series around the mean values of the random parameters, as for instance done in classical reliability analyses. The results obtained show analytically how the variance of the errors propagated to the MAC/COMAC values and the structural flexibility matrix relate to the variance of the errors that occur in the mode shape estimates. The results are also validated numerically through a Monte Carlo simulation using an 8 story shear–building model.

The implications of this mismatch in the order of propagated error can be interpreted from two differing points of view. For the first point of view, one may assume that the error-free analytical mode shapes of the structure are available beforehand, and one uses the estimated experimental mode shapes for damage detection and/or model updating purposes. In this case, the mismatch would imply that the error in the estimated flexibility matrix would be different than that suggested by the MAC and COMAC values comparing the estimated mode shapes with the true ones. Although the true mode shapes are not available in practice, this scenario can be analyzed in numerical simulations to evaluate the relative efficiency of different mode shape estimation and expansion techniques. For the second interpretation, one can assume that the error free mode shapes represent the undamaged state of the structure, and the estimated mode shapes represent the damaged state. In this situation, the estimated mode shapes are also error free and their difference from the undamaged ones is representative of damage. Thus, in this case, error propagation from the mode shapes to the flexibility matrix, and to MAC and COMAC values, is in essence the propagation of "damage severity information". The mismatch of the propagated error in this case will therefore suggest that the severity of damage indicated by the MAC and COMAC values is not the same as the severity of damage indicated by a change in the structural flexibility matrix.

After the propagation analysis, two new indices are proposed, both of which try to mimic the order of "error" that is to occur in the flexibility matrix. The first complements MAC; it can be used to compare two different mode shapes, but it will provide a measure of the difference one can expect in the flexibility matrices obtained using the two different mode shapes. The second index is complementary to COMAC; it can be used to compare corresponding mode shapes from two different sets at the same DOF, and it will also give a measure of the difference one can expect in the flexibility matrices obtained using the two different sets of mode shapes.

D.2 Error Propagation Analysis: MAC, COMAC and Flexibility Matrix

In this study it is assumed that the mode shapes are real, as for instance the mode shapes that can be obtained for a classically damped system, and that they are evaluated at every DOF. Let $\mathbf{v}_i \in R^{N\times 1}$ and $\widehat{\mathbf{v}}_i \in R^{N\times 1}$ denote, respectively, the analytical and experimental mode shapes for the ith mode of vibration for an N DOF system. Here the subjective "analytical" refers to an initial model, obtained possibly through a finite element analysis, and "experimental" refers to the actual in situ situation. Also, let $\mathbf{v}_i$ and $\widehat{\mathbf{v}}_i$ be related as

$$\widehat{\mathbf{v}}_i = \boldsymbol{\beta}_i \mathbf{v}_i \tag{D.1}$$

where $\boldsymbol{\beta}_i$ is an $N \times N$ diagonal matrix representing the mismatch, due to error and/or damage, between $\mathbf{v}_i$ and $\widehat{\mathbf{v}}_i$. In the case of no damage or if the analytical model perfectly matches the real structure, the matrix $\boldsymbol{\beta}_i$ becomes equal to

$$\boldsymbol{\beta}_i = \alpha_i \mathbf{I} \tag{D.2}$$

where α_i is a scalar constant.

The MAC value, MAC_i, for the mode shapes $\mathbf{v}_i$ and $\widehat{\mathbf{v}}_i$ is given by

$$\text{MAC}_i = \frac{|\widehat{\mathbf{v}}_i^T \mathbf{v}_i|^2}{|\widehat{\mathbf{v}}_i^T \widehat{\mathbf{v}}_i||\mathbf{v}_i^T \mathbf{v}_i|} \tag{D.3}$$

Using Eqs. (D.1) and (D.3), the MAC_i value can be expressed in terms of $\boldsymbol{\beta}_i$ and $\mathbf{v}_i$ as

$$\text{MAC}_i = \frac{(\sum_{k=1}^{N} \beta_{i,k} v_{k,i}^2)^2}{(\sum_{k=1}^{N} \beta_{i,k} v_{k,i}^2)^2 + \frac{1}{2}\sum_{k=1}^{N}\sum_{j=1}^{N}(\beta_{i,k} - \beta_{i,j})^2 v_{k,i}^2 v_{j,i}^2} \tag{D.4}$$

where $\beta_{i,k}$ is the kth element in the principal diagonal of $\boldsymbol{\beta}_i$, corresponding to the kth element $v_{k,i}$ in the vector $\mathbf{v}_i$. Remembering that MAC_i should ideally be 1 if $\mathbf{v}_i$ and $\widehat{\mathbf{v}}_i$ match perfectly, the error in MAC_i, denoted by eMAC_i, can then be written as

$$\text{eMAC}_i = 1 - \text{MAC}_i = \frac{\frac{1}{2}\sum_{k=1}^{N}\sum_{j=1}^{N}(\beta_{i,k} - \beta_{i,j})^2 v_{k,i}^2 v_{j,i}^2}{(\sum_{k=1}^{N} \beta_{i,k} v_{k,i}^2)^2 + \frac{1}{2}\sum_{k=1}^{N}\sum_{j=1}^{N}(\beta_{i,k} - \beta_{i,j})^2 v_{k,i}^2 v_{j,i}^2} \tag{D.5}$$

It should be noted that the eMAC$_i$ becomes zero (i.e. MAC$_i$ becomes 1) when all $\beta_{i,k}$ for $k = 1, 2, ..., N$, are equal to each other, in which case $\mathbf{v}_i$ and $\widehat{\mathbf{v}}_i$ differ only by a scalar multiplicative constant, and thus are exactly the same mode shape. On the other hand, if the differences between the different $\beta_{i,k}$ values become very large eMAC$_i$ tends to go to 1.

The $N \times N$ estimated flexibility matrix $\widehat{\mathbf{F}}$ for an N-DOF system can be expressed in terms of the experimental modal parameters as:

$$\widehat{\mathbf{F}} = \widehat{\mathbf{V}}\widehat{\mathbf{\Lambda}}^{-1}\big(\widehat{\mathbf{V}}^T\mathbf{M}\widehat{\mathbf{V}}\big)^{-1}\widehat{\mathbf{V}}^T \tag{D.6}$$

In this expression, $\mathbf{M}$ is the $N \times N$ mass matrix of the system, $\widehat{\mathbf{\Phi}}$ is the experimental mode shape matrix defined as

$$\widehat{\mathbf{V}} = [\widehat{\mathbf{v}}_1 \quad \widehat{\mathbf{v}}_2 \quad \cdots \quad \widehat{\mathbf{v}}_N] \tag{D.7}$$

and $\widehat{\mathbf{\Lambda}}$ is the $N \times N$ diagonal experimental eigenvalue matrix

$$\widehat{\mathbf{\Lambda}} = \text{diag}\big(\widehat{\lambda}_1, \widehat{\lambda}_2, \cdots, \widehat{\lambda}_N\big) \tag{D.8}$$

with $\widehat{\lambda}_i$ being the ith experimental eigenvalue, and $\widehat{\omega}_i = \sqrt{\widehat{\lambda}_i}$ being the ith natural frequency of the system obtained through the experiment. Here it is assumed that the mass matrices of the analytical and experimental system are equal: this is a widely used assumption, especially where changes in modal parameters are due to damage, as evidenced in several papers (see, e.g., [108–111]). Furthermore, mode shape changes due to modeling errors are less likely to be indicative of a change in mass rather than a change in flexibility, as the initial estimate of mass is generally accepted to be more reliable than an initial estimate of flexibility. Due to the same reason, mode shape mismatch due to measurement errors will be more likely to be reflected as errors in the updated/identified flexibility matrix.

The analytical flexibility matrix can similarly be written as

$$\mathbf{F} = \mathbf{V}\mathbf{\Lambda}^{-1}(\mathbf{V}^{\mathrm{T}}\mathbf{M}\mathbf{V})^{-1}\mathbf{V}^{\mathrm{T}} \tag{D.9}$$

where

$$\mathbf{V} = [\mathbf{v}_1 \quad \mathbf{v}_2 \quad \cdots \quad \mathbf{v}_N] \tag{D.10}$$

is the analytical mode shape matrix, and

$$\mathbf{\Lambda} = \text{diag}\big(\lambda_1, \lambda_2, \cdots, \lambda_N\big) \tag{D.11}$$

is the diagonal matrix of analytical frequencies. Since the mass matrix $\mathbf{M}$ is unaltered, both the experimental and analytical mode shapes are orthogonal with respect to $\mathbf{M}$. It is furthermore assumed that the analytical mode shapes are mass normalized, so that,

$$\mathbf{V}^T\mathbf{M}\mathbf{V} = \mathbf{I} \tag{D.12}$$

while the experimental mode shapes satisfy the following mass normalization condition:

$$\widehat{\mathbf{V}}^T\mathbf{M}\widehat{\mathbf{V}} = \mathbf{S} \tag{D.13}$$

where $\mathbf{S}$ is an $N \times N$ diagonal matrix, with the ith element on its principal diagonal given by

$$S_i = \widehat{\mathbf{v}}_i{}^T\mathbf{M}\widehat{\mathbf{v}}_i = \mathbf{v}_i{}^T\boldsymbol{\beta}_i{}^T\mathbf{M}\boldsymbol{\beta}_i\mathbf{v}_i = \sum_{k=1}^{N}\sum_{j=1}^{N} m_{jk}\beta_{i,j}\beta_{i,k}v_{j,i}v_{k,i} \tag{D.14}$$

where m_{jk} is the (j,k)th element, i.e. the element on the jth row and kth column, of the mass matrix $\mathbf{M}$.

Using Eqs. (D.12) and (D.13) in Eqs. (D.9) and (D.6), the analytical and experimental flexibility matrices, $\mathbf{F}$ and $\widehat{\mathbf{F}}$, can respectively be written as

$$\mathbf{F} = \sum_{i=1}^{N}\mathbf{F}_i, \qquad \widehat{\mathbf{F}} = \sum_{i=1}^{N}\widehat{\mathbf{F}}_i \tag{D.15}$$

where,

$$\mathbf{F}_i = \frac{\mathbf{v}_i\mathbf{v}_i^T}{\lambda_i}, \qquad \widehat{\mathbf{F}}_i = \frac{\widehat{\mathbf{v}}_i\widehat{\mathbf{v}}_i^T}{S_i\widehat{\lambda}_i} \tag{D.16}$$

The expressions in Eq. (D.15) describe the total analytical and experimental flexibility matrices as sums of the corresponding flexibility matrices obtained from each mode, whereas the expressions in Eq. (D.16) describe the contribution of a single mode to the analytical and the experimental flexibility matrices. Thus, the error in the flexibility matrix from the contribution of the ith mode due to $\boldsymbol{\beta}_i$ of Eq. (D.1) can be written as

$$\mathbf{eF}_i = \mathbf{F}_i - \widehat{\mathbf{F}}_i = \frac{\mathbf{v}_i\mathbf{v}_i^T}{\lambda_i} - \frac{\widehat{\mathbf{v}}_i\widehat{\mathbf{v}}_i^T}{S_i\widehat{\lambda}_i} \tag{D.17}$$

where the (j,k)th element of $\mathbf{eF}_i$, denoted by $\mathrm{ef}_{i,jk}$, is given in terms of $\beta_{i,j}$ and $\beta_{i,k}$ by

$$\mathrm{ef}_{i,jk} = \frac{v_{j,i}v_{k,i}}{\lambda_i} - \frac{\beta_{i,j}\beta_{i,k}v_{j,i}v_{k,i}}{S_i\widehat{\lambda}_i} \tag{D.18}$$

So the error in the (j,k)th element of $\widehat{\mathbf{F}}_i$ relative to the (j,k)th element of $\mathbf{F}_i$, denoted by $\text{ref}_{i,jk}$, is given by

$$\text{ref}_{i,jk} = \frac{\text{ef}_{i,jk}}{f_{i,jk}} = 1 - \frac{\lambda_i}{\widehat{\lambda}_i}\frac{\beta_{i,j}\beta_{i,k}}{S_i} \tag{D.19}$$

The representative error in the flexibility matrix associated with the ith mode, $\overline{\text{ref}}_i$, is defined here as the mean of the principal diagonal elements of the relative flexibility error matrix:

$$\overline{\text{ref}}_i = 1 - \frac{\lambda_i}{\widehat{\lambda}_i}\frac{\sum_{k=1}^{N}\beta_{i,k}^2}{NS_i} \tag{D.20}$$

If it is further assumed that the changes in natural frequencies are insignificant as compared to the changes in the mode shapes, Eq. (D.20) simplifies to

$$\widetilde{\text{ref}}_i = 1 - \frac{\sum_{k=1}^{N}\beta_{i,k}^2}{NS_i} \tag{D.21}$$

Although natural frequencies do change due to damage and/or measurement errors, our main purpose is to quantify how errors in the mode shapes propagate to MAC/COMAC and the flexibility matrix. Furthermore, since MAC/COMAC values depend only on the mode shapes and not on frequencies, neglecting the frequency changes will provide a more consistent comparison when the errors in flexibility are compared with the errors in MAC. It has also been discussed (see, e.g., [103]) that mode shapes are more sensitive to damage than natural frequencies, with changes in natural frequencies becoming significant only when there is substantial structural damage.

The $\beta_{i,k}$, for all k, are assumed to be independent and identically distributed normal random variables with unit mean and standard deviation equal to σ_i:

$$\text{E}\{\beta_{i,k}\} = 1,\ \text{Var}\{\beta_{i,k}\} = \sigma_i^2 \quad \forall \quad k \in \{1, 2, \cdots, N\} \tag{D.22}$$

σ_i is the standard deviation corresponding to the ith mode and it may be expected to have higher values for higher modes. The means and variances of the error in MAC_i (given by Eq. (D.5)) and the error in the flexibility matrix for no error in natural frequency (given by Eq. (D.21)) can now be calculated. To this end, both eMAC_i and $\widetilde{\text{ref}}_i$ are expanded in a Taylor series about $\text{E}\{\beta_{i,k}\}\ \forall\ k$ [112, chap. 4]. It is found that, for a first order Taylor series approximation of eMAC_i, both the mean and variance in eMAC_i come out to be zero:

$$\text{E}\{\text{eMAC}_i\} \approx (\text{eMAC}_i)\Big|_{\beta_{i,k}=\text{E}\{\beta_{i,k}\}\,\forall k} = 0 \tag{D.23}$$

$$\text{Var}\{\text{eMAC}_i\} \approx \sum_{k=1}^{N} c_k^2 \text{Var}\{\beta_{i,k}\} = 0 \tag{D.24}$$

where

$$c_k = \frac{\partial \text{eMAC}_i}{\partial \beta_{i,k}}\Big|_{\beta_{i,j}=\text{E}\{\beta_{i,j}\}\,\forall j} = 0 \tag{D.25}$$

In order to get a dependence of $\text{Var}\{\text{eMAC}_i\}$ on σ_i, a second order Taylor series approximation of eMAC_i is employed to get:

$$\text{E}\{\text{eMAC}_i\} \approx (\text{eMAC}_i)\Big|_{\beta_{i,k}=\text{E}\{\beta_{i,k}\}\,\forall k} + \frac{1}{2}\sum_{k=1}^{N} d_k \text{Var}\{\beta_{i,k}\} = \frac{\sigma_i^2}{2} \tag{D.26}$$

$$\begin{aligned}\text{Var}\{\text{eMAC}_i\} \approx & \sum_{k=1}^{N} c_k^2 \text{Var}\{\beta_{i,k}\} - \frac{1}{4}\sum_{k=1}^{N} \left(d_k \text{Var}\{\beta_{i,k}\}\right)^2 \\ & + \sum_{k=1}^{N} c_k d_k \text{E}\{(\beta_{i,k} - \text{E}\{\beta_{i,k}\})^3\} \\ & + \frac{1}{4}\sum_{k=1}^{N} d_k^2 \text{E}\{(\beta_{i,k} - \text{E}\{\beta_{i,k}\})^4\} \\ & = \frac{\sigma_i^4}{2} \frac{\sum_{k=1}^{N} v_{k,i}^4}{\sum_{l=1}^{N}\sum_{j=1}^{N} v_{l,i}^2 v_{j,i}^2}\end{aligned} \tag{D.27}$$

where $c_k = 0$ as per Eq. (D.25), and

$$d_k = \frac{\partial^2 \text{eMAC}_i}{\partial {\beta_{i,k}}^2}\Big|_{\beta_{i,j}=\text{E}\{\beta_{i,j}\}\,\forall j} = \frac{v_{k,i}^2}{\sum_{j=1}^{N} v_{j,i}^2} \tag{D.28}$$

Since $\beta_{i,k}$ are normally distributed for all k,

$$\text{E}\{(\beta_{i,k} - \text{E}\{\beta_{i,k}\})^3\} = 0; \;\; \text{E}\{(\beta_{i,k} - \text{E}\{\beta_{i,k}\})^4\} = 3\sigma_i^4 \tag{D.29}$$

The fact that the mean of eMAC_i is not equal to zero can be explained by the fact that MAC_i is a variable which is bounded upwards by 1 and for the ideal case of zero estimation error in the ith mode shape it should be equal to 1. Therefore eMAC_i should also have a distribution which is bounded downwards by zero, and thus should have a mean slightly greater than zero. Also, from Eq. (D.27) it can be said that the variance in eMAC_i is always less than $\sigma_i^4/2$ as $\sum_{k=1}^{N} v_{k,i}^4$ will always be lesser than $\sum_{l=1}^{N}\sum_{j=1}^{N} v_{l,i}^2 v_{j,i}^2$.

Similarly using a first order Taylor series expansion, the mean and variance of the flexibility error $\widetilde{\text{ref}}_i$ can be expressed respectively as

$$\text{E}\{\widetilde{\text{ref}}_i\} \approx (\widetilde{\text{ref}}_i)\Big|_{\beta_{i,k}=\text{E}\{\beta_{i,k}\}\,\forall k} = 0 \tag{D.30}$$

and

$$\text{Var}\{\widetilde{\text{ref}}_i\} \approx \sum_{k=1}^{N} c_k^2 \text{Var}\{\beta_{i,k}\} = 4\sigma_i^2 \Big(\sum_{k=1}^{N} \Big(\sum_{j=1}^{N} m_{jk} v_{j,i} v_{k,i} \Big)^2 - \frac{1}{N} \Big) \tag{D.31}$$

where

$$c_k = \frac{\partial \widetilde{\text{ref}}_i}{\partial \beta_{i,k}}\Big|_{\beta_{i,j}=\text{E}\{\beta_{i,j}\}\,\forall j} = -\frac{2}{N}\Big(1 - N \sum_{j=1}^{N} m_{jk} v_{j,i} v_{k,i}\Big) \quad \forall \quad k \tag{D.32}$$

Comparing the variances in eMAC$_i$ and $\widetilde{\text{ref}}_i$ and noting that σ_i would, in most cases, be expected to realize a value between 0 and $+1$, the errors in flexibility are identified to be of a higher order than the error in MAC. Of course, this comparison also involves the coefficients of σ_i^4 and σ_i^2 in Eqs. (D.27) and (D.31). It will later be demonstrated, via Monte Carlo simulations, that the variance of the error in flexibility as defined by Eq. (D.21) is indeed of a higher order than the variance of the error in MAC defined by Eq. (D.5).

It should be noted that, if a second order Taylor series expansion for $\widetilde{\text{ref}}_i$ is assumed, it will result in only adding an expression containing σ_i^4 to the σ_i^2 expression of Eq. (D.31). Remembering that variance is never negative, a second order expansion for $\widetilde{\text{ref}}_i$ will even further increase the variance of $\widetilde{\text{ref}}_i$ given by Eq. (D.31). As the resulting expressions involve too many terms, and do not add any significant information to that already obtained by comparing Eqs. (D.27) and (D.31), these second order expansion expressions are not included here.

Until this point the focus has been on how any error in the estimation of a single mode shape affects the contribution of that mode to the estimate of the structural flexibility matrix, and how this error changes the MAC value obtained by comparing this estimated mode shape with the corresponding actual one. It would also be interesting to know how the estimation errors in several estimated mode shapes propagate to any (k,k)th element of the estimated flexibility matrix, and whether this propagated error correlates well with the COMAC value at the kth DOF. To this end, it is assumed that N_m estimated mode shapes and natural frequencies are available for the N DOF system being considered ($N_m \leq N$). The COMAC value for the kth DOF, calculated using the estimated and the

actual mode shapes, can then be expressed as:

$$\text{COMAC}_k = \frac{\big(\sum_{i=1}^{N_m} \widehat{v}_{k,i} v_{k,i}\big)^2}{\sum_{i=1}^{N_m} \widehat{v}_{k,i}^2 \sum_{i=1}^{N_m} v_{k,i}^2} = \frac{\big(\sum_{i=1}^{N_m} \beta_{i,k} v_{k,i}^2\big)^2}{\sum_{i=1}^{N_m} \beta_{i,k}^2 v_{k,i}^2 \sum_{i=1}^{N_m} v_{k,i}^2} \tag{D.33}$$

Noting that COMAC_k should ideally be 1 when all $\beta_{i,k}$ (for $i = 1, 2, ..., N_m$) are equal to each other, the error in COMAC_k can be written as

$$\begin{aligned} \text{eCOMAC}_k &= 1 - \text{COMAC}_k \\ &= \frac{\frac{1}{2}\sum_{i=1}^{N_m}\sum_{j=1}^{N_m}(\beta_{i,k} - \beta_{j,k})^2 v_{k,i}^2 v_{k,j}^2}{(\sum_{i=1}^{N_m} \beta_{i,k} v_{k,i}^2)^2 + \frac{1}{2}\sum_{i=1}^{N_m}\sum_{j=1}^{N_m}(\beta_{i,k} - \beta_{j,k})^2 v_{k,i}^2 v_{k,j}^2} \end{aligned} \tag{D.34}$$

Furthermore, from Eqs. (D.15) and (D.16), the error in the (j,k)th element of the flexibility matrix obtained using these N_m estimated mode shapes can be written (using Eq. (D.18)) as

$$\sum_{i=1}^{N_m} \text{ef}_{i,jk} = \sum_{i=1}^{N_m} \Big(\frac{v_{j,i} v_{k,i}}{\lambda_i} - \frac{\beta_{i,j}\beta_{i,k} v_{j,i} v_{k,i}}{S_i \widehat{\lambda}_i} \Big) \tag{D.35}$$

If this error is scaled with the value of the true flexibility coefficient that would be obtained with the actual N_m modes, the following expression is obtained for the relative flexibility coefficient error:

$$\text{reF}_{jk}^{(N_m)} = \frac{\sum_{i=1}^{N_m} \Big(\frac{v_{j,i} v_{k,i}}{\lambda_i} - \frac{\beta_{i,j}\beta_{i,k} v_{j,i} v_{k,i}}{S_i \widehat{\lambda}_i} \Big)}{\sum_{i=1}^{N_m} \frac{v_{j,i} v_{k,i}}{\lambda_i}} = 1 - \frac{\sum_{i=1}^{N_m} \frac{\beta_{i,j}\beta_{i,k} v_{j,i} v_{k,i}}{S_i \widehat{\lambda}_i}}{\sum_{i=1}^{N_m} \frac{v_{j,i} v_{k,i}}{\lambda_i}} \tag{D.36}$$

where the superscript (N_m) denotes the number of modes used in the computation.

Since COMAC_k indicates the degree of agreement between the estimated and actual mode shapes at the kth DOF, it may be interesting to see whether the order of error in COMAC_k due to the estimation error in the mode shapes is the same as the order of error in the (k,k)th element of the flexibility matrix derived using these mode shapes, since this term indicates the "flexibility" for the kth DOF. To this end, eCOMAC_k and $\text{reF}_{kk}^{(N_m)}$ are compared in an analysis similar to the one undertaken for comparing eMAC_i and $\widetilde{\text{ref}}_i$. It is assumed here for simplicity that all $\beta_{i,k}$, for $k = 1, 2, ..., N$ and $i = 1, 2, ..., N_m$, are independent and identically distributed normal random variables with

$$\text{E}\{\beta_{i,k}\} = 1, \quad \text{Var}\{\beta_{i,k}\} = \sigma^2 \tag{D.37}$$

The first order Taylor series expansion about $\mathrm{E}\{\beta_{i,k}\}$ lead to zero mean and variance for eCOMAC_k, while with the second order expansion one finds:

$$\mathrm{E}\{\mathrm{eCOMAC}_k\} \approx \frac{\sigma^2}{2} \tag{D.38a}$$

$$\mathrm{Var}\{\mathrm{eCOMAC}_k\} \approx \frac{\sigma^4}{2} \frac{\sum_{i=1}^{N_m} v_{k,i}^4}{\sum_{i=1}^{N_m}\sum_{j=1}^{N_m} v_{k,i}^2 v_{k,j}^2} \tag{D.38b}$$

On the other hand, the first order Taylor series expansion of $\mathrm{reF}_{kk}^{(N_m)}$ about $\mathrm{E}\{\beta_{i,k}\}$ leads to:

$$\mathrm{E}\{\mathrm{reF}_{kk}^{(N_m)}\} \approx 0 \tag{D.39a}$$

$$\mathrm{Var}\{\mathrm{reF}_{kk}^{(N_m)}\} \approx \sigma^2 \Big(\sum_{\substack{j=1 \\ j\neq k}}^{N} \sum_{i=1}^{N_m} c_{i,j}^2 + \sum_{i=1}^{N_m} c_{i,k}^2 \Big) \tag{D.39b}$$

where

$$c_{i,j} = \begin{cases} \dfrac{2v_{k,i}^2}{\lambda_i} \dfrac{\sum_{l=1}^{N} m_{lj} v_{l,i} v_{j,i}}{\sum_{i=1}^{N_m} \frac{v_{k,i}^2}{\lambda_i}}, & \text{if } j \neq k \\ \dfrac{2v_{k,i}^2}{\lambda_i} \dfrac{\sum_{l=1}^{N} m_{lk} v_{l,i} v_{k,i} - 1}{\sum_{i=1}^{N_m} \frac{v_{k,i}^2}{\lambda_i}}, & \text{if } j = k \end{cases} \tag{D.40}$$

Once again the results of the second order Taylor series expansion for $\mathrm{reF}_{kk}^{(N_m)}$ are not presented, since this expansion simply adds a σ^4 term to the σ^2 term in Eq. (D.39b), and thereby further increases the variance of $\mathrm{reF}_{kk}^{(N_m)}$ given by Eq. (D.39b) for $0 < \sigma < 1$. Based on Eqs. (D.38b) and (D.39b), the error in the (k,k)th element of the flexibility matrix estimated from the N_m estimated mode shapes can, in general, be expected to be of a higher order than the error in COMAC_k, the variance of the former being proportional to σ^2 while that of the latter being proportional to σ^4.

D.3 Monte Carlo Simulation

To numerically compare the order of the errors in MAC_i and COMAC_k with the order of the errors in $\widetilde{\mathrm{ref}}_i$ and $\mathrm{reF}_{kk}^{(N_m)}$, respectively, Monte Carlo simulations using an 8 DOF shear–type system are performed: the lumped masses are taken as $m_i = 2500$kg for $i = 1, 2, ..., 7$, and $m_8 = 2000$kg, while the spring stiffnesses considered are $k_i = 5 \times 10^6$N/m for $i = 1, 2, ..., 8$. First an eigenvalue analysis

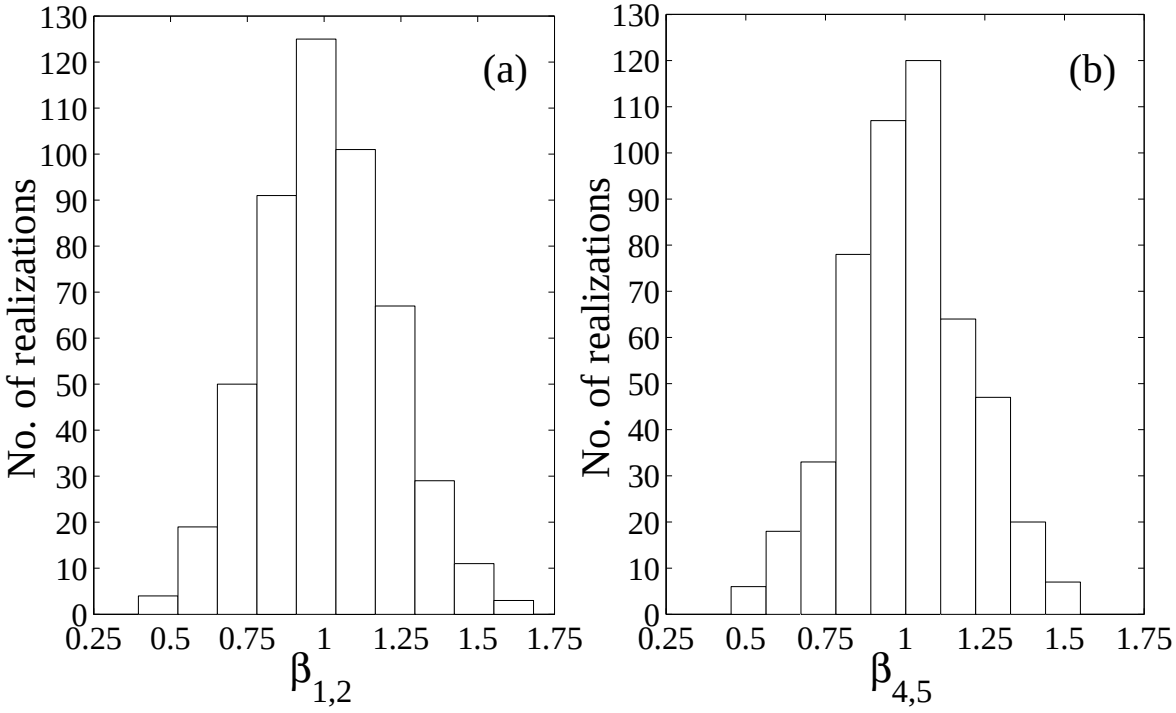

Figure D.1: Distribution of (a) $\beta_{1,2}$ and (b) $\beta_{4,5}$ for the 500 realizations.

of this 8 DOF system is performed to obtain its frequencies and mode shapes. It is assumed that only the first 5 mode shapes have been estimated from experiments; i.e. $N_m = 5$ for the COMAC$_k$ and reF$_{kk}^{(N_m)}$ calculations. The estimated mode shapes are obtained by perturbing the true mode shapes as in Eq. (D.1) for 500 sets of random realizations of $\beta_{i,k}$ (for $i = 1, 2, ..., 8$ and $k = 1, 2, ..., 5$) from a normal distribution with unit mean and $\sigma = 0.2$. Fig. D.1 shows the distributions of the 500 realizations of $\beta_{1,2}$ (with a mean of 1.0046 and variance of 0.0443) and $\beta_{4,5}$ (with a mean of 1.0070 and variance of 0.0380), i.e. the multiplicative perturbations for the mode shape components of second DOF for the first mode, and fifth DOF for the fourth mode, respectively.

Figs. D.2 and D.3 respectively show the distributions of the eMAC$_i$ and $\widetilde{\text{ref}}_i$ values, obtained from the true and the estimated 500 realizations of the first and the fourth mode shapes. It is evident from these figures that the variances of errors in MAC$_i$ are of a lower order than the variances of $\widetilde{\text{ref}}_i$, as could be anticipated from comparing Eqs. (D.27) and (D.31) in the last section. In fact, eMAC$_i$ has a mean of 0.0314 and a variance of 0.0004 for the first mode, and a mean of 0.0325 and a variance of 0.0004 for the fourth mode, whereas $\widetilde{\text{ref}}_i$ has a mean of -0.0111 and a variance of 0.0082 for the

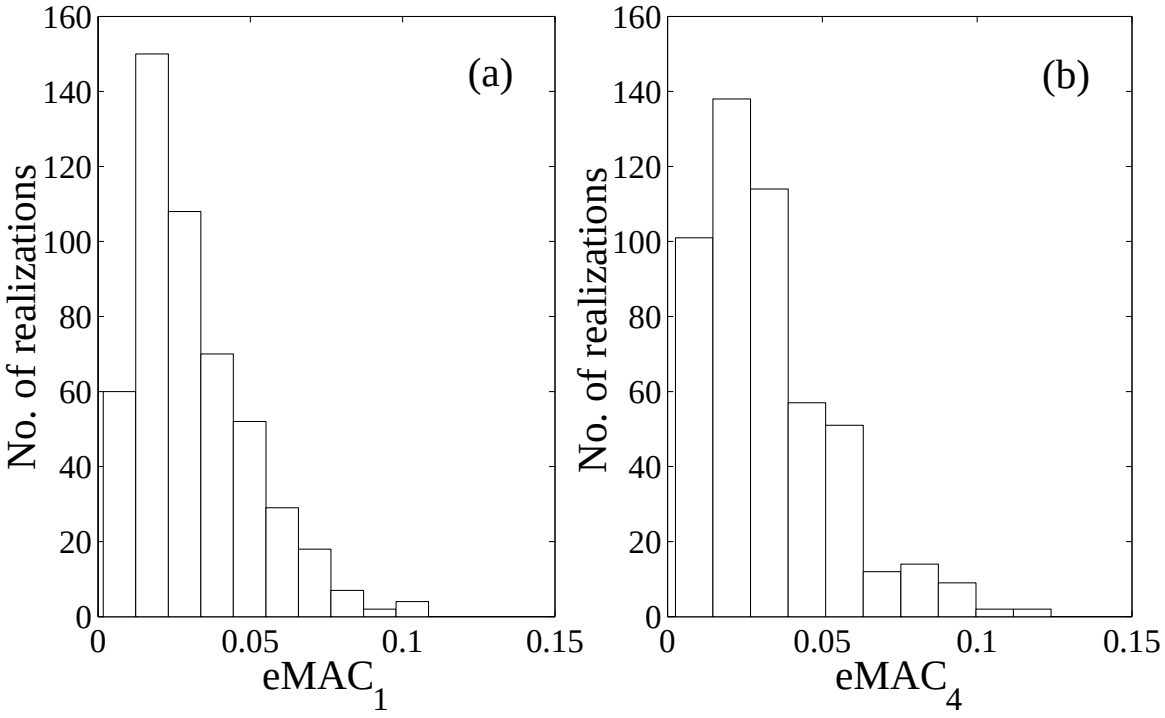

Figure D.2: Distributions obtained for (a) eMAC_1 and (b) eMAC_4.

first mode, and a mean of -0.0123 and a variance of 0.0085 for the fourth mode. Fig. D.4 shows the comparison of MAC_i with $\widetilde{\text{ref}}_i$ for the first and the fourth modes.

Figs. D.5 andD.6 respectively show the distributions of the eCOMAC_k and $\text{reF}_{kk}^{(N_m)}$ values, obtained for the second and the fifth DOFs from the 500 realizations of the first 5 estimated modes shapes and the corresponding first 5 true mode shapes. These figures also validate the reasoning of the last section that the variances in eCOMAC_k can be expected to be of a lower order than the variances in $\text{reF}_{kk}^{(N_m)}$. In these figures, eCOMAC_k has a mean of 0.0325 and a variance of 0.0004 for the second DOF, and a mean of 0.0317 and a variance of 0.0004 for the fifth DOF, while $\text{reF}_{22}^{(N_m)}$ has a mean of -0.0175 and a variance of 0.0561, and $\text{reF}_{55}^{(N_m)}$ has a mean of 0.0018 and a variance of 0.1101. Fig. D.7 compares COMAC_k with $\text{reF}_{kk}^{(N_m)}$ for the second and fifth DOFs.

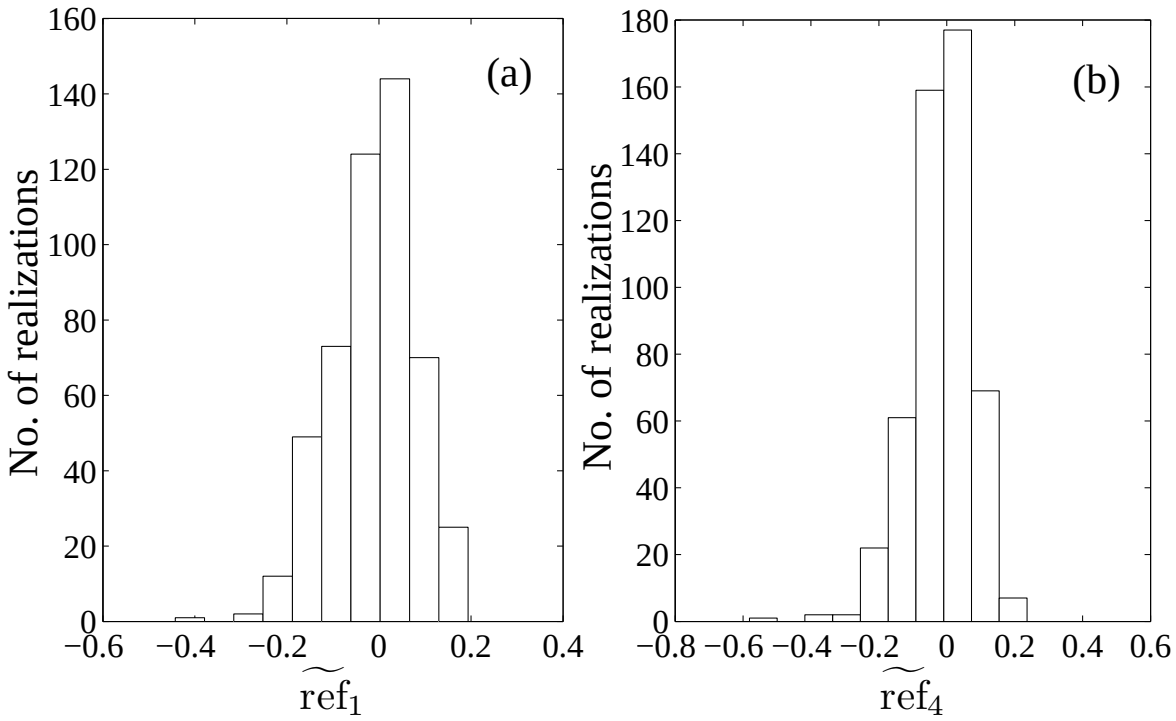

Figure D.3: Distributions obtained for (a) $\widetilde{\text{ref}}_1$ and (b) $\widetilde{\text{ref}}_4$.

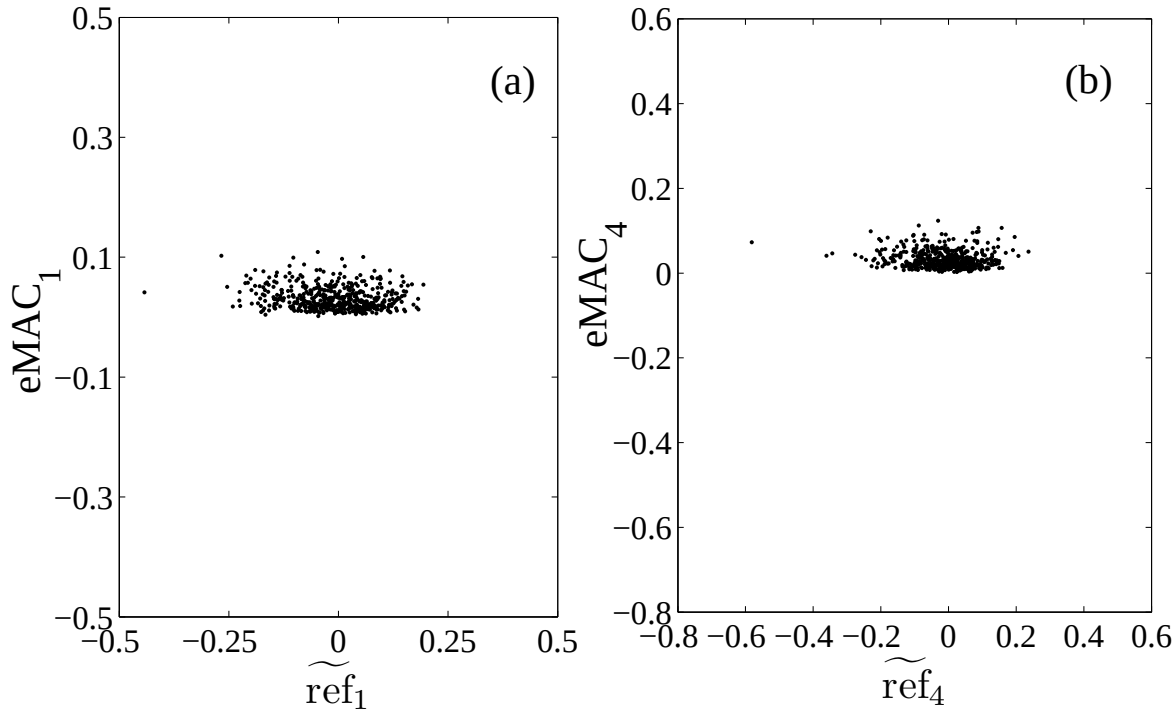

Figure D.4: Comparisons of (a) eMAC_1 with $\widetilde{\text{ref}}_1$ and (b) eMAC_4 with $\widetilde{\text{ref}}_4$.

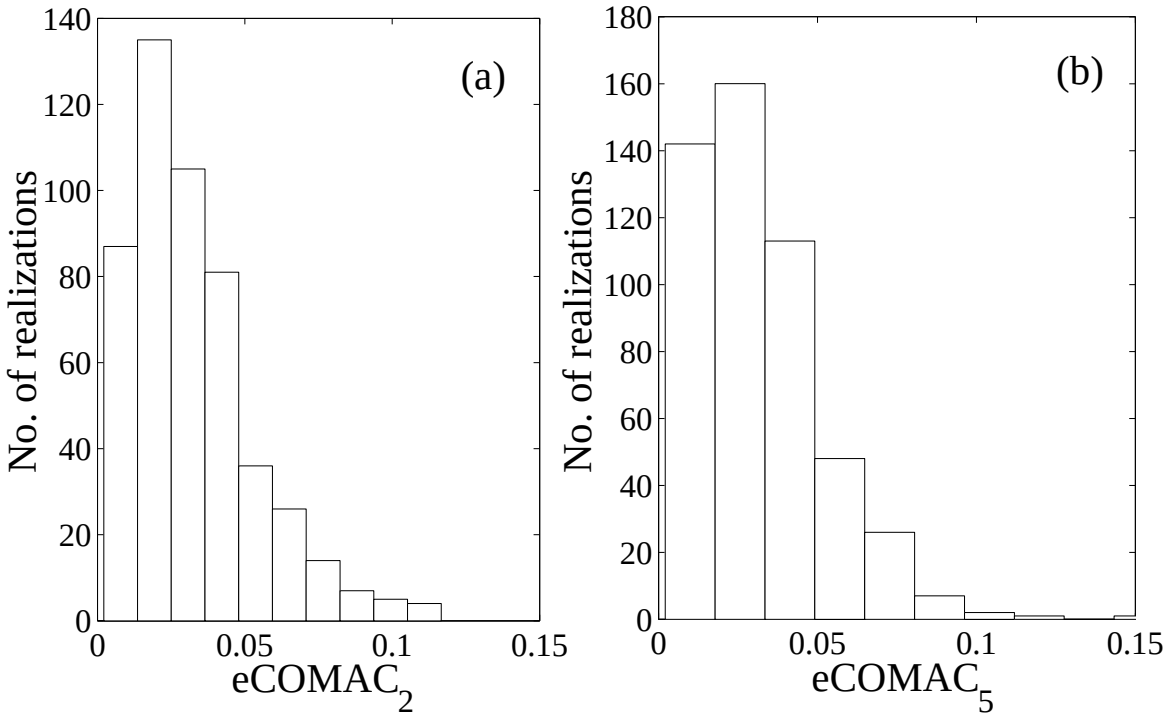

Figure D.5: Distributions obtained for (a) eCOMAC_2 and (b) eCOMAC_5.

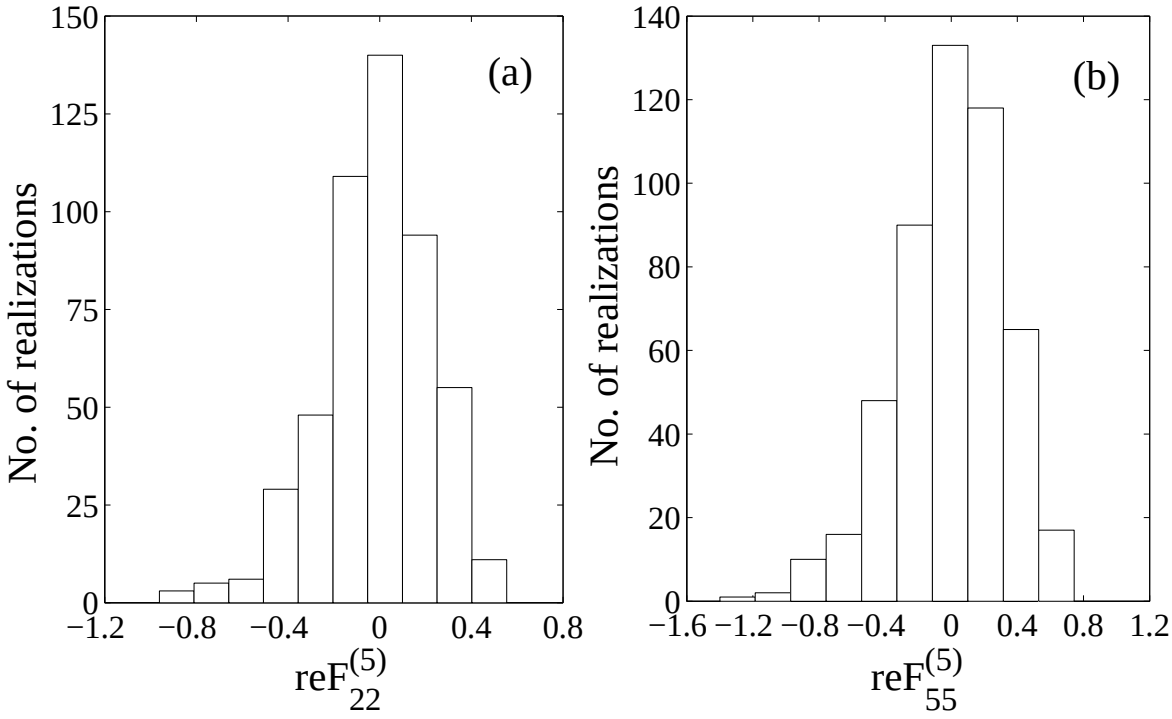

Figure D.6: Distributions obtained for (a) $\text{reF}_{22}^{(5)}$ and (b) $\text{reF}_{55}^{(5)}$.

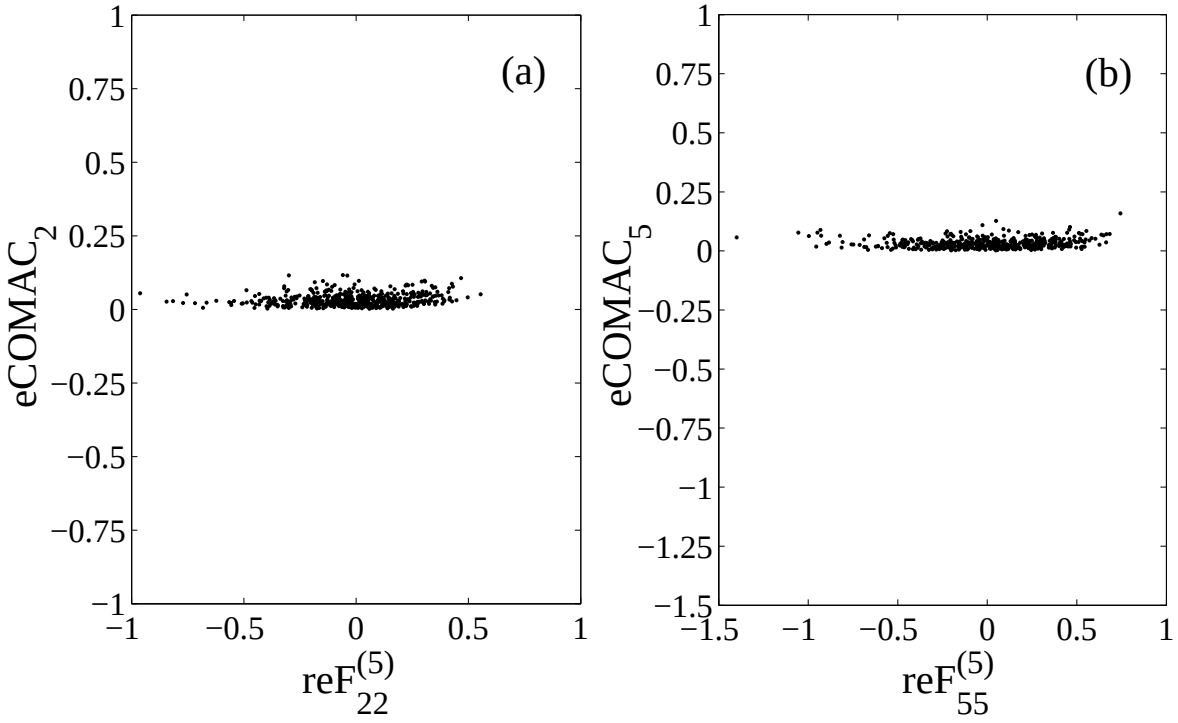

Figure D.7: Comparisons of (a) eCOMAC$_2$ with reF$_{22}^{(5)}$ and (b) eCOMAC$_5$ with reF$_{55}^{(5)}$.

D.4 Complementary Indices

D.4.1 Flexibility Proportional MAC and COMAC

From the preceding sections it is concluded that the error in the estimated flexibility matrix, due to an error in an estimated experimental mode shape, is of a higher order than the error in the MAC value comparing this estimated mode shape with the corresponding "true" mode shape. In this section an attempt is made to develop a criterion complementary to MAC, for comparing an estimated mode shape with its corresponding true mode shape, which at the same time also gives a measure of the error in the flexibility matrix that one can expect when comparing the flexibility matrices obtained using the two different mode shapes. Thus, in essence this section tries to define a mode shape comparison criterion whose deviation from 1 tries to mimic the flexibility error of Eq. (D.21), with the criterion being equal to 1 signifying that the two mode shapes are exactly similar,differing at most by a scalar multiplicative constant. This alternative criterion is named Flexibility Proportional Modal Assurance Criterion (FPMAC).

From an analysis of Eq. (D.21) it can be seen that, to be well correlated with the error in flexibility $\widetilde{\text{ref}}_i$, FPMAC for the ith mode may be of the form

$$\text{FPMAC}_i = 1 - \widetilde{\text{ref}}_i = \frac{\sum_{k=1}^{N} \beta_{i,k}^2}{NS_i} \tag{D.41}$$

Eq. (D.41) involves normalization by S_i, which in turn involves the mass matrix of the system. However the mass matrix may not be known in certain situations, or may have errors introduced from mass matrix reduction [113]. Thus, it may be useful if the normalization through S_i in Eq. (D.41) is replaced by a similar normalization not involving the mass matrix. To this end, normalized analytical and experimental mode shapes, $\mathbf{v}_i^*$ and $\widehat{\mathbf{v}}_i^*$, respectively, are first defined such that these normalized mode shape vectors are of unit length:

$$\mathbf{v}_i^* = \frac{\mathbf{v}_i}{\|\mathbf{v}_i\|} \tag{D.42}$$

$$\widehat{\mathbf{v}}_i^* = \frac{\widehat{\mathbf{v}}_i}{\|\widehat{\mathbf{v}}_i\|} \tag{D.43}$$

where $\|.\|$ denotes the Euclidean norm of the concerned vector argument. $\mathbf{v}_i^*$ and $\widehat{\mathbf{v}}_i^*$ are then related as

$$\widehat{\mathbf{v}}_i^* = \boldsymbol{\beta}_i^* \mathbf{v}_i^* \tag{D.44}$$

where

$$\boldsymbol{\beta}_i^* = \frac{\|\mathbf{v}_i\|}{\|\widehat{\mathbf{v}}_i\|} \boldsymbol{\beta}_i \tag{D.45}$$

Also, from Eq. (D.43) it can be said that

$$(\widehat{\mathbf{v}}_i^*)^T (\widehat{\mathbf{v}}_i^*) = 1 \tag{D.46}$$

Using Eqs. (D.44) and (D.45) in Eq. (D.46), one can obtain the expression

$$(\mathbf{v}_i^*)^T \boldsymbol{\beta}_i^T \boldsymbol{\beta}_i (\mathbf{v}_i^*) = \frac{|\widehat{\mathbf{v}}_i^T \widehat{\mathbf{v}}_i|}{|\mathbf{v}_i^T \mathbf{v}_i|} = \frac{\|\widehat{\mathbf{v}}_i\|^2}{\|\mathbf{v}_i\|^2} \tag{D.47}$$

On comparing Eq. (D.47) with Eq. (D.14) for S_i, it can be realized that the left hand side of Eq. (D.47) may serve as a potential replacement of S_i to be used as the normalization in Eq. (D.41), as both Eq. (D.14) and Eq. (D.47) have the same form. For instance, both Eqs. (D.14) and (D.47) will give the same value of α^2 when the estimated mode shape differs only by a constant multiplicative scalar, α, from the analytical mode shape, and thus all $\beta_{i,k}$ will be equal to the constant α. Similarly,

both will give a value of 1 when the estimated and true mode shapes are exactly the same and are mass normalized, i.e. when all $\beta_{i,k} = 1$. Note that the expression $\|\widehat{\mathbf{v}}_i\|^2/\|\mathbf{v}_i\|^2$ in Eq. (D.47) is exactly equal to S_i if the mass matrix is proportional to the identity matrix; otherwise it is an approximation.[2] The discrepancy introduced by this approximation is examined later in this section. Using this normalization based on Eq. (D.47) in Eq. (D.41) instead of S_i, and remembering that $\beta_{i,k} = \widehat{v}_{k,i}/v_{k,i}$, FPMAC$_i$ be defined as follows:

$$\text{FPMAC}_i = \frac{\|\mathbf{v}_i\|^2}{\|\widehat{\mathbf{v}}_i\|^2} \frac{\sum_{k=1}^{N} (\frac{\widehat{v}_{k,i}}{v_{k,i}})^2}{N} \tag{D.48}$$

The error term, which is defined as the deviation of FPMAC$_i$ from 1 and expressed as,

$$\text{eFPMAC}_i = 1 - \text{FPMAC}_i = 1 - \frac{\sum_{k=1}^{N} \beta_{i,k}^2}{N \frac{\|\widehat{\mathbf{v}}_i\|^2}{\|\mathbf{v}_i\|^2}} \tag{D.49}$$

should then indicate the measure of flexibility matrix error $\widetilde{\text{ref}}_i$ of Eq. (D.21). Fig. D.8 compares eFPMAC$_i$ with $\widetilde{\text{ref}}_i$ for the two cases of (a) first mode, and (b) fourth mode, from the Monte Carlo simulation discussed in the last section. A comparison of Fig. D.8 with Fig. D.4 illustrates that the FPMAC$_i$ values perform appreciably better than MAC$_i$ values, through their respective deviations from 1, in indicating the error that would be incurred in the flexibility matrix, $\widetilde{\text{ref}}_i$, due to an estimation error in the ith mode. In fact as indicated by Fig. D.8, eFPMAC$_i$ almost exactly replicates the error in flexibility $\widetilde{\text{ref}}_i$.

It should be noted that, unlike MAC$_i$, FPMAC$_i$ is not bounded upwards by 1. Since eFPMAC$_i$ tries to mimic $\widetilde{\text{ref}}_i$, and since flexibility error can be both positive and negative, FPMAC$_i$ can take values both greater and lesser than 1. When $\mathbf{v}_i$ and $\widehat{\mathbf{v}}_i$ are exactly the same mode shape and hence all $\beta_{i,k}$ are equal to each other, FPMAC$_i$ takes a value of 1. Also, FPMAC$_i$ cannot be negative since its numerator is a product of a sum of squares with the square of an Euclidean norm, while its denominator is also a product of two positive numbers. This is in line with expectations since if FPMAC$_i$ were to assume a negative value, it would entail that some diagonal terms of the flexibility matrix were to take on negative values, which is physically not possible. This also implies that eFPMAC$_i$ would always be lesser than 1. In order to ensure that FPMAC$_i$ becomes zero when the

[2] I would like to thank Ms. Luciana Balsamo for bringing this issue to my attention.

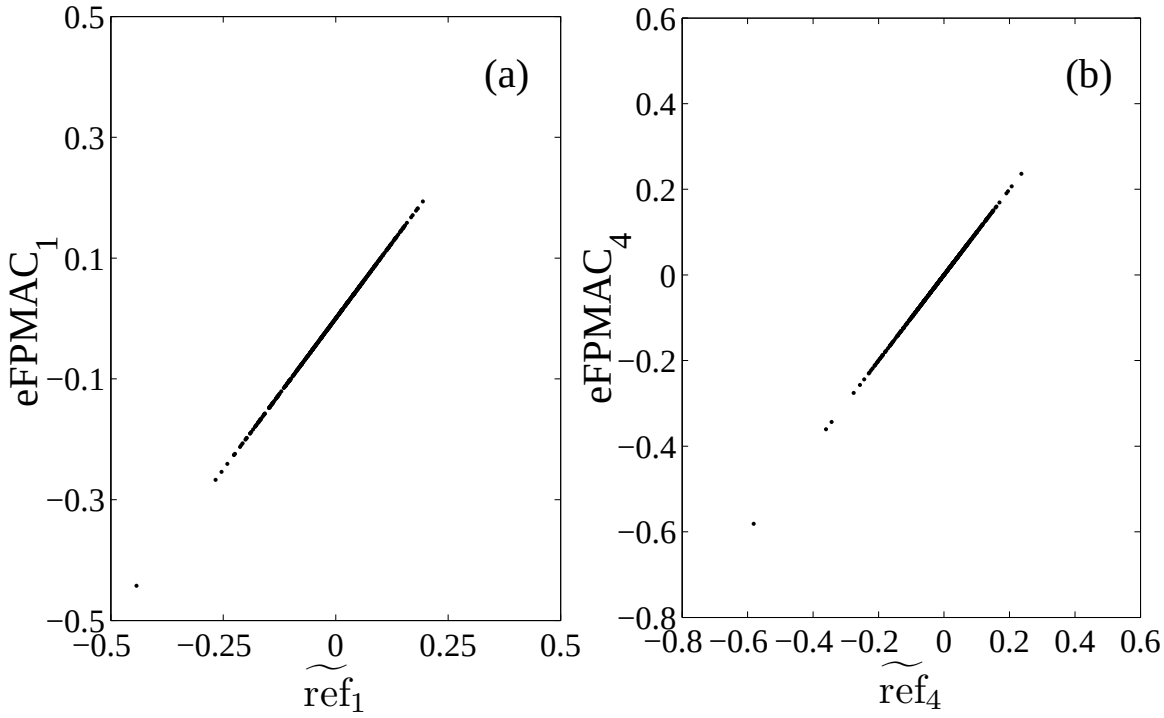

Figure D.8: Comparisons of (a) eFPMAC$_1$ with $\widetilde{\text{ref}}_1$ and (b) eFPMAC$_4$ with $\widetilde{\text{ref}}_4$ (based on the FPMAC$_i$ of Eq. (D.48)).

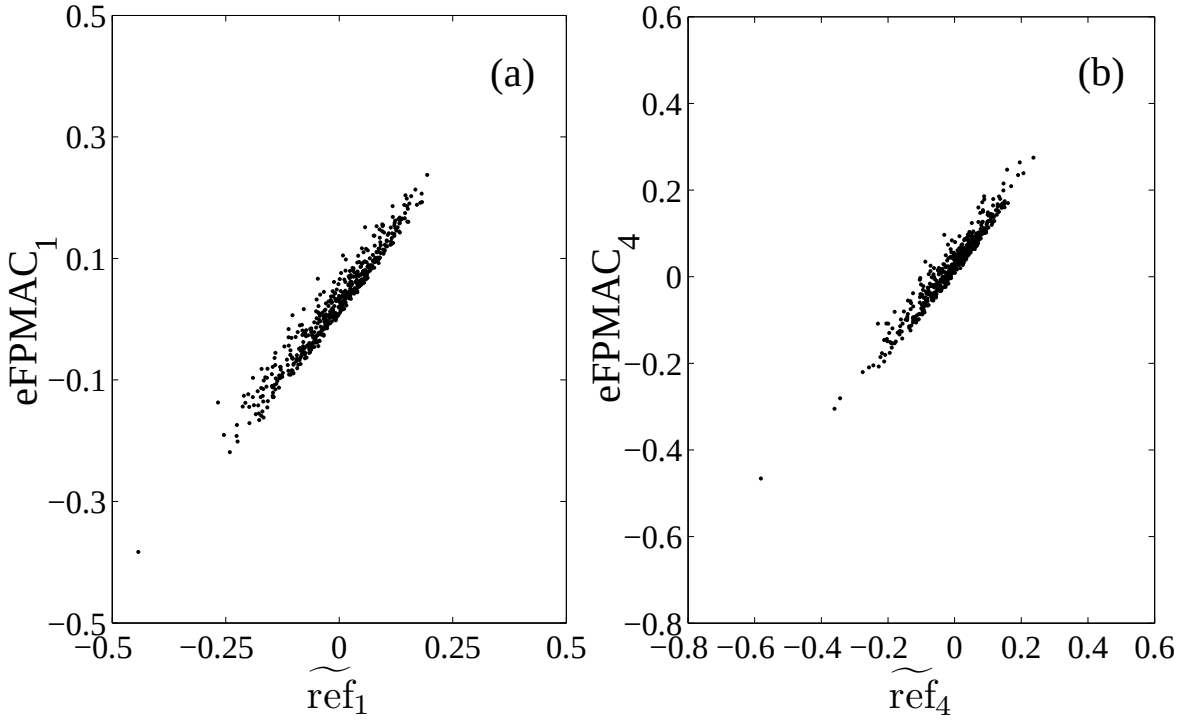

Figure D.9: Comparisons of (a) eFPMAC$_1$ with $\widetilde{\text{ref}}_1$ and (b) eFPMAC$_4$ with $\widetilde{\text{ref}}_4$ (based on the modified FPMAC$_i$ of Eq. (D.50)).

two mode shapes being compared are orthogonal to each other, one can redefine FPMAC$_i$ as the product of the definition in Eq. (D.48) and MAC$_i$, i.e.

$$\text{FPMAC}_i = \left(\frac{\|\mathbf{v}_i\|^2}{\|\widehat{\mathbf{v}}_i\|^2} \frac{\sum_{k=1}^{N} (\frac{\widehat{v}_{k,i}}{v_{k,i}})^2}{N} \right) (\text{MAC}_i) = \frac{|\widehat{\mathbf{v}}_i^T \mathbf{v}_i|^2}{|\widehat{\mathbf{v}}_i^T \widehat{\mathbf{v}}_i|^2} \frac{\sum_{k=1}^{N} (\frac{\widehat{v}_{k,i}}{v_{k,i}})^2}{N} \tag{D.50}$$

As can be seen from Fig. D.9, this definition of FPMAC$_i$ can also be used to estimate $\widetilde{\text{ref}}_i$ from the value of eFPMAC$_i$ almost accurately, although the dispersion in this case is slightly higher than that presented in Fig. D.8.

The definitions of FPMAC$_i$ as per Eqs. (D.48) and (D.50) suffer from a limitation in that if any component of the analytical mode shape $\mathbf{v}_i$ is very close to zero, then the ratio $\widehat{v}_{k,i}/v_{k,i}$ becomes extremely large for that k value, and consequently the FPMAC$_i$ becomes very high, making the eFPMAC$_i$ very high as well. This is a consequence of the objective of obtaining a mode shape comparison criterion whose error reflects the error in the flexibility matrix and the definition of flexibility

error used, which is relative to the true flexibility. The (k,k)th element of the true flexibility matrix estimated from the ith analytical mode shape is approximately zero if $v_{k,i} \approx 0$, and in such cases the error in the (k,k)th element of the estimated flexibility matrix becomes misleadingly large when considered relative to this "close to zero" value. One possible way to overcome this limitation is to drop the $\widehat{v}_{k,i}/v_{k,i}$ term for which $v_{k,i} \approx 0$ in the expression for FPMAC$_i$. This seems a reasonable approach in the sense that $v_{k,i} \approx 0$ does not contribute anything to the (k,k)th element of the true flexibility matrix, and so calculation of the error including the corresponding $\widehat{v}_{k,i}/v_{k,i}$ is not meaningful to begin with. In following this approach, the eFPMAC$_i$ will give a measure of $\widetilde{\text{ref}}_i$ involving all the degrees of freedom except for the one for which $v_{k,i} \approx 0$.

Just as eMAC$_i$ is of a lower order than $\widetilde{\text{ref}}_i$, the preceding sections also show that the error in any (k,k)th element of the estimated flexibility matrix from a set of N_m estimated modes, due to errors in the N_m estimated mode shapes, is of a higher order than the error in the COMAC value comparing these N_m estimated mode shapes with the corresponding true mode shapes at the kth DOF. Here it is now attempted to develop a criterion complementary to COMAC, hereonwards referred to as Flexibility Proportional Coordinate Modal Assurance Criterion, or FPCOMAC$_k$, whose deviation from 1 gives a measure of the error in the (k,k)th element of the estimated flexibility matrix constructed using the N_m mode shapes. In order that the deviation of FPCOMAC$_k$ from 1 mimics the flexibility error of Eq. (D.36), FPCOMAC$_k$ may be expected to be of the form:

$$\text{FPCOMAC}_k = \frac{\sum_{i=1}^{N_m} \frac{\beta_{i,k}^2 v_{k,i}^2}{S_i \widehat{\lambda}_i}}{\sum_{i=1}^{N_m} \frac{v_{k,i}^2}{\lambda_i}} \tag{D.51}$$

It can be seen that, as in case of Eq. (D.41), Eq. (D.51) too depends on the mass scaling factors S_i, and thus on the mass distribution of the system. Following the same procedure as for FPMAC$_i$, the S_i of Eq. (D.51) is replaced with the left hand side of Eq. (D.47), to define FPCOMAC$_k$ as

$$\text{FPCOMAC}_k = \frac{\sum_{i=1}^{N_m} \frac{\|\mathbf{v}_i\|^2}{\|\widehat{\mathbf{v}}_i\|^2} \frac{\beta_{i,k}^2 v_{k,i}^2}{\widehat{\lambda}_i}}{\sum_{i=1}^{N_m} \frac{v_{k,i}^2}{\lambda_i}} = \frac{\sum_{i=1}^{N_m} \frac{\|\mathbf{v}_i\|^2}{\|\widehat{\mathbf{v}}_i\|^2} \frac{\widehat{v}_{k,i}^2}{\widehat{\lambda}_i}}{\sum_{i=1}^{N_m} \frac{v_{k,i}^2}{\lambda_i}} \tag{D.52}$$

For the FPCOMAC$_k$ of Eq. (D.52) to meet this study's objective, the error defined as the deviation of

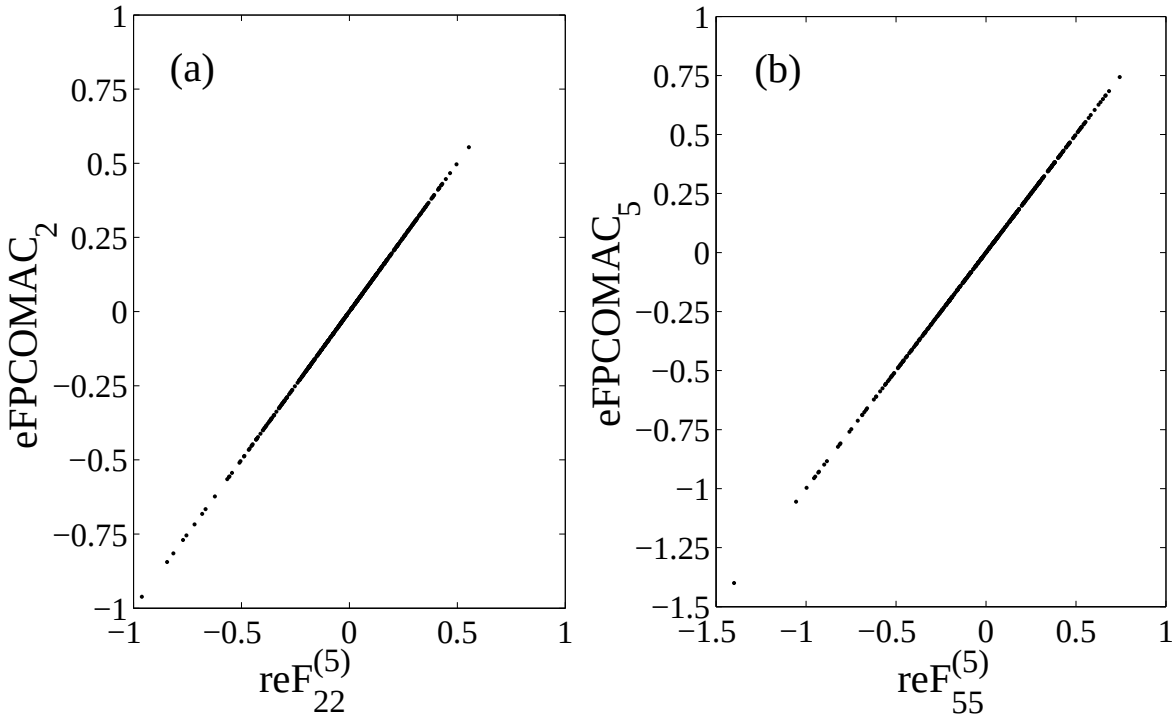

Figure D.10: Comparison of (a) eFPCOMAC$_2$ with reF$^{(5)}_{22}$ and (b) eFPCOMAC$_5$ with reF$^{(5)}_{55}$ for the 500 realizations.

FPCOMAC$_k$ from 1 as

$$\text{eFPCOMAC}_k = 1 - \text{FPCOMAC}_k = 1 - \frac{\sum_{i=1}^{N_m} \frac{\|\mathbf{v}_i\|^2}{\|\hat{\mathbf{v}}_i\|^2} \frac{\beta_{i,k}^2 v_{k,i}^2}{\widetilde{\lambda}_i}}{\sum_{i=1}^{N_m} \frac{v_{k,i}^2}{\lambda_i}} \tag{D.53}$$

should reflect the measure of the error in the (k,k)th element of the estimated flexibility matrix, reF$^{(N_m)}_{kk}$, as defined by Eq. (D.36). Fig. D.10 illustrates the comparison of eFPCOMAC$_k$ with reF$^{(N_m)}_{kk}$, with $N_m = 5$ (using the first 5 modes), for the two cases of (a) second DOF, and (b) fifth DOF of the 8 DOF shear–type system from the Monte Carlo simulations described in the last section. On comparing Fig. D.10 with Fig. D.7, it is observed that eFPCOMAC$_k$ is a much better indicator than eCOMAC$_k$ of the error in the flexibility matrix due to an estimation error in the N_m estimated modes. In fact, eFPCOMAC$_k$ almost accurately replicates reF$^{(N_m)}_{kk}$.

Just like FPMAC$_i$, FPCOMAC$_k$ is also not bounded upwards by 1 as eFPCOMAC$_k$ tries to mimic the reF$^{(N_m)}_{kk}$, which can be both positive and negative, thus making FPCOMAC$_k$ also capa-

ble of assuming values both greater than as well as less than 1. When all $\widehat{\mathbf{v}}_i$ differ from the corresponding $\mathbf{v}_i$ only by constant multiplicative scalars, FPCOMAC$_k$ takes a value of 1. It should be noted that for COMAC$_k$ to be equal to 1 it is necessary that all these constant multiplicative scalars differentiating $\mathbf{v}_i$ from $\widehat{\mathbf{v}}_i$ be equal to each other. Also, based on reasons similar to those put forth for FPMAC$_i$, FPCOMAC$_k$ cannot be negative, i.e. eFPCOMAC$_k$ would always be lesser than 1 (the case of eFPCOMAC$_k = 1$ will indicate inifinte rigidity, a practically unlikely possibility). FPCOMAC$_k$ is less likely to become zero when compared with FPMAC$_i$ since this would require all the N_m estimated modes to have a node at the same kth DOF. Furthermore, by virtue of its definition, FPCOMAC$_k$ is not affected to any significant extent if any one/some of the N_m true mode shapes has a zero component at the kth DOF.

D.4.2 Effect of non-uniform mass distribution

As stated before, S_i of Eq. (D.14) is exactly equal to $\|\widehat{\mathbf{v}}_i\|^2/\|\mathbf{v}_i\|^2$ of Eq. (D.47) if the mass matrix is proportional to the identity matrix. In general, using this normalization from Eq. (D.47) to replace S_i is an assumption. To see how this assumption affects the computed eFPMAC's and eFPCOMAC's, we consider a similar 8-DOF system as used before (Section E.3), but with the lumped masses: $\{m_1, m_2, \cdots, m_8\} = \{5000, 3500, 3000, 4000, 2500, 4500, 2000, 1500\}$ kg. As in Section E.3, 500 sets of estimated mode shapes are computed by perturbing the true mode shapes with random realizations of $\beta_{i,k}$ from a normal distribution with unit mean and $\sigma = 0.2$ (Eq. (D.1)). In the computations of FPCOMAC and reF$_{kk}^{(N_m)}$ it is again assumed that only the first 5 modes are available. Figs. D.11 and D.12 respectively compare the resulting (a) eFPMAC$_i$ with $\widetilde{\text{ref}}_i$ for all the modes, and (b) eFPCOMAC$_k$ with reF$_{kk}^{(N_m)}$ at all the DOFs. These figures also show the correlation coefficients (ratio of covariance to product of standard deviations) between the computed eFPMAC$_i$'s and $\widetilde{\text{ref}}_i$'s, and eFPCOMAC$_k$'s and reF$_{kk}^{(5)}$'s, for all the modes and DOFs. From these figures and correlation coefficients, it is evident that using the normalization of Eq. (D.47) for a system with non-uniform mass distribuition does not introduce any serious discrepancy in the computed eFPCOMAC$_k$'s, i.e. the eFPCOMAC$_k$'s still mimic the corresponding reF$_{kk}^{(5)}$'s with reasonably high accuracy. This is also true for the computed eFPMAC$_i$'s corresponding to the higher frequency modes; albeit for low frequency modes the eFPMAC$_i$'s do not strictly mimic the corresponding $\widetilde{\text{ref}}_i$'s, they still show moderate to high positive correlations. While the above example considered a case of moderate (rea-

sonable) non-uniformity in the mass distribution, we also consider two cases of extreme localized mass differences by repeating the above example with: (a) $m_1 = 50000$ kg and $m_8 = 15000$ kg, and (b) $m_1 = 50000$ kg, $m_4 = 40000$ kg and $m_8 = 15000$ kg. In the first case, the correlation coefficients between the eFPMAC$_i$'s and $\widetilde{\text{ref}}_i$'s are $\{0.66, 0.76, 0.69, 0.95, 0.99, 0.98, 0.95, 0.97\}$ for modes 1 to 8, while the correlation coefficients between the eFPCOMAC$_k$'s and reF$_{kk}^{(5)}$'s are $\{0.81, 0.94, 0.94, 0.95, 0.96, 0.93, 0.96, 0.97\}$ at DOFs 1 to 8; in the second case, the correlation coefficients between the eFPMAC$_i$'s and $\widetilde{\text{ref}}_i$'s are $\{0.40, 0.69, 0.92, 0.96, 0.99, 1.00, 1.00, 0.98\}$, while those between the eFPCOMAC$_k$'s and reF$_{kk}^{(5)}$'s are $\{0.93, 0.94, 0.94, 0.93, 0.94, 0.94, 0.95, 0.88\}$. Evidently, even in these extreme cases, there are strong positive correlations between the corresponding eFPCOMAC$_k$'s and reF$_{kk}^{(5)}$'s at all DOFs, while the eFPMAC$_i$'s and $\widetilde{\text{ref}}_i$'s are strongly positively correlated at higher modes, and show moderate positive correlations in the low frequency modes. The strong correlations between the corresponding eFPCOMAC$_k$'s and reF$_{kk}^{(m)}$'s, even with $N_m \leq N$ available modes, and even when the uniform mass distribution assumption, made by replacing S_i with $\|\widehat{\mathbf{v}}_i\|^2/\|\mathbf{v}_i\|^2$, is violated, suggest the possible use of eFPCOMAC as a damage sensitive feature in structural health monitoring, with structural damage represented as localized increase in flexibility.

D.4.3 An example with a 2-D Pratt truss

As a final example, we consider the 12-DOF Pratt truss of Fig. D.13; the properties of the truss elements, and the DOFs (numbered arrows), are also shown in the figure. It is assumed to be an ideal truss, i.e. all members are two-force members, only subjected to axial stresses. In order to obtain a reasonable fundamental frequency, additional lumped masses, as listed in Fig. D.13, are added to the top and bottom chord nodes; these lumped masses may be seen as the weight of the deck and deck girders (for the bottom chord), and the weight of the roof truss (for the top chord). The mass matrix is constructed by adding these lumped masses to the FE consistent mass matrix; the fundamental frequencies with and without these lumped masses are respectively 6.22 Hz and 14.84 Hz. Note that the addition of the lumped masses make $\mathbf{M}$ diagonally dominant, although not strictly diagonal; it also makes the mass distribution non-uniform, with the lumped masses at the bottom nodes being 10 times those at the top nodes.

As before, after obtaining the analytical frequencies and mode shapes of the system, the estimated mode shapes are obtained by perturbing the analytical ones using Eq. (D.1), for 500 sets of random

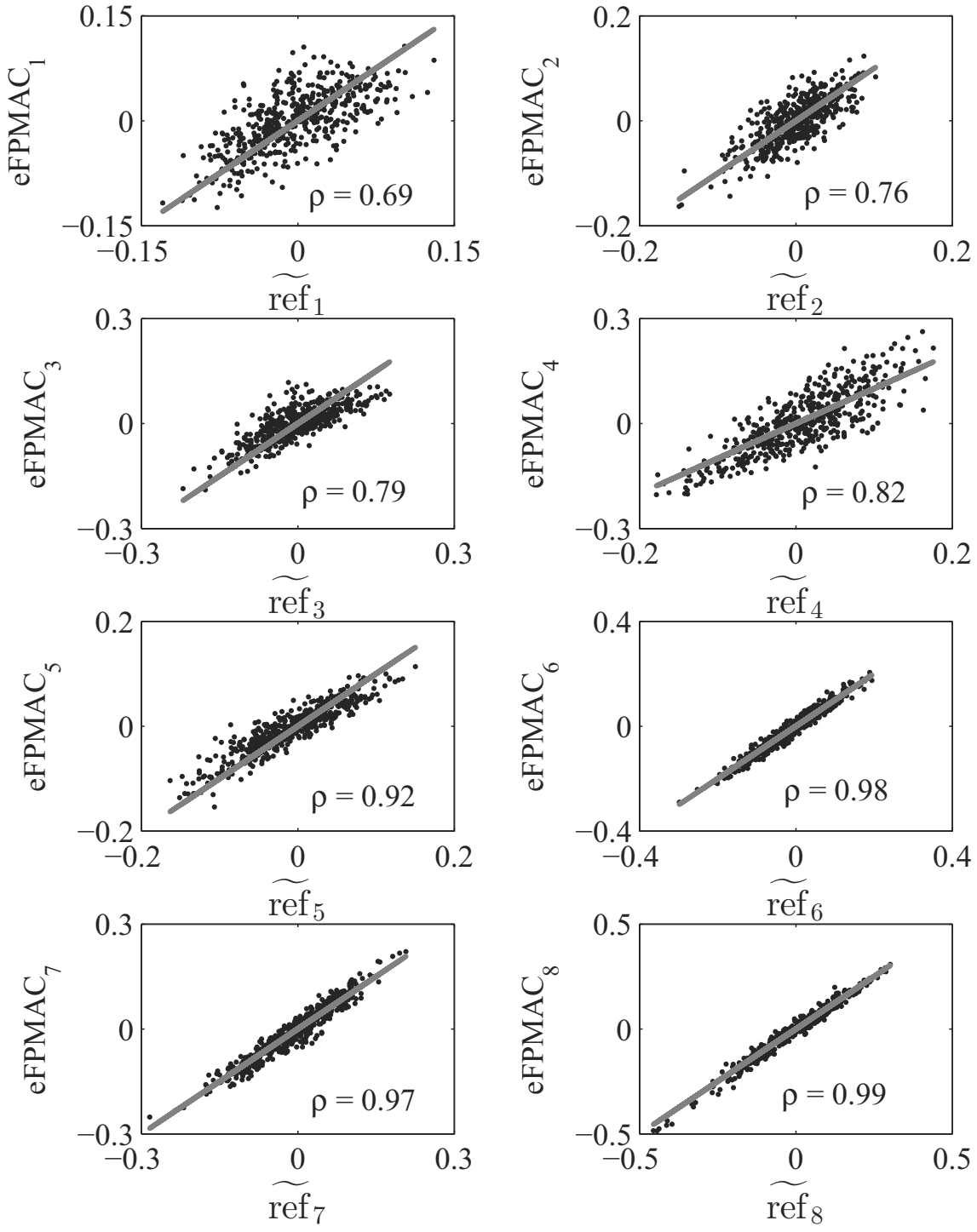

Figure D.11: Comparison of eFPMAC$_i$ with $\widetilde{\text{ref}}_i$ for the 500 realizations (dots), for all the modes (based on the FPMAC$_i$ of Eq. (D.48)). The line is the 45^0 line. Also shown are the correlation coefficients (ρ) between the computed eFPMAC$_i$'s and $\widetilde{\text{ref}}_i$'s.

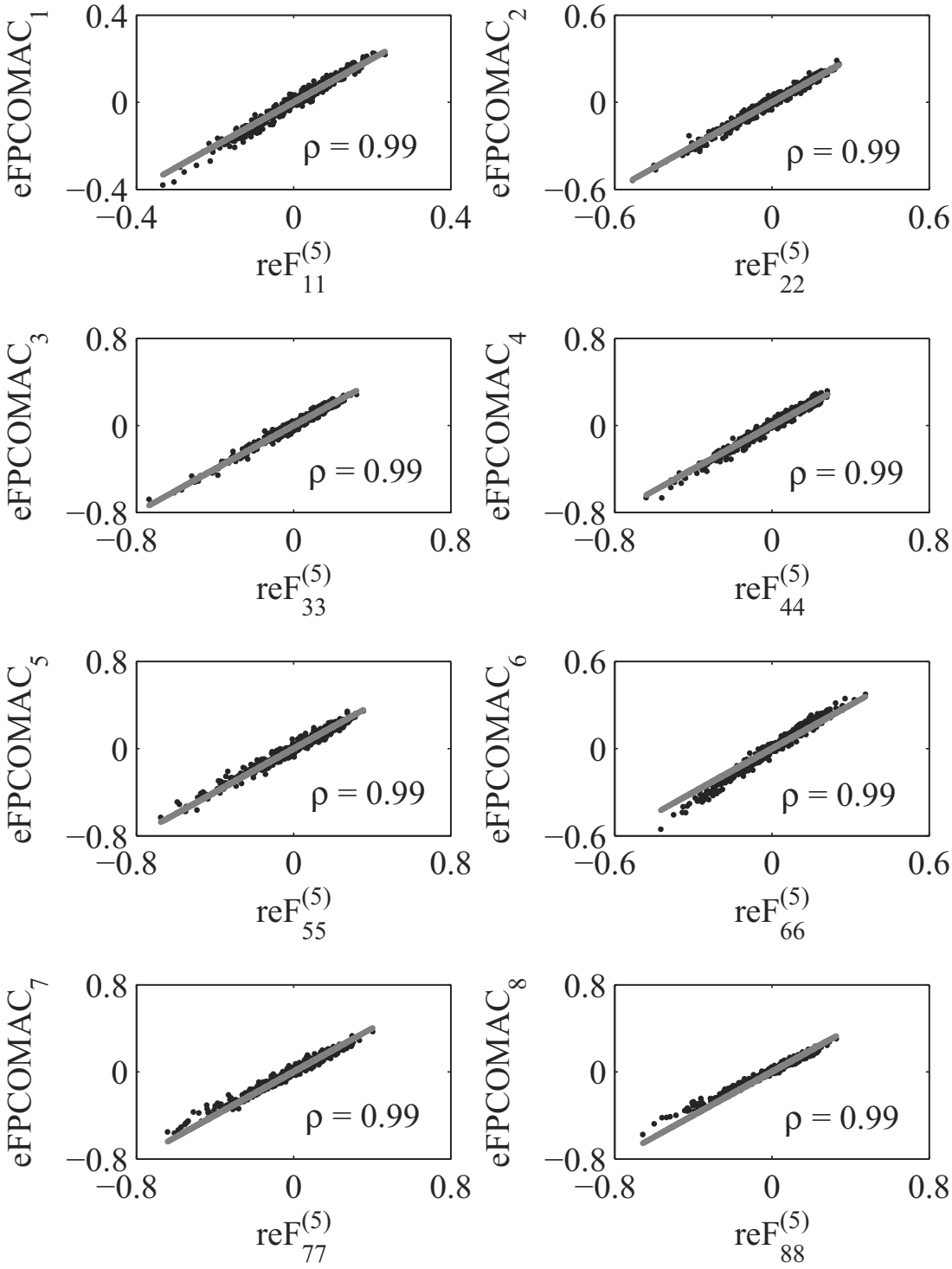

Figure D.12: Comparison of eFPCOMAC$_k$ with reF$^{(5)}_{kk}$ for the 500 realizations (dots), at all the DOFs. The line is the 45^0 line. Also shown are the correlation coefficients (ρ) between the computed eFPCOMAC$_k$'s and reF$^{(5)}_{kk}$'s.

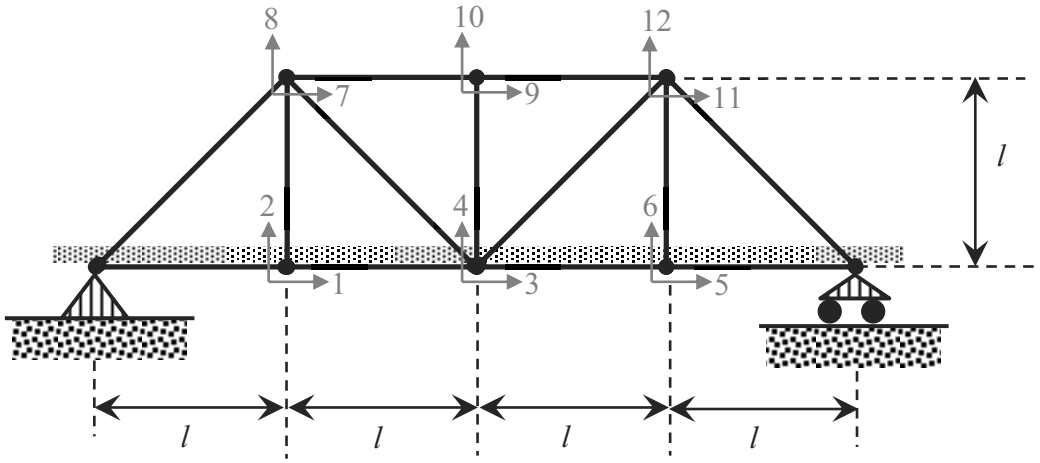

E (Young's modulus, all members)	2×10^{11} N/m^2
ϱ (mass density, all members)	8×10^3 kg/m^3
A (c/s area, all members)	25×10^{-4} m^2
l (length, horizontal and vertical members)	10 m
m_b (additional lumped mass, bottom nodes)	3000 kg
m_t (additional lumped mass, top nodes)	300 kg

Figure D.13: The 2-D Pratt truss used in the numerical example.

realizations of $\beta_{i,k}$ ($\forall\ i,k = 1, 2, \cdots, 12$) from a normal distribution with unit mean and $\sigma = 0.2$. In the computations of FPCOMAC and reF$_{kk}^{(N_m)}$, it is assumed that only 4 modes, viz. the modes 1, 2, 4 and 5, are available from the experimental data. Figs. D.14 and D.15 respectively compare the thus computed (a) eFPMAC$_i$ with $\widetilde{\text{ref}}_i$ for all the 12 modes, and (b) eFPCOMAC$_k$ with reF$_{kk}^{(4)}$ at all the 12 DOFs, and also show the corresponding correlation coefficients. Fig. D.16 shows a similar comparison, but using eMAC/eCOMAC instead of eFPMAC/eFPCOMAC, for 3 of the modes and 3 of the DOFs; the comparisons for the other modes and DOFs are similar. From these figures, it is evident that the results for the Pratt truss example corroborate the different analytical discussions, and the observations from the 8-DOF shear–type system examples, made earlier. (Note: in the case without the additional lumped masses, the correlation coefficients between the proposed indices and the corresponding flexibility errors are much stronger, viz. 1.00 between the eFPCOMAC$_k$'s and reF$_{kk}^{(4)}$'s at all the DOFs, and from 0.87 to 1.00 between the eFPMAC$_i$'s and $\widetilde{\text{ref}}_i$'s for the different modes.)

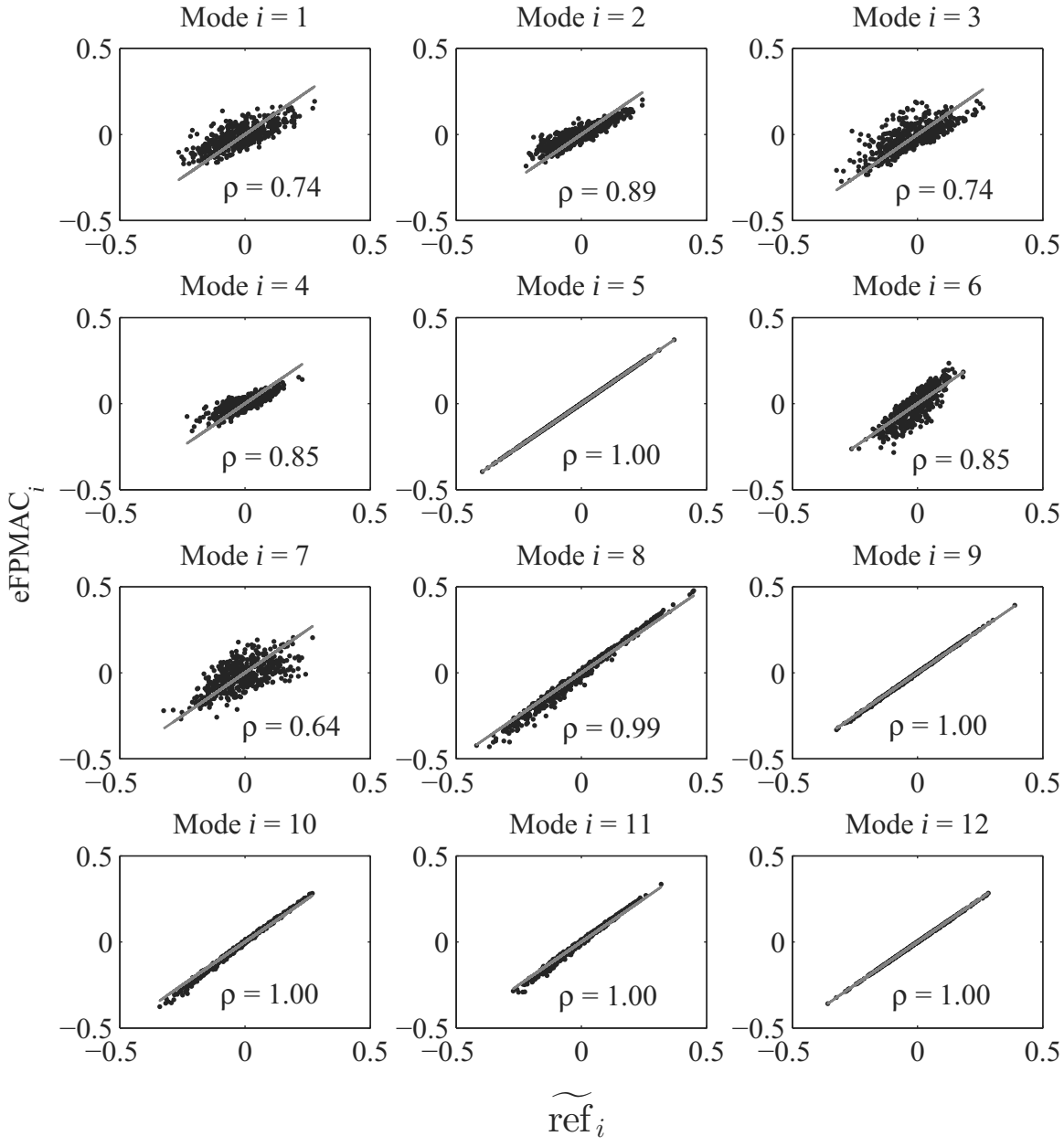

Figure D.14: Comparison of eFPMAC$_i$ with $\widetilde{\text{ref}}_i$ for the 500 realizations (dots), for all the modes of the example Pratt truss (using FPMAC$_i$ of Eq. (D.48)). The line is the 45^0 line. Also shown are the correlation coefficients (ρ) between the computed eFPMAC$_i$'s and $\widetilde{\text{ref}}_i$'s.

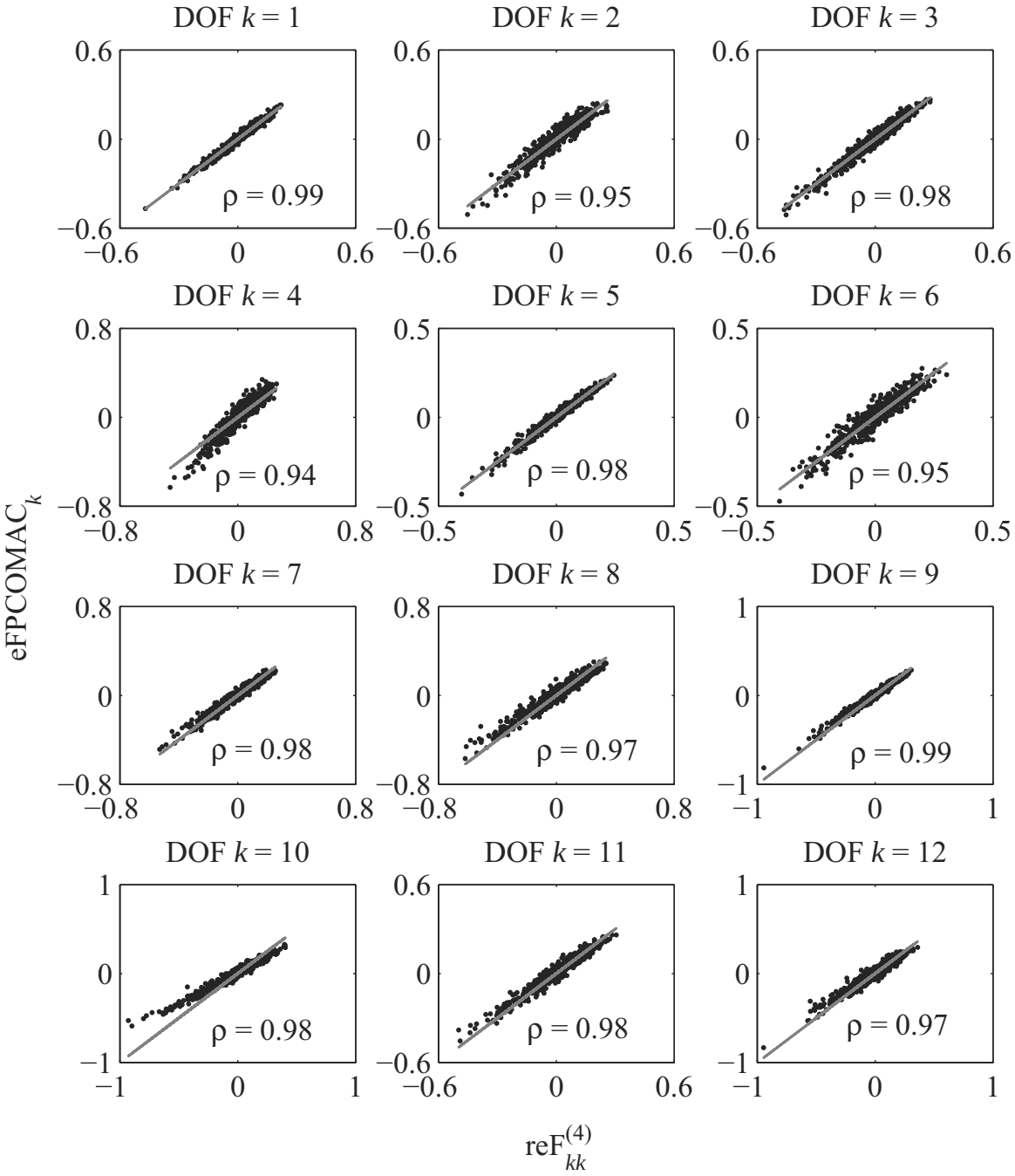

Figure D.15: Comparison of eFPCOMAC$_k$ with reF$^{(4)}_{kk}$ for the 500 realizations (dots), at all the DOFs of the example Pratt truss. The line is the 45^0 line. Also shown are the correlation coefficients (ρ) between the computed eFPCOMAC$_k$'s and reF$^{(5)}_{kk}$'s.

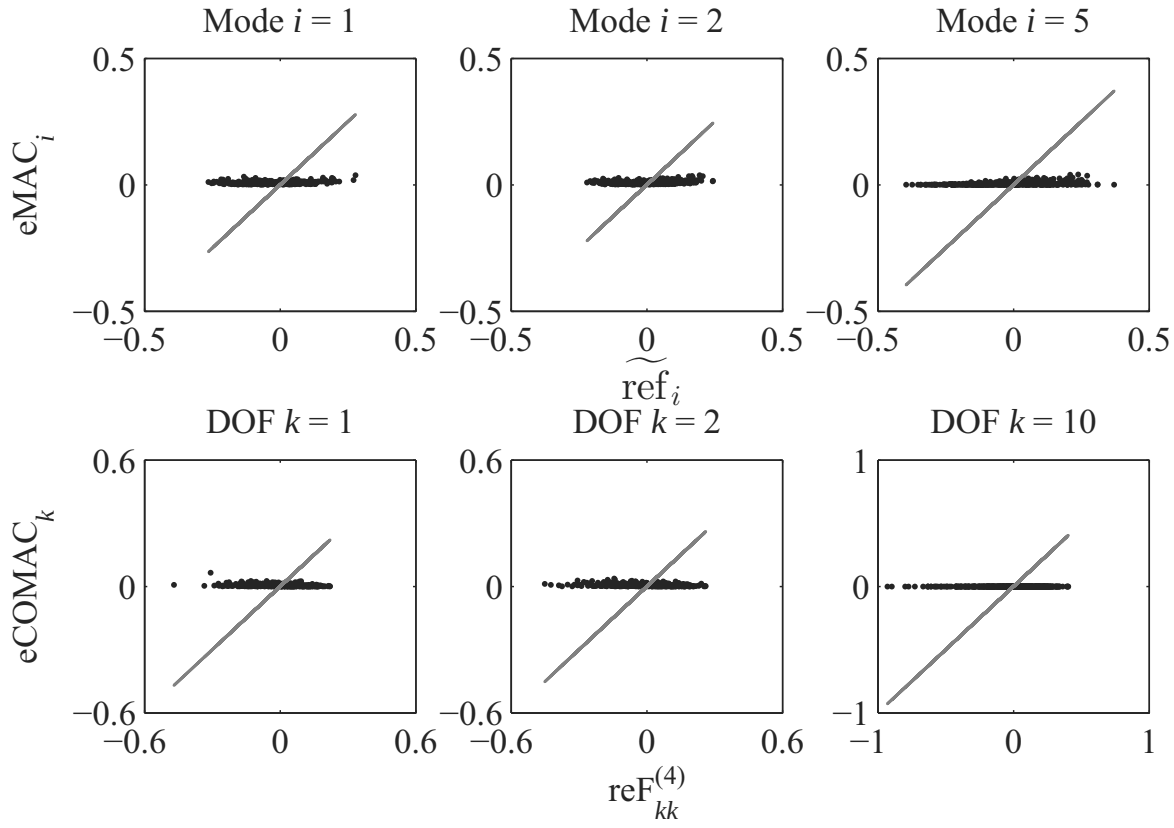

Figure D.16: Comparison of eMAC$_i$ with $\widetilde{\text{ref}}_i$ for modes $i = 1$, 2 and 5, and eFPCOMAC$_k$ with reF$^{(4)}_{kk}$ at DOFs $k = 1$, 2 and 10, for the Pratt truss example, based on the 500 realizations (dots). The line is the 45^0 line.

D.5 Conclusions

This study is an attempt to analyze how "errors" in the estimated mode shapes of linear classically damped systems propagate to the structural flexibility matrix and to quantify how these errors are reflected in the MAC and COMAC values obtained by comparing the estimated mode shapes with the corresponding exact (analytical) ones. The analyses are undertaken in a probabilistic framework wherein multiplicative errors in each component of each mode shape are treated as random variables. Both analytical derivations and Monte Carlo simulations are employed to show that, in terms of the variances, the orders of the errors in MAC and COMAC are lower than the orders of the corresponding errors in the structural flexibility matrix. This discrepancy leads to significant inconsistencies between the results obtained from comparison of identified mode shapes and the results for the structural flexibility matrix obtained using these estimated mode shapes: the general trend is that the flexibility terms are in more significant error even when the identified mode shapes correlate well, in the MAC/COMAC sense, with the analytical ones. To overcome this inconsistency, two criteria to complement MAC and COMAC, namely FPMAC and FPCOMAC, are proposed. These new criteria may be used for direct comparison of mode shapes, and they attempt to mimic the expected flexibility error that will be observed due to the mismatch of the estimated and the "true" mode shapes. Through numerical simulations it is shown that these criteria perform with reasonable accuracy in predicting the error in the flexibility matrix. Applying these complementary indices in model updating problems, possibly integrated with the traditional MAC/COMAC/frequency change based objective functions, define a direction of future research.

Since these new indices relate directly to changes in the flexibility matrix, it is expected that these indices may be used for damage detection purposes, where the damage is characterized by localized increase in flexibility. This is especially true for FPCOMAC, whose deviation from 1, based on the numerical examples, is shown to bear a strong positive correlation with changes in the elements of the structural flexibility matrix; both FPCOMAC and the flexibility matrix are constructed using only a reduced set of modes, and are affected by modal truncation to the same extent. While the FPMAC values, being particular to modes, may be used to detect if the structure has suffered any damage, the FPCOMAC values, being particular to structural DOFs, may even possibly be used to identify the most likely damage location(s)/damaged element(s). Moreover, while FPMAC includes only the effect of mode shape changes, FPCOMAC additionally includes also the effect of frequency

changes. In Chapter 5 of this thesis, and also within a statistical pattern recognition framework in [23], some preliminary damage detection applications using these indices have shown reasonable success. Further applications and comparisons with other popular modal parameter based damage detection methods (e.g. [72, 101, 102, 114, 115]) are however necessary, and defines another potential direction of future research.